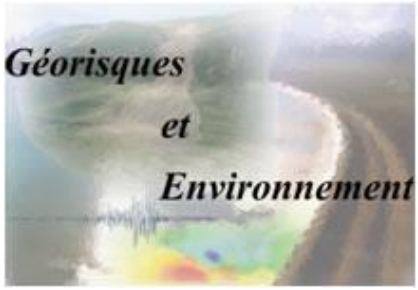

Université de Liège
Departement de Géologie
Géorisques et Environnement

Assessment of landslide hazard in the environmental hotspot areas of the Kyrgyz Tien-Shan:

Spatial analysis and Numeric modelling

A thesis submitted for the degree of
Doctor of Sciences

presented by
Torgoev Almazbek

December 2016

Acknowledgement

I use this nice moment to restore in my mind the whole story of my PhD research. By looking back I understand that this professional milestone would not be possible without support of other people. The most valuable and most important input comes from the promoter Prof. Havenith Hans-Balder. Without his help regarding both scientific and practical issues, the completion of this thesis would definitely not have been possible. There were several periods in my research when I did not believe that I could reach the end. In these moments the support of Hans was decisive and, obviously, not in vain. I would like to thank him for this as well as for all funny and nice moments of my research, such as the field trip to Gobi desert, the happy-end affair with the Chinese intelligence service, the banana trees in Burundi, the geophysical survey in the Eifel forest, the beer parties in Belgium and many other events all around the world.

I would also like to outline that during my numerous stays in Belgium I was kindly hosted in the house of Hans. Therefore, I would also like to express my deepest gratitude to his whole family, including his mother and relatives. Special thanks go to Hans' wife, Verena, who always gave me a warm welcome during my stays in their house in Raeren.

The other sincere thanks of mine are directed to Kyrgyzstan. I would like to express my deepest gratitude to SEC "Geopribor" with special thanks to Isakbek Torgoev and Yury Alishin. The results of their 25-year research in Kyrgyzstan formed a sound background for my PhD studies. The biggest portion of the input data and baseline information of my thesis originates from their field studies in Mailuu-Suu and Minkush target areas.

I would also like to mention the INTAS project which was a "seed" further grown into the fully-developed "tree" of my PhD thesis. In respect to that I am very grateful to Prof. Dr. Schneider, J. (BOKU University, Vienna, Austria), Prof. Dr. Casagli, N. (Università degli Studi di Firenze, Florence, Italy) and Prof. Dr. Guzzetti, F. (CNR IRPI, Perugia, Italy). I am also very thankful to numerous colleagues from these scientific organisations who have helped me during my INTAS fellowship. A special thank is also directed to Prof. Dr. Beier, G. (WHZ, Zwickau, Germany) who has certain input in the success of my research. Additionally, I would like to thank the NATO SfP LADATASHA project for a scientific and financial support of my research.

Finally, I would like to thank my close family and my wife Saniya for the hot support along the track. Their strong belief in the success of my research was always an additional impetus and "light in the tunnel" which brought me to the desired destination. A special gratitude is expressed to my mother Roza, as she has a personal input in this milestone due to the time and efforts she spent in past. I dedicate this work to my children wishing that they climb the higher summits in their life than I have done.

Благодарность

Я хочу использовать этот прекрасный момент, чтобы вспомнить всю историю этого личного проекта. Обарачиваясь назад, я понимаю, что это профессиональное достижение было бы невозможным без помощи других людей. Самый значимый вклад и самая важная поддержка была оказана моим руководителем Проф. Др. Хавеницем Хансом-Балдерем. Эта диссертация определенно не увидела бы свет без его всесторонней помощи, как в отношении научных аспектов, так и с практической точки зрения. На протяжении моей работы было несколько критических моментов, когда я уже не верил в успешное завершение моих начинаний. В такие моменты Ханс оказывал решающую поддержку, которая, очевидно, не была напрасной. Вместе с этим, я хотел бы поблагодарить его за все прекрасные, местами смешные, моменты моей исследовательской работы, такие как полевые работы в пустыне Гоби, история с китайской секретной службой (со счастливой концовкой), банановые плантации в Бурунди, геофизические исследования в Айфеле, веселые вечеринки в Бельгии и т.д.

Хотелось бы особо подчеркнуть, что во время моих многочисленных визитов в Бельгию я пользовался великодушным гостеприимством Ханса. В связи с этим, я также хочу поблагодарить его мать, а также родственников его жены. Я особенно благодарен Верене, которая была очень доброжелательна и терпелива ко мне во время моего проживания в их доме в Ранене.

Также хотелось бы передать искреннюю благодарность в Кыргызстан. Большое спасибо НИЦ «Геоприбор», а также лично Исакбеку Торгоеву и Юрию Алешину. Результаты их 25-летних исследований в Кыргызстане послужили твердой основой для написания моей диссертации. Значительная часть вводных данных и сопутствующей информации берет свое начало из их полевых работ в Майлуу-Суу и Мин-Куше.

Хотелось бы особо отметить проект ИНТАС, который послужил в качестве «зерна» из которого впоследствии выросло «дерево» моей кандидатской диссертации. В связи с этим я выражаю свою признательность Проф. Др. Шнайдеру Ж. (Университет BOKU, г. Вена, Австрия), Проф. Др. Касагли Н. (Università degli Studi di Firenze, г. Флоренция, Италия) и Проф. Др. Гуззетти Ф. (CNR IRPI, г. Перуджа, Италия). Я также очень благодарен тем сотрудникам вышеобозначенных огранизаций, которые помогли мне в ислледования в рамках ИНТАС проекта. Также хотел выразить особую признательность Проф. Др. Баеру Г. (WHZ, г. Цвиккау, Германия), который внес определенный вклад в успех моих исследований. В дополнение к вышесказанному, я хочу поблагодарить проект NATO SfP LADATASHA за помощь моим исследованиям, как в финансовом отношении так и научном плане.

В заключении, хотел бы поблагодарить мою семью и супругу Санию за их горячую поддержку. Их несгибаемая вера в успех всегда была дополнительным импульсом и «светом в конце туннелля», которые вели меня к желаемой цели. Отдельное спасибо моей маме Розе, так ее усилия и время, потраченные на меня в прошлом, обеспечили вклад в успех данного проекта. Эту работу я посвящаю своим детям с пожеланием того, чтобы они покорили более высокие вершины, чем это сделал я.

Abstract

This PhD research was initiated in parallel with the Nato Science for Peace project "Prevention of Landslide Dam Disasters in the Tien Shan, Kyrgyz Republic". During this project a large amount of thematic data on slope instabilities and landslide dams in the Kyrgyz Tien-Shan was collected. The thesis uses this information to investigate applied and fundamental aspects of the regional mapping of the landslide susceptibility, hazard and, partially, risk. The target areas selected for the PhD research are the Mailuu-Suu River Valley (southern Kyrgyzstan) and the surroundings of the Minkush settlement (central Kyrgyzstan). They represent the areas of former uranium mining hosting numerous storage sites of tailing material and waste rock. Additionally, these areas are characterised by a high level of landslide activity induced by the human and environmental impacts. The landslides in those areas present a high risk to the society and infrastructure, potentially triggering serious environmental consequences.

Structurally, the thesis is composed of two parts: Part A and Part B. These parts are different both with respect to the research methodology and the scientific targets. The common goal of both parts is the development effective techniques to regionally assess landslide hazard in mountainous areas marked by complex geomorphological, tectonic and geological settings. Due to the remote access, such areas are often lacking background information and in-situ data that are required for the precise prediction of landslide occurrence and impacts. In such cases the spatial analysis often helps to better characterise regional and, partly, local landslide susceptibility. The regional studies allow us to outline the basic relationships between affecting factors and landslide occurrence. Such results also become the basis for effective planning of in-situ investigations and localised measurements.

Part A of thesis is focused on the applied aspects of spatial analysis. This part assembles a set of the well-established approaches and methods to model landslide susceptibility, hazard and risk. The studies start with the compilation of database spatially combining various thematic information. The first type of such thematic data is represented by the multi-temporal landslide inventories. These inventories are extracted applying different sources of remote sensing data, including the satellite and aerial imagery. The second type of thematic data describes the spatial distribution of factors affecting the level of landslide activity. The mapping of affecting factors is performed by applying conventional remote sensing techniques and spatial analysis tools.

The collected thematic data are then used to extract the landslide susceptibility, hazard and risk maps. In total, four conceptually different approaches are applied to map the landslide susceptibility, both on a qualitative and quantitative basis. The results of the quantitative susceptibility mapping and thematic data are further used to calculate the landslide hazard for each part of the studied area. The calculated landslide hazard is characterized both by spatial and temporal components. The results of the landslide hazard assessment are finally used to estimate the risk of the direct impacts of landslides on selected exposed elements, including the uranium tailings sites.

One of the well-established approaches used in Part A is the Newmark method. It maps the seismically triggered landslide susceptibility based on the computed co-seismic displacements. The simplicity of this method is attractive to many researches around the world studying seismically-triggered landslide hazards. Nevertheless, the simplifications adopted in this method strongly limit the reliability of the final predictions.

In the second part of thesis we provide a critical overview of the Newmark method and attempt to propose conceptual improvements of the existing mapping practice. To reach the targeted challenges we combine the spatial analysis with the dynamic simulations in the 2D and 3D domains. The studied models represent the actual topographic and geologic settings of the landslide-prone slopes. The simulations provide acceleration time histories that are recorded in different parts of the model surface. The analyses of these records allow us to outline the amplification impacts related to the topographic and geological site effects.

The modelled amplification factors are analysed with respect to their link to the local geological and topographic settings. Thus, we study how the structural or material settings of the model can impact the recorded geological amplification. Such impacting parameters can be represented by the layer thickness, inclination of the underground contacts or the contrast of the shear wave velocity (Vs) values. The 2D topographic modelling investigates the way how the pure topographic amplification factors can be predicted

based on the surface morphology. The studies show that the surface curvature can be considered as a key parameter to predict the amplification factors. This idea is further investigated in the 3D modelling studies applying different input signals and the materials of varying Vs. The results of this modelling are integrated into a single database which is subjected to spatial analysis. This finally allows us to develop a simple proxy which maps the impacts of the topographic site effects based on morphological parameters extracted from the Digital Elevation Model of the target area.

Additionally, the subset of the 2D dynamic tests analyses the shear displacements triggered by the seismic shaking. Those displacements are recorded in the models with simplified geometry, as well as in the ones presenting the real topographic settings. The recorded displacements are cross-correlated with parameters characterising the seismic impacts. The results of analyses allow us to develop a new law which can easily be used in the GIS-based studies. The proposed law applies a set of the conventional parameters as well as a novel predictor which has never been used by any regional law before.

The conceptual improvements proposed in Part B are finally tested by applying them to the geodatabase compiled in the first part of thesis. Related results are then compared with those that were produced by using the conventional Newmark method. The validation tests should assess performance of the developed proxies to improve the predictions of seismically-triggered landslides.

Table of content:

Part B: Newmark Displacement method: dynamic studies and conceptual improvements

B.I Earthquake-triggered landslides and Newmark method: current state and problems

B.II 2D dynamic numerical modelling: methodology

B.III 2D dynamic numerical modelling: topographic site-effects

B.IV 2D dynamic numerical modelling: combined geological and topographic site effects

B.V Shear displacement versus Newmark displacement: 2D studies

Introduction

The United Nations organization declared the 1990s as the International Decade for Natural Disaster Reduction (IDNDR). The worldwide concern was due to an increasing number of major catastrophic events, including landslides, while associated damage was also steadily growing over the past decades. According to Munich Re (2001), the number of natural hazards increased threefold over the 1990s in comparison with the 1960s, while the rate of economic losses increased by a factor of almost nine over the same period.

For many mountainous countries landslide hazards are of primary concern. An increasing rate of landslide activity is often attributed to an intensified human influence, environmental degradation and climate change (CRED-OFDA, 2002). Kyrgyzstan belongs to the list of countries where among all natural hazards the landslide activity brings the highest annual rate of economic losses and death toll. According to the Ministry of Emergency Situation of Kyrgyz Republic (2013), for the period between 1988 and 2010, the mean annual death toll attributed to the landslide activity is four times higher than the one due to earthquakes, twenty times more than the one due to snow avalanches and fifty times more than the one due to floods.

The Mailuu-Suu River Valley (southern Kyrgyzstan) and the surroundings of the Minkush settlement (central Kyrgyzstan) present two examples of areas where the landslides pose the significant threat to society and existing infrastructure. The situation is aggravated by the presence of some active landslides in close proximity to the tailing storage facilities, the legacy sites of former uranium mining in those areas. The direct and indirect landslide impacts can result in the destruction of protective infrastructure of those storage sites, potentially leading to environmental pollution. Due to this situation, both sites are recognized to be the environmentally hot-spot areas where the implementation of the remediation measures is urgently needed. Some risk reduction measures have already been applied in some of the most hazardous sites. For instance, large part of tailing № 3 in the Mailuu-Suu area was relocated to another place where it is less threatened by landslide impacts. Nevertheless, there are still many other places where the landslide activity could result in local disasters.

The Kyrgyz government and international agencies try to improve the current situation. Thus, in October 2015 the European Union has launched the project named as “Conducting an integrated environmental impact assessment and feasibility study for the safe management and remediation of the uranium legacy complex of Minkush”. A similar project for the Mailuu-Suu target area is planned to be launched in the first half of 2017. The overall objective of these projects is to conduct an integrated environmental impact assessment and feasibility study for the possible remediation and related management activities at targeted sites. Among numerous other topics, the projects goals comprise the characterisation of the landslide activity in the target area. The results of such characterisation strongly impact the selection of the remediation strategy. For example, for the Tuyuk-Suu storage site near Minkush, an on-going EU project has already selected the option of the total relocation of the tailing material to another safer place. This decision was taken due to the high probability of negative landslide impacts and water infiltration problems existing in the present location of the Tuyuk-Suu tailing. Similarly, the planned project for the Mailuu-Suu target area has an objective to characterise the landslide hazard area. The results of such characterisation can help to select the most efficient remediation options.

Both aforementioned sites are selected to be the target areas in present thesis. The developed research is structurally divided into two parts which use spatial analysis and dynamic modelling as the main research tools. The thesis has both applied and scientific objectives. The first, practically oriented part is presented in detail below.

Part A: Landslide susceptibility, hazard and risk – spatial analysis

I.1 Landslide classification and terminology, susceptibility versus hazard

Many countries around the world are exposed to a high level of landslide hazard and risk. This situation is especially critical for the poorest and, therefore, the most vulnerable regions of the world. In response to that, the significant resources have been invested in attempt to assess the landslide susceptibility/hazard and to produce the maps portraying its spatial distribution (CRED-OFDA, 2002). During that time, the scientific community had also put certain efforts into finalizing the common definitions of terms, such as "landslide", "landslide susceptibility" and "landslide hazard".

The basic concept of a "landslide" is the one of a gravitational movement of masses down a slope (Nemčok et al., 1972; Varnes, 1978; Hutchinson, 1988; WP/WLI, 1990). Landslides are classified according to the type of moving material and the type of failure (see Table AT.1). The moving material can normally consist of bedrock, consolidated soil, regolith, loose debris, various mixtures of sediment and pure water in a form of snow or ice (Bryant, 2005). According to Varnes (1978), the moving material is classified next: hard material (bedrock) and soils with coarse (debris) or fine (earth) grain size (see Table AT.1).

Table AT.1: Classification of slope movements (by Varnes, 1978).

Type of movement		Type of material		
		Bedrock	Engineering soils	
			Coarse	Fine
Fall		Rock fall	Debris fall	Earth fall
Topple		Rock topple	Debris topple	Earth topple
Slide	Rotationnal	Rock slump	Debris slump	Earth slump
	Translationnal	Rock (block) slide	Debris (block) slide	Earth (block) slide
Lateral spread		Rock spread	Debris spread	Earth spread
Flow		Rock flow	Debris flow	Earth flow
Complex slope movement (i.e. combination of two or more types)				

Figure AF.1 demonstrates the main types of landslide movement. Falls occur when the moving material separates along joints, bedding or other weaknesses (Keller, 2005; Figure AF.1a). They are normally characterized by little displacement prior to failure and have very rapid to extremely rapid displacement rates (Varnes, 1978). The toppling movement listed in Table AT.1 is referred to be one variety of falling mechanism, when the forward rotation of the unit/units around some pivot point occurs (Varnes, 1978; Keller, 2005).

Flow is the downslope displacement of unconsolidated material in which particles move and mix within the mass (Keller, 2005; Figure AF.1b). The flows normally have a water content which controls the behaviour of the moving material. When the fine-grained material dominates the moving mass it is referred to as mudflow/earthflow, while debris flows normally contain coarser material (Bryant, 2005). Flow initiation and failure normally occur over a few hours to a few days, when the movement is extremely rapid with a rate of hundreds of meters per a few tens of seconds (Evans and DeGraff, 2002).

Slides are the coherent movements of material over one or more failure surfaces (Keller, 2005; Figure AF.1c). These failure surfaces can have curved or planar shape. The first case, i.e., curved failure surface is characteristic for the rotational slides/slumps (see Figure AF.1d). Translational slides and lateral spreads normally have planar sliding surfaces, such as faults, joints, a clay layer or a contrast between soft and hard rocks (Abbott, 2009).

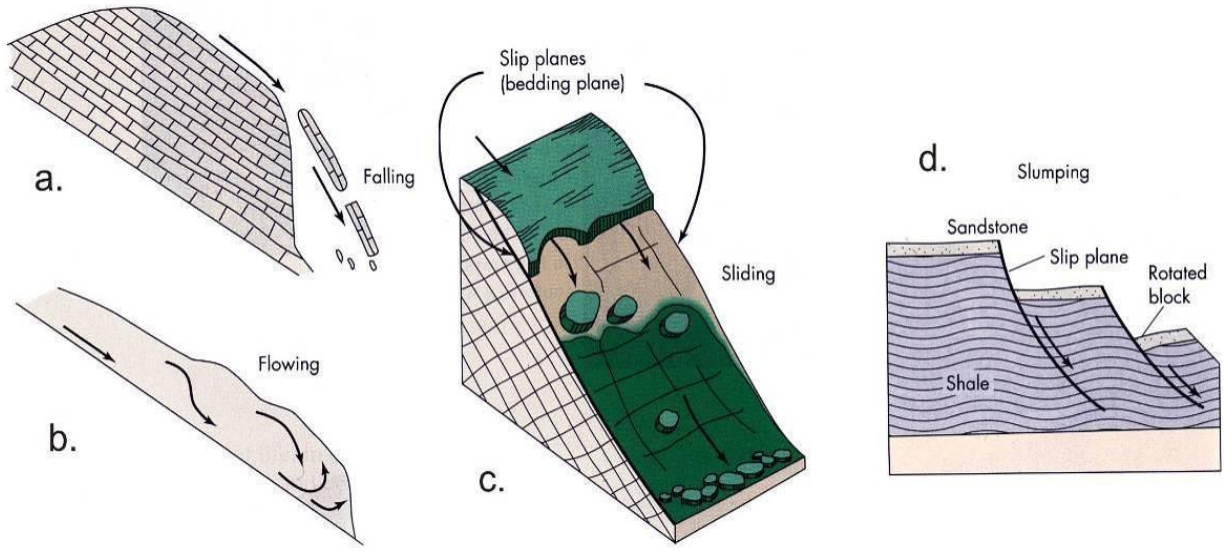

Figure AF.1: Types of landslide movements (by Keller, 2005).

A literature review suggests that the terms of "landslide susceptibility" and "landslide hazard" are often mixed, while there is a clear concept separating them. The landslide susceptibility is considered to be the likelihood of a landslide occurring in an area depending on the local terrain conditions (Brabb, 1984). Another definition proposes that landslide susceptibility indicates the degree to which a terrain can be affected by slope movements and shows an estimation of "where" landslides are likely to occur (Guzzetti, 2006). Susceptibility does not consider the temporal probability of failure (i.e., when or how fast/frequently landslides occur), nor the magnitude of the expected landslide (i.e., how large or destructive the failure will be; Committee on the Review of the National Landslide Hazards Mitigation Strategy, 2004).

Landslide hazard is the probability that a landslide of a given magnitude will occur within a given period and in a given area. Besides predicting "where" the slope failure will occur, landslide hazard forecasts "when" or "how frequently" it will occur, and "how large" it will be - in this matter, landslide susceptibility is considered to be the spatial component of landslide hazard (Guzzetti et al., 2005).

According to Guzzetti (2006), landslide susceptibility and hazard mapping involves the degree of interpretation, which relies on several wide-adopted assumptions:

1. Slope failures are marked by features which can be recognized, classified and mapped in the field or through remote sensing;
2. Landslides are controlled by mechanical laws which can be determined empirically, statistically or deterministically. These instability conditions can be regionally mapped and applied in predictive models for the mapping of landslide susceptibility/hazard;
3. The future slope failures will most likely occur under the conditions which also led to past and present instability cases;
4. Spatial and temporal landslide occurrence can be inferred from heuristic investigations, computed through the analysis of environmental information or inferred from the physical models.

Ideally, any method of landslide susceptibility/hazard mapping should rely on all assumptions. Practically, all existing methods use just some of them, which limit the final reliability of these methods. The main concept of landslide susceptibility zoning involves a rating of the terrain units according to their propensity to produce landslides, i.e. landslide occurrence probability (Fell et al., 2008). There are various methods of landslide susceptibility mapping and they vary depending on input data, landscape, purposes and available resources. The next section reviews a classification of all existing method and presents a short description of them.

I.2 Classification of landslide susceptibility mapping methods

A review of existing landslide susceptibility mapping methods is presented by Guzzetti (2006) and Mouchel (2011). The authors outlined four main groups of the mapping methods, namely: (i) geomorphological; (ii) heuristic (index-based); (iii) process-based (conceptual) and (iv) statistical modelling. In general, these mapping methods are subdivided into the direct/non-direct and qualitative/quantitative ones (Varnes and IAEG Commission on Landslides and other Mass-Movements, 1984; Carrara and Guzzetti, 1995; Hutchinson, 1995 among others). The proposed classification of methods is "fuzzy", as involved concepts and/or applied computational solutions often have a certain degree of similarity.
The classification into quantitative and qualitative methods reflects the output provided by these methods (see Figure AF.2). The qualitative ones provide subjective and pure descriptive (non-quantitative) estimates of the landslide susceptibility level. The quantitative methods provide the output in numerical terms, i.e. a probability of landslide occurrence in any given area.

	Geomorph-ological	Heuristic	Physical	Statistical
Quantitative		Attribute Scoring Schemes	Factor of Safety	Regressions Neural Networks
Qualitative	Mapping Observation	Logic lookup tables		

Figure AF.2: Classification of existing mapping methods based on provided output (by Mouchel, 2011).

Direct methods are based on the geomorphological mapping of landslide susceptibility applying field observations and data gained from interpretation of the aerial photographs or satellite images (Verstappen, 1983; Nossin, 1989). In most cases, but not necessarily, direct methods are associated with a production of the landslide inventory maps, which become a basis for further susceptibility ranking. The direct methods apply an expert-based opinion and normally do not involve a lot of automatic data post-processing.
Indirect methods are considered to be essentially stepwise and should normally contain the next investigation/processing stages: (i) preparation of the landslide inventory map; (ii) identification and mapping of the instability factors; (iii) estimate of a relative input of all instability factors into a final susceptibility level; (iv) classification of a studied area into the domains with certain level of landslide susceptibility; (v) assessment of model performance and model fit.
As it was noted above, the boundaries between different methods are not rigid. Some methods present a certain grade of hybridization. Nevertheless, there is certain conceptual difference between four main groups of methods. The next sub-sections review in more details a concept and methodology involved in each group.

I.2.1 Geomorphological mapping

The geomorphological mapping represents a direct (sometimes indirect) method which can be considered as an expert-based mapping methodology. This qualitative approach relies on the ability of investigator to track

a relationship between the landslide activity and the factors, affecting instability level (see an example in Figure AF.3). Normally this method also considers a historical evolution of landslide activity together with an analysis of possible consequences (Humbert, 1977; Kienholz et al., 1978; Bosi et al., 1985; Zimmerman et al., 1986; Seeley and West, 1990; Hansen et al., 1995 among others). The collected information provides a basis for a landslide susceptibility mapping, when the susceptibility ranking strongly depends on the observed relationship between the affecting factors and instability cases. Such kind of mapping is considered to be a form of an expert judgment which involves certain subjectivity depending on the investigator experience. It is very difficult to formalize the mapping methodology due to a presence of subjective opinion. Nevertheless, for example, Cardinali et al. (2002) and Reichenbach et al. (2005) present the attempts to develop the semi-automated expert-based mapping techniques.

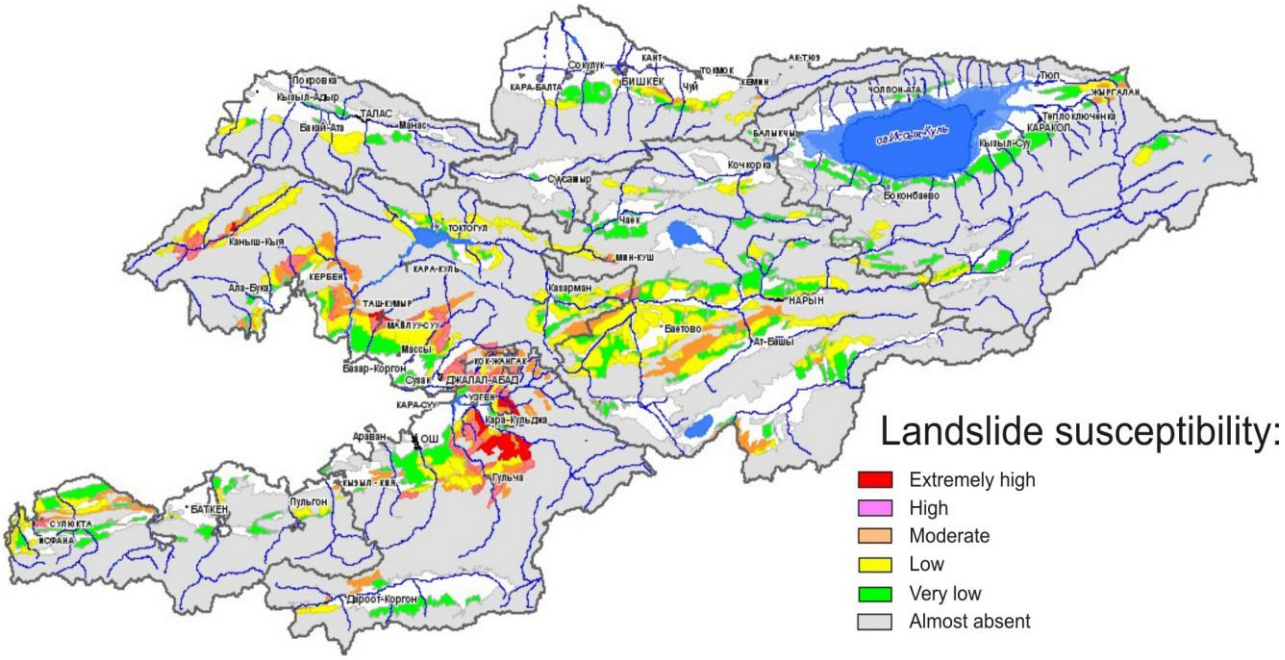

Figure AF.3: An example of the geomorphological mapping of the landslide susceptibility for the target area presented by the whole territory of Kyrgyzstan (by Ministry of Emergency Situation of Kyrgyz Republic, 2013).

I.2.2 Heuristic methods

The heuristic or index-based approach is considered to be the indirect or semi-direct, mostly qualitative mapping method. It is based on the priory knowledge on the link between landslide activity and instability factors. The method application normally involves classification, ranking and weighting of the instability factors with a following mapping of the landslide susceptibility. To some extent this method is considered to be an expert-based approach, as a selection of affecting factors and analysing procedure directly depend on the investigator (see an example in Figure AF.4). There are several applied examples, when the heuristic decision rules were employed for a mapping of the landslide susceptibility in the different target areas (Nilsen and Brabb, 1977; Hollingsworth and Kovacs, 1981; Neeley and Rice, 1990; Montgomery et al., 1991; Pachauri and Pant, 1992; McClelland et al., 1997; Nagarajan et al., 2000; Lee et al., 2002; Liu et al., 2004; Moreiras, 2005 among others).

The main disadvantage of an index-based approach originates from the subjective consideration of the involved affecting factors. Another disadvantage comes from the point that this approach does not consider a complex interaction between different factors. For example, Guzzetti (2006) comments that this method separately considers slope and lithology, like it is in Figure AF.4, while a complex interaction of them should be taken into account.

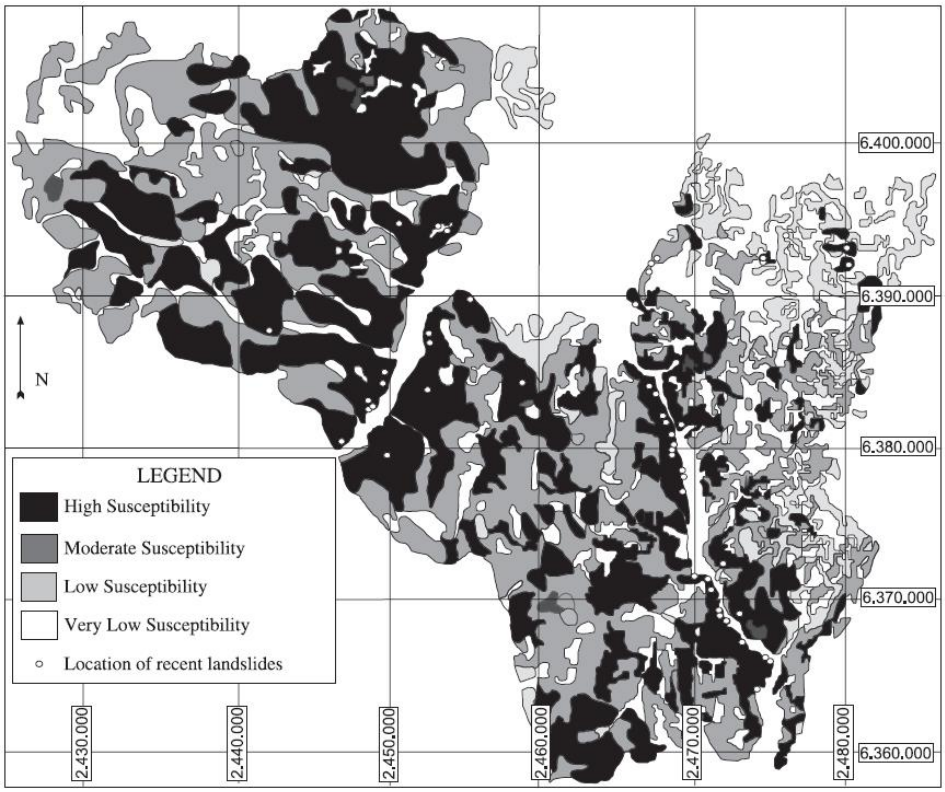

Figure AF.4: The index-based landslide susceptibility mapping in the Rio Mendoza Valley, Argentina applying lithologic and slope angle thematic layers (by Moreiras, 2005).

I.2.3 Process-based methods

Another group of landslide susceptibility mapping methods is presented by the process-based or conceptual models. This set of methods relies on the physical laws controlling the slope stability, i.e., they estimate the balance between stabilizing and driving forces acting along a potential sliding surface. These models often apply a simplified concept generalizing all specific cases of the landslide occurrence under one single model. The simplification often considers a planar sliding surface situated at a fixed depth and parallel to the topographic surface. Such models are mostly developed to study a particular type of landslides (e.g., shallow soil slides, debris flows, rock falls, etc.) or to investigate the effect of a specific trigger, i.e. an intense rainfall period or an earthquake.

In our studies we apply the regional Newmark method which belongs to the group of the process-based models. The Newmark models are developed for a regional seismic slope stability analysis. It is based on an original technique developed by Newmark (1965). The author suggested that co-seismic slope displacement can be calculated by the double integration of the part of the impacting acceleration-time history exceeding the critical acceleration value, which is a function of the Factor of Safety of the studied slope. Several authors have later adapted this concept to a regional application. These adapted concepts are relying on the empirical laws rather than on the precise stability calculations and integration of the affecting seismic signal (Wilson and Keefer, 1983; Wieczorek et al., 1985; Jibson, 1993; among others). As an example, Figure AF.5 presents the results of seismic landslide susceptibility mapping in the Oat Mountains, California obtained by application of the regional Newmark method (Jibson et al., 1998).

Part B of this thesis applies the set of the dynamic simulations to analyse the original Newmark (1965) technique as well as its regional models. It will be shown that our simulations suggest some conceptual improvements of the existing mapping methodology. These improvements should finally increase the reliability of model predictions.

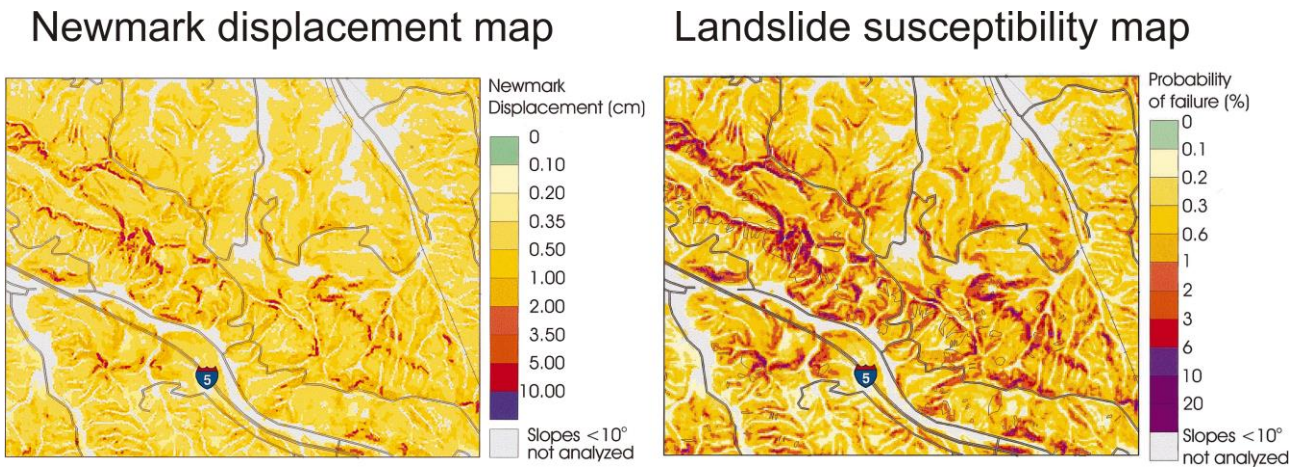

Figure AF.5: The distribution of Newmark displacement and landslide susceptibility mapped by regional Newmark method in the Oat Mountains, California (by Jibson et al., 1998).

Some other process-based methods consider the rainfall as the main factor triggering slope instability. These models basically analyse the shallow rainfall-induced landslides and they normally employ simplified stability models widely adopted in geotechnical engineering. The analysis includes a complex consideration of the conventional parameters such as the normal stress, angle of internal friction, cohesion, pore water pressure, external loads, etc. Many authors present applications of the regional models studying the rainfall-induced landslides (Ward et al., 1981, 1982; Dunne, 1991; van Ash et al., 1999; Gritzner et al., 2001; Lan et al., 2005 among others).

The physical-based models studying the regional rock fall potential are presented by van Dijke and van Westen (1990). Following this concept, Guzzetti et al. (2002) apply Digital Elevation Model (DEM) and spatially distributed information to simulate three dimensional rock fall failure for areas ranging from a few thousands of square meters to several hundreds of square kilometers. The results of these studies normally include the extent/location of the areas potentially subjected to the rock falls, the estimates of the maximum velocity and the maximal travel distance.

I.2.4 Statistical methods

The statistical modelling is an indirect and quantitative method. It determines the landslide susceptibility through a description of functional relationships between the instability factors and the past and/or present distribution of slope failures (Carrara, 1983).

The simplest statistical methods are based on a determination of the relative abundance (proportion, percentage, frequency) of the landslides in the ranked classes representing the geographical distribution of the stability/instability factors. In general, these methods are classified according to a general instability index (e.g., Carrara, 1978), a landslide susceptibility/hazard index (e.g., Sarkar et al., 1995), a frequency index (e.g., Parise and Jibson, 2000) and a surface percentage index (e.g., Uromeihy and Mahdavifar, 2000). These indexes provide a direct or weighted measure of a relative/absolute abundance of a landslide area or a number of them in the different terrain categories. This information is further applied by the investigator to establish the susceptibility levels in different parts of study area.

Michie et al. (1994) made an overview of more advanced statistical methods (Figure AF.6). These methods employ different "philosophical" concepts and can be classified as follows: (i) classical (frequentist or Fisherian) statistical techniques, (ii) modern (subjectivist or Bayesian) statistical methods, (iii) fuzzy logic systems, (iv) artificial neural networks and (v) expert systems.

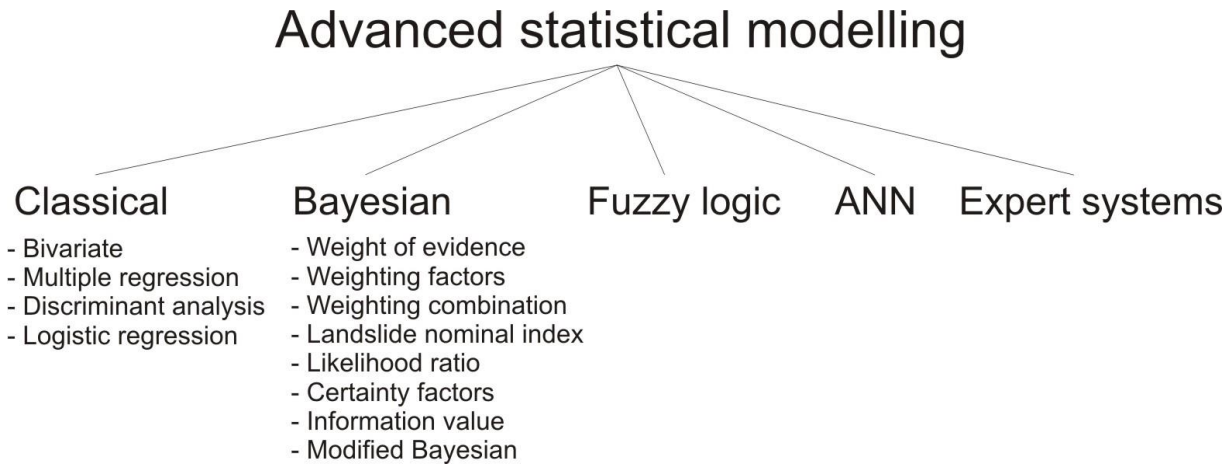

Figure AF.6: Classification of advanced statistical modelling (by Michie et al., 1994).

The classical, "frequentist" approach is further subdivided into the next techniques: (i) bivariate analysis, (ii) multiple regression analysis, (iii) discriminant analysis (DA) and (iv) logistic regression analysis. DA and logistic regression analysis are recognized to be the most wide-spread techniques (Guzzetti, 2006).
DA employs a classification of the samples or cases into one of several mutually exclusive groups based on their values for a set of predictor variables (Fisher, 1936). For the landslide susceptibility mapping the classification cases are presented by the landslides, while the exclusive groups are presented by the mapping units with instability potential (with landslides) and those without instability potential (free of landslides). The interaction between predictor variables (affecting factors) and the landslide occurrence is further analysed. It provides a basis to establish the instability potential in any part of the study area expressed via the value of the sliding probability (see an example in Figure AF.7).

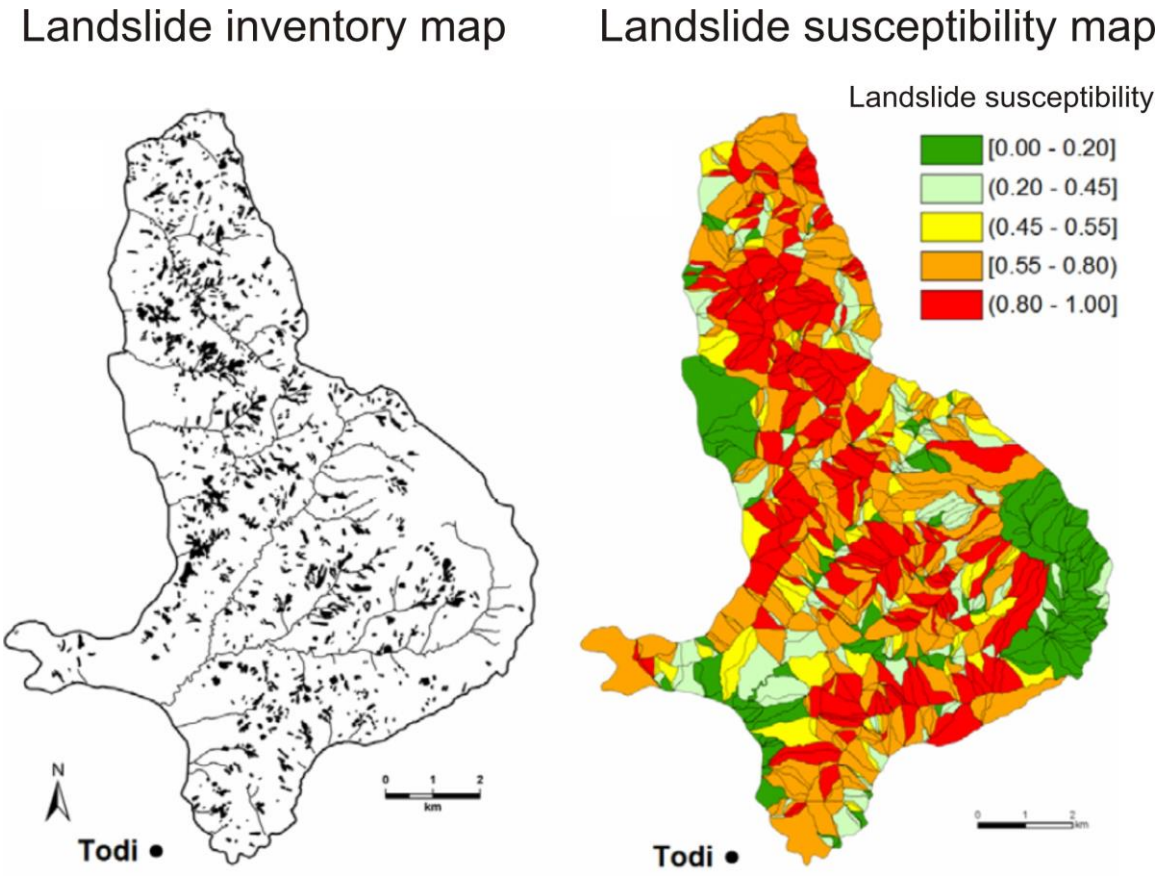

Figure AF.7: Landslide inventory and landslide susceptibility maps for Collazzone study area, Italy (landslide susceptibility is mapped by the DA method - by Guzzetti, 2006).

Cox (1958) was the first to introduce the Logistic Regression Analysis (LRA) to investigate a binary response from a set of measurements. This technique predicts the success or failure of a process based on a set of the measurements (Michie et al., 1994; Brown, 1998). Landslide susceptibility studies often employ a curvilinear model relationship between the independent variables (affecting factors) and the response (landslide presence/absence). The mapped distributions of affecting factors are later used to estimate the instability potential in a study area on the basis of the Bernoulli probability. This value indicates if a certain area belongs to a stable or non-stable mapping unit.

Another group of advanced statistical methods employs the Bayesian theorem for the conditional probability, which represents a chance of a hypothesis being true or false given a piece of evidence (Gorsevski et al., 2003). This approach proposes the way to deal with the uncertainties normally involved in the landslide susceptibility mapping (Chung and Fabbri, 1999; Gorsevski et al., 2003). The Bayesian theorem is applied to determine the probability that a region will have slope failures considering the local environmental conditions. According to Guzzetti (2006), there are several techniques which employ a similar idea, namely: weight of evidence methods, weighting factors, weighted linear combination of instability factors, landside nominal risk factor, likelihood ratio, certainty factors, information value and modified Bayesian estimation. These methods are often difficult to differentiate, as they often mix with each other. An advantage of the Bayesian probabilistic modelling is the possibility to introduce uncertainty into the susceptibility model and to explicitly consider an expert knowledge which often exists for the investigated area (Chung and Fabbri, 1999).

Figure AF.6 also presents a group of techniques referred to as the fuzzy logic system. Zadeh (1975) developed a fuzzy set theory which updated the ordinary set theory. The original technique, i.e., ordinary set theory, allows an element to have only 0 or 1 values as possible membership degrees. The fuzzy set theory allows the membership degree (landslide susceptibility) to be any value from 0 and 1. In the case of the landslide susceptibility mapping each affecting factor is ranked into the classes and the following analysis establishes a membership degree for a link between the landslide presence/absence and the parameter class (e.g., the presence of landslides in the 10-20 degree slope class). Such kind of analysis is performed for all affecting factors and the analysis results are integrated at the end to get the final value of landslide susceptibility. Figure AF.8 presents an example of fuzzy logic application – the authors analysed lithology, slope angle, slope aspect, land cover, level of weathering, fault distance and anthropogenic impact as affecting factors in this study (Champati ray et al., 2007)

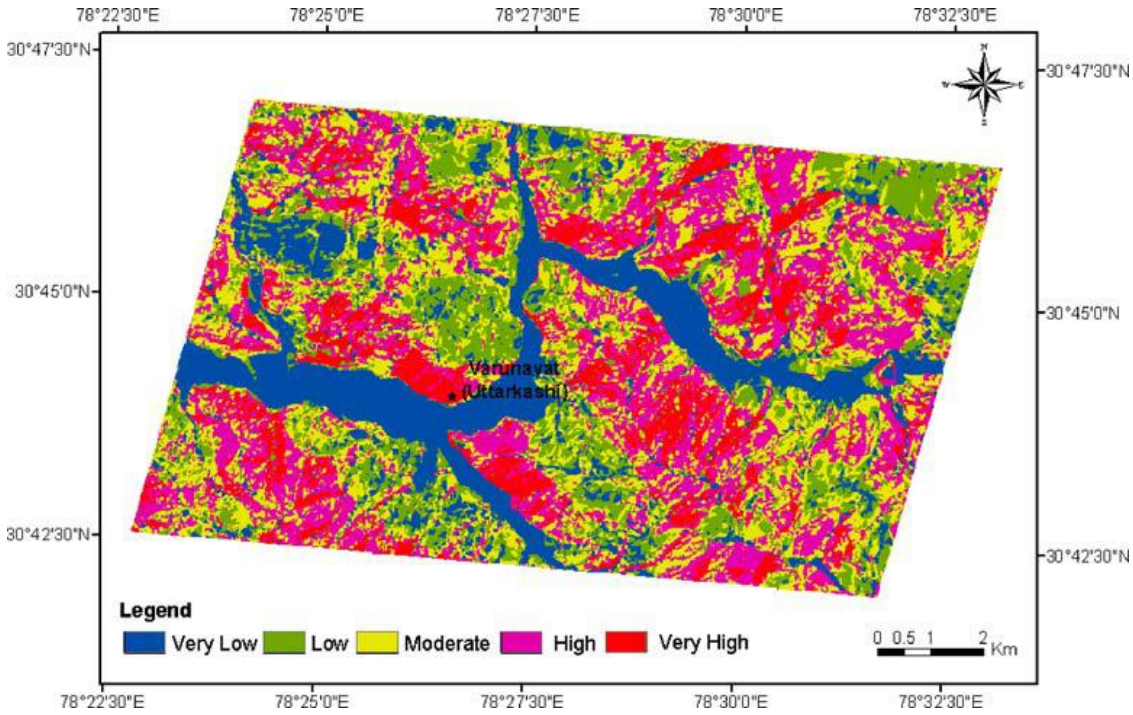

Figure AF.8: Landslide susceptibility mapping for Bhagirathi valley, Himalaya applying fuzzy integration of membership values (by Champati ray et al., 2007).

The Artificial Neural Networks (ANN) and expert system methods presented in Figure AF.6 are integrated into one common group referred as an expert knowledge approaches. A more detailed description of ANN is presented in the section, where it is applied to the mapping of landslide susceptibility in our target area. Conceptually, ANN reproduces the behaviour of human brain in solving complex problems (Michie et al., 1994). At first, the training areas are applied to establish a link between a distribution of affecting factors and landslide occurrence. At the last step, the observed relationships are "spread" over the rest of a study area to estimate the landslide susceptibility level for each part of it (see an application example in Figure AF.9).

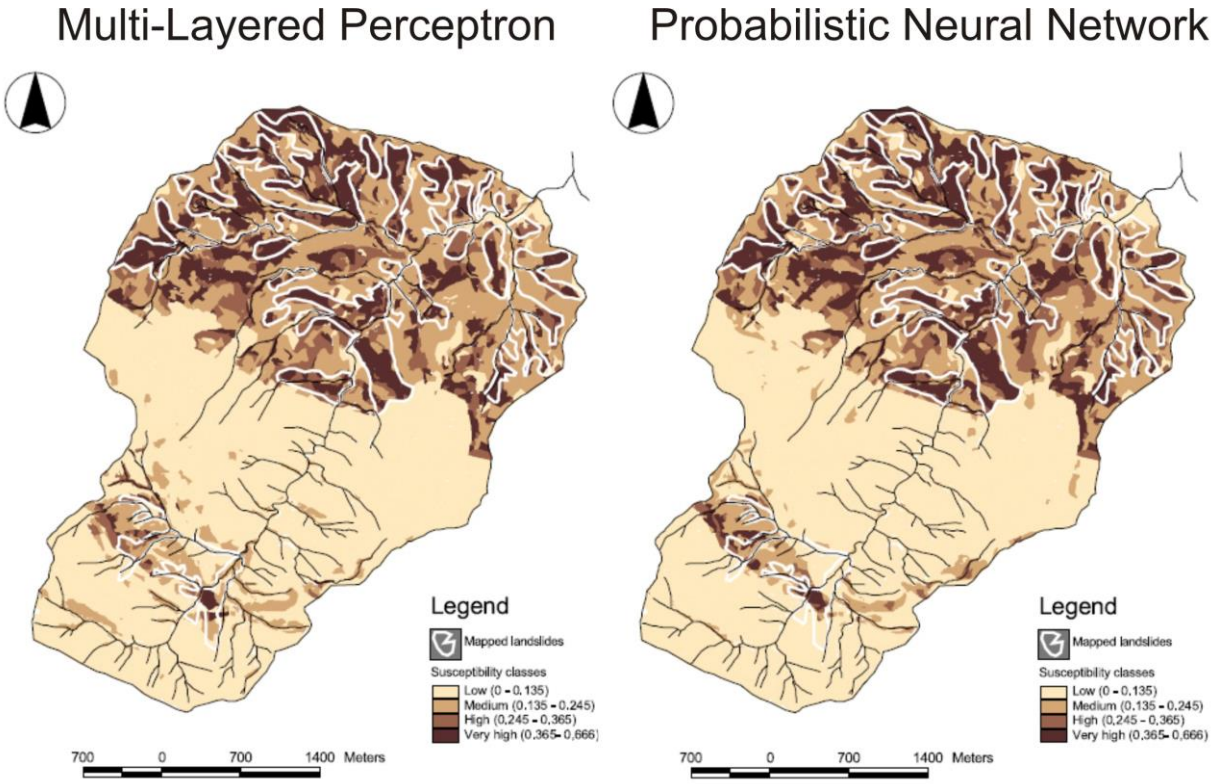

Figure AF.9: Landslide susceptibility mapping for the Riomaggiore River valley, Italy, applying different techniques of Artificial Neural Networks (by Ermini et al., 2005).

Expert systems are computer programs capable of exploiting complex information to make decisions based on a set of the rules (Michie et al., 1994). The decisions taken by the expert system include categorization, which means selection between the possible alternatives. The rules applied in the expert systems can be established a priori or defined by the same system by learning from the errors. The expert systems provide a possibility to establish rules for the special cases or individual instability events, which cannot be performed by other statistical or physically based models. There are several documented cases, when rule-based expert systems are employed for the landslide susceptibility mapping (Al-Homoud and Masanat, 1998; Al-Homoud and Al-Masri, 1999; Pistocchi et al., 2002).

Data mining can be considered as part of the expert systems. Its implementation in the quantitative landslide susceptibility mapping has strongly advanced during the last decade. The data mining algorithms simulate the process of expert decision making by classifying the terrain into stable and unstable regions according to particular parameters (Fernandez-Steeger, 2002). An ability to deal with non-linear problems is considered to be the major advantage for analysis of slope stability problems (Lee et al., 2003). This tool has also proved to be robust for the analysis of incomplete or noisy data, which is often a problem for spatially distributed information (Melchiorre et al., 2008). As both categorical and continuous data are allowed, it avoids a data classification which normally involves subjectivity. The data mining algorithms are often referred to as

"black box" models, and their application demands a deep understanding of the data preparation and post-processing steps (Fayyad et al., 1996).
A good example of application of data mining tools to landslide susceptibility mapping is presented by Braun (2010). The author applied three different techniques (ANN, Bayesian network and Ensemble) to map the landslide susceptibility in the Mailuu-Suu River Valley, Southern Kyrgyzstan. Figure AF.10 presents snapshots of some of the landslides in the study area. The author shows that ANN mainly outlines areas with landslides, while Bayesian network proved to be a perspective technique for the landslide susceptibility mapping (it has better prediction capabilities, while ANN is best in recognition).

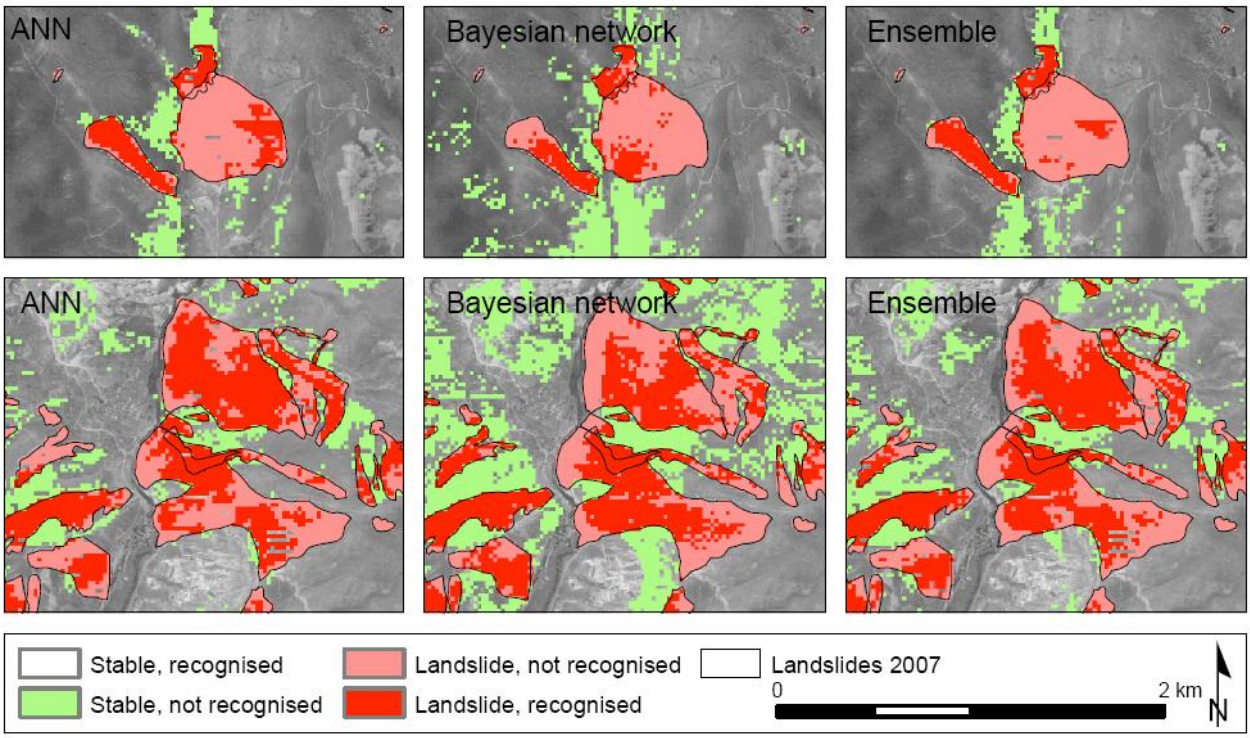

Figure AF.10: The zoom to some of the landslides in the Mailuu-Suu River Valley, Kyrgyzstan together with the results of automatic recognition of existing landslides applying ANN, Bayesian network and Ensemble models (by Braun, 2010).

I.3 Landslide hazard mapping

The well-adopted concept of landslide hazard states that it represents the probability of the potentially damaging landslide to occur within a specified period of time and within a given area (Varnes and the IAEG Commission on Landslides and other Mass-Movements, 1984). Guzzetti et al. (1999) modified this definition by inclusion of the landslide magnitude. Thus, the authors mathematically expressed the landslide hazard (H_L) as follows:

$$H_L = M_L * S_L * T_L \qquad \text{(AE.1)},$$

where M_L is the probability of landslide magnitude exceedance, S_L is the spatial probability (landslide susceptibility) and T_L is the temporal probability of the landslide occurrence.
Different methods of the landslide susceptibility (S_L) mapping have already been described in the preceding section. According to Equation AE.1, it is obvious that only quantitative mapping methods are suitable to landslide hazard zonation, as it applies a numeric measure of S_L. The geomorphological and some index-based methods do not fulfil this criterion, while the groups of conceptual and statistical methods provide a numeric measure of landslide susceptibility (see Figure AF.2).

There is no common opinion on the definition of the landslide magnitude exceedance probability (M_L). For example, Guzzetti (2006) proposes the landslide area (size/volume) to be a proxy of landslide magnitude measure. The authors analysed five multi-temporal landslide inventories for the Staffora River basin, Italy and estimated the distribution of the mean landslide area (see Figure AF.11) which later was considered as proxy to estimate M_L. Many other authors prefer to relate the landslide magnitude to a measure of energy released during landslide failure. For instance, Hungr (1997) relates the landslide magnitude to its destructive potential. Raetzo et al. (2001) introduces an intensity scale for the damage magnitude. This last term, i.e., landslide destructive/damaging potential is suggested to be a function of the landslide volume and the expected landslide velocity (Cardinali et al., 2002; Reichenbach et al., 2005).

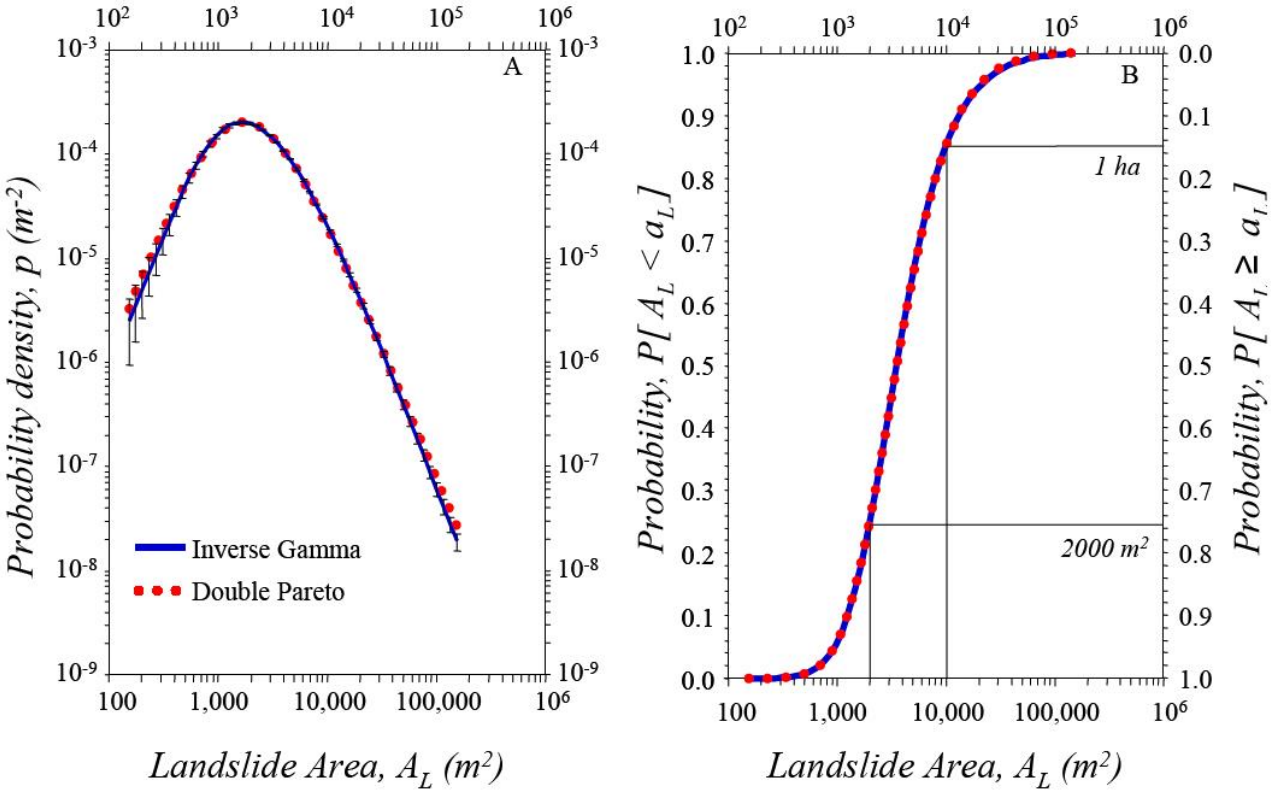

Figure AF.11: (a) Probability density and (b) probability for the mean landslide area in the Staffora River basin, Italy - solid blue line is inverse gamma distribution and dotted red line is a double Pareto distribution (by Guzzetti, 2006).

The third term in Equation AE.1 is presented by the temporal probability of the landslide occurrence (T_L). It is estimated by an analysis of the multi-temporal landslide inventories (Coe et al., 2000; Guzzetti et al., 2003; Guzzetti et al., 2005). To calculate this parameter the landslides are considered to be independent point events randomly distributed in time (Crovelli, 2000). Two models are commonly applied to investigate the occurrence probability of these point events: the Poisson and the binomial models (Crovelli, 2000; Coe et al., 2000; Önöz and Bayazit, 2001; Vandine et al., 2004; Roberds, 2005 among others). Other models of the landslide temporal probability can include the Weibull distribution (Bebbington and Lai, 1996) and the mixed exponential distribution (Nathenson, 2001).

Crovelli (2000) compared the Poisson and the binomial probability models for a set of multi-temporal landslide inventories. It was shown that both models differ for the short prediction period (recurrence interval), while the larger time periods are characterized by very similar estimates. Figures AF.12b and AF.12c present the examples of temporal probability mapping applying five multi-temporal inventories, summarized in Figure AF.12a (Guzzetti, 2006). The Poisson probability model was adopted to map the temporal probability for 25-year (Figure AF.12b) and 50-year (Figure AF.12c) recurrence intervals.

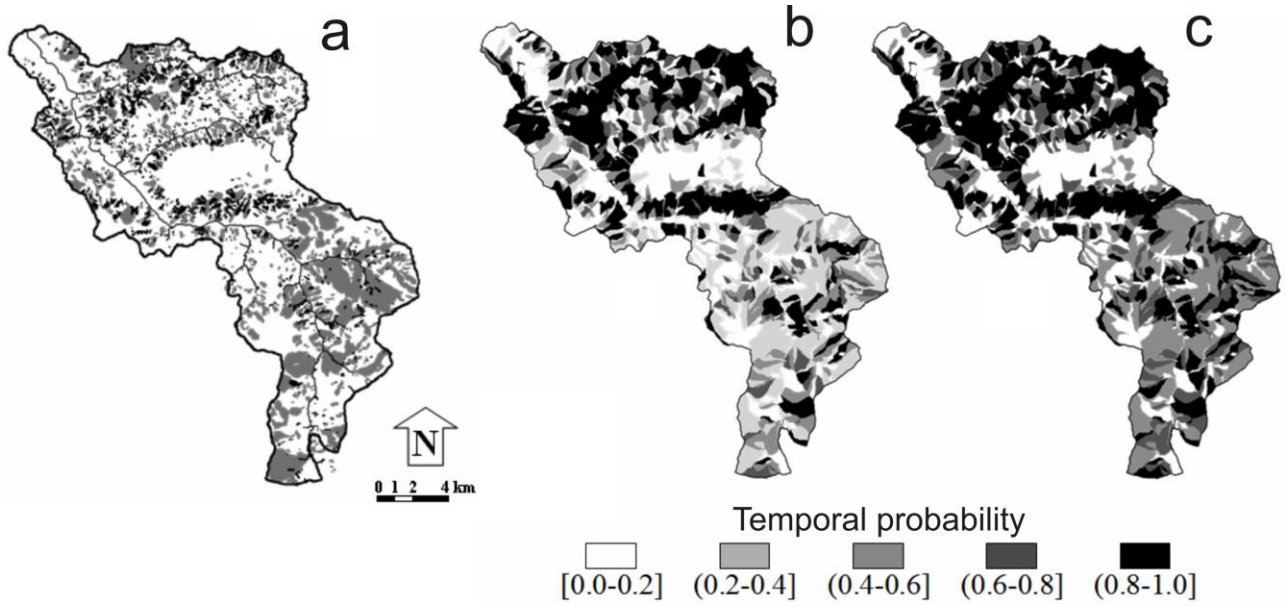

Figure AF.12: (a) Cumulative landslide inventory compiled on the base of five multi-temporal inventories, including relict and old landslides (grey poligons) for the Staffora River Valley, Italy; (b) temporal probability map for 25-year recurrence interval and (c) temporal probability map for 50-year recurrence interval (by Guzzetti, 2006).

I.4 Mapping units

The preceding sections reviewed the main methods of landslide susceptibility and hazard mapping. These methods are applied in a given study area and one of the main parameters in this regional analysis is the type of mapping unit. It represents a portion of land surface which contains a set of ground conditions that differ from the adjacent units across definable boundaries (Hansen, 1984). The regional landslide susceptibility/hazard studies normally employ six groups of mapping units, namely: (i) grid cells, (ii) terrain units, (iii) unique condition units, (iv) slope units, (v) geo-hydrological units, (vi) topographic units, and (vii) geographical units. Figure AF.13 presents extracts of landslide susceptibility maps illustrating different types of mapping units, like grid cells (Figure AF.13a), unique condition units (Figure AF.13b) and slope units (Figure AF.13c).

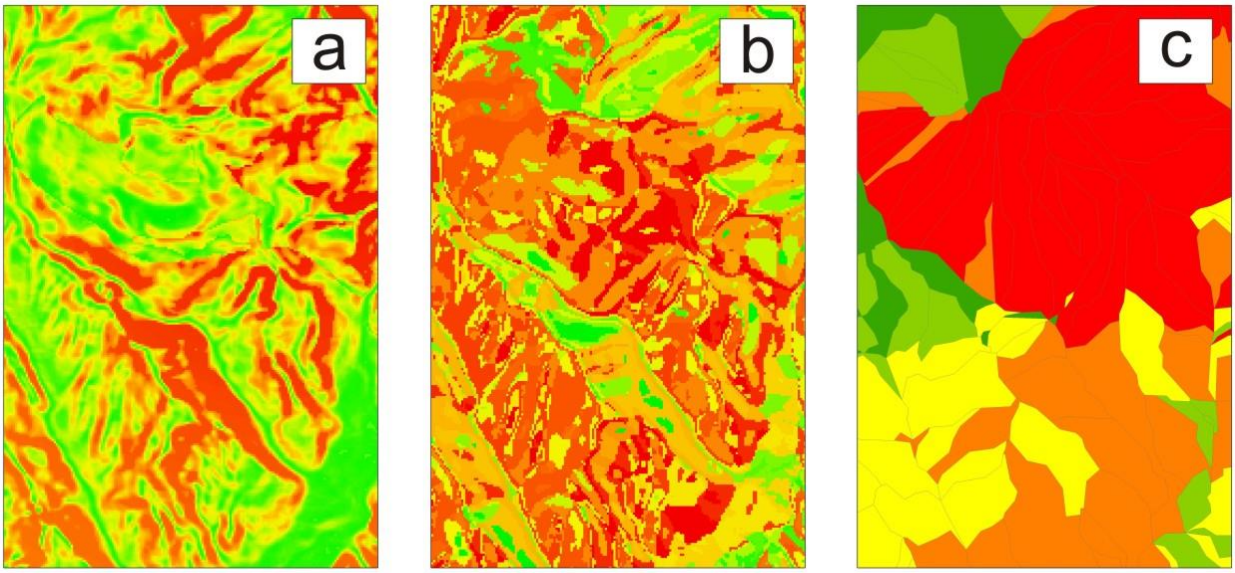

Figure AF.13: The results of the landslide susceptibility mapping, portrayed by different types of mapping units, like (a) grid cells, (b) unique condition units and (c) slope units.

According to Carrara and Guzzetti (1995) the selection of an appropriate mapping unit depends on a number of factors, like: (i) studied type of landslide, (ii) scale of the studies, (iii) available resources, (iv) quality, resolution and type of the input thematic information, (v) availability of the analysis tools (software) and (vii) type of the method applied for the landslide susceptibility/hazard mapping.
Table AT.2 summarizes the application of different mapping units in the groups of the susceptibility mapping methods, described above. The grid cells are preferred by the heuristic, statistical modeling and process-based methods. The unique conditions units are mostly used in the heuristic methods and statistical modelling (van Westen et al., 1993; Carrara and Guzzetti, 1995; Ardizzone at al., 2002). The slope units and geo-hydrological units are often used for the statistical modelling (Carrara et al., 1991; Ardizzone et al., 2002), whereas topographic units are used in the process-based models (Montgomery and Dietrich, 1994).

Table AT.2: Application of the mapping units in the different methods of the landslide susceptibility mapping (by Guzzetti, 2006).

	Geomorphological mapping	Heuristic (index-based)	Statistical modelling	Process-based (conceptual)
Grid cell		x	x	x
Terrain unit	x			
Unique conditions unit		x	x	
Slope unit			x	
Geo-hydrological unit			x	
Topographic unit				x
Geographical unit			x	

The grid cells subdivide the target area into a set of the regularly distributed elements (pixels) which can have square, rectangular, triangular or hexagonal shapes (see an example in Figure AF.13a). It works well for areas where the input parameters/properties have sharp and distinct boundaries. The cases of gradual and smoothed change of parametric limits can also be presented by grid cells, but this requires an adaptation of the cell size.
The terrain unit subdivision is considered to be an expert-based approach, when the study area is delineated based on the similarity of geomorphologic and geologic conditions. The subjectivity of delineation is a disadvantage of these mapping units. Additional disadvantage comes from the fact that landslide susceptibility can often not be related to specific geomorphologic and geologic settings.
The unique condition units (UCUs) may be partly similar to the terrain units. They are extracted through a subdivision of the target area into the zones of similar properties (unique conditions). For example, this subdivision can represent the zones of similar geology, elevation and slope angle, like it was for a case shown in Figure AF.13b. Once all thematic layers are ranked, the further extraction of UCUs can be performed automatically. This process can often create a large number of small groups of unique conditions. Additional disadvantage is the subjectivity involved during a choice and ranking of the input thematic layers.
The slope units represent hydrologic regions, in other words, small-scale drainage and catchment areas (see an example in Figure AF.13c). The subdivision process can be provided manually or automatically based on the DEM of target area. The problems often appear when a scale/size of slope unit should be adapted to the size of studied landslides. For example, a study of the big deep-seated landslides would need bigger scale slope units, while small and shallow slides would need a finer subdivision.
The extraction of geo-hydrological units is based on the slope units which are further subdivided into the zones of similar conditions, e.g. of similar lithology. This subdivision can also be based on a change of land use or land cover. It works well when the landslide susceptibility is strongly related to a change of some key factors, e.g., to a change of rock type.
The topographic units result from a vector-based subdivision, when a catchment area or a single slope is subdivided into the stream tube elements of irregular size and shape (Guzzetti, 2006). The upper and lower boundaries of a stream tube are defined by the adjacent contours, and the lateral boundaries are delineated by the flow lines orthogonal to the contours (O'Loughlin, 1986; Moore et al., 1988; Moore and Grayson, 1991). The topographic and geo-hydrological units are the special cases of the slope units. Therefore, these mapping units are also impacted by the subjectivity introduced during delineation process.
The geographical units are based on the national, political, administrative or demographic borders. This type of units is often applied to the big-scale landslide susceptibility studies, like country scale, for example. The

main limitation of these units is that they do not reflect the morphologic, hydrological, lithological and other parametric boundaries, while landslide susceptibility is directly related to them. Nevertheless, some landslide susceptibility methods can apply these units. For example, Guzzetti and Tonelli (2004) employed the historical records to estimate the landslide susceptibility for different regions in Italy. A data representation in a shape of geographical units is very appealing to the politicians and decision-makers working at the regional/national scales (Guzzetti, 2006).

I.5 Spatial analysis tools: Geographic Information Systems and Remote Sensing

The conceptual framework of landslide susceptibility/hazard assessment was reviewed in the previous sections. In the following one we will describe the tools and software solutions applied in these studies. The instrumental tools widely applied in the regional mapping of landslide susceptibility/hazard are referred to as spatial analysis tools and include Geographic Information Systems (GIS) and Remote Sensing (RS) techniques. According to the most general definition, RS is an acquisition of information about an object/phenomenon without making a physical contact with them, and GIS is a system designed to capture, store, manipulate, analyse, manage and present all types of geographic data with main application in 2D (Williams, 2001). Earth Remote Sensing (ERS or simply RS) can be defined as the measurement of object properties on the Earth's surface using data acquired from aircrafts and satellites (Prost, 2001). From a broader scope, ERS or RS can be defined as the set of scientific and applied approaches which utilise aerial or satellite sensor technologies to detect and classify objects on the Earth by the means of propagated signals, e.g., electromagnetic radiation (Campbell, 2011).
Early discussions on a link between these spatial tools only considered RS as a source of a spatial information for the GIS database (Peplies and Keuper, 1975), while interpretation of the RS imagery was considered to be a separate research domain (Marble et al., 1983). More recent concepts tend to treat RS and GIS in a more general framework, as both tools can be mutually related (e.g., Parker, 1988; Star and Estes, 1990 among others). For example, while RS provides additional input into the spatial database, GIS is often applied to improve imagery quality/accuracy (Sabins, 1996).
At present time, GIS and RS are widely applied in numerous domains, spanning from the engineering/planning to insurance/business activities. The regional studies are highly demanded in earth sciences. For instance, GIS and RS are employed in atmospheric sciences, oceanography, geology and physical geography. A more detailed overview of these spatial analysis tools is presented in the next sub-sections.

I.5.1 Geographic Information Systems

From a technical point of view, GIS is considered to be an organised database, which assembles and relates different types of information based on their geographic location (Prost, 2001). GIS, as a spatial analysis tool, has 40 years of history which started from the initial attempts of the Canadian Geographic Information Survey to employ geographically related polygons in assessing land use properties (Williams, 2001). A growing importance of GIS is related to the large number of possibilities available in this tool:
- to locate studied objects in a desired geographic coordinate system (georeference);
- to relate the georeferenced objects with respect to each other;
- to convert and adapt spatial data in the formats applied for further analysis or data modelling;
- to visualise a set of the spatial data in a user-friendly format.

Due to these options GIS is a very perspective tool for a lot of tasks in engineering, science, social studies and economics. A progress of GIS application is strongly related to the hardware/software developments, as data manipulation needs a rapid processing. An increasing calculation capacity gives more perspectives for the data modelling/representation in the 3D domain, while in some applied areas, e.g., construction, geological prospecting and mining engineering 3D GIS tools have already been widely applied during the last 15-20 years.
The RS imagery or a georeferenced topographic map often become a basic platform to which other data are related based on their geographic location. These data include any types of physical information, like geology, road network, engineering constructions, technical infrastructure, lifelines, etc. It can also include an output from a preceeding data analysis, i.e., the results of geophysical surveys, sampling data, etc.

A series of options is provided by a compiled GIS database. These options include a rapid and convenient data visualization, complex data analyses and data update/export. All these possibilities form a background for a following planning/prognostic activity.
There are two main data representation formats in GIS: raster and vector. The raster format is represented by a set of regular-shaped elements (pixels), structured by rows and columns. Each pixel has one data value averaging a data variability within it. Satellite imagery or other RS data, as well as DEM (represeted in pixel format) are examples of raster data. This format is intrinsic to some type of spatial analyses. For example, the extraction of a slope and aspect map from DEM demands raster representation of input data.
The vector format does not rely on a regular data network. It depicts the key moments of a data variation via the changing limits and attributes. Topologically, the vector format can be represented by the polygonal, polyline or point shapes – each of these shapes has its own applications. A lot of spatial data are best represented by the vector format, such as the road network and lifelines (represented by polylines), administrative borders (represented by polygons), sampling data/boreholes (represented by points), etc.
The spatial analysis tools are characterized by the low unit/labor costs which are strongly determined by the modern software/hardware capabilities. These modern Information Technology (IT) achievements determine the flexibility and efficiency with which the spatial database can be processed and managed. That way spatial analysis presents an indispensible solution to perform the regional generalization of analysed data. The RS imagery, as a part of the GIS database, provides unique spectral information for vast areas, which could hardly be collected by in-situ measurements. The negative aspect of pure spatial analysis is the lacking "ground truth". Therefore, related tools should best be coupled with field surveys and in-situ studies – such coupled approach gains a full coverage of a studied problem. In this matter, spatial analysis is considered to be an additional research possibility, rather than independent scientific domain.
A general overview of different types of GIS software is presented by Steiniger and Weibel (2009), and Steiniger and Hunter (2013). The authors note that nowadays there are more than several tens of GIS codes or other geospatial processing tools available to the end-user. Among those the best known tools are the next: ArcMap and ArcGIS (by ESRI Inc.), Mapinfo (by Pitney Bowes), AutoCAD (by Autodesk), Smallworld (GE), Microstation (Bentley), as well as open source software such as Quantum GIS, gvSIG, POSTGIS, OpenLayer and GRASS.
Figure AF.14 presents the main types of commonly applied GIS codes together with a standard/optional functionally included by this software. Regional landslide studies use almost all presented types of tools. Mobile GIS in combination with Global Positioning System (GPS) is often applied in field studies and mapping of landslides. Desktop GIS, Spatial Database Management System, GIS extensions are applied in the stages of data preparation and data analysis. Server GIS is used to manage a spatial database with a big number of investigators/end-users. Internet-based platforms, like WebMap Server and WebGIS client (e.g. Google Maps and Google Earth) experience growing application during the last years, as they provide a data access to a wide auditorium of end-users. Through these platforms the end-users can overview, visualize, download and sometimes update spatial data. Therefore, these internet-based codes are often used in a data representation and data dissemination stages.

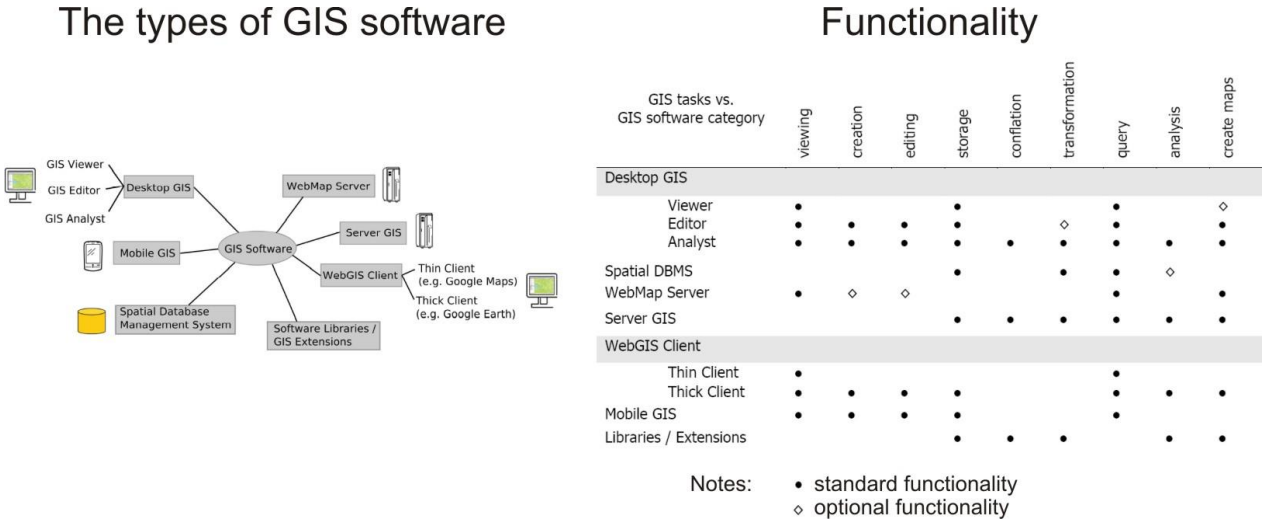

Figure AF.14: The types of GIS software (by Steiniger and Weibel, 2009).

I.5.2 Remote Sensing

Acquired imagery is the main source of information for RS. The imagery indicates how a studied medium (earth surface and objects on it) interacts with different fields, e.g. electromagnetic (EM) or gravitational ones. At present, the main focus of RS is a wide range of EM radiation, from ultraviolet till microwave (see the EM spectrum in Figure AF.15). The way how the EM radiation will interact with the earth surface depends on the physical properties of both the studied object and the incident EM radiation. This interaction can be expressed via refraction, reflection, absorption or radiation.

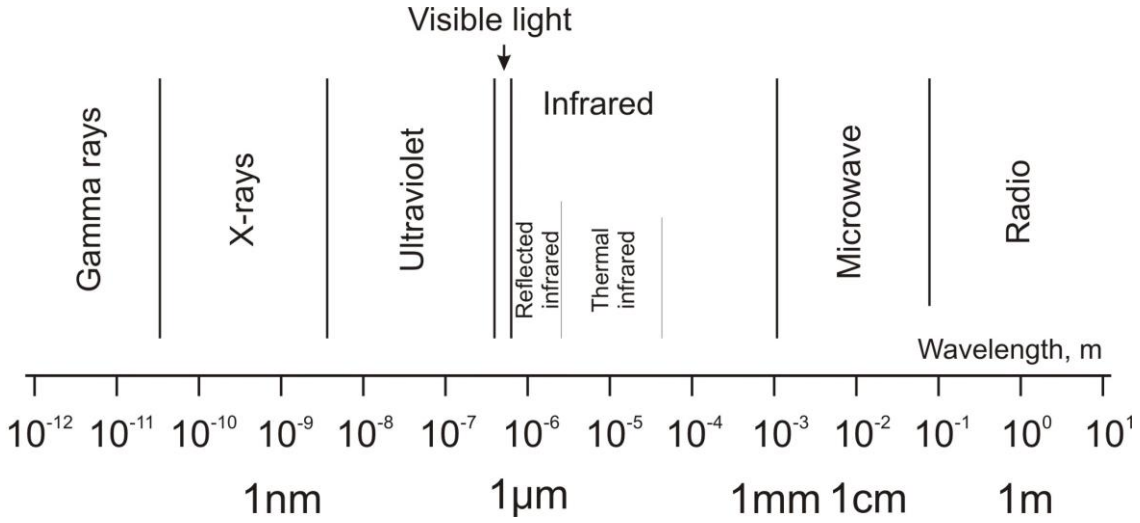

Figure AF.15: The main spectral ranges of the EM radiation (by Jain, 2004).

The different atmospheric agents, e.g., ozone, carbon dioxide, water vapor, etc., create the absorption bands with a low atmospheric transparency. These bands strongly reduce the application of RS in these ranges. Figure AF.16 shows the areas of high atmospheric transparency, also called atmospheric windows. For example, the EM radiation with a wavelength of less than 0.3 μm is totally absorbed in atmosphere. It includes gamma rays, x-rays and the major part of the ultraviolet (UV) radiation. Therefore, RS starts to operate from photographic UV range, where atmospheric absorption starts to be less pronounced (see the range of Photo UV in Figure AF.16). There are several absorption bands in the other EM ranges – all RS missions bypass them and work in the atmospheric windows (see a position of working bands for different missions in Figure AF.16).

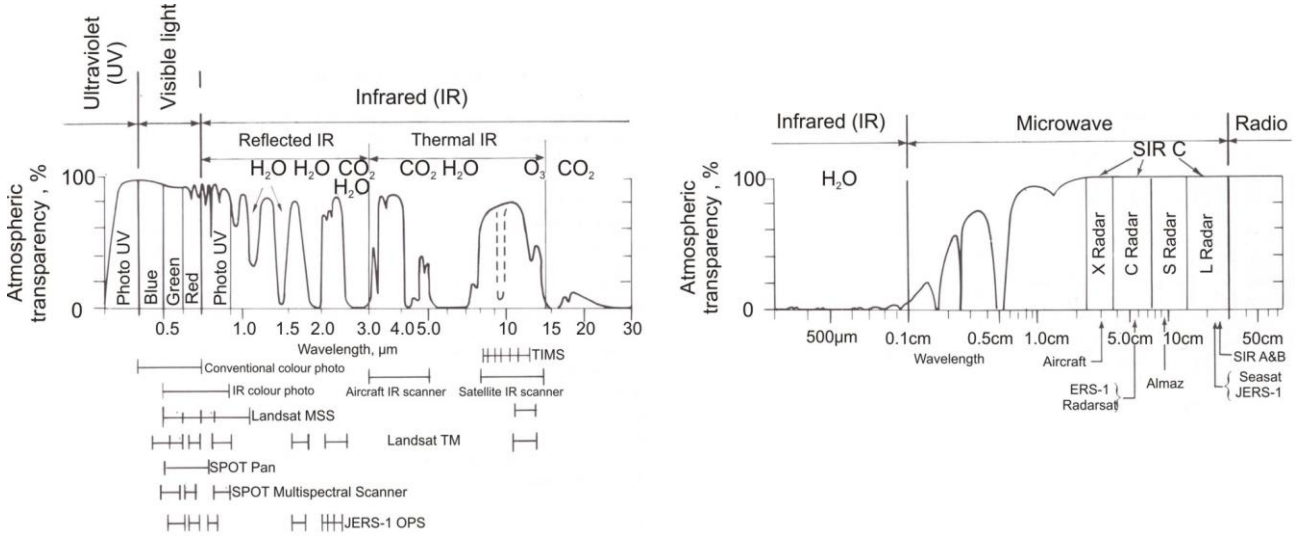

Figure AF.16: Atmospheric transparency in different ranges of the EM spectrum and the working bands of some RS missions (chemical formulas indicate absorption bands provided by different agents in the atmosphere; by Jain, 2004).

The EM spectrum is also subjected to an atmospheric scattering which results from interaction with air agents and aerosol particles. The scattering intensity decreases starting from the ultraviolet radiation with a minimum at the microwave range. Radar waves are almost not subjected to atmospheric scattering, reflection and absorption and are, therefore, widely applied in RS.
The atmospheric effects determine the passive and active regimes of RS. The passive regime works only with natural part of a reflected and emitted energy (such as sun light reflected by the Earth surface), while the active regime uses its own source of emitting radiation. Radar RS is an example of the active regime. The radar radiation is first sent by the emitting source, and a part of energy, reflected back from the earth surface, is acquired by a sensor. The active regime of RS is not applied in other EM ranges, as related energy is too much attenuated by the two-way travel through the atmosphere.
The instrumental factors, i.e., sensor properties, also put some negative effects during the acquisition and post-processing stages. These factors include optic/geometric distortion of the acquired imagery. Some RS missions apply their own correction procedures and include them into the final product, while other ones leave this option to the end-user.

I.5.2.1 Remote Sensing missions

A complex system with a combination of technological/instrumental solutions designed to capture and/or postprocess RS data (aerial/satellite imagery) is called RS mission. At present time there are more than one hundred missions working in different spectral ranges. A final product of these missions, i.e. RS imagery, is characterized by the next main parameters:
-spectral properties (number of spectral bands, their spectral position and spectral width);
-spatial resolution (pixel size);
-spatial extent (surface area coverage).
All these parameters depend on the technical settings of a given RS mission, which, in turn, are strongly determined by the research targets. For example, the applications targeting oceanic and atmospheric studies normally have a coarse spatial resolution (more than 200 m) and larger spatial extent. RS missions targeting the Earth surface monitoring are normally characterized by a finer spatial resolution (less than 30 m) and smaller spatial extent. The spectral properties of RS missions also depend on the external limitations, such as the atmospheric transparency, as it was described in the previous section.
Till the 1960s an application of RS was limited to the observations and photos from planes, air balloons and other aircrafts in the ranges of visible light or infrared radiation. Space discovery provided new possibilities for RS. During the last 30 years RS experienced the most intensive development regarding the quality of acquired imagery, periodicity of acquisition, processing software, price politics and public access to the data. A periodicity of imagery acquisition is one of the most pronounced advantages, as it allows us to reconstruct historic changes of studied processes. To better demonstrate the possibilities of different RS missions the following sub-sections present a short description of RS imagery applied in our studies.

I.5.2.2 Middle resolution imagery: Landsat and ASTER

One of the research tasks completed in this thesis was the land cover mapping in the Mailuu-Suu target area. This task was performed with the help of the Landsat imagery, which is the common product of the United States Geological Survey (USGS) and the National Aeronautics and Space Administration (NASA). The Ladsat project was designed as a kind of tool, which provides periodical monitoring of the earth surface conditions and tracks the changes on it (Sabins, 1996). Landsat was one of the pioneer missions, which formed RS as a separate scientific domain regarding the involved technologies. The Landsat database was also pioneering about survey periodocity, applied spectral and spatial properties.
The Landsat mission has started in 1972 from the launch of the first generation satellite (Landsat 1). It had on board a multispectral scanner (MSS) with four spectral bands and spatial resolution of 79x79 m (see Table AT.3 for the spectral properties). At present, the first generation of satellites (Landsat 1, 2 and 3) have terminated their activity, but their operation provided several hundreds of thousands of images for different parts of the world.

Table AT.3: The spectral properties and spatial resolution for the imagery, acquired by different Landsat satellites (www.landsat.gsfc.nasa.gov).

	Multispectral scanner (MSS); (Resolution; spectral range)	Thematic mapper (TM); (Resolution; spectral range)	Modernized thematic mapper (ETM+); (Resolution; spectral range)	Operational Land Imager/Termal Ifrared Sensor (OLI/TIRS); (Resolution; spectral range)
Missions	Landsat 1, 2, 3	Landsat 4, 5, 6	Landsat 7	Landsat 8
Blue 1	-	-	-	30 m; 0.433-0.453 μm
Blue 2	-	30 m; 0.450-0.515 μm	30 m; 0.450-0.515 μm	30 m; 0.450-0.515 μm
Green	79 m; 0.520-0.600 μm	30 m; 0.525-0.605 μm	30 m; 0.525-0.605 μm	30 m; 0.525-0.600 μm
Red	79 m; 0.630-0.690 μm	30 m; 0.630-0.690 μm	30 m; 0.630-0.690 μm	30 m; 0.630-0.680 μm
Near-Infrared	79 m; 0.760-0.900 μm	30 m; 0.775-0.900 μm	30 m; 0.775-0.900 μm	30 m; 0.845-0.885 μm
Short wave Ifrared 1	-	30 m; 1.550-1.750 μm	30 m; 1.550-1.750 μm	30 m; 1.560-1.660 μm
Short wave Ifrared 2	79 m; 2.080-2.350 μm[1]	30 m; 2.090-2.350 μm	30 m; 2.090-2.350 μm	30 m; 2.100-2.300 μm
Long wave Infrared 1	-	60 m; 10.00-12.50 μm	60 m; 10.00-12.50 μm	100 m; 10.30-11.30 μm
Long wave Infrared 2	-	-	-	100 m; 11.50-12.50 μm
Panchromatic	-	-	15 m; 0.520-0.900 μm	15 m; 0.520-0.900 μm

Note: [1]Only Landsat 3 had a working band in this spectral range

The second generation of Landsat satellites started in July 1982 with the launch of Landsat 4. At present time, Landsat 4 and Landsat 5 stopped their activity, while the launch of Landsat 6 was non-successful. Landsat 7 and Landsat 8 were launched in 1999 and 2013, respectively – both of them operate until now. They acquire imagery in several spectral bands with a spatial resolution ranging from 30 m till 100 m, while there is also one panchromatic band with the resolution of 15 m (see Table AT.3 for working bands of both missions).

Another type of middle resolution imagery applied in our studies is ASTER, which means Advanced Spaceborne Thermal Emission and Reflection Radiometer. This mission was launched in 1999 as part of NASA's Earth Observing System (EOS). It has a 705 km flight elevation, sun synchronous orbits and 16 days returning time period. This mission is equipped by three sensors surveying temperature, radiation and reflection from the Earth surface. It was lauched to assist scientists and society in surveying the changes on the Earth surface, ocean and lower layer of atmosphere. One of the main monitoring targets of this mission is the global carbon cycle which is tracked by a study of a relationship between human activity and nature.

Table AT.4 lists the sensors and working bands of ASTER mission. It has 15 spectral bands, while one, called 3B, gives a stereoscopic possibility in combination with the 3N band. Our studies employ this possibility to reconstruct a DEM of the target area, which is later applied to landslide susceptibility/hazard mapping.

Table AT.4: Spectral bands of ASTER mission (www.asterweb.jpl.nasa.gov).

Spectral range/Sensor	Spectral band	Spectral range, μm	Spatial resolution, m
VNIR (visible and near unfrared range)	1	0.52-0.60	15
	2	0.63-0.69	
	3N	0.78-0.86	
	3B	0.78-0.86	
SWIR (short-wave infrared range)	4	1.60-1.70	30
	5	2.145-2.185	
	6	2.185-2.225	
	7	2.235-2.285	
	8	2.295-2.365	
	9	2.360-2.430	
TIR (thermal infrared range)	10	8.125-8.475	90
	11	8.475-8.825	
	12	8.925-9.275	
	13	10.25-10.95	
	14	10.95-11.65	

Figure AF.17 compares the spectral bands of Landsat 7 (ETM+ sensor) and ASTER missions. As it can be seen, these two missions are complementary to each other. In the VNIR range ASTER has improved spatial resolution, while Landsat 7 has a panchromatic band in this range. ASTER imagery proposes higher spectral/spatial resolution in the SWIR and TIR ranges, while Landsat 7 gives more generalized information in these ranges. A big advantage of ASTER mission in comparison to Landsat 7 is a stereoscopic option provided by 3N and 3B bands.

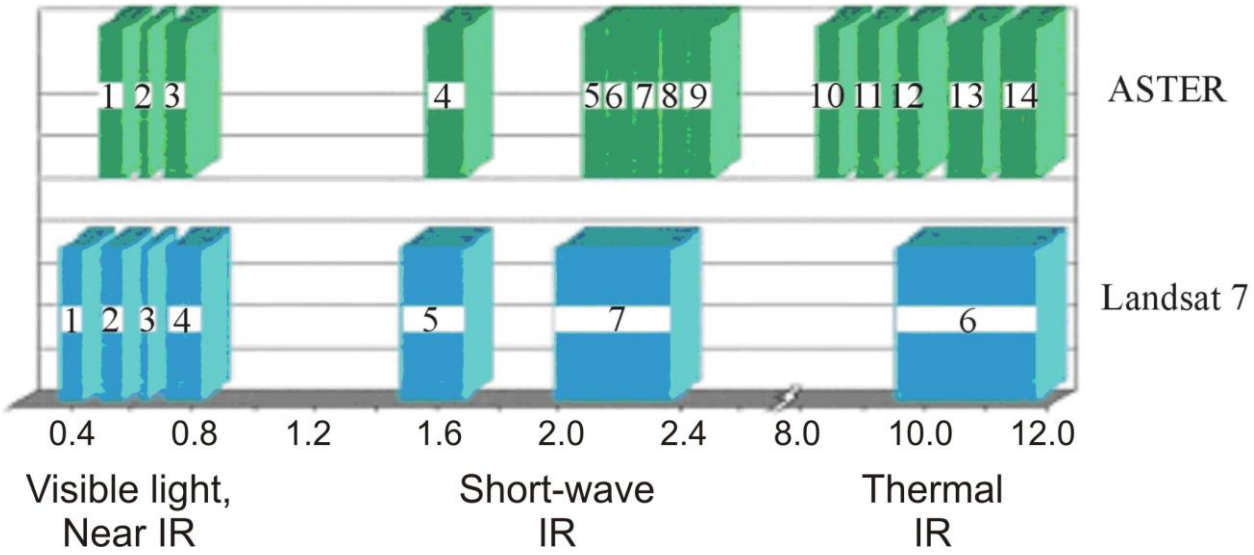

Figure AF.17: Comparison of spectral bands for ASTER and Landsat 7 missions (courtesy of NASA LP DAAC).

ASTER is one of the pioneering missions which showed that lithological mapping in the vegetation-free areas can be based on the spectral reflectance curves of rocks/lithologic units (Rowan et.al., 2001). For example, mapping of clays, carbonates, hydryd sulphats and iron oxide minerals can be based on their reflectance/absorbtion properties in the VNIR/SWIR ranges. Rowan et al. (2001) and Ellis (1999) show that ASTER spectral bands 10, 11 and 12 in TIR range can provide good indicators for such a basic minerals, like quartz and feldspar.

I.5.2.3 High resolution imagery: Quickbird and SPOT

The high resolution (HR) satellite imagery is characterized by a spatial resolution of less than 10.0 m. At present time, there are several RS missions acquiring HR imagery - they include, e.g., GeoEye, Ikonos, Pleiades, WorldView, RapidEye among others. This imagery is widely applied in the city planning, buisness and environmental tasks. Their application can be especially important in those earth sciencies which study small-scale events/processes.

One example of such RS missions is presented by Quickbird which is operated by DigitalGlobe. This mission was launched in 2001 and stopped its operation in the beginning of 2015. It had an operational altitude of 482 m, sun-synchronous orbits and a periodicy of the imagery acquisition around 1-5 days, depending on the site location. The spatial coverage of single image is 18x18 km.

Quickbird mission offers the imagery with sub-meter resolution, high geolocational accuracy, and large on-board data storage (www.digitalglobe.com). There are four spectral bands with a spatial resolution of 2.44 m (blue:0.45–0.52 μm; green: 0.52-0.60; red: 0.63–0.69 μm; near IR: 0.76-0.90 μm). Additional panchromatic band (0.445–0.90 μm) has a finer spatial resolution of 0.61 m.

At present time, the Quickbird imagery is applied in such research domains as land cover/land use mapping, infrastructural planning, lifeline monitoring and environmental studies. For example, Schlögel et al. (2011) apply the multi-temporal Quickbird imagery to identify and map landslide events.

Another example of the high resolution imagery is presented by SPOT. This mission was launched in 1982 and included seven satellites out of which three are still operating (SPOT 5, 6 and 7). The specifications of the imagery acquired by all gererations of SPOT satellites are presented in Table AT.5. As it can be seen, compared to the first generation, the latest SPOT satellites have a significantly improved spatial resolution in both multispectral and panchromatic bands (compare those of SPOT 1-4 with SPOT 6,7 in Table AT.5).

Thanks to these improvements, the latest imagery can be classified as high resolution data, while the older imagery (SPOT 1-4) is still characherized by the middle scale spatial resolution. Another significant improvement is related to the stereoscopic option included in SPOT 5.

Table AT.5: The spectral properties and spatial resolution for the imagery acquired by different SPOT satellites (www.eoedu.belspo.be).

	Visible High-Resolution Sensor (HRV); (Resolution; spectral range)	Visible&Infrared High-Resolution Sensor (HRVIR); (Resolution; spectral range)	High-Resolution Stereoscopic (HRS); (Resolution; spectral range)	New AstroSat Optical Modular Instrument (NAOMI); (Resolution; spectral range)
Missions	SPOT 1, 2, 3	SPOT 4	SPOT 5[1]	SPOT 6, 7[1]
Blue	-	-	-	6 m; 0.45-0.52 μm
Green	20 m; 0.50-0.59 μm	20 m; 0.50-0.59 μm	10 m; 0.50-0.59 μm	6 m; 0.53-0.59 μm
Red	20 m; 0.61-0.68 μm	20 m; 0.61-0.68 μm	10 m; 0.61-0.68 μm	6 m; 0.62-0.69 μm
Near-Infrared	20 m; 0.78-0.89 μm	20 m; 0.78-0.89 μm	10 m; 0.78-0.89 μm	6 m; 0.76-0.89 μm
Middle Ifrared	-	20 m; 1.58-1.75 μm	20 m; 1.58-1.75 μm	-
Panchromatic	10 m; 0.50-0.73 μm	10 m; 0.61-0.68 μm	2.5 or 5.0 m; 0.51-0.73 μm	1.5 or 2.0 m; 0.45-0.75 μm

[1] Stereoscopic option is included

At present time, SPOT mission provides three general types of products: orthorectified multispectral imagery (SPOTView ortho), natural-colour compositions (SPOTMaps) and 3D products automatically built from the stereoscopic pairs (SPOT DEM). For the territory of Kyrgyzstan the SPOTView ortho and SPOT DEM data are particularly interesting, as these products cover almost the entire territory of the country. For instance, the SPOT DEM is used in our 3D modelling studies performed for the Min-Kush target area.

I.5.2.4 Data analysis and Remote Sensing software

The interpretation of RS imagery is based on numerous image analysis/processing techniques. They are targeted at an extraction of a specific information and a choice of certain tool depends on the goals of each individual project. The list of the most wide-spread techniques includes expert-based interpretation, supervised/unsupervised classification, multiband transformation and spatial topographical analysis (Schowengerdt, 2006).

Through expert-based interpretation the investigator manually maps/identifies different features/properties from the analysed imagery. This activity is performed through the analysis of true-colour or pseudo-colour imagery. The true-colour imagery, otherwise called true-colour composition, corresponds to a natural colour rendition, which means that the colours in imagery appear the same way as it can be seen in reality. The pseudo-colour composition, in contrast, has non-natural colour rendition, when, for example, the displayed red colour represents the spectral band different from the one acquired in the range of red light.

Table AT.6 lists the examples of the most wide-spread application areas for the spectral bands of Landsat TM imagery (see a more detailed specifications for the spectral bands in Table AT.3). For example, near-infrared radiation is totally absorbed by water - this feature is widely applied for the mapping of ocean-/sea-/river-side. In that application case, the Near-Infrared spectral image can be represented by any colour from RGB (red-green-blue) composition, and a lack of refraction in this pseudo-colour range allows the interpreter to distinguish pure water from other objects/materials in the analyzed imagery.

A similar feature is presented by the Short Wave Infrared 2 spectral band (see the one in Table AT.6). The hydrooxides in the hydrothermally-altered rocks strongly absorb EM radiation in this spectral range. Therefore, a mapping of these rocks can be based on this feature. The analogous interpretation proxy is applied in this case: the Short Wave Infrared 2 spectral image is displayed by any colour out of RGB set and a lack of refraction in the displayed pseudo-colour range indicates the presence of the hydrothermally-altered rocks.

Table AT.6: The examples of the application areas for the spectral bands of Landsat TM imagery (see a more detailed description of spectral bands in Table AT.3).

Spectral band	Wavelength, μm	Wide-spread application areas
Blue 2	0.450-0.515	- Bathimetric studies due to a maximum penetration through water; - Mapping of coniferous/deciduous vegetation;
Green	0.525-0.605	- Mapping of vegetation cover
Red	0.630-0.690	-Mapping of vegetation cover
Near-Infrared	0.775-0.900	-Mapping of vegetation cover; -Biomass studies; -Mapping of ocean/sea/riverside
Short wave Ifrared 1	1.550-1.750	-Study of soil moisture content; -Mapping of different vegetation types
Short wave Ifrared 2	2.090-2.350	-Mapping of hydrothermally-altered rocks
Long wave Infrared 1	10.000-12.500	- Study of soil moisture content; - Thermal mapping of rock/soil via the imagery acquired at nightime.

The supervised/unsupervised classification, multiband transformation and the mapping of spatial parameters can be integrated into a group of automatic processing techniques. These tools apply pre-defined algorithms of data processing/assembling which allow end-user to extract specific features from the analysed imagery.
The supervised/unsupervised classification groups the pixels of imagery into the clusters based on similarity of reflectance properties (Blaschke, 2010). The pixel clustering in supervised classification is driven by the user-controlled sampling, while unsupervised classification applies automatic sorting technique. Figure AF.18 presents an application example, where Heenkenda et al. (2014) applied the supervised classification of the aerial imagery to identify the mangrove species. In this case the authors apply a sampling of spectral data, which is supported by the field studies. As it can be seen, the supervised classification identifies five different species solely based on the reflectance properties.

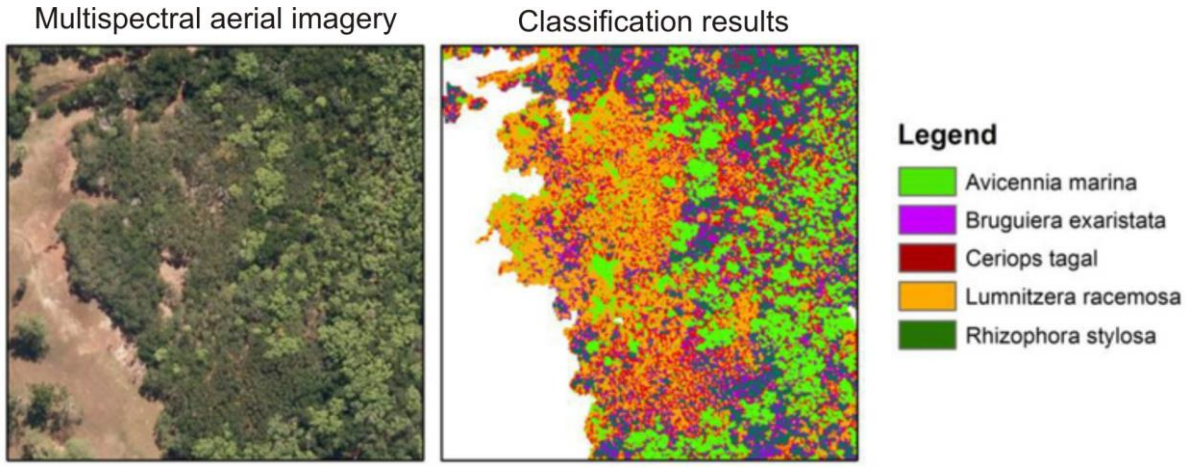

Figure AF.18: The example of the mangrove species identification applying multispectral aerial imagery and supervised classification technique (by Heenkenda et al., 2014).

Multiband transformation applies mathematic operations to combine multiple bands into one or more transformed bands (Nag and Kudrat, 1998). The applied band manipulations can include such simple techniques like addition, subtraction or ratioing, as well as more complicated algorithms like principal component analysis (PCA), tasseled cap (TC), intensity hue saturation (IHS), etc. The final goal of these transformations is to enhance interpretability of RS data and to better highlight the reflectance variability.
An application example of the transformed Landsat ETM+ data for the Xiemisitai target area, China is presented in Figure AF.19. Liu et al. (2013) applied this data to identify copper-mineralized zones as well as to improve existing geological map of target area. The original Landsat imagery was modified applying PCA, a decorrelation procedure which statistically reorganizes reflectance values of multiple spectral bands. The authors show that the results of PCA allowed them to clarify existing facial boundaries, refine fault/fold position and assisted in a discovery of copper-mineralized zones (see black dots in Figure AF.19).

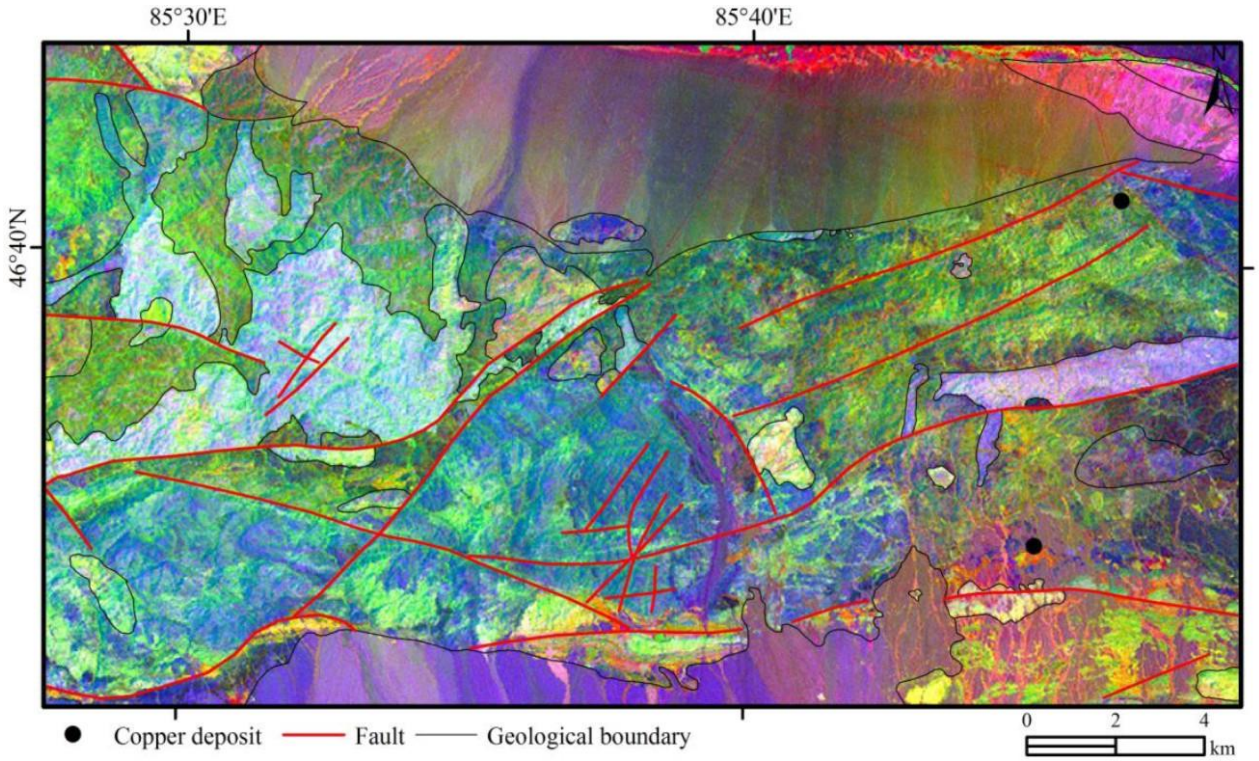

Figure AF.19: The PCA transformed Landsat ETM+ imagery for the Xiemisitai target area, China overlaid with the interpreted geologic/structural features and copper-mineralized zones (by Liu et al., 2013).

The specific case of multiband transformation, when the multiband rationing is applied is called as the spectral ratio or spectral index analysis. The core concept of this tool relies on a fact that each material/substance has unique reflectance, absorption and emission properties (Harris, 1987). To better demonstrate that, Figure AF.20 presents some sample reflectance curves, i.e., the plots of the reflectance values as a function of wavelength. Here, the reflectance curves for three rock types and vegetation are overlaid with the working bands of ASTER and Landsat TM missions. As it can be seen, the shape of the curves is varying. This variation shows a difference in a position of reflectance/absorption peaks.

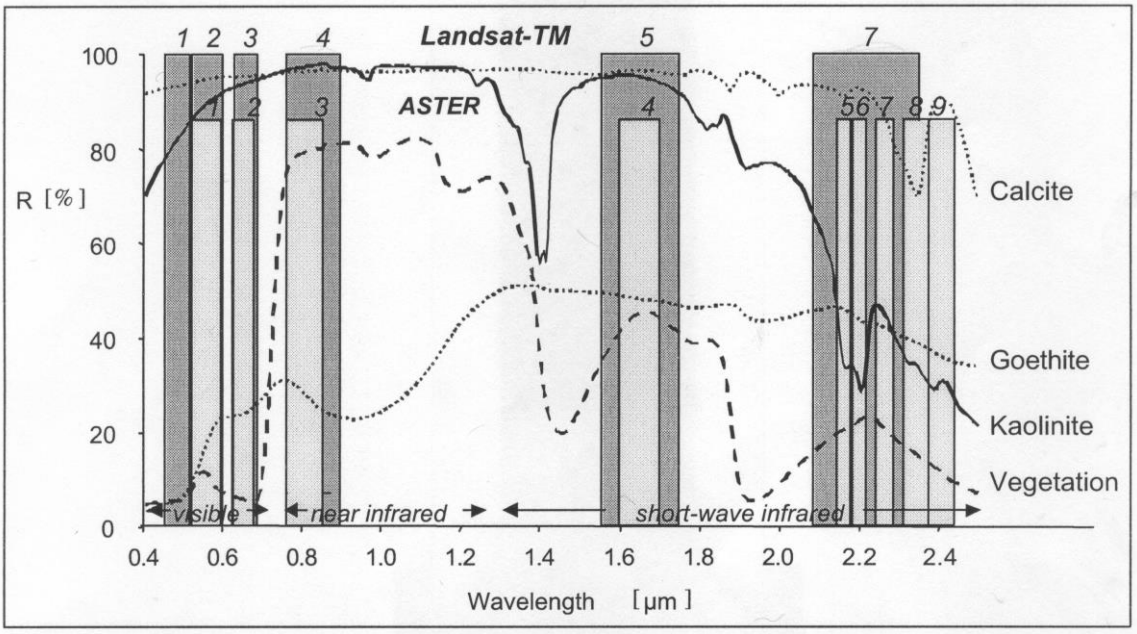

Figure AF.20: The reflectance curves for some rock types and vegetation overlaid with the working bands of the Landsat TM (dark-grey bars) and the ASTER (light-grey bars) missions (by Roessner et al., 2002).

The spectral index analysis applies the variation of the reflectance/absorption features to discriminate different materials/substances. This discrimination is based on a ratio between spectral reflectance values. For example, the ratios between short-wave infrared and near-infrared reflectance values is applied for a mapping of clay and ferrous minerals, while the ratio between red and blue light reflectance values detects the iron oxides. The ratios between reflectance values in red light and short-/thermal-infrared radiation are applied for identification of the burned areas, as well as for a mapping of forest fires.
Normalized Difference Vegetation Index (NDVI) is among the list of the most commonly applied spectral ratios. Its rationale employs a specific feature of healthy vegetation, which normally has 5-7 times more reflectance in the range of the near infrared radiation comparing to one in the range of red light. This feature is applied to map the richness of the vegetation cover and the calculation of NDVI is based on the next expression:

$$NDVI = \frac{IR - R}{IR + R} \qquad \text{(AE.2)},$$

where IR is the reflectance value in the infrared range and R is the one for the range of red light. As Figure AF.20 shows, IR corresponds to Band 4 for Landsat TM and Band 3 for ASTER, while R stands for Band 3 (Landsat TM) and Band 2 (ASTER).
According to Equation AE.2, NDVI values are ranging between -1 and 1. The highest positive values of NDVI indicate thick and healthy vegetation, while negative values of this index show an absence of it. Figure AF.21 demonstrates the application example, where the high-resolution Ikonos imagery is applied for the biomass studies performed via NDVI analysis (Tapiador, 2009). As it can be seen in Figure AF.21b, vegetation-free areas have negative values of NDVI, while the highest positive NDVI values are revealed for the cultivated croplands. The results of the study allowed the author to estimate a total biomass production and helped him detect the sites where the irrigation management was ineffective. Due to its simplicity and effectiveness, NDVI analysis is widely applied in numerous domains, including forestry, environmental/biological studies as well as agriculture, urban management/planning, etc.

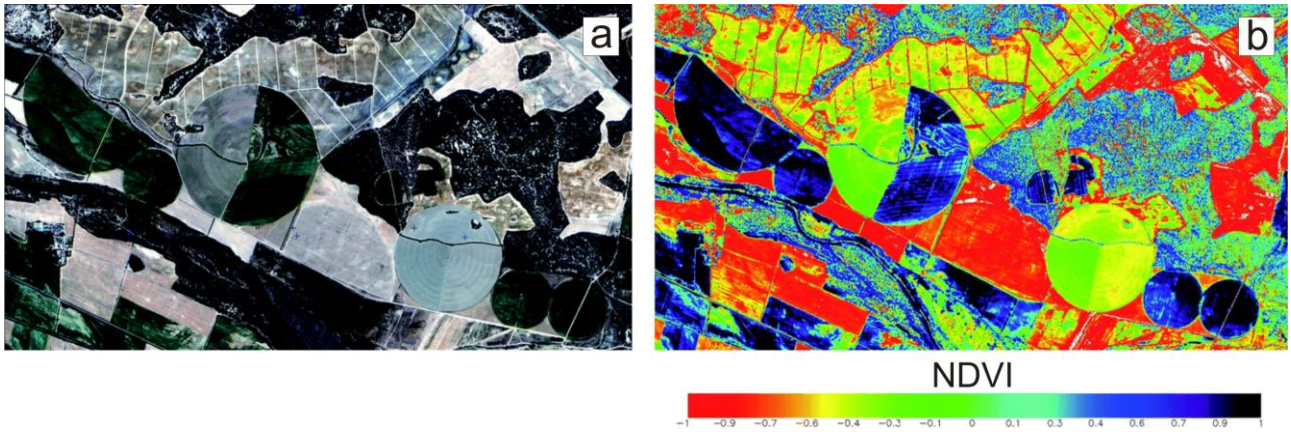

Figure AF.21: (a) True-colour composition of Ikonos imagery and (b) NDVI map applied for the biomass assessment studies (Tapiador, 2009).

Another commonly applied processing technique is represented by the spatial topographical analysis. This tool works with 3D topographic data, otherwise called as DEM or DTM (Digital Terrain Model). These data can be freely available or supplied as commercial products. The examples of the free-of-charge data are presented by GTOPO30 (approx. 1 km of resolution), SRTM DEM (formely near 90 m, now mostly with 30 m of resolution) and ASTER DEM (around 30 m of resolution). The commercially-supplied DEMs are mainly characterized by finer resolution, like 20 m for SPOT DEM, 12 m for TerraSAR-X and submeter resolution for national lidar datasets. A user-controlled DEM reconstruction can be performed with the help of specialized software – it is the case for the the aerial DEMs and radar data. The last technique applies very sophisticated principle of 3D data acquisition/processing, therefore, it demands a deep knowledge and interpretation experience. A deep overview and detailed analysis of radar techniques can be found at Massonnet and Feigl (1998), Burgmann et al. (2000) and Hanssen and Ramon (2001).

An important analysis option, provided by 3D topographic data, is a possibility to regionally map such important morphologic settings, as slope angle, slope aspect, curvature, etc. It presents a special interest to landslide studies, as landslide susceptibility/hazard mapping often employs this layers as input data. 3D topographic data are widely applied in other domains, especially 3D GIS applications, like 3D geological modelling, mineral prospecting/mining, urban planning/construction, etc.

According to the Global Marketing Insights, Inc. (2005) there are several tens of specialized codes which process/analyze RS data. The list of the most commonly applied solutions includes ERDAS Imagine, Mapinfo, ERMapper, ENVI, ESRI and AutoDesk. In this list only ERDAS Imagine and ENVI are considered as specialized RS applications, while ERMapper, ESRI, Mapinfo and AutoDesk are more refferred to be the GIS-based platforms. It shows that some processing techniques can be performed within conventional GIS codes. This is the case for some simple tools, like, e.g., expert-based interpretation and spectral index analyses. More sophisticated analyses require an application of specialized codes. For example, image classification and sophisticated multiband transformation can only be performed within customized RS applications, like ERDAS Imagine and ENVI.

Parts of the spatial analysis techniques and types of remote sensing data that were introduced here have been applied to the landslide hazard mapping in an area of Kygyzstan that has been one of the most impacted by mass movements in this country over the past 25 years: Mailuu-Suu.

II. The Mailuu-Suu target area

II.1 Kyrgyzstan

The Kyrgyz Republic, or Kyrgyzstan, is located in Central Asia and has common borders with Tajikistan, Uzbekistan, Kazakhstan and China (Figure AF.22). Almost the whole the territory of country is occupied by the Tien-Shan Mountains which are part of the Himalayan orogenic belt that resulted from a Cenozoic collision of the Indian and Eurasian plates (see more details in next section). From a geographic point of view the Tien-Shan is delimited in the north by the relatively flat Kazakh platform and in the south by the Tarim Basin and the Pamir mountain belt. The mean altitude of the Tien-Shan is 2750 m, while the highest peak, called as the Victory Peak, has an altitude of 7429 m. Morphologically, the Tien-Shan consists of a set of EW-trending subparallel mountain ranges (4000-7000 m of altitude) separated by intra-montane basins (1000-2500 m of altitude).

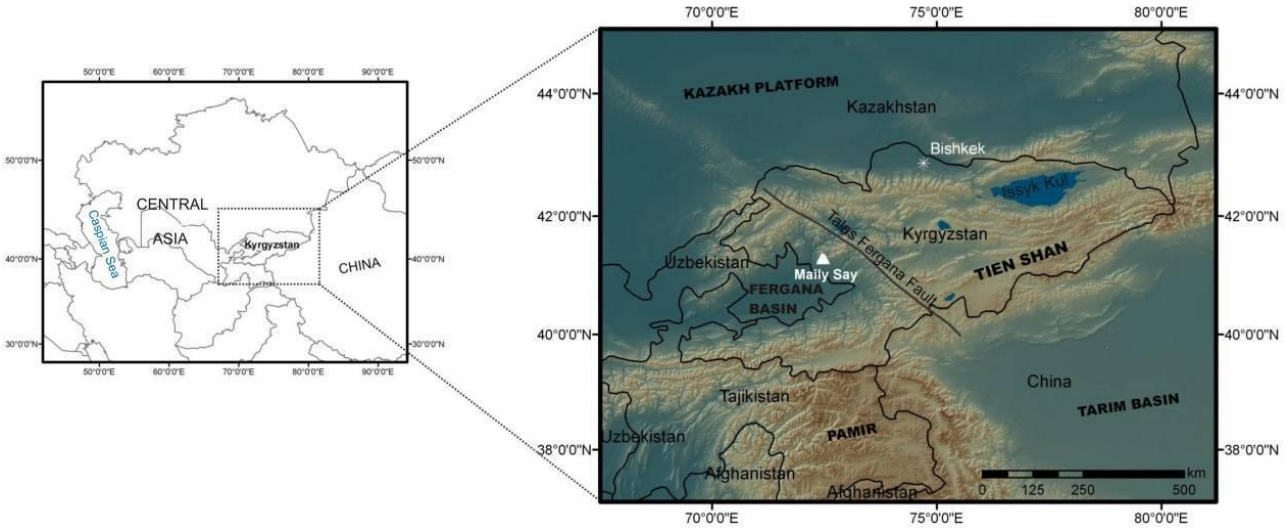

Figure AF.22: The general map of Central Asia together with zoom to Kyrgyzstan, indicating the location of the capital (Bishkek) and the Maily-Say City (by Schlögel et al. 2011).

The territory of Kyrgyzstan is subjected to a high level of natural risk due to its mountain topography, active tectonics and geology. The most critical natural hazards are earthquakes, landslides and flooding. Impacts of natural hazards clearly hamper the social and economical development of the country. The average annual damage related to the negative effects of the natural hazards is estimated at about 35 million USD - it becomes a major problem for the state budget, suffering from the lack of necessary financial resources (GO-ELS Ltd., 2008).

Mass movements are among the most damaging types of the natural hazards. Approximately 7.5% of the whole country territory are exposed to landslide hazards, while southern Kyrgyzstan is marked by the highest level of landslide hazard and risk (Torgoev et al., 2005). According to Alioshin and Torgoev (2000), during the period from 1993 to 2005 more than 300 large-scale landslide events have been registered here.

Southern Kyrgyzstan has several hot-spot areas, where landslides may produce significant damage and trigger environmental problems. Maily-Say City situated in the Mailuu-Suu River Valley is one example of such areas (see a location in Figure AF.22). Here, the landslides not only directly affect the population, but also pose a threat to the stability of uranium tailings, the results of former mining activity. The issues related to landslide risk management in this area attract significant attention of the responsible agencies and society. The selection of this area as research target for this thesis was partially based on these considerations: our studies would produce both scientific and practical results which may later support mitigation of the landslide risk. The high rate of landslide activity here is strongly related to the neo- and seismotectonic settings. Therefore, the regional overview of these settings is presented in the next section.

II.2 Neotectonic and seismic settings

Kyrgyzstan is situated in an active collision zone between the Indian plate and the stable Eurasian platform (Figure AF.23). This collision started 55 Ma ago, while most of the Cenozoic belt of the Tien-Shan was

formed during the last 10 Ma (Molnar and Tapponnier, 1975). In the first collisional stage (35-20 Ma ago), the Indian plate thrusted under the Tibet and Pamir platforms, inducing the growth of the Himalayan Mountains, uplift of the Tibetan Plateau and subsidence of the Tarim and Fergana depressions (see location in Figure AF.23). In the second stage (20-11 Ma ago) the Tarim plate thrusted under the central and eastern parts of the southern Tien-Shan, triggering its uplift.

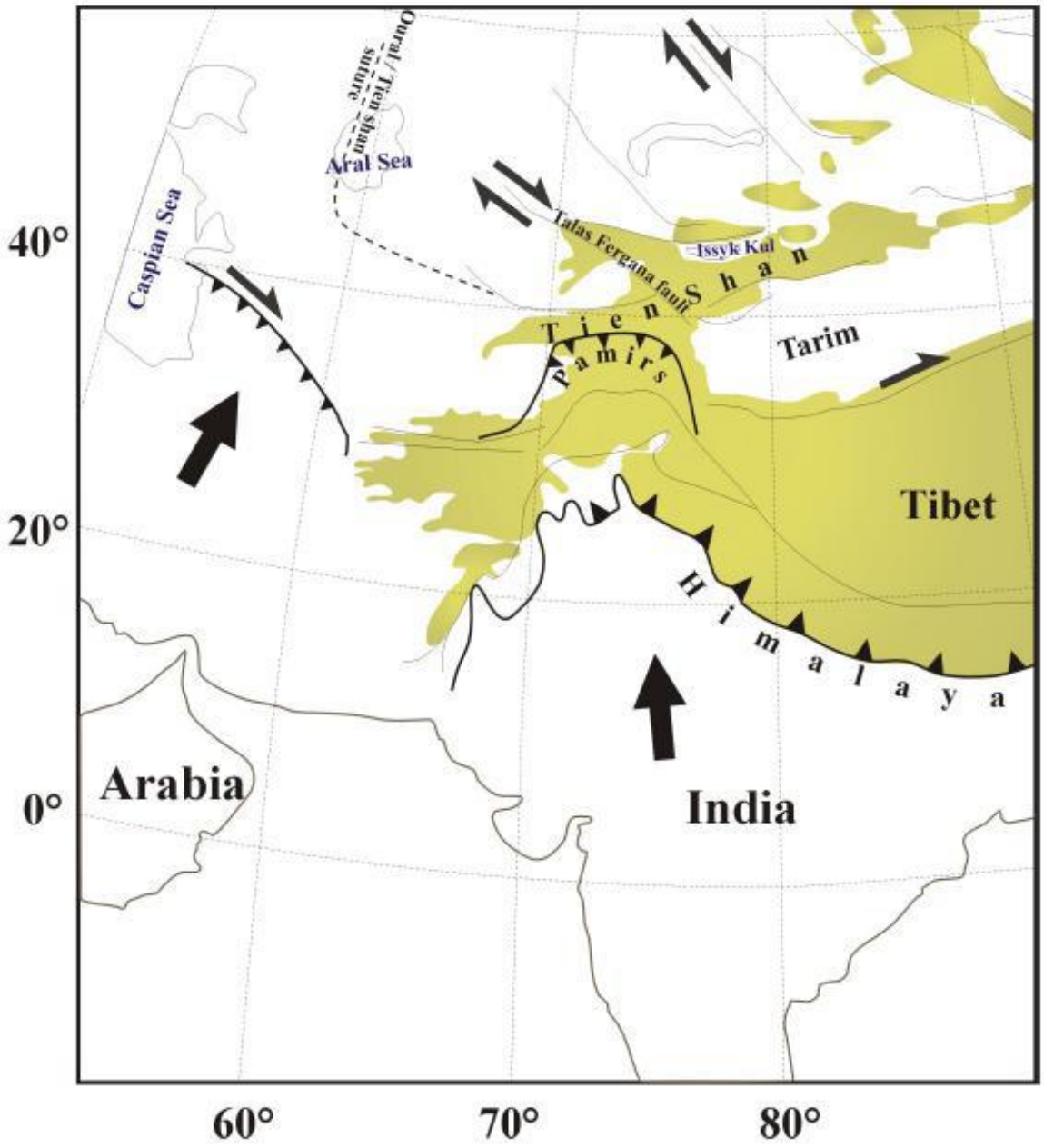

Figure AF.23: The schematic tectonic map of the Tien-Shan - Pamir – Himalaya zone with the areas of more than 2000 m altitude shaded in green-brown colour. The large arrows indicate the current motion of India (and Iran) in relation to Asia (modified by Havenith 2002, from Bossu and Grasso, 1996).

The active orogenic processes appeared in the second half of the Cenozoic Era. According to Molnar and Tapponnier (1975), the tectonic settings and deformation rates changed very drastically starting from the Middle Oligocene. This stage is characterized by a high rate of tectonic deformations, active faulting and folding leading to sedimentation of thick Tertiary molasses layers. Due to a change of the tectonic settings, in the north-eastern part of the Fergana Valley the rate of the accumulation and uplift exceeded the rate of denudation.

The highest rate of the tectonic activity was in the Miocene. The Pliocene-Quaternary uplift of the Tien-Shan had a strong impact on the distribution of the stress induced by the India-Eurasia collision at a rate of 50 mm/year, principally N-S oriented. During the third stage (10-3 Ma ago), dextral strike-slip movements along the Talas-Fergana fault crossed the Tien-Shan from SE to NW at a rate of about 10-15 mm/year. The reactivation of the Issyk-Kul microcontinent and its surroundings in the northern Tien Shan started to form the mountain ranges. Finally, the interplay of the Tarim and Pamir convergence with the Tien-Shan (about 3 Ma ago) gave rise to the maximum uplift and formation of the modern Tien-Shan in its present shape, while the dextral strike-slip displacement along the Talas-Fergana Fault Zone is now reduced to 1 mm/year (Buslov et al., 2007). It led to the formation of the existing topographic/morphologic patterns which represent the basic reason for the present-day high landslide activity in many parts of the Tien Shan.
The Quaternary tectonic deformations formed of the modern faults within the rims of the Fergana Valley. The high rates of tectonic uplift resulted in an intense deposition of the proluvium, colluvium and aeolian sediments (Rygkov, 1963). The intense uplift of some areas has also resulted in their glaciation, which is witnessed by the thick moraine deposits in the different parts of the south-eastern Fergana Valley. Schulz (1947) studied the unconformities in conglomerates layers and revealed five main tectonic phases in the Quarternary period. These tectonic phases are summarized into one single folding process started in the period between the Neogene and Quarternary. The folding process was accompanied by a high rate of uplift along in the rims of the Fergana Valley. The erosional depth of the Pliocene valleys indicates that the uplift amplitude from the Pliocene until now reached the value of 1000 m. Thus, the erosional patterns that are normally typical for the low-altitude areas can now be found at an elevation of 2000 m – it evidences the high-rate uplift occurred during a short period of geological time. Nikitin et al. (1974) indicate that the maximum uplift rates are found in the source area of the Sarydariya River with an estimated value of the uplift of not less than 0.4 cm/year.
Due to the high rate of tectonic deformation in recent geological periods, the whole territory of Kyrgyzstan, including the rims of the Fergana Valley, is characterized by intense seismicity. Several strong earthquakes struck the Kyrgyz part of the Tien-Shan (Figure AF.24) in the last century, including: the M=8.2 Kemin earthquake in 1911, the M=7.6 Chatkal earthquake in 1946 and the Ms =7.3 Suusamyr earthquake in 1992 (Abdrakhmatov et al. 2003). The instrumental observations show that the target area is characterized by a moderate to high seismic hazard with the prognostic seismic intensity of 8-9 on the MSK-64 scale (Djanuzakov et al., 1996). These studies indicate that the recurrence interval for such seismic events is between 500 and 1000 years.

Figure AF.24: Shaded relief map of the Tien-Shan mountains (from NOAA DEM) with location of Kyrgyzstan, neighboring countries, Talas-Fergana fault, the Chatkal earthquake (Ms =7.6, 1946), the Suusamyr earthquake (Ms =7.3, 1992), the Kemin earthquake (Ms =8.2, 1911) and the Ms =6.2 event in 1992 that occurred in the northern part of the Fergana Basin, 30 km south of Maily-Say (by Havenith et al., 2006).

The last strong earthquake near the Fergana Basin, the Ms=6.2 Kochkor-Ata earthquake of May 15, 1992, hit also the Mailuu-Suu target area. It was located about 30 km south from the Maily-Say City (see location in Figure AF.24) and is supposed to be a factor, which triggered the reactivation of several mass movements (Torgoev et al., 2005). The triggering impact together with the basic characterization of the target area are analysed more in detail in the next sections.

II.3 The Mailuu-Suu target area: mining history and environmental conditions

Maily-Say City and the Mailuu-Suu River Valley are situated near the northern border of the Fergana Valley. The target area is characterized by a combination of geologic, tectonic and climatic settings favouring intense landslide activity (Alioshin and Torgoev 2000; Torgoev et al. 2002). The biggest concern is related to the high probability of environmental pollution, possibly triggered by the landslide activity. The protective infrastructure of some radioactive tailings might be impacted by landslide failure or could be eroded by river flooding, possibly induced by downstream landslide dams or upstream breaching of such dams. Some of these sites are the sources of a gradual environmental pollution – due to these problems Maily-Say City has once been ranked as one of the ten most polluted sites around the world (Blacksmith Institute, 2006).
The environmental problems in the Mailuu-Suu River Valley originate from the past uranium mining and the associated with the urban development. The first stage of the urbanization started from the oil mining initiated in 1901. These findings gave the name to the city and river, as “mai” in Kyrgyz language means “oil” and “suu” means “water”. Another mining perspective appeared in 1929, when radium-hosting rocks were discovered in this area. Active uranium mining started in 1946 and lasted until 1968. It finally resulted in the creation of 23 uranium tailings and 13 waste dumps stored along the banks of the Mailuu-Suu River (Vandenhove et al., 2003). Presently, these storage sites are under the direct threat of destruction due to the river erosion, seismic impacts and gravitational mass movements – it can potentially lead to a radioactive pollution of the Mailuu-Suu River, flowing to the densely populated Fergana Valley (Alioshin and Torgoev, 2000).
Certain types of remediation activity have been initiated in some of the hazardous sites. It includes the sliding mass removal on the Tektonik landslide threatening to the tailings situated downslope (Minetti et al., 2002). The environmental risk at tailing №3 has been totally eliminated through relocation of the whole tailing to another place with safer geoenvironmental conditions (Kunze and Schmidt, 2008). Nevertheless, there are still several other sites where the negative natural impacts may cause significant environmental damage. The negative scenarios are illustrated by several cases. For example, the destruction of one tailing dam in 1958 brought intense river pollution; more recently, a landslide failure in 1994 caused 8 deaths, infrastructural damage and partial erosion of the tailing dam with following river pollution (Alioshin and Torgoev, 2000).

II.4 Landslide activity and its link with anthropogenic and environmental factors

Torgoev et al. (2005) studied several cases of the ancient slope movements in the target area. The authors show that the landslide position and their evolution are related to a combination of environmental factors, such as the lithology, tectonics, climatic settings and seismic activity. Alioshin and Torgoev (2000) further consider anthropogenic influences and the presence of very soft loess deposits as additional landslide triggering factors.
Figure AF.25 presents the topographic map of the target area with outlines of identified landslides and the underground uranium mining sites that had been active from 1946 until 1968. Alioshin and Torgoev (2000) indicate that very large areas (around 2.2 km^2) were affected by mining during these 22 years. A large volume of the rock material (more than $7*10^6$ tons) was removed, transported, partially processed and deposited (see location of the uranium tailings in Figure AF.25). Torgoev and Alioshin (2009) list several

cases of earth subsidence around underground mining sites, which led to slope instability problems. The list of the negative impacts originating from oil/coal/uranium mining also includes numerous cases of slope undercutting, slope loading and underground water inflow.

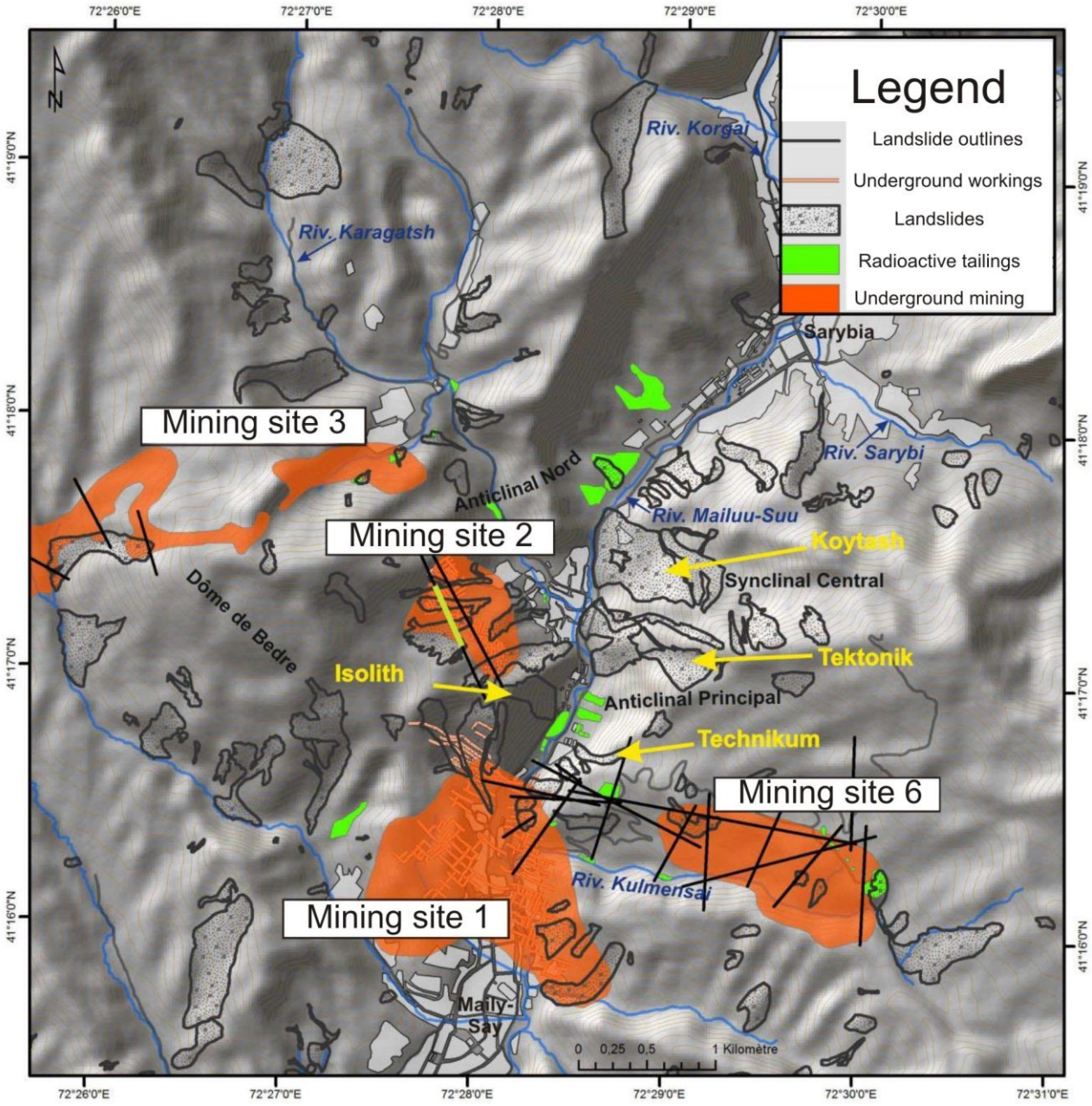

Figure AF.25: Topographic map and hillshade of the 20 m SPOT DEM of the target area with the location of landslides, underground mining sites and tailings (by de Marneffe, 2010).

According to Torgoev and Alioshin (2009), the uranium mining activity brought the most negative anthropogenic impact. The Cold War between USA and USSR resulted in a high pace of the mining which disregarded the natural hazard/risk components. This finally led to a situation, when almost half of the radioactive tailings (11 out of 23) are under the direct threat of destruction through landslide failure or under the risk of river erosion due to river damming (see example in Figure AF.26). At present time, the society and state agencies are highly concerned about these issues, as landslide activity could finally result in the contamination of the Mailuu-Suu River.

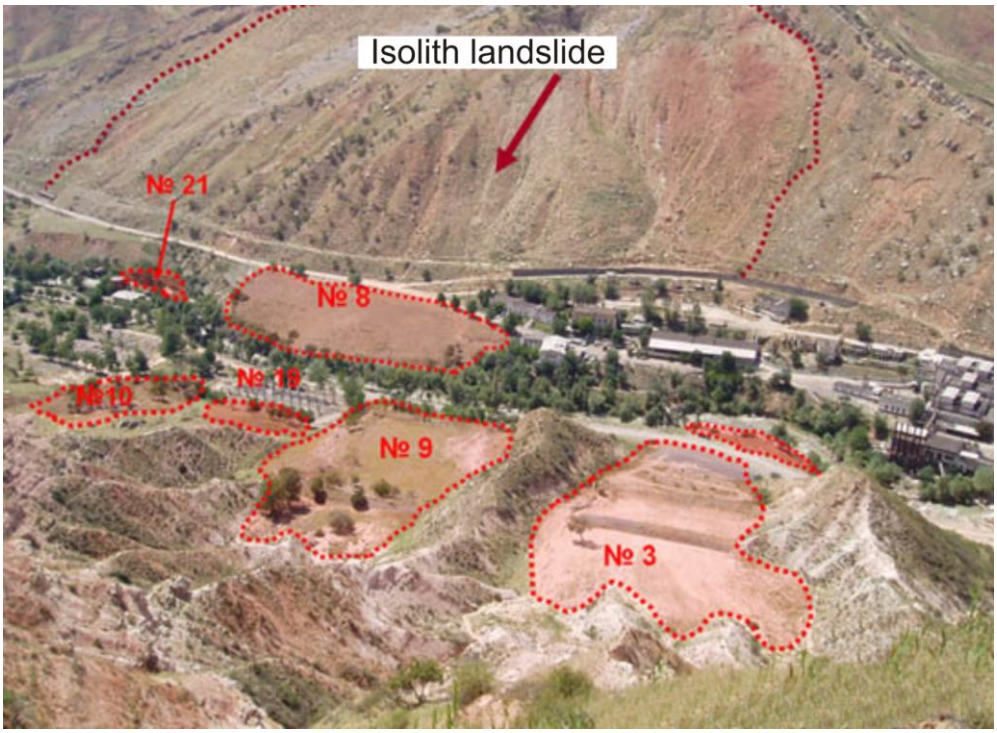

Figure AF.26: The radioactive tailings (red dotted outlines) situated in a narrow river valley, subjected to the negative impacts of the landslide activity (the courtesy of the Ministry of Emergency Situations Agency of Kyrgyzstan)

According to Alioshin and Torgoev (2000) and Torgoev et al. (2005) the seismic activity is among the most crucial factors triggering the landslide re-/activation (see those example below). The climatic settings are the next important factor affecting the rate of landslide activity in the target area (Alioshin et al., 2000). The climate of the Mailuu-Suu River valley is considered to be continental, marked by sharp temperature changes in the nocturnal-diurnal periods and with comparatively low precipitation rate (Gidrometeoizdat, 1989). The average annual temperature is around 12.0-14.5ºC, while the average annual precipitation rate is 463.2 mm. The maximum temperature values are recorded in July-August (30.0-36.0ºC), while the minimum ones are registered for December-January (down to -5.0 ºC). A comparative analysis of the landslide activity and average precipitation rates during the last 50 years (Figure AF.27) reveals a direct link between them (Havenith et al., 2006). The authors show that the peaks of landslide activity are observed during, or just after the years with abundant precipitation, such as in 1954, 1969, 1978, 1994 and 2003 (compare the data in Figure AF.27).

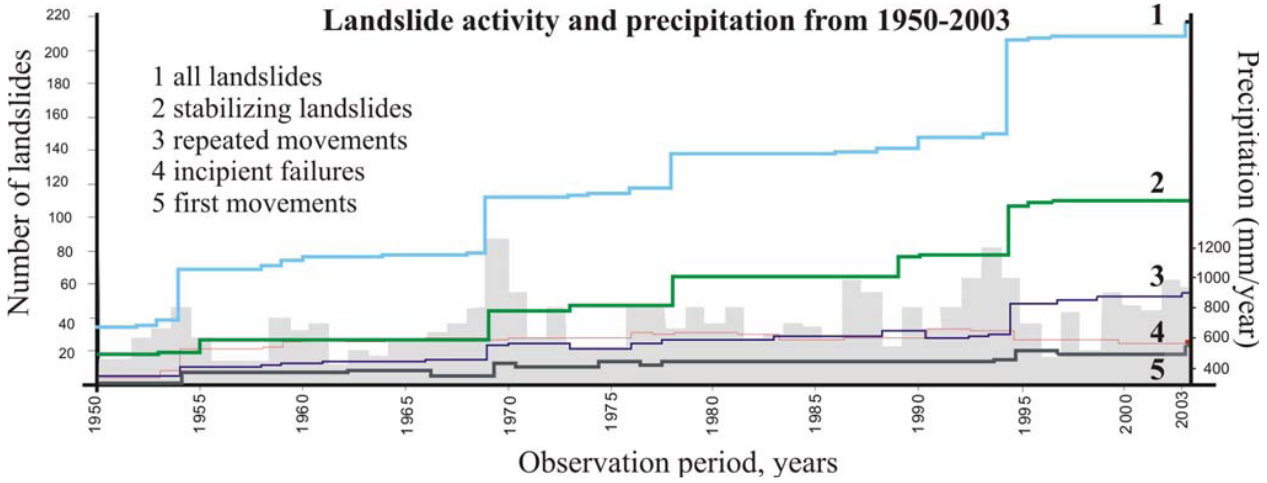

Figure AF.27: The plot of the landslide activity (a number of landslides) versus precipitation (grey) for the period between 1950 and 2003 (by Havenith et al., 2006).

The link between environmental factors and landslide activity has also been instrumentally studied. Alioshin and Torgoev (2000) and Torgoev et al. (2005) present results of extensometric measurements performed in several landslide sites over a period of 8 years (1996-2004). Figures AF.28b and AF.28c present the cumulative downslope displacement for the Upper Koytash landslide (see a location in Figures AF.25 and AF.28a) with overlays of the precipitation records and seismic events. As it can be seen, the rate of the sliding activity is the highest in mid-spring time, when the snow melting overlaps with the high precipitation rate. The authors show that the climatic triggering can be magnified in case of preceding seismic event, such as in the spring of 1998 (see the data in Figures AF.28b and AF.28c).

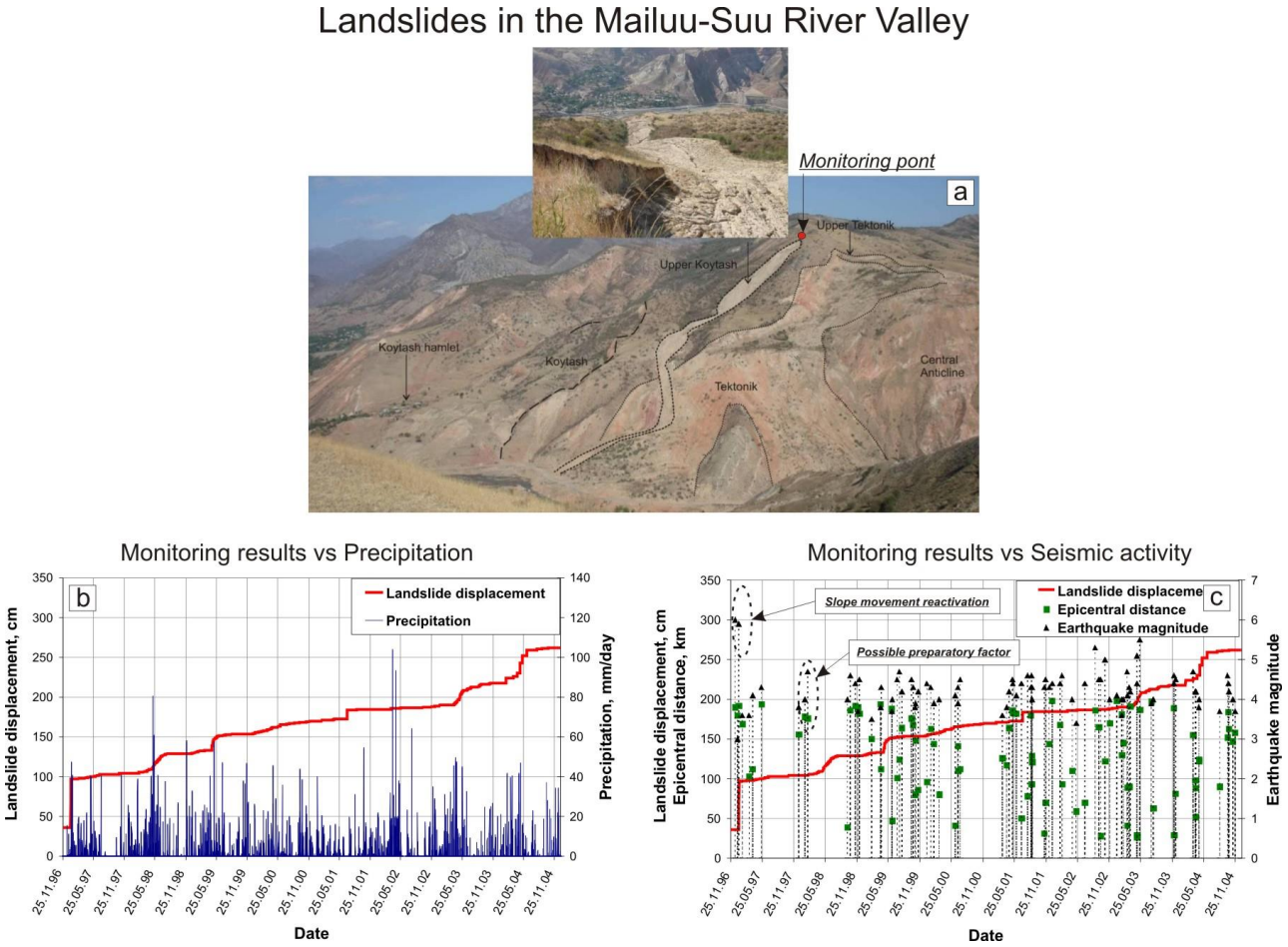

Figure AF.28: (a) General view (September, 2008) at the eastern slopes of the Mailuu-Suu River Valley with location of the Koytash, Upper Koytash, Tektonik, etc. landslides (the Upper Koytash monitoring area is marked by red point); (b) and (c) results of the Upper Koytash landslide monitoring (extensometric data) plotted versus the daily precipitation and seismic activity for a period from 25.11.1996 till 25.11.2004.

Figure AF.29 presents the cumulative displacement curves for the Tektonik and Isolit landslides (see their location in Figure AF.25). The displacement curves are overlaid with the data on precipitation, snow cover and seismic activity. The plots show that both landslides have the highest rates of downslope displacements in a spring time, such as it was for the Upper Koytash landslide. Alioshin and Torgoev (2000) note that the Tektonik landslide is more sensitive to seismic effects. This is due to combined morphologic (high elevation difference between toe and crest of ustable slope), lithologic (presence of Loess in the upper part of the landslide) and hydrogeological (high groundwater table) settings of this landslide. The authors suggest that the partial failure of the Tektonik landslide in 1992 was induced by the Ms=6.2 Kochkorata earthquake that had occurred seven weeks earlier. The Isolit landslide, in turn, is more sensitive to the underground water inflow related to the snow melting (compare the data in Figure AF.29a). This landslide is less sensitive to seismic effects, while some seismic triggering is still revealed in 1998 (see the displacement data in Figure AF.29b).

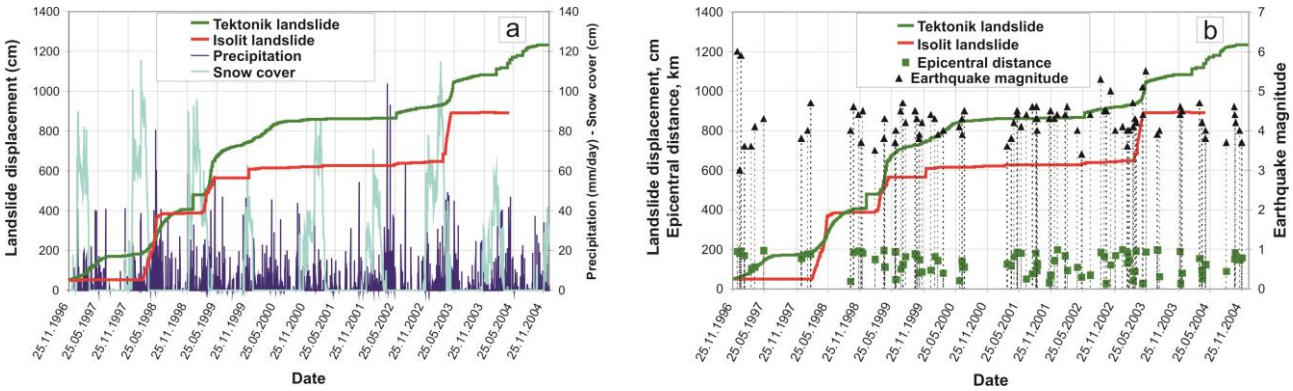

Figure AF.29: The results of the extensometric measurements for the Tektonik and Izolit landslides plotted versus: (a) daily precipitation and snow cover thickness; (b) seismic activity.

Alioshin and Torgoev (2000) highlight that among the list of the triggerring/affecting factors it is not possible to mark the most critical one. This is due to the fact that most known landslides in the target area are normally impacted by a specific combination of several factors and rarely by just one of them. For example, in case of the Technikum landslide (see location in Figure AF.25) the main reason leading to slope failure was anthropogenic impact (surface subsidence and road undercutting). Koytash landslide (see location in Figure AF.25), another critical mass movement in the target area, is strongly affected by groundwater flow and climatic effects. The instrumental recordings show that the higher parts of this deep-seated rotational slide are more impacted by the precipitation, while the lower parts are more impacted by the underground water inflow. The authors conclude that the landslide susceptibility/hazard mapping in the target area should involve a combination of the environmental factors. Those inputs for the mapping are documented in the next chapters, the first one presenting primary input, the landslide database, and the following ones analysing the related landslide susceptibility and hazards.

III. Landslide database

III.1 Methodology

The information about landslide evolution and landslide activity plays a significant role for the landslide susceptibility/hazard assessment. Guzzetti (2005) points out that any serious attempt to estimate landslide susceptibility/hazard/risk must begin with the collection of information on where these events are located and on how they evolve. This activity normally includes the mapping of the landslides, a retrospective research about their evolution and a collection of other information about the landslide activity and its impacts. These studies normally end with a compilation of the landslide events database, which summarizes all temporal and geographic information available for the landslides in the target area. The multitemporal landslide inventories are among the most widespread representations of this data. They are normally compiled on a GIS-based platform, when all existing information about the landslide evolution, the type of movement, the recorded impacts and other relevant information are attached as attributes.
In our research we adopt a similar idea of the landslide database compilation. The main types of the research activity include the compilation of the multi-temporal landslide inventories, the mapping of landslide types and the mapping of the landslide features (scarps and landslide outlines). Additional studies aim at identification of the landslide activity on the basis of multi-temporal Landsat and Quickbird imagery. Part of the landslide inventories are compiled from the analysis of aerial stereopairs. Some other inventories were compiled through the novel semi-automatic technique developed by Schlögel (2009). The mapping of the landslide types was provided by manual photointerpretation of the satellite imagery (Braun, 2010).
Several types of software are applied in our research (see Table AT.7). Correct georeferencing of landslide inventories was strongly focused, as these products resulted from different imagery. The latest and most precisely georeferenced inventories are considered as a basis for the geocorrection.

Table AT.7: Short description of software, data sources and tasks accomplished at the stage of the landslide database compilation.

Software	Utilized data sources	Tasks
ArcGIS	Multi-temporal landslide inventories, results of automatic landslide mapping and landslide activity detection	Landslide inventories compilation, spatial and geometric corrections, compilation of attribute information
ENVI	Quickbird imagery	Radiometric and geometric correction of imagery, pre-processing for the semi-automatic landslide mapping
SPSS (Clementine)	Postprocessed Quickbird imagery	Application of data mining for semi-automatic landslide mapping
Erdas Imagine	Landsat imagery	Landslide activity detection

III.2 Landslide inventories

Landslide inventories give basic information needed for landslide susceptibility and hazard mapping. They represent the simplest form of landslide mapping which indicates the location, outlines and, where known, the date of occurrence and the type of the mass movements (Hansen, 1984; McCalpin, 1984; Wieczorek, 1984). Guzzetti (2006) suggests that the procedure involved in the compilation of the landslide inventories depends on their purpose, the extent of the study area, the scale of the base maps and the availability of input data (satellite and aerial imagery). The main concept of a mapping activity is based on the idea that

landslides leave discernible signs, most of which can be recognized, classified and mapped in the field or from stereoscopic aerial photographs and satellite imagery (Turner and Schuster, 1996).
There are only limited case studies dealing with the landslide inventory compilation in Kyrgyzstan. Figure AF.30 presents a case study for the Central Tien-Shan area that was completed by Burette (2012). The mapping of the landslide outlines, landslide scarps and an identification of the different types of the mass movements was done on the basis of satellite imagery (mainly SPOT) available in the Google Earth software platform. The coverage of the studied area is approximately 130x230 km and includes the upper Mailuu-Suu River Valley (see the lower lef corner in Figure AF.30). This inventory was later included by Havenith et al. (2015a) into the large database of the landslide scarps and landslide outlines covering the territory of the whole Tien-Shan.

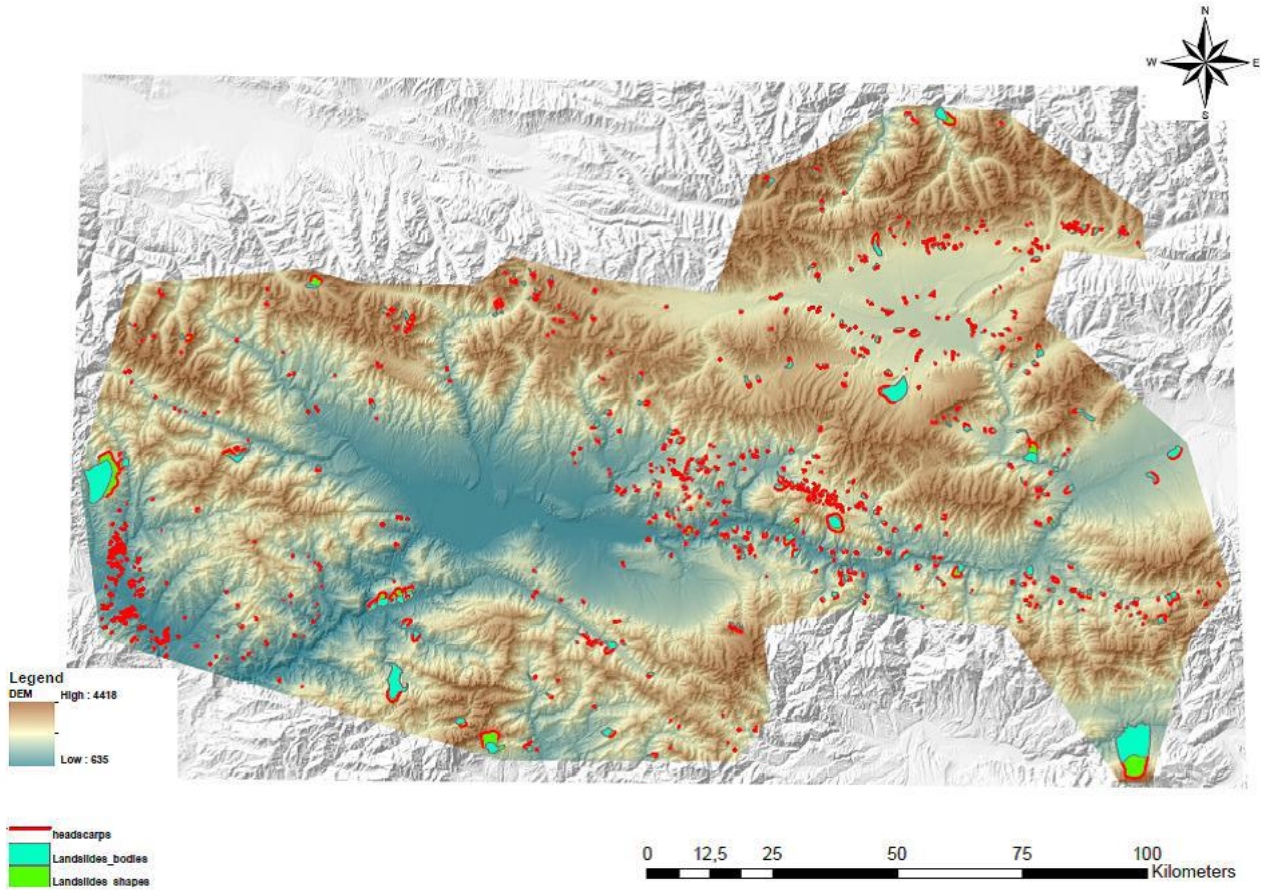

Figure AF.30: The results of landslide inventory compilation at regional scale using the Google Earth software platform; the size of the territory is approximately 130x230 km (by Burette, 2012).

The high-resolution satellite and aerial images were used to compile the landslide inventories in the Mailuu-Suu target area (see Table AT.8). The archival information, i.e. topographic maps and existing inventories, are also applied at this stage. The most recent inventory (for 2007) was checked by field studies (Schlögel et al., 2011).

Table AT.8: The data sources applied for the compilation of the multitemporal landslide inventories.

Year	Data
1962	Soviet maps, aerial photographs (1:25000), archival 1962 inventory
1984	Soviet maps, aerial photographs (1:33000) , archival 1977 inventory
1996	Soviet maps, aerial photographs (1:10000), archival 1977 inventory
2002	Satellite images (Quickbird)
2007	Satellite images (Quickbird)

The landslide inventory dataset consists of five inventories dating back to 1962 and covering the periods of 1984, 1996, 2002 and 2007 (Figure AF.31). All inventories contain only landslides that could be identified from imagery of a certain year and, thus, are likely to have been (re-) activated by the studied periods of time (ancient mass movements have not been included in those catalogues). Landslide inventories for the period between 1962 and 1996 were compiled through photointerpretation of aerial stereo-pairs, while those for 2002 and 2007 were compiled on the basis of the Quickbird imagery.

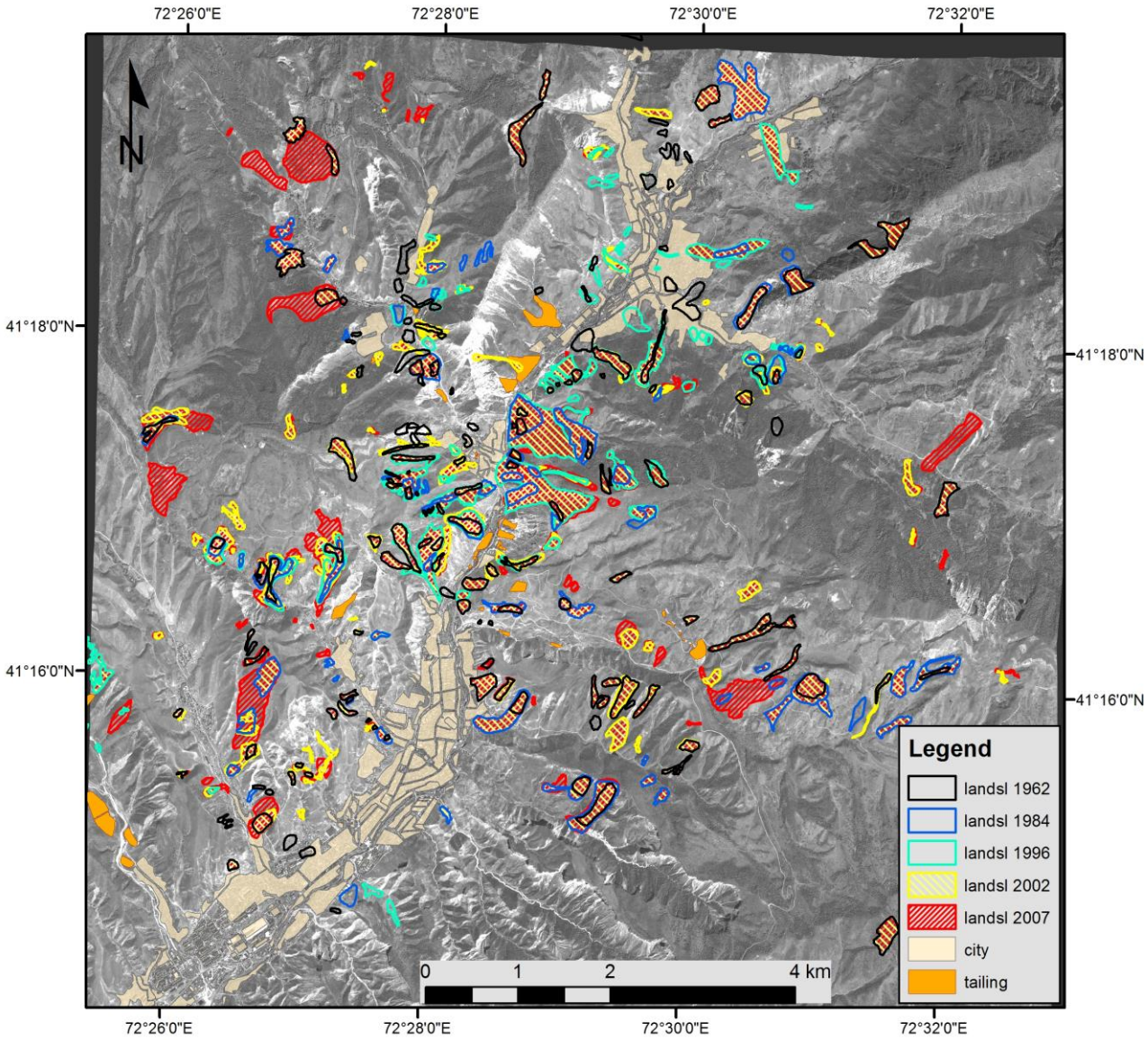

Figure AF.31: The landslide inventory dataset overlaid on Quickbird image (2002) with an indication of the urbanized territory and the radioactive waste tailings (by Schlögel et al., 2011)

The analysed imagery have different quality and acquisition scale (see Figure AF.32 and Table AT.8). The inventories for 1962, 1977 and 1996 were compiled by the Ministry of Emergency Situation of Kyrgyz Republic: the original inventories can be found in Havenith et al. (2006). In our mapping activity we corrected the inventory of 1977, which was finally replaced by a new one of 1984 based on the analysis of 1984 aerial imagery (Schlögel, 2009). The landslide scarp inventories for the same periods of time were also compiled. Each scarp basically represents the upper third of the whole landslide outline.

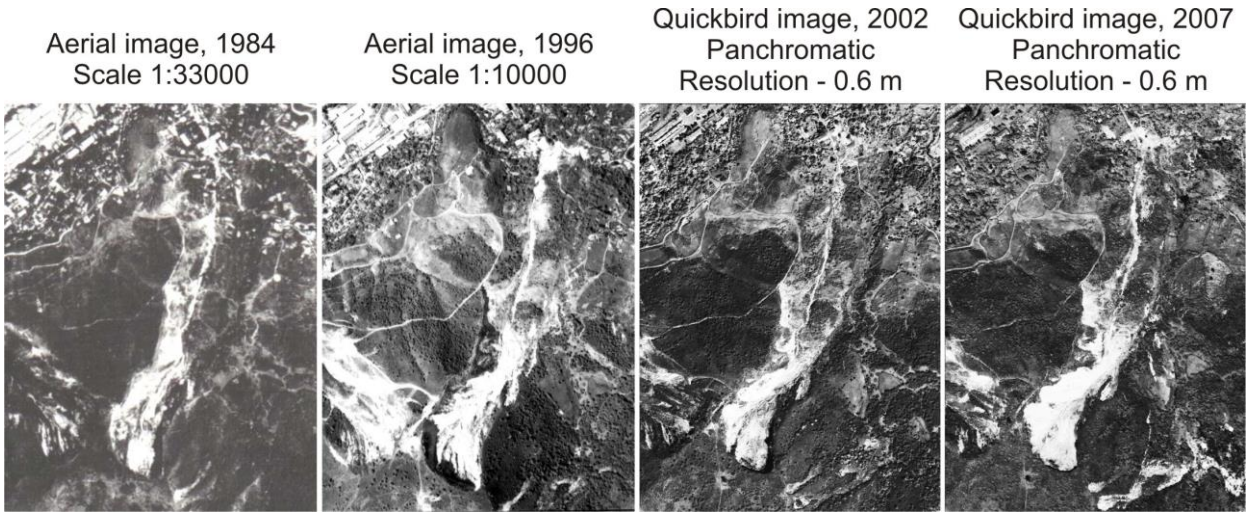

Figure AF.32: Comparison of the different imagery applied in the landslide inventories compilation.

The landslide inventories for 2002 and 2007 were compiled through the semi-automatic identification of slope failures from the Quickbird images (Schlögel et al., 2011). This approach consists of the NDVI analysis of the multitemporal Quickbird imagery, which has comparatively high spatial resolution (2.44 m). The post-processing stage also involves data mining techniques. The basic idea of this approach considers that a moving landslide disturbs the vegetation cover. Therefore, the subtraction of the multi-year NDVI products provides a basis for the semi-automatic identification of the landslide activity. Figure AF.33 presents some results of this study, where the active slope processes are characterized by a degraded vegetation cover (see the areas marked by red colour).
This technique can also be applied for the landslide activity detection – some case studies are presented in the next section. This approach has some limitations, which are discussed below. Nevertheless, it proved its effectiveness and promises good perspectives for the tasks of the landslide mapping and the landslide activity detection.

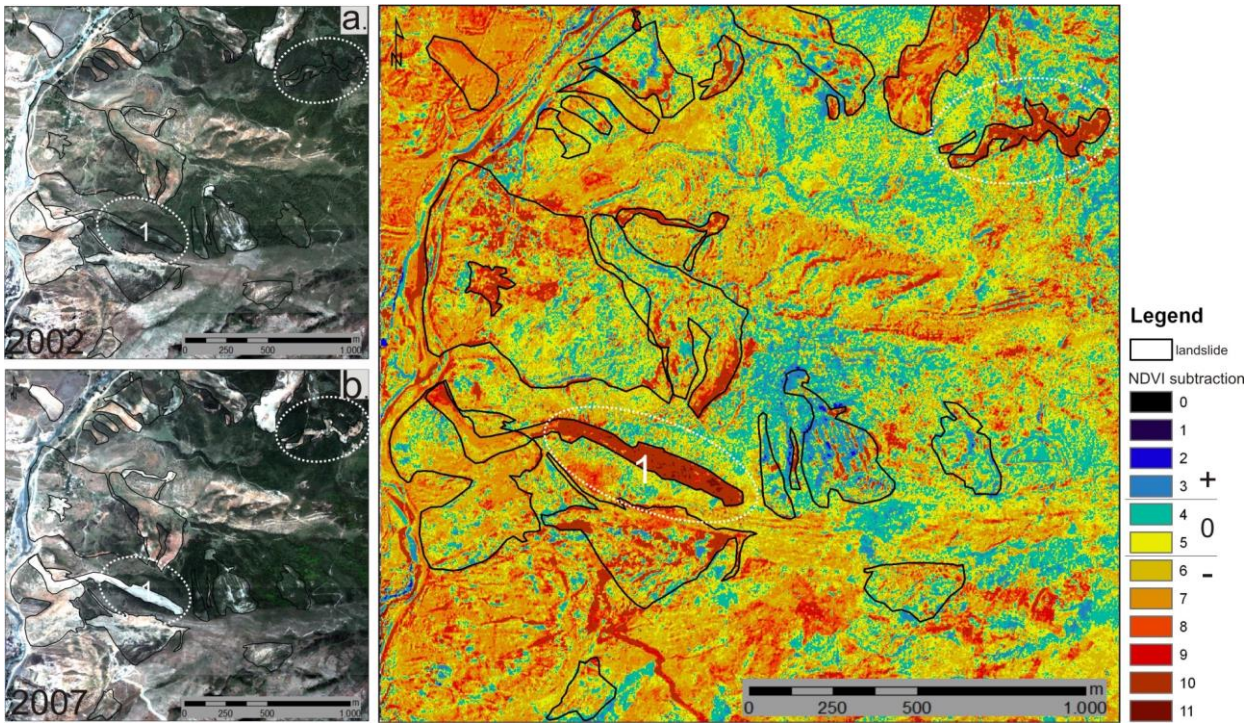

Figure AF.33: The result of the NDVI subtraction for the Quickbird imagery (2002 and 2007) in the central part of the target area together with the landslide outlines - the landslide marked by 1 presents the failed Upper Koytash landslide (by Schlögel et al., 2011).

Braun (2010) provided another type of mapping in the target area. The different types of mass movements were identified using 2007 Quickbird imagery, namely: complex landslide, earthflow/debris flow, rockfall and slump/rotational slide (see Figure AF.34). All these types were manually identified from analysed satellite imagery based on the principle that different landslide types leave specific features on the earth surface. Field checks of the mapping results confirmed the reliability of this mapping in most of the cases.

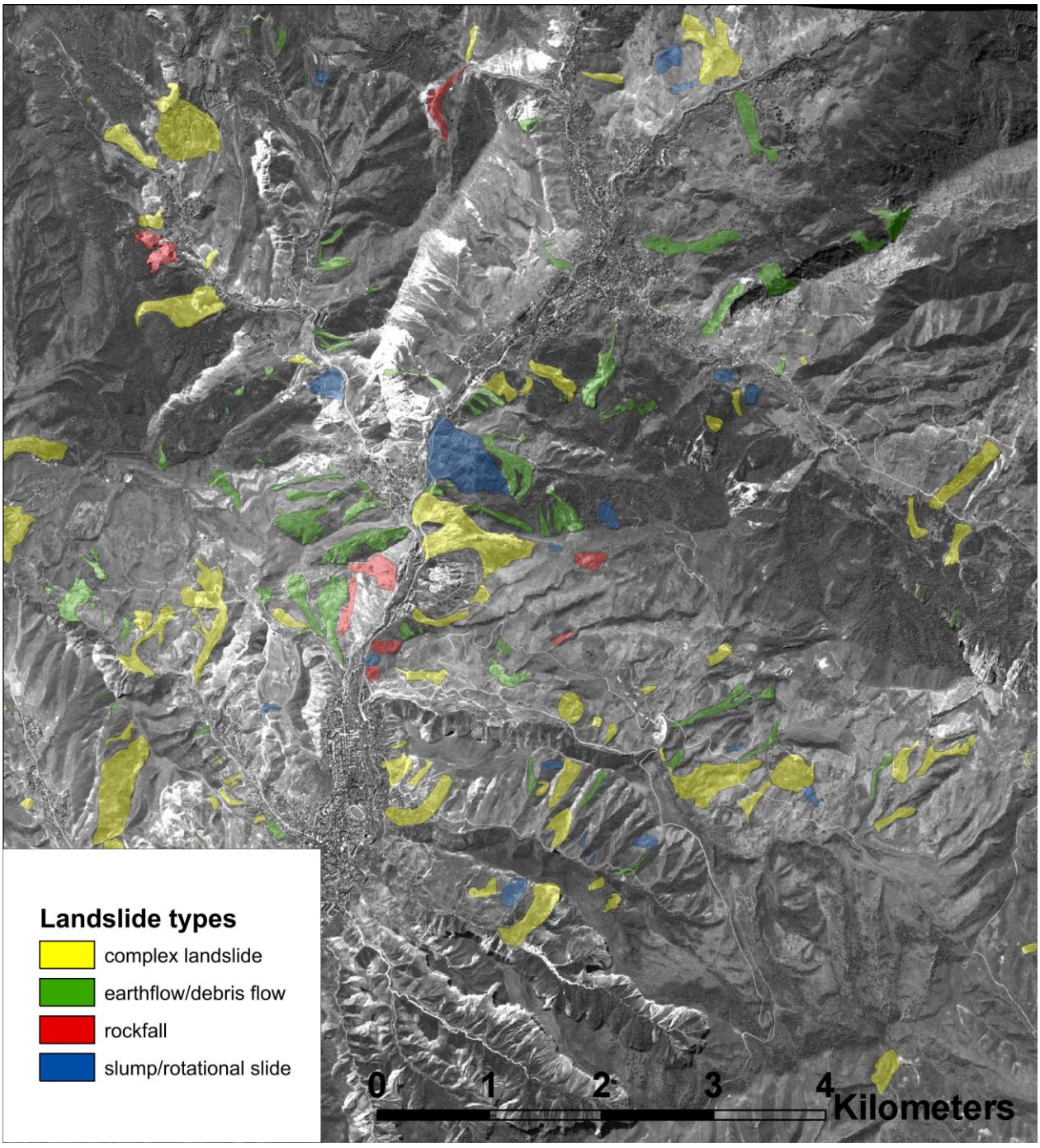

Figure AF.34: The landslide inventory for 2007 with an identification of the different types of mass movements plotted on top of the 2002 Quickbird image (by Braun, 2010).

Figure AF.35 presents a set of multi-temporal landslide inventories compiled for the target area. The analysis of these inventories shows that the landslide activity was intensified over the past sixty years. The total area affected by the landslides increased from 1.0 % in 1962 (~ 0.2 km^2) to 3.3 % in 1984, 4.5 % in 1996, 4.3 % in 2002 and 5.6 % (~ 6.7 km^2) in 2007 compared to the entire investigated area along the Mailuu-Suu River Valley. The analysis also shows that the landscape in the target area is continuously changing due to the high

landslide activity. The landslide size is quite variable - it ranges from 335 m^2 for the smallest detected landslide to 348425 m^2 for the largest one in 2007. The mean landslide size is also increasing over time, from 15170 m^2 in 1962 to 31000 m^2 in 2007.

The number of the landslide events is continuously changing. There were 162 slopes marked by landslide phenomena in 1962, 206 cases in 1984, 222 cases in 1996, 189 cases in 2002 and 208 cases in 2007. The extreme number of the landslide events registered in 1996 is related to the high precipitation rates and to the higher seismic activity observed in the target area in the beginning of the 1990s (Torgoev et al., 2002).

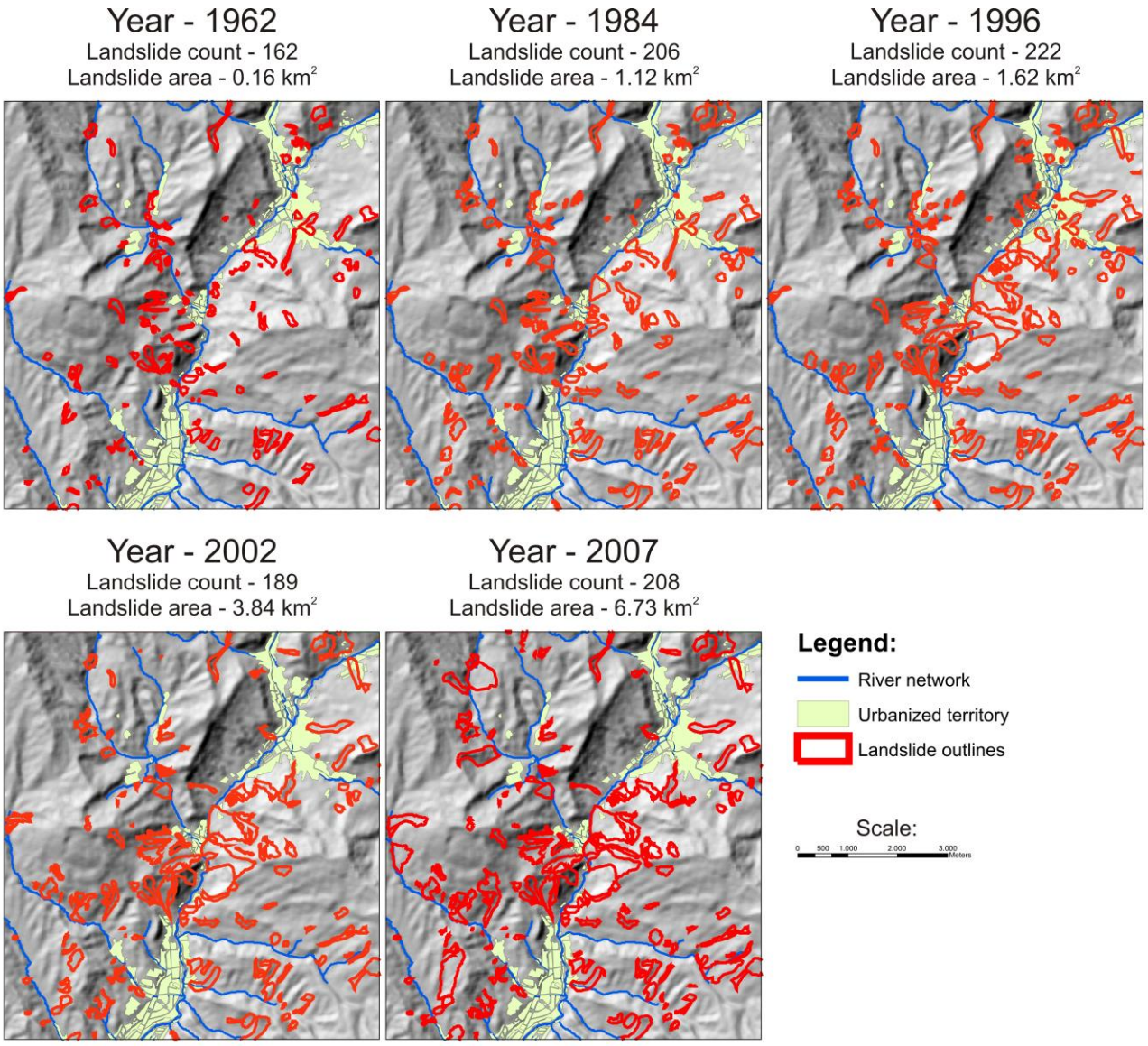

Figure AF.35: The multitemporal landslide inventories overlaid over the hillshaded relief, the outlines of the urbanized territory and a river network.

III.3 Landslide activity detection

In this part of our research we apply multi-temporal Landsat imagery to detect landslide activity in the target area. As it was shown above, the active mass movements can modify the vegetation cover – other impacts can include slope cracking, topographic perturbation, surface changes, etc. These effects tend to modify a surface reflectance and its alteration can be studied through the analysis of the multi-temporal satellite imagery.

Sabins (2007) lists several examples how this principle is applied to the landslide activity detection. An expansion of a landslide scarp is often followed by a degradation of the vegetation, which can be studied through the NDVI analysis. The topographical perturbations result in a change of the earth surface reflectance, especially in the range of the visible light. The change of a slope hydrological/hydrogeological regime often incurs changes of the earth reflectance in the far-infrared and thermal-infrared ranges.
As it is shown in the previous section, Schlögel (2009) and Schlögel et al. (2011) apply two multi-year Quickbird images to map/detect the landslide activity for a period between 2002 and 2007. In our studies we analyse three multi-year Landsat images to detect landslide activity for two target periods (1975-1992 and 1992-2001). Table AT.9 lists the specifications for the analysed Landsat imagery. The data for the Qiuckbird scenes analysed by Schlögel (2009) and Schlögel et al. (2011) are also presented in this table. As it can be seen, the Landsat imagery is acquired by different missions, therefore, only the overlapping bands are employed in our analysis (see more details in Table AT.9). The Quickbird imagery has 5 working bands, but the landslide detection is based on the NDVI analysis, which applies only two working bands: the red and the infrared bands (see more details by Schlogel et al., 2011).

Table AT.9: Specifications of Landsat and Quickbird satellite imagery used in the analysis (based on http://landsat.usgs.gov and http://glcf.umiacs.umd.edu/data/quickbird)

Acqusition	Mission	Number of bands	Resolution, m
June, 1975	Landsat 2 (MSS)	4 (the 1975-1992 period applies only 3 bands)	57x79
August, 1992	Landsat 5 (TM)	7 (the 1975-1992 period applies only 3 bands; the 1992-2001 period applies all 7 bands)	30x30 (band 6 has 120x120 m resolution)
August, 2001	Landsat 7 (ETM+)	8 (the 1992-2001 period applies only 7 bands)	30x30 (band 6 has 60x60 m and band 8 has 15x15 m resolution)
July, 2002	Quickbird	5 (NDVI index was used in the analyses)	2.44x2.44 (panchromatic resolution – 0.61)
June, 2007	Quickbird	5 (NDVI index was used in the analyses)	2.44x2.44 (panchromatic resolution – 0.61)

Figure AF.36 presents the generalized analysis scheme demonstrated on the basis of the 1992 and 2001 Landsat imagery. These images have 7 overlapping bands in the visible, infrared and far-infrared ranges (see Table AT.9). The first analysis step consists of a normalization of the pixel values (reflectance values) applying the mean and the standard deviation of reflectance for each spectral image. Originally, these pixel values are represented by the digit numbers ranging from 0 up to 256, showing the reflectance of the earth surface in a certain EM range. The normalized reflectance value shows how far the original reflectance is from the mean value for this spectral image. For example, if a given pixel value is 150, the mean value for a given spectral image is 100 and its standard deviation is 50, then the normalized pixel value would be 1: it shows that an original reflectance value is one standard deviation far from the mean.
At the second analysis step the multi-year normalized spectral images are subtracted to analyze a change of these values over the studied period of time. The results of the multiband subtraction are further stacked into one single pseudo-image, which summarizes a change of the reflectance values within all analysed spectral bands. To better highlight the change of the reflectance values, the resulting pseudo-images are subjected to the Principal Component Analysis (PCA). It presents a mathematical procedure which summarizes the multiband data variability into the smaller number of bands. For example, a change of the reflectance values for the period 1992-2001 was presented by 7 subtracted bands, and PCA summarized these bands into 3 ones (see the result of the Principal Component Analysis in Figure AF.36).

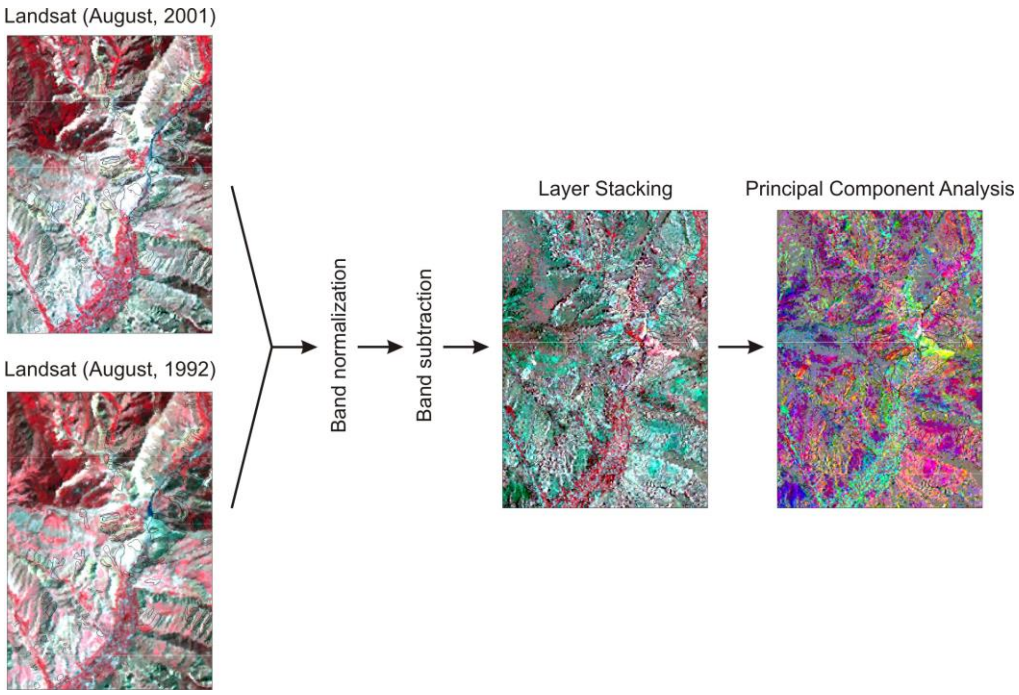

Figure AF.36: The scheme of applied analysis shown on the examples of Landsat imagery for the period between August, 1992 and August, 2001

The basic analysis criterion implies that reflectance values inside the active landslides would experience more drastic changes compared to the surroundings. Figure AF.37 shows some examples of the landslide activity detection for two analysed periods. It can be seen, that active landslides are characterized by more drastic changes of the reflectance values. These results can also infer the temporal variation of the landslide activity. For example, the landslide in Figure AF.37a was active during the both analyzed periods, while those in Figure AF.37b and c were more active between 1992 and 2001, rather than between 1975 and 1992. The landslide in Figure AF.37d presents an example of the slope movement, which was active during the both analysed periods, even though more drastic changes of the reflectance values are revealed for the period between 1992 and 2001 (especially in the right upper part of the landslide).

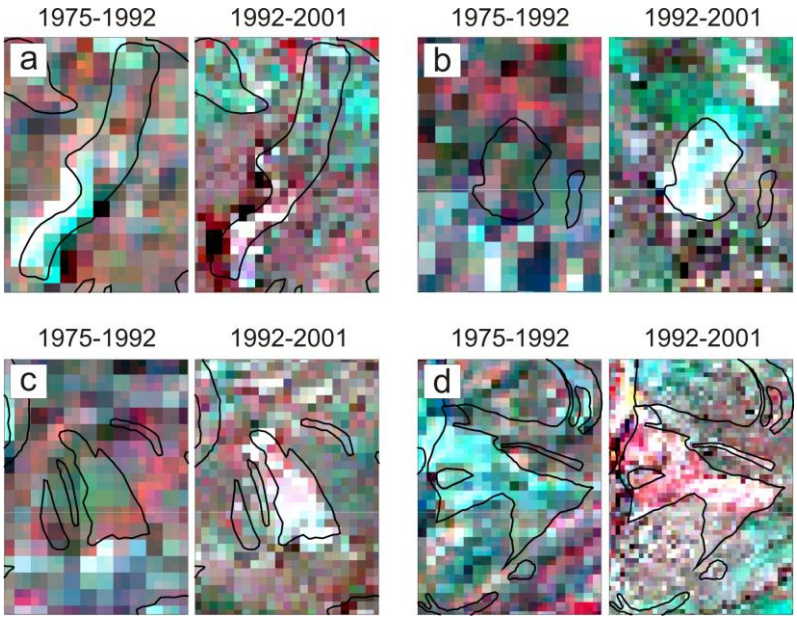

Figure AF.37: Examples of the landslide activity detection applying the pseudo-images of reflectance value change (the detection is based on the colour contrast separating the active landslide from stable surroundings).

Schlögel (2009) applies the values of the NDVI index instead of the real reflectance values in her analysis of the Quickbird images (see *Sub-section A.I.5.2.4* for the explanation of the NDVI analysis). The improved spatial resolution of these scenes provides more detailed information for the target area (compare the results in Figure AF.38). In addition to the landslide activity detection, these results are applied to a semi-automatic mapping of the landslide outlines, when the additional analysis tools (data mining) are employed.
Figure AF.38 summarizes the results of the landslide activity detection for a part of the target area, situated in the eastern slope of the Mailuu-Suu River (note: Schlögel (2009) analyzed a period of 2002-2007). There are three well-known landslides, situated in this area, namely Koytash (1), Upper Koytash (3) and Tektonik (4) landslides. These slope movements pose a high destruction threat to the radioactive waste tailings situated along the Mailuu-Suu River. Additional threat comes from a possible river damming, when following upstream/downstream flooding can inundate the protective infrastructure of the tailing sites.

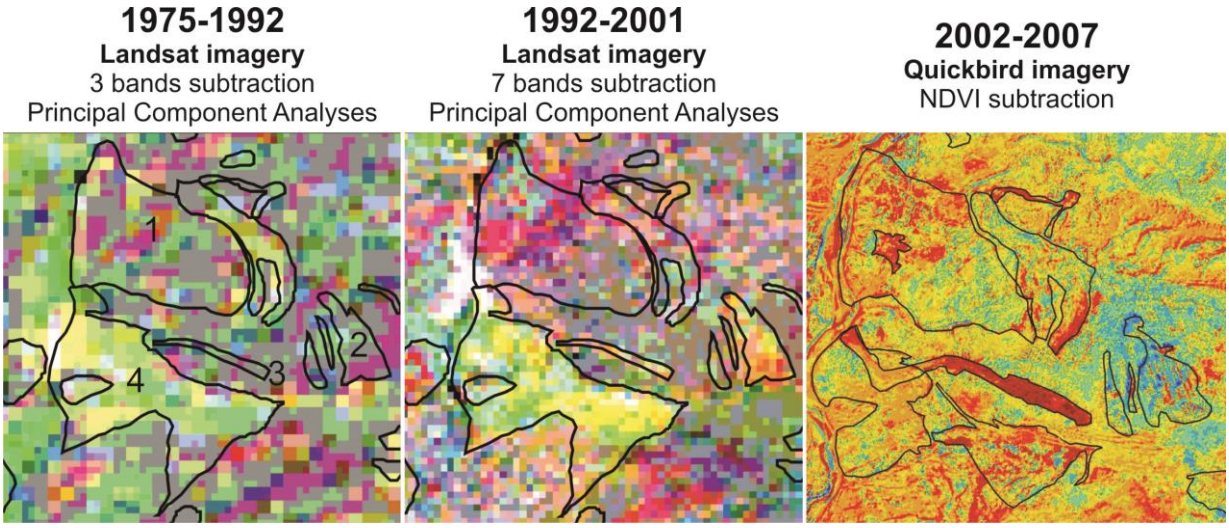

Figure AF.38: The results of landslide activity detection for some famous landslides, situated in the central part of target area, namely: Koytash (1), Upper Koytash (3) and Tektonik (4). The analysis of the Qiuckbird imagery is performed by Schlögel (2009): the colours indicate a change of the vegetation cover over the studied period (red = degradation of vegetation cover; yellow = no changes; blue = richer vegetation cover).

According to Torgoev et al. (2002), the Tektonik landslide poses the highest level of the landslide risk due to its high activity and due to the close proximity to the radioactive waste tailings situated downslope. The field observations show that during the last 10 years some of the landslide scarps reached the height of 9 m, while in the beginning of the years 2000 only a very small scarp of a few decimeters was observed in the same place (see a scarp evolution in Figure AF.39).
The landslide activity detection for the periods 1975-1992 and 1992-2001 shows that the Tektonik landslide experienced some sliding activity during these periods of time (see Figure AF.38). The rough resolution of the Landsat imagery (57x79 m and 30x30 m) does not allow us to make more detailed conclusions. The Quickbird imagery (resolution 2.44 m) provides more detailed information on the surface changes incurred by the slope movements: the areas with a degraded vegetation cover are identified near the scarp (see the areas, marked by the brown colour for a period 2002-2007 in Figure AF.38).
The Upper Koytash landslide (number 3 in Figure AF.38) is marked by a pure earthflow sliding mechanism. The landslide detection studies suggest that this landslide was activated between 1992 and 2001, as no changes of the reflectance values are identified for the period between 1975 and 1992. As it can be seen, this landslide is also characterized by a very clear contrast of the vegetation cover in the period between 2002 and 2007. It indicates that this landslide was very active during that period and posed significant threat to the areas below. Actually, a major failure in 2005 hit the road and caused some downslope damage (Schlögel et al., 2011).
The unnamed landslide 2 (see Figure AF.38) is also marked by earthflow sliding mechanism. The analysis suggests that it was more active in the period between 1992 and 2001 than in the later period. It is confirmed by the fact, that in period 2002-2007 this landslide was partially revegetated (see the area marked by a blue colour in Figure AF.38). The richer vegetation witnesses the slope stabilization.

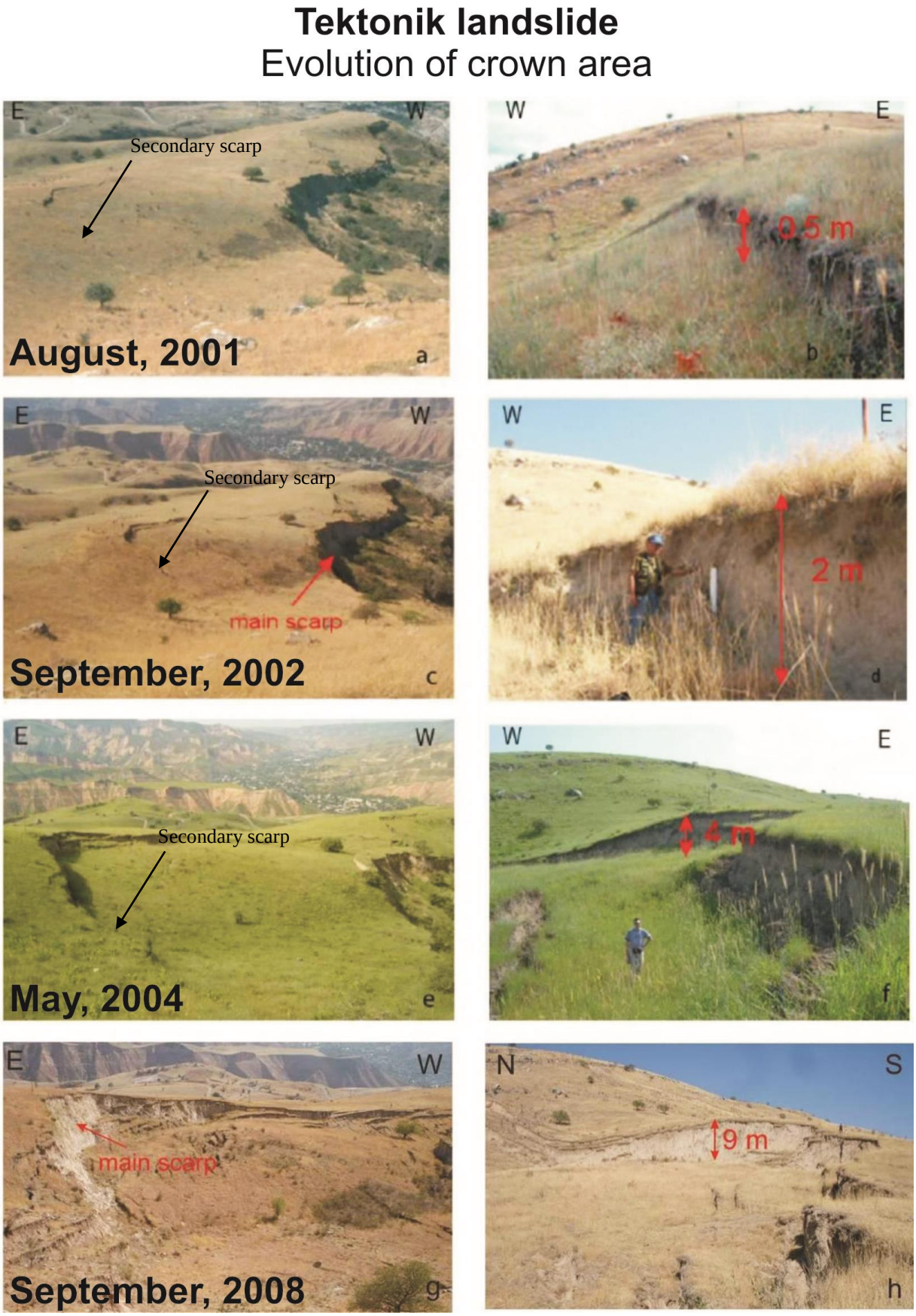

Figure AF.39: The evolution of the Tektonik landslide crown area: (a and b) August 2001, (c and d) September 2002, (e and f) May 2004 and (g and h) September 2008. Arrows in the left general views mark the main and secondary scarps, while right photos show the evolution of the secondary scarp (by Havenith et al., 2006; modified).

The Koytash landslide, number 1 in Figure AF.38, has a translational-rotational sliding movement along a deep-seated sliding surface. Such large landslides with low movement rate are generally not marked by significant changes on the earth surface, i.e., those which affect the vegetation cover. Therefore, the landslide activity detection can be less efficient in this case. Indeed, the analysis of the multi-temporal Landsat imagery (the periods of 1975-1991 and 1991-2001) does not provide any clear indication of a sliding activity, while Alioshin and Torgoev (2000) instrumentally show that at the end of the 90s and in 2000 it moved up to 8.0-10.0 cm per year. The recent field surveys show that this landslide still moves several centimeters per year (Schlögel et al., 2011). The analysis of the high-resolution Quickbird imagery (the period between 2002 and 2007) shows that there are some patterns of degraded vegetation cover, even though some parts of the landslide are classified to be stable (see the yellow-blue areas for the period 2002-2007 in Figure AF.38).

This last example suggests that the (semi-)automatic technique of landslide activity detection may produce poor results for some of the landslide types. The technique works best for translational flows which normally result in drastic changes on the earth surface. The slides and slumps often have low movement rates and the changes on the earth surface can not be easily identified. The falls and topples normally occur at rock outcrops which are often free of the vegetation cover - in this case any application of NDVI subtraction becomes useless. Reliable results are anticipated only for the big-scale falls/topples, which involve relocation of a significant volume of sliding material and bring significant changes to the initial landscape.

Compiled landslide inventories represent the main outcome of current chapter. These inventories are futher applied to map the landslide susceptibility, hazard and risk in target area. The input data for such analysis also include the maps of factors contributing to landslide activity. The next chapter reviews in more details the mapping of the contributing factors, as well as presents the results of the landslide susceptibility analysis.

IV. Landslide susceptibility

IV.1 Factors contributing to landslide susceptibility

One of the key assumptions, applied for a landslide susceptibility mapping, states that a prediction of future landslide occurrence is based on a study of conditions led to past/present slope instability (Hutchinson, 1988; Dietrich et al., 1995). These conditions directly or indirectly control the slope instability and they are referred to as the factors contributing to landslide activity, otherwise called as the predictor variables or thematic layers. A link between contributing factors and slope instability is controlled by the mechanical laws which can be determined empirically, statistically or in deterministic fashion (see more details in introductory sections). It finally determines the way how these factors are further applied for a mapping of the landslide susceptibility.
Alioshin and Torgoev (2000) studied the landslide activity in the target area and outlined three main groups of the contributing factors: anthropogenic impact, regional tectonic settings and distribution the soft rock types. The anthropogenic impact is mainly expressed via the earth subsidence leading to the slope instability. Danneels (2004) studied the link between landslide occurrence and position of the underground mine workings. The author could not clearly outline this link due the uncertain position of the areas characterized by surface subsidence. In our study the anthropogenic impact is partially taken into account in a land cover/land use thematic layer. The groups of the environmental/geotechnical factors, outlined by Alioshin and Torgoev (2000), are summarized in two thematic layers: the structural control (tectonic settings) and the geological units (rock types). Torgoev et al. (2005) note that the slope stability in the target area is also affected by the surface morphology, especially by the slope inclination. Due to that, our studies included the additional group of predictor variables connected to the surface morphology. More detailed information on a collection and mapping of the selected thematic variables (land cover/land use, structural control, rock types and surface morphology) is presented in the sub-sections below.

IV.1.1 Surface morphology

The surface morphological features originate from the landform geometry and include important parameters such as slope angle, slope curvature and slope exposition. These features are normally mapped applying the DEM of target area which is the 3D representation of a real earth surface. The DEM can be represented both in raster or vector-based formats, while the majority of the conventional mapping tools, e.g. Spatial Analyst in ArcGIS, demand the raster format.
There are several options to reconstruct the DEM of the target area. A direct topographic survey can be carried out to map the topography of small areas with very high precision and resolution, while this method is time-consuming and not applicable for wide areas. Remote Sensing proposes a good alternative for this case. These techniques include the traditional photogrammetry (aerial stereo-pairs) as well as more advanced processing tools, which employ stereoscopic satellite imagery, for example ASTER, SPOT, IKONOS, GeoEye, Pleiades, etc.
An additional option is represented by the aerial/satellite missions working in the range of the radar waves. These missions acquire two or more so-called synthetic aperture radar (SAR) images. Data processing generates the DEM of the surveyed area based on the difference of the phase of the radar waves returning to the aircraft/satellite. A similar idea is adopted by the aerial or terrestrial LiDAR techniques, which work in the ultraviolet, visible and infrared ranges. The SAR and LiDAR techniques can potentially provide a sub-centimeter precision, but the costs of the products limit their present application.
An example of DEM generation in the target area is presented by Danneels et al. (2006). It is performed on the basis of stereo-pairs of ASTER and SPOT images. The extraction procedure is carried out within the PCI Geomatica 8.0 Orthoengine software platform. First, a rigorous mathematical Toutin's model is computed for the stereo images to get a correct geometric correction of the analyzed imagery. The ground control points (GCPs) are collected from the Landsat image (longitude/latitude) and from the SRTM DEM (elevation data – see a short description below). Second, so-called tie points are generated between two images in order to rectify one image towards another one. This rectification creates a pair of the stereo-overlapped images, which is finally applied for the DEM generation. The elevation values of the final DEM are determined by the parallax values, which are gained by a comparison of the grey colour contrast.

The SPOT DEM is extracted on the basis of two cross-track SPOT-4 images with a resolution of 10 m (see Figure AF.40). The processed SPOT images have 4 month acquisition difference, which affected the quality of the constructed DEM. The horizontal accuracy of the resulting DEM is +/- 10 m, while the vertical one is +/- 20 m.

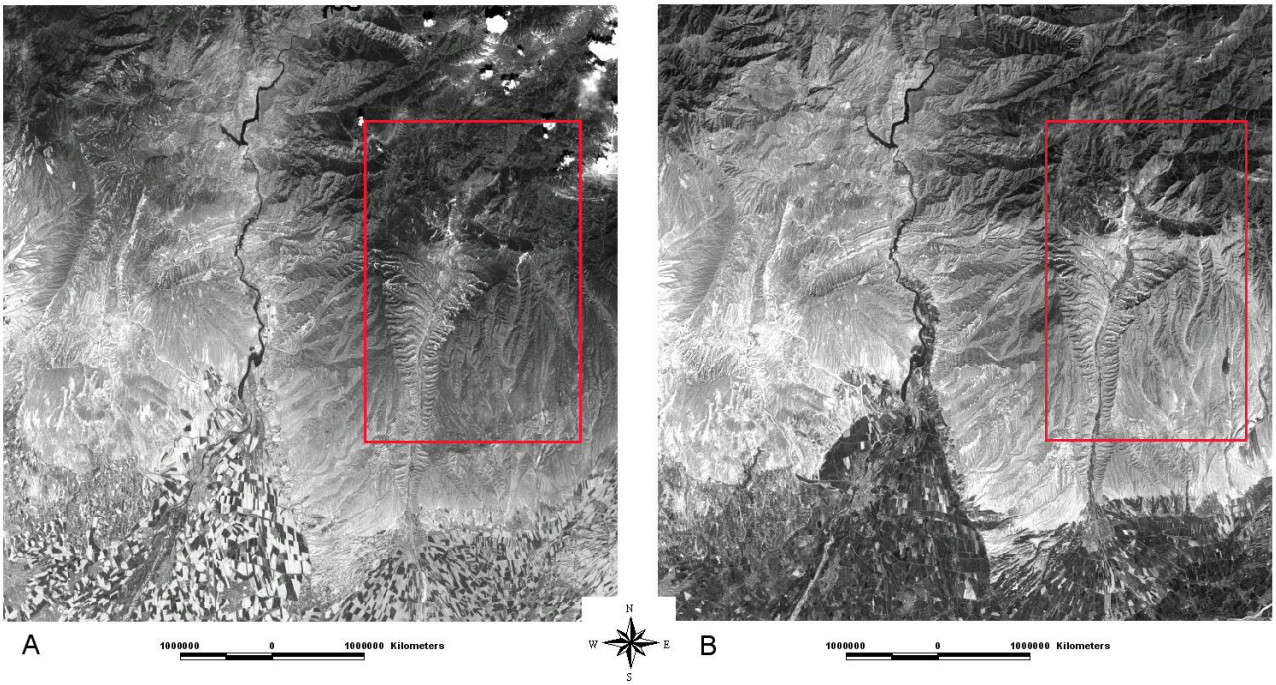

Figure AF.40: The SPOT-4 images applied for the stereocoverage in the target area: (a) 20 May, 2000 and (b) 31 August, 2000 (the area of the DEM generation is marked by a red rectangle - by Danneels et al., 2006).

The ASTER DEM is generated by application of the nadir-looking 3N and the backward looking 3B ASTER bands, both with a resolution of 15 m (see the 3D view in Figure AF.41). The analysed imagery was acquired in 2001. The horizontal accuracy of the final ASTER DEM is +/- 15 m, while the vertical one is +/- 30 m.

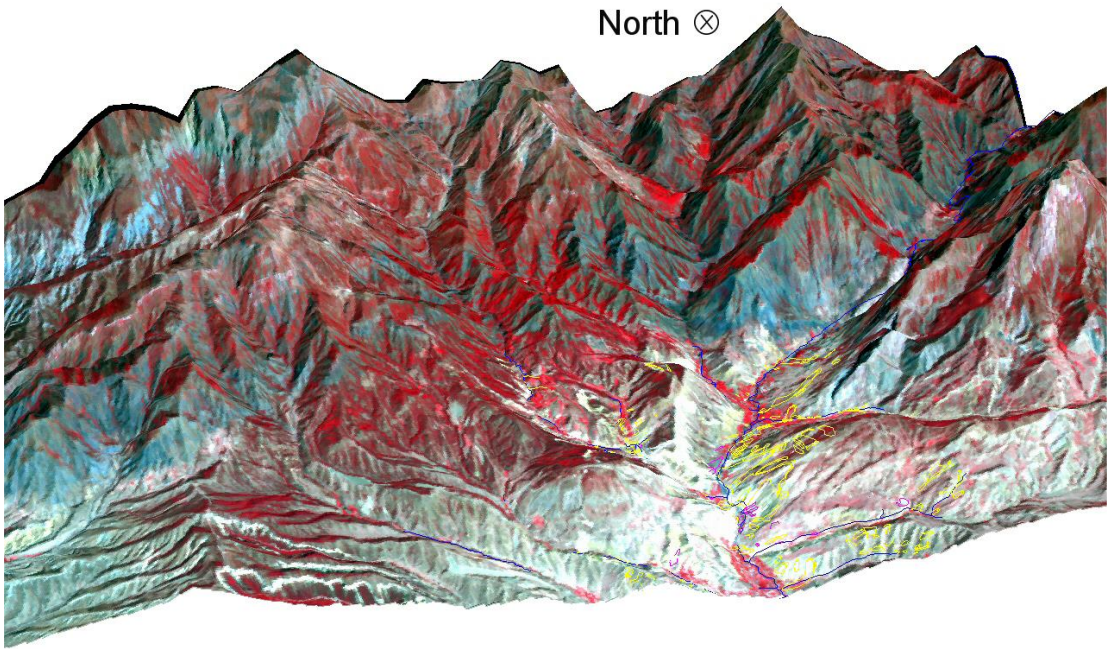

Figure AF.41: The 3D view of the ASTER DEM for the northern part of the target area generated with the ArcScene (ArcGIS) software; the pseudo-colour ASTER 2001 imagery together with the river (blue) and landslide (yellow) outlines are draped over the ASTER DEM (by Danneels, 2006).

The similar processing technique is applied to two sets of aerial photos acquired in 1984 (acquisition scale is 1:33000) and in 1996 (acquisition scale is 1:10000). The aerial DEMs are generated with the ERDAS Imagine software (see Figures AF.42a and AF.42b for the sample snapshots). The horizontal information for the GCPs, i.e. latitude/longitude, is collected with the Quickbird imagery available in the Google Earth software. The elevation data are collected from the SPOT DEM 2010 with a spatial resolution of 20 m, which is acquired as a complete product (see a sample snapshot in Figure AF.42c). Due to the lack of precise GCPs, the aerial DEMs have a poor accuracy in some parts of the target area. Therefore, the aerial DEMs are not applied for mapping of the geomorphologic features.

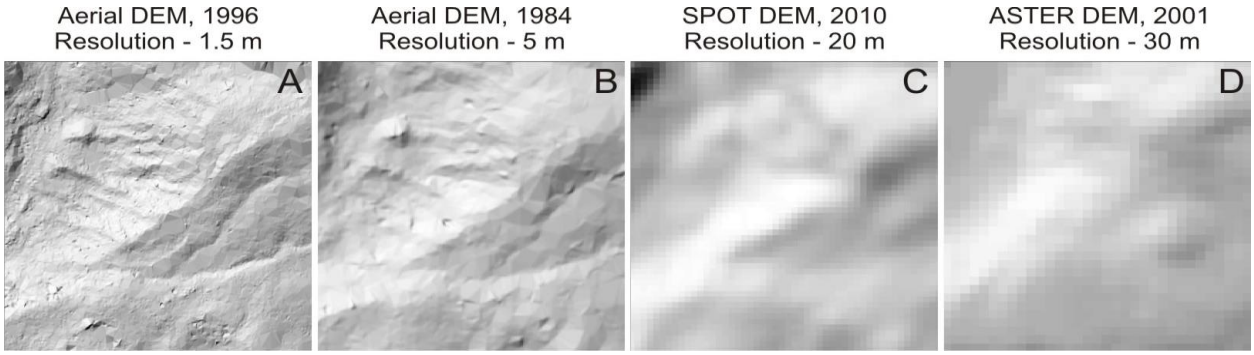

Figure AF.42: Sample snapshots of the DEMs with the different spatial resolution (see titles), presented by the shaded relief view.

The Shuttle Radar Topography Mission DEM (SRTM DEM) is an additional source of the topographic information freely available for the most parts of the world, including Kyrgyzstan. This product is globally provided by the National Geospatial-Intelligence Agency (NGA) and the National Aeronautics and Space Administration (NASA). The SRTM DEM is generated by the SAR technique and since the end of 2014 it has a spatial resolution of 30 m for most parts of the world. The low resolution of this product available at the time of our analysis (90 m before the end of 2014) was not suitable for our susceptibility studies at local scale. Therefore, the SRTM DEM was only used for the collection of GSPs to generate the DEMs from the SPOT 2000 and ASTER 2001 stereo-imagery. Meanwhile, Havenith et al. (2015a) used the SRTM DEM for the landslide susceptibility analysis applied to the whole Tien-Shan.
The purchased SPOT DEM 2010 is selected to be the main source of the topographic information in our studies (see a snapshot in Figure AF.42c). It has appropriate vertical accuracy (+/- 10 m) and its spatial resolution falls within those of other thematic layers (i.e., 20-30 m - see details in further sub-sections). Figure AF.43 presents the results of automatic mapping of main geomorphological features (slope exposition, slope curvature and slope angle) performed in the ArcGIS software (Spatial Analyst extension).

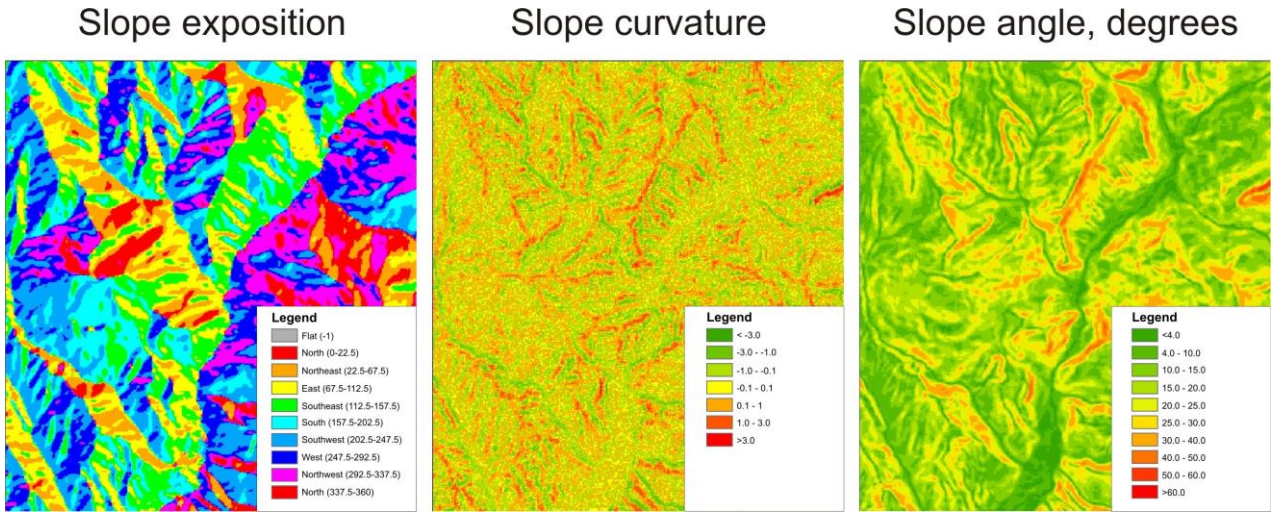

Figure AF.43: The results of the automatic mapping of the geomorphologic features performed in the ArcGIS software (Spatial Analyst) and applying the SPOT DEM 2010 (20 m resolution).

IV.1.2 Land cover/land use

The terms of the land cover and land use are often mixed with each other, even though there is a fundamental difference between them (Sabins, 1996). Comber et al. (2005) define land cover as the type of the material or substance covering a certain part of the ground surface – these substances/materials can be represented, e.g., by the grass, trees, asphalt, bare surface, water, etc. The land use is a description of how people utilize the land or part of the studied surface, i.e. a type of a socio-economic activity on the earth surface – the urban and agricultural land use can be the examples of the land use gradation (Prost, 2001).
The land cover and land use are among the most important factors affecting the rate of landslide activity, especially in case of the shallow events. Glade (2003) suggests that the type of the land cover can drastically change an underground water regime in unstable slope sites. The type of land use can provide a hint at how an anthropogenic activity provides an instability impact. Therefore, these parameters are often used for the mapping of the landslide susceptibility as one of the main impact factors.
A well-adopted practice of the land cover/land use mapping includes the classification of the existing vegetation cover according to the vegetation richness, namely: bare surface, grass, shrubs and forest. According to Guzzetti (2006), this gradation provides information on the hydrogeologic site conditions, even though there can be an opposing effect, when the landslide activity itself affects the vegetation cover in the surroundings. It is often very difficult to separate these effects. Therefore, there is certain risk of mixing up the landslide susceptibility mapping with the landslide inventory compilation (or landslide activity detection).
As it is described in *Sub-section A.I.5.2.4*, each material or substance has unique reflectance curve. Remote Sensing applies this property to differentiate the types of land cover: for example, NDVI analysis is applied to map the areas covered by healthy and rich vegetation. Some other materials cannot be easily discriminated due to a number of reasons, like similarity of the reflectance properties, position of the working bands, etc.
Danneels (2005) tested the potential to discriminate different rock types in the target area on the basis of Landsat data. The author collected 40 rock samples and tested them in the lab spectroscope. These samples represent five different geologic formations in the target area. Figure AF.44 shows the generalized shapes of the reflectance curves, gained for these geologic formations. All curves have a similar shape, but the values of the IR/R ratios are different (a ratio of the infrared reflectance over the red one for the Landsat spectral ranges - see Figure AF.44). The highest value of the IR/R ratio is revealed for the RED formation (1.8), while the lowest one is revealed for LIM (1.2). It demonstrates that an application of the spectral ratios/indexes can potentially be applied to discriminate analysed rock types.
Nevertheless, an application of the IR/R ratio in the target area is impractical since existing geological formations are characterized by a mixed rock composition and the analyzed samples do not fully reproduce this sequence. Moreover, almost all formations in the study area are characterized by a very similar rock composition. An additional limitation comes from the presence of the surface sediments/debris that may cover the rock outcrops. Nevertheless, Sabins (1996) shows that the spectral indexes can be successfully applied for the mapping of the lithological/rock units in the case when the rock composition is uniform and the sediment cover is absent.

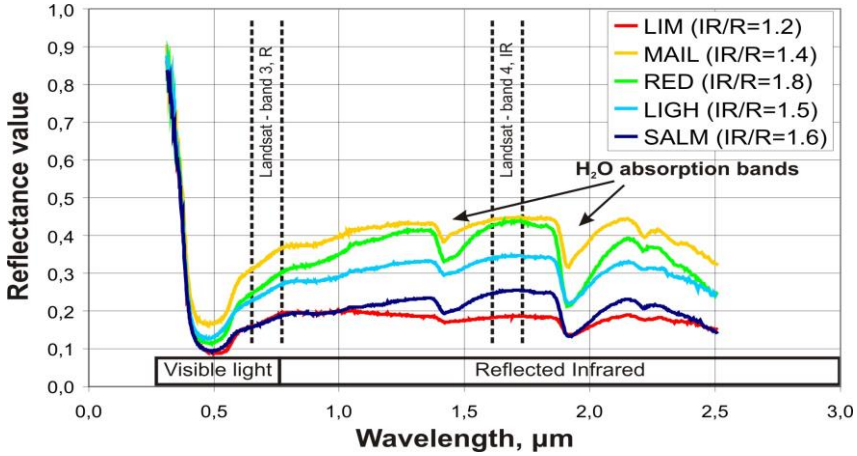

Figure AF.44: Generalized spectral reflectance curves together with the calculated values of IR/R spectral indexes for the different formations presented in the Mailuu-Suu target area (by Danneels, 2005).

To map the land cover/land use in the target area we employ the Landsat image (August, 2001) with a spatial resolution of 30 m. Figure AF.45 presents a flow chart of the applied mapping methodology. The Landsat image is first subjected to the NDVI analysis. A supervised classification technique (performed with the ERDAS Imagine software) is applied to map three classes of vegetation richness, namely rich vegetation, poor vegetation and bare surface. The urbanized territory and predominantly rural area are manually mapped applying the thematic maps and existing knowledge on local infrastructure. The final thematic layer consists of five classes of land cover/land use, namely bare surface, poor vegetation, rich vegetation, urbanized territory and predominantly rural area (see the final layer of the land cover in Figure AF.45).

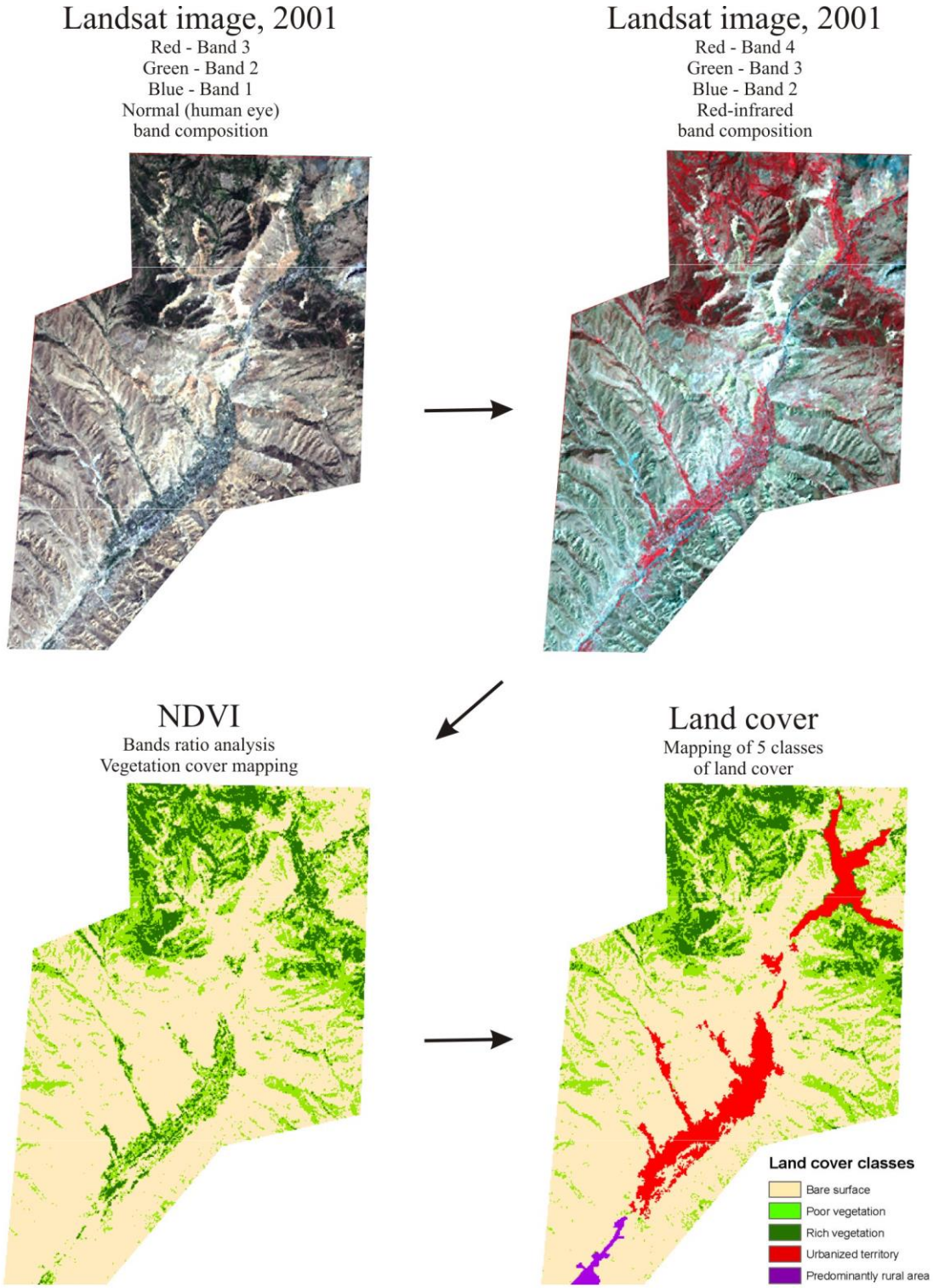

Figure AF.45: Flow chart of a land cover/land use mapping in the target area applying the Landsat image.

IV.1.3 Geological units

The type of geological unit or rock type is another important factor contributing to the landslide susceptibility. The sliding potential of a given rock type is determined through its geotechnical properties, including internal friction angle, cohesion, shear strength, etc. Other factors impacting the sliding potential can include the weathering rate, cracking, water saturation, liquefaction potential, as well other geotechnical/hydrogeological specifications. The rock units should ideally be ranked (classified) according to the spatially distributed geotechnical data. In reality, they are often ranked based an expert-based opinion which takes into consideration the landslide concentration within certain geological units.
The thematic geological layer in the target area was compiled from the results of de Marneffe (2010). The author provided a new geological map of the target area which improved the results of former research performed by Iliyn (1959), Krestnikov (1962) and Konaev (1964). The research of de Marneffe (2010) was especially targeted at the precise location of the borders between different formations. The final results of this mapping activity with indication of main structural features (faults, fold axis) are presented in Figure AF.46.

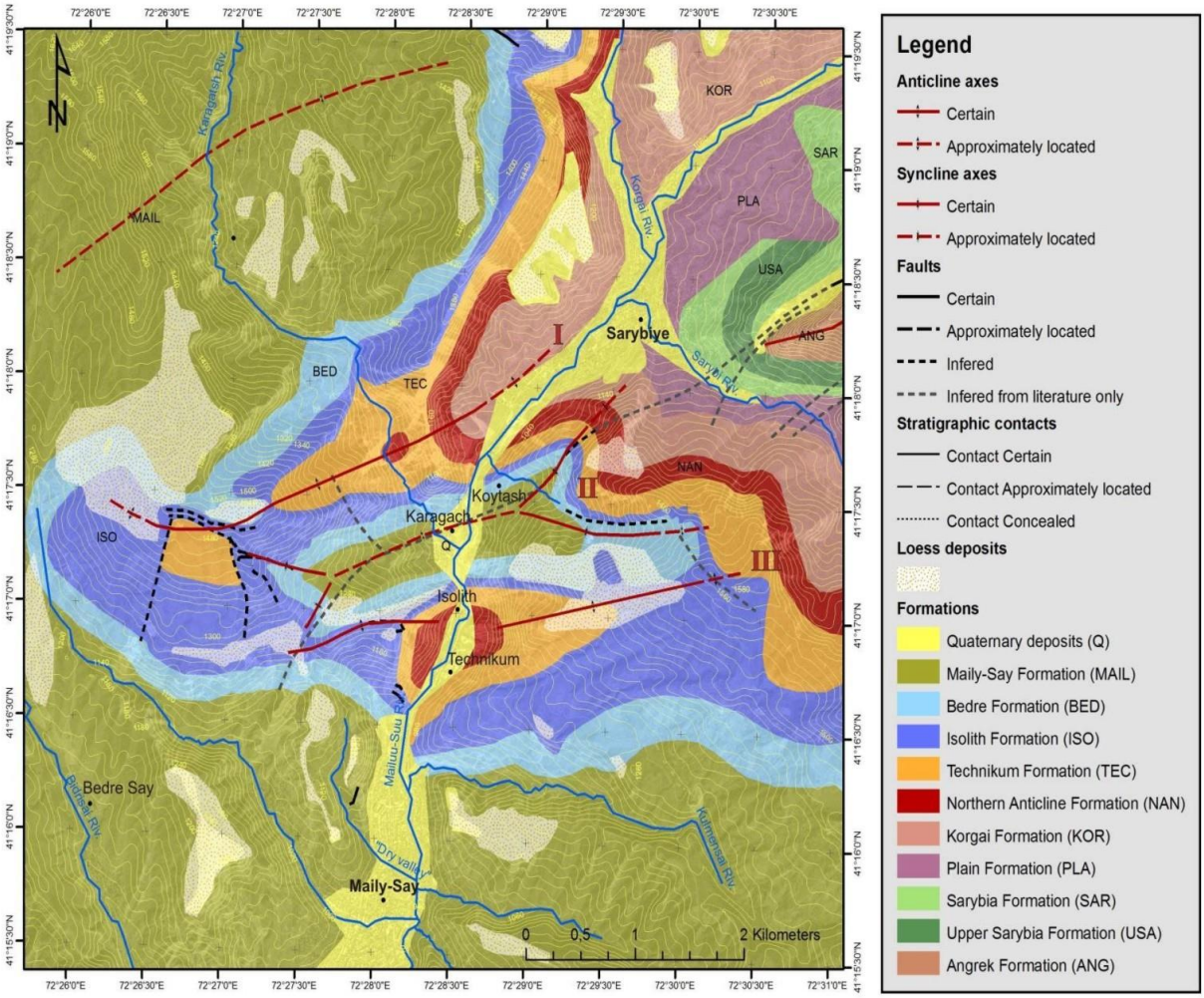

Figure AF.46: Geological map of the Mailuu-Suu target area: I is the Northern Anticline, II is the Central Syncline and III is the Central Anticline (axes marked in red); the loess deposits are marked by the semi-transparent white dotted zones (de Marneffe, 2010; modified by Schlögel et al., 2011).

As it can be seen in Figure AF.47, there are three main tectonic features, presented in the target area: the Northern Anticline (I), the Central Syncline (II) and the Central Anticline (III). According to Konaev (1964) the main phase of the neotectonic activity is registered in the Early Pleistocene. Alioshin and Torgoev (2000) discriminated two main types of the topographic features: the oldest ones, mainly Paleozoic, are more

impacted by the tectonic activity, while the youngest ones (Pliocene-Quarternary) are mainly marked by the erosional effects. The high rate of tectonic activity created specific patterns of the river network situated in the deep canyons crossing the layers. Konaev (1964) indicates that a rate of the Neogene-Querternary uplift changed from 0.4 mm/year in Miocene-Pliocene up to 10 mm/year in Pleistocene-Holocene. The high rate of a tectonic activity accompanied by the erosional processes has resulted in a high level of the landslide susceptibility in the target area.

Figure AF.47a presents a litho-stratigraphic column constructed by de Marneffe (2010). As it can be seen, all formations are composed of the interlaying sedimentary rocks. The volcanogenic rocks (not shown in the column) are present only in the upper part of the river valley, 10-15 km to the north from the Saribiye village (see village location in Figure AF.46). According to Alioshin and Torgoev (2000) these rocks are very hard, and, therefore, have very low level of landslide susceptibility.

The results of the landslide statistics for the rock formations are presented in Figure AF.47b. The level of the landslide susceptibility for each geologic formation can be estimated through the percentage of the area affected by the landslides. As it can be seen, the most susceptible formation is BED. The other most susceptible formations are MAIL, ISO, TEC, NAN and KOR. The least susceptible formations are ANG, PLA and SAR.

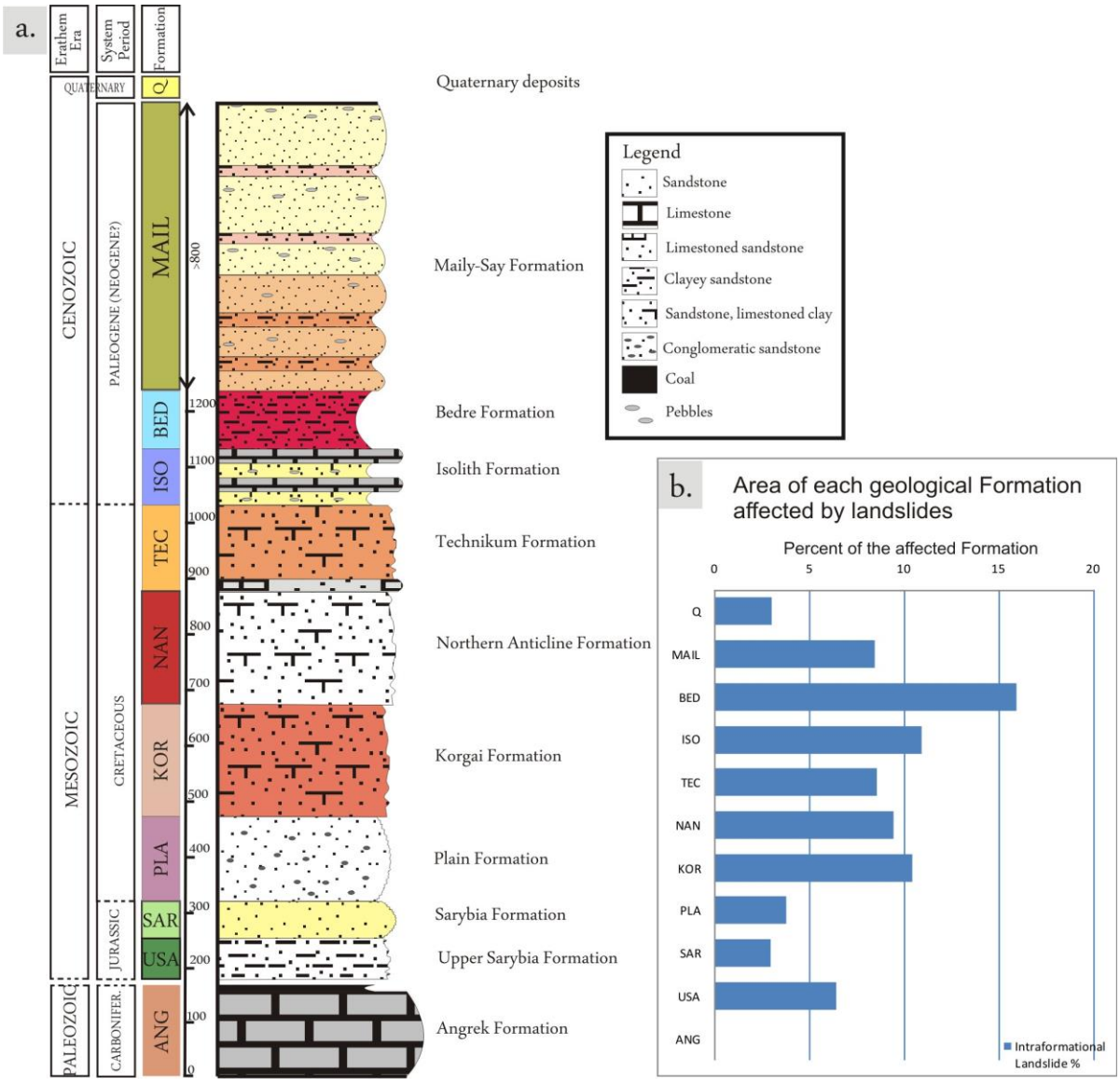

Figure AF.47: (a) Litho-stratigraphic column of the rocks and deposits mapped in the Maily-Say River valley; (b) graph showing the density of slope instabilities (of 2007 inventory) within each geological formation (de Marneffe, 2010; modified by Schlögel et al., 2011).

The Angerek formation (ANG) is the oldest one presented in Figure AF.47a. It is mainly composed of the Carboniferous limestone which is characterized by a high stability potential. In some areas these rocks can be less stable due to inclusions of sandstone and gravel. A lot of convex morphologies (hills, cliffs) in the target area are composed of this rock type due to a high erosional resistance. This formation has the lowest level of landslide susceptibility among those shown in Figure AF.48a. However, according to de Marneffe (2010), if buried, this limestone layer can represent the sliding surface for some landslides in the target area.

The two Jurassic formations, Sarybia (SAR) and Upper Sarybia (USA), are mainly composed of the sandstone and clayey sandstone. These formations have an average level of landslide susceptibility (see Figure AF.48b). The sliding potential of these rocks is strongly related to a weathering rate, underground water conditions and lateral rock inclusions (Alioshin and Torgoev, 2000). According to Torgoev et al. (2005), the Jurassic rocks are highly exposed to weathering, especially along the bedding. Therefore, a conformable bedding of these rocks with slope surface often favours sliding activity.

There are four Cretaceous formations in the target area: Plain (PLA), Korgai (KOR), Northern Anticline (NAN) and Technicum (TEC). These formations are charachterized by a medium to high landslide susceptibility (see Figure AF.48b) determined by the weathering rate and underground water conditions (Torgoev et al., 2005). Alioshin and Torgoev (2000) note that the inclusion of gypsum and siltstone strongly enhances the instability potential, as most of the landslides in these formations are observed in those rock types. An opposite, stabilizing, effect is noted for thick sandstone and gravelite beds which normally have a quartz cement resisting well to weathering and erosion.

The Cenozoic rocks are presented by the Isolith (ISO), Bedre (BED) and Maily Say (MAIL) formations. These rocks were formed during the active orogenic processes and they occupy the biggest portion of the target area. All formations are characterized by the interlaying sandstone and conglomerate. The composing rocks have a very low erosional resistance due to the weak carbonatic or sulfatic cementation. The ISO formation containes some limestone interlayers, but due to their relatively small thickness (compared to the thickness of the entire formation) they do not support slope stability (Alioshin and Torgoev, 2000). An additional destabilizing effect is related to the high water absorption in those rocks which results in a significant drop of the shear strength in the wet periods of year. Due to these reasons, the Cenozoic formations are charachterized by the highest level of the landslide susceptibility (see Figure AF.47b).

The Quaternary sediments in the target area are represented by the the colluvium, prolivium, deluvium, alluvium and aeolic sediment. Most of the landslides in this formation occur in the aeolic sediments (loess-like loam). These sediments are often situated on the mountain tops or inclined slopes and have a thickness of up to 20-25 m. The loess-like loam has a moderate natural water content (9-18%). It is very plastic and and almost impervious; therefore, these sediments often become unstable after periods of intense precipitation, especially when preciding seismic activity caused initial surface rupturing (Torgoev et al., 2005). In this later case surface water flows in the cracks and stops at the bedrock, which forms a sliding mass moving along the contact between stable bedrock and overlying aeolic sediments (de Marneffe, 2010).

According to Figure AF.47b, the Quarternary sediments (other than loess-like loam) have a comparatively low percentage of area affected by the landslide activity. This can be explained by the fact that most of these deposits are located on gentle slopes and are generally not very thick (about 10-15 m, personal communication – de Marneffe, 2011). The extent and position of loess sediments in Figure AF.46 are not precise, as it was not the main focus of the field survey (personal communication – de Marneffe, 2011). Therefore, these sediments were not considered for the final compilation of this thematic layer.

The presented geological map and outlined formations are the basic inputs for the compilation of thematic layer (see the ranking of formations according to rock unit classes in Table AT.10). This expert-based classification relies on observed landslide susceptibility of certain formations (see Figure AF.47b). The applied procedure involves certain subjectivity, as it does not directly account for the geotechnical and hydrogeological properties. Figure AF.48 compares the compiled thematic layer with the overlaid landslide outlines for 2007. As it can be see, the extracted map contains 6 classes of the rock units: the biggest portion of area is occupied by the rock type of class 6, while the smallest one is occupied by rock unit of class 4, mainly represented by very stable volcanogenic rocks.

Table AT.10: Classification of the rock formations within thematic layer (see a formation code in Figure AF.49).

Geological code	Composing rocks	Formation	Rock unit class
Q IV	Gravel, sand	Q	1
Q III-IV	Colluvium, deluvium, proluvium	Q	1
Q III	Colluvium material of big grain size	Q	1
Q I-II	Sand and material of middle grain size	Q	1
P3 – N1 – ms1	Conglomeratic sandstone, conglomerate	MAIL	6
P3 – N1 – ms2	Conglomeratic sandstone, conglomerate	MAIL	6
P2 - 3	Clay, siltstone	BED	2
P1 – 2	Limestone, clay, sandstone, conglomeratic sandstone, conglomerate	ISO	5
K2 – Sn2	Clay, sandstone with limestone	TEC	3
K2t - Sn	Limestone, clay	NAN	5
K2s	Clay, sandstone, gravelite, limestone	KOR	3
K1n + al	Clay, limestone, sandstone	KOR	3
K1hd	Conglomerate, conglomeratic sandstone, sandstone, basalt	PLA	4
J2	Sandstone, siltstone	SAR	6
J1ts2	Clay, siltstone	USA	2
J1ts1	Clay, siltstone	USA	2
C1v – s	Limestone	ANG	5
D 1-2 ab	Laves, silicates, siltstone	-	4
S1 – 2 asA	Effusive sillicates	-	4
S1 – 2 as	Effusive sillicates	-	4

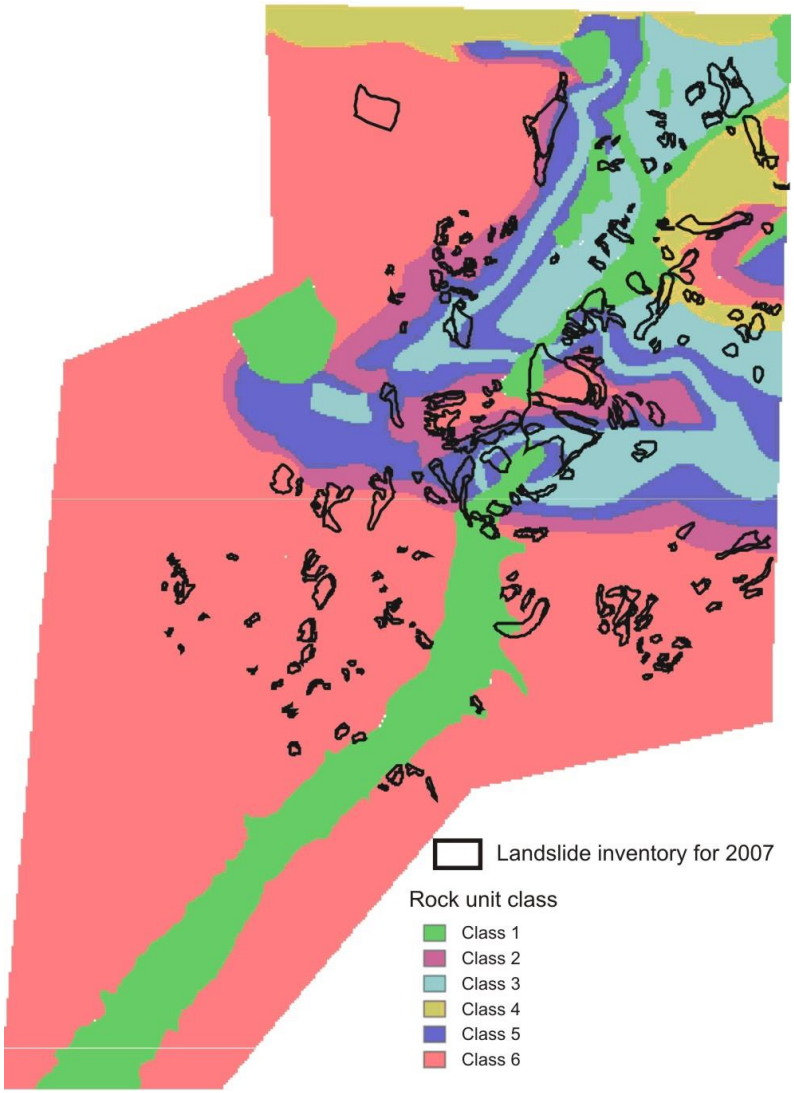

Figure AF.48: Thematic layer of the rock units (6 classes) with the overlaid landslide outlines for 2007.

IV.1.4 Structural control

Several authors highlight the role of the structural settings with respect to their influence on slope stability (Fookes and Wilson, 1966; Varnes, 1978; Cruden, 2000; Prager et al., 2009 among others). The authors conclude that the mass movements often occur along the bedding planes of the contact zones, which is related to the contrast of the geotechnical properties and the intense fracturing within these zones. They also note that the water saturation increases near these contacts which additionally contributes to slope instability. Therefore, the structural settings of the studied slopes are often considered to be a basic aspect in landslide susceptibility studies.

Grelle et al. (2011) propose a semi-automatic methodological approach to map the structural control features on the basis of the southern Italy study case. The authors define three main types of interaction between the slope aspect and the rock dip orientation measured in the horizontal plane, namely cataclinal (slope and layers are roughly inclined in the same direction), orthoclinal (slope inclination and layer dip are roughly perpendicular to each other) and anaclinal slopes (slope inclination and layer dip are roughly opposite, see Figure AF.49). All slopes in the target area were classified into these three groups, applying a tolerance angle value which is calculated as the difference between the slope aspect (Ψ_S, º) and the rock dip orientation (Ψ_L, º). For example, if the tolerance angle is 45º, then all slopes with $|\Psi_S - \Psi_L| \leq 45º$ are classified as cataclinal (slope and layers are roughly inclined in the same direction). The authors show that for any values of the tolerance angle the cataclinal slopes are the most susceptible to the landslide activity. The orthoclinal and anaclinal slopes are much less subjected to the slope instability, while the anaclinal slopes proved to be the most stable ones.

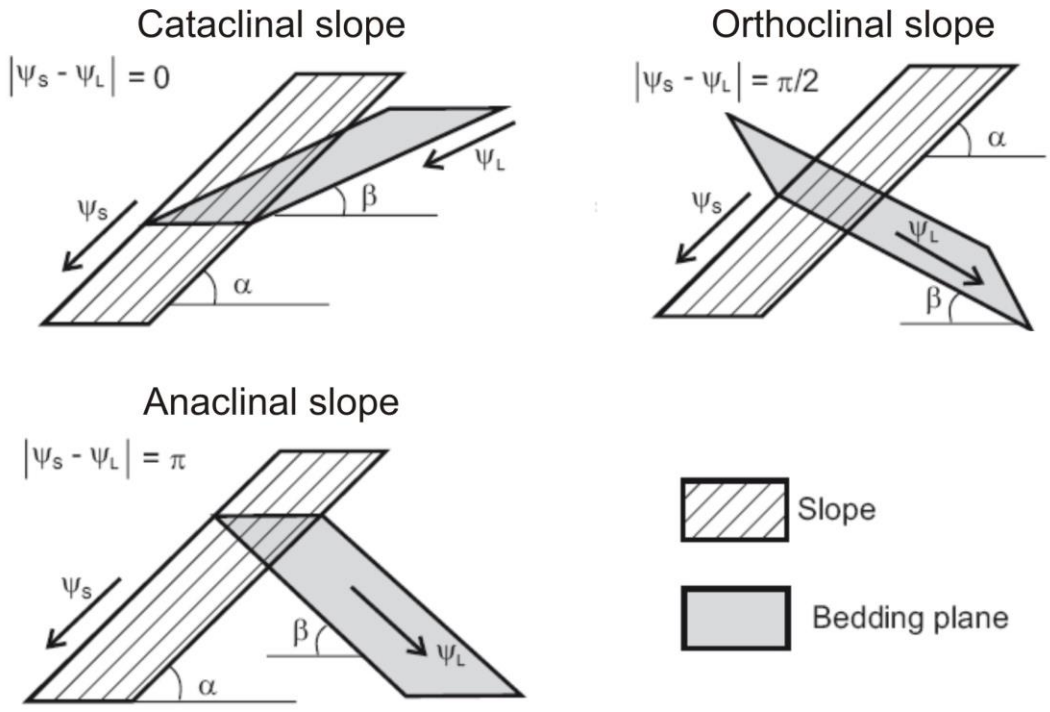

Figure AF.49: Types of an interaction between the slope aspect (Ψ_S, º) and the rock dipping (Ψ_L, º), applied for a mapping of the structural control features (by Grelle et al., 2010).

Qi et al. (2010) present field evidences of the structurally controlled landslides, triggered by the M=7.9 Wenchuan, China earthquake in 2008. For example, Figure AF.50 presents a view to the river slopes situated in the Beichuan study area. The right bank slope (see Figure AF.50a) is almost orthoclinal, since the difference between the dipping direction of the rocks and the slope exposition is about 80-90°. The left bank slope (see Figure AF.50b) is considered as cataclinal, as the corresponding difference is less than 20-30°. It can be seen that the right bank slope kept stable, while the left bank one, named as Magongyan landslide, has failed and blocked the river. The authors note that a majority of the landslides triggered by the Wenchuan earthquake were situated on cataclinal slopes. The list of the cataclinal landslides includes the famous Tangjiashan, Daguangbao, Laoyingyan, Xiaojianping and Chenjiaba landslides.

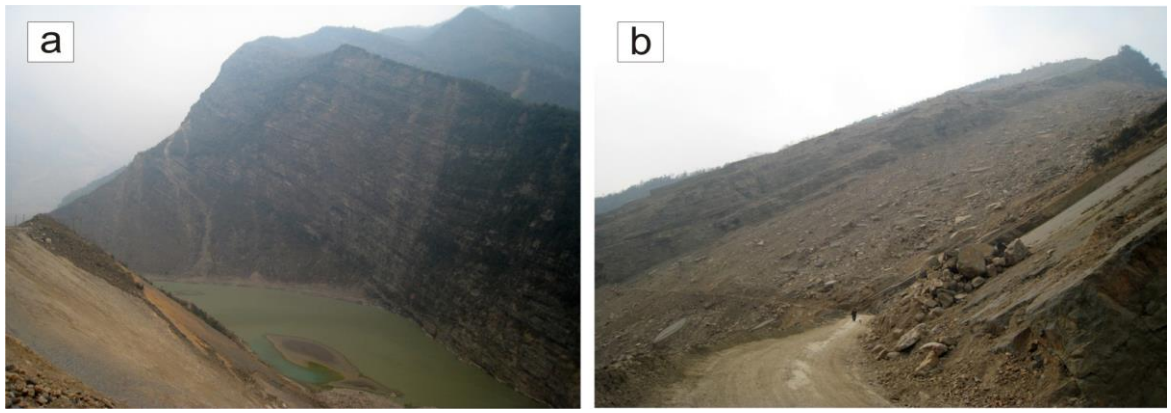

Figure AF.50: (a) View to a right-bank slope, where the layer dipping is almost perpendicular to the slope inclination (camera is oriented towards the north); (b) view of the left-bank slope (camera is oriented to the south) which hosts Magongyan landslide (by Qi et al., 2010).

To compile the structural control thematic layer we adopt the aforementioned concept proposed by Grelle et al. (2010), which classifies the slopes into cataclinal, orthoclinal and anaclinal groups (see Figure AF.49). The first analysis step is a regional mapping of the sedimentary rock dipping, which is accomplished by an interpretation of the 1984 aerial stereo-imagery (M 1:33000). This imagery is panchromatic (black-white colour). The Google Earth software provides an additional interpretation option, as the high-resolution Quickbird imagery can be viewed in the 3D domain. This imagery is represented by a true colour composition such as seen by the human eye; therefore, it strongly helps in discrimination of different rock formations.

The basic guidelines of the photo-geologic interpretation are presented by Ray (1960), Allum (1975), Drury (1986) and Dirik (2005). The main interpretation principle implies that most features of the rock bedding can be identified on the stereo-imagery. Figure AF.51 presents the case, when the structural settings (strike, dip) can be studied from a sample 3D view, presented by the Quickbird imagery. Here, the strike of the bedding plane can be easily reconstructed solely on the basis of the imagery. A precise value of the dipping angle can be reconstructed from the DEM or topographic map of the target area.

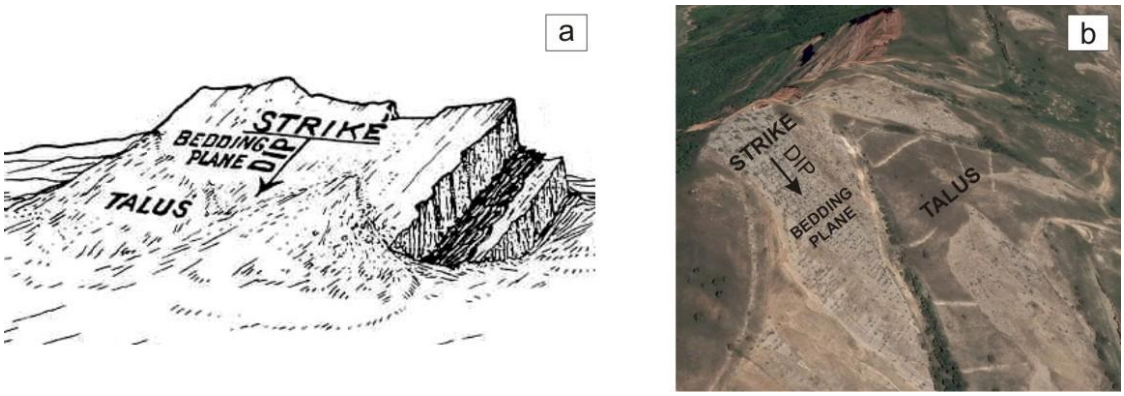

Figure AF.51: (a) Schematic representation of the relation between strike-dip-bedding plane and talus (by Dirik, 2005); (b) sample 3D view of the Quickbird image with an indicated strike/dip directions.

Figure AF.52a provides a schematic representation of the morphologic features in the horizontally layered strata (Dirik, 2005). These features normally include a dendritic drainage network, deep canyons and ring structures, which can be easily identified on the aerial or satellite imagery. Figure AF.52b represents a sample view from the south-eastern part of the study area (the 1984 aerial imagery). The deeply-incised canyon and ring structures are well-expressed here, which indicate a horizontal rock layering. The 3D views,

presented in Figure AF.52c, AF.52d and AF.52e demonstrate that these ring structures are mainly due to richer vegetation growing in the talus between the rock outcrops.

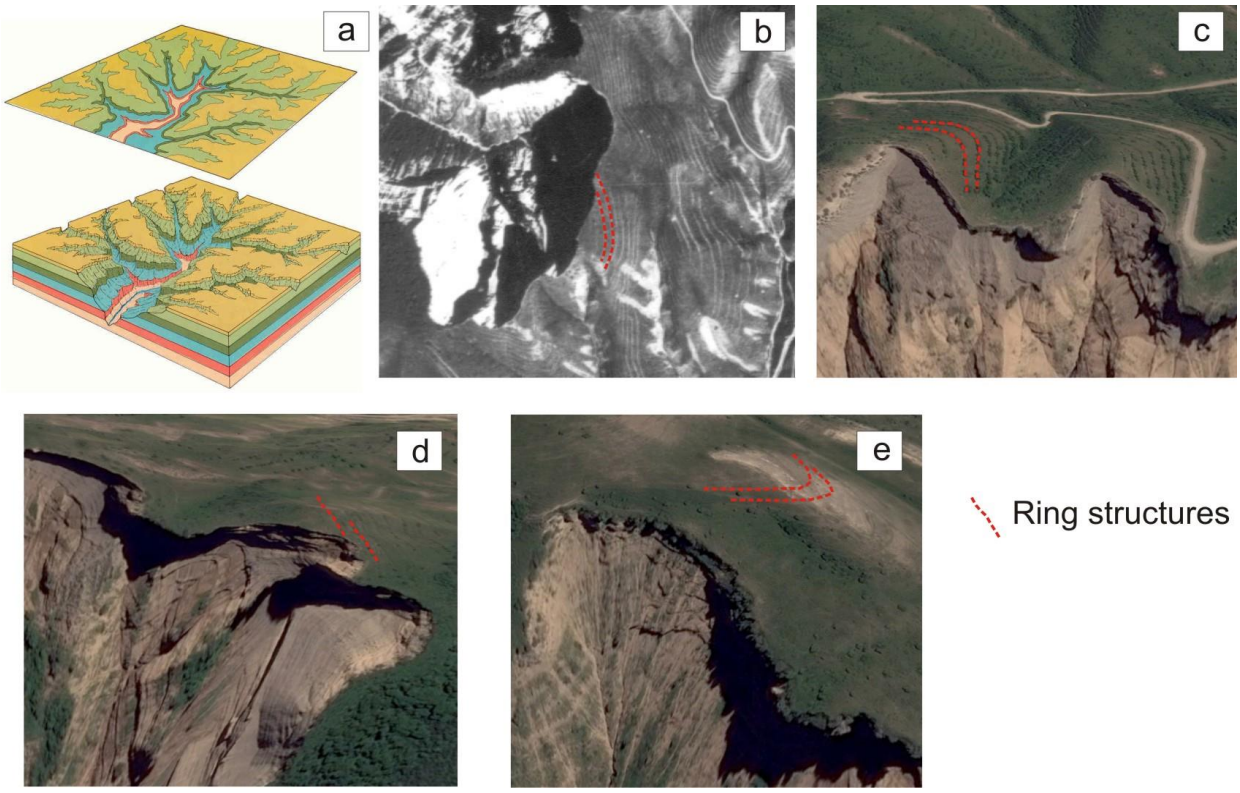

Figure AF.52: (a) Schematic representation of a dendritic drainage network and the deep canyons in a horizontally layered strata (by Dirik, 2005); (b) view from above at the deep canyon and ring structures in the target area (the 1984 aerial imagery); (c), (d), (e) sample 3D views of the deep canyons and ring structures in the target area (the Quickbird imagery, Google Earth software).

The patterns of the inclined bedding in the cataclinal slopes are normally identified via so-called V-shape structures (see Figure AF.53a). These structures originate from the erosion and their size is inversely proportional to the dipping angle – the low dipping angle results in large V-shape structures, while the steeper dipping decreases their size. Figure AF.53b presents a comparison of two types of the V-shape structures in the Central Syncline. The western ones are bigger than the eastern ones – it shows that the dip of the layers in the eastern part is steeper compared to the dip of the layers in the western part of the Central Syncline. The V-shape structures do not normally exist in orthoclinal and anaclinal slopes.

Figure AF.53: (a) Schematic representation of roughly parallel outcrop patterns in a cataclinal slope (by Dirik, 2005); (b) and (c) sample views from above at the V-shape structures in the target area (the Quickbird imagery, Google Earth software).

The symmetric or asymmetric form of a hill is another important feature to track the bedding patterns. Figure AF.54a shows that cataclinal slopes are normally gentler than anaclinal ones due to the different resistance to erosion (see Figures AF.54b, AF.54d and AF.54e). This asymmetry disappears for steeper rock bedding: Figure AF.54c shows an almost symmetric hill observed for the steeply inclined layers. Figures AF.55b, AF.54d and AF.54e also show that cataclinal slopes, in comparison to anaclinal ones, are more susceptible to the landslide activity (see the landslide scarps, marked by the blue solid lines).

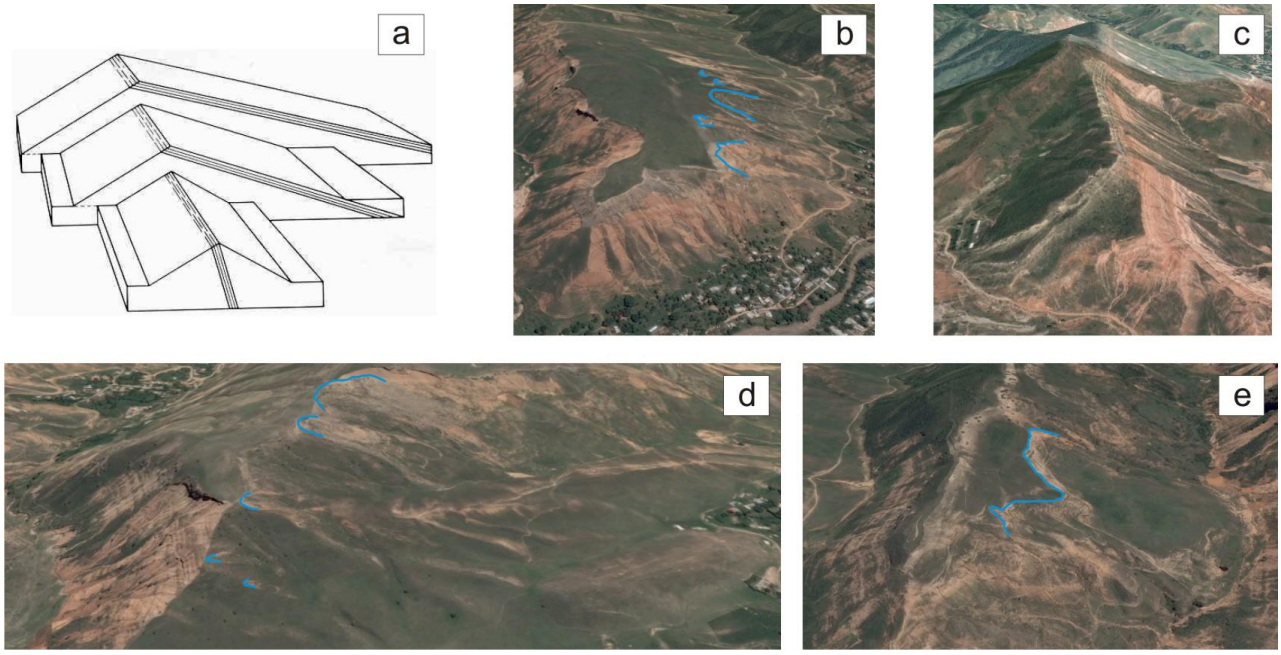

Figure AF.54: (a) Schematic representation of a hill asymmetry resulted from the cataclinal and anaclinal slopes (by Dirik, 2005); (b), (c), (d) and (e) the Google Earth views at the hills with a different degree of asymmetry (the blue lines are the landslide scarps).

Figure AF.55 presents the 3D snapshots of the fold axis. A true colour composition of the Quickbird imagery helps in identifying the bedding patterns (see the red dotted lines). The surroundings of the anticline axis can be subjected to landslide activity, especially when the slopes are cataclinal. For example, a majority of the slopes in the axial part of the Central Anticline (see Figure AF.55a) are cataclinal and there are several landslides in this proximity (see blue solid lines in Figure AF.55a). The slopes in the axial part of the Northern Anticline are orthoclinal or anaclinal (see Figure AF.55b) and it results in much higher slope stability. Figure AF.55c shows that the axial part of the Central Syncline is also susceptible to landslide activity. The structural control is proved by the fact that a majority of the landslides the Central Syncline occur along the layer bedding.

Figure AF.55: The Google Earth views at the fold axis for: (a) the Central Anticline, (b) the Northern Anticline and (c) the Central Syncline (the red dotted lines are the rock outcrops, the black dotted lines are the fold axis and the blue solid lines are the landslide scarps).

The final results of the photo-geologic mapping are presented in Figure AF.56a (marked as rock bedding - Ψ_L). The target area is subdivided into 30 structural zones of uniform rock bedding. The interpreted values of layer inclination are also presented here – it ranges from a horizontal layering up to 50°. Figure AF.56b also presents a map of a slope aspect (marked as Ψ_S). The ArcGIS software (Spatial Analyst extension) is applied to extract this map from the SPOT DEM.

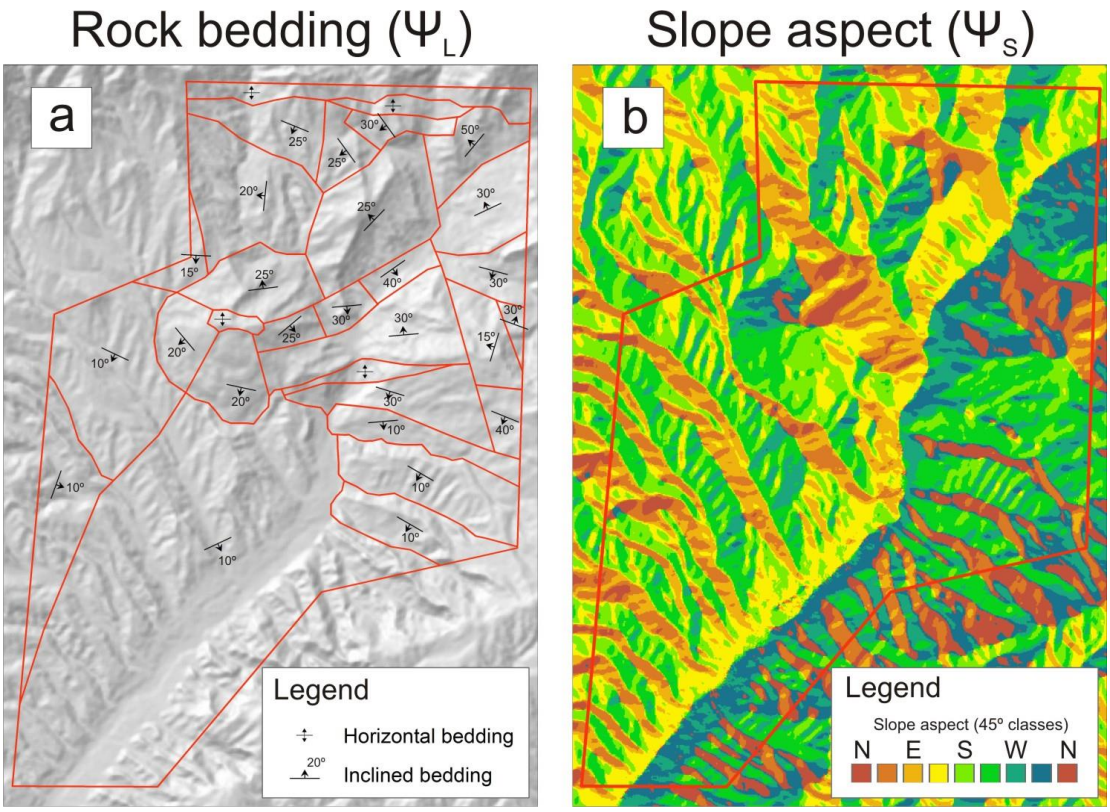

Figure AF.56: (a) Results of the photogeologic mapping showing the areas with an uniform direction of the rock bedding; (b) map of slope aspect extracted for the SPOT DEM.

Following the concept of Grelle et al. (2011), the value of $|\Psi_S - \Psi_L|$ determines the type of an interaction between the rock bedding and slope aspect (see the classification in Figure AF.49). Three different values of a tolerance angle (30°, 45° and 60°) are applied by us to separate the cataclinal, orthoclinal and anaclinal slopes (see the description in Table AT.11). Figure AF.57 presents the models constructed for these values of a tolerance angle. All models have four slope classes: cataclinal, orthoclinal, anaclinal and massive. The first three classes are determined by a value of $|\Psi_S - \Psi_L|$. The last class, called "massive", is applied to areas where no bedding could be identified, where the rocks are marked by horizontal bedding or to the slopes with the inclination of less than 7°.

Table AT.11: A description of the classes, applied for different models of the structural control thematic layer.

Class / Model	Tolerance angle	Cataclinal slope	Orthoclinal slope	Anaclinal slope	Massive
Model 1	30º	$\|\Psi_S - \Psi_L\| \leq 30º$	$30º < \|\Psi_S - \Psi_L\| < 150º$	$\|\Psi_S - \Psi_L\| \geq 150º$	-horizontal rock layering; -slope inclination less than 7º.
Model 2	45º	$\|\Psi_S - \Psi_L\| \leq 45º$	$45º < \|\Psi_S - \Psi_L\| < 135º$	$\|\Psi_S - \Psi_L\| \geq 135º$	-horizontal rock layering; -slope inclination less than 7º.
Model 3	60º	$\|\Psi_S - \Psi_L\| \leq 60º$	$60º < \|\Psi_S - \Psi_L\| < 120º$	$\|\Psi_S - \Psi_L\| \geq 120º$	-horizontal rock layering; -slope inclination less than 7º.

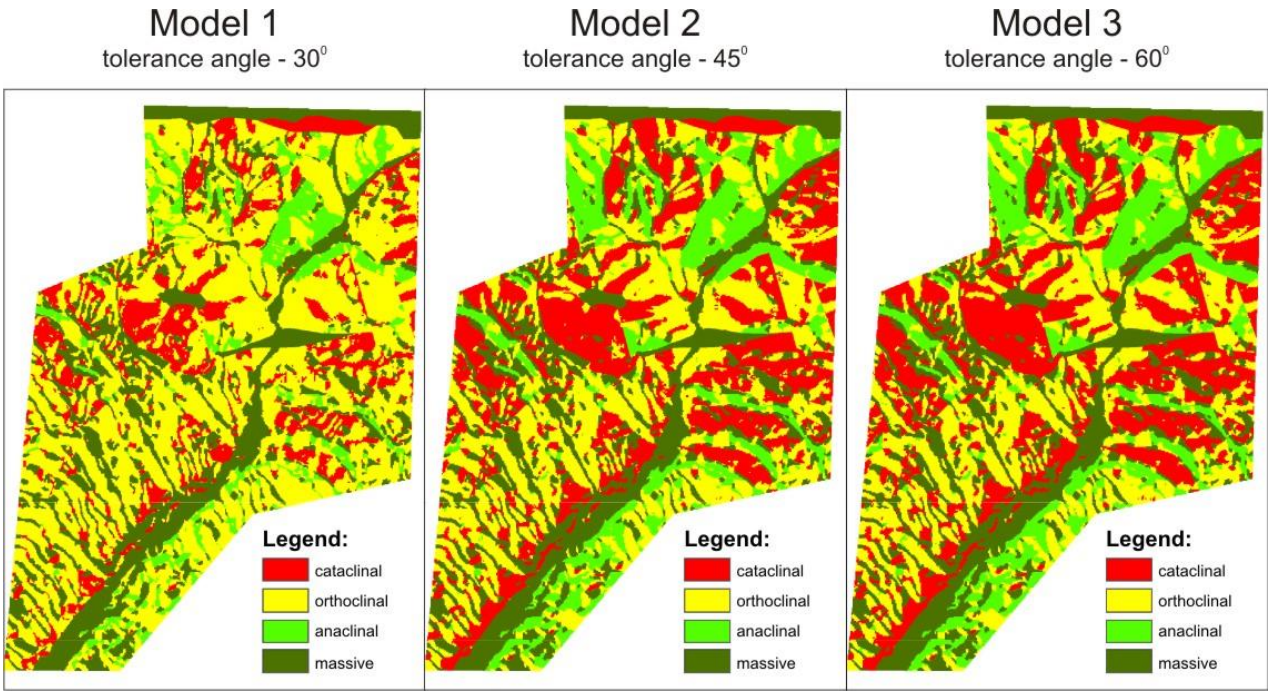

Figure AF.57: The models of the structural control thematic layer, extracted for the different values of the tolerance angle.

IV.2 Landslide susceptibility mapping

The mapping of thematic layers is reviewed in the previous section. These layers assemble the spatial information on the factors contributing to the landslide activity. The thematic layers together with landslide inventories present the basic input data for the mapping of the landslide susceptibility which is reviewed in this section.

Four different mapping methods are applied here to rate and rank all terrain units of target area with respect to their propensity to produce slope instabilities. These methods represent the groups of heuristic, statistical and process-based methods (see *Section A.I.2* for more details). The heuristic mapping is presented by the Index-based method, the statistical mapping is presented by the Discriminant Analysis and Artificial Neural Networks, while process-based mapping is presented by the Newmark method. All methods are indirect: first, the affecting factors are ranked/estimated based on their influence on the instability potential and, then, the susceptibility mapping is performed. The Index-based and Newmark methods are qualitative, i.e. they produce non-quantitative estimates of the landslide susceptibility level. The statistical methods applied in our studies are quantitative, as they provide numeric outputs. More detailed overview of applied mapping methods, i.e. concept, methodology and results, are presented in the sub-sections below.

IV.2.1 Index-based mapping

The index-based or heuristic mapping is indirect and mostly qualitative method (see *Sub-section A.I.2.2* for more details). Prior to the mapping itself the instability factors/thematic layers should be ranked and weighted according to their expected importance with respect to the triggering of mass movements. It becomes a basis for the decision rules further applied for the landslide susceptibility mapping. A certain degree of subjectivity is involved in the preparation of the thematic layers and in establishment of the rules. This subjectivity is often considered to be the main drawback of this method.

The first analysis step is the ranking of all thematic layers, i.e. their conversion into a categorical/interval/ dichotomous representation. Some thematic layers can naturally contain necessary data format, like it is for the layer of structural control with four categorical classes (see *Sub-section A.IV.1.4*). The ranking specifications (number of classes and sampling interval) can be determined by the landslide statistic or via the established independent rules. The independent ranking (e.g., fixed sampling interval) is often more preferred, since the following weighting in this case is not biased.

The next analysis step is the weighting of ranks/classes of the thematic layers according to their potential to bring destabilizing effect. In our study this weighting is performed via the parameter, called as the map-scaled density (*Dm*; Chung and Fabbri, 2003):

$$Dm = \frac{q}{r} \Big/ \frac{\alpha}{t} \Rightarrow Dm = \frac{q * t}{r * \alpha} \qquad \text{(AE.3)},$$

where q is a pixel count for the landslides/scarps within given class of the thematic layer, r is a total pixel count for the landslides/scarps, α is a pixel count for the given class of the thematic layer and t is the total pixel count for the thematic layer.

Logically, the *Dm*-value exactly equal to 1 implies that a given class of the thematic layer has an equal probability to be classified as susceptible or non-susceptible class. The *Dm*-value > 1 should indicate a destabilizing impact of given class, while *Dm*-value < 1 should show opposing effect. Chung and Fabbri (2003) propose several guidelines to estimate the prediction significance based on the numeric value of *Dm*. The authors indicate that a "powerful and effective" prediction class should have either a very large (>3) or a near zero (<0.2) value of *Dm*. A high landslide susceptibility is marked by a *Dm*-value of more than 6 and very low landslide susceptibility is indicated by a value of less than 0.1.

Six thematic layers are applied in the index-based mapping in our target area, namely slope angle, slope aspect, slope curvature, land cover, rock units and structural control (see *Sub-sections A.IV.1.1-A.IV.1.4*). The layers of land cover, rock units and structural control have a categorical representation, i.e. they do not need ranking. The surface morphological layers are subjected to independent ranking, i.e. one which employs fixed sampling intervals. The thematic classes are weighted applying the 2002 landslide/scarp outlines.

Figure AF.58 shows the distribution of the *Dm*-values within the different classes of the slope angle. The most susceptible class in the 10-degree ranking is marked by slope angle values of 20 to 30º, while the least susceptible class is marked by values between 0 and 10 º (see *Dm*-values in Figure AF.58a). A more detailed ranking (5-degree intervals in Figure AF.58b) reveals that the class of 25-30º has the highest value of *Dm*, while the classes of 0-5º and 40-45º are the least susceptible. According to guidelines of Chung and Fabbri (2003), only the class of 40-45º can be considered as an effective prediction class, as the value of *Dm* is around 0.2.

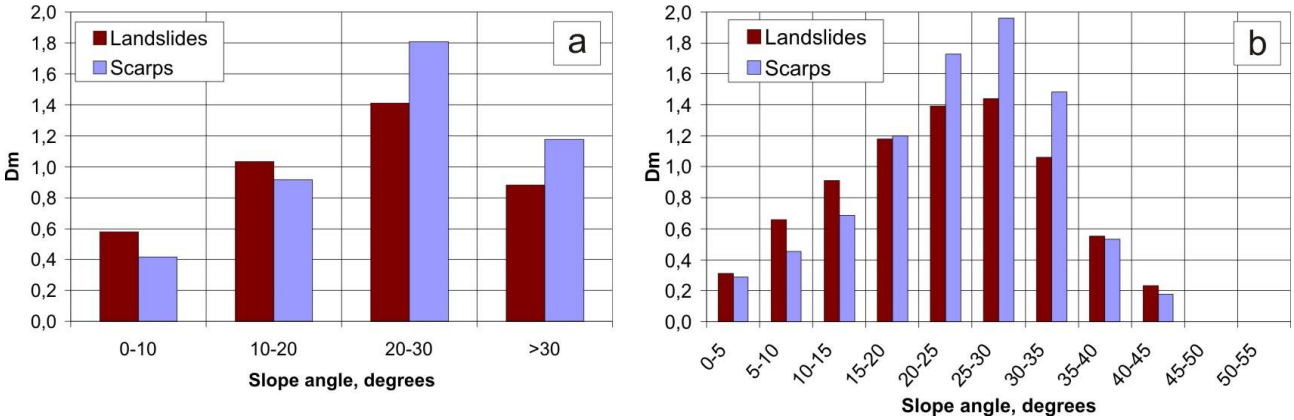

Figure AF.58: Plots of the *Dm*-values versus the classes of slope angle in the ranking with: (a) 10-degree and (b) 5-degree intervals.

The distribution of the *Dm*-values for the slope aspect classes is presented in Figure AF.59. The 90- degree ranking shows that all classes have very similar values of *Dm* (see Figure AF. 59a). A more detailed ranking (45-degree classes in Figure AF. 59b) reveals that the slopes with a northern and western exposition have the highest values of *Dm*, while those marked by eastern exposition have the lowest *Dm*-values. The low and high susceptibility classes in both rankings are far from the *Dm*-ranges recommended by Chung and Fabbri (2003) – it indicates that the classes of slope aspect have an inefficient prediction power.

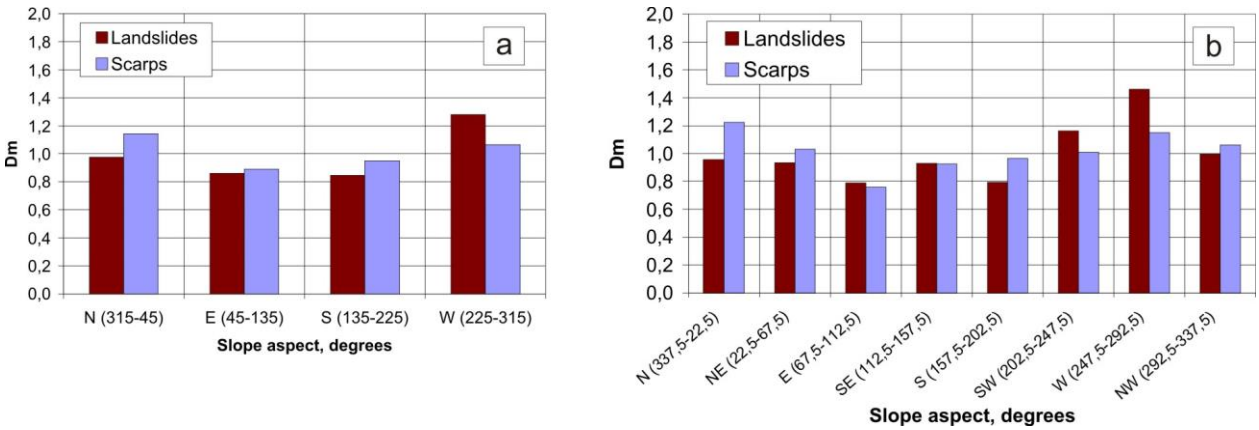

Figure AF.59: Plots of the *Dm*-values versus the classes of slope aspect in the ranking with: (a) 90-degree and (b) 45-degree intervals.

Statistics for the different ranking of the total curvature are presented in Figure AF.60. A clear trend for the change of the *Dm*-values can be observed. In almost all graphs, the *Dm*-values for the landslides are steadily decreasing from the concave (negative values) to the convex curvature (positive values). Varnes (1978) provides an explanation for these statistics – the author observed that for a majority of the active landslides the concave depletion zone is larger than the convex zone of accumulation. The landslide scarps have an opposite trend: the *Dm*-values are normally higher for the convex curvature than for the concave one. It can be explained by the fact that the scarps of the seismically triggered landslides tend to be situated close to the convex mountain/ridge crest. As it can be seen, the *Dm*-values range between 0.40 and 1.72. According to guidelines of Chung and Fabbri (2003), all classes of the total curvatures do not have an effective prediction power, even though the clear link between curvature and landslide activity can be outlined.

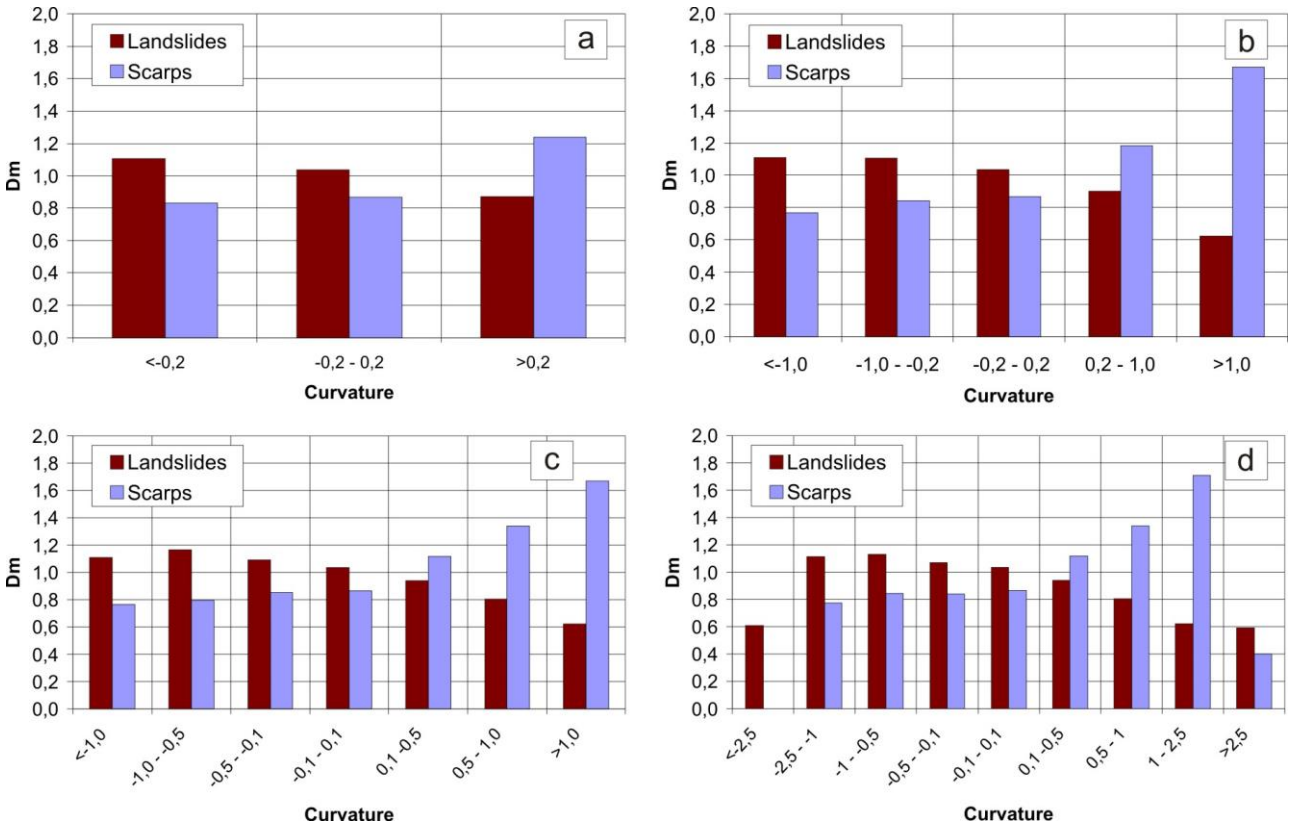

Figure AF.60: Plots of the *Dm*-values for the total curvature represented by: (a) 3 classes, (b) 5 classes, (c) 7 classes and (d) 9 classes.

The plot of the *Dm*-values versus five classes of the land cover/land use is presented in Figure AF.61. Only the class of rural area is considered to be an effective prediction class, as the corresponding *Dm*-value is equal to zero. The class of urbanized territory is very close to the effective prediction class, as the *Dm*-values range from 0.1 up to 0.45. Three classes of vegetation cover do not have the effective prediction power due to the fact that their *Dm*-values are very close to 1. For example, the class of the bare surface contains 65% of all landslides and it occupies 59% of a total area of this thematic layer - therefore, the corresponding *Dm*-value is 1.1 (see the one in Figure AF.61).

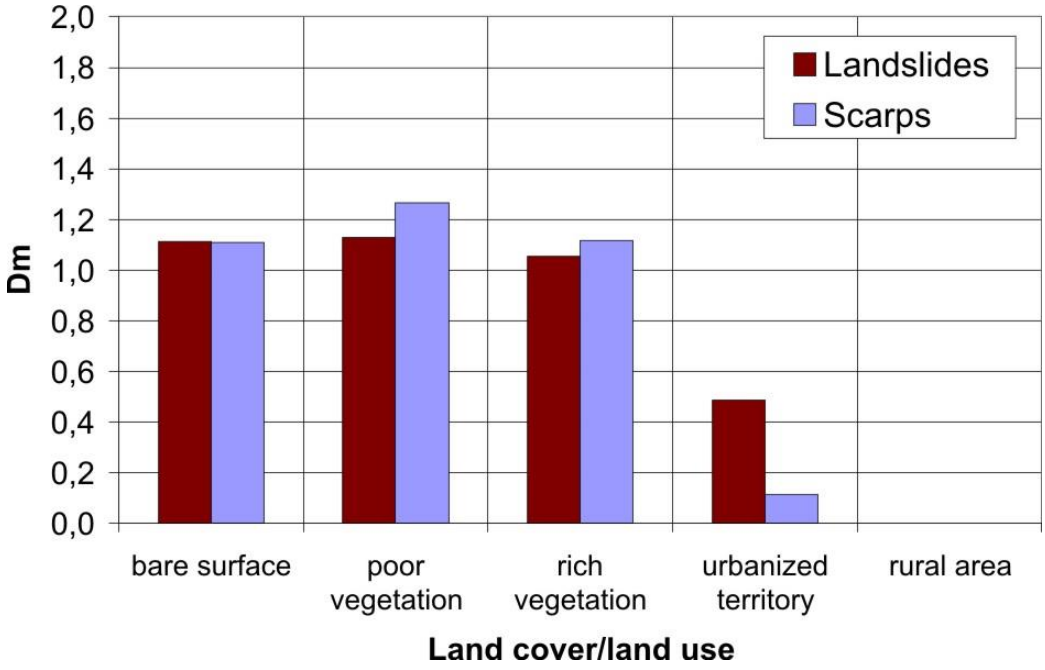

Figure AF.61: Plot of the *Dm*-values versus the land cover/land use classes.

Statistics for the rock formations and the rock unit classes are presented in Figure AF.62. The most susceptible formations are KOR, ISO and BED, while ANG and USA formations are the least susceptible ones (see Figure AF.62a). The ranking of the rock formations that uses six classes (see details in *Sub-section A.IV.1.3*) indicates that class 2 and class 5 are the most susceptible ones, while class 1 and class 4 are the least susceptible (see Figure AF.62b).

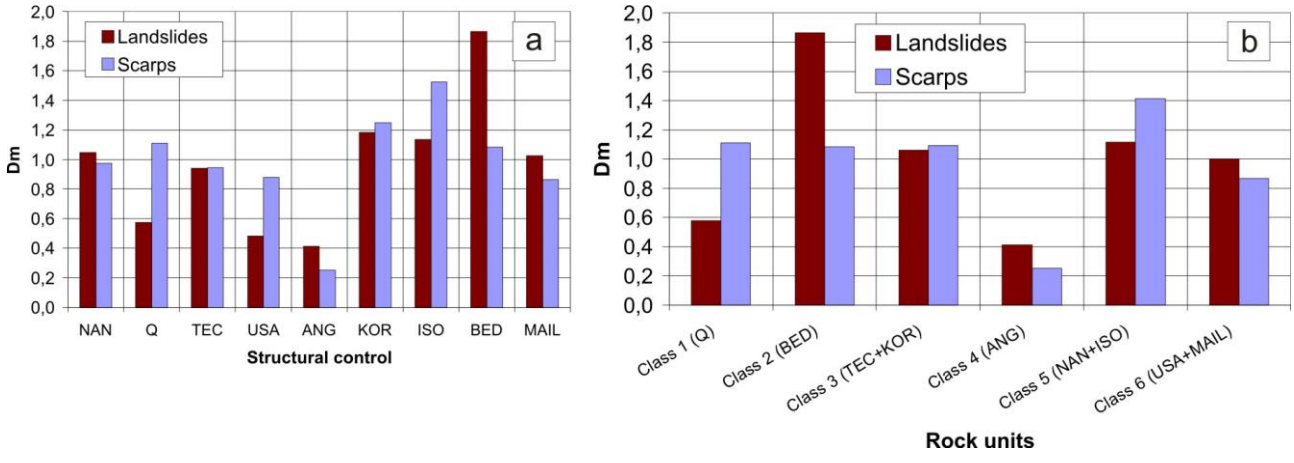

Figure AF.62: Plots of the Dm-values versus classes of: (a) rock formations and (b) rock unit classes.

Figure AF.63 presents the statistics for the thematic layer of structural control. Two values of tolerance angle are studied, namely 45º (Figure AF.63a) and 60º (Figure AF.63b). It can be seen that the tolerance angle does not significantly affect the final values of *Dm* (compare the ones in Figure AF.63). As it could be expected, the most susceptible class is the one representing cataclinal slopes, while the classes of massive structure and anaclinal slopes are the least susceptible ones. None of the classes of the structural control is marked by an effective prediction power, as the *Dm*-values range between 0.41 and 1.4.

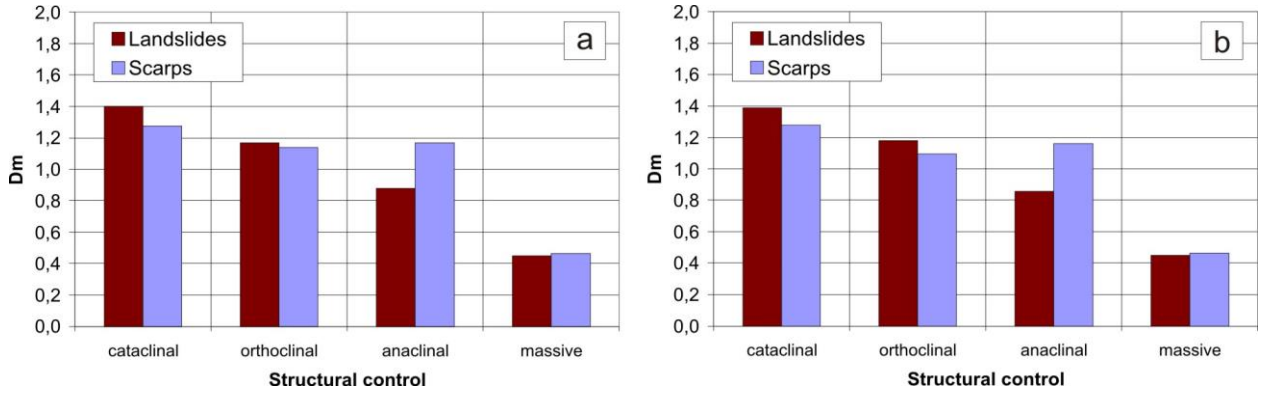

Figure AF.63: Plots of the *Dm*-values versus the classes of the structural control applying: (a) 45-degree and (b) 60-degree tolerance angles.

Two different approaches are employed here to map the landslide susceptibility based on the above-described input data. The first methodology is simplified and it analyzes how the specific combination of thematic layers can be successful to map the landslide susceptibility. Any number of thematic layers can be analysed. The landslide susceptibility level is assessed via the mean *Dm*-value (Dm_m) calculated from a set of specific *Dm*-values as next:

$$Dm_m = \frac{Dm_1 + Dm_2 + ... + Dm_n}{n}, \qquad \text{(AE.4)},$$

where *n* is the number of the analyzed thematic layers and Dm_1, Dm_2…. Dm_n are the specific *Dm*-values, i.e. the ones gained for the analysed thematic layers (see the statistics on these values in Figures AF.59-AF.64). Then, the landslide susceptibility level is assigned to all terrain units based on the resulting Dm_m-values (see the ranking scheme in Table AT.12). The guidelines of Chung and Fabbri (2003) are taken into account to determine the classes of the very low, low and moderate landslide susceptibility. The lower limit for the class of very high landslide susceptibility is less than the value recommended by the authors (>3), as the *Dm*-values for all thematic layers are less than 2 (see Figures AF.59 – AF.64).

Table AT.12: Ranking of the landslide susceptibility classes according to the resulting value of Dm_m.

The range of the Dm_m	Landslide susceptibility class
$Dm_m \leq 0.25$	Very low
$0.25 < Dm_m \leq 0.95$	Low
$0.95 < Dm_m < 1.05$	Moderate
$1.05 \leq Dm_m < 1.50$	High
$Dm_m \geq 1.50$	Very high

Figure AF.64 presents the results of the landslide susceptibility mapping applying specific combinations of thematic layers. For instance, Figure AF.64a presents Model IB1, which assembles all six thematic layers, namely slope angle, slope aspect, slope curvature, land cover, rock unit and structural control (note: the number of classes for each thematic layer is indicated in legend). As it can be seen, only three classes of the landslide susceptibility (low, moderate and high) can be outlined by this combination of thematic layers (see Figure AF.64a). Model IB2 (see Figure AF.64b) presents a simple composition of two layers (slope angle and rock units) which are often considered to be those that have the strongest effect on the slope instability

potential. Model IB3 in Figure AF.64c assembles the rock units with the surface morphological features (slope angle, total curvature, slope aspect). Model IB4 in Figure AF.64d combines Model IB2 with the structural control and Model IB5 in Figure AF.64e combines Model IB2 with the land cover.

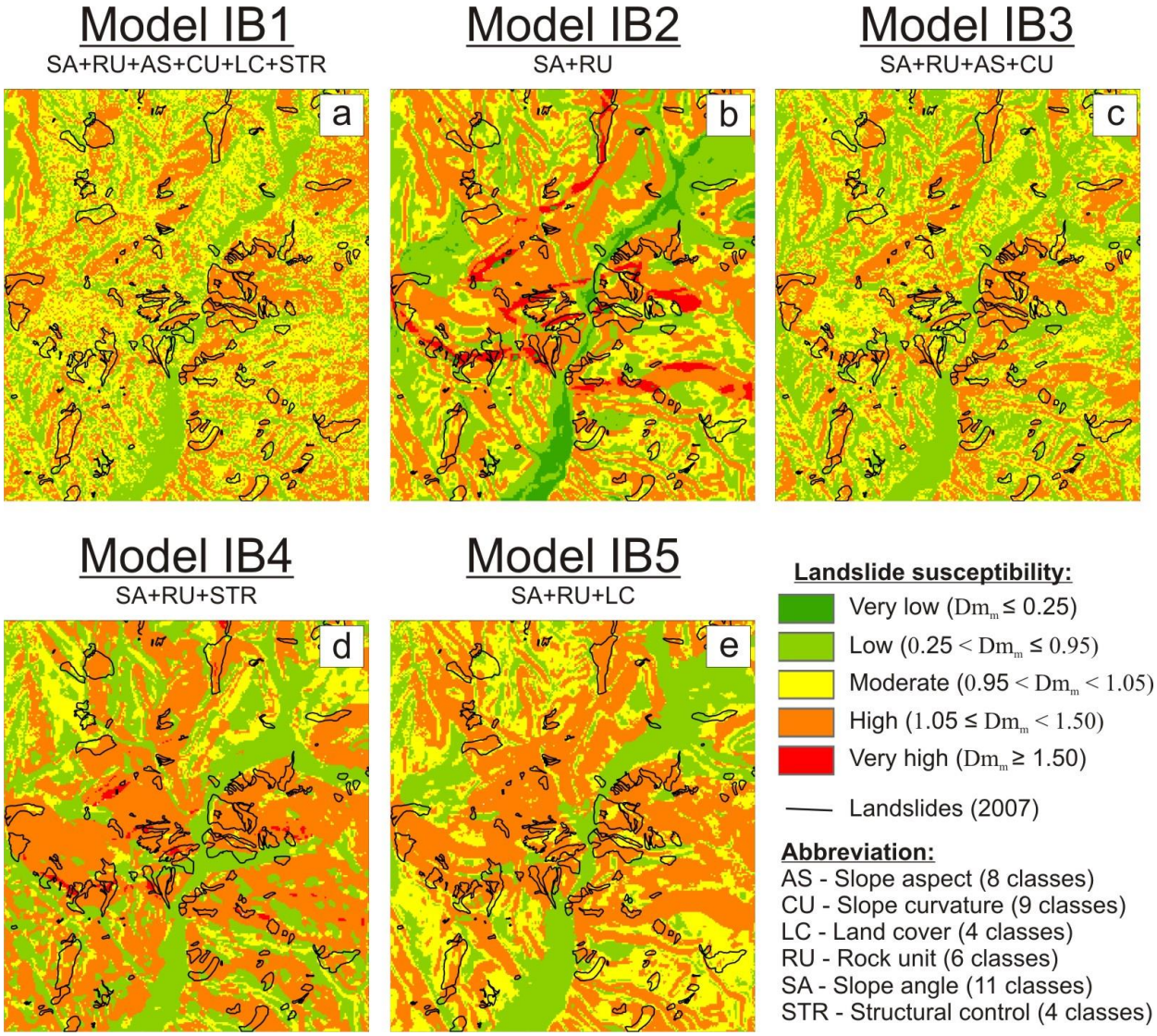

Figure AF.64: Five models of landslide susceptibility assessment based on different combinations of thematic layers (the level of landslide susceptibility is assigned according the Dm_m-values).

As it is indicated above, the landslide susceptibility models (Figures AF.65 a-e) are compiled based on the Dm_m-values which, in turn, are evaluated with respect to the 2002 landslide/scarp inventories. These extracted models are further validated applying the latest inventories: the 2007 landslide/scarp outlines are applied here to calculate the *Dm*-values for all susceptibility classes of extracted models. The resulting distribution of the *Dm*-values should indicate the prediction performance of susceptibility models.
Figure AF.65 summarizes the results of the validation studies applying the 2007 landslide and scarp inventories. All models are characterized by a gradual increase of the *Dm*-values for the increasing susceptibility levels. However, most models do not contain a full sequence of the susceptibility classes and only Model IB2 has all five susceptibility classes. The distribution of the *Dm*-values shows that Model IB4 has the highest Dm-value for the class of the very high landslide susceptibility (compare the *Dm*-values in Figure AF.65). It indicates that a combination of the slope angle, rock units and structural control predicts best the 2007 landslide and scarp occurrence. One of the poorest predictions is made by Model IB1 which combines all thematic layers – the model performance is negatively affected by the layers with poor prediction power.

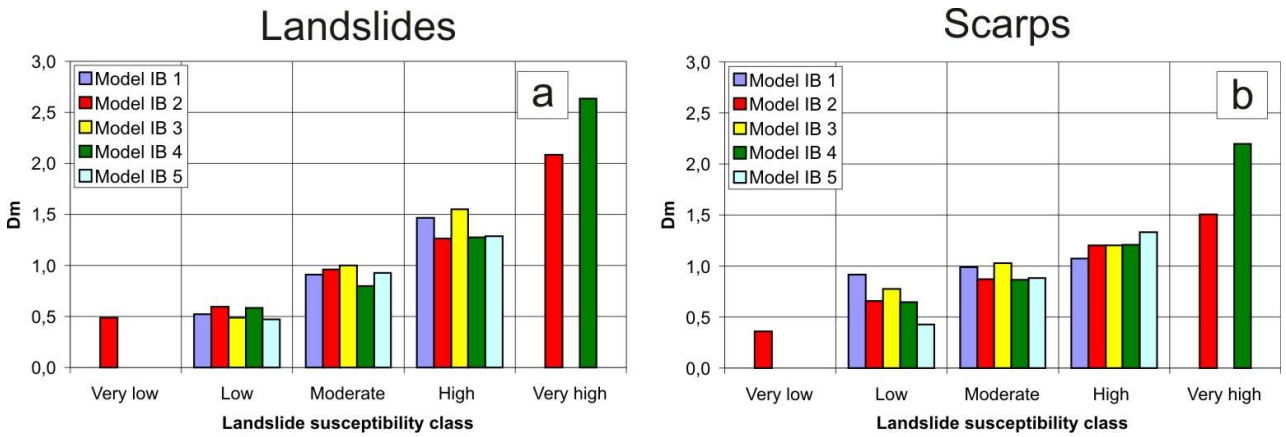

Figure AF.65: Results of the validation studies for Models IB1-IB5 applying: (a) the 2007 landslides and (b) the 2007 landslide scarps.

The second mapping approach accounts for a complex interaction of the input parameters. The thematic layers are integrated into a single product, when the entire area is subdivided into the unique condition units or UCUs (see more info on UCUs in *Sub-section A.I.4*). The values of *Dm* are calculated for each group of UCUs separately and the ranking of the landslide susceptibility relies on Table AT.12. Special attention should be paid to the ranking of the thematic layers: too detailed intervals can lead to data overfitting, i.e. a situation when a large amount of unique UCUs are created and they can not be used to define the general guidelines to differentiate stable and unstable slopes. In this case the landslide susceptibility mapping is impractical, as it basically delineates the analyzed landslide outlines. Figure AF.66a presents a snapshot to the area with more than 12000 UCUs resulted from a very detailed ranking of six thematic layers. Figure AF.66b shows that high *Dm*-values are mainly concentrated within the analysed landslide outlines which makes susceptibility mapping ineffective.

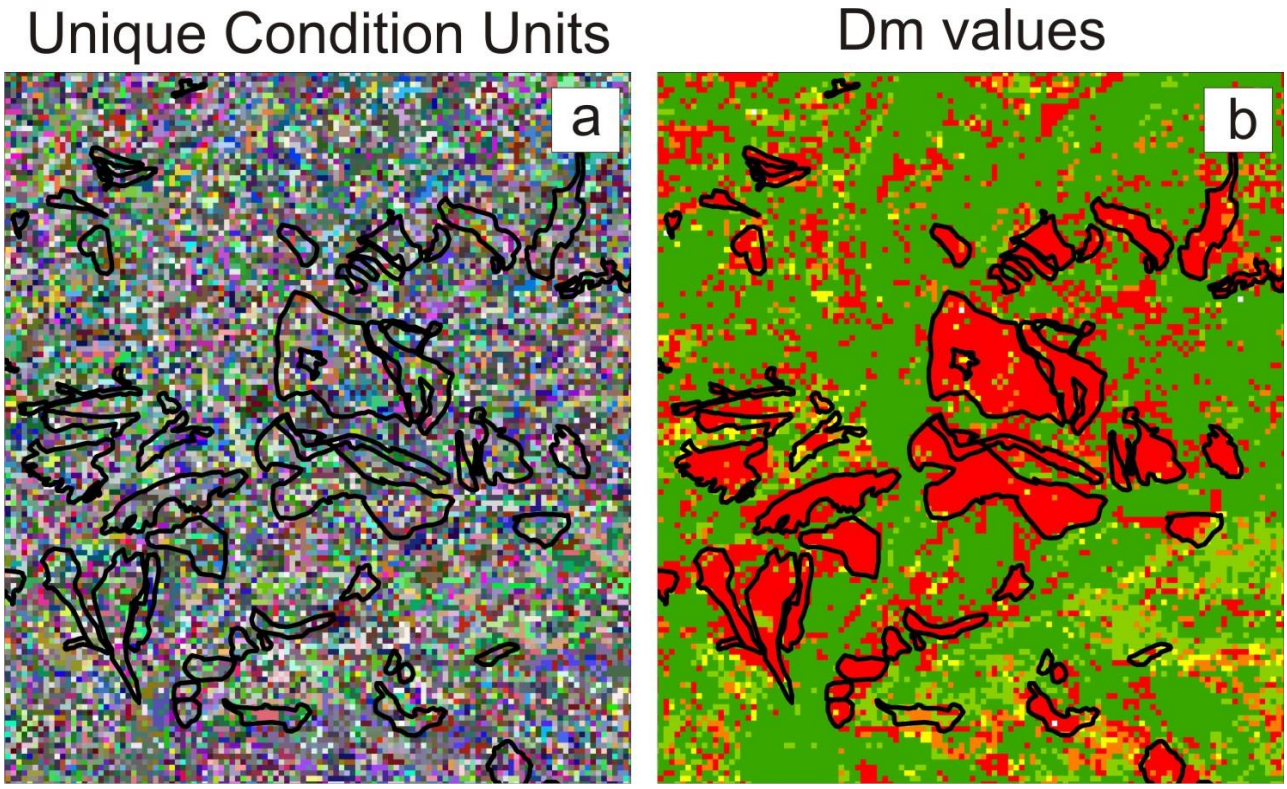

Figure AF.66: (a) Distribution of the UCUs in the central part of the study area gained for a combination of six thematic layers with a detailed ranking; (b) resulting distribution of the Dm-values.

Figure AF.67 presents the susceptibility models for the different variants of UCUs. The analysed combinations of thematic layers are similar to those presented in Figure AF.64. The land cover, rock units and structural control have the same ranking in both mapping approaches (compare a ranking for LC, RU and STR in legends for Figures AF.65 and AF.68). The layers of surface morphology, i.e. slope angle, slope aspect and slope curvature, are subjected to a less detailed ranking to decrease the number of analysed UCUs (compare a ranking for SA, AS and CU in legends for Figures AF.64 and AF.67).

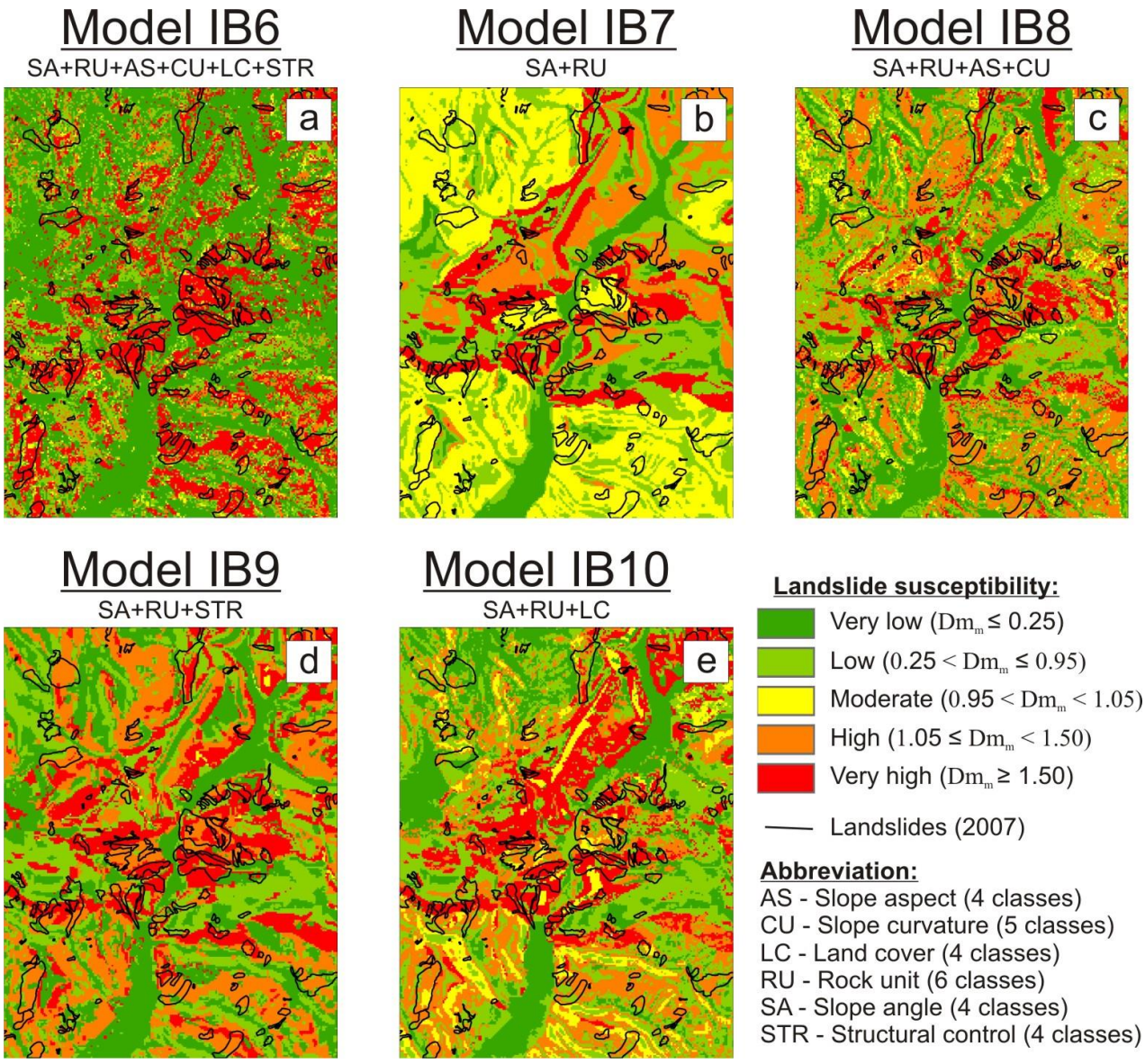

Figure AF.67: Five models of the landslide susceptibility for the different variants of UCUs.

The results of the validation studies for Models IB6-IB10 are presented in Figure AF.68. Here, again, the validation is based on the 2007 landslide/scarps inventories. Most of the models have a full sequence of the landslide susceptibility classes and only Model IB9 does not have a class of the moderate landslide susceptibility. Almost all models present good statistics: the *Dm*-values are growing in parallel with the increasing landslide susceptibility. Some of the models have an inconsistency in the distribution of the *Dm*-values. For example, Model IB6 has a higher *Dm*-value in the low landslide susceptibility class compared to the class of moderate landslide susceptibility (see Figure AF.68b). The statistics shows that the best models are the next: Model IB6 (all six thematic layers), Model IB7 (slope angle and rock unit) and Model IB8 (slope angle, rock unit, slope aspect and slope curvature). Model IB6 has the highest *Dm*-value for the class of the very high landslide susceptibility (compare the *Dm*-values in Figure AF.68a). It indicates that UCUs incorporating all six thematic layers present the best prediction of the 2007 landslide occurrence.

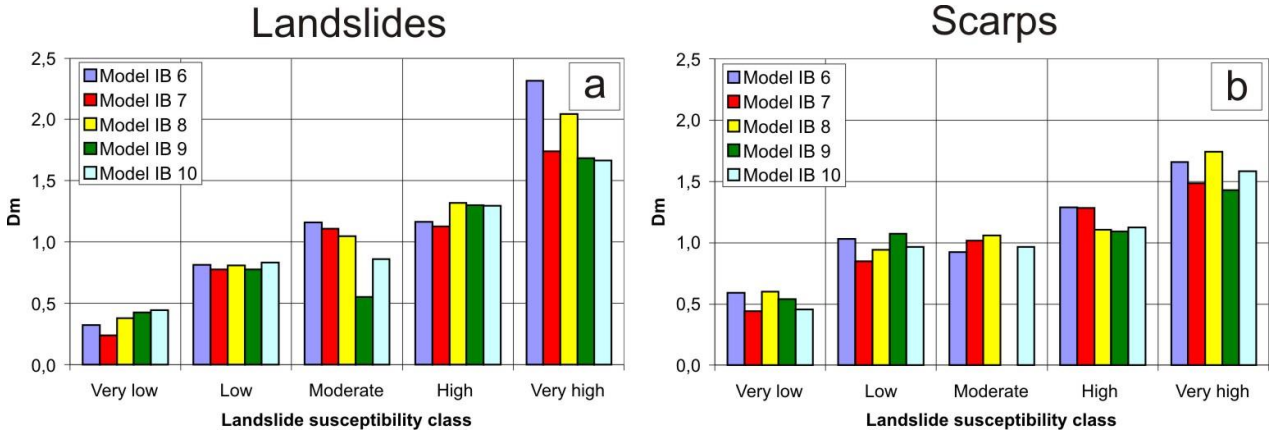

Figure AF.68: Results of the validation studies for Models IB6-IB10 applying: (a) the 2007 landslides and (b) the 2007 landslide scarps.

IV.2.2 Discriminant analysis

The Discriminant Analysis (DA) represents a group of the advanced statistical methods. This method is indirect and provides a quantitative output of the landslide susceptibility mapping. Guzzetti (2006) comments that DA can be performed with almost all types of mapping units, while the most widespread types include grid cells and slope units.

Fisher (1936) is the founder of the DA method. The author presented it as a proxy to classify a given set of data/events/objects into the mutually exclusive groups/classes. Most commonly, landslide susceptibility studies establish two groups, namely: (i) mapping units free of landslides, i.e. stable slopes, and (ii) mapping units with landslides, i.e. unstable slopes. The classification itself is based on a combined parameter calculated from a set of the predictor variables, which provide an interval or dichotomous representation of the analysed affecting factors. These affecting factors in the landslide susceptibility studies normally include morphological, lithological and structural settings. The affecting factors can also include such the thematic layers as land use, mean precipitation, land cover, etc.

The DA technique is based on a linear (or curvilinear) combination of the predictor variables, which best discriminates the predefined classes/groups of data (Michie et al., 1994). The classification applies the value of the discriminant score (D), which is calculated through the linear combination of the predictor variables (V_1, $V_2 \ldots V_n$) as follows:

$$D = a_1 * V_1 + a_2 * V_2 + ... + a_n * V_n \qquad \text{(AE.5)},$$

where a_1, $a_2 \ldots a_n$ are the slope constants for a given set of the predictor variables. It should be noted that any number of predictor variables can be employed in DA. If only one variable is employed, then Equation AE.5 is reduced to linear equation; if n independent variables are involved, then a group discrimination is performed over a functional surface in (n-1) dimensions (Hastie et al., 2001).

The applied technique determines the mean values of D for all classification groups, i.e., those for the group centroids. For the landslide susceptibility studies the values of D are determined for stable (D_0) and unstable (D_1) slopes. The D-values for all mapping units in the study area are schematically represented as the dataset of points, lying on the line between D_0 and D_1. The likelihood of a certain mapping unit to belong to a group of unstable slopes is determined through the distance between the D-value of this mapping unit and D_1, i.e. the one of the unstable slope. This likelihood shows the sliding probability value (P_1), while the probability to belong to a group of stable slopes is defined as P_0=1-P_1.

Figure AF.69 shows two examples of data point clouds with bad and good separation potential (Schwardt and du Preez, 2005). As it can be seen, this potential depends on the ratio between the class centroids distance and the inner-class data deviation. The bad classification potential is represented by those cases, for which the distance between class centroids is comparable to or even less than the inner-class data deviation (see example in Figure AF.69a). The reliable classification can be performed only for the datasets with the inner-class data deviation to be smaller than the distance between class centroids (see example in Figure AF.69b).
Figure AF.69c presents a sample dataset which consists of three classes. The discriminant score values calculated according to Equation AE.5 for the worst and the best linear combinations of the predictor variables are also presented here. As it can be seen, the worst prediction variant cannot be applied for the classification, as the between-centroid distances are comparable to the inner-class data deviation. The best classification variant can be used for the class separation, as the centroid distances are larger than the data deviation within given classes.

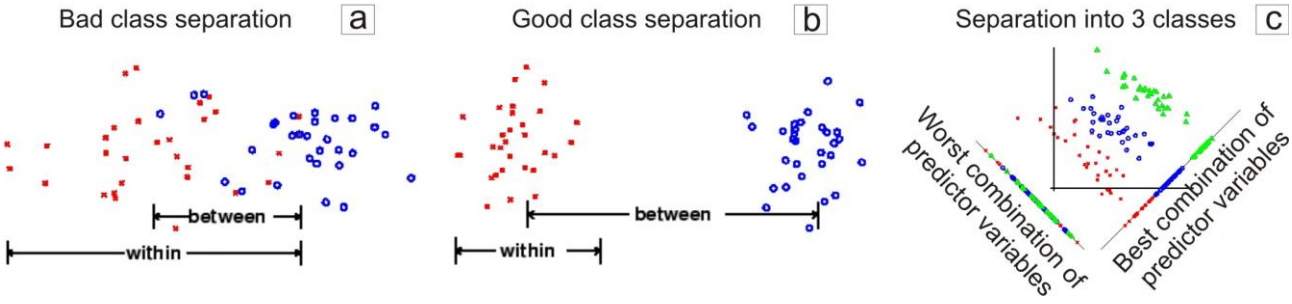

Figure AF.69: The examples of data point clouds with: (a) bad and (b) good classification potential; (c) the sample cloud of data points with the worst and the best linear combinations of the predictor variables, applied for a separation of given dataset into 3 classes (by Schwardt and du Preez, 2005).

Thus, the main goal of DA is to find the linear combination of the predictor variables which best discriminates given dataset into the predefined groups. At present time, there are several statistical packages which perform this classification automatically (XLSTAT, Unistat, MASS, NCSS among others). In our studies we employ SPSS package which has already been used, for example, by Guzzetti (2006) for the landslide susceptibility mapping in the Collazzone study area, Italy. In this case, the user has to select the type of mapping unit, to determine the predictor variables, to convert them into interval/dichotomous representation and to define the classification groups. The optimal linear combination of the predictor variables is automatically detected according to Equation AE.5 through the several iterations performed by the SPSS code.
As it is noted above, the application of DA method starts with the selection of the mapping unit. In our study we select the slope unit to be the main analysed type. According to Carrara (1988), the slope units partition the territory into hydrological regions, which are bounded by drainage/stream and divide/watershed lines. Figure AF.70 schematically represents all processing steps, involved in the slope units extraction based on the DEM of study area. The extraction is automatically performed with the ArcGIS software, applying Spatial Analyst extension (Hydrology tools). The first processing step is an extraction of the flow direction raster which shows the direction of the steepest descent from each cell (Jenson and Domingue, 1988). This product is later applied to extract the flow accumulation raster indicating the accumulated flow discharge for each pixel of the study area. The stream network can be constructed based on flow accumulation raster - it is performed by export of raster data into the vector dataset. The flow direction raster and stream network dataset are then applied to extract the watershed outlines. An integration of the stream and watershed networks provides the outlines of slope units (see the slope unit outlines overlaid over the hillshaded DEM in Figure AF.70).

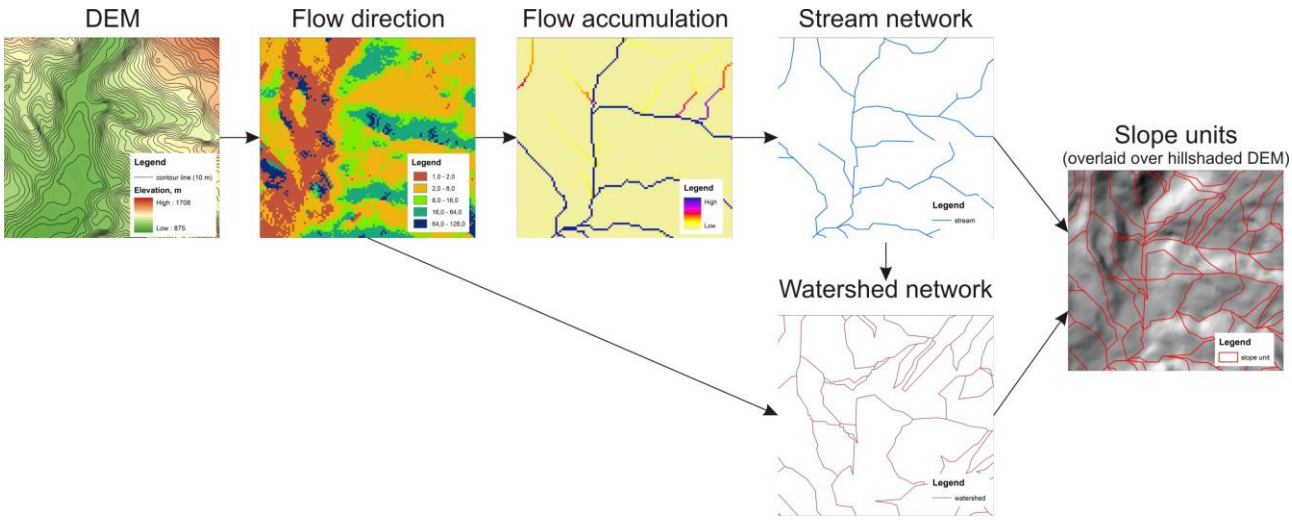

Figure AF.70: Schematic representation of the slope unit extraction based on the DEM of the study area.

For our susceptibility analysis we employ several thematic layers which represent the distribution of topographic features, land cover, structural control and rock units. The topographic data are the products of the DEM and include minimal/mean/maximal/standard deviation values of elevation and slope angle. These parameters have a continuous representation, i.e. one which incorporates a real value of the thematic parameter. For example, if certain slope unit has V_n=9 for the variable of "minimal slope angle" it shows that the minimal slope angle withing this slope unit is equal to 9°.

The land cover, structural control and rock unit thematic layers are converted into different formats. They are first subjected to discretization. It means, for example, that layer of structural control is decomposed into "cataclinal", "anaclinal", "orthoclinal" and "massive" variables. Then, each descrete variable is subjected to the dichotomous ("yes"/ "no") classification: e.g., if a certain slope unit contains the anaclinal slopes, then it is assigned to the "yes"-value of the "anaclinal" variable, and if this slope unit does not contain anaclinal slopes then it is assigned to the "no"-value of this variable. The variable value of each slope unit (V_1, V_2 … V_n in Equation AE.5) is determined by the percentage of slope unit area occupied by this variable. For example, if 30% of some slope unit area is occupied by the cataclinal slopes, then "cataclinal" variable for a given slope unit would have a value of V_n=0.3.

The prepared input layers (variables and analysed landslide inventory) are further subjected to the SPSS processing. This software first iterates to find an optimal linear combination of variables to discriminate stable and non-stable slopes. These iterations are performed within so-called training set which can combine, for example, several landslide inventories (cumulative inventory) or use just one of them. The studied DA models have different training sets as well as different combination of the analysed variables. At the last processing step the optimal linear combination is applied to the whole extent of target area to map the numeric value of the landslide susceptibility.

Figure AF.71 presents the final results of the landslide susceptibility mapping applying DA. The training sets for Models DA1, DA2, DA3 and DA4 present the cumulative inventory which combines the 1984, 1996 and 2002 landslides. The training sets for Models DA5 and DA6 contain only the 2002 landslide outlines which represent the recent re-/activations of slope processes. The training set can also contain a certain set of slope units, as it is for a case of Model DA6. This training set analyses the slope units in the central part of the study area and coincides with the one applied by the Artificial Neural Networks (see next sub-section).

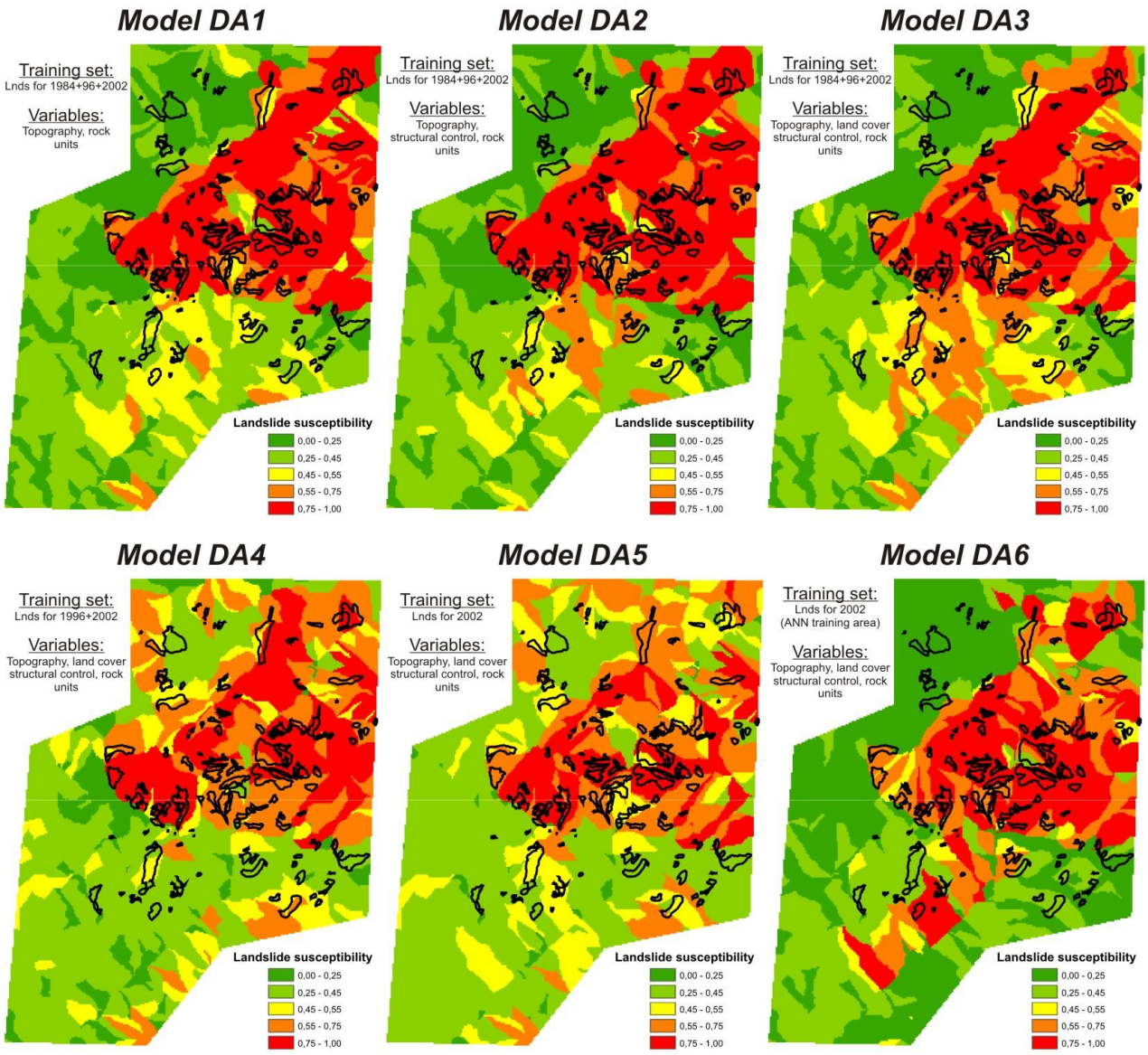

Figure AF.71: The set of the landslide susceptibility models obtained for the varying combinations of the training set and analysed variables (acronym "Lnds" corresponds to the landslide inventory; black solid outlines – landslide inventory for 2007).

The analysis of extracted models shows that all thematic layers have a different level of importance with respect to the discrimination between stable and non-stable slopes. This level of importance is defined by a slope value (a_1, a_2 … a_n in Equation AE.5) returned by SPSS for each variable. If this value is close to 0, then this variable is considered to be insignificant for the discrimination. For example, the minimal/maximal/standard deviation values of elevation and slope angles are considered as insignificant discrimination variables, as the slope values returned by SPSS are close to 0. The same is true for some groups of rock units, especially those which consist of limestone and sandstone. The variables with high positive/negative slope values are considered to be significant with respect to the discrimination. The most significant variables which best discriminate unstable slopes are the next: mean value of the slope angle, cataclinal slopes, bare surface and group of rock units, which mainly consists of the quaternary and clayey rocks. The variables which best discriminate stable slopes include rich vegetation cover, anaclinal/massive slopes and the class of the volcanogenic rocks.

The prediction performance of the compiled models is studied through the values of the map-scaled density (*Dm*), calculated for each susceptibility class of the models based on 2007 landslide inventory (see Equation AE.3). As mentioned above, the classes of high landslide susceptibility should be characterized by a *Dm*-value of more than 1, while the classes of low landslide susceptibility are marked by $Dm < 1$. Table AT.13 lists the values of *Dm* obtained for each class of extracted models. As it can be seen, all models are characterized by a gradual increase of the *Dm* values for the increasing landslide susceptibility level. Model DA4 presents the best statistics, as it has the lowest *Dm* value for Class 1, and the highest *Dm* value for Class 5. This model analysed all thematic layers, while discrimination was based on the training set of cumulative landslide inventory (the 1996 and 2002 landslides).

Table AT.13: The map-scaled density values (*Dm*) obtained for the landslide susceptibility classes of extracted models.

Susceptibility class (P_1, sliding probability)	***Model DA1***	***Model DA2***	***Model DA3***	***Model DA4***	***Model DA5***	***Model DA6***
Class 1 (0.00-0.25)	0.52	0.49	0.47	0.12	0.3	0.54
Class 2 (0.25-0.45)	0.6	0.49	0.53	0.55	0.46	0.62
Class 3 (0.45-0.55)	0.94	1.47	1.39	0.88	1.25	0.56
Class 4 (0.55-0.75)	1.49	1.44	0.89	1.48	1.36	1.65
Class 5 (0.75-1.00)	1.77	1.74	1.70	1.86	2.08	1.78

IV.2.3 Artificial Neural Networks

In this sub-section we apply the Artificial Neural Networks (ANN) which are considered as an indirect and quantitative mapping method. According to the classification, this method belongs to the group of the advanced statistical models. During the last 30 years, ANN has been employed in a wide range of applications of pattern/shape recognition and classification in natural sciences. A number of authors have also applied ANN to the landslide susceptibility studies: e.g., Fernandez-Steeger (2002), Lee et al. (2003), Yesilnacar and Topal (2005), Ermini et al. (2005), Melchiorre et al. (2008) and Falaschi et al. (2009) among others. The growing use of ANN is due to its possibility to handle data at any measurement scale, when input thematic layers can be represented in nominal, ordinal, linear or ratio formats (Wang et al., 1995). In addition, ANN can easily handle qualitative variables making it widely used in an integrated analysis of the multiple-source spatial data (Kawabata and Bandibas, 2009).

Basically, ANN is a computational network which tries to simulate a behaviour of the human brain in solving complex problems (Michie et al., 1994). The decision-making is performed over a network of connected processing units, so called artificial neurons (Fernandez-Steeger and Czurda, 2001). This network provides a prediction based on an analysis of training dataset with known input and output parameters/data (Lee et al., 2003). A commonly applied type of ANN is the back-propagation learning algorithm which employs an input layer, the hidden layer/layers and an output layer of neurons (Figure AF.72a). The training is performed over these layers, when the system investigates the link/links between training input and output. These links are studied though the adjustment of the weights in response to the errors between the predicted and the expected result (Lee et al., 2003). The training stage finishes at the moment when a targeted minimal

error is achieved. After that, the resulting network (i.e. links between neurons) is applied via a feed-forward structure to produce a prediction for the whole dataset.

Figure AF.72b schematically shows how the ANN-driven algorithm is applied to the landslide susceptibility mapping (Kawabata and Bandibas, 2009). As it can be seen, the thematic layers are arranged into a network of input neurons. The following application of the training and feed-forward structure provides the prediction output. This output is presented via a distribution of the sliding probability values, i.e. those values showing a likelihood of a certain mapping unit to belong to the group of the unstable slopes. It should be noted that the output could also be represented in the opposite way, i.e. through the probability/likelihood of a unit to belong to group of stable slopes.

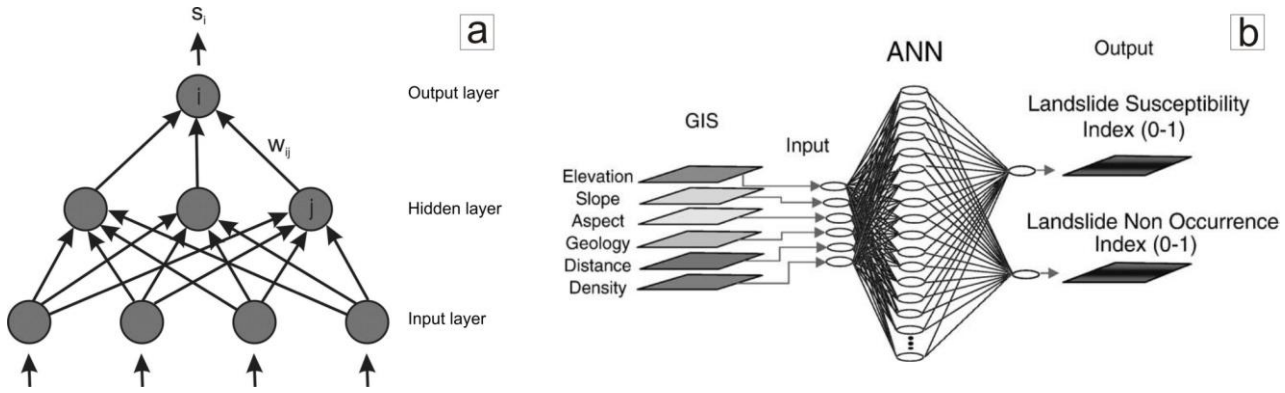

Figure AF.72: (a) Feed-forward ANN with neurons in the input/hidden/output layers, applied in a back-propagation learning algorithm (by Fernandez-Steeger, 2002); (b) schematic representation of the landslide susceptibility mapping via ANN-driven algorithm (by Kawabata and Bandibas, 2009).

Lee et al. (2003) note that the conceptual advantage of ANN over other classification methods lies in the fact that ANN is independent from the input data distribution and their format, although the neural networks are calibrated by using the input data and this calibration defines the functionality of the network. Also, ANN normally requires less data for training than other statistical methods. The main limitation of ANN originates from its "black-box" operation principle, leading to the fact that the user often does not know how the system works and which input neurons are the most important for the final prediction. Therefore, the role, functionality and significance of the applied weights are difficult to be interpreted. It limits the possibility to generalize the mapping rules and to apply them in the areas different from the studied one. Due to that, ANN is considered as a mapping tool aimed at case-specific studies with a low potential to generalize the applied methodology.

The application of ANN in our study area is completed by using the pixel-based mapping units. The ANN analyses apply the same combinations of thematic layers and training sets as those that were used in DA. The topographic variables are expressed via the slope angle, slope azimuth and slope curvature layers. The other input parameters include land cover, structural control and rock unit thematic layers.

Figure AF.73 presents a set of the ANN models. The training sets for Models ANN 1-3 use the cumulative landslide inventories for 1984, 1996 and 2002. Models ANN4 analyses the cumulative landslide inventories for 1996 and 2002, while Model ANN5 accounts only for the recent re-/activation of slope processes occurred in 2002. Model ANN6 has a specific configuration of the training area which covers the central part of the target area (see a black dotted rectangle in Model ANN6 presented in Figure AF.73).

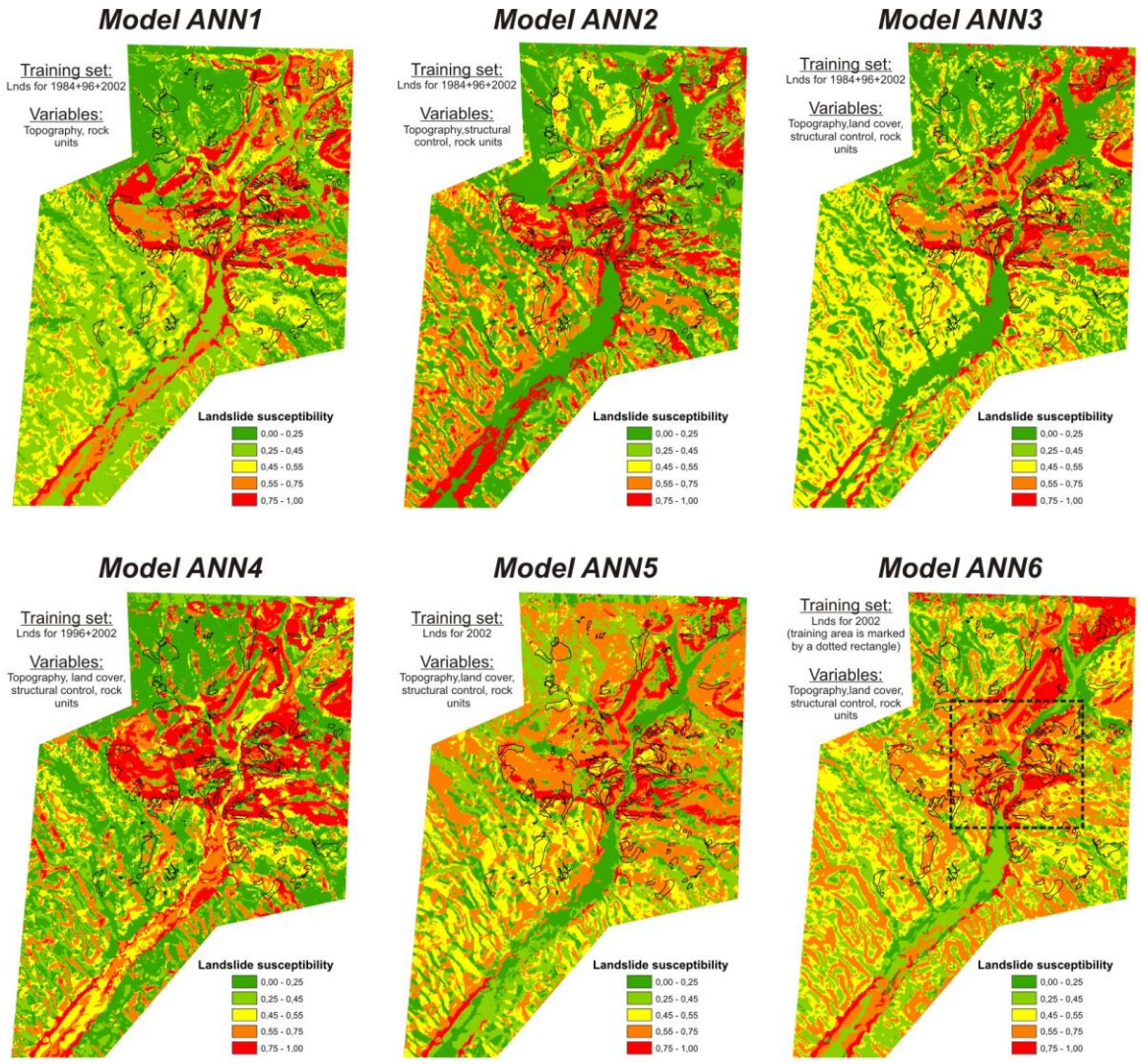

Figure AF.73: Landslide susceptibility models extracted by application of ANN for the varying combinations of the analyzed variables and training sets (acronym "Lnds" corresponds to the landslide inventory; black solid outlines – landslide inventory for 2007).

Table AT.14 analyses the prediction performance of the models based on the map-scaled density values (*Dm*). The validation studies are based on the 2007 landslide inventory. Most of the models have consistent distribution of the *Dm*-values: the classes of the higher susceptibility have the higher values of *Dm*. Only Model ANN1 has some inconsistency (compare the *Dm*-values for class 1 and 2 of landslide susceptibility in Table AT.14). Models ANN 3 and ANN 5 have the best statistics, while Model ANN5 has the lowest *Dm*-value for Class 1 (sliding probability is 0.00-0.25) and the highest *Dm*-value for Class 5 (sliding probability is 0.75-1.00).

Table AT.14: The map-scaled density values (*Dm*) obtained for the landslide susceptibility classes of extracted models (validation set includes the 2007 landslide inventory).

Susceptibility class (P_1, sliding probability)	***Model ANN1***	***Model ANN2***	***Model ANN3***	***Model ANN4***	***Model ANN5***	***Model ANN6***
Class 1 (0.00-0.25)	0.78	0.48	0.41	0.71	0.37	0.42
Class 2 (0.25-0.45)	0.66	0.90	0.59	0.83	0.63	0.49
Class 3 (0.45-0.55)	1.26	1.43	1.04	0.92	1.12	0.98
Class 4 (0.55-0.75)	1.28	1.26	1.53	1.11	1.21	1.37
Class 5 (0.75-1.00)	1.67	1.63	2.07	1.61	2.18	1.80

IV.2.4 Newmark Displacement

The Newmark method belongs to the group of the conceptual or process-based models. This method applies a set of the regional predictors to map the values of co-seismic slope displacement (the Newmark Displacement, ND). These displacement values are the indicators of the seismically-induced landslide susceptibility. The historic evolution and more detailed analysis of the Newmark method are presented in Part B, where dynamic studies propose the conceptual improvements of the existing methodology. Therefore, here we only review the technical aspects of susceptibility mapping, while theoretical issues are more deeply analyzed in the second part of this thesis.
The regional Newmark method was developed on the basis of the simplified model proposed by Newmark (1965), which calculates the co-seismic displacement of a rigid block sliding on an inclined plane (see Figure AF.74a). This value of ND is estimated through the double integration of impacting acceleration-time history (see in Figures AF.75b, AF.75c and AF.75d). Only the part of the history exceeding the critical acceleration value (see a_c in Figures AF.75a and AF.75b) should be integrated to get the value of the co-seismic slope displacement. Originally, this rigid-block model was applied to the stability analyses of dams and embankments at the scale of a single slope. The main reason constraining the application of the original model to the local scale was the difficulty to get a regional distribution of the input parameters (a_c, acceleration time histories), which is a prerequisite of the spatial studies.

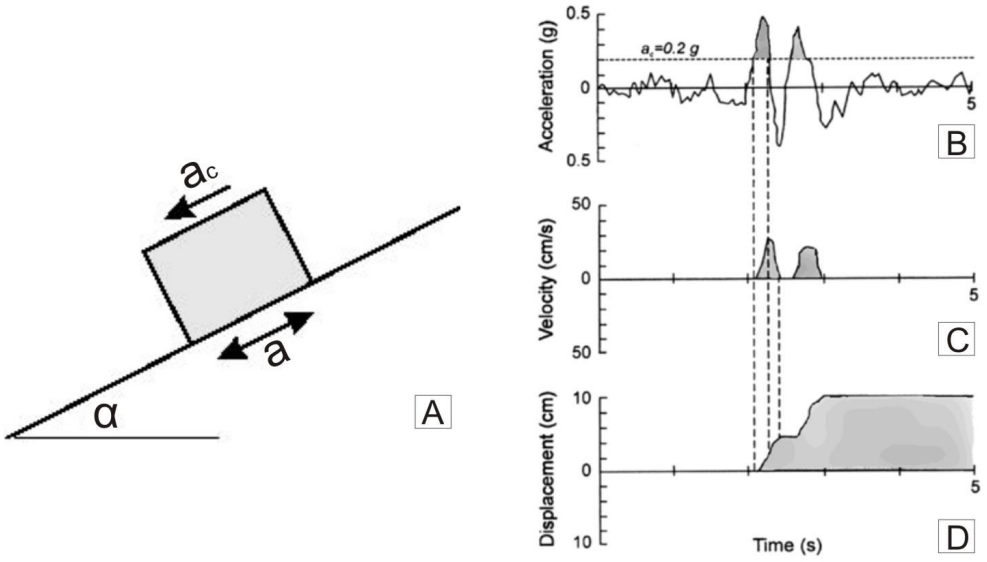

Figure AF.74: (a) Simplified model of a rigid block sliding on an inclined plate, analyzed by Newmark (1965); (b) dynamic impact expressed via an acceleration-time history; (c) predicted behaviour of a co-seismic shear velocity; (d) predicted behaviour of a co-seismic shear displacement (by Wilson and Keefer, 1985, modified by Jibson et al., 1998).

A series of modified concepts (regional Newmark models) have overcome this limitation. The earliest models are proposed by Wilson and Keefer (1985), Wieczorek et al. (1985), Ambraseys and Menu (1988) and Jibson (1993). Four main and partly interrelated parameters are involved in these models: Arias Intensity, critical acceleration, earthquake magnitude and maximum acceleration or PGA. In our studies we apply the Jibson (1993) model, which regionally maps the values of the co-seismic displacement (D, cm) based on the next relationship:

$$\log(D) = 1.46 * \log(Ia) - 6.642 * Ac + 1.546 \qquad \text{(AE.6)},$$

where Ia (m/sec) is the Arias Intensity and Ac (in term of g) is the critical acceleration.
In Equation AE.6 the value of Ia represents the potentially destabilizing impact of seismic shaking intensity. This parameter was first introduced by Arias (1970): the value of Ia is calculated through the integration of the squared acceleration time history over the recorded time period. As it is impossible to get the acceleration time history for each point of the investigated area, the regional ND models apply a modified mapping concept. In this concept the value of Ia is calculated on the basis of an attenuation law. This law defines the

dependence of Ia on the earthquake magnitude (M) and the hypocentral distance (R, km). In our studies we apply the attenuation law developed by Wilson and Keefer (1985):

$$\log Ia = -4.1 + M - 2 * \log R \qquad \text{(AE.7)}.$$

Figure AF.75 presents the distribution of the Ia-values obtained for two scenarios of the earthquakes studied through an application of ND in our target area. The first scenario (see Figure AF.75a) analyses the effect of the M=6.2 earthquake in 1992 that occurred at a distance of 30 km SSE from the target area. The second studied scenario is based on a hypothetical earthquake in the Central Fault zone (M=5.5 – see Figure AF.75b). As it can be seen, the Ia isolines are concentric for the both studied cases – according to Equation AE.7, the Ia-values are decreasing with increasing hypocentral distance.

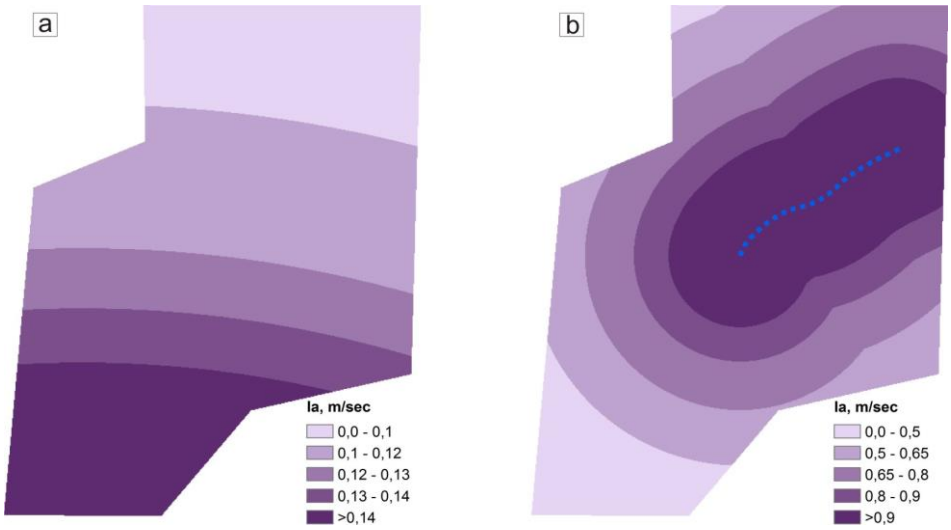

Figure AE.76: The distribution of the Ia-values, obtained for two studied earthquake scenarios: (a) the M=6.2 earthquake in 1992; (b) a hypothetical M=5.5 earthquake in the Central Fault zone, marked as the blue dashed line.

The second parameter involved in Equation AE.7 is the critical acceleration (Ac, m/sec^2 or in terms of g). This parameter is directly related to the static Factor of Safety (FS) of a given slope and its inclination angle (α,°):

$$Ac = (FS - 1) * g * \sin\alpha \qquad \text{(AE.8)},$$

where g is the acceleration due to gravity (9.81 m/sec^2).
At present, most regional ND models map the value of FS by applying the Janbu (1973) approach which is adapted to translational sliding of an infinite layer. In this equation the value of FS is related to the set of geotechnical and morphological settings as follows:

$$FS = \frac{c}{\gamma * t * \sin\alpha} + \frac{\tan\varphi}{\tan\alpha} - \frac{m * \gamma_w * \tan\varphi}{\gamma * \tan\alpha} \qquad \text{(AE.9)},$$

where c is the cohesion (kPa), φ is the internal friction angle (°), α is the slope angle (°), t is the total layer thickness (m), m is the fraction of the total layer thickness that is saturated by water, γ is the material unit weight (kN/m^3) and γ_w is the unit weight of water (kN/m^3).
Figure AF.76 presents the distribution of the geotechnical properties (cohesion, internal friction angle and material unit weight) that was used for the mapping of the FS values according to Equation AE.9. Table AT.15 lists the geotechnical properties for all presented rock units. These values were compiled from the available historic data (Iliyn, 1959; Krestnikov, 1962; Konaev, 1964) and recent geophysical studies in the target area (Alioshin and Torgoev, 2000; de Marneffe, 2010).

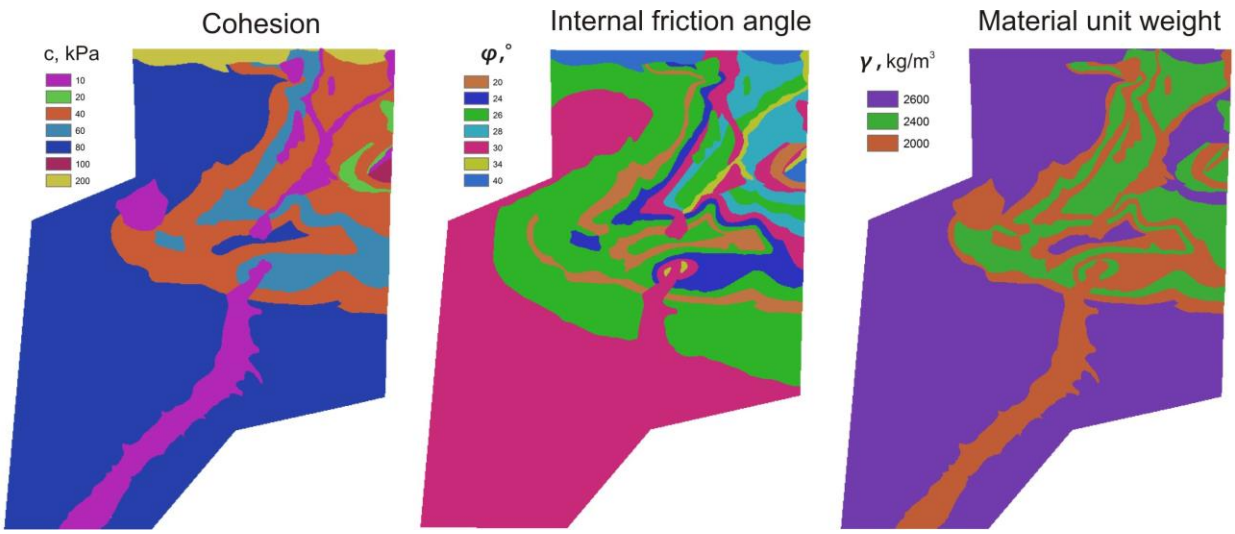

Figure AF.76: Distribution of the geotechnical parameters (cohesion, internal friction angle, material unit weight) applied in the mapping of the FS values.

Table AT.15: Assigned values of geotechnical parameters for all rock units presented in target area

Rock unit	Composing material	Cohesion *c*, kPa	Internal friction angle φ, °	Material unit weight, kg/m³
Q IV	coarse loose sediments	10	34	2000
Q III-IV	mixed loose sediments	10	30	2000
Q III	coarse loose sediments	10	34	2000
Q I-II	fine loose sediments	10	26	2000
P3-N1-ms1	sandstone, brecchia	80	26	2600
P 3-N1-ms2	sandstone, brecchia	80	30	2600
P 2-3	clay	40	20	2000
P 1-2	clay, sand-limestone	40	26	2400
PR 2 kb	metamorphic rocks	200	40	2600
K2 - Sn2	clay	60	24	2000
K2t-Sn	clay, limestone	60	30	2400
K2s	clay, sand-limestone	40	28	2400
K1n+al	clay, sand-limestone	40	26	2400
K1hd	sandstone, brecchia	40	28	2600
J2	sandstone	20	30	2400
J1ts2	clay	40	20	2000
J1ts1	clay	40	20	2000
C1v-s	limestone	100	40	2400
D 1-2 ab	acid volcanic	200	40	2600
S 1-2 asA	acid volcanic rocks	200	40	2600
S 1-2 as	acid volcanic rocks	200	40	2600

The mapped distributions of the Ac (Equation AE.8) and FS (Equation AE.9) values are presented in Figure AF.77. Four main landslides models are studied: shallow/deep landslides (t=5 m and t=20 m, correspondingly) in dry conditions and with water saturation (m=0 and m=1, correspondingly). An increasing value of the landslide thickness and water saturation results in decreasing values of FS and Ac – the lowest values of these parameters are found for the deep landslides in the water-saturated conditions (t=20 m and m=1). The highest values of FS and Ac are found for the shallow landslides in dry conditions (t=5 m and m=0). According to Equations AE.8 and AE.9, the values of FS and Ac also depend on the slope inclination – the flat areas have the highest values of FS and Ac, while steeply inclined slopes are characterized by the lowest values of these parameters.

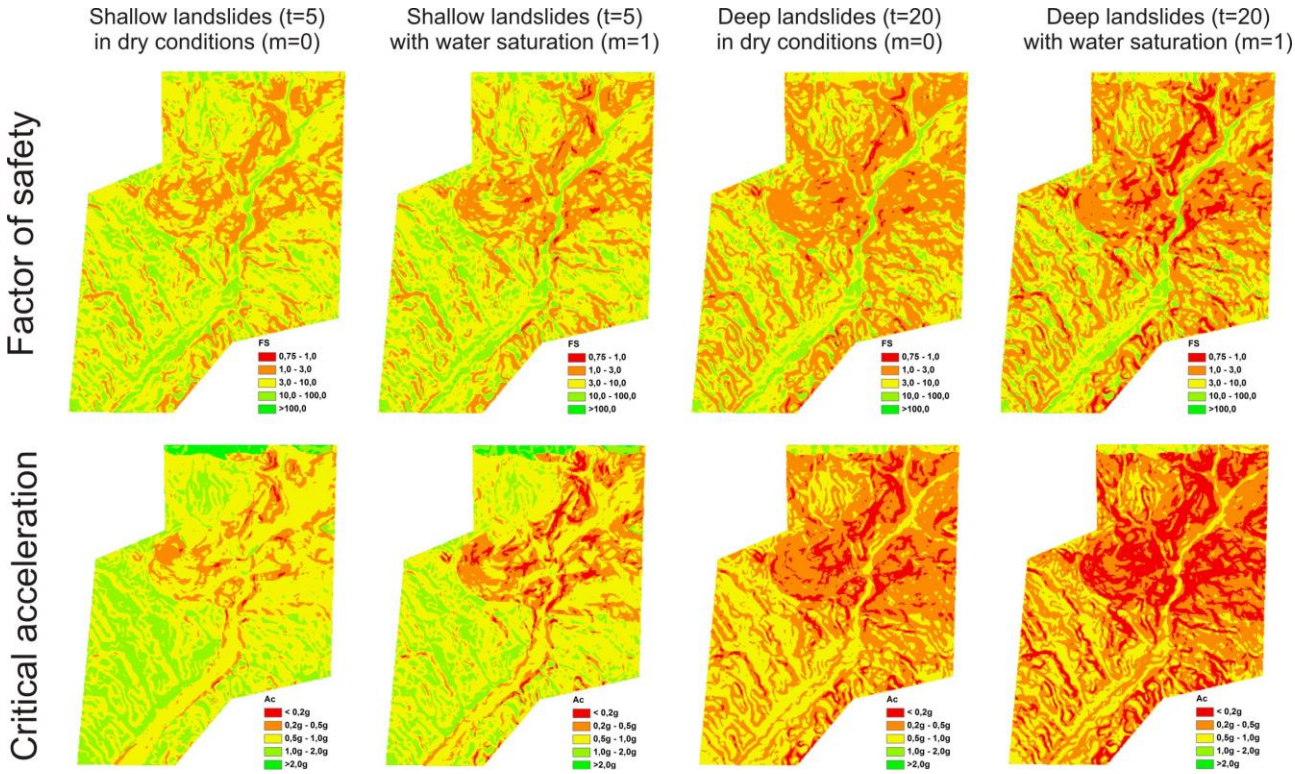

Figure AF.77: Distribution of the Factor of Safety and Critical Acceleration values obtained for shallow/deep landslides in dry conditions and with water saturation.

Figure AF.78 presents four ND models, constructed for the first studied scenario of the M=6.2 earthquake that occurred in 1992 at a distance of 30 km to SSE from the target area. The models are constructed for four specific combinations of conditions, i.e. shallow and deep landslides in dry or water-saturated states (see Figure AF.77). The landslide susceptibility class for every pixel is assigned according to the calculated value of the Newmark Displacement, i.e. the co-seismic shear displacement. The class of the very low landslide susceptibility (class 1) is marked by very small displacement values between 0.0 and 0.1 cm, class 2 is marked by slightly larger ND values (0.1- 0.5 cm), class 3 – by ND values between 0.5 and 0.9 cm, class 4 - by ND values between 0.9 and 5.0 cm, while the highest susceptibility (class 5) is marked by large displacements of more than 5.0 cm.

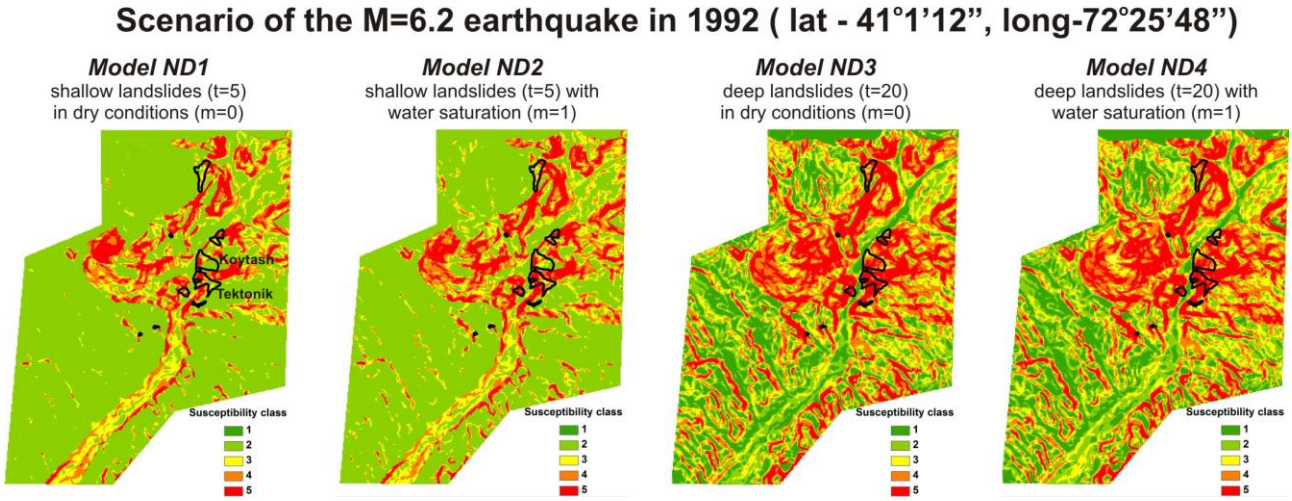

Figure AF.78: Models of the landslide susceptibility for the scenario of the M=6.2 earthquake in 1992 (black solid outlines mark the landslides re-/activated during this earthquake).

The validation set for this earthquake scenario contains 10 landslides, which are reported to be re-/activated by this seismic event (Alioshin and Torgoev 2000; Torgoev et al. 2005). One of the biggest disaster occurred when the Tektonik landslide failed 7 weeks after the M=6.2 earthquake in 1992. It is very likely that this seismic event was one of the main preparatory factors for the landslide failure (Havenith et al., 2006). This landslide with a volume of 1.5×10^6 m^3 incurred significant economical losses and sensitive environmental damage (Vandenhove et al., 2003). The validation set also includes the Koytash and Technikum landslides, where a partial slope failure and surface cracking were registered in a postseismic period. It should be noted that a high level of the landslide activity was also registered one year later, when an anomalous precipitation resulted in a loss of stability in these sites (Torgoev et al. 2005).

Table AT.16 lists the values of the map-scaled density (*Dm*) obtained for the model classes, applying the validation set of the above-mentioned 10 landslides. As it can be seen, model ND3 has the best statistics over four presented models – it has the lowest *Dm* value for class 1 and the highest *Dm* values for class 5. It shows that the model of the deep landslides in dry conditions fits best the studied earthquake scenario.

Table AT.16: The map-scaled density values (*Dm*) obtained for model classes in the scenario of the M=6.2 earthquake in 1992 (validation set includes 10 landslides, shown in Figure AF.79).

Susceptibility class	***Model ND1***	***Model ND2***	***Model ND3***	***Model ND4***
Class 1 (very low)	0.04	0.04	0.03	0.05
Class 2 (low)	0.63	0.39	0.16	0.18
Class 3 (intermediate)	1.88	1.94	0.58	0.63
Class 4 (high)	1.93	2.09	1.73	1.65
Class 5 (very high)	2.1	2.36	2.51	2.21

The second earthquake scenario analyses a hypothetical event in the Central Fault zone (M=5.5; see blue dashed line in Figure AF.75b). The extracted landslide susceptibility models are shown in Figure AF.79. The ranges of the co-seismic displacement values used for the mapping of landslide susceptibility are similar to those which were used for the previous earthquake scenario.

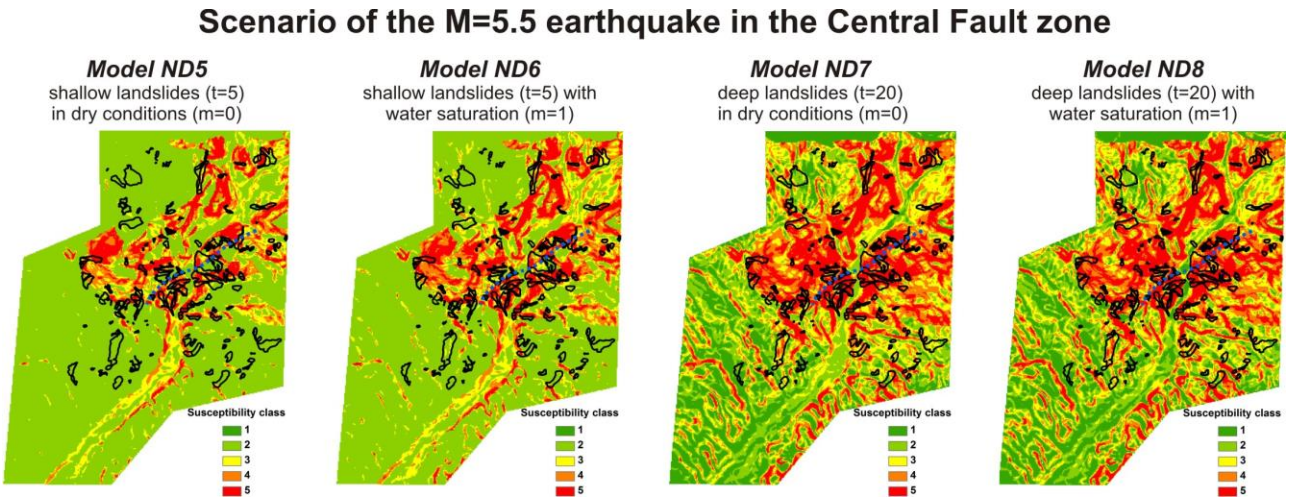

Figure AF.79: Models of landslide susceptibility for the scenario of the M=5.5 earthquake in the Central Fault zone (blue dashed line is the hypothetical rupture zone and black solid outlines mark the landslides of the 2007 inventory).

Table AT.17 presents the *Dm*-values calculated for the susceptibility classes of the resulting models. Here, the validation set is represented by the 2007 landslide inventory. As it can be seen, model ND7 is marked by the best statistics: the *Dm*-value for class 1 is the lowest one, while class 5 has the highest *Dm*-value among the presented models. This indicates that the model of deep landslides in dry conditions best explains the location of the analysed landslides. Thus, both seismic scenarios show that the best predictions are yielded by the same model of landslides with t=20 m (deep landslides) and m=0 (dry, no water conditions). The models with water saturation (m=1) have worse performance comparing with those that have dry conditions (m=0). It can be explained by fact that under the state of water saturation a big portion of stable slopes are classified as unstable areas: it impacts the *Dm*-value and final model performace.

Table AT.17: The map-scaled density values (*Dm*) obtained for model classes in the scenario of the M=5.5 earthquake in the Central Fault zone (validation set includes landslide inventory for 2007).

Susceptibility class	***Model ND5***	***Model ND6***	***Model ND7***	***Model ND8***
Class 1 (very low)	0.19	0.21	0.19	0.27
Class 2 (low)	0.82	0.73	0.51	0.56
Class 3 (intermediate)	1.07	1.22	0.91	0.93
Class 4 (high)	1.60	1.43	1.44	1.43
Class 5 (very high)	1.84	1.79	1.85	1.78

The mapping results for two seismic scenarios present quite similar results with respect to the spatial distribution of the landslide susceptibility (compare the models in Figures AF.79 and AF.80). It is related to the fact that in the applied mapping law (Equation AE.6) the value of the co-seismic displacement (D) is much more sensitive to a change of the critical acceleration (Ac) than to a change of the Arias Intensity (Ia). A stronger impact of Ia is anticipated for the case when there are rapid changes of Ia-values due to local topographic and geological amplification effects. Part B of the thesis provides an in-depth analysis of such amplification effects via the dynamic studies in the 2D and 3D domains. The techniques to account for these amplification effects in the mapping of ND values are also presented in Part B. The goal of these studies is to improve existing methodology which would finally lead to a more reliable mapping of the seismically-induced landslide susceptibility.

V. Landslide hazard and landslide risk.

V.1 Landslide hazard mapping

According to the Committee on the Review of the National Landslide Hazards Mitigation Strategy (2004), the landslide hazard is a combined parameter which indicates where, how often/when the landslides are likely to occur and what is their expected magnitude (see more details in the *Section A.I.1*). The landslide susceptibility studied in *Section A.IV.2* is considered to be a spatial component of the landslide hazard, i.e., it outlines the areas where the slope failures most likely occur. The temporal component of the landslide hazard provides an answers to question of how often/when the landslides are likely to occur. At regional scale, this parameter can be studied through the analysis of the multitemporal landslide inventories; at local scale, it can be supported by monitoring surveys of the landslide activity. The last component of the landslide hazard informs on the expected size of the slope instabilities, i.e., it indicates how large/fast and, thus, how "potentially" destructive the landslide events can be.
Schlögel et al. (2011) show that the Mailuu-Suu target area is characterized by a high variability of the landslide size, which ranges from 335 m^2 for the smallest detected landslide to 348,425 m^2 for the largest one in 2007. The authors also show that the variability of the landslide size strongly depends on the site morphologic, geothechnic and geologic settings. The existing approaches are not developed enough to account for all these impacts. Therefore, in our hazard studies the magnitude component is not taken into account. Thus, the regional mapping of the landslide hazard (H) in our target area is only based on two components which can be expressed next:

$$H = S * T \qquad \text{(AE.10)},$$

where *S* is the landslide susceptibility, i.e. a spatial probability of the landslide occurrence, and *T* is the temporal probability of the landslide re-/activation.
Equation AE.10 suggests that both components (*S* and *T*) should be expressed in terms of a quantitative measure. The Artificial Neural Network (ANN) and Discriminant Analysis (DA) give the numeric value of the landslide susceptibility (*S*); therefore, these results can be applied in Equation AE.10. The qualitative results provided by the Index-based (IB) and the Newmark Displacement (ND) methods can generally not be applied in Equation AE.10. It is, however, possible to adapt the ND method in order to supply quantitative estimates of *S* and *T* – this would require validation inventories of the landslides triggered by several seismic events, each one being marked by a specific occurrence probability. In our study cases (see *Sub-section A.IV.2.4*) the reliable validation inventories were lacking. Therefore, the ND method gave only qualitative results.
The second component applied in Equation AE.10 is presented by the temporal probability of the landslide occurrence (*T*). This information is extracted here from the set of the multitemporal landslide inventories. Figure AF.80 presents this dataset of five inventories covering a time span of 45 years (between 1962 and 2007). The minimal time span between succesive inventories is 5 years (for the period between 2002 and 2007), while the maximal one is 22 years (for the period between 1962 and 1984).

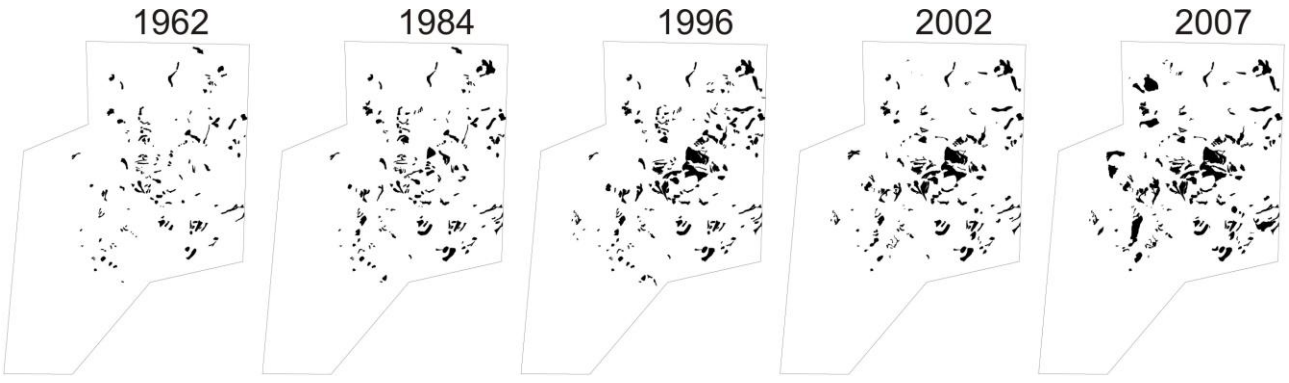

Figure AF.80: Set of the multi-temporal landslide inventories for the Mailuu-Suu target area.

Crovelli (2000) describes two models applied to map the variable *T* based on the analysis of the multitemporal landslide inventories: (i) the Poisson model and (ii) the binomial model. According to the author, both models should return quite similar results in our case, as the interval between succesive inventories is irregular and generally exceeds 3-5 years. We select the Poisson model which returns the value of *T*, otherwise called as the landslide exceedance probability, based on the next equation:

$$T = 1 - e^{-\frac{t}{m}} \quad \text{(AE.11)},$$

where *t* (years) is the predictive period of time and *m* (years) is the mean recurrence interval for the landslide re-/activation in the target area. In this equation the value of *t* is defined by user to indicate the period of time for which the prediction of the *T*-value is performed (e.g., for 1, 5, 10…100 years). The second parameter (*m*) is regionally mapped with the multi-temporal landslide inventories applying the next equation:

$$m = \frac{I}{n} \quad \text{(AE.12)},$$

where *I* (years) is the time interval between the oldest and the youngest landslide inventories (in our case 45 years) and *n* is the number of the landslide re-/activations, registered for *I* period of time.
The last parameter, i.e. *n*, is estimated based on the set of the multi-temporal landslide inventories. Figure AF.81 presents a part of the study area with the landslides identified from the 2002 and 2007 Quickbird imagery. The analysis of older inventories (for 1962, 1984 and 1996) shows that this area was free of landslides, i.e. all pixels inside of this area has *n*=0 for a period between 1962 and 1996. Figure AF.81a shows that two new landslides are identified on the 2002 Quickbird imagery, which means that all pixels within activated landslides have *n*=1 for a period between 1996 and 2002. The 2007 Quickbird image (Figure AF.81b) shows that in a period between 2002 and 2007 these two landslides reactivated and expanded upslope, while completely new landslide also activated in the surroundings. The final results of the mapping of the *n*-values are presented in Figure AF.81c. As it can be seen in this figure, the intersected parts of the reactivated landslides have *n*=2, while the landslide, freshly activated during period between 2002 and 2007, has *n*=1. The mapping results also show that a pixel-based analysis is sensitive to the selected pixel size – a rougher pixel size results in less accurate distribution of *n*-values (see a discrepancy between landslide outlines and pixel values in Figure AF.81c).

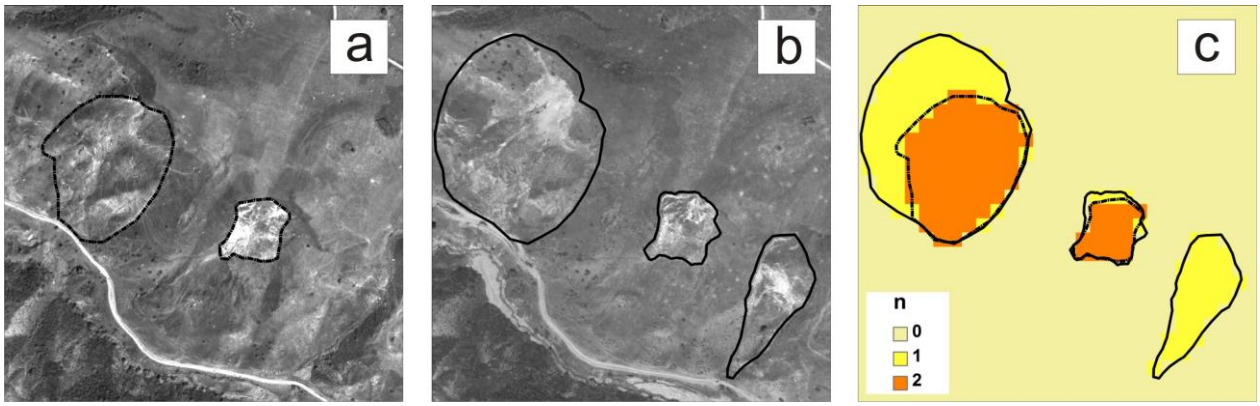

Figure AF.81: The 2002 (a) and 2007 (b) Quickbird imagery with the identified outlines of active landslides and the results (c) of the mapping of the landslide re-/activations number.

The regional mapping of the landslide re-/activation number is also performed applying the slope units (SUs). The configuration of SUs is similar to the one applied by the DA method (see more details in *Sub-section A.IV.2.2*). Figure AF.82 presents the snapshots to a part of study area with the SU outlines overlaid by the multi-temporal landslide inventories (see the ones for 1962, 1984, 1996, 2002 and 2007). The final map showing a distribution of *n*-values is presented in Figure AF.82f. During the analysis, a re-/activation record is assigned to the whole SU, even if only a part of it is affected by the landslide activity. It can be seen that more than one half of the presented area has the n-value equal or larger than 4 – this shows that most of

the presented SUs were partially affected by the landslide (re)activations during the studied period of time (see Figure AF.82f). Only some of the presented SUs have n=0, as they have never been affected by the landslides (see SUs in left part of Figure AF.82f).

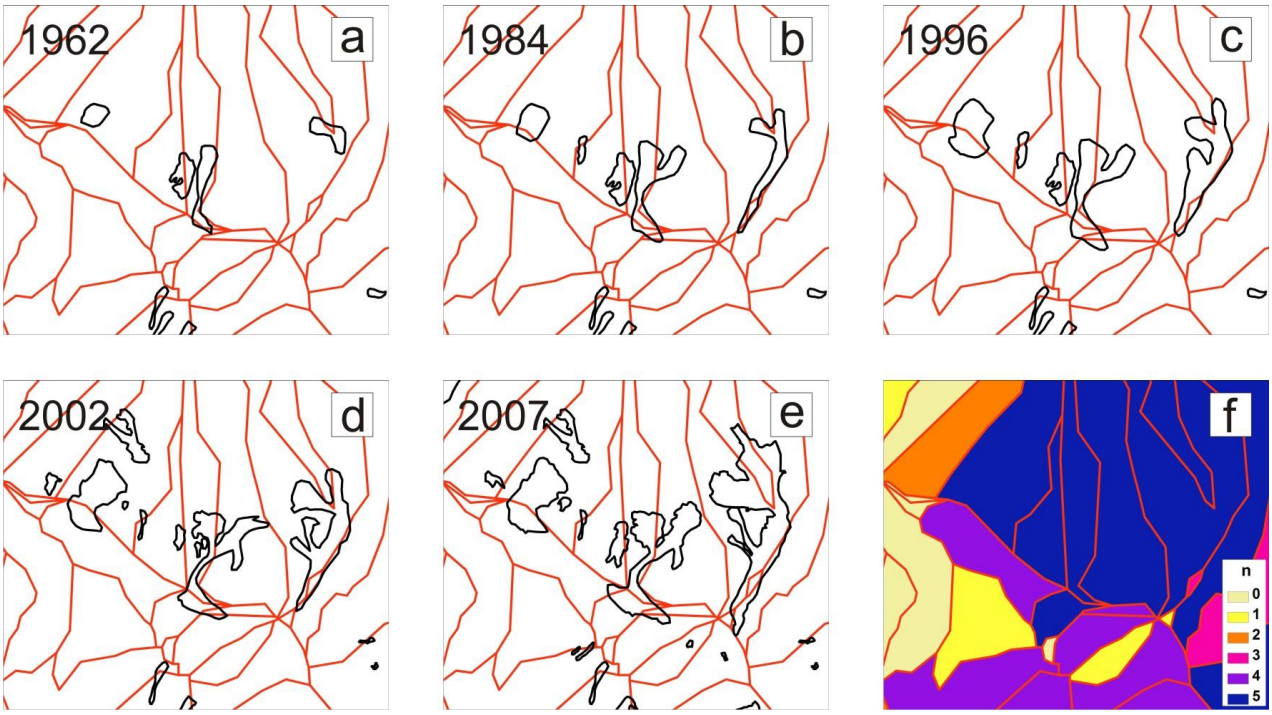

Figure AF.82: (a-e) Snapshots to a part of study area with the SUs outlines (red outlines) overlaid over the multi-temporal landslides inventories for 1962, 1984, 1996, 2002 and 2007 (black outlines); (f) distribution of the landslide re-/activation number.

Figure AF.83 summarizes the results of mapping of the landslide re-/activation number (*n*) and the recurrence interval (*m*). These results were obtained by applying the pixel- and SU-based analyses. As it is shown in Figures AF.82 and AF.83, the distribution of *n* is mapped on the basis of five multi-temporal inventories presented in Figure AF.80. The values of *n* are ranging between 0 and 5: for pixel-based analyses only the pixels falling inside of the former/existing landslides are marked by *n*>1. The SU-based map have larger area with *n*>0, as every landslide re-/activation spread its impact over several neighbouring SUs. The values of *m* are mapped applying Equation AE.12. As our dataset consists of five inventories the minimal value of *m* is equal to 9 years (45/5 = 9 years), while the maximal one is infinite.

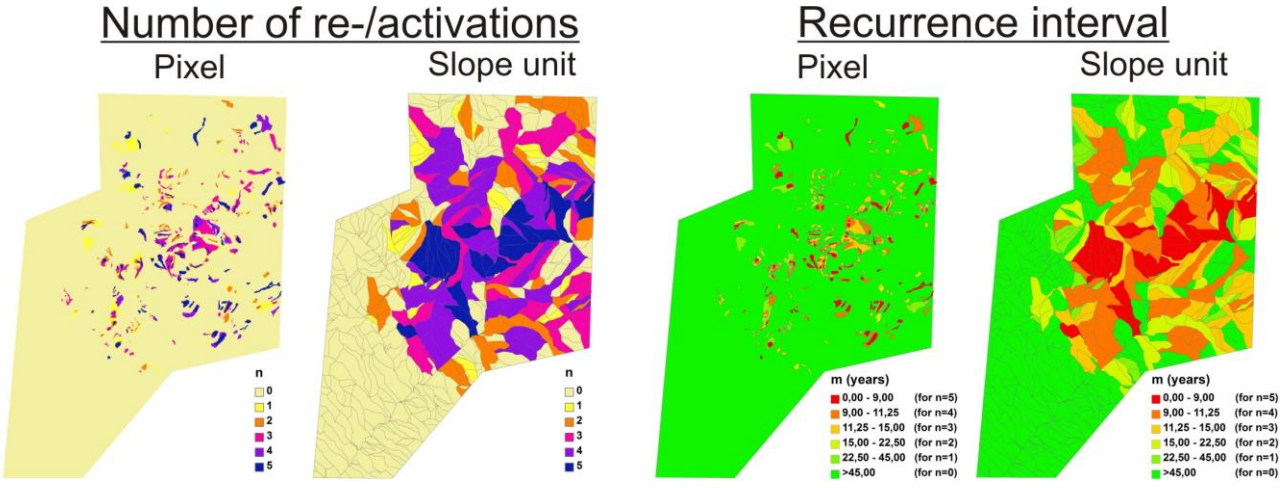

Figure AF.83: The distribution of the number of re-/activations (*n*) and the mean recurrence interval (*m*) mapped by the pixel- and SU-based analyses.

Figures AF.85 and AF.86 present the results of the temporal probability (*T*) and the landslide hazard (*H*) mapping, performed for the pixel- and SU-based mapping units. Four values of the predictive period are applied: *t*=5, 10, 20, 50 years. The values of *T* are mapped by applying Equation AE.11 and using corresponding distributions of *m* shown in Figure AF.83. The landslide hazard is mapped by applying Equation AE.10, where the values of *S* are given by Model ANN5 (pixel-based analysis) and Model DA4 (SU-based analysis). The applied susceptibility models are considered to be the best ones according to the validation studies (see more details in *Sections A.IV.2.2* and *A.IV.2.3*).

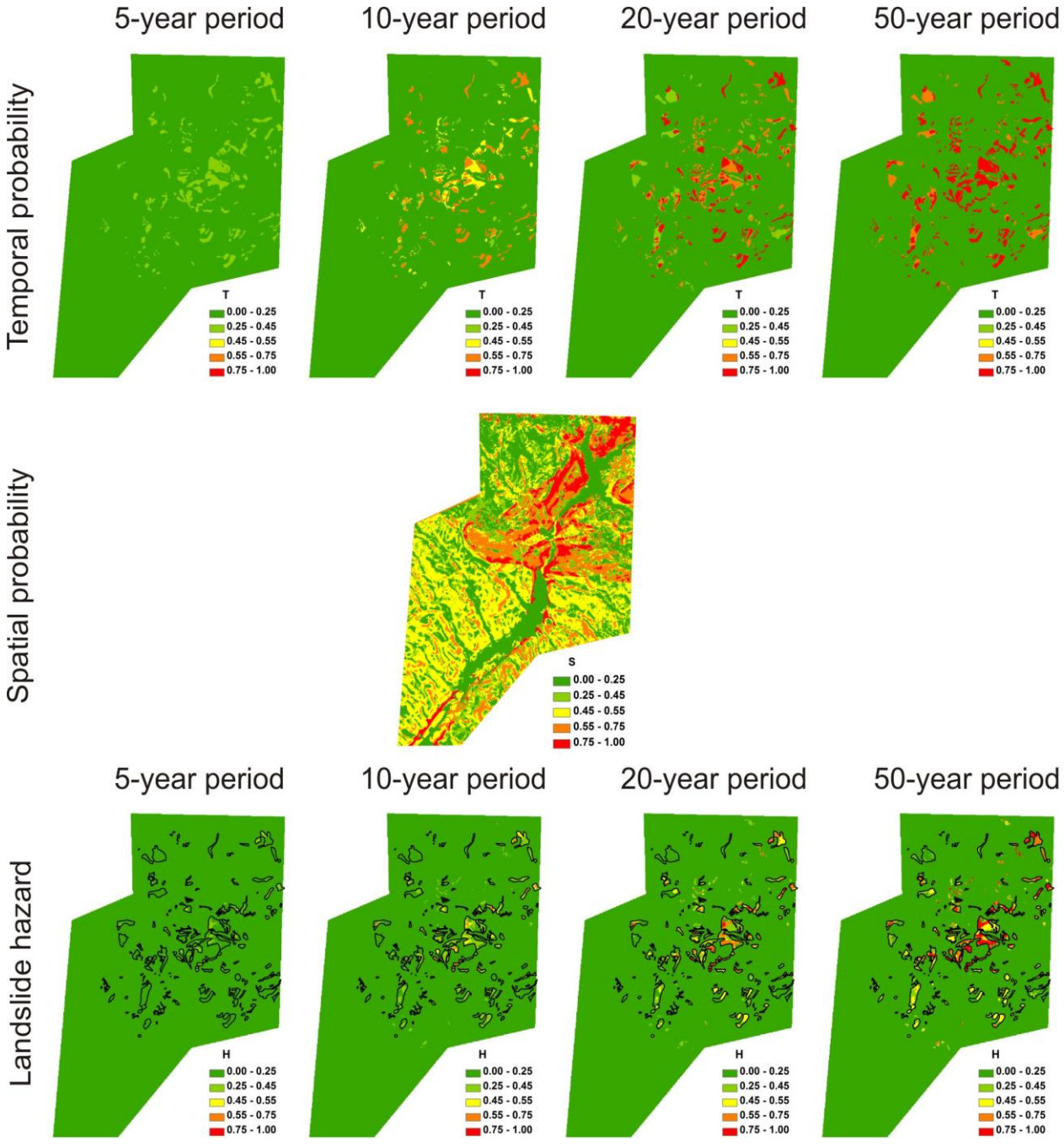

Figure AF.84: The results of the temporal probability, spatial probability (model ANN5) and the landslide hazard mapping for t=5, 10, 20, 50 years applying pixel-based mapping units (the black solid outlines in the landslide hazard maps coincide with the landslide inventory for 2007).

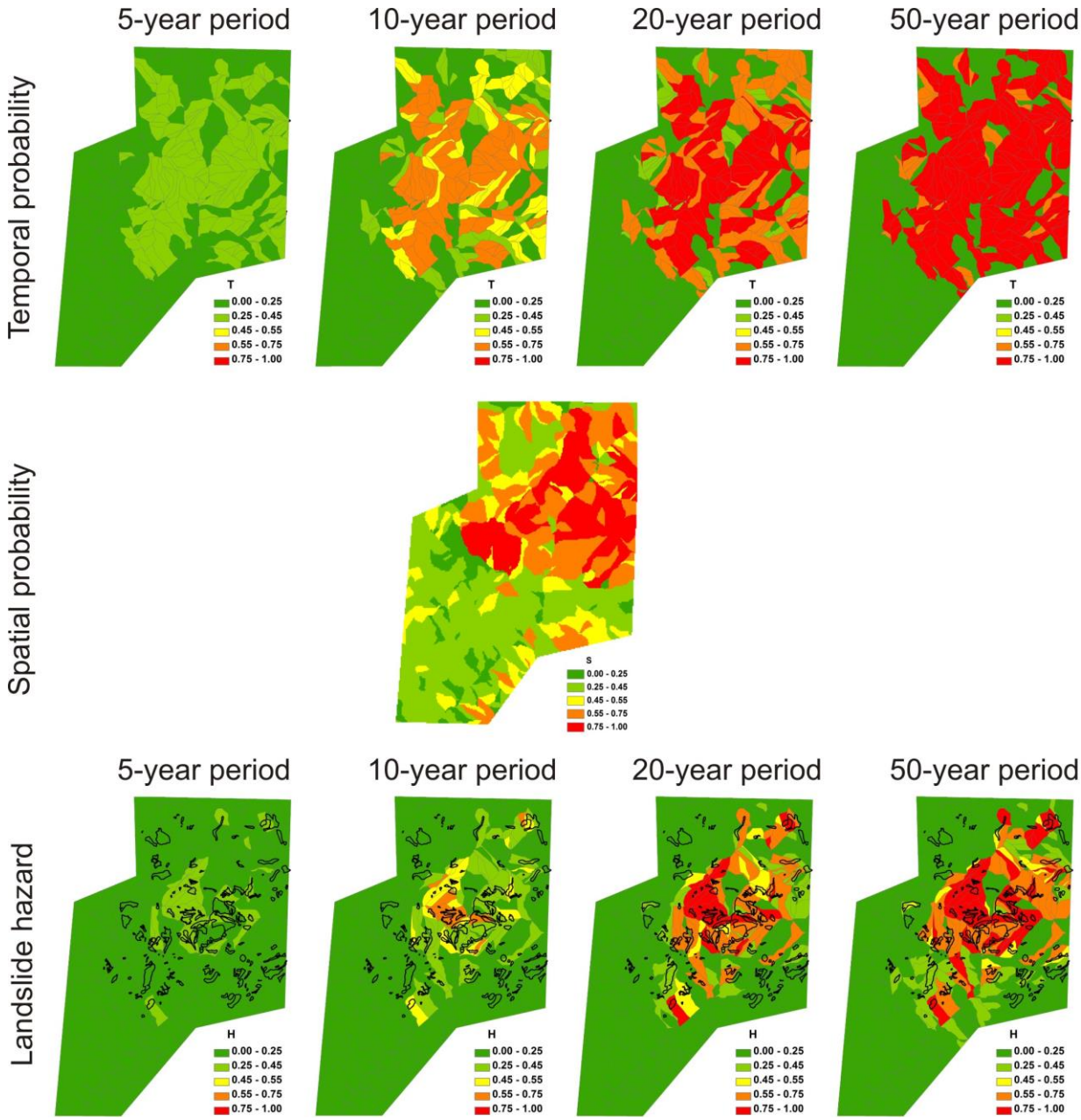

Figure AF.85: Results of the temporal probability; spatial probability (model DA4) and the landslide hazard mapping for t=5, 10, 20, 50 years applying SU-based mapping units (the black solid outlines in the landslide hazard maps coincide with the landslide inventory for 2007).

According to Crovelli (2000), the Poisson model in Equation AE.11 reliably estimates the *T*-value only in the case when the predictive period of time (*t*) exceeds the time span between successive landslide inventories. As it can be seen in Figure AF.80, the time span between analyzed inventories is ranging between 5 and 22 years. This means that in our case the most reliable predictions for *T* (and *H*, correspondingly) can be performed only for $t \geq 22$ years which is true only for $t=50$ years. The shorter-term predictions of *T* and *H* are much less reliable, as the time spans between some inventories exceed the *t*-value. For example, the time span between the 1962 and 1984 inventories (22 years) is more than 4 time larger than $t=5$ years applied in the shortest-term predictions. The reliability of such predictions can be improved by using landslide inventories separated by shorter time intervals, especially for the period between 1962 and 1996.

Figures AF.85 and AF.86 suggest some similarities between the pixel- and SU – based products. First of all, the predicted values of *H* are directly depending on the analysed *t*-value: the larger the *t*-value is, the bigger

portion of target area is occupied by the mapping units with moderate to very high level of the landslide hazard ($H \geq 0.45$). For example, for t=5 years both pixel- and SU-based maps are marked by an absence of areas with $H \geq 0.45$. The highest percentage of the area with the very high landslide hazard ($H \geq 0.75$) is recorded for t=50 years: on the pixel-based map about 0.5 % of area is marked by a hazard value of $H \geq 0.75$, while on the SU-based map more than 10 % of the area have $H \geq 0.75$. Such discrepancy is due to the above-mentioned reason: even if a landslide affects only a small part of certain SU, it adds a re-/activation record and increases the value of H for the whole mapping unit. It further suggests that the SU-based product accounts for a future landslide expansion, while the pixel-based analysis predicts the distribution of H with the present landslide outlines. Meanwhile, the SU-based predictions can actually overestimate the H-value, as the re-/activation record for part of the SU is extrapolated over the whole SU. In this matter, the SU hazard model presents more conservative estimates compared to the pixel-based product.
The results of the landslide hazard mapping are used in the *Sub-section A.V.2.2* to perform the qualitative risk studies. These studies apply the SU-based hazard model for t = 50 years. Following the above discussion, this model conservatively accounts for the future landslide expansion and the long-term predictive period (t = 50 years) gives the most reliable estimates of H among the studied models. The results of the qualitative landslide risk studies, as well as some important theoretical aspects are reviewed in more detail below.

V.2.1 Risk and landslide risk: concept and underpinning issues

The human being and its activity are always exposed to the threat of the negative impacts coming from different types of hazards which can be of natural or anthropogenic origin. In that broader sense, 'hazards' are defined as those processes and situations, actions or non-actions that have the potential to bring the damage, loss or other adverse effects to any attributes valued by mankind (Crozier and Glade, 2005). For example, in our study we treat the hazards as any direct or indirect impacts of the landslide activity. The exposed attributes are generally referred to as the elements at risk and in our study case these elements include human life/health, land, resources, social and physical infrastructure, productive/non-productive activities and environmental quality.
In response to hazards, the human society tries to protect the valued attributes from the negative impacts. For example, the river banks are reinforced to reduce the erosional effects and the active landslides are equipped by early warning systems to allow the people to escape just after initiation and before full development of the landslide failure. That way mankind reduces the vulnerability of the elements at risk, i.e. it diminishes the rate or degree to which a given element at risk is susceptible to be affected by the negative impacts of threatening hazards. In other words, the vulnerability of the element at risk reflects the ability of a given element to resist or withstand the adverse impacts of hazards. The "behaviourist" paradigm suggests that the vulnerability of the element at risk is strongly determined by the social awareness and readiness or the possibility to invest enough resources to deal with the threatening impacts (Smith, 2011). For example, the author shows that the developing countries are often lacking necessary resources to reduce their vulnerability to the landslides. Therefore, slope failures of a comparable magnitude or destructive potential often incur much more losses and victims in the developing countries compared to the developed ones.
Both aforementioned components, i.e. the hazard and vulnerability of the element at risk, complexly interact with each other to determine the level of risk for that element (see Figure AF.86; by Alexander, 2002). The concept suggests that both affecting components are independent in their inputs which shape the existing level of risk. The interaction of both components also suggests that absence of any component, i.e. either hazard or vulnerability is zero, will result in zero-risk for the studied element. This concept shows that risk can be managed via three main options: reduction of hazard alone, mitigation of vulnerability alone or reduction/mitigation of both components simultaneously. The selection of the appropriate

reduction/mitigation measures is normally based on the cost/benefit analysis which should outline the most effective options.

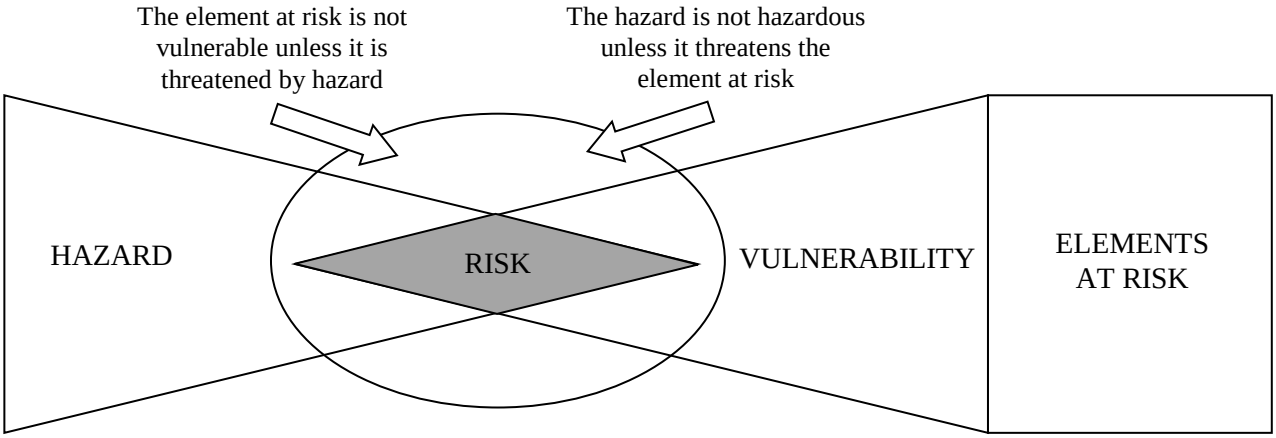

Figure AF.86: Relationship between hazard, vulnerability and risk for a given elements at risk (Alexander, 2002; modified).

The concept of the landslide risk follows the theoretical framework discussed above. Most authors define the landslide risk as a measure of the probability and severity of loss affecting the elements at risk resulting from any direct or indirect consequences of the landslide activity (Fell and Hartford, 1997; Australian Geomechanics Society, 2000). The hazard component in this case is presented by the destructive potential of moving mass and other secondary effects which can accompany the landslide failure (e.g., blockage of the roads, damming of river with following flooding, etc.). The endangered attributes/assets, i.e. elements at risk, often include the human life/health, infrastructure, lifelines and land. The landslide risk is usually managed via the vulnerability mitigation measures, like relocation of the population at risk, building the protective infrastructure, installation of the early warning systems or different capacity building actions. In some important sites the landslide risk can be mitigated via the hazard reduction measures which can include revegetation of the landslide surface, deviation of the surface runoff, toe reinforcement, sliding mass removal, etc.

The landslide risk can be studied both qualitatively and quantitatively. The qualitative studies first rate the landslide hazard and vulnerability (input components) according to the pre-defined progressive scales which have several classes, usually not more than 5. These classes reflect the probability of hazard or indicate the current state of vulnerability of elements at risk: from very low (very improbable hazard or very low vulnerability) till very high (very probable hazard or very high vulnerability). The rated input components are then represented in the so-called risk matrix. This matrix assesses the level of risk based on the combination of hazard and vulnerability classes defined for the studied elements at risk. All described manipulations are usually based on the expert-based opinion and consider site- or project-specific conditions. Therefore, applied ranking rules and the classification matrix could not be readily formalized under the uniform methodology.

The quantitative risk studies are usually referred to as the risk calculation which requires the input components to be represented in the quantitative measure. For example, Crozier and Glade (2005) introduce a general equation which calculates the risk (R) for a given element at risk or its value (E) based on the probability of negative impact originating from the landslide activity (H) and vulnerability of studied element at risk (V):

$$R = H * E * V \qquad \text{(AE.13)}.$$

The *H*-value in this last equation represents the result of the landslide hazard studies. Ideally, this value should be determined for every type of landslide (rockfall, flow, slide, etc.) and for every specific impact of landslide activity (rapid failure, creeping, road blockage, river damming, etc.). This discrimination of the *H*-

values is recommended due to fact that every type of hazard produces a specific type of risk: for example, a creeping slope usually poses the highest threat to the neighbouring infrastructure and buildings/homes, while the risk to the human life is very negligible. In practice, landslide hazards are normally analysed either for one specific landslide type or for all of them together without considering such discrimination. In addition, the hazard studies usually analyse only the specific impact of landslide activity, generally represented by the probability of rapid failure down the slope: in such analyses the type of the sliding mechanism is rarely taken into account. These assumptions and simplifications adopted in landslide hazard studies further affect the reliability of final estimates, as a given slope can have different *H*-values for the failure of the rapid moving earthflows and for the slowly creeping slope.

The *E*-value in Equation AE.13 gives the quantitative measure or value of the element at risk. In some cases this parameter can readily be quantified, for example, through the number of humans living in the area potentially affected by the landslide failure or through the total cost of the houses on the creeping slope. In several other cases the elements at risk are very hard to quantify. For example, the studied element can be represented by the quality of live which is very difficult to convert into measurable units.

The remaining parameter used in Equation AE.13 is the vulnerability of studied element at risk (*V*). This parameter usually represents the proportion of total value which can be potentially lost due to the negative impacts of landslide activity. In this case *V* ranges from 0 to 1: *V*=0 meaning no loss at all and *V*=1 meaning the total loss of value of the studied element at risk. The vulnerability quantification should often account for the interdisciplinary considerations. For example, if element at risk is represented by human life, then the vulnerability studies should account for the structural stability of buildings (construction engineering), the time that people stay withing the target area (sociology) and even the difference between the behaviour of adults and of children during an emergency situation (psychology). Crozier and Glade (2005) comment that the vulnerability of element at risk in Equation AE.13 is the most difficult to quantify among the three existing components. The authors further note that there are only very few studies which analyse the vulnerability to landslide hazards and even fewer studies review the vulnerability with respect to specific impacts of different landslide types.

The next sub-section presents an attempt to study the landslide risk in the Mailuu-Suu target area. These studies should be considered as purely qualitative. A quantitative risk analysis is not possible in our case, as some important data are missing, especially those regarding the vulnerability of elements at risk with respect to specific landslide hazards. The studied risk scenarios include three different elements at risk which are exposed to the direct effects of the landslide failure. The secondary impacts of landslide failure, like, e.g., river damming, upstream and downstream flooding are not analysed, as the required high-resolution topographic data are missing. A more detailed overview of the risk ranking and related results are presented below.

V.2.2 Landslide risk in the Mailuu-Suu target area: main results

The landslide risk in the target area is qualitatively analysed for three types of elements at risk: buildings, automobile roads and uranium waste tailings. The performed analyses are very simplified and do not propose the full coverage of targeted issues. Therefore, the final results of risk mapping should be treated as very indicative data, rather than as precise and reliable risk estimates.

The level of landslide hazard for all elements at risk is assigned via the SU-based model (*t*=50 years) extracted in *Sub-section A.V.1*. This model represents the spatial distribution of the *H*-values which show the probability of the landslide failure for the 50-year predictive period. Following the basic methodology discussed above, these *H*-values are converted into five progressive ranks: very low hazard (*H*=0.00÷0.25), low hazard (*H*=0.25÷0.45), intermediate hazard (*H*=0.45÷0.55), high hazard (*H*=0.55÷0.75) and very high hazard (*H*=0.75÷1.00). This rated model is further used to attribute the hazard ranks to all studied elements at risk based on their spatial location. That way one component of risk, i.e. the hazard, is determined for all analysed elements.

According to Figure AF.86, the second component of risk is represented by the vulnerability of the elements at risk. This component was never regularly studied in target area and the limited reports provide just some

indicative data (see, e.g., Alioshin and Torgoev, 2000). Due to the lack of regular data, the vulnerability of two elements at risk (buildings and automobile roads) is evaluated by us based on some secondary attributes and features. The selection of these secondary features and vulnerability ranking involve expert-based opinion supported by the site-specific knowledge (Torgoev I. and Alioshin Y., 2013 – oral communication). Thus, we assume that the vulnerability of local roads is directly related to their traffic density. That way, every segment of the existing road network was assigned by one out five possible classes of traffic density: from the lowest (class 1) till the highest one (class 5). Five classes of traffic density are further converted into five classes of vulnerability: from the very low (the lowest traffic density) till the very high vulnerability (the highest traffic density). The segmentation of existing network and determination of the traffic density classes purely relies on the knowledge of the local situation and do not involve any on-site records of traffic density.

The same five classes of vulnerability are applied to the buildings as the elements at risk: from the lowest (class 1) till the highest vulnerability (class 5). Here, it is assumed that the vulnerability is related to the structural resistance of the building, the parameter which can be characterized through the construction type. Thus, two main types of buildings are outlined here for the following vulnerability ranking: the multi-storey apartment blocks and single-storey houses. The lowest vulnerability, i.e. the highest structural resistance, is assigned to the multi-storey apartment blocks which are often situated inside the city. The highest vulnerability (with the lowest structural resistance to the landslide impacts) is assigned to the single-storey houses, often made of adobe and normally situated in the rural areas. In this ranking approach the intermediate classes of vulnerability are assigned to areas covered by a mixture of those two building types according to the percentage of presence of each type of building.

The clusters of building types are mapped by using the 2007 Quickbird imagery. Figure AF.87 shows some examples of such cluster identification. For instance, the highest vulnerability (class 5) is assigned to the area with predominating presense of single-storey houses (Figure AF.87a). The domination of multi-storey blocks in Figure AF.87c is considered to represent an area marked by the lowest vulnerability (class 1). The intermediate vulnerability (class 3) is determined by an almost equal proportion of each of the two building types (see Figure AF.87b).

Figure AF.87: Snapshots of the 2007 Quickbird imagery showing clusters of inhabited area with very high (a), moderate (b) and very low (c) vulnerability, assigned based on the interpreted proportion between two building types.

The final results of the vulnerability mapping applied to the two studied elements at risk are presented in Figure AF.88. The vulnerability map for buildings contains the set of clusters interpreted from the Quickbird image (see examples in Figure AF.87). As it can be seen, the highly vulnerable buildings mainly concentrate in the suburbs and rural areas, especially in the northern part of target area (see the clusters marked by red colour). Almost half of the city territory is marked by a low vulnerability due to the presence of highly stable apartments blocks (see the areas marked by green colour). An opposite distribution is observed for the road vulnerability map. Here, the highly vulnerable elements at risk are concentrated within the city, while the outskirts and rural areas are marked by the lowest vulnerability.

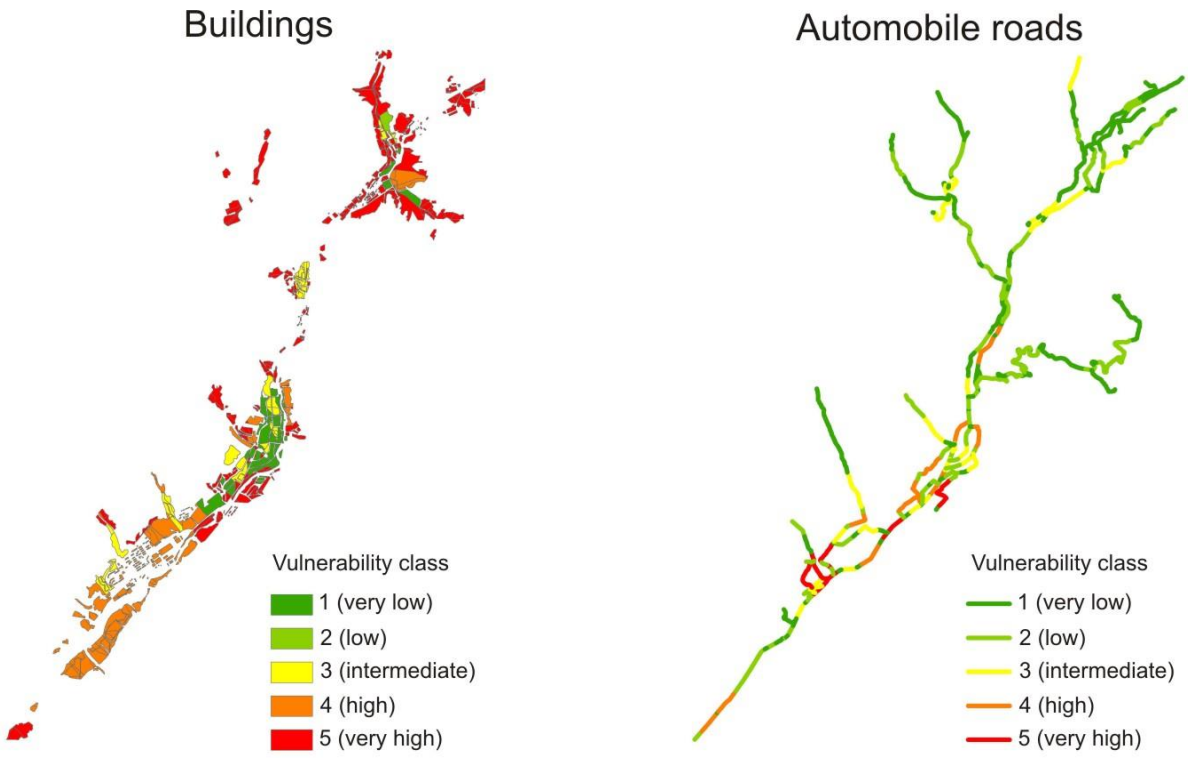

Figure AF.88: Mapped distribution of the vulnerability for the buildings (left) and roads (right).

Thus, hazard and vulnerability ranks ranging from very low (class 1) to very high (class 5) are assigned to the clusters/segments of two studied elements at risk (buildings and automobile roads). These results are further applied in the ranking of the landslide risk applying the classification matrix presented in Table AT.18. This matrix returns the class of the landslide risk based on the interaction between hazard and vulnerability ranks. In total, five risk classes can be defined based on this matrix: from very low risk (class 1) till very high risk (class 5). Similar to the vulnerability ranking, the risk classification relies on the aforementioned expert opinion. Torgoev and Alioshin (2013) suggest that the landslide risk in target area is more sensitive to the vulnerability variation, rather than to the change of the hazard class. Therefore, e.g., the interaction between very low hazard and very high vulnerability already produces an intermediate risk, while very high hazard and very low vulnerability results in a low level of risk.

Table AT.18: Classification matrix returning the class of landslide risk based on the interaction between hazard and vulnerability ranks (based on Torgoev I. and Alioshin Y., 2013 – oral communication).

		Landslide hazard				
		1 (very low)	2 (low)	3 (intermediate)	4 (high)	5 (very high)
Vulnerability	1 (very low)	1 (very low risk)	2 (low risk)	2 (low risk)	2 (low risk)	2 (low risk)
	2 (low)	1 (very low risk)	2 (low risk)	3 (intermediate risk)	3 (intermediate risk)	3 (intermediate risk)
	3 (intermediate)	2 (low risk)	2 (low risk)	3 (intermediate risk)	4 (high risk)	4 (high risk)
	4 (high)	2 (low risk)	3 (intermediate risk)	3 (intermediate risk)	4 (high risk)	5 (very high risk)
	5 (very high)	3 (intermediate risk)	3 (intermediate risk)	4 (high risk)	4 (high risk)	5 (very high risk)

The resulting distribution of the landslide risk for buildings and roads is presented in Figure AF.89. As it can be seen, the biggest portion of city territory is characterized by very low to intermediate landslide risk. The neighbouring villages are exposed to higher risk, while the highest levels (classes 4 and 5) are assigned to the remote places in the northern and north-eastern parts of the study area. The analyzed road network is mainly characterized by an intermediate level of landslide risk. Some roads within the city and its surroundings are marked by high to very high levels of landslide risk, which is related to the active landslides in this parts of the target area.

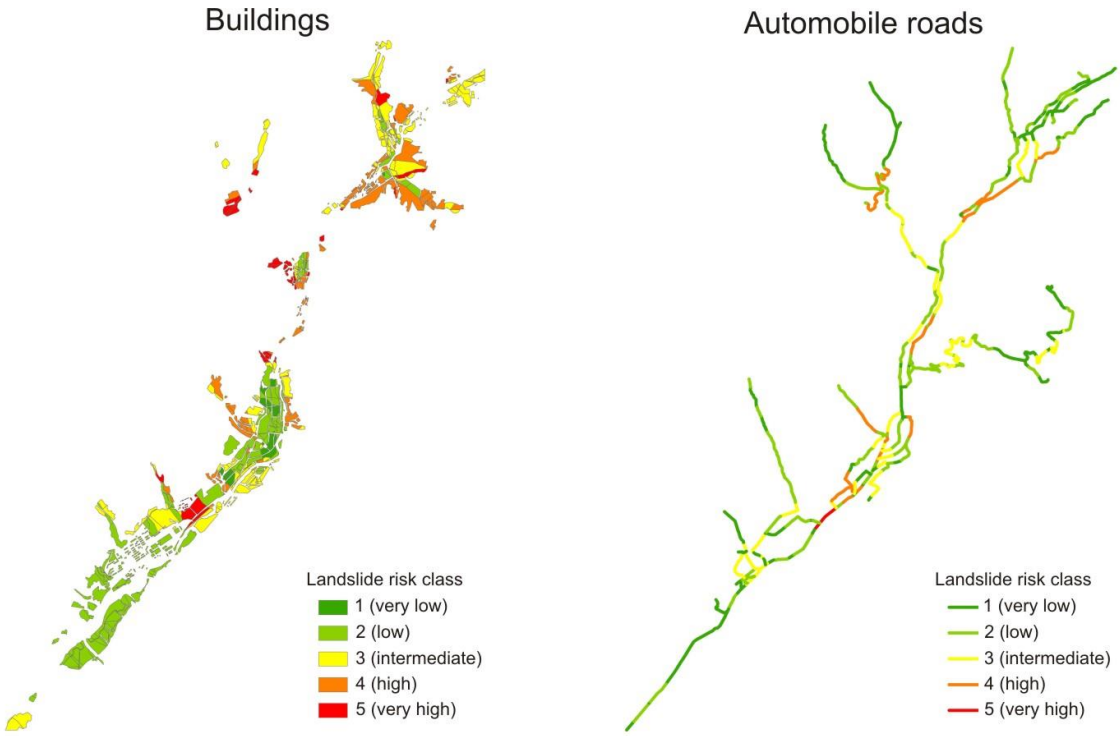

Figure AF.89: Mapped distribution of landslide risk for buildings (left) and roads (right); the risk classes are estimated based on the classification matrix presented in Table AT.18.

A slightly different methodology is applied to the uranium waste tailings, the third type of the elements at risk studied here. We do not use the classification matrix presented in Table AT.18, as there is no reliable approach to rank the vulnerability of the tailing sites to the damaging impacts of the landslide failure. Meanwhile, some indicative information on this parameter can be found. For example, Alioshin and Torgoev (2000) note that these tailings were deposited more than 50 years ago and protective infrastructure was not maintained in between. As a result, all these sites are very vulnerable to adverse impacts. Therefore, it can be conservatively assumed that all tailings in the target area have very high level of vulnerability with respect to the damaging impact of the landslide failure.

Assuming that the vulnerability of all tailings is uniformly very high, we prefer to use the landslide hazard model as the proxy for the landslide risk characterization. It is assumed that the *H*-values extracted for the 50-year predictive period should directly indicate the probability of the direct destruction due to slope instability.

Thus, Figure AF.90a presents the central part of the target area with the indicated position of tailing sites, landslides, river network and inhabited territory overlaid on the 2007 Quickbird image. Figure AF.90b further overlays these tailing sites on the landslide hazard model extracted for the 50-year predictive period. According to Alioshin and Torgoev (2000), the highest environmental concern is related to the tailings situated along the Mailuu-Suu River valley (see the tailings № 5, 6, 7 and 9 in Figure AF.90a). The destruction of these tailings can result in the river pollution with potential transboundary impacts. Due to high risk posed by the Tektonik landslide the biggest part of material from tailings №3 was relocated to another place with safer geoenvironmental conditions (see old and new storage sites in Figure AF.90a; Kunze and Schmidt, 2008).

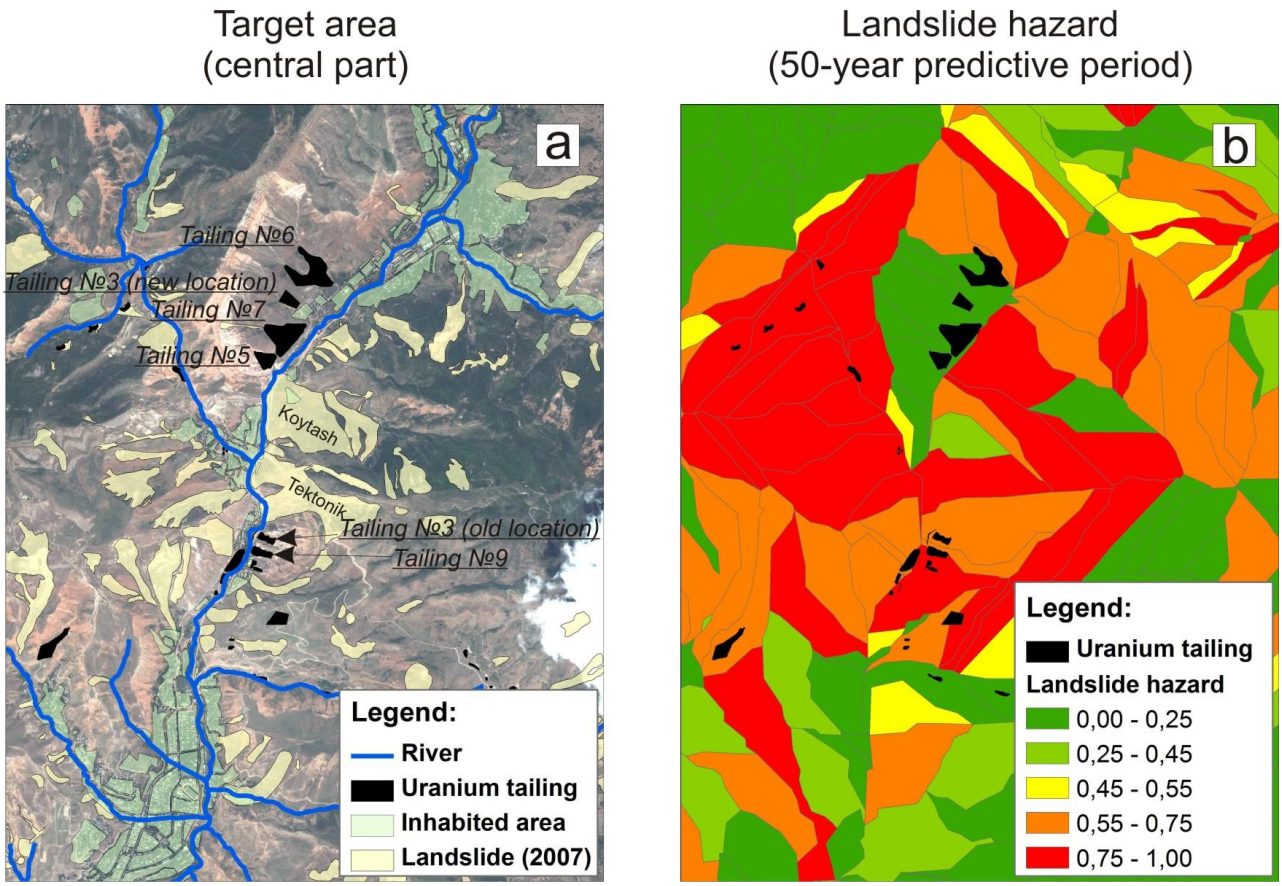

Figure AF.90: (a) Schematic view of the central part of the target area with indicated position of uranium tailings situated along the Mailuu-Suu River valley; (b) uranium tailings overlaid over the landslide hazard map the 50-years prognostic period.

Figure AF.90b shows that the tailings № 5, 6, 7 and new storage site for tailing № 3 are exposed to a very low level of landslide hazard (H=0.0-0.25 for the 50-year predictive period). This shows that relocation of biggest part of material from tailing № 3 was an effective mitigation measure, which finally reduced the risk of river pollution. The low level of landslide hazard here is proved by the analyzed dataset of landslide inventories. This dataset shows that during the last 45 years there was only one small-scale debris flow observed in the surroundings of tailing №5. According to Alioshin and Torgoev (2000), this event did not bring any significant damage to the protective infrastructure. It further suggests that these sites are marked by very low level of landslide risk, i.e., by low probability of destruction potentially induced by landslide failure.

Tailings № 9 and old location of tailing № 3 are marked by high to very high levels of landslide hazard which are mainly related to the active Tektonik landslide (H=0.55-1.0 for the 50-year predictive period). Indeed, Vandenhove et al. (2003) list several evidences of the high destruction impacts caused by the failure of the Tektonik landslide in 1994. Following this event, some part of the sliding mass of the Tektonik landslide was removed withing the frame of the World Bank funded project (see, e.g., Kunze and Schmidt, 2008). It should be highlighted that the impact of this mitigation measure was not analysed by our hazard studies, as applied mapping methods do not have readily available algorithms to deal with such factors. Therefore, the actual level of landslide hazard and risk at tailing № 9 and old location of tailing № 3 should be reanalyzed. Such analyses should account for the stabilization impacts originating from these mitigation measures.

As it can be seen, the landslide risk in target area is studied via very simplified scenarios. These scenarios introduce expert-based assumptions which are not verified by any on-site measurements. Therefore, the results should be more considered as qualitative indications, rather than as precise estimates of the landslide risk in the target area. Additionally, the analysed scenarios cover just limited aspects of the full risk related to

the landslide activity. For instance, one important risk component not studied here is the possible blockage of the river channel induced by the landslide failure. This blockage can lead to negative impacts both upstream and downstream from the landslide dam. The upstream water impoundment can cause, e.g., inundation of engineering structures, river bank erosion or structural damage to infrastructure. The potential threat to downstream areas mainly originates from the abrupt breaching of the landslide dam. The breached water can have very high destructive potential which pose significant threat to inhabited area, infrastructure and any valued elements at risk situated in exposed zone.

Regarding this risk aspect, Alioshin and Torgoev (2000) highlight the high threat attributed to possible failure of big-scale Tektonik or Koytash landslides. The authors say that a following upstream flooding can inundate the protection of tailings № 5 and 7. These impacts can finally lead to tailing destruction when significant volume of tailing material can spill into the river network. That way these sites are exposed to much higher level of the total risk attributed to the landslide impacts, while the risk related to the direct destruction due to landslide failure is very low (see Figure AF.90b). Torgoev (2010) performed a simplified analysis of these flooding scenarios. According to the author, the failure of Koytash landslide with a dam height of about 10 m can already lead to partial inundation at these tailing sites. The author also shows that a critical volume of water can be accumulated within 5-10 hours, which leaves a short time for response, such as the removal of the blocking mass or reinforcement of inundated sites. These results show that such aspects of landslide risk in the target area require further attention. The risk analysis in this case should then deliver information for the implementation of risk mitigation measures.

VI. Research summary

Part A of this thesis presented the results of research focused on spatial analysis and mapping of the landslide susceptibility, hazard and risk in the surroundings of the town of Mailuu-Suu, situated in southern Kyrgyzstan. The target area is characterized by a combination of environmental settings and anthropogenic impacts resulting in a high level of landslide hazard. The studies show that the number of active landslides is gradually increasing over last decades. The expansion of the total area affected by the landslides could be documented by remote imagery and other data collected primarily at 6 distinct moments during the period between 1962 and 2007.

This situation is aggravated by the proximity of some active landslides to the uranium tailings, the legacy sites of previous mining here. Landslides can directly or indirectly impact the tailings, which could lead to extreme environmental pollution, potentially with transboundary effects. These aspects outline an urgent need for the risk reduction measures to be implemented in the Mailuu-Suu arae. Giving the lack of available resources, the mitigation strategies should be optimized to select the most effective actions.

One practical input for such optimization is delivered by the results of this thesis, as we developed a spatial database that can be used to improve decision making. According to Table AT.19, this database was compiled as the result of five research tasks. These tasks include the compilation of the landslide database, the mapping of the affecting factors and final assessment of the landslide susceptibility and hazard (see Tasks 1-4). In the frame of the final research task a qualitative risk study was performed for three elements at risk: buildings, roads and some critical uranium tailing sites (see Task 5).

The main deliverables of these tasks are the maps which portray the spatially distributed information on factors influencing landslide activity, as well as the levels of landslide susceptibility, hazard and of risk. Some of these maps can directly be used for decision making. For example, the hazard models can characterize, both spatially and temporally, the exposure of elements at risk to the impact of landslide failure. The other products provide important inputs for more advanced analyses that should be completed in future. Thus, the quantitative estimates of landslide hazard can be used for risk calculation which is the most reliable way to characterize the local risk due to the landslide impacts. In this last case, the additional research quantifying the vulnerability of elements at risk would be needed.

Table AT.19: Summary of research tasks of Part A with short description of reached milestones.

Task	Milestones/deliverables
1. Landslide database	Compilation of the multitemporal landslide inventories; Landslide activity detection.
2. Affecting factors	Compilation of thematic layers for: -surface morphology; -land cover/land use; -geological units; -structural control.
3. Landslide susceptibility	Applied mapping methods: -Index-based (IB); -Discriminant Analysis (DA); -Artificial Neural Networks (ANN); -Newmark Displacement (ND).
4. Landslide hazard	Temporal probability analysis; Landslide hazard mapping.
5. Landslide risk	Quailitative risk mapping for buildings and automobile roads; Estimates of exposure of tailings №3,5,6,7,9 to landslide hazards.

The first research task outlined in Table AT.19 is referred to as ‘Landslide database’. The main deliverable here is the set of multi-temporal landslide inventories compiled for 1962, 1984, 1996, 2002 and 2007. Three earliest products (for 1962, 1984 and 1996) are extracted on the basis of the aerial stereo-imagery. The

landslide inventories for 2002 and 2007 are compiled by Schlögel et al. (2011) applying two Quickbird scenes. All resulting inventories were geo-referenced in order to determine a relatively precise position of landslides mapped from different imagery. These results provided necessary inputs for successive mapping of landslide susceptibility (Task 3). Thus, the earliest inventories are applied to the susceptibility analysis itself, while the latest one (for 2007) is employed in validation studies. These deliverables also provided important inputs for the landslide hazard mapping (Task 4), as the temporal probability of landslide occurrence was estimated based on the multi-temporal inventories.

Additional research of Task 1 included the detection of landslide activity. Three main periods were studied: 1975-1992, 1992-2001 and 2002-2007. The multispectral Landsat scenes for 1975, 1992 and 2001 are applied here to detect the landslide activity within two earliest periods (1975-1992, 1992-2001). The detection principle implies that landslide activity incurs the change of reflectance values. This change can be identified by spectral analysis of the overlapping Landsat bands. Schlögel (2009) performed a similar study for the period of 2002-2007 on the basis of two high-resolution Quickbird scenes. The author assumed that the landslide activity can alter the Normalized Difference Vegetation Index (NDVI). Thus, the temporal change of NDVI-values was studied and it represented the basis for following mapping of active landslides. The results showed that multispectral imagery can be successfully applied to detect landslide activity. The final accuracy of such mapping is strongly determined by the resolution of input imagery. For example, the resolution of the Landsat images is sufficient only for the scale of slope unit. The high resolution of Quickbird imagery allows not only the landslide detection, but gives the opportunity to precisely map the active landslides.

Task 2 in Table AT.19 performs the collection of thematic data. These data are further used in the landslide susceptibility mapping. Four main groups of affecting factors were analysed: surface morphology, land cover/land use, geological units and structural control. The surface morphological data (slope angle, slope exposition, slope curvature) were spatially mapped on the basis of the SPOT DEM. The land cover/land use thematic layer was mainly compiled by analysing the 2001 Landsat imagery. The thematic map of geologic units was extracted from the results of de Marneffe (2010), who created a geological map and a 3D geological model of the central part of the target area. The layer of the structural control was generated on the basis of photo-geological interpretation performed over the 1984 aerial stereo-imagery. This last thematic layer combined the interpreted structural patterns (layer dipping) with surface morphology (slope exposition) to define four classes of structural control.

The landslide susceptibility mapping is the main goal of Task 3. Four different mapping methods were applied here: Index-based (IB), Discriminant Analysis (DA), Artificial Neural Networks (ANN) and Newmark Displacement (ND). These methods represent three conceptually different groups of methods: heuristic (IB), statistical (DA, ANN) and process-based (ND) techniques. The outcome of the applied methods was represented by a qualitative ranking of landslide susceptibility (IB, ND), as well as in terms of numeric measure indicating the sliding probability values (DA, ANN). The models of the landslide susceptibility are produced using the 1962, 1984, 1996 and 2002 landslide inventories. The 2007 inventory allowed us to validate the models and to assess their predictive power. The models with the best predictive power were used in landslide hazard studies.

Task 4 in Table AT.19 is focused on the landslide hazard analyses. Two types of mapping units are used here: pixel and slope unit (SU). The DA and ANN models with the best predictive power are used here to characterize the spatial component of landslide hazard. The DA model is applied to the SU-based mapping and ANN model is used in the pixel-based analysis. The temporal component of the landslide hazard is analysed by applying the set of the multi-temporal landslide inventories. As the time span between successive inventories is irregular, it is considered that the long-term predictions of the landslide hazard (for 20-50 years) are more reliable than the short-term ones (for 5-10 years). Regarding the applied mapping units the final preference is given to the SU as they more accounts for future upslope and lateral expansion of landslide activity. Therefore, it is assumed that the best landslide hazard model has the SU-based mapping units with a predictive period of 50 years.

Qualitative studies of landslide risk were performed in the frame of Task 5. Three types of elements at risk were analysed: buildings, automobile roads and uranium waste tailings. The studied risk scenarios were very

simplified and reviewed just selected aspects of full risk associated to landslide activity. Two different approaches were used here. The first one studied the risk for buildings and automobile roads. First, the component of hazard exposure for these elements at risk was characterized. It was done using the SU-based hazard model predicting the probability of the landslide failure for the 50-year period. Then, the vulnerability of these elements at risk was laterally assessed through some features and attributes established by expert-based opinion. Thus, it was assumed that vulnerability of building is determined by its structural type, while the road vulnerability is linked to the traffic density. The spatially distributed hazard and vulnerability ranks were further combined to determine the class of landslide risk. The mapping results indicate that the northern and north-eastern parts of study area are marked by the highest risk for buildings, while the road network is generally affected by a moderate level of landslide risk.

For the uranium waste tailings the risk study did not involve any vulnerability ranking. Actually, due to a bad state of protective infrastructure, it can be conservatively assumed that all tailings in the target area are marked by a uniformly high vulnerability to destruction by landslide failure. The landslide risk in this case was purely characterized through the SU-based hazard model: that way the landslide risk for all tailings was described through their exposure to hazard within the 50-year prediction period. The results of these studies indicate that tailing № 9 and old location of tailing № 3 are exposed to the highest threat of direct impacts due to landslide failure (H=0.55-1.0 for 50 year period). The tailings № 5, 6, 7 and new location of tailing № 3 are less exposed to such direct threats. These results indicate that relocation of tailing № 3 was an effective measure to decrease the risk of river pollution that had been posed by this tailing at the old location.

It should be highlighted that total risk associated with the landslide impacts may have some other important aspects. Thus, Torgoev (2010) shows that tailings № 5, 6, 7 and new location of tailing № 3 may be exposed to indirect impacts related to the possible damming of river finally leading to a partial inundation at these sites. The study of the simplified flooding scenarios shows that the most negative impact is related to a possible failure of the Koytash landslide. This study demonstartes that all aspects of the landslide risk in the target area need to be further analysed.

The research of Part A was mainly based on existing methods and approaches that are widely-adopted in the international practice. The study focused on the integration of these methods in order to provide results that can be useful for the future management of landslide risk in the Mailuu-Suu Valley. The developed methodology can be considered as comprehensive approach that may also be applied to other regions marked by a similar level of landslide risk – especially to those located in remote areas. Such studies can act as a proxy for the site characterization giving background data for more detailed and localised investigations.

The second part of this thesis presents results of more fundamental studies. We provide a critical analysis of Newmark mapping methodology which assesses the seismically-induced landslide susceptibility through the calculation of co-seismic shear displacements. Applying 2D and 3D dynamic modelling studies we try to develop some proxies that will account for some of the problem complexities not considered by the existing methodology. These developments should finally improve the predictions of seismically-induced landslide displacements and related susceptibility. A detailed review of modelling studies and results is presented in the next part of thesis.

Part B: Newmark Displacement method: dynamic studies and conceptual improvements

I. Earthquake-triggered landslides and Newmark method: current state and problems

I.1 Earthquake triggered landslides

According to Varnes (1978) earthquakes together with climatic and anthropogenic factors are among the most widespread triggers of the slope movements. Such as liquefaction and tsunami, seismically-triggered landslides are considered as 'side effects' of earthquakes. Past and recent examples around the world show that most moderate and large earthquakes in mountainous regions trigger landslides. It is demonstrated by several seismic events that occurred worldwide during last 20-30 years. For instance, the M=6.7 Northridge, California earthquake in 1994 triggered more than 11,000 landslides (Harp and Jibson, 1996a), the M=7.3 Chi-Chi, Taiwan earthquake in 1999 triggered more than 20,000 landslides, adding significant infrastructural damage and 10% of fatalities to the total earthquake impact (Lin et al., 2003).
In many cases these landslides account for a significant proportion of total earthquake damage and/or death toll (Jibson, 2007). Table BT.1 provides information on the earthquakes that triggered the deadliest landslides. The M=8.5 Gansu, China earthquake in 1920 brought the highest historic death records attributed to seismically-triggered landslides. The huge loess flows buried several towns which resulted in more than 100,000 casualties (Alexander, 1989). The second deadliest event listed in Table BT.1 is also registered in China. The M≈7.7 Kangding-Luding (Sichuan) earthquake in 1786 resulted in the landslide damming of the Dadu River. The 70 m high dam was destabilised ten days later by an aftershock impact, and the following downstream flooding resulted in more than 100,000 fatalities (Dai et al., 2005). The 'side effects' of this seismic event are remarkable compared to the reported number of 500 people directly killed by the earthquake through the destruction of buildings.

Table BT.1: List of seismic events, that triggered the most deadliest landslide activity ([1]U.S. Department of the Interior, 1970; [2]Alexander, 1989; [3]Rachowiecki and Beech, 2004; [4]Petley et al., 2005; [5]Petley et al., 2006; [6]Evans et al., 2009; [7]Liu et. al, 2009; [8]Yin et al., 2009; [9]Lynn, 2010; [10]Huang and Fan, 2013).

Earthquake (location)	Date	Total fatalities, resulted from seismic event	Fatalities due to triggered landslide activity
Gansu (China)[1, 2]	16/12/1920	273,400	more than 100,000
Kangding-Luding (China)[1,2]	10/06/1786	more than 100,000	more than 100,000
Kashmir (North Pakistan and India)[4, 5]	08/10/2005	more than 100,000	26,500
Wenchuan (China) [7,8,9,10]	10/06/2008	69,227	more than 20,000
Ancash (Peru)[3]	31/05/1970	66,000	more than 18,000
Khait (Tajikistan)[2,4,6]	10/07/1949	28,000	7,200-12,000

Table BT.1 also lists some other seismic events that occurred recently. The M=7.6 Kashmir earthquake triggered numerous large landslides and the largest one is the Hattian Bala rock avalanche with a volume of $80*10^6$ m^3. According to Petley et al. (2006), the total death toll attributed to the earthquake-triggered landslide/rockfall activity is estimated to be around 26,500 fatalities. It is around one-third of the total number of victims related to this seismic event.
The M=7.9 Wenchuan, China earthquake in 2008 represents a very spectacular example. This seismic event triggered between 60,000 and 200,000 destructive slope movements (Huang and Fan, 2013; Xu et al., 2014). The Daguangbao landslide is cited to be the largest (Figure BF.1). The triggered landslides caused serious infrastructural damage and brought secondary effects, like river damming (Gorum et al, 2011). The seismically-triggered landslides resulted in more than 20,000 fatalities which is about one-third of a total earthquake death toll (Huang and Fan, 2013). While thousands of people became homeless due to the

landslide activity, around one million of people were threatened downstream from the Tangjiashan landslide dam (Liu et. al, 2009). Numerous cases of road blocking hindered rescuing and remediation activity in the immediate earthquake aftermath.

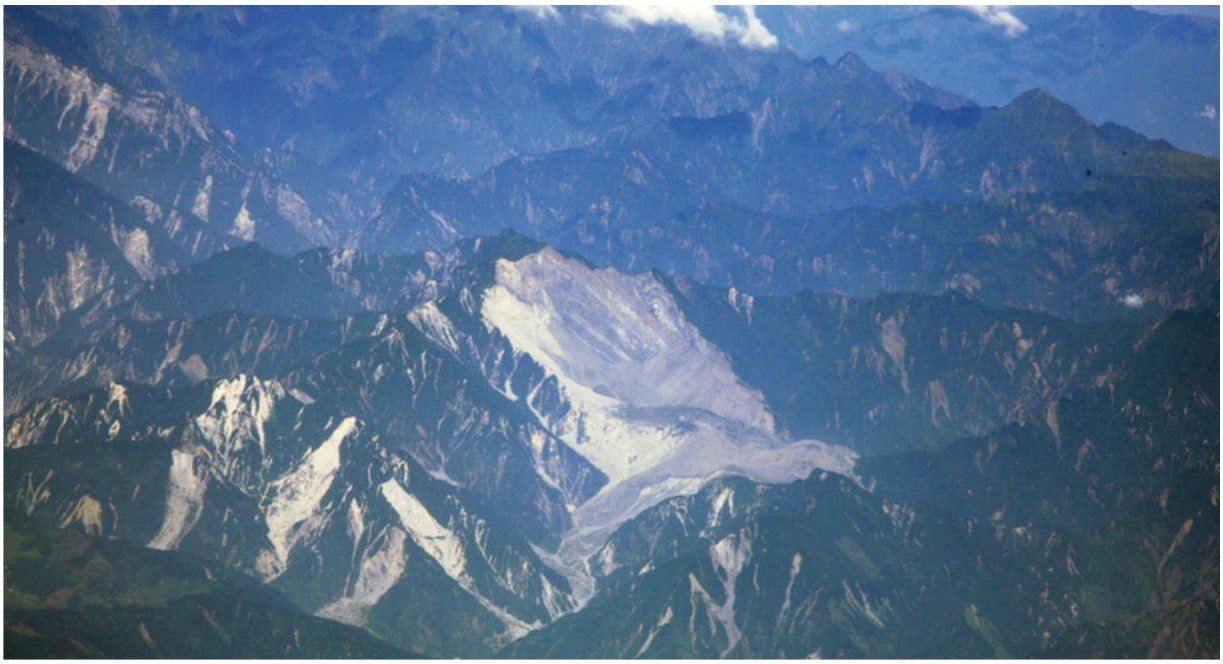

Figure BF.1: The photo of the Daguangbao landslide – the largest slope movement triggered by the M=7.9 Wenchuan, China earthquake in 2008 (by Huang and Fan, 2013).

The M=7.9 Ancash earthquake in 1970 is the most catastrophic natural disaster that ever hit the territory of Peru. Therefore, this seismic event is often referred to as the Great Peruvian earthquake. The seismic shaking destabilised the northern side of the Mount Huascaran which finally resulted in a huge flowslide of mixed material made of rock, ice and snow (Cluff, 1971). The sliding mass buried the towns of Yungay and Ranrahirca, which resulted in more than 18,000 victims. This number of casualties approximately accounts for one-third of the total earthquake victims, similar to the proportion that was indicated above for the 2005 Kashmir and the 2008 Wenchuan earthquakes.

The last event listed in Table BT.1 is the M=7.4 Khait earthquake which struck the territory of Tajikistan in 1949. According to several authors, between 7,200 and 12,000 life losses are attributed to the seismically-triggered landslides (Alexander, 1989; Petley et al. 2005; Evans et al., 2009). This earthquake induced several hundreds of landslides. Around half of victims, associated with the slope failures, were caused by the Khait rock avalanche and the Yasman loess landslide.

There are several other remarkable cases of earthquake-triggered landslides in the Central Asian region. One of them is the famous Usoi rockslide triggered by the M=7.4 Sarez, Tajikistan earthquake in 1911. The giant rockslide failure with an estimated volume of 2.2 km^3 dammed the Murgab River valley which finally created the 75 km long Sarez Lake (Preobrajensky, 1920; Gaziev, 1984; Schuster and Alford, 2004; Evans et al., 2006). The present-day stability of this lake is of great concern for the Tajik government and population living downstream from this lake (Risley et al., 2006).

The territory of Kyrgyzstan is also highly susceptible to the earthquake-triggered landslides, even though known examples are less catastrophic than the above cited ones due to the low population density in the affected areas. The M=8.2 Kemin earthquake in 1911 triggered tens of large-scale landslides in the epicentral area (Bogdanovich et al., 1914; Delvaux et al., 2001). A retrospective analysis shows that a significant percentage of total earthquake fatalities is related with the landslide failures caused by this seismic event. The most recent example in Kyrgyzstan is the M=7.3 Suusamyr earthquake in 1992. This earthquake hit a weakly populated area and resulted in around 50 fatalities in total (Ghose et al., 1997). Meanwhile, tens of landslides of different size were triggered by this seismic event, including the biggest Belaldy rockslide. These mass movements brought significant infrastructural damage and resulted in the long-term negative impacts.

I.2 Seismic slope stability at a scale of single slope

The problem of slope stability under the impact of the seismic shaking became more and more important during the second half of the 20th century. It was mainly due to the wide expansion of construction activity in the seismically active regions. Such engineering constructions include dams, river embankments, pit walls, road-cuts, etc. Jibson (2007) made an overview of all methods for the analysis of single slope seismic stability and defined three groups of them: (1) pseudo-static analyses, (2) stress-deformation analysis and (3) permanent-displacement analysis.

The earliest and the simplest group of the methods is the pseudo-static analysis. Terzhagi (1950) is considered as the first author to include seismic shaking as additional static force into the analysed force-body diagram. A normal practice of this analysis includes only the horizontal earthquake component via the pseudo-static coefficient. The vertical component of seismic shaking is not included, as its projection onto the sliding surface is considered to be negligible. The widely accepted drawback of this approach is the simplified consideration of seismic impact which is assumed to be a permanent, unidirectional body force. The uncertainty associated with the selection of an appropriate value of the pseudo-static coefficient is another obvious drawback (Kramer, 1996). Nevertheless, the pseudo-static analyses are still applied by the engineering community.

A certain progress in the single slope stability analysis was reached by Clough (1960) who developed the finite-element method for engineering analysis. It uses a mesh of elements to model the behaviour of a deformable system. The deformation of each node in response to the applied stress could be measured by this method. Soon after the development, this method was widely applied for the modelling of earth dams. A later evolution of these numericalal methods led to the development of the finite-difference, distinct-element, and discrete-element approaches. These modelling tools are integrated into one group called stress-deformation analysis. Its application requires detailed information on the slope setting (topography, geotechnical properties, discontinuity, etc.) - it often becomes the hardest task of this analysis. Due to the overall complexity of the method additional difficulties appear during the model preparation stage and during analysis itself. Therefore, the stress-deformation analysis is only employed in important projects, when the quality of input data can be assured and total investments are justified. At present, there are numerous application examples of this method at local and regional scales (Prevost, 1981; Griffiths and Prevost, 1988; Elgamal et al., 1990; Peng et al., 2009 among others).

Permanent-displacement analysis represents an approach which bridges a gap between simplified pseudo-static analysis and the complicated stress-deformation technique. This approach is the direct focus of our studies: therefore, the next sections describe in detail the original technique as well as the later modifications of this concept adapted to the regional applications.

I.3 Newmark model for a rigid block behaviour

Newmark (1965) is considered to be a founder of the permanent-displacement analysis. His original concept is based on at a simplified model reproducing a rigid block sliding on an inclined plate (Figure BF.2a). The developed approach initially aimed at a stability analysis of dams and embankments using the impacting acceleration time history as key element to predict the co-seismic sliding behaviour.

One of the core points of this approach is the calculation of the critical acceleration value (a_c), the parameter which directly depends on the static Factor of Safety (FS) of the studied slope:

$$a_c = (FS - 1) * g * \sin\alpha, \qquad \text{(BE.1)},$$

where g is the acceleration due to gravity (≈9.81 m/sec^2) and α is the slope angle (see Figure BF.2a).

The traditional stability analysis can be employed to estimate the value of FS. For example, the Janbu (1973) method describing a translational sliding mechanism is often applied as next:

$$FS = \frac{c}{\gamma * t * \sin\alpha} + \frac{\tan\varphi}{\tan\alpha} - \frac{m * \gamma_w * \tan\varphi}{\gamma * \tan\alpha}, \qquad \text{(BE.2)},$$

where c is the cohesion (kPa), φ is the internal friction angle (°), α is the slope angle (°), t is the total layer thickness (m), m is the fraction of the total layer thickness that is saturated by water, γ is the material unit weight (kN/m³), γ_w is the unit weight of the water (kN/m³).

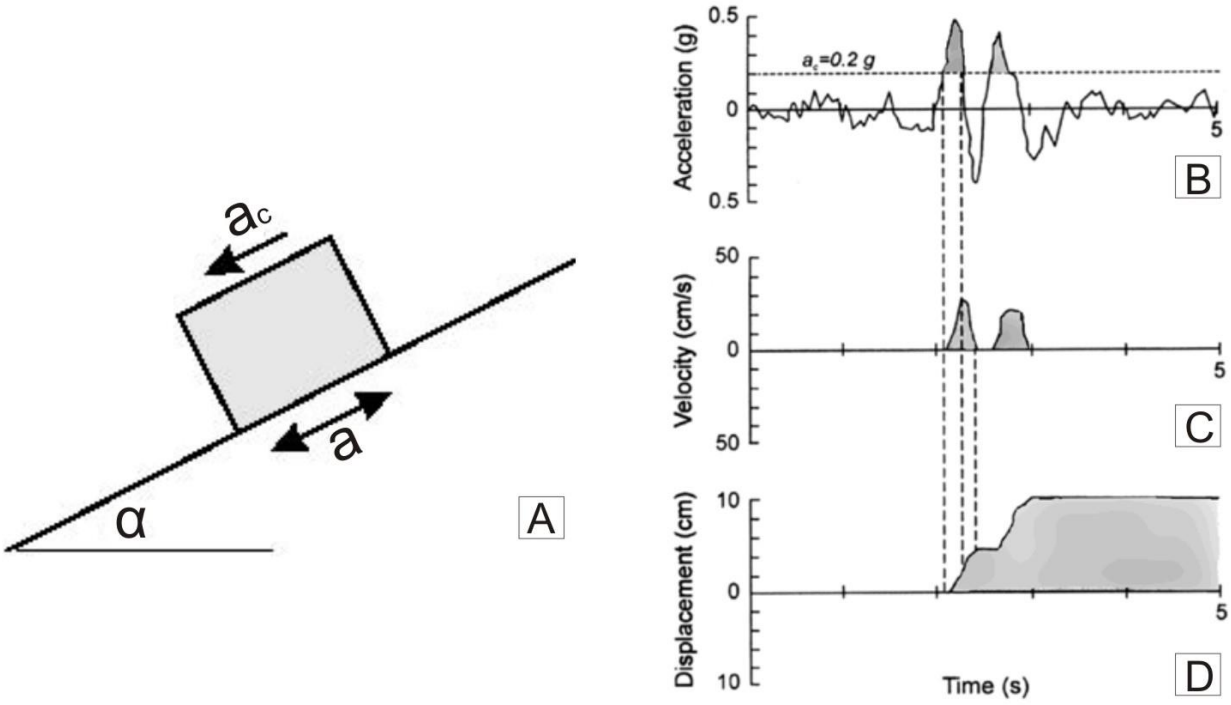

Figure BF.2: (a) Simplified model of a rigid block sliding on an inclined plate, analysed by Newmark (1965); (b) dynamic impact expressed via an acceleration-time history; (c) predicted behaviour of a co-seismic shear velocity; (d) predicted behaviour of a co-seismic shear displacement (by Wilson and Keefer, 1985, modified by Jibson et.al., 1998).

The co-seismic sliding behaviour and the final value of the cumulative displacement, the so-called Newmark displacement (see diagram in Figure BF.2d), are calculated by a double integration of the earthquake acceleration-time history (see diagram in Figure BF.2b). A key moment of this double-integration states that only a part of the acceleration-time history, exceeding the critical acceleration value (a_c in Figure BF.2b), should be subjected to the integration. These principles suggest that the history with peak ground acceleration (PGA) less than value of a_c will not trigger any co-seismic sliding.

The simplified theoretical background of the Newmark analysis relies on the next key assumptions considering:

- the rigid block behaviour neglecting the internal deformations;
- the values of the critical acceleration (a_c) that are not strain dependent and remain unique;
- the upslope displacement that is not possible due to infinitively large upslope resistance;
- that there is no difference between static and dynamic shear resistance of the sliding block;
- that the change of a dynamic pore pressure is negligibly small and not taken into account.

The adopted assumptions limit the application of the proposed technique. The conceptually improved modifications of this method apply the strain-dependent critical acceleration, the dynamic values of FS as well as bi-lateral displacements. The decoupling technique tries to account for an internal deformation taking place during seismic shaking. The most widespread decoupled analysis (Makdisi and Seed, 1978) proposes design charts, where the co-seismic displacement values are functionally related to the slope geometry, earthquake magnitude and the ratio of yield acceleration to peak acceleration.

A rigorous decoupled analysis proposes a stepwise procedure: at first, the dynamic response of the studied slope is analysed, and, then a modified acceleration-time history is employed to estimate the co-seismic displacement behaviour. The fully coupled technique proposes a simultaneous proceeding of these steps. The

dynamic response of the sliding mass and the permanent displacement are modelled together – thus, the effect of the sliding displacement on the ground motions is taken into account.
The rigid block of Newmark (1965) applies a very simple concept which was confirmed by some laboratory tests (Goodman and Seed, 1966; Wartman et al., 2003) and by the studies of the earthquake-induced landslides in natural conditions (Wilson and Keefer, 1983). This concept has been intensively applied to analyse the seismic stability of the artificial embankments at site-specific scale (Wilson and Keefer, 1985). The main reason constraining its application to a local scale is the difficulty to get a regional distribution of the input parameters (A_c, acceleration-time histories), which is a prerequisite of the regional studies. This limitation was overcome by a set of the modified mapping concepts which are deeper analysed below.

I.4 The regional Newmark method

The first modifications of the regional Newmark method have appeared in the middle of 1980s. In particular, Ambraseys and Menu (1988) analysed strong-motion records from several earthquakes and proposed an empirical law to map the Newmark displacement value (D_n) based on a known distribution of the ratio of critical acceleration (A_c) over maximum acceleration (A_{max}):

$$\log D_n = 0.9 + \log((1-\frac{A_c}{A_{\max}})^{2.53}(1-\frac{A_c}{A_{\max}})^{-1.09}) \pm 0.30, \quad \text{(BE.3)},$$

Wilson and Keefer (1985) studied the earthquake-triggered landslides in the vicinity of Los-Angeles, USA. The authors attributed the specific values of critical displacement to every landslide types. It was assumed that predicted displacements exceeding critical values should potentially result in slope failure. For example, coherent slides have a critical displacement value of 10.0 cm, while rock falls have one of 2.0 cm. Thus, the calculation of A_c via FS (Equation BE.1) was replaced by the unique value of A_c: e.g., A_{c10} for coherent slides and A_{c2} for rock falls. The original Newmark (1965) technique represents a destabilising impact of a seismic shaking through the acceleration-time history, while Wilson and Keefer (1985) employed the Arias Intensity (I_a, m/sec) as triggering factor. This parameter was firstly introduced by Arias (1970) and is calculated as next:

$$I_a = \frac{\pi}{2*g} * \int_0^{T_d} [a(t)]^2 dt \quad \text{(BE.4)},$$

where a(t) is a single component acceleration-time history (m/sec^2), T_d is the total duration of the acceleration recording (sec), t is time (sec) and *g* is the acceleration of gravity.
A set of the strong-motion records was analysed to get the unique triggering value of I_a for each landslides type. For example, it was assumed that the coherent landslides/lateral spreads (10.0 cm of critical displacement) are triggered by I_a=0.5 m/sec, while the rock falls/disrupted landslides (2.0 cm of critical displacement) are triggered by I_a=0.15 m/sec.
According to Equation BE.4, the calculation of the I_a values requires the availability of the acceleration-time histories. As it is impossible to get a regional distribution of this parameter, an alternative mapping proxy was proposed based on the next empirically-approved assumptions:

- for a given distance from the seismic source, the logarithm of I_a is a linear function of the earthquake magnitude;
- for a given earthquake magnitude, an inverse square relation between the I_a value and the source distance exists.

These assumptions led to a development of the linear attenuation law, where the value of logI_a was directly related to the earthquake moment magnitude (M) and inversely related to the logarithm of the source-site distance (logR):

$$\log I_a = K_0 + K_M * M - 2 * \log R + K_c * P \quad \text{(BE.5)},$$

where K_0 and K_M are the proportionality constants, K_C is the standard deviation for the I_a values, and P is exceedance probability.

The authors further analysed a dataset for the Los-Angeles area and proposed the next shape of the linear attenuation law for it:

$$\log I_a = -4.1 + M - 2 * \log R + 0.44 * P \qquad \text{(BE.6)},$$

Applying these simplifications the authors mapped the landslide occurrence probability zones for a case of a hypothetical earthquake in one of the fault zones. The developed approach also defined the triggering probability zones for the different landslide types. For example, Figure BF.3 shows the mapping results for the coherent landslides triggered by the hypothetical M=6.5 earthquake.

Figure BF.3: An example of the landslide susceptibility mapping performed by Wilson and Keefer (1985) - the external outline shows the maximum landslide occurrence zone and the inner outlines denotes 50% occurrence probability zone (by Wilson and Keefer, 1985).

Further conceptual progress was reached by Jibson (1993). On the basis of strong-motion records and field data he proposed the following law:

$$\log D_n = 1.460 \log I_a - 6.642 A_c + 1.546 \pm 0.409 \qquad \text{(BE.7)},$$

where D_n (cm) is the value of the co-seismic displacement, I_a (m/sec) is the Arias Intensity value and A_c (m/sec^2) is the critical acceleration value.

According to Jibson (1993) the values of A_c are calculated using Equation BE.1, while the spatial mapping of the FS values is performed by Janbu's method (Equation BE.2). The mapping of the I_a values is empirical, i.e., it is based on analysis of strong-motion recordings in the study area.

This model became a basis for further developments. Several authors proposed the updated forms and introduced certain modifications, including Ambraseys and Srbulov (1995), Crespellani et al. (1996), Miles and Keefer (2000), Del Gaudio et al. (2003), Bray and Travasarou (2007), among others. Jibson (2007) concluded that there are four main, and partially interrelated, factors included in all presented models: Arias intensity, critical acceleration, earthquake magnitude and maximum acceleration or PGA. A model developed by Hsieh and Lee (2007) for Taiwan data presents one example of later modifications:

$$\log D_n = 1.756 \log I_a - 2.780 \log A_c - 2.728 \pm 0.658 \quad \text{(BE.8)}$$

Presently, all models map the values of I_a through the attenuation laws. A general form suggested by Wilson and Keefer (1985) and presented in Equation BE.5 was analysed by several researchers applying strong-motion recordings (Frankel and Wennerberg, 1989; Wald et al., 1990; Harp and Wilson, 1995; Hsieh and Lee, 2007 among others). In the most of the attenuation laws the value of I_a depends only on the earthquake magnitude and epicentral distance. Some laws try to account for more complex inputs. For example, Travasarou et al. (2003) included the average shear-wave velocity in the upper 30 meters (V_{S30}), as one of the affecting parameters:

$$\ln I_a = c_1 + c_2(M-6) + c_3 \ln(\frac{M}{6}) + c_4 \ln(\sqrt{R^2 + h^2}) + c_5 \ln(\frac{V_{S30}}{1130}) + c_6 F_N + c_7 F_R + \eta + \varepsilon \quad \text{(BE.9)},$$

where M is the moment magnitude of an earthquake, R is the closest distance to the rupture plane (rupture distance) for large earthquakes and epicentral distance for others in km, h is a fictitious hypocentral depth (in km) determined by the regression, V_{S30} is the average shear-wave velocity in the upper 30 meters of the soil profile, assuming that the V_{S30} of hard rock is equal to 1130 m/s, F_N and F_R are dummy variables for the fault types (both being 0 for strike-slip faults, 1 and 0 for normal faults, and 0 and 1 for reverse or reverse-oblique faults, respectively; a rake angle of less than 45 degrees or greater than 135 degrees is classified as a strike-slip fault), η is earthquake inter-event errors and ε is intra-event errors.
For example, Lee et al. (2012) applied this equation to develop the attenuation law for Taiwan:

$$\ln I_a = 3.757 - 1.043(M-6) + 18.077 \ln(\frac{M}{6}) - 2.251 \ln(\sqrt{R^2 + 9.56^2}) - 1.042 \ln(\frac{V_{S30}}{1130}) - 0.214 F_N + 0.220 F_R \quad \text{(BE.10)},$$

Equations BE.9 and BE.10 show that the most advanced I_a attenuation laws try to account for the amplification/deamplification effects of surface geology. However, these laws do not consider the influence of other geological or geomorphological settings, i.e., layer dipping, layer thickness etc. Moreover, the existing I_a attenuation laws do not consider the influence of topography. This influence is referred to as the topographic site effects and they depend on a set of morphologic settings, like a slope height, slope width, slope concavity/convexity etc. Meanwhile, some numericalal studies show that the topographic site effects can significantly modify the values of I_a. For example, Peng et al. (2009) demonstrates that I_a values at hilltops are up to 3-4 times larger than the values at the hill toes.
Due to the assumptions adopted by Newmark (1965), any modification of original concept can only be applied to fairly stiff material, coherently moving on a well-defined sliding surface. The field studies of seismically-triggered landslides indicate that 90% of the triggered slope movements, especially the shallow ones, fall inside of this idealized behaviour (Harp et al., 1981; Harp et al., 1996a; Jibson et al., 2006). Nevertheless, there are still a lot of cases, when an actual landslide behaviour is quite different from the predicted one. It means that the predictions provided by the regional Newmark method should be treated as indicative information rather than a precise evaluation of co-seismic slope displacements.
One of the most obvious limitations is related to the assumption of linear or sub-linear attenuation of I_a values with distance. Jibson (2007) recognizes the fact, that the site conditions can significantly affect some of the strong-motion characteristics. Nevertheless, the way to take these effects into account still remains unclear and proposes a big research challenge. Therefore, the sections below are focused on more detailed overview of the issues related to the seismic site effects.

I.5 Seismic site effects

The propagation of seismic energy through the Earth is considered to be a manifold process in classic seismology and engineering seismology (Figure BF.4). The initial parameters of the seismic waves, i.e. signal central frequency, amplitude, shaking duration directly depend on the source settings (e.g., the earthquake magnitude and the length of the crustal disruption). The initiated seismic energy further travels through the Earth crust (path) and already at this stage it is subjected to the modifications referred to as the path effects. They mainly include attenuation and boundary effects (reflection, refraction, scattering, etc.).

When the waves finally arrive at the earth surface (site) they are again subjected to the alterations which are directly related to the site settings. These surface effects are called site effects that are depending on the local geology and topography. In this respect the site effects denote the modifications of the arriving seismic signal imposed by the topographic and geological site settings. The site effects normally modify the frequency content of incoming seismic waves, amplify/deamplify PGA, alter the signal duration and induce other related impacts.

A well-adopted practice of the instrumental studies of the site effects requires an installation of, at least, two seismic stations. One station, the reference one, is installed in a place which is likely not affected by the site effects. Therefore, the reference station is often installed within a flat area on bedrock outcrop, sometimes also in a boreholes. The other seismic station/stations are installed in an area of interest, e.g., near in the crest of a hill/mountain or within a sedimentary basin. This configuration of recording network tends to separate the site effect from other effects mentioned above, as recordings at all stations are equally subjected to source and path effects. The sections below present some examples of the instrumental studies and provide a more detailed overview of the geological and topographic site effects.

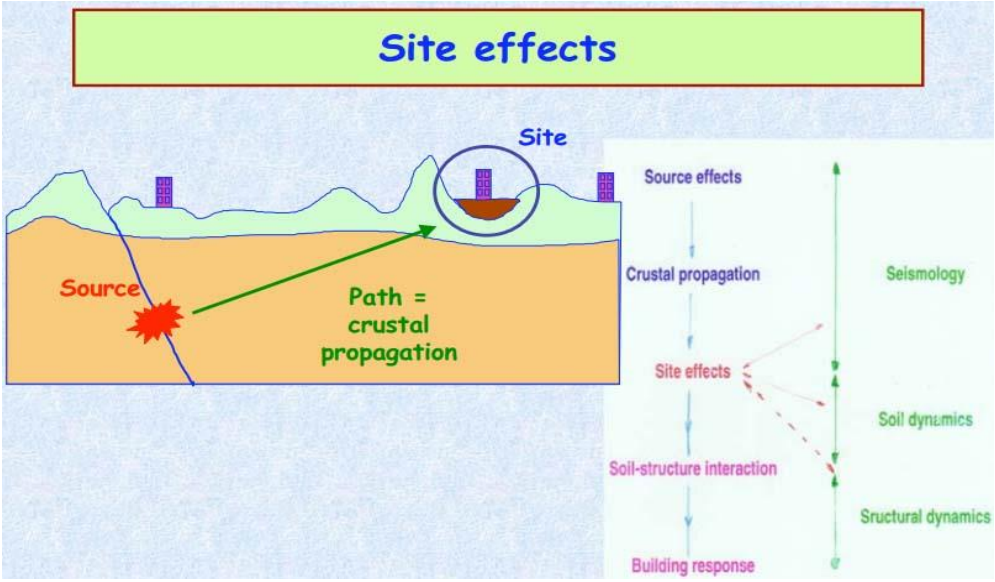

Figure BF.4: A draft of a main concept of the seismic wave propagation and signal modification effects (by Bard, 2007).

I.6 Geological site effects

The seismic energy entering the near-surface geological medium is subjected to reflection, refraction, scattering and other related impacts occurring at the contacts of changing geotechnical/dynamic properties, e.g., density, seismic wave velocity, etc. The geological site effects are directly depending on these processes occurring at the contrast boundaries. For example, loose sediments are generally marked by lower shear-wave velocity values than the underlying hard bedrock; this difference is often referred to as the V_s impedance contrast. Due to this contrast the shear waves can easily travel from the hard rocks to the loose sediments, while in the opposite direction they are reflected/refracted back into the loose rocks. It finally favours the entrapment of the seismic energy within the domain with lower values of V_s and results in much longer duration of the seismic shaking.

The geological site effects can also amplify/deamplify the peak ground motion characteristics, i.e. peak ground acceleration (PGA), peak ground velocity (PGV) and peak ground displacement (PGD). Thus, the same loose rocks are normally characterized by the amplified PGA values compared to the bedrock outcrops. It is often referred to as the main aspect of the geological amplification effects and from the engineering point of view it has the highest damaging potential. The PGA amplification in this case is explained through the energy conservation law. Geiger and Gutenberg (1912) state that the energy of the seismic wave (E) is directly proportional to the seismic wave velocity (C) and the square of the wave's amplitude or PGA (A):

$$E \sim CA^2 \qquad \text{(BE.11)}.$$

If the seismic wave comes from a high velocity medium into a low velocity one without significant energy losses (reflection, refraction, heating, etc. are negligible), the reduction of the seismic velocity (C) should be compensated by the increment of the wave amplitude (A). According to Equation BE.11 this increment of the A value is inversely proportional to the reduction of the square root of the C value.

The spectral deamplification/amplification is another aspect of the geological site effects. Here, again, the sedimentary basin represents the best example. Several authors studied these patterns of spectral amplification through the numerical analysis and instrumental experiments. The numericalal studies of the 1D soft layer model show that the layered half-space is marked by the amplification at specific frequencies which are also referred to as the natural resonance frequencies of this layer (Aki and Larner, 1970; Borcherdt, 1970). Nevertheless, the 1D model fails to address the total complexity of the spectral amplification processes. The studies in 2D and 3D domains show that the really observed amplification patterns are strongly impacted by the lateral heterogeneities and the underground basin geometry (Bard and Bouchon, 1980; Graves, 1993; Steidl et al., 1996; Riepl, 1997; Faccioli, 2000; Semblat et al., 2002; Seriani et al., 2002). For example, Graves (1993) shows that a significant amplification impact originates from the waves refracted or reflected at the basin rims or near the inclined contacts. Due to that, the spectral amplification and its connection with site geological and structural settings are considered to be very complicated issues. Their study often demands site-specific analyses which should combine numerical modelling with on-site instrumental experiments.

Celebi et al. (1987) presents a very comprehensive study demonstrating the importance of geological site effects on the basis of four instrumental records of the M=8.1 Michoacan, Mexico earthquake in 1985 (see Figure BF.5). Those acceleration histories show that the highest PGA values were recorded at the most distant SCT station situated in the vicinity of the Mexico City. The sedimentary basin strongly amplified PGA values and enlarged the duration of seismic shaking in the SCT station (compare the shaking characteristics at all stations). The significance of amplification becomes obvious when comparing the SCT record with the one at UNAM station, situated at 20 km far from the SCT station, at the rim of the basin; the UNAM acceleration history is characterized by much lower values of PGA and, at least, 2 times shorter shaking duration. Thus, according to Murillo and Manuel (1995), the geological effects are the key factors responsible for the distribution of the earthquake-induced damage observed in Mexico City. These effects resulted in, at least, 10,000 fatalities and incurred significant damage to the Greater Mexico City area.

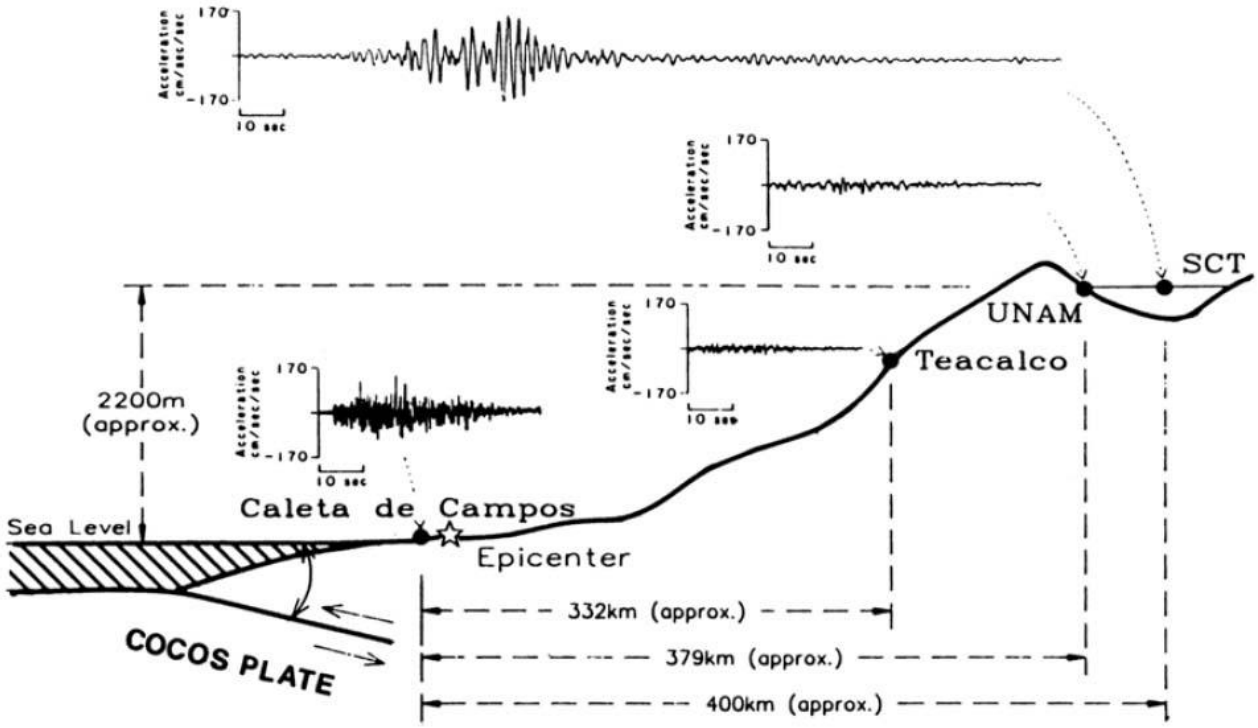

Figure BF.5: The recordings of the M=8.1 Michoacan earthquake, Mexico in 1985 - station SCT is situated inside the Mexico basin (by Celebi et al., 1987).

Jongmans and Campillo (1993) show similar amplification patterns based on the instrumental survey in the Ubaye Valley, France. They show that all seismic recordings over the sedimentary basin experience a certain grade of amplification in comparison with the reference station, situated on the bedrock. The amplification effect results in a longer duration of a seismic shaking and the higher values of PGA. The most pronounced amplification is revealed in the stations situated over the thicker sediments.
A distribution of the earthquake-induced damage can also be related to the spectral amplification patterns. For example, Jongmans (1989) studied the M=4.9 Liege earthquake in 1983 and revealed a higher grade of the infrastructural damage in sites where the internal period of the buildings was very close to the internal periods of the underlying sediments/geological structures.

I.7 Topographic site effects

The patterns of topographic site effects were most probably identified well before those of the geological amplification effects. For example, Barlow (1933) already cited the words of Charles Darwin (1809-1882) who described some patterns of hilltop amplification that occurred during the Chilean earthquake in 1835. The earliest documented observations are dated back to the beginning of the 20th century, when the distribution of the seismic damage in the Rognes earthquake, France in 1909 was directly correlated with the proximity to the crest of the hill (see Figure BF.6 - Bard, 2007).

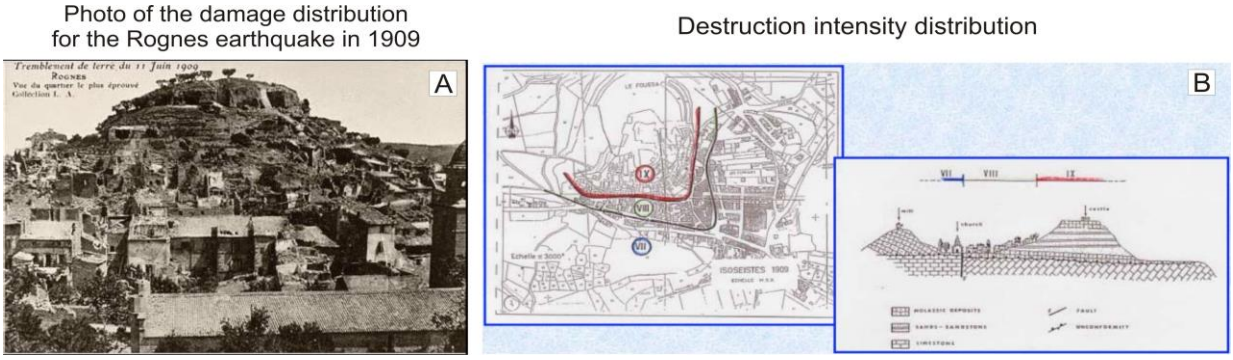

Figure BF.6: (a) Photograph showing the damage distribution caused by the Rognes earthquake in 1909 showing a more intense destruction close to the crest of the hill; (b) sketch of the seismic intensity distribution indicating higher level of destruction in the topographically high areas (by Bard, 2007).

Many other, more recent, studies confirm that constructions situated on the crest or in the higher parts of hills/mountains often experience more severe destruction. For instance, the damage distribution study for the Kozani-Greneva (Greece) earthquake in 1995 revealed more destruction in the upper parts of the Egion Town due to the topographic amplification effects (Athanasopoulos et al., 1999). Other experimental examples include observations from the 1971 San Fernando earthquake (Boore, 1972), the 1983 Coalinga earthquake (Celebi, 1991), the 1985 Chile earthquake (Celebi, 1987), the 1987 Superstition Hills earthquake (Celebi, 1991) and the 1994 Northridge earthquake (Ashford and Sitar, 1994). All these studies conclude that topography can play a very important role in the site amplification phenomenon and may contribute to a larger damage.
There are some spectacular examples of instrumental recordings highlighting the importance of topography with respect to the general site amplification. Spudich et al. (1996) present the aftershock recordings for the M = 6.7 Northridge, California earthquake in 1994 (Figure BF.7). The measurements were performed along two seismic arrays crossing the 20 m high Tarzana Hill in sub-perpendicular directions (see a topographic map in Figure BF.7a). Figure BF.7b demonstrated that the highest values of PGA and the longest seismic shaking could be found at the stations situated close to the crest of the hill (see recordings for W02, W01, C00 and S01). Meanwhile, the authors note that these recordings demonstrate unusually high values of PGA comparing to the surroundings. Bouchon and Barker (1996) concluded that these extremely high values of PGA can be referred to as the geological site effects. Rial (1996) suggests that this hill represents an old landslide reactivated during this seismic event which finally resulted in the high acceleration records. Nevertheless, a common opinion of all studies states that a role of topography is still well expressed in these recordings.

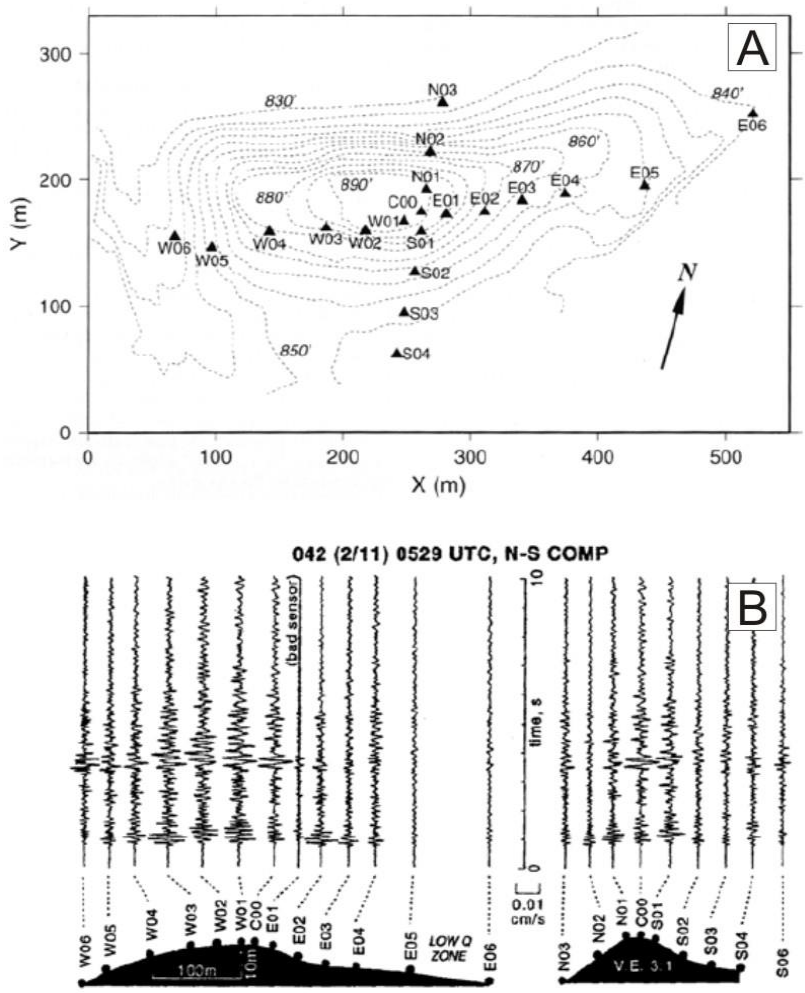

Figure BF.7: (a) Topographic map of the studied Tarzana Hill with a position of the seismic stations; (b) N-S component seismograms of an aftershock for the M = 6.7 Northridge, California earthquake in 1994 recorded at all stations (by Bouchon and Barker, 1996; Spudich et al., 1996).

According to Bard (1995), the origin of the topographic amplification effects is principally related to a focusing of the reflected waves below the ridge-crest morphologies. In this matter, a hill surface behaves like a surface of a curved mirror, which focuses optic radiation at certain areas. Differently from mirrors, which normally have almost ideal parameters (regular shape and smooth surface), the natural topographic features (hills, mountains, crests, etc.) are more irregular. The asymmetry of the hill/mountain and the surface roughness (concavity/convexity of different scale) cause overlying patterns of the reflected/refracted waves. These patterns strongly complicate the final distribution of the amplification parameters.

Starting from the 1970s, the studies of topographic site effects were conducted through the numericalal reconstruction of the amplification process. Boore (1972) provided one of the first numericalal studies applying the finite-difference method. Other numericalal analyses of the topographic site effects used finite elements (e.g., Smith, 1975), boundary elements (e.g., Sanchez- Sesma et al., 1982) and discrete wavenumber methods (e.g., Bard, 1982). All these studies analysed an isolated two-dimensional ridge and yielded consistent results: (1) PGA amplification with a factor generally less than 2 near the crest, with maximum spectral amplification for a wavelength roughly equal to the ridge width, and (2) PGA attenuation at the mountain base for the wavelengths larger than the mountain width, while other frequency ranges can experience alteration of the amplification/attenuation effects due to interaction between the primary/reflected/refracted seismic waves (Geli et al., 1988).

However, most of the numericalal studies of an isolated mountain considerably underestimated recorded PGA amplification, which often ranges from 2 to 10, with extreme values up to 30 (Ashford et al., 1997). For that reason, Geli et al. (1988) analysed a more complicated site configuration, combining a layered profile and topographic features. The authors highlighted the complex distribution of the amplification/attenuation

pattern over the hill sides, especially in the upper parts of the hill. These studies also showed that higher PGA values can be related to the neighbouring ridge effect coupled with an effect of the underground geology.

I.8 Combined topographic and geological site effects

The natural conditions often involve a complex combination of prominent topographic features (mountains, canyons, hills, basins, etc.) and different structural-geological elements (faults, folds, underlying bedrock, dipping layers, etc.). These site settings directly affect on the seismic site effects due to a complex interaction between amplification patterns imposed by the topography and the underground geology.
The numericalal reconstructions coupled with the field measurements showed that a separate consideration of the topographic input often fails to reproduce a reality. For example, as it is mentioned above, the study of the Tarzana Hill revealed unusually high values of PGA (see Figure BF.7). These amplification patterns could not be explained through numericalal modelling of the pure topographic effects. Additional numericalal studies concluded that a misfit between the modelled and the observed parameters can only be explained by the complex interaction of the topography and underlying geology (Bouchon and Barker, 1996; Rial, 1996).
Figure BF.8 presents the instrumental recordings performed by Pederson et al. (1999). Five seismic stations were installed in the surrounding of Mont St. Eynard, Grenoble, France and performed the recording of the velocity-time histories. These recordings demonstrate that the highest PGV values and the longest duration of seismic shaking can be found at the stations situated over the thick sediments in the NW part of profile, especially at the station S5. Comparatively thin sediments in the SE part of profile also induce site amplification (compare the PGV values and shaking duration at the S1 and S2 stations). These recordings show that the geological site effects are much more important than the topographic amplification which can be found at stations S2 and S3.

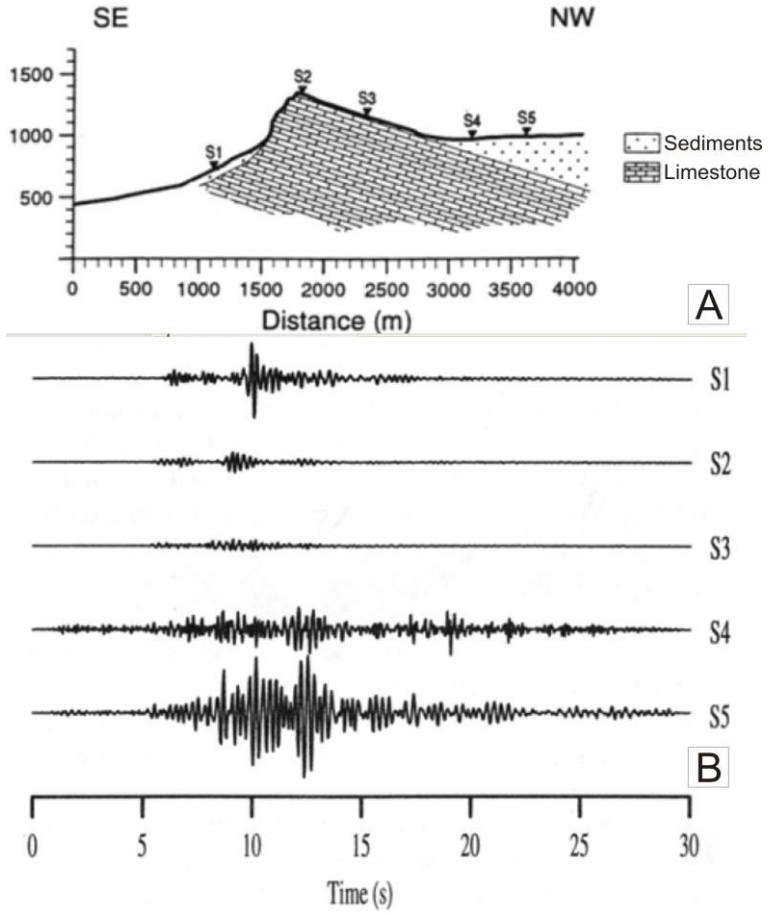

Figure BF.8: (a) Schematic geological cross-section of the Mont St. Eynard, Grenoble, France with an indication of installed seismic stations; (b) velocity-time histories recorded at five stations (by Pedersen et al., 1994).

A comparison of the spectral amplification patterns is carried out by Le Brun et al. (1999) based on the instrumental recordings on a limestone ridge close to Kitherion, Corinth. The largest spectral amplification at the top of the ridge was observed at 2.5 Hz. The spectral amplification at 0.7 Hz was 5 times less than at 2.5 Hz. The authors relate the low frequency peak (0.7 Hz) to the topographic fundamental frequency, while the 2.5 Hz peak is attributed to the geological site effects. This study shows that, like for the PGA amplification, the geological site effects have a much more important influence on the spectral amplification than the pure topographic effects.

Several researches applied numerical studies to compare the pure topographic effects with the combined effects of geology/topography (Sanchez-Sesma and Campillo, 1993; Athanasopoulos et al., 1999; Anderson et al., 2006 among others). Bourdeau and Havenith (2008) numericalally studied a landslide-prone slope in Kyrgyzstan and confirmed the findings of the instrumental recordings: pure topographic effects were considerably smaller than the combined topographic-geological effects. For the input signal with a central frequency of 1.0 Hz the combined spectral amplification effects at the crest of the slope were more than four times larger than the pure topographic ones. The authors note that the combined site effects can not be easily decoupled into the pure geological and pure topographic inputs. Nevertheless, a decoupling procedure is recommended by some of the seismic design codes (e.g., Eurocode 8); therefore, the validity of the decoupling technique still remains unclear.

The conceptual framework of the seismic site effects is developed through numerous instrumental experiments and numericalal studies. It is soundly confirmed that the geological site effects often produce much more intense amplification compared to the topographic effects. Nevertheless, the combined influence of geology and topography on seismic shaking still requires further analyses. The performed studies have demonstrated that those combined effects are very sensitive to the site-specific conditions, which strongly limits a rule generalization.

However, generalized rules are needed in several applied domains, especially for a planning and construction in the seismically active regions. Landslide-related studies also require a deeper understanding of the site effects, as a triggering potential of amplified seismic shaking is proved by many field studies. The role of seismic site effects in the initiation of slope failures and the possible ways to improve existing mapping methodologies are deeply analysed below.

I.9 Site effects and the landslide-related studies

Several authors reported on the significance of site effects in the triggering of slope failures during seismic shaking (Seed, 1968; Cotecchia et al., 1986; Hansen and Franks, 1991; Del Gaudio et al, 2000 among others). For instance, Harp and Jibson (1996b) compared two intense seismic events affecting the same study area in California (USA) in 1971 and 1994. They revealed a similarity in the concentration of the triggered slope failures. Thus, the area of the Pacoima Canyon had the highest concentration of the triggered rock falls that resulted from both earthquakes. The studies conclude that it was due to the topographic amplification effects in this area. The instrumental recordings have shown that those site effects result in larger values of PGA compared to the surroundings.

Observation of landslides triggered by the M=7.9 Wenchuan (China) earthquake in 2008 also highlight the role of topographic site effects. Yin et al. (2009) indicate that a significant part out of the 60,000 triggered slope movements were situated close to mountain ridges and peaks which were most likely affected by topographically amplified shaking. This assumption was confirmed by earthquake recordings clearly showing some deamplification patterns at the base of the mountains, while higher areas experienced stronger shaking.

The studies of the M=8.5 Gansu, China earthquake in 1920 have also indicated that a majority of the triggered landslides were situated in sites that had experienced topographic amplification of the seismic shaking (Zhang and Wang, 2007). The authors note that more than 80% of the triggered landslides were situated on the convex slopes that are the most susceptible to topographic amplification.

Thus, the field observations show that the site effects have profound impacts on the initiation of slope failures. Due to that, the single slope stability analyses (see the classification of methods in *Sub-section B.I.2*) attempt to account for these impacts. In the simplest pseudo-static method the site amplification effects are accounted in the value of the pseudo-static coefficient. Nevertheless, these coefficient values are selected empirically which is often limit the final reliability of this method.

The stress-deformation analysis proposes more possibilities in this case. More complex models can be applied to analyse the combined topographic and geological amplification effects. In general, these

approaches propose a site-specific solution, but the right combination of the model settings can provide a good option for a rule generalization. For example, a series of numericalal studies aimed at the analysis of the seismic wave's behaviour inside unstable slopes (Martino and Mugnozza, 2005; Sepulveda et al., 2005; Del Gaudio and Wasowski, 2007; Bourdeau and Havenith, 2008; Bozzano et al., 2008; Bozzano et al., 2011). These studies describe both the landslide mechanism and the triggering conditions, when the seismic input parameters (seismic energy, frequency content, directivity, PGA, etc.) are taken into account. Nevertheless, most of the studies are still site-specific and focus on the selected issues of the amplification processes. The whole concept of the site effects and their triggering potential is still a challenge for future studies.

The permanent displacement analysis proposes alternative solutions to study the influence of site effects. The original concept proposed by Newmark (1965) does not take into account any site effects due to its simplicity and, especially, due to the assumed block rigidity. The later modifications of this concept (coupled/decoupled approaches) try to consider the dynamic response of the studied slope, i.e., the site amplification effects.

The decoupled analysis applies a stepwise procedure, when a modified acceleration-time history is employed for an estimation of the co-seismic displacement following the original Newmark (1965) procedure (Seed and Martin, 1966; Makdisi and Seed, 1978; Lin and Whitman, 1983; Bray and Travasarou, 2007 among others). The most widespread approach (Makdisi and Seed, 1978) proposes a set of the design charts, where the co-seismic displacement is a function of slope geometry, earthquake magnitude, and the ratio of yield acceleration to peak acceleration. The studies of the seismically triggered landslides have demonstrated several cases when the decoupled analysis accurately predicted the actual field behaviour (Pradel et al., 2005).

The fully coupled analysis applies simultaneous modelling of the dynamic response and the co-seismic displacements (Lin and Whitman, 1983; Rathje and Bray, 2000, Bray and Travasarou, 2007 among others). This method is more sophisticated and computationally intensive compared to the decoupled approach. It often needs more input parameters, like, for example, the shear-wave velocities of the materials above and below the sliding surface, the damping ratio and the thickness of the potential landslide.

The increasing computation capacities favour a wider expansion of the fully coupled analysis. In comparison with the decoupled approach it yields the best results because it accounts for more problem complexities (Jibson, 2011). But, still, there are the conditions when the decoupled and rigid-block analyses can yield quite reliable estimates. Rathje and Bray (2000) propose the general guidelines for a selection between the rigid-block or plastic-block (decoupled/coupled) behaviours. The procedure involves the calculation of the period ratio, T_s/T_m, where T_s is the fundamental site period, and T_m is the mean period of the earthquake motion. The value of T_s (sec) is proposed to be calculated next:

$$T_S = \frac{4 * H}{V_S} \qquad \text{(B.12)},$$

where H is the maximum landslide thickness (m), and V_S is the shear wave velocity inside of the landslide body (m/sec). These two parameters, H and V_S, can be determined, for example, through surface waves analyses based on ambient noise recordings and/or seismic profiles (see, e.g., Danneels et al., 2008; Torgoev et al., 2013b).

The mean spectral period of an earthquake motion, i.e. T_m (sec), is defined as an average value weighted by the Fourier amplitude coefficients over a frequency range of 0.25-20 Hz (Rathje, et al. 1998). Rathje et al. (2004) analysed data from North America and proposed a model estimating the mean period (T_m, sec) for shallow crustal earthquakes and rock site conditions as a function of earthquake moment magnitude (M_w) and source distance (r, km):

$$\ln(T_m) = -1.00 + 0.18 * (M_W - 6) + 0.0038 * r \qquad \text{for } M_W \leq 7.25 \qquad \text{(BE.13a)},$$

$$\ln(T_m) = -0.775 + 0.0038 * r \qquad \text{for } M_W \leq 7.25 \qquad \text{(BE.13b)},$$

Figure BF.9 presents the guidelines to compare the rigid-block analysis versus the decoupled one applying the ratio of these period values, i.e. T_s/T_m. These guidelines suggest that the fully coupled approach always provides good results, but the availability of this approach is often problematic, therefore, it is considered as

a limited option. Following the guidelines, it is recommended to apply the rigid-block analysis for the thin stiff landslides having a period ratio of 0.1 or less. Between 0.1 and 1, the rigid-block analysis yields non-conservative results and should not be used, while the decoupled analysis presents conservative to very conservative results in this range. For the period ratios between 1 and 2, the rigid-block analysis gives conservative predictions, while the results of the decoupled and coupled analysis are close to each other. For the period ratios greater than 2, rigid-block analysis tends significantly overestimate displacements. The decoupled analysis can be either conservative or non-conservative in this range of period ratio - therefore, only the coupled analysis should be applied in this range.

Slide type	T_s/T_m	Rigid-block analysis	Decoupled analysis
Stiffer, thinner slides	0 – 0.1	Best results	Good results
↓	0.1 – 1.0	Unconservative	Conservative to very conservative
↓			
Softer, thicker slides	1.0 – 2.0	Conservative	Conservative
	> 2.0	Very conservative	Conservative to unconservative

T_s is the site period

T_m is the mean period of the earthquake shaking

Figure BF.9: The guidelines for the selection of the appropriate sliding-block analyses (by Rathje and Bray, 2000; modified by Jibson, 2011).

The guidelines, presented in Figure BF.9, indicate that the rigid-block behaviour can only be reliably applied at $T_s/T_m \leq 0.1$, i.e. when a site (i.e., landslide) resonance frequency is at least ten times more than the central frequency of the impacting seismic shaking. Such kind of conditions are often met in the shallow and stiff landslides, mainly small scale rock falls and earthflows that are situated at a certain distance from the earthquake epicenter. For the mid- and large-scale slope movements the corresponding period ratio is often more than 0.1. Therefore, an application of the rigid-block analysis in this case is often limited. The period ratio may even approach the value of 1.0 for the large-scale landslides at a significant distance from the earthquake epicenter. In this later case the dynamic response of the landslide becomes a mandatory factor of analysis.

As it is described in *Section B.I.3*, the original Newmark method is only based on the rigid-block sliding mechanism. Moreover, the regional approaches do not directly use this original technique developed by Newmark (1965). These methods introduce additional simplifications to adapt the original concept to a regional application. The linear or sub-linear I_a attenuation laws present the example of such simplifications. As it is shown in *Section B.I.4*, the most sophisticated I_a attenuation laws try to account for the geological site effects through the average shear-wave velocity in the upper 30 meters (Travasarou et al., 2003; Lee et al., 2012). Nevertheless, it is clear that these advanced laws can propose only partial solution as the topographic and the mixed topographic-geological site effects are not accounted for by any existing laws. This limitation poses a significant research challenge, as possible solutions should bridge the gaps between different research areas: from numericalal modelling to GIS, and from engineering geology or seismology to the regional landslide mapping. An attempt, at least partial, to bridge these research gaps is presented in the following part of the thesis.

II. 2D dynamic numerical modelling: methodology

II.1 Methodology and applied software

The previous chapter discussed the issues related to the seismic triggering of slope failures and reviewed the methods to study the seismic slope stability. The main focus was put on the regional Newmark method which predicts seismically-induced landslide susceptibility based on the calculated values of the co-seismic shear displacement. These values of displacement are estimated applying a set of regional predictors which include the Arias Intensity (I_a). This last parameter is mapped through the I_a attenuation laws where its value mainly depends on the earthquake magnitude and epicentral distance. Those laws do not account for the amplification/deamplification impacts of the geological and topographic site effects. This strongly constraints the final reliability of the model predictions.
In order to propose some conceptual improvements we apply the 2D dynamic studies to six long profiles with real topographic and geological settings. The impacts of the topographic and combined topographic-geological site effects are analysed through the observed amplification/deamplification of the I_a values. The results of studies outline the relationships which can later be applied in the regional Newmark method to predict the I_a amplification factors. The patterns of topographic site effects are also analysed by the 3D dynamic studies and these results allow us to develop a proxy for a spatial mapping of the topographic amplification factors (see more details in *Chapter B.VI*). The proposed solutions should potentially improve the existing Newmark method and make it more reliable for the mapping of the earthquake-induced landslide susceptibility.
The 2D numericalal studies are performed with the Universal Distinct Element Code (UDEC, version 4.01) developed by the ITASCA engineering company. This code simulates the response of the discontinuous media (e.g., jointed rock mass) subjected to either static or dynamic loading (Itasca, 2006). The modelled media is represented by an assemblage of the blocks separated by the joints or contacts with a possibility of large shear displacements along these contacts. The blocks themselves can be either rigid or deformable and are filled by the finite-difference (FD) zones. During modelling these zones behave according to prescribed linear or non-linear stress-strain laws. The relative motion of the blocks is also determined by the force-displacement relationships in both normal and shear directions. The recordings of different dynamic parameters, e.g., acceleration, velocity or displacement, can be performed in any part of the studied medium. Due to these capabilities, the UDEC code is considered as a very powerful tool for a wide range of engineering and scientific domains, including the stability analysis, underground mining, earthquake engineering, hydrogeology (especially in studying the fractured soils or rocks), etc.

II.2 Modelled profiles

The 2D dynamic studies are focused both on topographic and geological site effects. Therefore, two types of models are analysed here. The first type applies a combination of real topography with unique underground material and analyses the pure topographic site effects. The second type of constructed models includes the geological layers and surface topography to model the combined topographic-geological site effects.
Figure BF.10a presents the geological map of the Mailuu-Suu target area together with a position of six studied profiles. The set of the models with real topographic-geological settings constructed for these six profiles is shown in Figure BF.10b (see more details on modelled material sequence and properties in *Section B.II.5*). The total length of the studied profiles is 22.76 km. As two types of models are constructed for each profile (i.e., 6 profiles=12 models), the total length of constructed models is 45.52 km. The average depth of the models is around 400-500 m and 372 receivers are spread along the surface of 12 models to provide the dynamic recordings.
Profiles 1, 2 and 3 are designed to study some expressive structural features in the study area. The longest Profile 1 (the length = 5.73 km; see a model in Figure BF.10b) reproduces a fold axis with the sedimentary basins at the both ends of profile. Profile 2 (the length = 4.60 km) is used to analyse the effects of the almost horizontal layering of the comparatively hard sedimentary rocks. The important feature of the sedimentary basin is reproduced by Profile 3 (the length = 4.53 km).
Profiles 4, 5 and 6 cross some of the landslides in the target area which are believed to be re-/activated due to seismic shaking (Torgoev Isakbek, 2013 – oral communication). Thus, Profile 4 (the length = 4.60 km) passes through the Koytash landslide which is one of the biggest events presented in the target area. Profile 5

(the length = 2.70 km) crosses the large Tektonik landslide and Profile 6 (the length = 2.20 km) passes through a smaller landslide situated at the flank of the anticline. As it can be seen, the profiles attributed to the landslides are significantly extended at both ends. This extension diminishes the boundary effects negatively impacting the analysed recordings (see more details in *Sub-section B.II.6*). The extension of the profiles also allows us to identify the site effects due to the larger topographic and geological features.

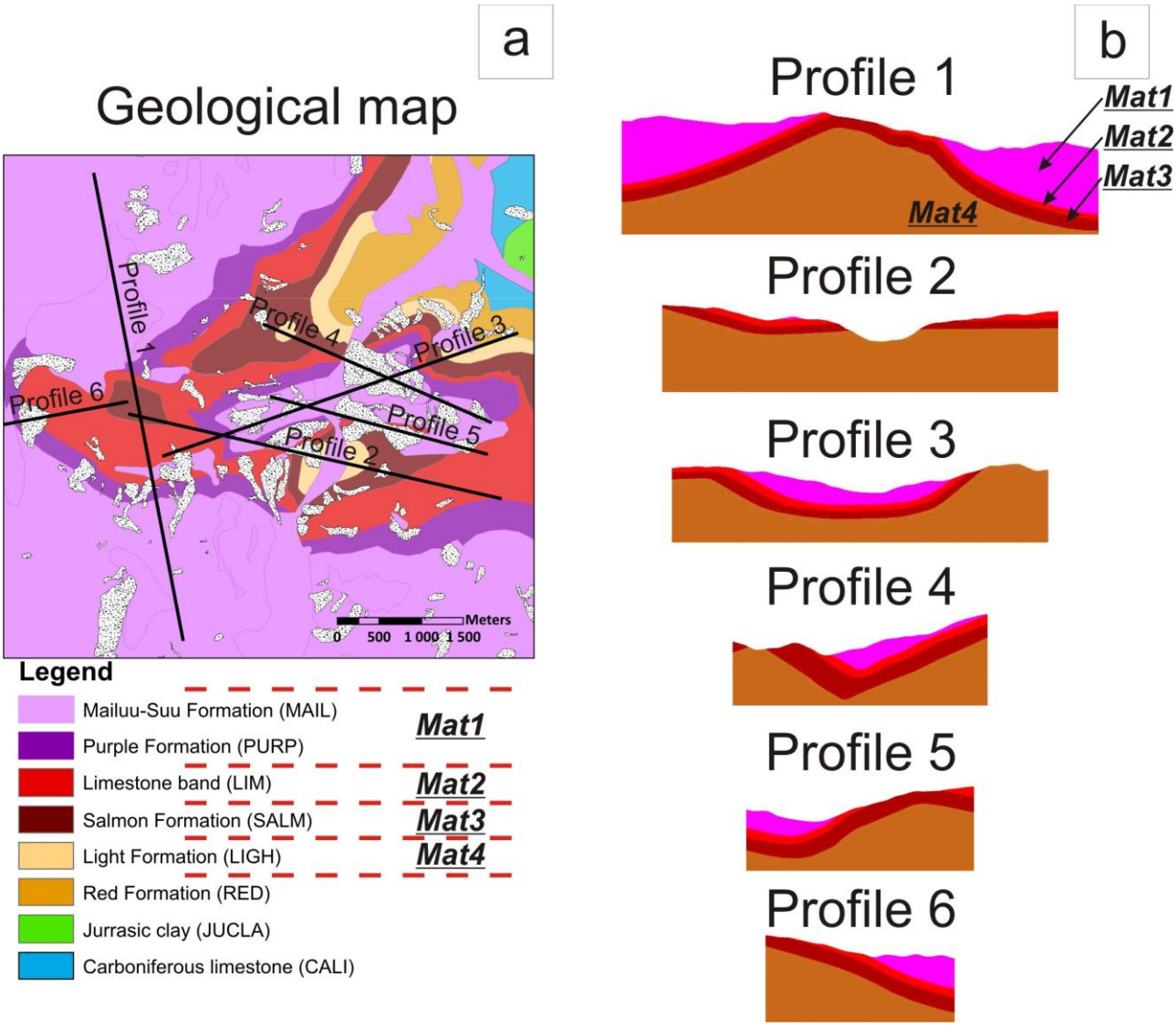

Figure BF.10: (a) Geological map of the target area with a position of modelled profiles and the 2007 landslides presented by dotted outlines (by de Marneffe, 2010; modified); (b) models with combined topographic-geological settings constructed for the studied profiles (see the legend of the geological map for the applied material types).

II.3 Model geometry

The starting point of our analyses is referred to as the model extraction step. Here, the geometry of the model (surface, lateral boundaries and inner structure) is determined. The surface of all models is reconstructed applying the 2010 SPOT DEM (see *Sub-section A.IV.1.1*). First, all studied profiles are spatially overlaid over this DEM applying the ArcGIS code. Then, the elevation values are sampled every 21 m along these profiles. Following this sampling, some elevation values are manually corrected to reconstruct the smoothness of model surface. This manual correction is needed due to artificial holes/spikes which input SPOT DEM inherited from the automated DEM extraction.

As it is previously indicated, there are two types of models constructed for each of six studied profiles. The first type of models aims at the pure topographic site effects and, therefore, includes a unique underground

material. The second type of models is designed to analyse the combined topographic-geological site effects and is made of different materials (see examples in Figure BF.10b). In this later case the underground model geometry is restored based on the digital geological map and the 3D geological model presented by de Marneffe (2010). Figure BF.11 presents this geological map and shows the extent of the 3D geological model which covers the central part of the study area. To construct these products the author incorporated several sources of historical information, especially those originating from former uranium mining. These data included the geological cross-sections, boreholes description, geophysical data, etc. An extensive field work allowed him to detail the position of the contacts and provided precise information on the structural settings (dipping/strike) of the geological layers.

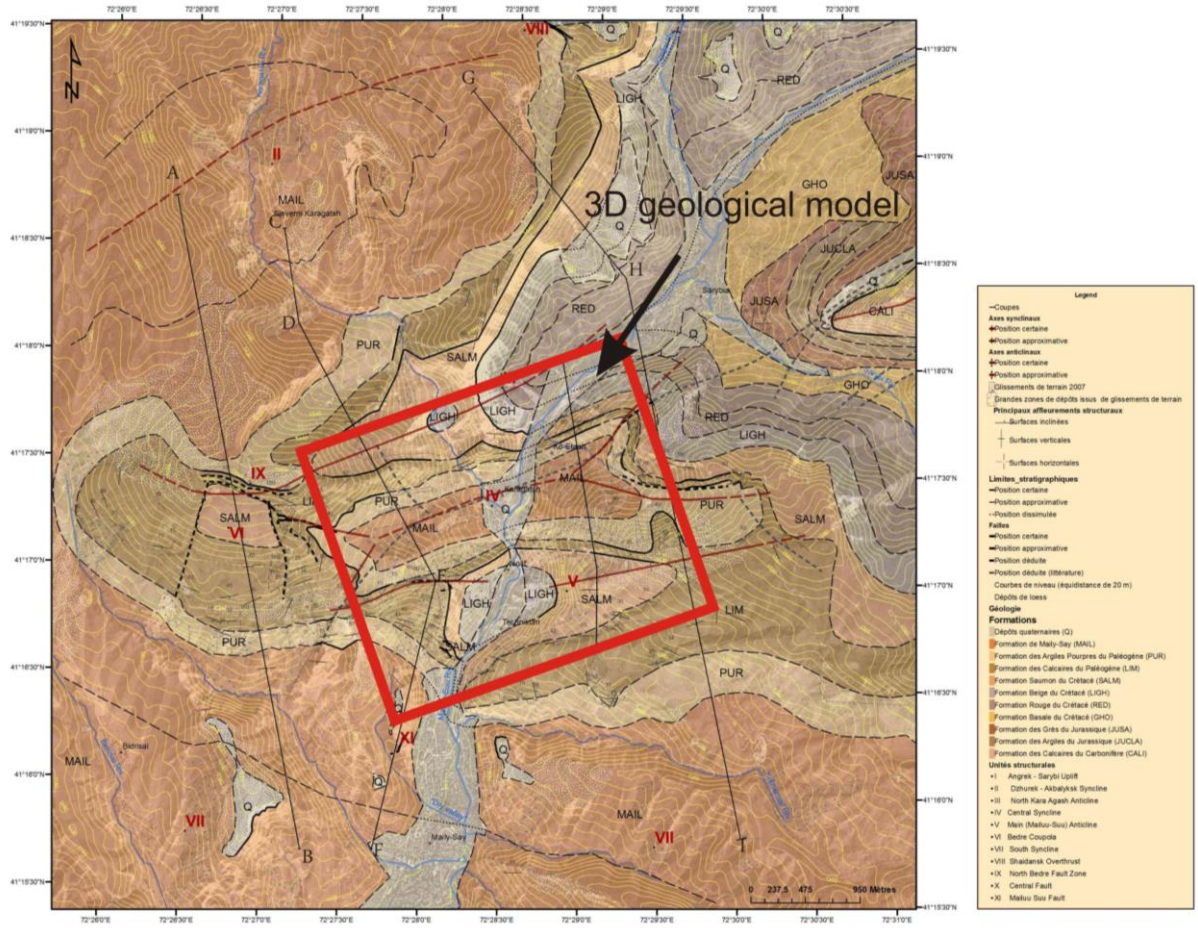

Figure BF.11: Geological map of the target area with indicated limits of the 3D geological model (by de Marneffe, 2010; modified).

The 3D geological model was produced with the GOCAD software (Paradigm Epos). The structural information, such as the contact location, the layer thickness and dipping are extracted from this model. This information is further applied by us to reconstruct the central parts of the topographic-geological models for Profiles 2, 3, 4 and 5. In places where the 3D geological model is missing (e.g., Profile 1 and 6), the structural data are inferred from the geological map and the field data presented by de Marneffe (2010).

For example, Figures BF.12 and BF.13 show the 3D geological data which are used to construct the topographic-geological model for Profile 4 (see this model in Figure BF.10b). According to Figure BF.10a, this profile is attributed to the Koytash landslide. The sample views to the 3D geological model with the cross-sections passing through this landslide are presented in Figure BF.12. As it can be seen, the electrical tomography data is partially applied here to interpret the layer dipping. The other structural settings are interpreted through the field data and the geological map showing the position of the geological layers. The final variant of the interpreted 3D layer geometry is presented in Figure BF.13. This data are finally applied to reconstruct the numerical model of Profile 4.

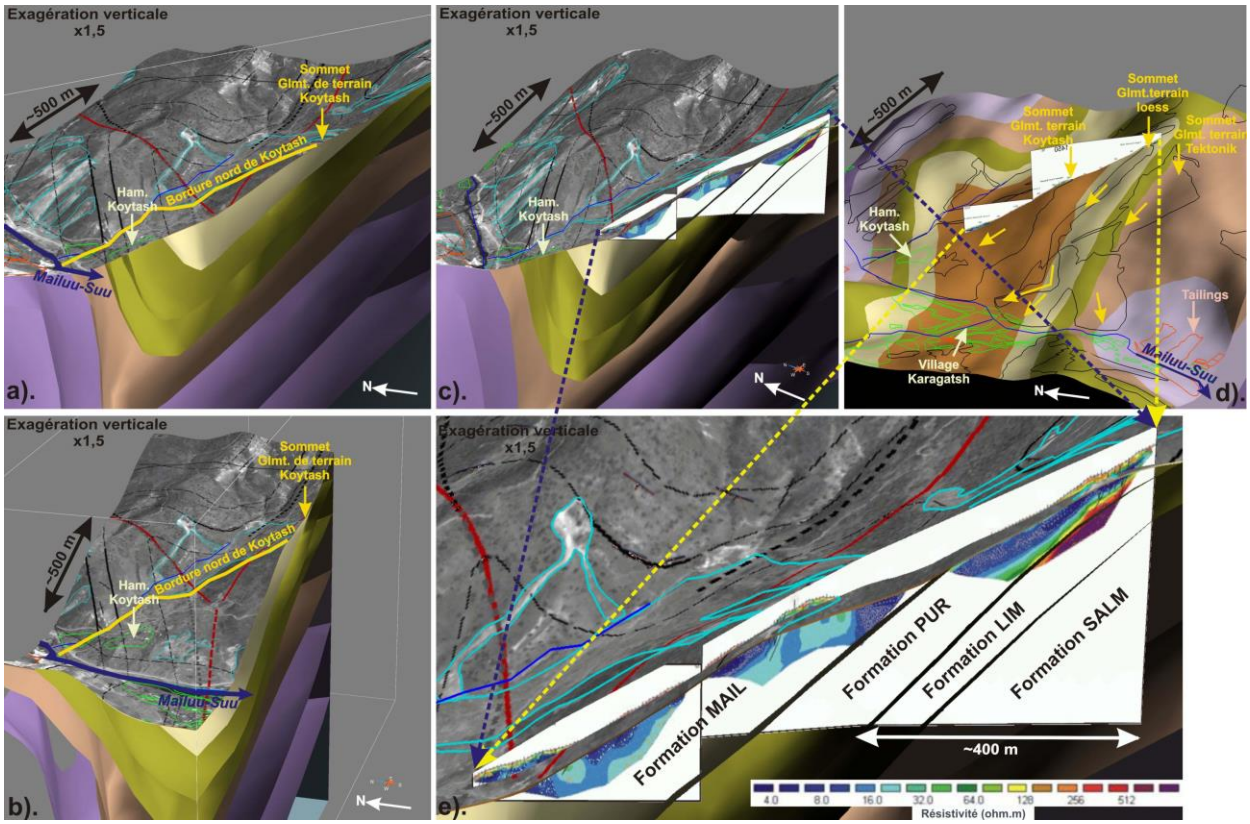

Figure BF.12: Views of the 3D geological model (a, b, c, d) in the surroundings of Koytash landslide with location of the available electrical tomography data (by de Marneffe, 2010).

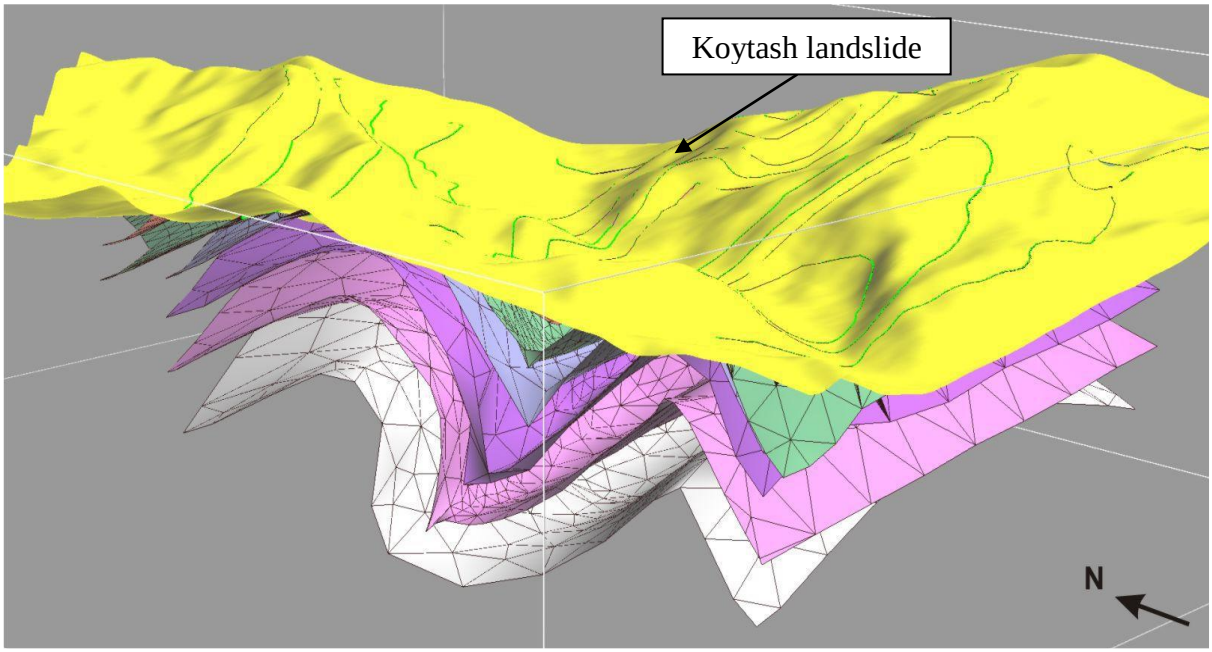

Figure BF.13: Final 3D geological model for the surroundings of Koytash landslide (in the central syncline of the model, marked by slight shadows as situated north of the ridge to the right) with an indication (green-blue lines) of the intersection between the topographical surface and the underground geological layers (by de Marneffe, 2010).

The extracted models use three types of contacts to reconstruct the underground model geometry: material, separation and subdivision contacts. Figure BF.14 presents two models of Profile 4 which show the ways how these contacts are applied. As it can be seen, the material contacts separate various material types. These

contacts are applied only in the combined topographic-geological models, as only one material is used in pure topographic simulations.
The separation contacts split the model into the domains filled by the finite difference (FD) zones with varying zone edge length. Thus, the upper parts of models are filled by 5.0 or 10.0 m FD-zones (the selection of the zone edge length is reviewed in next section). The lower parts of models are filled by two times bigger zones. These separation contacts are always horizontal and situated at the depth of 100-200 m from the model surface.
The third type of contacts, i.e., the subdivision contacts splitting the big blocks into several parts to produce sub-blocks of smaller size. This procedure is required due to the processing limitations of the UDEC code. Thus, the zonation of the big-size blocks often involves extensive processing memory which may exceed the capacity of common computers (Itasca, 2006). The subdivision contacts are always horizontal or vertical to optimize the block zonation.

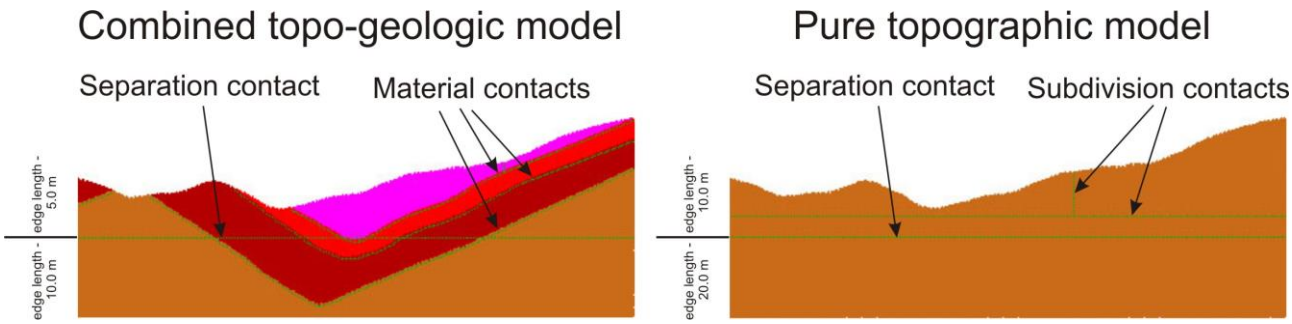

Figure BF.14: Topographic-geological and pure topographic models of Profile 4 showing different types of contacts used for model extraction.

II.4 Size of FD-zones

The FD-zones represent the elementary units of the model and their size (zone edge length) plays an important role in the dynamic simulations. The coarser zones result in faster calculations, while they do not properly transmit the high frequency seismic signal. The finer FD-zones better transmit the high frequency signal, but the calculations are much longer. These considerations are used to select the optimal value of zone edge length.
Kuhlemeyer and Lysmer (1973) propose a rule to select the size of the FD-zone based on the central frequency of the modelled seismic wave. The authors say that the accurate representation of wave transmission through a model requires a size of the FD-zones (Δl, m) that is about ten times smaller than the wavelength (λ, m) associated with the highest frequency component of the input shear wave, i.e.:

$$\Delta l \le \frac{\lambda}{10} \Rightarrow \Delta l \le \frac{V_s}{10 * f} \qquad \text{(BE.14)},$$

where Vs (m/sec) is the shear wave velocity and f (Hz) is the upper limit of the modelled frequency range.
Among the material types used in the topographic-geological models the lowest value of Vs is attributed to Mat1 and is equal to 550 m/sec (see more details in *Section B.II.5*). The upper limit of the modelled frequency range is around 10.0 Hz (see *Section B.II.7*). Therefore, according to Equation BE.14, the FD-zones with Δl =5.0 m are applied in the upper parts of the combined topographic-geological models. The pure topographic models are made of a single material with Vs=1300 m/sec. Therefore, here, FD-zones with Δl =10.0 m are applied. As it is mentioned in the former section, the lower parts of all models are filled by coarser FD-zones with two times larger edge length. This subdivision allows us to perform faster calculations of the seismic energy propagation.
The nodes of the neighbouring FD-zones should precisely fit with each other. Otherwise, artificial reflection patterns are created. Figure BF.15 shows examples of precise node fitting, which is especially important at the contact between blocks with different edge length (see contact between 5.0 m and 10.0 m FD-zones). The generation of the FD-zones with precise fitting of the nodes is computationally intensive and often requires the introduction of additional subdivision contacts (see example in Figure BF.14).

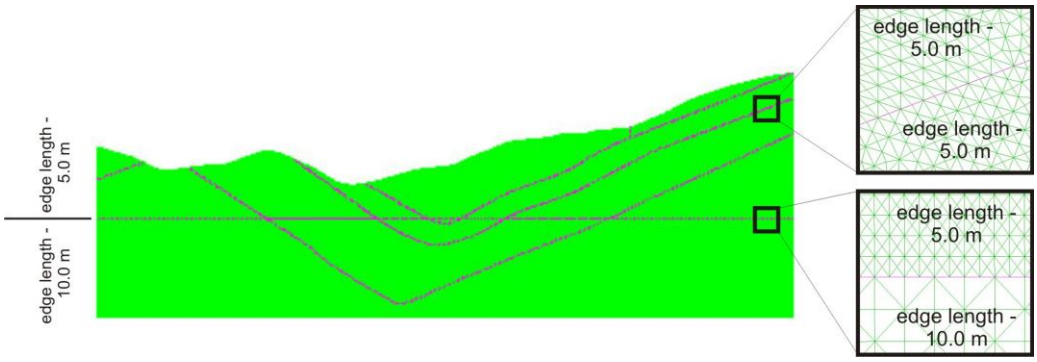

Figure BF.15: Examples of the precise fitting of the FD-zone nodes.

II.5 Modelled materials and properties

The geological formations and rock types composing the target area are deeply analysed in *Section A.IV.1.3.* According to available data and field studies there are in total 11 geological formations (de Marneffe, 2010). There are only rough data on the distribution of the geotechnical and dynamical properties of existing rock types. The mean values of these parameters can be partially estimated based on former investigations in the target area (Sinicyn, 1948; Nikitin, 1974; Kyrgyzgiiz, 1986, etc.) and on results of geophysical studies (Torgoev et al., 2002; Minetti et al., 2002; Havenith et al., 2006). However, new reliable data are lacking. Meanwhile, our parametric analysis does not require precise values of V_s, V_p or density. The estimates of these parameters are precise enough for our analysis. Therefore, the final classification of the modelled materials relies on the expert-based opinion (Torgoev I. and Havenith H.-B., 2012 – oral communication).
Figure BF.16 shows how the sequence of geological formations in the target area is used to determine the modelled materials. Thus, four material types summarize all formations. Table BT.2 lists the applied values of the geotechnical/dynamic properties further used in dynamical simulations. According to the shear wave velocity (V_s) values, the weakest material type is Mat1. The limestone layer (Mat 2) represents the hardest material. Mat3 is attributed to weak material and Mat4 represent the second hardest material in the modelled sequence.

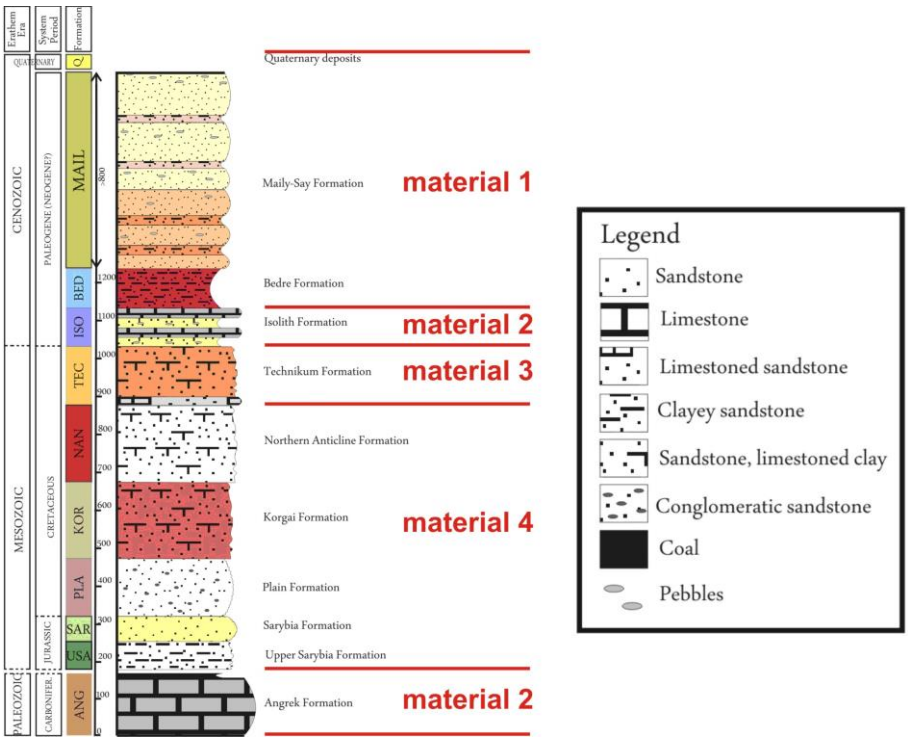

Figure BF.16: Classification of the modelled material types (shown by red colour) in relation to the formations and rocks presented in the target area (de Marneffe, 2010; modified).

Table BT.2: Applied values of the geotechnical/dynamical properties for the modelled material types.

Material code	Geological code	Cohesion, MPa	Friction angle, deg	Density, kg/m^3	V_p, m/sec	V_s, m/sec	Bulk modulus (K), MPa	Shear modulus (G), MPa
Mat1	Q, MAIL, BED (Quarternary, Paleogene-Neogene loose sediments)	0.04	26	2200	1000	500	1467	550
Mat2	ISO, ANG (limestone layers with average thickness of 100 m)	0.1	30	2400	4000	2200	22912	11616
Mat3	TEC (Cretaceous loose sediments with average thickness of 155 m)	0.03	30	2200	1500	800	3073	1408
Mat4	NAN, KOR, PLA, SAR, USA (cretaceous bedrock)	0.08	30	2200	2500	1300	9592	4056

All three types of contacts used in the models are characterized by joint normal stiffness (jkn), joint tangential stiffness (jks), joint cohesion (jcoh) and joint tension (jten). The parametric values of jkn and jks are empirically selected based on preliminary numericalal tests. These tests show that the wave transmission through the contacts is least disturbed when jkn=jks=10000 Pa/m. Extremely high values of jcoh and jten are assigned to all contacts. This feature inhibits any shear displacements along them.

II.6 Model stabilization and boundary conditions

After determination of the model geometry, filling the FD-zones and specification of material codes/properties, the prepared models are subjected to the computational analysis starting with the numerical stabilization. This procedure intends to equilibrate the forces and stresses acting in the newly constructed model. In other words, the numerical stabilization brings the models to the state where the potential energy in it has the minimal value. Technically, it is performed via a number of numericalal iterations during which the residual stresses and unbalanced forces are eliminated. The iterations stop when the balance of force/stress reaches a preset minimal value.

The numerical stabilization is performed through a sequence of intermediate steps. First, all model boundaries are fixed in proper directions to reproduce the dynamic constraints valid in reality for the near-surface rock layers. Thus, the model bottom is fixed in vertical direction, i.e. vertical movement is inhibited. The same procedure is applied to left and right boundaries to inhibit their movement along horizontal directions. After that the numericalal iterations are applied to reach the predefined minimal limit of the mechanical force ratio (rat). According to Itasca (2006), in general conditions, including our modelling case, the stabilization is insured when $rat=10^{-5}$. The convergence of iterations can be accelerated by applying the material damping which attenuates the seismic energy created through the numerical cycling.

After that an additional type of boundary conditions is assigned. These conditions reproduce important feature which significantly impacts the dynamic simulations. In reality the seismic waves are traveling in an infinite medium and reflection, refraction, diffraction normally occur in places with changing material properties (density, seismic velocity, etc.). In the case of the numerical model with limited dimensions all boundaries may act as the strong reflectors. These reflectors create the aforementioned effects which strongly impact the final results of dynamic modelling.

The numericalal codes employ techniques trying to eliminate these boundary effects. Two options are proposed by the UDEC code. The first one is represented by the so-called quiet boundaries. All model rims, excluding the model surface, are set to be extremely viscous. This viscosity strongly absorbs incoming seismic energy and prevents its refraction or reflection. According to Lysmer and Kuhlemeyer (1969), this solution is considered to be effective for the body waves approaching the model boundaries at the incidence angle greater than 30º. The authors recommend this technique for pure geomechanical studies. The second option proposed by the UDEC code is the so-called free-field boundary conditions. This procedure reproduces a medium attached to the model boundaries: this medium “enforces” the free-field motion in such

a way that boundaries retain their non-reflecting properties, i.e., outward waves originating from the boundaries are properly absorbed (Cundall et al., 1985).
To select between those two options we performed some test simulations (see the snapshots of x-velocity profiles in Figure BF.17). As it can be seen, the quiet boundaries have lateral impacts spreading 100-200 m deep into the model. This impact is expressed through the attenuation of x-velocity related to assigned viscosity. The free-field boundaries almost do not produce these lateral effects: the wave front is not subjected to any alterations of velocity values close to the model rims. These results show that viscous boundaries are much less effective compared to the free-field conditions. Therefore, this last option is applied for all studied models.
Once the free-field conditions are assigned, the model should again be stabilized. The applied numericalal iterations reach the predefined limit of the unbalanced force (for). This limit is set to for=10^{-5} N, such as it is recommended by Itasca (2006). These procedures complete the model stabilization step. The stabilised models are prepared for further dynamical simulations which are deeply reviewed below.

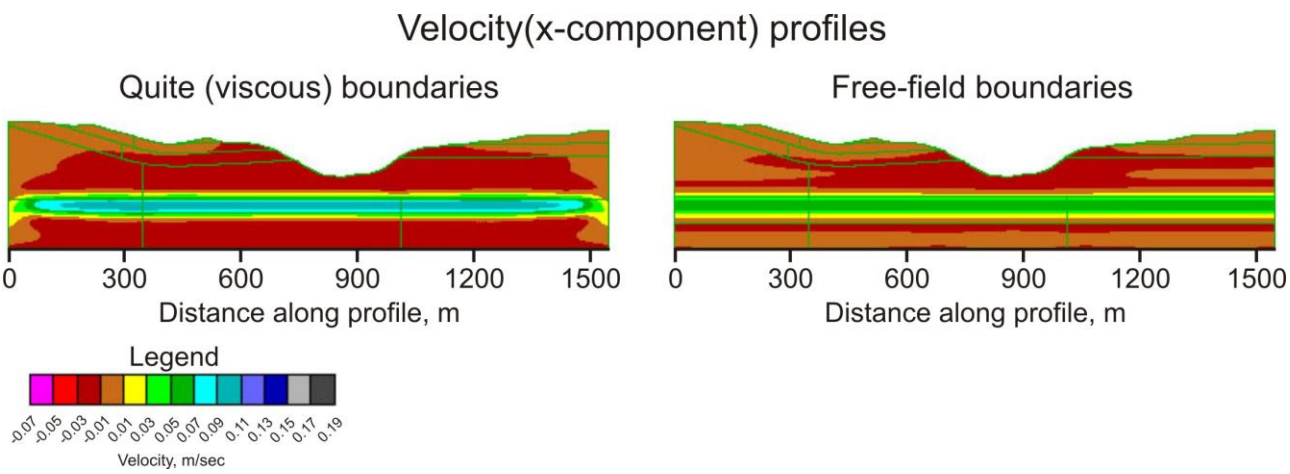

Figure BF.17: The velocity profiles (x-component, 1.7 sec after the impeding of the input signal), comparing the seismic wave propagation for the cases of the quiet (viscous) and the free-field boundaries.

II.7 Dynamic loading and recordings

There are two main options to define the dynamic loading in the UDEC code. The first one expresses the loading in terms of velocity applied in the normal, shear, x- and y-directions. The second option expresses the loading in terms the stress for which the xx-, xy- and yy-components can be determined. Both options establish the loading as a permanent factor, while variations of it can be determined by an additional time-dependent multiplier. This multiplier can have a simple functional shape described by FISH which is the programming language used in combination with all Itasca codes. The shape of the multiplier can also be expressed by the pre-defined time histories of the studied variables.
In our case the loading cannot be expressed in terms of velocity amplitude, as vertical movements are inhibited along the bottom of all models, i.e., the y-velocity is equal to zero. Therefore, we determine the dynamic loading in terms of stress amplitudes. To impede a loading both along x- and y-directions we apply the shear stress: only the xy-component of stress is used as input, while xx- and yy-components are zero. The shear stress dynamic loading is impeded from the whole extent of the model bottom.
The shape of the applied multiplier is programmed by using the FISH language. It represents the integrated curve resulting from a sum of two Ricker wavelets having different values of central frequency (1.4 and 3.5 Hz – see Figure BF.18). The Ricker wavelet is widely applied in engineering seismology, as it is among the functions which best approximate the spectral content of real seismic recordings (Gholamy and Krienovich, 2014). The Ricker wavelet, also called as the “Mexican hat”, was first introduced by Ricker (1953) using the equation below:

$$A = (1 - 2\pi^2 f^2 t^2) e^{-\pi^2 f^2 t^2} \qquad \text{(BE.15)},$$

where A is the amplitude value, f (Hz) is the central frequency (here 1.4 and 3.5 Hz) and t (sec) is the dynamic time.

Figure BF.19 shows the final shape of stress-time history applied as loading in our dynamic studies. This history is the product of two factors: the fixed value of the xy-component of the shear stress (-0.4 MPa) and the multiplier which combines two Ricker wavelets (see one in Figure BF.18). As it can be seen, the effective time of the dynamic loading does not exceed 1.3 sec (approximately from 0.8 sec till 2.1 sec). Nevertheless, the dynamic simulation and dynamic recordings are performed during 15 sec. The extended duration of the dynamic simulations insured the recording of all secondary seismic effects (i.e., reflection/refraction/etc.). A long record duration is especially important for models simulating the combined effects of the geology and topography, as those secondary effects can be delayed in time.

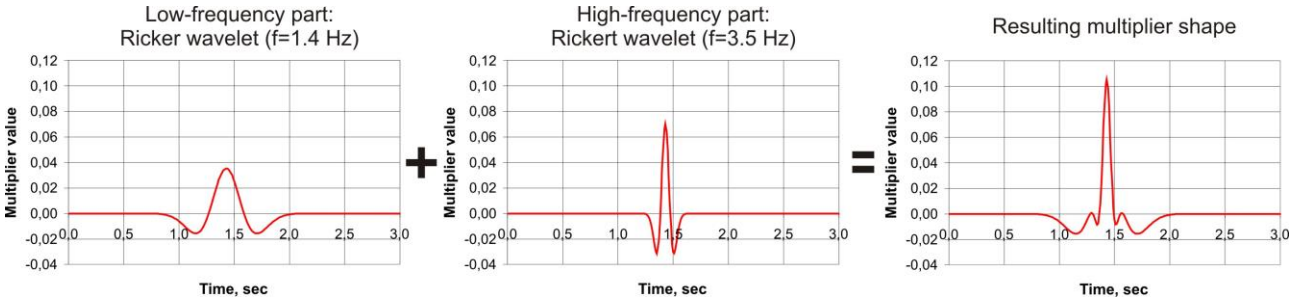

Figure BF.18: Shape of multiplier resulted from a sum of two Ricker wavelets: with f=1.4 Hz and f=3.5 Hz.

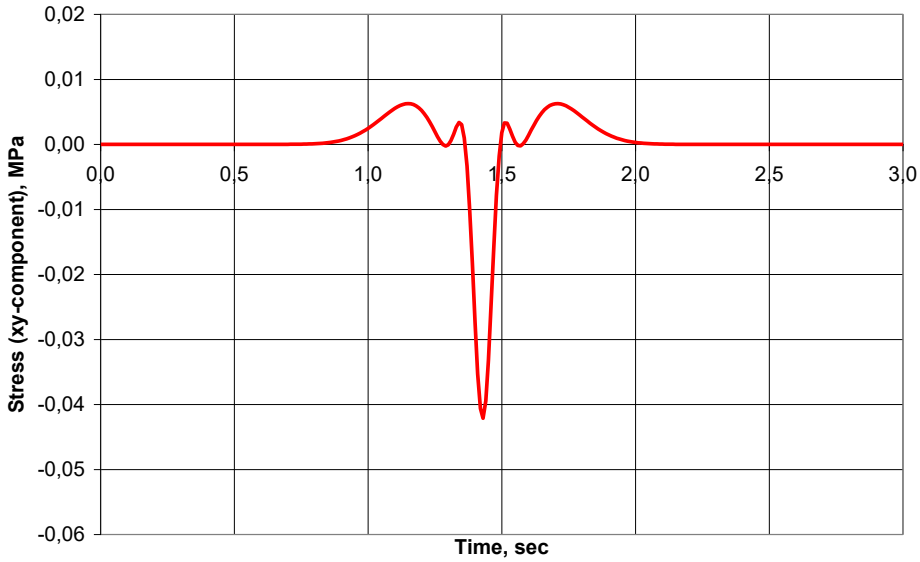

Figure BF.19: Dynamic loading expressed via the stress-time history (xy-component of the stress).

Figure BF.20 presents the x-component acceleration and velocity histories recorded at reference receiver of the pure topographic model of Profile 3 (30 m above the model bottom). These histories are the same for all models, as the same dynamic loading is used everywhere. The recordings show that the free-field conditions are performing well, as reflection patterns registered after 2.0 sec are negligible (compare the time histories in Figure BF.20 versus the duration of effective loading in Figure BF.19). As it can be seen, the applied dynamical loading results in PGA values of around ±1.5 m/sec^2, which is approximately 0.15g. The recorded PGV values are ranging from around -0.02 m/sec up to 0.1 m/sec.

Figure BF.20 also shows the spectral amplitude curves for both recordings. The acceleration history has two frequency peaks (at around 2.2 and 4.1 Hz) which originate from two peaks of input shear stress. The velocity-time history also has two peaks, but they are shifted towards the low frequency domain.

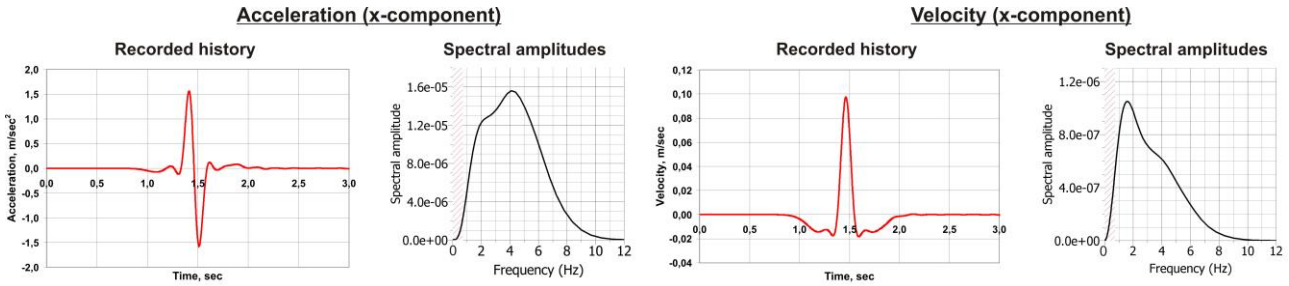

Figure BF.20: Time histories and spectral amplitude curves for the x-component acceleration and velocity recorded at the reference point situated 30 m above the model bottom.

As it is indicated above, the duration of dynamic simulation is 15 sec. During that period of time the x-component acceleration and velocity time histories are recorded at surface receivers. There are, in total, 186 receivers distributed along the surface of 6 purely topographic models. The same receivers are used for the topographic-geological models. Those receivers are normally situated on the sites marked by a characteristic morphology. For the pure topographic modelling the characteristic sites are the hill/mountain crest and basis, the central part of topographic depression, hill slopes, etc. For the mixed topographic-geological modelling the characteristic sites are, for example, the central part of a sedimentary basin, the crest of an anticline, the outcrop of hard rock, etc. The surface receivers are always placed at minimum of 70 m far from the model boundaries due to the residual impacts of the free-field conditions.
Two models of the same profile always have similar configuration of the surface receivers, i.e. a given receiver has the same x- and y-coordinates in these models. This configuration allows us to decouple the mixed topographic-geological effects into pure topographic and pure geological components. This decoupling procedure and the related data analyses are deeply reviewed in the following section.

II.8 Analysis of the Ia amplification

The main outputs of the dynamic simulations are the recorded acceleration and velocity time histories. The acceleration recordings are further used to calculate the values of I_a (see Equation BE.4). According to Harp and Wilson (1995), the landslide triggering is mainly caused by the horizontal component of the seismic shaking, while the vertical component generally has a negligible impact. Therefore, we only analyse the x-component of I_a values which are calculated based on the x-acceleration recordings. Actually, these values should be referred to as the I_{ax} values, while I_a is a sum of I_{ax} and I_{ay}. Meanwhile, in our studies the y-component is not taken into consideration. Therefore, here we assume that $I_a = I_{ax}$ and this assumption is used in further analysis.
The I_a values for all receivers are calculated as follows: first, the acceleration-time history (x-component) is squared, and, second, this squared history is integrated over the recorded time span which is equal to 15 sec. The surface recordings are directly subjected to these calculations, while reference recordings require pre-processing. At first, these reference histories are multiplied by 2 to eliminate the free-surface amplification effect at all surface recordings. Then, these modified histories are filtered which allows us to eliminate the reflections coming from the model surface. Figure BF.21 shows an example of the unfiltered reference recordings. The reflections coming from the model surface can be seen after 2.1 sec, i.e. after the time when effective loading is finished. The filtered recordings are also shown in Figure BF.21. As it can be seen, the filtering removes this reflections appearing after 2.1 sec.
The modified reference histories (multiplied by 2 and filtered) are further squared and integrated over 15 sec to get the I_a values for the reference receivers. The analyses show that all those recordings in both topographic and topographic-geological simulations have the same value of I_a=0.09 m/sec. It should be note, that this value of I_a is attributed to the Ricker wave with central frequency of 1.4 and 3.5 Hz. Some limited tests also use different input signals which, correspondingly, have different values of I_a.

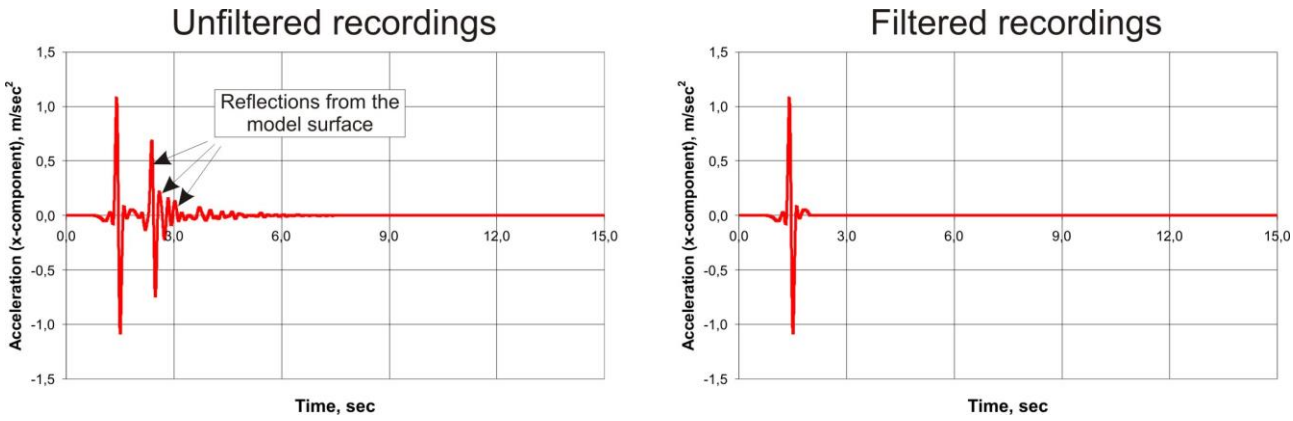

Figure BF.21: Comparison of unfiltered and filtered acceleration time histories recorded at the reference receiver of Profile 3 in the pure topographic modelling.

The calculated values of I_a are further used to study the amplification patterns. The impacts of the topographic site effects are analysed via the pure topographic I_a amplification factor (A_t) which is calculated applying the next equation:

$$A_{nt} = \frac{I_{ant}}{I_{a0t}} \Rightarrow A_t = \frac{I_{ant}}{0.09} \quad \text{(BE.16)},$$

where A_{nt} is the pure topographic I_a amplification factor registered for the n-th surface receiver, I_{ant} (m/sec) is the I_a value obtained for the n-th surface receiver in the pure topographic simulations and I_{a0t} (m/sec) is the I_a value for the reference receiver (here and for all models it is equal to 0.09 m/sec).
The same calculation approach is applied to get the combined topographic-geological I_a amplification factor (A_{tg}):

$$A_{ntg} = \frac{I_{antg}}{I_{a0tg}} \Rightarrow A_{tg} = \frac{I_{antg}}{0.09} \quad \text{(BE.17)},$$

where A_{ntg} is the combined topographic-geological I_a amplification factor registered for the n-th surface receiver, I_{antg} (m/sec) is the I_a value gained for the n-th surface receiver in the combined topographic-geological simulations and I_{a0tg} (m/sec) is the I_a value for the reference receiver (I_{a0tg}=0.09 m/sec).
Both amplification factors (A_{nt} and A_{ntg}) are obtained for the same surface receiver which here is referred to as the n-th receiver. Therefore, the pure geological I_a amplification factor (A_{ng}) for the n-th surface receiver can be calculated as next:

$$A_{ng} = \frac{A_{ntg}}{A_{nt}} \quad \text{(BE.18)}.$$

Equation BE.18 presents the decoupling procedure, when the combined topographic-geological site-effects are decomposed into the pure topographic and pure geological inputs. According to equations BE.16, BE.17 and BE.18 the values of A_t, A_{tg} and A_g are calculated for every surface receiver. The dataset of these amplification factors is further analysed to outline the links between amplification and critical topographic-geological settings. This analysis is focused on the topographic and geological parameters which can act as the regional predictors in the Newmark method. The data analyses also include the spectral amplification studies, as it can be linked to the amplification of the I_a values. A detailed review of the methodology and technical aspects of the spectral analysis is presented in the next section.

II.9 Spectral studies

The spectral amplification studies are performed by the open-source GEOPSY software which is applied in many geophysical and seismological domains (see, e.g., Di Giulio et al., 2006; Köhler et al., 2007; Wathelet

et al., 2008 among others). As a product of the SESAME European project, this software contains a set of tools to process and analyse seismic data.
Special focus of GEOPSY is on the site characterization through processing of the ambient vibrations. One of those tools analysing ambient vibrations is based on the "H/V spectral ratio" technique and is implemented in the HV-toolbox. It partially applies the analytical technique originally proposed by Nogoshi and Igarashi (1971) with conceptual improvements of Nakamura (1989). The HV toolbox is designed to analyse the three-component recordings of ambient vibrations (2 horizontal components and 1 vertical). The applied algorithm estimates the ratio between the amplitudes of the Fourier spectra for the horizontal (H) and vertical (H) components which is also referred to as the HV-ratio. A value of the HV-ratio larger than 1 indicates spectral amplification, while a value smaller than 1 indicates spectral deamplification. The HV-ratio exactly equal to one shows an absence of any associated effects. The final output of this analysis is the HV-curve which shows distribution of the HV-ratios within the analysed frequency range.
Figure BF.22 presents the sample three-component acceleration recordings performed during 20 mins. This set of recordings is further subjected to the HV analysis. Firstly, the GEOPSY software extracts the Fourier spectra for all three components. These curves show the distribution of the spectral amplitudes within the frequency range between 0.0 and 10.0 Hz. The spectral curves for two horizontal components are combined to produce the averaged horizontal Fourier spectra. Finally, the HV-toolbox divides the amplitudes of averaged horizontal spectra over those of vertical spectra to get the spectral ratio curve, also referred to as the HV-curve. As it can be seen, this HV-curve conveniently demonstrates the spectral deamplification/amplification patterns. Thus, it can easily be inferred that significant amplification of horizontal component versus vertical one occurs at around 3.5 and 7.7 Hz. It can also be concluded that the low frequency range between 0.0 and 3.0 Hz is systematically deamplified. The magnitude of associated effects can also be inferred from this curve. Thus, the HV-values at two amplified peaks show that the second peak amplification at 7.7 Hz is almost two times more intensive than the first peak amplification at 3.8 Hz.

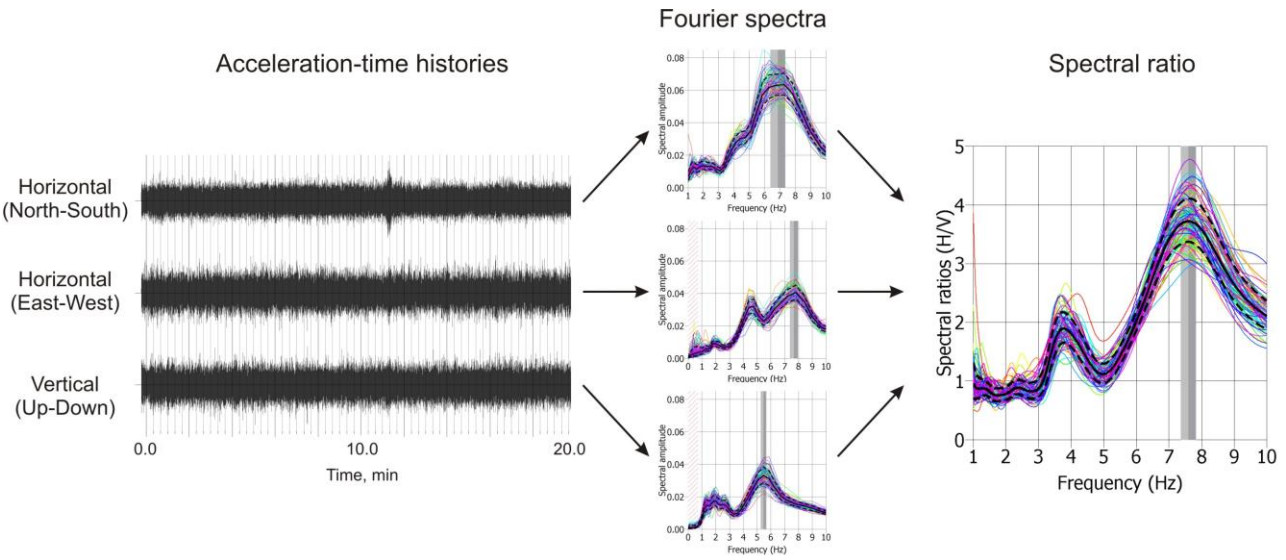

Figure BF.22: HV-toolbox, GEOPSY: analysis of sample three-component recordings to extract the spectral ratio curve showing the distribution of the HV-values over a range between 0.0 and 10.0 Hz).

This methodology is used by us to analyse the spectral patterns of the modelled data. Thus, all surface acceleration recordings (x-component) are compared with corresponding reference histories which are multiplied by 2 and filtered. For every analysed receiver an artificial dataset of three-component recordings is created (see Figure BF.23). In this dataset the surface history represents both horizontal components, while the vertical component is substituted by the reference recordings. This artificial dataset is further subjected to the HV-analysis schematically described in Figure BF.22. First, similar to the aforementioned example, the Fourier spectra for all recording are calculated. Then, the spectral amplitudes for the surface recordings are divided by the reference amplitudes, similar to the division of H by V in Figure BF.22. That way the spectral ratio curve for a given surface receiver is finally extracted.

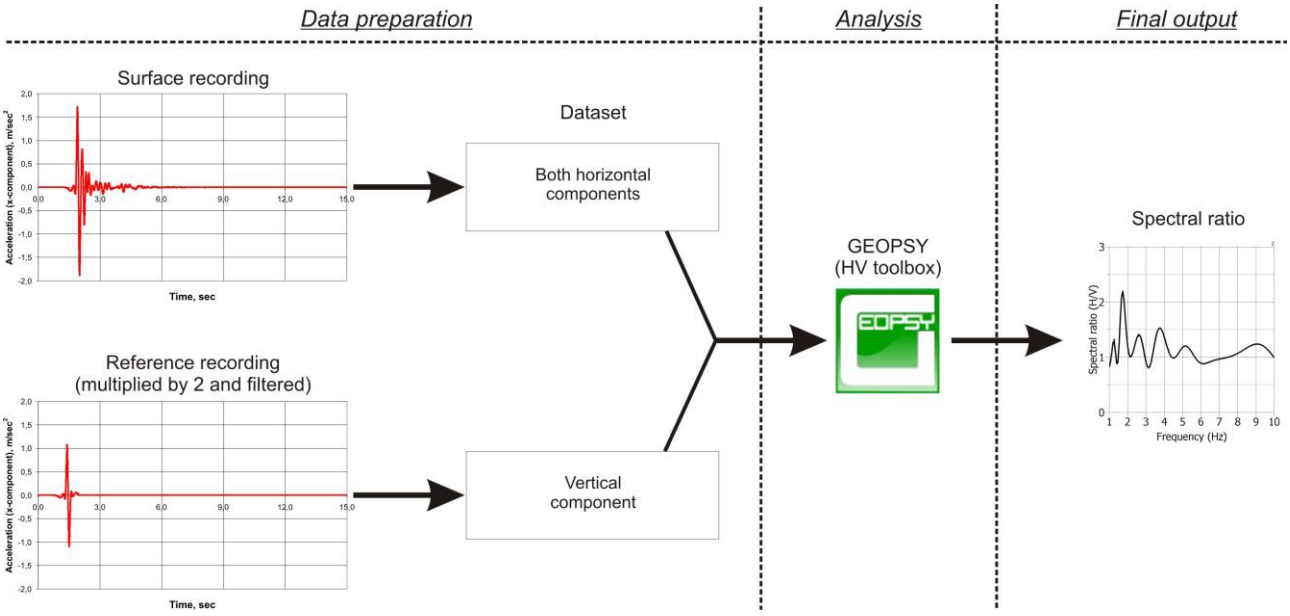

Figure BF.23: Schematic representation of data preparation and following data analyses applied in the spectral studies.

Similar to the example above, the extracted curve conveniently describes the spectral deamplification/amplification patterns. Thus, this curve in Figure BF.23 indicates that surface history is amplified at six spectral ranges in comparison to the reference recordings. The most significant amplification with factor of more than 2 occurs at around 1.7 Hz. The spectral deamplification is registered at three frequency ranges, while the most intensive deamplification occurs at 3.1 Hz.
The results of spectral studies are further used in our analysis to relate the spectral amplification with amplification of I_a. The link between those two processes is especially important in the studies of pure topographic seismic effects, as it allows us to outline the morphological factor which can regionally predict the distribution of I_a. A more detailed overview of this analyses as well as a summary of basic findings are presented in the next chapter.

III. 2D dynamic numerical modelling: topographic site-effects

III.1 Models

The models used for studying the pure topographic site effects combine a real topographic surface with unique underground material (Mat4). According to Table BT.2, Mat4 presents the hardest rocks among the four studied materials (V_p=2500m/sec, V_s=1300 m/sec, ρ=2200 kg/m^3, K=9592 MPa, G=4056 MPa). The model surface was extracted from the 2010 SPOT DEM with elevation points sampled every 21 m.
Figure BF.24 shows the SPOT DEM together with the studied profiles and constructed models. The total length of the models is 22.76 km. The longest model (Profile 1) has a length of 5.73 km, while the model for Profile 6 is the shortest one (2.20 km). The length of the models allows us to cover the topographic features of varying size: from the 40-80 m wide hills up to the 1.5 km wide mountains (one mountain is shown in the middle of Profile 1). The models also reflect the basic morphologic features marking the target area such as the river valley, curved morphology, inclined slopes, etc.

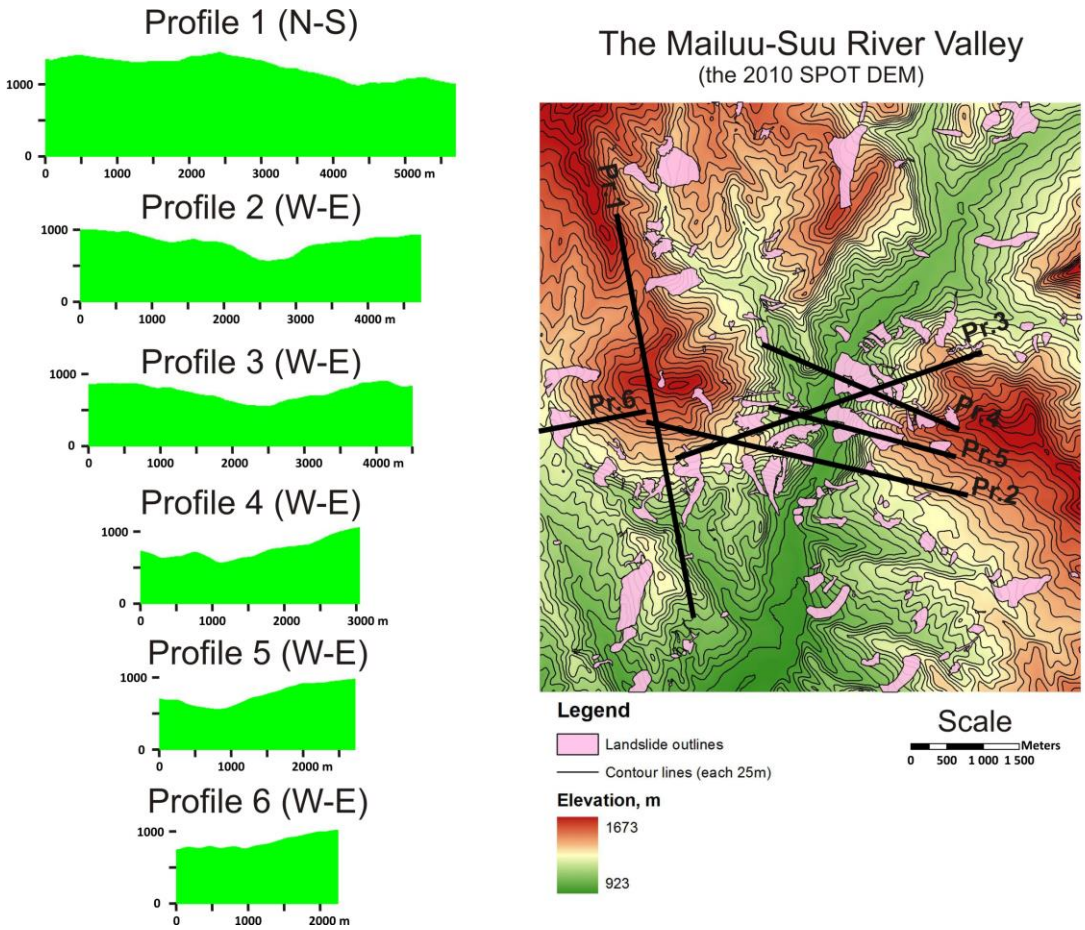

Figure BF.24: The 2010 SPOT DEM of the target area together with landslide outlines, studied profiles and constructed models applied for the pure topographic modelling.

III.2 Impact of contacts

According to *Section B.II.3* the model preparation requires the use of artificial contacts. The upper parts of all models are filled by the 10 m FD-zones, while the lower parts are filled by 20 m FD-zones. Separation contacts have been introduced between the blocks with varying length of the FD-zones. The number of the FD-zones within large blocks often exceeds the local storage allocated by the UDEC code. Therefore, such blocks should be further split into domains of smaller size. This split is performed through the horizontal and vertical subdivision contacts. Extremely high values of the joint cohesion and the joint tension are assigned to all artificial contacts. This inhibits the shear displacements along such contacts.

The dynamic studies of the topographic site effects assume that wave propagation is solely affected by the model surface. It means that any type of contact should be totally transparent to the seismic energy, i.e. these contacts should not produce any reflection, refraction or other lateral impacts. The joint normal and tangential stiffness (jkn and jks) are the critical parameters which affect the contact transparency. Preliminary tests show that jkn=jks=10000 Pa/m insure correct wave propagation without any artificial contact-induced effects.

Figure BF.25 shows a set of the multitemporal velocity cross-sections for Profile 3. The cross-sections represent the x-component velocity profiles. The covered modelling time (from T=0.0 till 5.0 sec) includes the moment when the seismic input is impeded (T=1.2 sec) and finishes at the moment when the seismic energy is reflected from surface and attenuated (T=5.0 sec). All profiles show that the velocity isolines are not interrupted near the contacts surroundings – this indicates that the seismic waves easily travel through the contacts and not reflected back from them. These results show that selected properties of the artificial contacts (jkn=jks=10000 Pa/m) do not affect the propagation of the seismic energy and do not impose any secondary impacts.

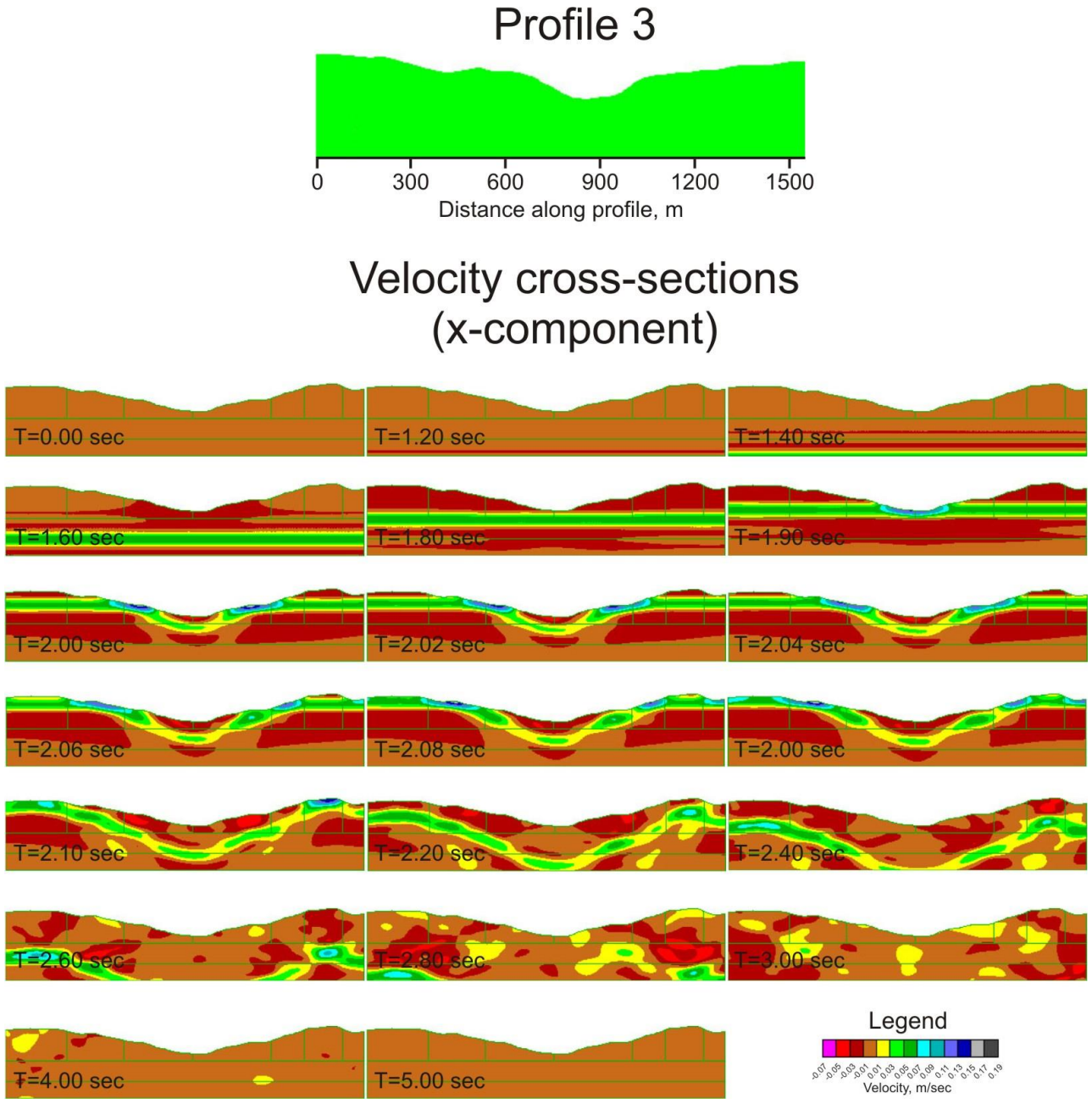

Figure BF.25: Multitemporal x-component velocity cross-sections for Profile 3 covering the modelling time from T=0.0 till 5.0 sec.

III.3 Wave focusing and PGV amplification

According to Bard (1995), the topographic amplification effects are directly related to the focusing of the reflected waves below the ridge-crest morphology. This focusing results in longer duration and larger amplitudes of the seismic shaking near the crest parts of convex morphologies.
Figure BF.26 presents a set of the x-velocity cross-sections for Profile 4 sampled from T=1.8 till 3.0 sec. These profiles show that the crest of the hill situated in the left part of the model is subjected to longer and more intense seismic shaking compared to its toes (compare the PGV values from T=2.00 till 2.06 sec). The wave focusing below this hill results in the highest values of PGV recorded in the whole model, even in comparison with the larger half-mountain situated in the right part of the model.

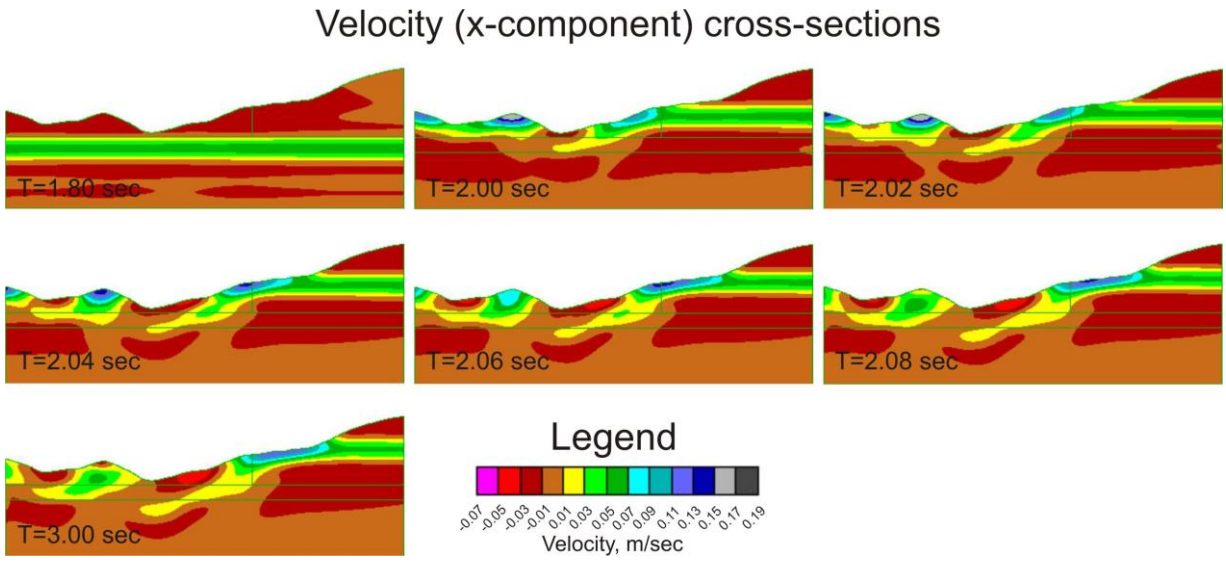

Figure BF.26: Set of the multi-temporal x-velocity cross-sections for Profile 4.

The focusing patterns and resulting PGV amplification on the crest parts are revealed for all analysed models. Figure BF.27 shows the x-velocity cross-sections for five studied models. For example, the PGV value along the left slope of Profile 5 is higher than one along the right slope – this is due to the fact that the left slope is more convex than the right one. The crest of the right mountain of Profile 3 is convex, while the crest of the left mountain is almost flat – it finally results in almost two times higher PGV value in the right part of the model. The highest PGV value among the studied models is revealed for the hill in the left part of Profile 4. These results confirm that all convex morphologies amplify the PGV values. These profiles also show that the most expressive convexities impose the strongest PGV amplification. In this case the expressiveness of the convexities is determined by the ratio of the hill height over the hill length: more expressive convexities are marked by higher values of this ratio.

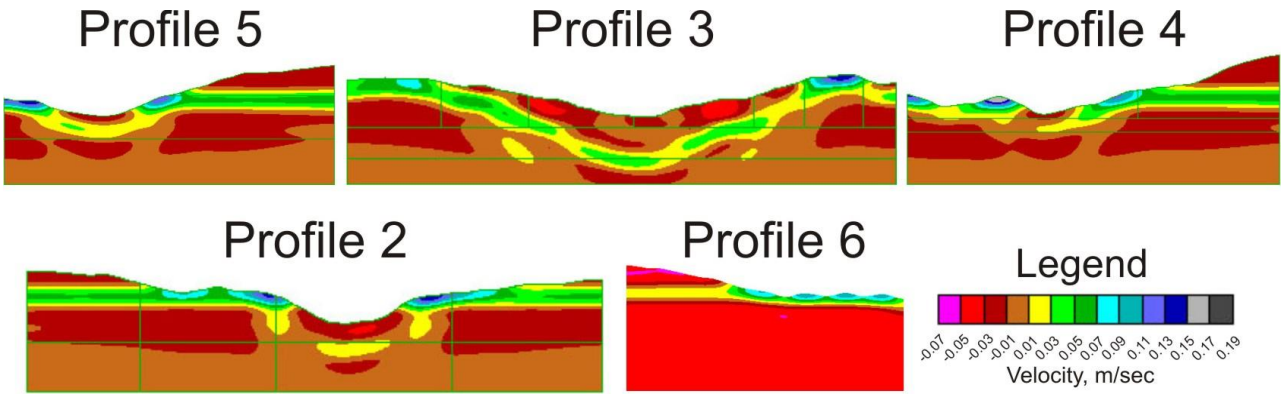

Figure BF.27: The x-component velocity cross-sections for five studied profiles showing the PGV amplification patterns imposed by the convex morphologies.

III.4 PGA amplification

Figure BF.28 shows that wave focusing below convex morphologies (here presented for a hill within Profile 4) results in PGA amplification as well. The modelled hill has a length of around 550 m and a height of around 200 m. The recorded acceleration time histories (x-component) clearly show that the PGA values on the hillcrest is higher than those at both toes. Thus, the hillcrest is affected by a PGA of 2.84 m/sec^2 and its toes by PGA values of 1.61 and 1.73 m/sec^2. In this case, the relative crest/toe PGA amplification ranges from 1.64 up to 1.76. It should be noted, that this hill produced the highest PGA amplification among all studied models.

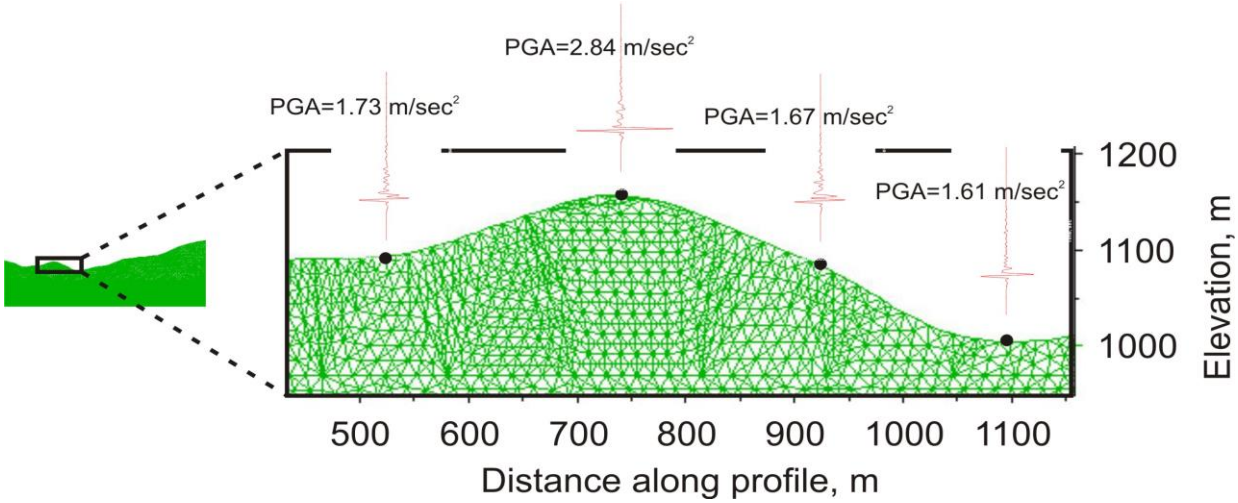

Figure BF.28: Distribution of the PGA values along the hill in left part of Profile 4.

Figure BF.29 summarizes examples of the convex morphologies together with the recorded PGA values. The size of these morphologies, i.e. the hill/mountain length, ranges from 150 m up to 1100 m. As it can be seen, all convexities are affected by amplification of the PGA values. The relative crest/toe amplification of the PGA value varies from 1.10 up to 1.76. A qualitative comparison of the amplification patterns again indicates that the most expressive convexities produce the strongest PGA amplification. It is especially confirmed by the hill analysed in Figure BF.28 which height over width ratio is the highest among all studied topographic features.

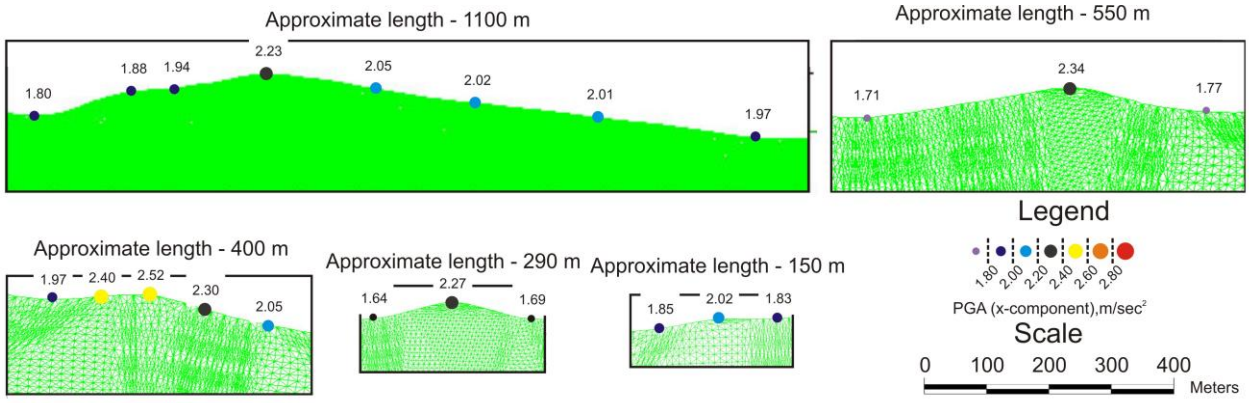

Figure BF.29: Distribution of the recorded PGA values along the sample convex morphologies of different size.

III.5 Arias Intensity vs PGA

According to Equation BE.4, the Arias Intensity (I_a, m/sec) is calculated by the integration of the squared acceleration time history over the recorded time span. This means that PGA amplification and longer duration of shaking observed over the convex morphologies should also result in I_a amplification over the hill/mountain crests. Figure BF.30 compares the I_a versus the PGA values registered for surface receivers of

Profile 3. As it can be seen, these values correlate with each other. Logically, the highest values of I_a are found at the hill tops, while the minimal I_a value is revealed in the middle of the topographic depression (see I_a=0.047 m/sec).

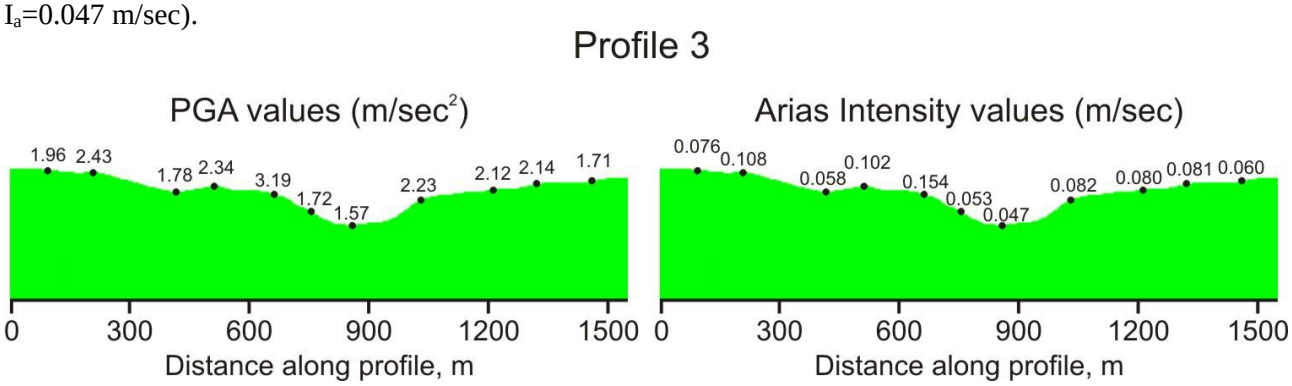

Figure BF.30: The values of PGA and I_a recorded for the surface receivers of Profile 3.

Figure BF.31 presents the plot of the calculated I_a values versus corresponding values of PGA. This plot combines the recordings from all studied models. The analysed PGA values range from 0.41 m/sec^2 up to 3.23 m/sec^2. As it can be seen, the presented distribution fits well the exponential law with correlation coefficient of 0.96 (see equation in Figure BF.31). It is assumed that this law can only be applied to our specific case of Ricker shape input signal. A significant difference is anticipated for the combined topographic-geological modelling, as in this case the significant patterns of lateral reflection and refraction could be created.

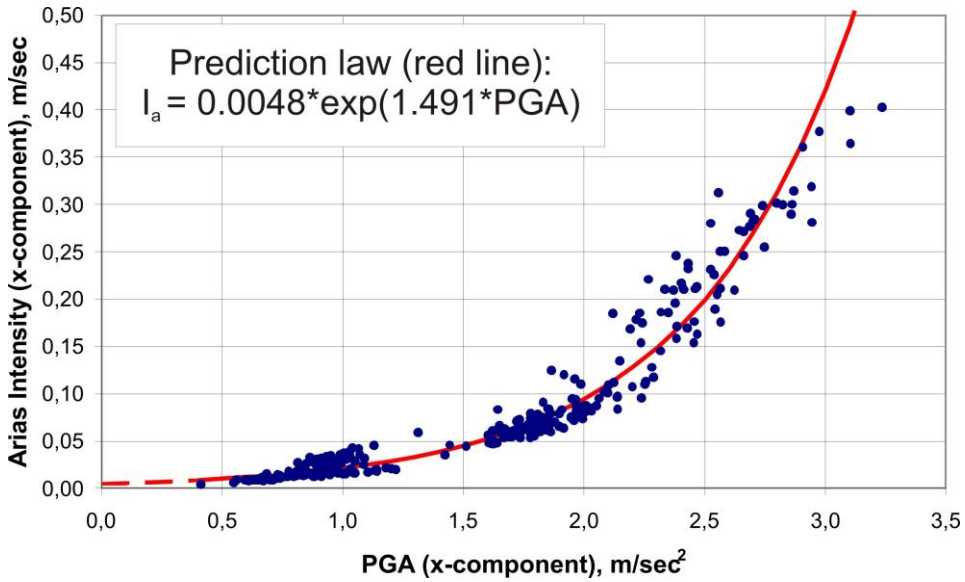

Figure BF.31: Plot of the calculated values of I_a versus corresponding PGA values showing the exponential trend line (red).

III.6 Spectral studies

Several authors studied the topographic site effects in connection with the spectral amplification/attenuation of seismic shaking (Bard, 1982; Geli et.al., 1988, Ashford et al., 1994; Graves et al., 2004; Peng et.al, 2009 among others). These studies provide some hints on how the topographic settings can spectrally modify the arriving seismic waves. Geli et al. (1988) performed one of the earliest numericalal studies and indicate that a significant spectral amplification may occur at the hilltops with respect to the mountain base. This amplification occurs at a wavelength roughly equal to the mountain width. Numerous other studies reveal that the height and the slope angle together with the surface convexity may also be responsible for spectral amplification (Celebi, 1987; Conte et al., 1992; Pedersen et al., 1994; Ashford et al., 1997; Athanasopoulos et al., 1999; Bouckovalas and Papadimitriou, 2005, Zhang et.al, 2007).

A snapshot of the central part of the longest Profile 1 is presented in Figure BF.32. It includes the big mountain marked by Baseline 1 with an approximate length of about 1400 m. Along the mountain surface some minor convexities can be found, such as the one marked by Baseline 2 (approximate length is about 250 m). The dynamic recordings are performed for fourteen receivers distributed along the surface of this mountain (see receivers P1.15t-P1.28t). The spectral attenuation/amplification patterns are analysed by the spectral ratio curves extracted for these surface receivers (see the methodology to construct these curves in *Section B.II.9*).

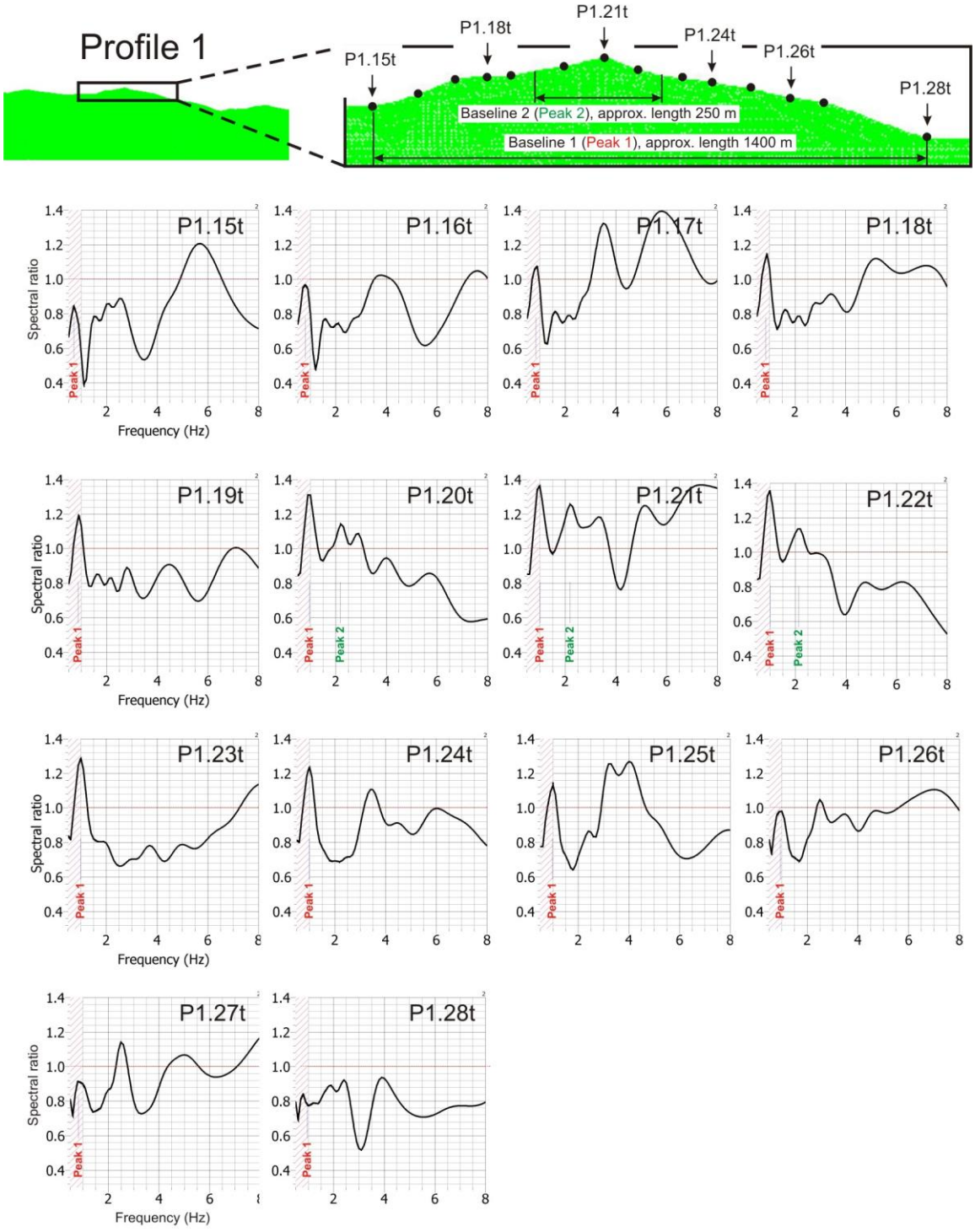

Figure BF.32: Central part of Profile 1 with a set of the spectral ratio curves constructed for fourteen surface receivers.

A careful analysis of the presented curves reveals that some amplification peaks systematically affect some types of convex morphologies. For example, Peak 1 can be found all over the mountain marked by Baseline 1 (see Figure BF.32). This low frequency peak (around 0.8-1.0 Hz) experiences the strongest amplification at

the mountain top (P1.21t) which is confirmed by the highest value of the spectral ratio at this surface receiver (around 1.37). It can also be seen that this peak gradually attenuates along both slopes. The strongest deamplification at the frequency of Peak 1 is found near the mountain base (the spectral ratio of 0.82 for P1.15t and the spectral ratio of 0.84 for P1.28t).
The similar amplification patterns are revealed for the minor convexity marked by Baseline 2. An analysis of the spectral ratio curves shows that Peak 2 can be associated with this convexity, as it is registered only at three surface receivers (P1.20t, P1.21t and P1.22t). Like for Peak 1, the highest value of the spectral ratio is revealed near the hill crest (P1.21t). The surface receivers P1.20t and P1.22t still experience spectral amplification at the frequency of Peak 2, while this peak almost disappears at P1.19t and P1.23t. This shows that the convexity amplifying this frequency range is situated somewhere between P1.19t and P1.23t.
Several convexities situated next to each other can behave like one feature amplifying ground motion over a specific spectral range. Figure BF.33 presents the zoom to the left half of Profile 6. It presents three hills of almost unique shape situated next to each other. The crests of these hills are systematically amplified within a range of 3.0-3.7 Hz (see Peak 2 for P6.14t, Peak 3 for P6.16t and Peak 4 for P6.18t). An additional spectral amplification is registered for all surface receivers. For example, Peak 1 at around 1.6-1.8 Hz is present all along the surface of those hills, but it is only really amplified at the crest of the central hill, i.e. at P6.16t. This peak is subjected to gradual deamplification at the other receivers, while the lowest value of spectral ratio is found at P6.13t. This distribution suggests that Peak 1 is most probably amplified by the feature which combines all three hills. There are also some amplified peaks in the higher frequency range which have unclear origin (see Peaks 5, 6, 7). They can be related to minor convexities or are caused by some neighbourhood effects such as those presented by Geli et al. (1988).

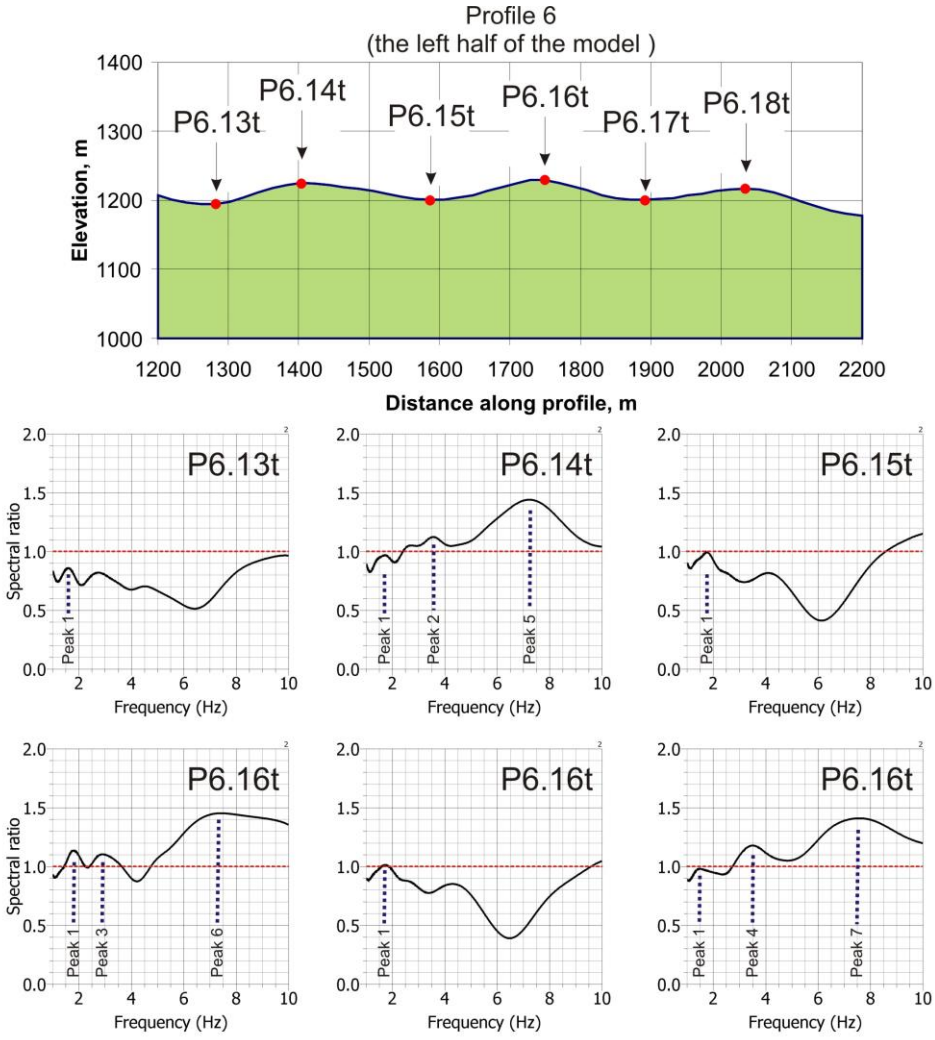

Figure BF.33: Spectral ratio curves for the surface receivers in left half of Profile 6.

The same principle of spectral amplification is revealed for all studied models. Figure BF.34 presents the results of spectral analysis for the surface receivers of Profile 3. This model has two major mountains separated by the river valley in between. The surface of both mountains also presents some minor convexities of different size and shape. The vertical exaggeration with factor of 2.5 is applied here to better demonstrate these minor convexities.

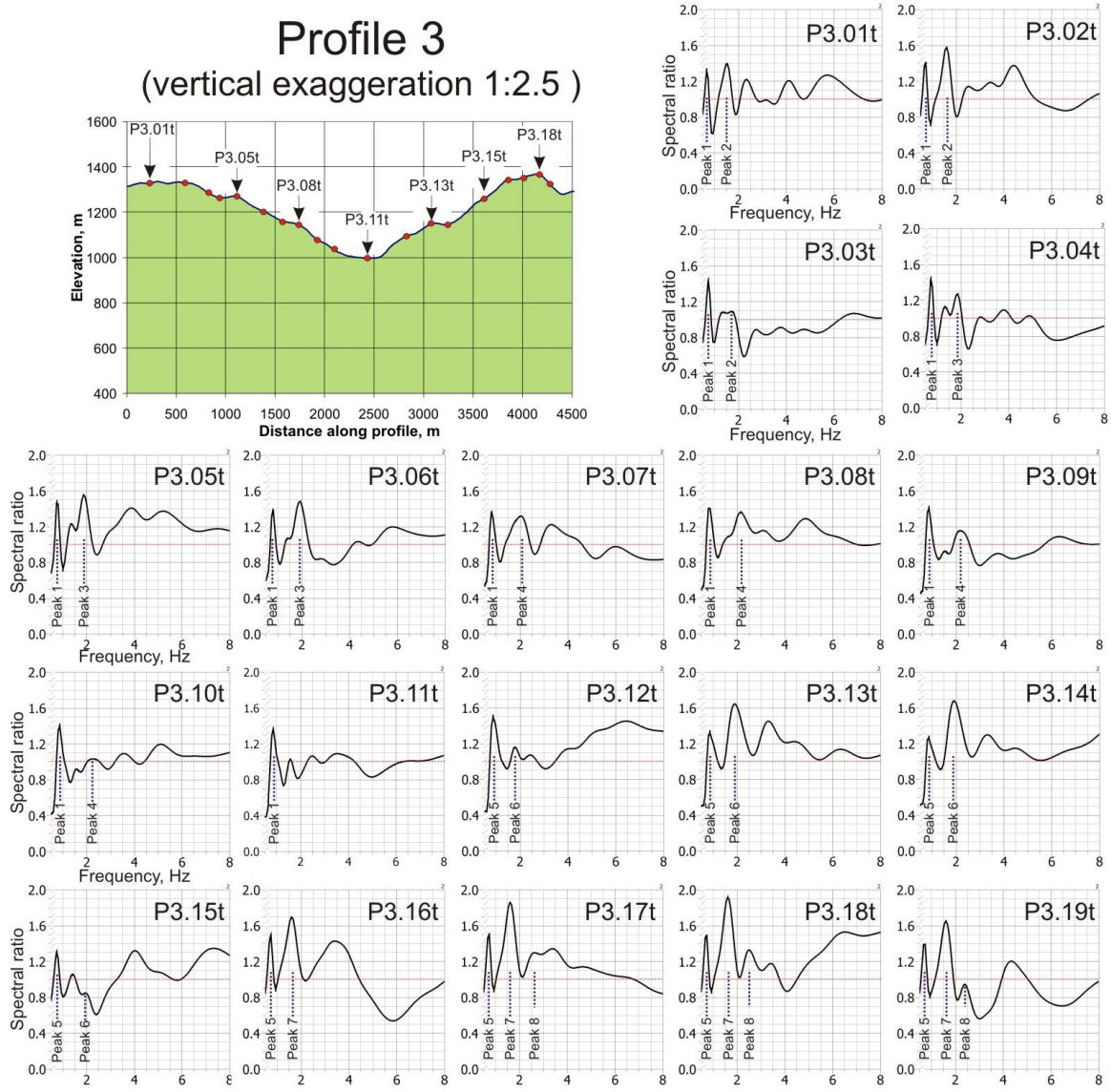

Figure BF.34: Results of spectral studies for surface receivers of Profile 3 (note: the vertical exaggeration 1:2.5 is applied to better highlight the convex/concave features).

There are in total eight amplified peaks which are structurally related to the presented convex morphologies. Such as for the previous examples, the low frequency peaks (less than 1.0-1.2 Hz) are associated with the larger mountains. For example, Peak 1 (≈0.7 Hz) is related to the entire mountain in the left part of the model. This mountain has a baseline length of at least 2500 m. In the right part of the model Peak 1 is replaced by Peak 5, which is related to another mountain with a width of 2000 m. Some residual amplification at Peak 1 is observed for receiver P3.12t, as the spectral ratio value of Peak 5 is larger than for the other receivers, situated higher in the slope.

The amplified peaks observed in the higher frequency range are attributed to minor convexities. One of the best examples is presented by the hill between the receivers P3.04t and P3.06t. Related receivers are characterized by an amplified frequency range between 1.8 and 1.9 Hz (see Peak 3 in Figure BF.34). The crest of this convexity (P3.05t) has the maximal value of spectral ratio at Peak 3. At both toes (P3.04t and

P3.06t) lower values of spectral ratios are observed. The same regularity can be revealed for other amplified peaks, such as for Peaks 2, 4 and 6.
The amplified peaks generally disappear at a certain distance from a given convexity, but some residual amplification can still be observed. For example, Peak 4 is associated with a hill between P3.07t and P3.09t. Meanwhile, it is still present at P3.10t, situated outside of this hill. This residual impact, so called neighbourhood effect, is similar to the ones aforementioned in Figure BF.33.
In all presented cases the hill crests have the highest value of spectral ratio within the amplified frequency range. The location of the receivers with amplified peaks indicates that low frequency amplification is related to the large-scale features, while smaller convex morphologies amplify ground motion in the higher frequency domain. Most of the amplified peaks could be associated with specific morphologies, while the origin of others is more complex or remains unclear. For example, Peak 1 at receiver P3.11t can be explained by the neighbourhood effect. In addition, this receiver also has two amplified peaks in the higher frequency range (see the ones at 2.5 and 3.5 Hz). These last peaks could hardly be explained, as the central part of a concavity should normally be characterized by spectral deamplification. The origin of these peaks should be clarified by additional studies that are beyond our current objectives.

III.7 Spectral amplification and hill dimensions

According to Geli et al. (1988) a hill amplifies the seismic signal at a range of the wavelengths comparable to a width of this hill. Alternatively, Ashford et al. (1997) relate the frequency of the peak amplification to the slope height. The performance of these relationships can be checked by our spectral data, as the amplified frequency values are sampled and both hill dimensions can be directly estimated applying the studied models.
Figures BF.35b and c present the plots of the amplified frequency values versus both hill dimensions (see H and L in Figure BF.35a). These plots summarize the experimental results obtained for all six models. The fit between our data and the previously established laws is also analysed. Figure BF.35b shows that the amplified frequency range can be quite reliably predicted on the basis of the hill length applying the Geli's law. It is confirmed by the high value of correlation coefficient (0.93) associated with the fit between experimental and predicted values. The analysis of Figure BF.35c shows that the value of the amplified frequency is more related to the square root of the hill height, rather than to its original value as indicated by Ashford et al. (1997). This discrepancy can be explained by the fact, that those authors analysed steep slope geometries, which is not our case. Nevertheless, the high value of correlation coefficient (0.91) shows that the spectral amplification is also related to the slope height.

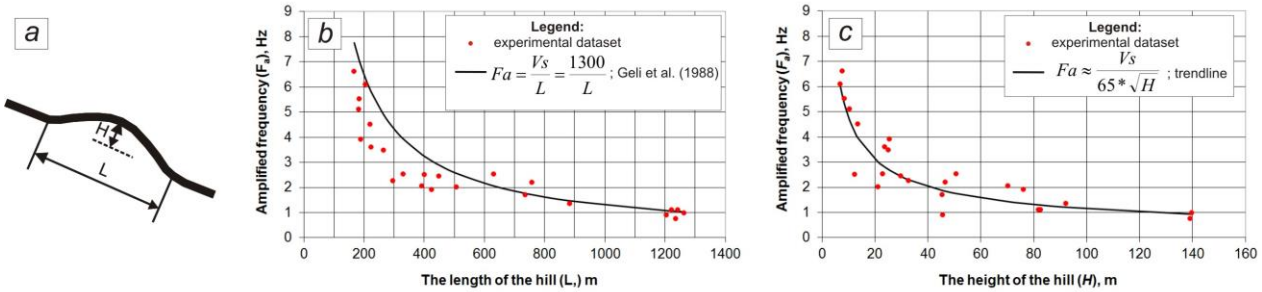

Figure BF.35: (a) Schematic representation of the analysed hill geometry; (b) plot of the amplified frequency values versus the hill length in comparison to the Geli's law; (c) plot of the amplified frequency values versus the hill height together with the resulting trendline.

The intensity of spectral amplification is characterized by the spectral ratio registered at the amplified frequency range. Figure BF.36 presents the plots of the spectral ratio values (R_s) versus the hill length, the hill height and the ratio of height over length. The analysis of the plots shows that the R_s values poorly correlate with the hill length (see Figure BF.36a), while they are slightly better correlate with the hill height (the linear correlation coefficient is around 0.39, see Figure BF.36b). The ratio of height over length provides the best predictions, as it is shown in Figure BF.36c (correlation coefficient is 0.79). This last relationship shows that more expressive convexities (higher values of H/L ratio) impose stronger spectral amplification compared to the morphological features with lower values of this ratio.

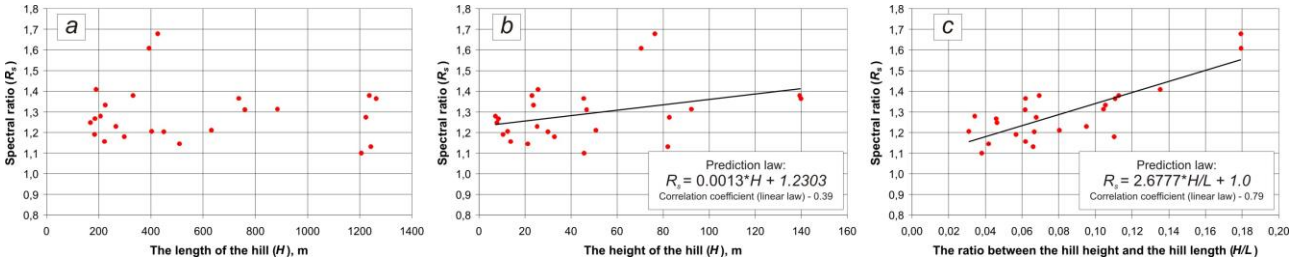

Figure BF.36: Plots of the spectral ratio values versus the hill length (a), the hill height (b) and the ratio of hill height over hill length (c).

These correlation studies confirm some important conclusions made by Geli et al. (1988), Ashford et al. (1997), among others. It is shown that larger mountains generally induce amplification at lower frequencies than smaller convexities. Further, the peak spectral amplification is not related to a single morphological factor - it was shown that the amplified frequency range should be predicted both on the basis of the hill length (L) and hill height (H). The hill geometry also determines the intensity of the spectral amplification. More expressive hills, i.e. those with higher values of the H/L ratio, induce more intensive amplification compared to less expressive convexities. This last conclusion is similar to one yielded for the PGA amplification, as in both cases more expressive convexities result in more intensive amplification (see *Section B.III.4*). Meantime, the main focus of our studies is the I_a amplification. Therefore, the amplification process and factors affecting this parameter are more deeply analysed in the next sections.

III.8 General patterns of I_a amplification

Figure BF.37 shows the distribution of the A_t values representing the I_a amplification factors that result from the pure topographic site effects (see Equation BE.16 to calculate A_t). These amplification factors are shown for the four longest profiles studied through our dynamical simulations (Profiles 1, 2, 3 and 4). As it could be expected, all mountain crests are systematically amplified in terms of A_t, while the topographic depressions and the hill toes are characterized by the lowest A_t values. Nevertheless, some amplification patterns require further clarification. For example, Profile 1 has three main hills, the central one being the largest one in terms of L and H (compare the size of the hills in Figure BF.37). However, the crest of this hill is less amplified (A_t=1.30) compared to the hill in the right part of the model (A_t=1.38). Similar patterns can be revealed for Profiles 2 and 3, where the less expressive and smaller convexities may be marked by the highest values of A_t (for example, compare the features with A_t = 1.17 and A_t = 1.76 in Profile 2).

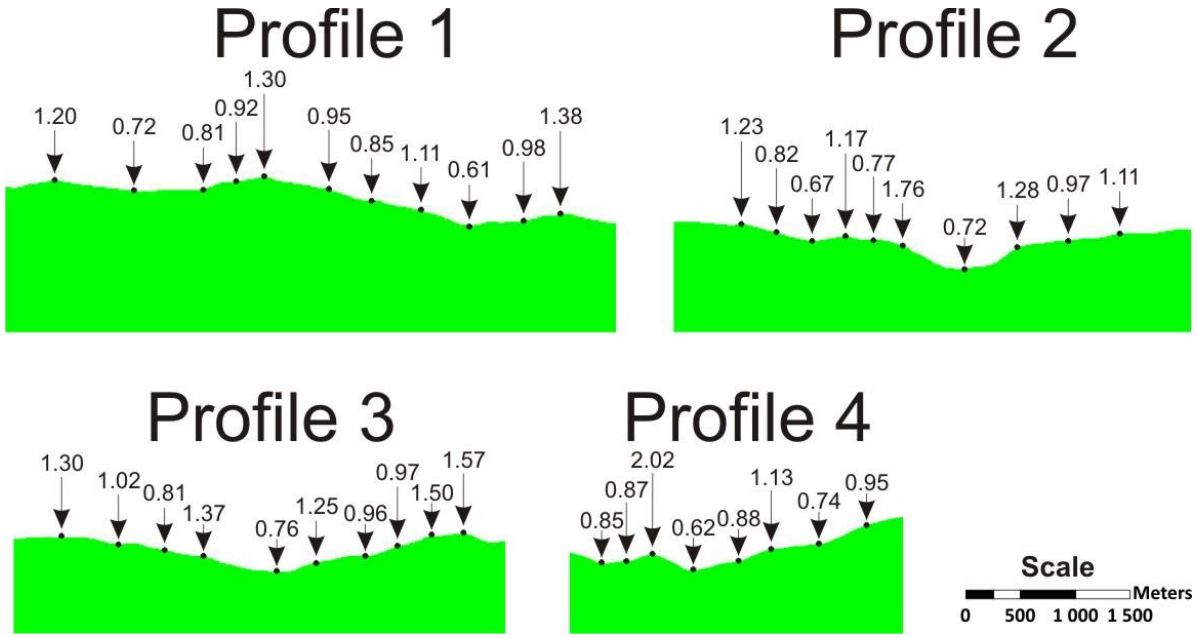

Figure BF.37: Distribution of the A_t values registered for the four longest profiles (Profiles 1, 2, 3 and 4).

The observed distribution suggests that the surface morphology plays some specific role in the I_a amplification, considering that larger hills/mountains may not necessarily result in more intensive amplification. According to the previous section, the surface morphology also determines the spectral amplification patterns. It implies that spectral amplification and I_a amplification are connected processes. The theoretical analysis of this relationship supported by the experimental data is presented in the next section.

III.9 Spectral amplification versus I_a amplification

To establish a link between the spectral amplification and the value of I_a (and A_t) we turn to Parseval's theorem (Parseval des Chênes, 1806). It states that an integral of the squared function is equal to an integral of the squared Fourier transform of this function. In our case, the acceleration time history is the function and, according to Equation BE.4, the integral of the squared function multiplied by a pre-defined constant is the value of I_a. The Fourier transform of the acceleration time history is its amplitude spectrum. It further means that the value of I_a for a given acceleration time history can be calculated by two ways:

$$I_a = \frac{\pi}{2*g} * \int_0^{T_d} \left[a(t)\right]^2 dt = \frac{\pi}{2*g} * \int_0^{\infty} \left[S(\varphi)\right]^2 d\varphi \qquad \text{(BE.19)},$$

where a(t) is acceleration time history (with dt as time interval) and S(φ) is spectral amplitude curve (with dφ as frequency interval).
Introducing Equation BE.19 into Equation BE.16 the value of A_t for the (n) surface receiver (A_{nt}) can be calculated as next:

$$A_{nt} = \frac{Ia_n}{Ia_o} = \frac{\frac{\pi}{2*g} * \int_0^{\infty} \left[S_n(\varphi)\right]^2 d\varphi}{\frac{\pi}{2*g} * \int_0^{\infty} \left[S_{0n}(\varphi)\right]^2 d\varphi} = \frac{\int_0^{\infty} \left[S_n(\varphi)\right]^2 d\varphi}{\int_0^{\infty} \left[S_{0n}(\varphi)\right]^2 d\varphi} \qquad \text{(BE.20)},$$

where $S_n(\varphi)$ is the amplitude spectrum for a given surface receiver and $S_{0n}(\varphi)$ is the amplitude spectrum for the reference receiver of the corresponding model.
According to *Section B.II.9,* $S_n(\varphi)$ can be represented by a multiplication of two products: the spectral ratio curve, $Rs_n(\varphi)$, and the reference amplitude spectrum, $S_{0n}(\varphi)$:

$$S_n(\varphi) = Rs_n(\varphi) * S_{0n}(\varphi) \qquad \text{(BE.21)}.$$

In this case Equation BE.20 can be represented as:

$$At_n = \frac{\int_0^{\infty} \left[S_n(\varphi)\right]^2 d\varphi}{\int_0^{\infty} \left[S_0(\varphi)\right]^2 d\varphi} = \frac{\int_0^{\infty} \left[Rs_n(\varphi) * S_{0n}(\varphi)\right]^2 d\varphi}{\int_0^{\infty} \left[S_{0n}(\varphi)\right]^2 d\varphi} \qquad \text{(BE.22)}.$$

Thus, all manipulations presented above outline two main options to calculate the values of A_t (note: the values of I_a themselves are not interesting any more, as we track the relative amplification of them). The first option calculated A_t on the basis of $S_n(\varphi)$ and $S_{0n}(\varphi)$ applying Equation BE.20. The second way to calculate A_t on the basis of $Rs_n(\varphi)$ and $S_{0n}(\varphi)$ is presented in Equation BE.22.
Figure BF.38 analyses how $S_n(\varphi)$, $S_{0n}(\varphi)$ and $Rs_n(\varphi)$ may be used to calculate A_t (and I_a, respectively). This is studied on the basis of P3.01t receiver (see Figure BF.34) which is subjected to two Ricker shape shear stress

input signals with varying frequency content. Thus, Figure BF.38a presents the reference (input) spectrum $S_{0n}(\varphi)$ and the surface spectrum $S_n(\varphi)$ for the Ricker signal with 1.4 and 3.5 Hz central frequencies. Figure BF.38b shows $S_{0n}(\varphi)$ and $S_n(\varphi)$ for the lower frequency Ricker signal (1.0 and 2.0 Hz central frequencies). Figure BF.38c shows the spectral ratio curves $Rs_n(\varphi)$ for those signals resulting from subdivision of $S_n(\varphi)$ by $S_{0n}(\varphi)$.

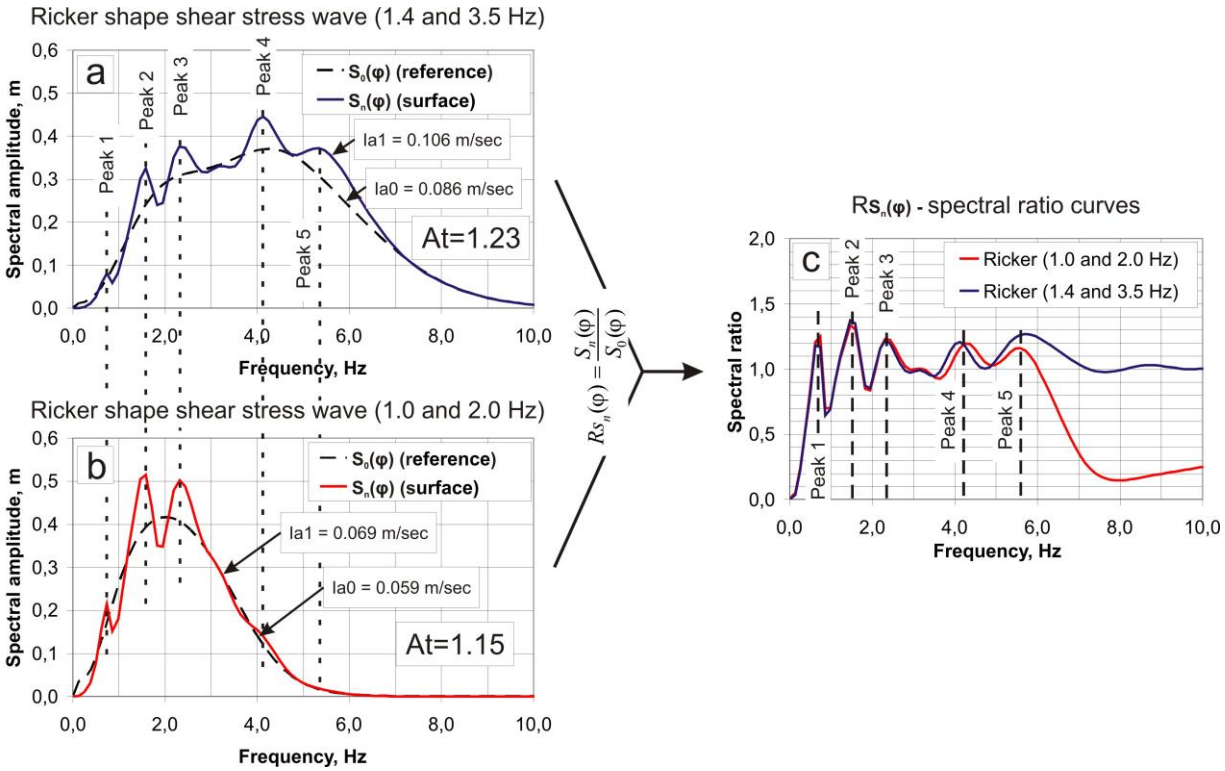

Figure BF.38: The reference amplitude spectra $S_0(\varphi)$, the surface amplitude spectra $S_0(\varphi)$ and spectral ratio curves $Rs_n(\varphi)$ gained for a sample surface receiver (see P3.01t in Figure BF.34) subjected to high and low frequency Ricker shape shear stress input signals.

As it can be seen, the shape of $Rs_n(\varphi)$ is almost identical for both signals and marked by five amplification peaks (se Peaks 1-5 in Figure BF.38c). A significant difference at the frequency of Peak 5 is artificial: the low frequency signal has negligible energy beyond 5.0 Hz which finally results in artificially low value of spectral ratio at Peak 5. The basic similarity of $Rs_n(\varphi)$ for two input signals suggests that, ideally, their shape depends only on the site morphologic/geotechnical settings, i.e. Vs, slope height and length, concavity/convexity, etc.

The reference amplitude spectrum $S_{0n}(\varphi)$ is a site-independent factor and its shape solely depends on the specifications of input signal (see the black dotted lines in Figures BF.38a and BF.38b). The surface spectra $S_n(\varphi)$ is the product of $S_{0n}(\varphi)$ and $Rs_n(\varphi)$: the shape of $Rs_n(\varphi)$ characterizes the site amplification potential, while the shape of $S_{0n}(\varphi)$ determines where and how strong this potential will affect the surface signal. Figures BF.38a and BF.38b show that $S_n(\varphi)$ for both signals have unique position of amplification peaks which reflects the impact of site via $Rs_n(\varphi)$. Meanwhile, the spectral amplitudes at these peaks are different and determined by $S_{0n}(\varphi)$: it demonstrates the impact resulting from $S_{0n}(\varphi)$.

All these links between $S_n(\varphi)$, $S_{0n}(\varphi)$ and $Rs_n(\varphi)$ have important implications with respect to the calculation of A_t for both signals. Thus, the final value of A_t in both aforementioned methods is strongly determined by the shapes of the integrated curves. The integration principle implies, that amplified spectral amplitudes of $S_n(\varphi)$ or larger $Rs_n(\varphi)$ will result in larger values of A_t. For example, this relationship in case of $S_n(\varphi)$ can be clearly identified based on the studied signals. Thus, the high frequency input signal has a broader spectral content. Therefore, $S_n(\varphi)$ for that signal is almost equally impacted by four amplification peaks, while the strongest impact comes from Peak 4 (see blue curve in Figure BF.38a). The low frequency input signal has a narrower spectral content. Due to that, only two amplification peaks are well expressed in $S_n(\varphi)$ and Peak 2 yields the strongest impact (see red curve in Figure BF.38b). Finally, such variation in amplification results in different values of A_t for both signals: A_t=1.23 for the high frequency signal and A_t=1.15 for the low

frequency signal. This shows that the high frequency signal is more amplified in terms of I_a compared to the low frequency signal.

Figure BF.39 presents the results for the same receiver (P3.01t) subjected to the signals made sinusoid shape shear stress waves (one full cycle) with central frequencies of 2.0, 3.5 and 5.0 Hz. To better highlight the amplification patterns the resulting spectral ratio curves (Figure BF.39a) are overlapped with the surface and reference spectra (Figure BF.39b). As it can be seen, the resulting spectral ratio curve has almost identical shape in all tests – it also coincides with one yielded by the Ricker shape input signals (compare the shapes of these curves in Figures BF.38c and BF.39b). The 5.0 Hz input signal has the highest value of A_t=1.20, as its central frequency coincides with two amplified peaks, namely Peak 4 at 4.1 Hz and Peak 5 at 5.6 Hz. The 2.0 Hz signal is strongly impacted by two amplified peaks (Peaks 2 and 3), but it has a lower value of A_t=1.15. This difference in the A_t values is explained by the very broad amplification provided by Peak 5 in the range between 5.1 and 6.9 Hz, while the range between Peaks 2 and 3 is even deamplified (see the range between 1.7 and 2.0 Hz in Figure BF.39a). The 3.5 Hz signal has the lowest A_t value (1.06), which is strongly related to the spectral deamplification at the range of 2.7-3.8 Hz.

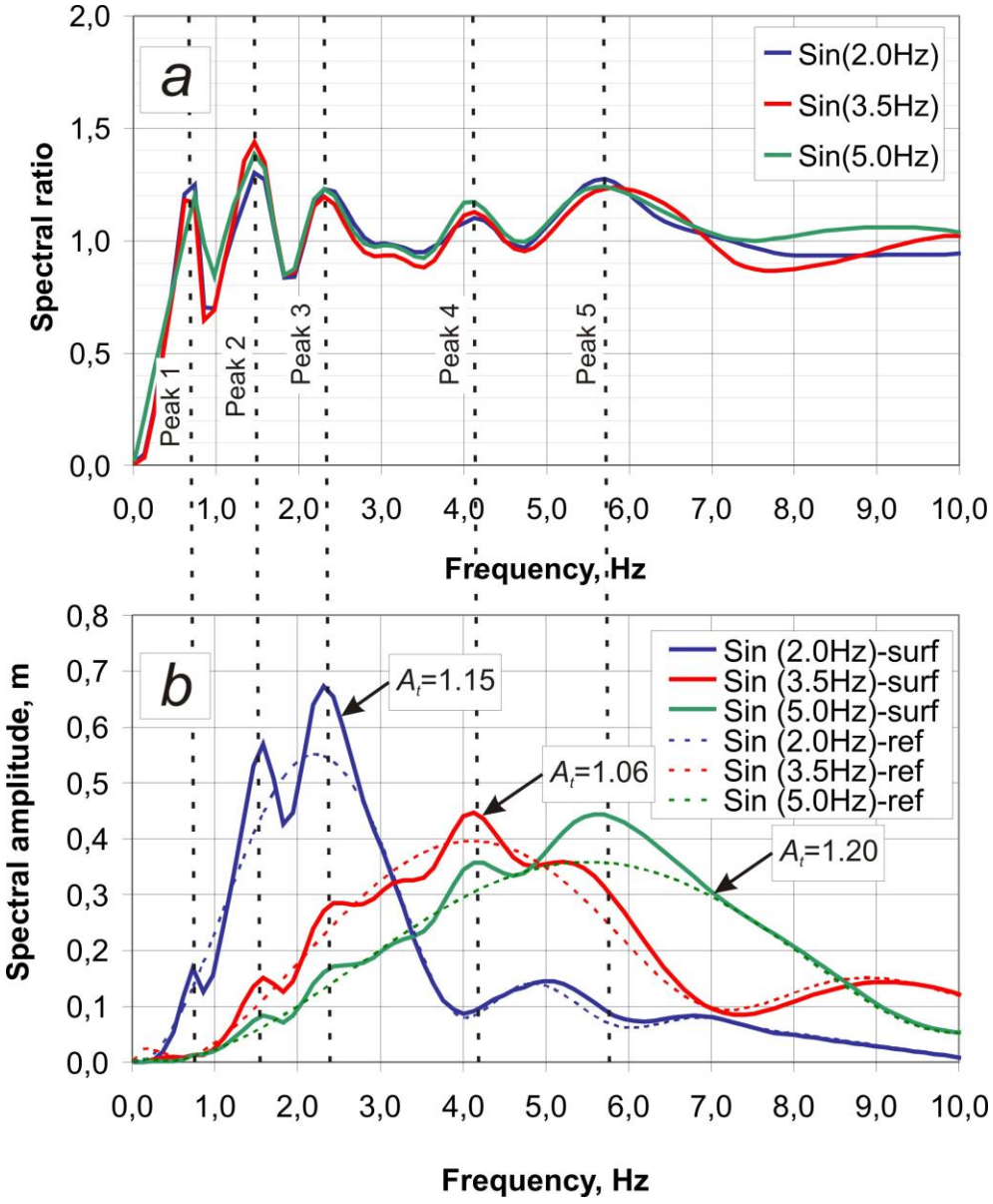

Figure BF.39: Results of the tests with sinusoid shape input signals having central frequencies at 2.0, 3.5 and 5.0 Hz (note: analysed P3.01t receiver is the same as in Figure BF.38).

The results of our analysis show that the final value of I_a and A_t are directly related to the spectral amplification patterns. This link is determined by two independent factors: the spectral ratio curve and the

input spectrum. The first factor, i.e. spectral ratio curve, depends on the site settings (surface morphology, V_s, etc.). This curve shows the amplification potential of given site, i.e. at which frequencies and at which intensity the arriving seismic shaking can potentially be deamplified or amplified. The second factor, i.e. input spectra, is the site-independent parameter and its shape determines the frequency ranges where the site amplification potential will be realized. In other words, the 2.0 Hz input signal will be marked by a deamplified value of I_a (A_t<1) at the site which is naturally characterized by the spectral deamplification at the range of 2.0 Hz. The other spectral ranges can also provide an input which depends on the shape of input spectra. This input is less pronounced for the signals which spectral content is concentrated around the central frequency. However, the broader input spectrum should result in a stronger impact coming from the neighbouring frequency ranges.
This link between A_t and spectral amplification shows a potential to predict the I_a amplification based on frequency scaled curvature (FSC). This parameter was introduced by Maufroy et al. (2015) and presents the surface curvature double-smoothed over a specific spatial extent. FSC is applied to regionally predict the spectral amplification patterns. The authors show that the best predictions are yielded by FSC when the smoothing extent is calculated according to Geli's law. As FSC presents a convenient regional predictor, we further analyse in more detail the issues related to surface curvature and its link with the amplification of I_a.

III.10 Curvature, FSC and smoothed curvature

The basic concept of curvature as one topographic index was reviewed by Evans (1979) and Zeverbergen & Thorne (1987). The authors analysed a part of the Digital Elevation Model (DEM) through a moving window with dimensions of 3 x 3 cells where the cell values denote elevation (see schematic view in Figure BF.40a). The presented distribution of nine elevation values is further fit by the polynomial functional surface (see the one in Figure BF.40a). The 1st spatial derivative of this polynomial function, i.e. change of elevation per unit of spatial extent, is defined as the slope. The 2nd spatial derivative of the same polynomial function is the curvature representing a change of slope per unit distance. The authors further define two basic directions along which the curvature can be calculated, i.e. along the direction of maximum slope (profile curvature) and transversely to it (planform curvature). Moore et al. (1991) incorporate both types of curvature to get the parameter termed as the general curvature. Figure BF.40a shows the technique adopted by the ArcGIS code to calculate the value of general curvature in the 3D domain. Here, D and E reflect the curvature in both orthogonal directions with the general curvature calculated for the central cell being marked as Z5. The positive value of general curvature shows upward convexity, while negative value represents downward concavity.

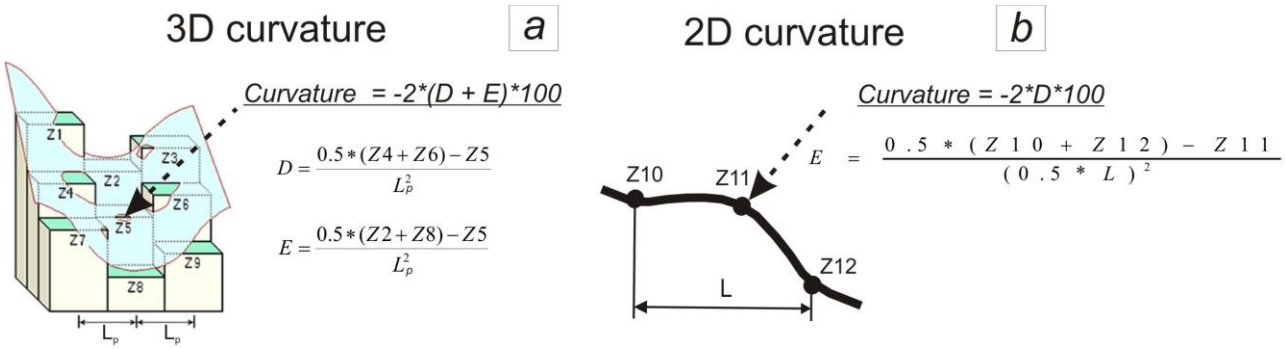

Figure BF.40: (a) Calculation of general curvature in 3D domain based on elevation data from DEM, where Z1, Z2…Z9 are the elevation values for the corresponding pixels (m) and Lp (m) is DEM pixel size (ESRI 2012; modified); (b) calculation of general curvature in 2D domain, where Z10, Z11 and Z12 are the elevation values (m) and L (m) is a curvature baseline length (note: L=2Lp).

Figure BF.40b shows how the concept of general curvature is adapted to the 2D domain. In this case curvature is calculated along a single direction, i.e. along the model surface. As a 2D cross-section normally shows the direction of the maximum slope, the value of D in this case is equal to 0. That way the 3D general curvature becomes the 2D general or 2D profile curvature. This concept of curvature calculation is applied to analyse our 2D data. The choice is driven by the fact that 2D and 3D curvatures in this concept are clearly interconnected which allows us to compare the 2D outputs with the 3D model results presented in *Chapter*

B.V. In this case the curvature baseline length, referred to as L in Figure BF.40b, corresponds to twice the DEM pixel size in Figure BF.40a, i.e. $L= 2L_p$. As the surface of our models is sampled every 21 m, the smallest baseline for which the value of curvature can be calculated corresponds to $L=2L_p=42$ m. For further convenience, those elementary curvature values, i.e. calculated for L=42 m, are referred to as Curv (not to be mixed with the conceptually different smoothed curvature which later will be referred as $Curv_{84}$, $Curv_{126}$, etc.).

The next critical issue is related to the smoothing of the curvature values. Regarding our topic, this smoothing expresses the procedure which returns the mean value of curvature over a given spatial neighbourhood which, in turn, is determined by the smoothing length. Actually, the smoothing of curvature values can be performed via two main options: the direct smoothing of the elementary curvature values or the extraction of the curvature based on the smoothed elevation data. The last option implies that, first, the elevation values should be smoothed and, then, the curvature is calculated. Moreover, the smoothing itself can be applied several times. For example, Maufroy et al. (2015) apply double-smoothing of original curvature values to get the parameter termed as FSC. In this respect, given the variety of smoothing options, we prefer to treat FSC as the particular case of smoothed curvature.

In our studies we do not apply FSC, as we prefer to first test the simplest and most direct way to extract the smoothed curvature. Figure BF.41a demonstrates a sample distribution of the Curv values around P4.05t receiver (Profile 4). These curvature values are calculated for every surface node according to Figure FB.40b: Z11 is the elevation at the studied node, while Z10 and Z12 are the neighbouring elevation values. Figure BF.41b shows the way how this distribution of Curv values is applied to calculate the smoothed curvature for the same surface receiver, i.e. for P4.05t. As it can be seen, the applied algorithm collects all Curv values within specific neighbourhood from P4.05t and returns the mean value. For example, $Curv_{84}$ presents the mean curvature over the neighbourhood of 84 m, while $Curv_{126}$ is calculated by averaging all Curv values over the neighbourhood of 126 m (see the smoothing neighbourhood in Figure BF.41a and sample calculations in Figure BF.41b). According to this approach the smoothed curvature values with L ranging from 84 m till 798 m are calculated for all surface receivers of six studied models. These smoothed curvature values are further analysed regarding their relationship with observed amplification of I_a. The details on this analysis are presented in next section.

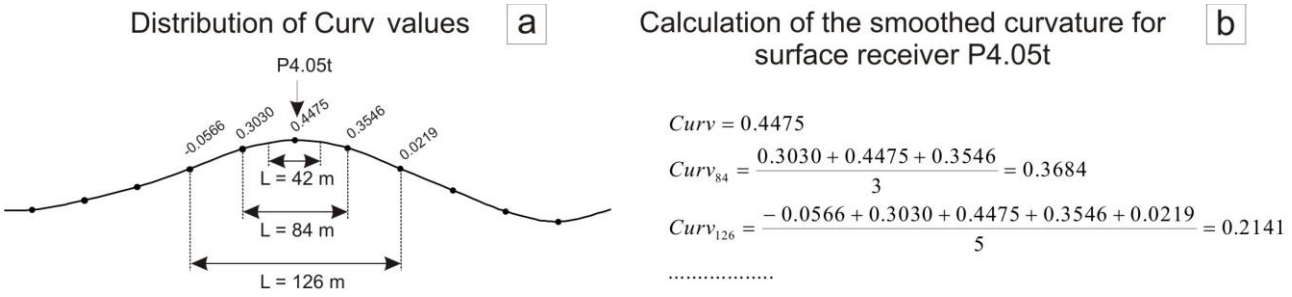

Figure BF.41: (a) 2D distribution of the Curv values around sample surface receiver (P4.05t from Profile 4); (b) calculation of the smoothed curvature values for L=84 m and L=126 m for the same surface receiver.

III.11 Link between A_t and smoothed curvature

To study the link between A_t and the smoothed curvature we present the scatter plots of the first variable against the second one (Figure BF.42). These plots summarize the data from all six models studied by the Ricker shape input signal (1.4 and 3.5 Hz). The distributions for both smoothed and original curvature are presented. The values of L used to get the smoothed curvature range between 84 and 798 m. The link between two variables in each plot is characterized by the linear correlation value. The other types of relationship between two variables (exponential, quadratic, etc.) are not tested here, as we aim at indicative information rather than looking for the precise law.

As it can be seen, the linear correlation values are distributed according to a certain rule. Starting from L=42 m these values are growing, reaching the maximum at L=294 m (see a graph marked by a dotted rectangle in Figure BF.42). For L of more than 294 m the correlation values are again decreasing. This distribution suggests that A_t for the studied input signal is best linearly predicted by a curvature with L=294 m, i.e. by $Curv_{294}$. That value of L we further refer as an effective smoothing length (L_e), while corresponding curvature is termed as effective curvature ($Curv_{Le}$).

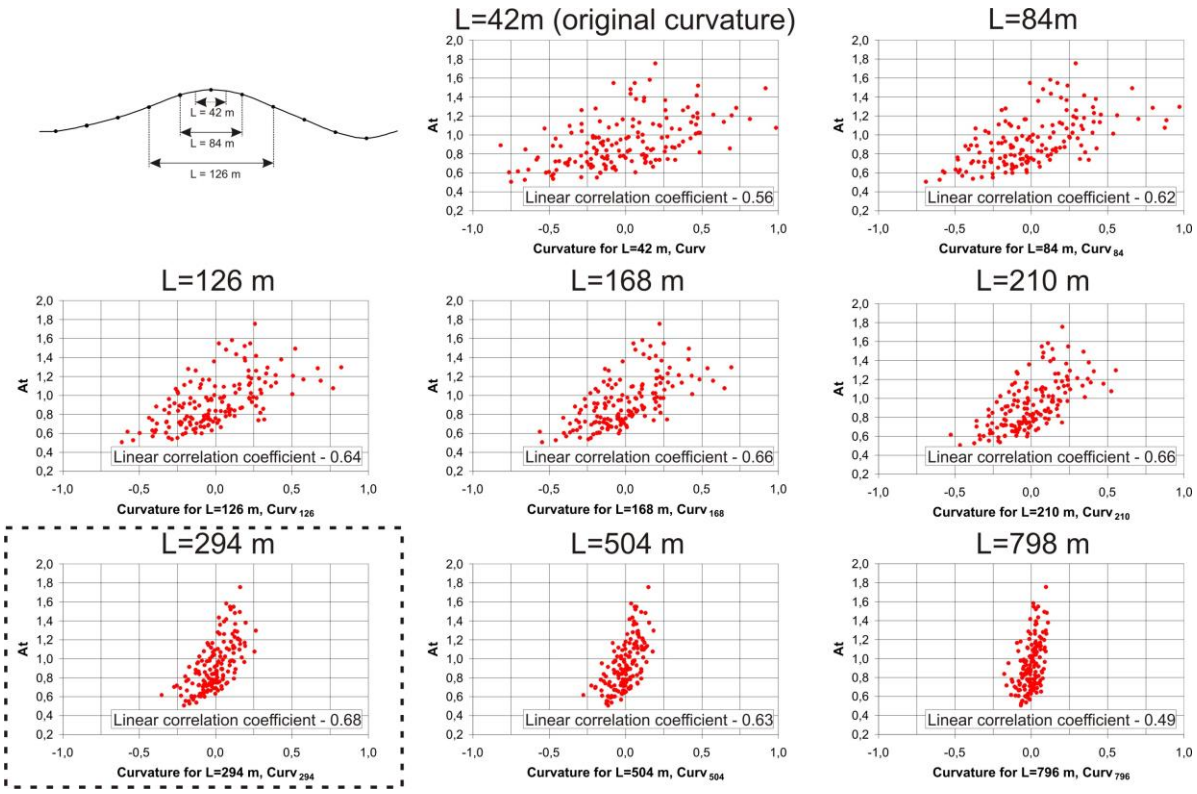

Figure BF.42: Plots of A_t values versus the original and smoothed curvature for the dynamical simulations applying a Ricker shape input signal (shear stress) with the central frequencies of 1.4 and 3.5 Hz (the best correlation is marked by a dotted rectangle).

To further analyse the link between A_t and original/smoothed curvature we study Profile 3 with different input signals. They include the low frequency Ricker signal (1.0 and 2.0 Hz central frequencies), as well as sinusoid-shape signal with varying central frequency. Figure BF.43 summarizes the results of all tests. Here, the linear correlation values are plotted against the values of L used to extract the smoothed curvature. According to the previous discussions, the maximal values of linear correlation depict L_e for each signal. The curvature smoother over L_e, i.e., $Curv_{Le}$ is the best linear predictor of the corresponding distribution of A_t. Presented graphs again demonstrate a consistent distribution of the correlation values. Thus, all curves have some peak value of correlation coefficient which is marked by L_e. To both sides from L_e the correlation coefficients gradually decrease. It is important to note that L_e and the central frequency value are inversely related. The sinusoid signals soundly confirm that link: Sin (2.0 Hz) signal has L_e=504 m, Sin (3.5 Hz) signal has L_e=336 m, Sin (5.0 Hz) signal has L_e=168 m and Sin (6.0 Hz) has L_e=126 m (see Figure BF.43b).

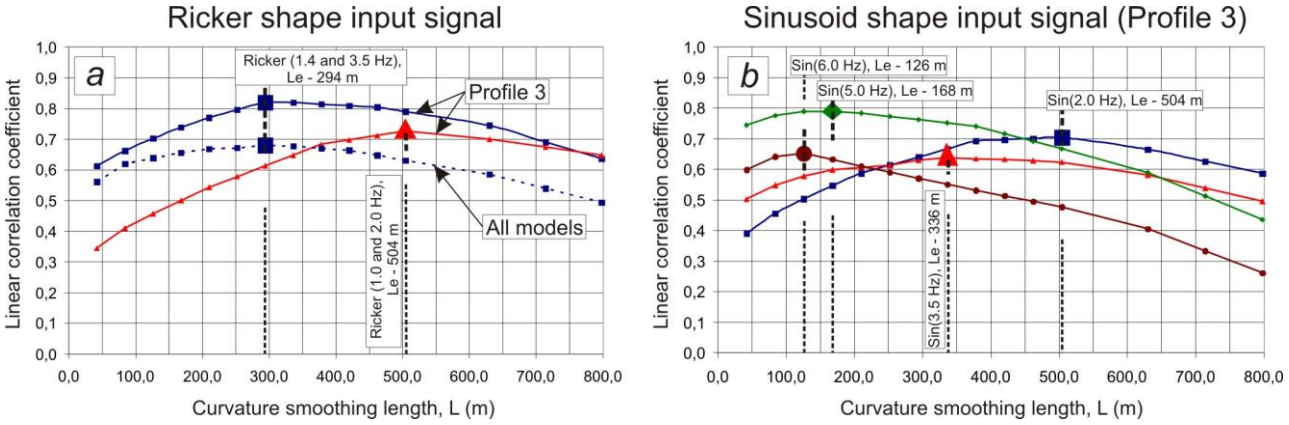

Figure BF.43: Distribution of the linear correlation coefficients to establish a link between A_t and the curvature with varying smoothing length: (a) for the tests with Ricker shape shear stress input signals; (b) for the tests with the sinusoid shape shear stress input signals (only Profile 3).

Some curves shown in Figure BF.43 are asymmetric. For example, the one for the low frequency Ricker signal (red curve in Figure BF.43a) is more inclined in a part with L<Le. The input spectrum shown in Figure BF.38b explains this asymmetry: as it is comparatively narrow (spectral range is from 0.0 up 6.0 Hz) it results in a smaller impact coming from the curvature with smaller L, while the curvature with larger L induces a more pronounced impact on the final value of A_t. The high frequency Ricker signal shown by blue curves in Figure BF.43a has a more symmetric shape. Figure BF.38a shows that this signal has a much broader input spectrum; therefore, the A_t values for this signal are almost equally impacted by the curvature with both small and large values of L.

Figure BF.44 further plots the resulting values of L_e against the central frequency of the tested input signals (red dots - Ricker signals, blue dots – sinusoid signals). Here we analyse the central frequency of the input acceleration time history (F_{ca}) which is derived from the input spectrum computed with the Geopsy software. The values of F_{ca} are higher than those for the input shear stress. For example, the 2.0 Hz shear stress corresponds to F_{ca}=2.2 Hz (point 1), while the 6.0 Hz shear stress already corresponds to F_{ca}=8.4 Hz (point 4). The presented distribution is also compared with Geli's law (see the trendline in Figure BF.44). It can be seen that the empirical values of L_e highly correlate with the calculated ones (correlation coefficient - 0.88). This fit is very important, as it suggests that the value of L_e can be predicted on the basis of two parameters: the shear wave velocity of the analysed material (V_s) and the central frequency of the input acceleration time history (F_{ca}).

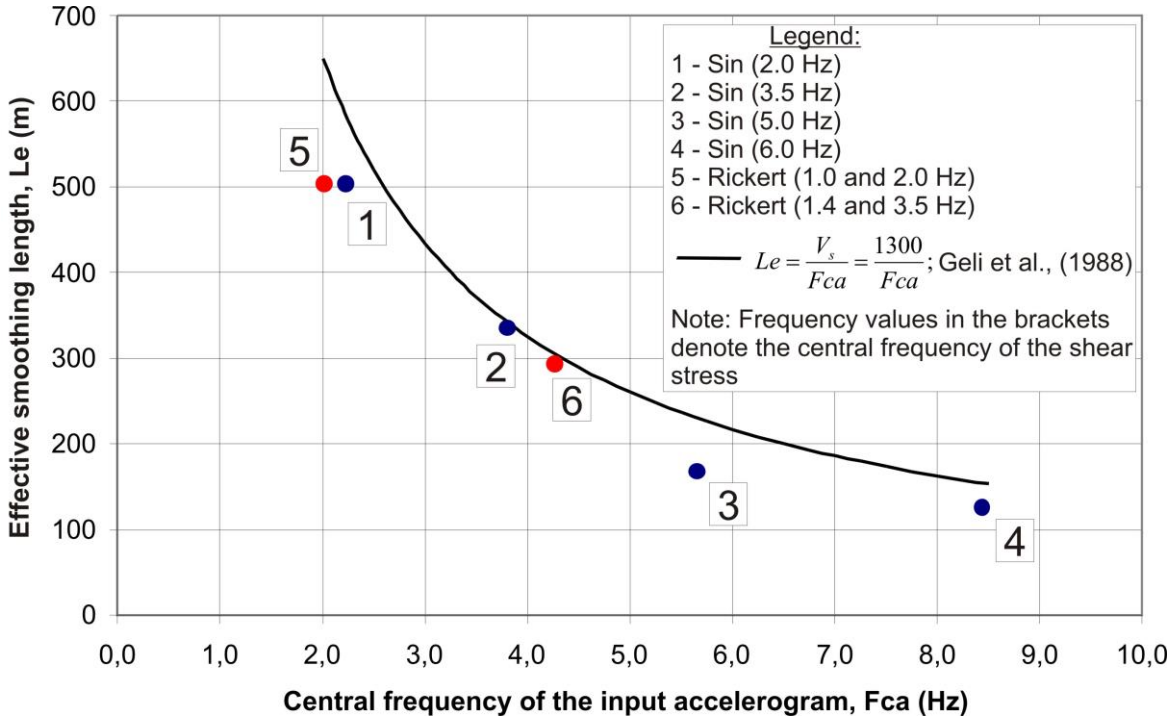

Figure BF.44: Plot of the effective curvature baseline length (L_e) versus the central frequency values for the input acceleration time history (F_{ca}) and comparison with the law of Geli et al. (1988).

Thus, Figure BF.44 shows how to estimate the value of L_e which is later used to map the effective curvature values ($Curv_{Le}$). We further investigate how successfully $Curv_{Le}$ can predict the distribution of A_t. This analysis is performed over dataset of 40 surface receivers from Profile 3. The analysed A_t distribution includes the results of tests with four sinusoid signals. Figure BF.45 plots A_t versus the corresponding $Curv_{Le}$ (note: in this case L_e is calculated according to Geli's law applying V_s=1300 m/sec and the corresponding F_{ca}). All graphs present the linear shape laws predicting A_t on the basis of $Curv_{Le}$ (see also linear correlation coefficients for these laws). These coefficients correspond to the peak values observed for the same signals in Figure BF.43b.

As it can be seen, the worst predictions of the A_t values are obtained for the F_{ca}=8.43 Hz signal (linear correlation coefficient at around 0.64). Slightly better predictions are performed for the F_{ca}=2.22 Hz and F_{ca}=5.65 Hz signals, as the corresponding coefficients are equal to 0.68 and 0.67. The best predictions are obtained for the F_{ca}=3.8 Hz signal, as the correlation coefficient equals to 0.78. The variation of the

correlation values seems to be non-systematic and not related to F_{ca}. This discrepancy between observed and predicted data is explained above: the A_t values are not solely impacted by the effective curvature, as some additional impacts also come from the curvature smoothed over other values of L.
The analysis of the prediction laws in Figure BF.45 reveals some regularity. First of all, the slope of the trends becomes flatter with an increasing value of F_{ca} (compare the slope coefficients). Second, all equations have an intercept equal to 1, i.e. for $Curv_{Le}$=0 the value of A_t is exactly equal to 1 which shows a lack of any deamplification/amplification of I_a value. These regularities allow us to define the general shape of prediction law which can be presented as below:

$$At = K * Curv_{Le} + 1 \qquad \text{(BE.23)},$$

where K is a frequency-dependent slope.
These four values of K for sinusoid signals are further compared with F_{ca} to get the relationship between these parameters. The analysis shows that K is best predicted by the next equation:

$$K = \frac{2.1770}{F_{ca}^{0.3905}} \qquad \text{(BE.24)}.$$

Introducing Equation BE.24 into BE.23 we would get the next form of the A_t prediction law (for the sinusoid-shape signals):

$$At = \frac{2.1770 * Curv_{Le}}{F_{ca}^{0.3905}} + 1 \qquad \text{(BE.25)}.$$

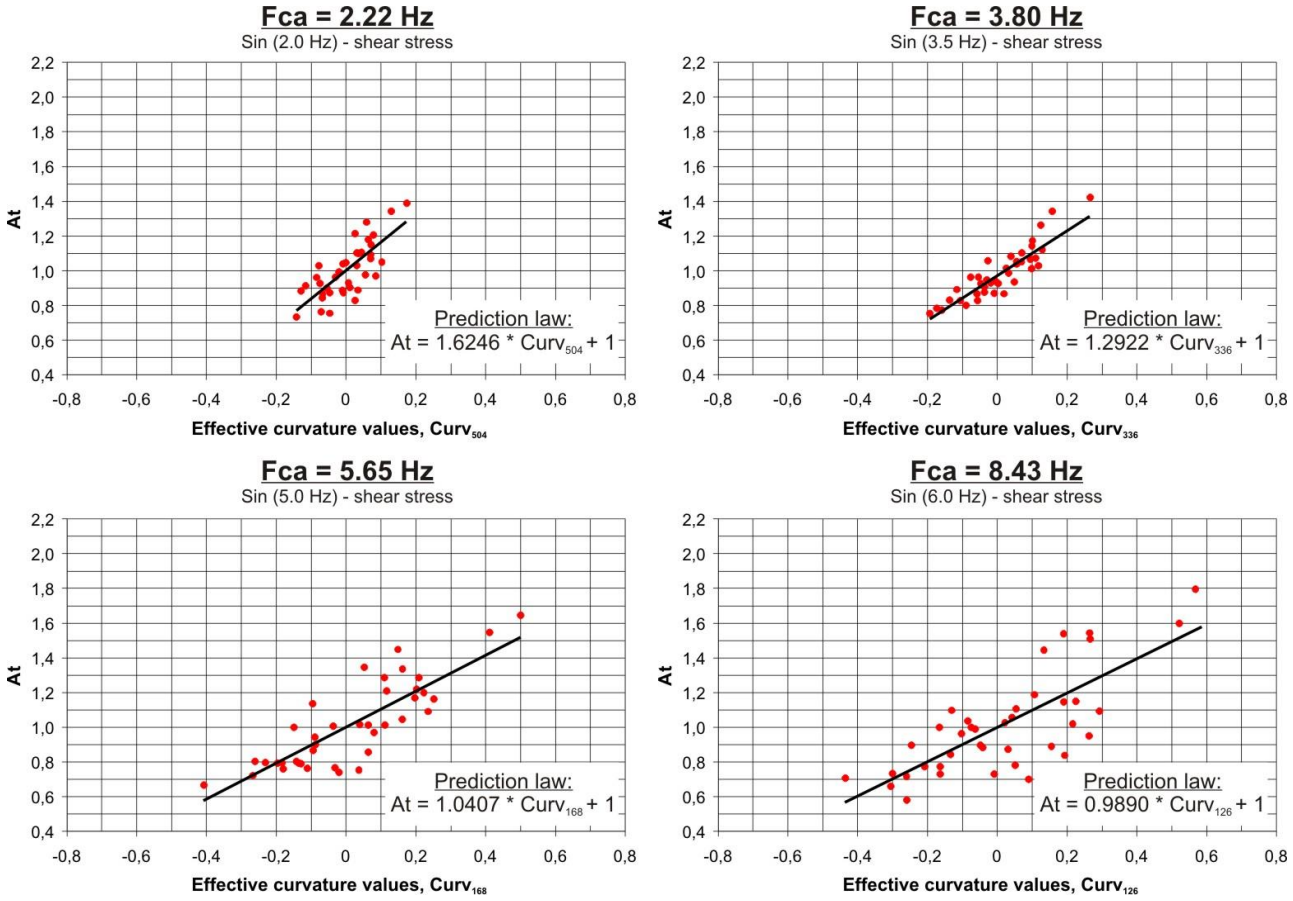

Figure BF.45: Plots of the At values versus the effective curvature observed for Profile 3 (40 surface receivers) applying sinusoid shape signals with varying frequency content.

The analysis of data from the Ricker tests confirmed that distribution of A_t can also be predicted according to the general law shown in Equation BE.23. Nevertheless, some difference is observed. For example, the prediction law for the sinusoid signal with F_{ca}=2.22 Hz has a value of K=1.6246, while the one for the low-frequency Ricker signal with a comparable value of F_{ca}=2.01 Hz is marked by K=1.9939. This difference of around 18-20% shows that the value of K does not only depend on F_{ca}, but also on the shape of the input spectrum. This further implies that the prediction of the I_a amplification based on the effective curvature should not only consider the central frequency of the input spectrum, but also its shape.

The relationship shown in Equation BE.23 cannot be directly integrated into the conventional I_a attenuation laws which work in the 3D domain. The extracted 2D law considers amplification of I_a only along one direction, while the 3D morphologies may amplify ground motion in both orthogonal directions. Nevertheless, some assumptions still allow us to apply this law in the 3D domain. For example, the long ridge may have a curvature variation only across the ridge, while the curvature in the orthogonal direction (along the ridge) is equal to 0. In this specific case, the I_a values should be amplified in only one direction and Equation BE.23 can be applied to predict this amplification. However, most morphologies have different shapes which can even be almost symmetric in the 3D domain. In that case the values of I_a are amplified in both horizontal directions and the curvature should account for the 3D shape. It finally implies that development of mapping proxy should be based on the 3D modelling studies.

Our concept developed in the 2D domain shows a certain similarity with the well-established FSC proxy developed by Maufroy et al. (2015). First, both concepts suggest that the best predictions are yielded by the curvature smoothed (or double-smoothed) over the spatial extent calculated according to Geli's law. Second, the FSC-proxy uses the trendlines which slope variation is similar to our case: the trendline for the low frequency signal has a steeper inclination compared to the one of the low frequency signal. It finally indicates that our concept proposed by the 2D analysis should also be valid in the 3D domain.

Therefore, we further apply this concept in the 3D dynamic studies which are described in *Chapter B.V*. These studies are performed on the model reconstructing the real topographic surface of the Min-Kush target area situated in the Central Tien-Shan. The I_a amplification patterns are studied in both horizontal directions available in 3D. This combined amplification factor is further compared with the 3D general curvature. The studies will allow us to develop a proxy for the mapping of the pure topographic I_a amplification factors based on the smoothed curvature derived from the DEM of the study area. This mapping proxy can be incorporated into the regional Newmark method. This should finally improve the reliability of predictions of the earthquake-triggered landslide susceptibility.

IV. 2D dynamic numerical modelling: combined geological and topographic site effects

IV.1 Models and material sequence

The models used for studying the patterns of the topographical-geological site effects combine real surface with changing material sequence. The studied profiles coincide with those analysed by the topographic modelling (see the position of profiles in Figures BF.10 and BF.24). Therefore, both combined topographic-geological and topographic models have an identical surface restored from the 2010 SPOT DEM. The pair of models attributed to the same studied profile always employs identical network of surface receivers, i.e. these receivers are always attributed to the same geometric nodes in both models.
Figure BF.46 present six profiles studied by the combined topographic-geological modelling. Similar to the topographic studies the total length of profiles is 22.76 km. The constructed models reflect different types of structural features presented in the target area. The longest Profile 1 analyses the crest of anticline, Profile 2 restores the sub-horizontal layering of different material types, Profiles 3 and 4 focus at the central parts of synclines, while Profiles 5 and 6 mainly study the inclined layering. Most of the profiles (Profiles 2, 4, 5 and 6) cross the landslides which activity is probably related to the earthquake triggering that occurred in near-past (see a detailed review in *Section B.II.2*).

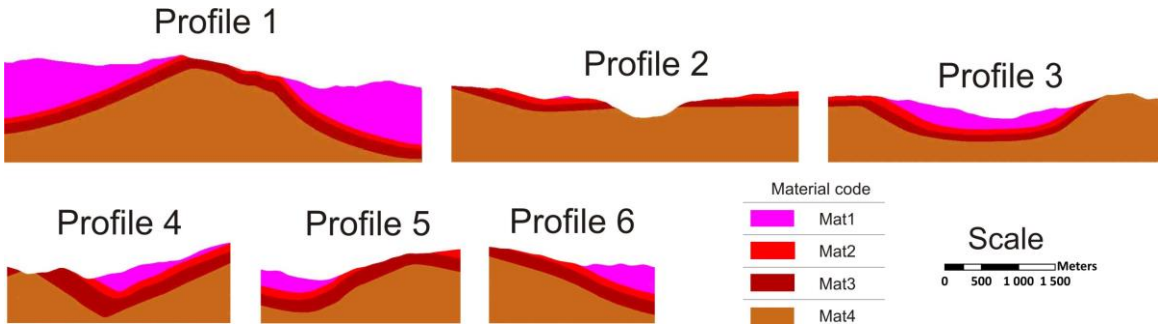

Figure BF.46: Models analysed by the combined topographic-geological dynamic studies.

The analysed material sequence employs four main material types further referred to as Mat1, Mat2, Mat3 and Mat4 (see Figure BF.46). These material types summarize eleven geological formations presented in the target area (see more detailed description of material classification in *Section B.II.5*). Table BT.3 lists the main dynamic properties assigned to Mat1-Mat4. The elastic properties of the given material in the UDEC code is described via three main parameters: density, bulk modulus (K) and shear modulus (G). These last parameters, i.e. K and G, are complexly related to the Young's modulus (E) and the Poisson's ratio (ν) as follows:

$$K = \frac{E}{3(1-2\nu)} \quad \text{(BE.26a)},$$

$$G = \frac{E}{2(1+\nu)} \quad \text{(BE.26b)},$$

The values of E and ν in the equations BE.26a and BE.26b, in turn, are related to the material density, as well as to V_p and V_s. The loose material is normally characterized by the lowest values of K and G. Based on this criterion Mat1 and Mat3 are considered as the loosest material types, while Mat2 and Mat4 represent the hard bedrock. This classification is also valid considering the applied values of V_s: Mat1 and Mat3 have the lowest value of V_s, while Mat2 and Mat4 have the highest V_s values.

Table BT.3: List of the dynamic properties assigned to the analysed material types.

Material code	Density, kg/m^3	V_p, m/sec	V_s, m/sec	Bulk modulus (K), MPa	Shear modulus (G), MPa
Mat1	2200	1000	500	1467	550
Mat2	2400	4000	2200	22912	11616
Mat3	2200	1500	800	3073	1408
Mat4	2200	2500	1300	9592	4056

The main aim of combined topographic-geological studies is to track the amplification of I_a values caused by the pure geological site effects. The targeted parameter in this case is presented by A_g which acts as the pure geological I_a amplification factor. One one hand, the values of A_g cannot be directly extracted from the studied models, as they always combine topographic and geological settings. Thus, our models estimate the value of A_{tg} which shows the I_a amplification incurred by the combined topographic-geological site effects. On the other hand, the pure topographic I_a amplification at each surface receiver has already been studied by us via the parameter termed as A_t (see *Chapter B.III*). It implies that A_g for all surface receivers can be estimated based on corresponding A_{tg} and A_t applying the next equation:

$$A_g = \frac{A_{tg}}{A_t} \qquad \text{(BE.27)},$$

This last equation represents a kind of decoupling procedure, when the combined topographic-geological impact (A_{tg}) is decomposed into topographic (A_t) and geological (A_g) inputs. Meanwhile, there is some critical difference regarding the way to estimate both inputs: A_t directly results from modelling studies, while A_g is laterally estimated based on combined topographic-geological modelling.
As our models cannot be used to directly track the pure geological amplification effects, we first analyse the models with simplified geometry which do not induce the topographic site effects. The next section analyses such models which represent the soft layer of regular shape lying on the domain representing the hard bedrock. The flat and horizontal surface of this model ensures the lack of topographic effects and guarantees that I_a amplification is solely related to the geological settings.

IV.2 Soft layer: spectral amplification and A_g

Figure BF.47 shows the quadratic shape model with dimensions of 1000 m. This model reproduces the soft layer (Mat5) which is horizontally lying on the hard material (Mat6). The soft layer has a regular shape which is characterized by the thickness (H) changing in our models between 10 m and 600 m. Two receivers are installed to perform the acceleration-time recordings: reference and surface receivers (see their position in Figure BF.47). The recorded acceleration-time histories are applied to calculate the corresponding I_a values for two receivers (see Ia_0 and Ia_1). These last parameters are further applied to analyse how the change of model settings impacts the value of A_g (note: $A_g = Ia_1/Ia_0$). The acceleration recordings are also applied in spectral studies, as it is proven that spectral amplification affects the amplification of I_a value.

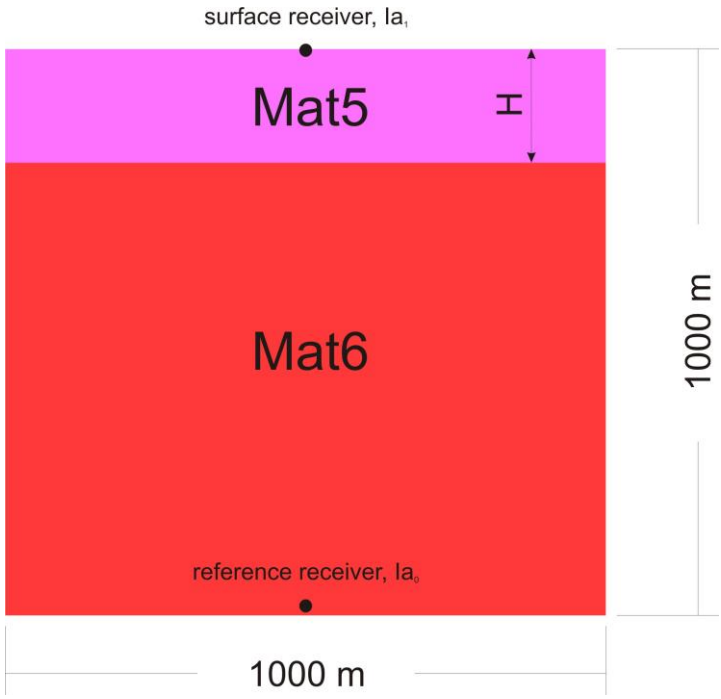

Figure BF.47: Model of a soft layer (Mat5) lying on the domain representing the hard bedrock (Mat6).

All tested variants of Mat5 and Mat6 have a fixed density value equal to 2400 kg/m^3. The values of V_s for Mat5 (Vs_1) are ranging between 500 m/sec and 2200 m/sec, while a factor of 2 is always applied to calculate the value of Vp_1, i.e. $Vp_1=2Vs_1$. The studied variants of Mat6 have the V_s values (Vs_0) ranging from 1000 m/sec to 3000 m/sec, while the same factor of 2 is applied to calculate the value of Vp_0. In all studied models $Vs_1<Vs_0$, as we reproduce the conditions of soft layer lying on the hard material. Thus, the V_s impedance contrast (Vs_0/Vs_1) which is further referred to as the Ivs is manly ranging from 1.25 to 4.4.
The tested input signals represent the Ricker shape shear stress waves with three central frequency values: 1.0, 2.0 and 4.0 Hz (see Figure BF.48a). All these input histories have identical stress amplitudes (see those in Figure BF.48a). The reference acceleration time histories have a varying shape of spectrum (see those in Figure BF.48b). The low frequency signal with Fca=1.28 Hz has the narrowest spectral content, while the Fca=4.95 Hz signal has the broadest input spectrum.

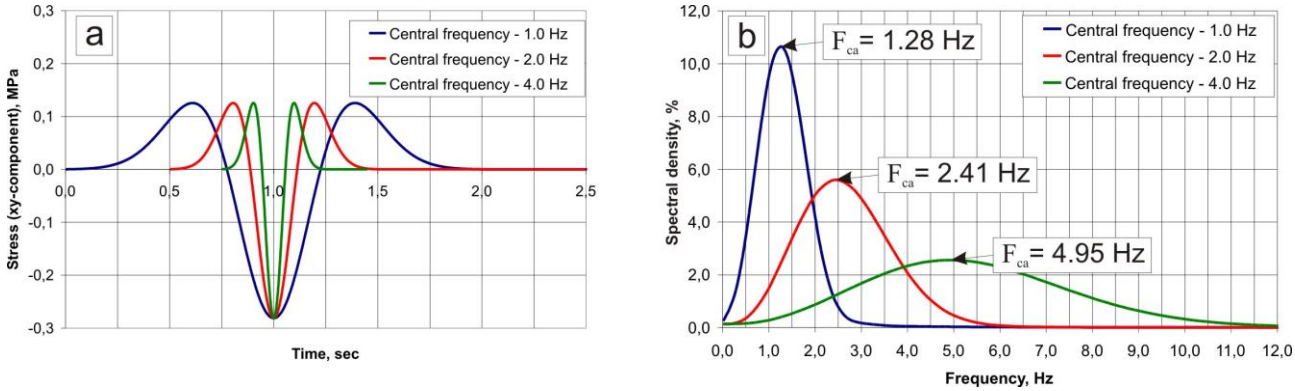

Figure BF.48: Three variants of applied input signals representing the Ricker shape shear stress waves: (a) stress–time histories (xy-component of stress) with changing values of central frequency; (b) input spectrum of acceleration-time histories (x-component).

The data analysis starts with the spectral studies which employ the spectral ratio curves reconstructed in the Geopsy software. In this case the surface acceleration time history is compared with the reference one to estimate the amplified frequency ranges. All modelling scenarios show certain regularity: the extracted spectral ratio curves always have the characteristic shape where several frequencies are amplified and the spectral ratio gradually decreases towards the high-frequency domain. For example, Figure BF.49a shows the curve constructed for model with Vs_0=2200 m/sec, Vs_1=800 m/sec and H=200 m. This curve contains several amplified frequencies referred as F_0 to F_3, while the highest spectral amplification is registered at F_0=1.0 Hz. The observed patterns of spectral amplification follow with links established by previous studies (see, e.g., Aki and Larner, 1970; Borcherdt, 1970; Bard and Bouchon, 1980; Riepl, 1997; Faccioli, 2000). These studies infer that layered half-space, i.e. soft layer, provides amplification at specific frequencies which can be predicted according to next equation:

$$F_n = (2n+1)F_0 = \frac{(2n+1)V_s}{4h} \qquad \text{(BE.28)},$$

where F_0 (Hz) is primary amplified peak, V_s (m/sec) is the shear wave velocity of soft layer (in our case Vs_1), h (m) is thickness of half-space/soft layer (in our case H) and n=0, 1, 2, 3…..
Indeed, in our case F_0=1.0 Hz corresponds to the value calculated by Equation BE.28 for n=0 (note: Vs_1=800 m/sec and H=200 m). The other amplified peaks also coincide with those predicted by Equation BE.28, i.e. $F_1\approx3F_0$, $F_2\approx5F_0$, $F_3\approx7F_0$. Figure BF.49b shows that this shape of spectral ratio curve stays almost the same for varying input signals. This effect is explained by us in *Section B.III.9* where we show that, ideally, this curve is only related to the model geometry and material properties, while the input signal does not affect its shape. The minor differences at high-frequency domain are attributed to the artificial errors: the same difference is observed by us in *Section B.III.9.*
Figure BF.50 further explores the performance of Equation BF.28. Here we plot the amplified frequency values versus the ratio of Vs_1/H for the model with fixed material properties and H changing between 100 m

and 600 m. As it can be seen, the observed spectral amplification is quite reliably predicted by Equation BE.28: F_0 is linked to Vs_1 and H, while F_1-F_3 can be calculated based on value of F_0.

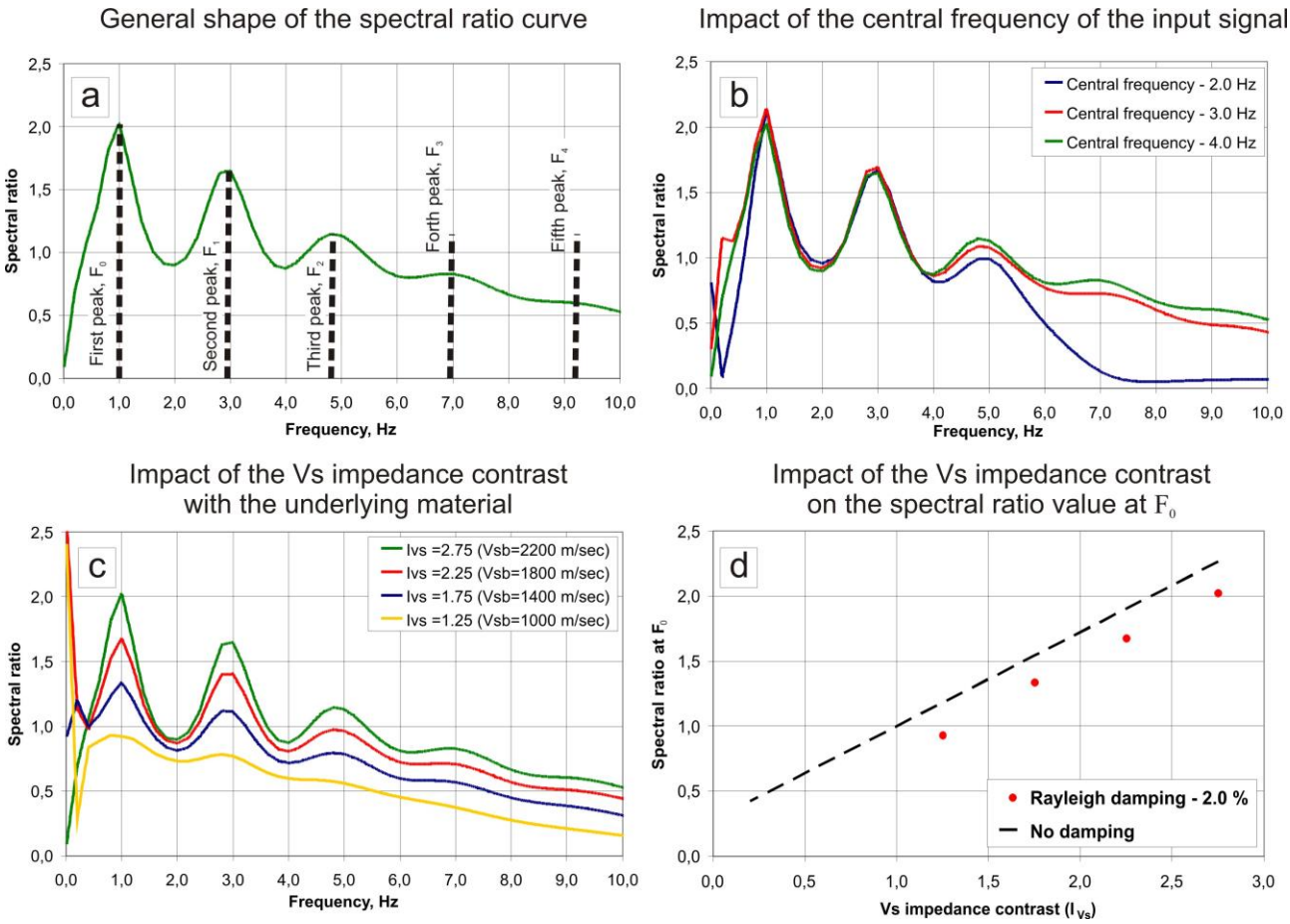

Figure BF.49: (a) Characteristic shape of the spectral ratio curve showing the number of amplified frequencies; (b) impact of changing input signal on a shape of the spectral ratio curve.

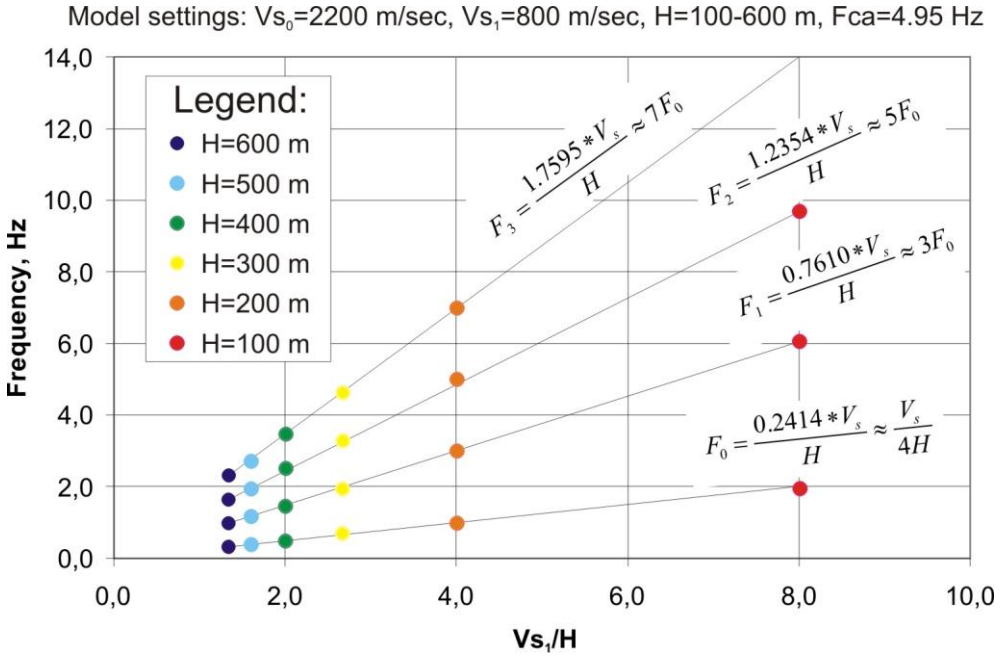

Figure BF.50: Plot of amplified frequency values versus ratio of V_s/H for the tests with changing geometry and fixed material properties.

The spectral studies also explore the impacts related to the changing properties of underlying material when the settings of soft layer are fixed. Figure BF.51a shows the spectral ratio curves constructed for the fixed values of Vs_1=800 m/sec and H=200 m, when Vs_0 varies from 1000 m/sec (Ivs=1.25) to 2200 m/sec (Ivs=2.75). It can be seen, that the change of V_s value for the underlying material does not shift the position of amplified frequency peaks. The impact is expressed via the changed intensity of spectral amplification: the lower values of Ivs result in less intensive spectral amplification.

The spectral ratio curve for the model with Ivs=1.25 (see yellow curve in Figure BF.51a) shows that the surface signal is even deamplified in comparison to the reference recording. This deamplification is explained by the material damping applied in the frame of our studies (Rayleigh damping of 2.0%). Figure BF.51b further analyses how the spectral ratio at F_0 changes in respect to Ivs for both damped and non-damped data. The trend for the non-damped data shows that for Ivs=1 the spectral ratio at F_0 will be equal to 1. It logically shows that in case of absent damping and for Vs_1= Vs_0 no spectral effects at F_0 will be registered. In case when material damping is applied there are two opposed processes which affect spectral amplification: on one hand, the soft layer spectrally amplifies certain frequency ranges, but, on the other hand, the material damping produces a general attenuation of the signal. Thus, in the case of a model with Ivs=1.25 the attenuation impact of damping prevails over the amplification effect of the soft layer: it results in general deamplification of tested signal, while the artefacts of the amplified frequencies can still be revealed (see the minor peaks of yellow curve in Figure BF.51a).

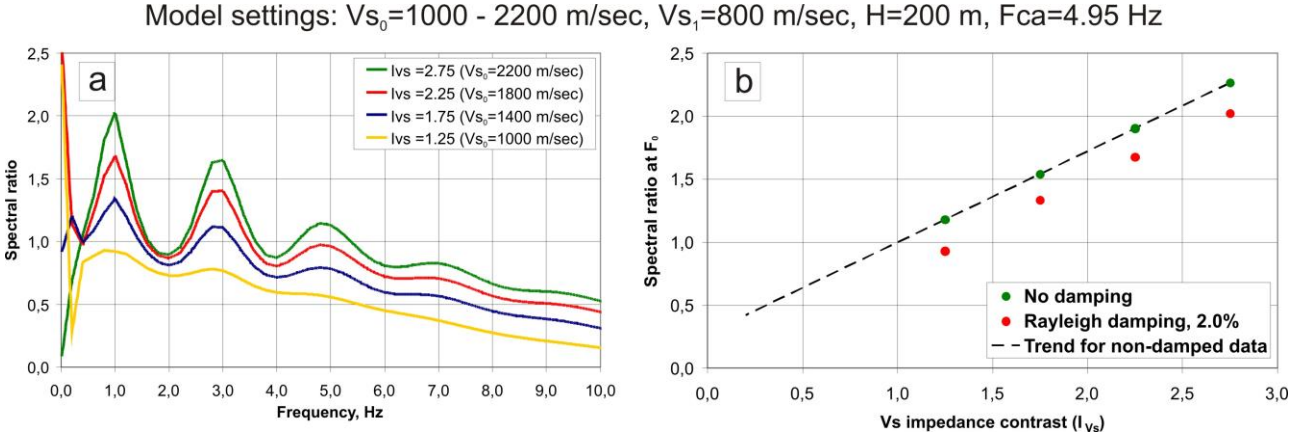

Figure BF.51: (a) Impact of the V_s impedance contrast (Ivs) on the shape of the spectral ratio curve; (b) effect of damping on the value of spectral ratio registered at F_0.

Section B.III.9 establishes a link between spectral amplification and amplification of I_a value which in our models is expressed via A_g=Ia_1/Ia_0. In general, the spectral amplification at the central frequency (Fca) for a given input signal results in an amplified value of I_a for same signal, i.e. A_g>1. This relationship is further investigated through our models when we compare the value of A_g versus the spectral amplification patterns.

Figure BF.52 plots the values of A_g versus changing H for the model with fixed material properties and applying the Fca=4.95 Hz input signal. The shallow thicknesses up to H=25 m are characterizing by increasing A_g values. The peak value of A_g is revealed for H=25 m: according to Equation BE.28 this value of H provides primary amplification at 4.95 Hz, i.e. at the central frequency of the tested signal. This value of H we further refer as the effective thickness (H_e): it shows the thickness of soft layer which yields the peak value of A_g related to the primary amplification at Fca. The part of the curve with H_e<H<2H_e has a negative trend of A_g values reaching the minimum at 2H_e. These patterns are also explained by the spectral effects: for H=2H_e=50 m the primary amplification occurs at 2.5 Hz with the second peak at 7.5 Hz, while Fca=4.95 Hz falls within the deamplified range between those two peaks. The region with 2H_e<H<3H_e has a positive trend, while the peak value at 3H_e is much lower than the one related to H_e: in this case H=3H_e=75 m has F_0≈1.66 Hz and Fca almost coincides to F_1=3F_0=5.0 Hz. The lower value of A_g at 3H_e comparing to the one at H_e is explained by the lower amplification normally observed at F_1 in comparison to F_0 (see, e.g., Figure BF.51a). At H>3H_e the values of A_g are gradually decreasing and at H=250 m the value of A_g starts to be less than 1. It shows that material damping in layers with H>250 m starts to be more pronounced than amplification effects.

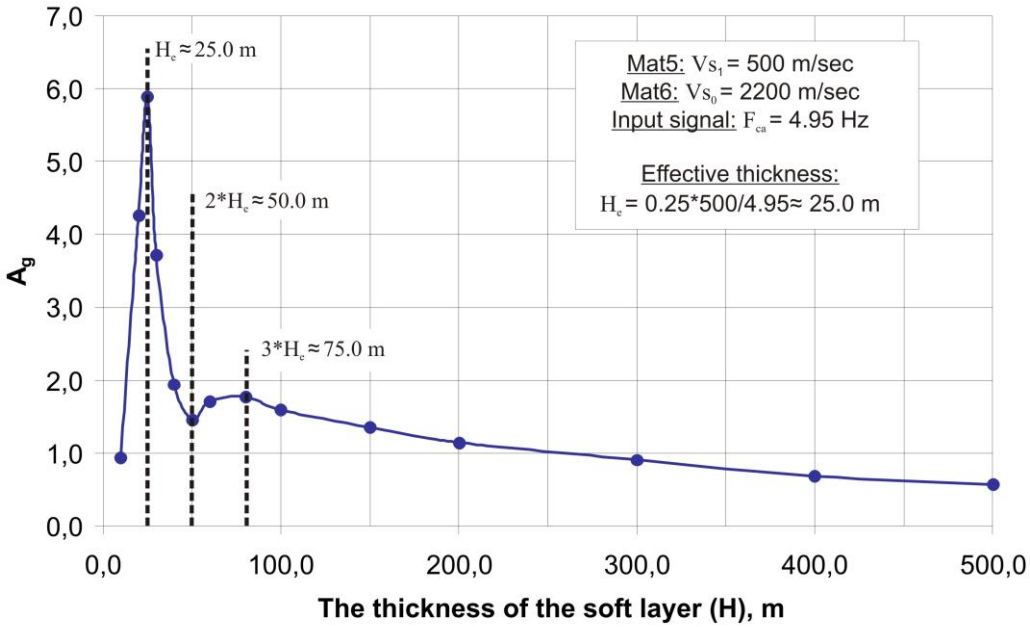

Figure BF.52: Plot of A_g values versus the soft layer thickness (H) for the model with fixed material properties and applying the Fca=4.95 Hz input signal.

Figure BF.53 combines the results of tests with different input signals applied to the same model as studied above. Logically, all curves have shifted values of H_e which can be calculated applying Fca and Vs_1 according to Equation BE.28. These curves also contain recurrent features with respect to the distribution of A_g when characteristic changes occur at H_e, $2H_e$ and $3H_e$. In general, increasing F_{ca} results in lower values of A_g, especially for a part with $H>3H_e$. This specific feature is related to the Rayleigh damping of 2.0% uniformly applied to all frequency ranges: in that case the high frequency signal is more damped than the low frequency one and it finally results in lower values of A_g.

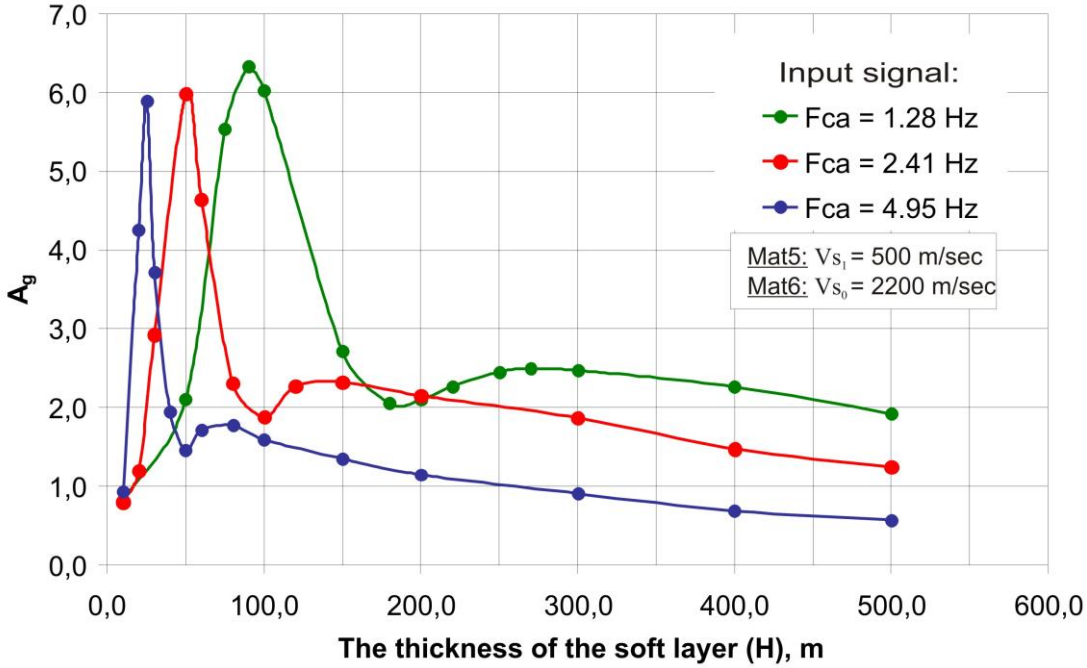

Figure BF.53: Plot of A_g versus H for three tested variant of input signal.

Figure BF.54 shows how A_g is affected by a change of Vs_1 of the soft layer. The models apply unique underlying material (Vs_0=2200m/sec) and test the Fca=2.41 Hz input signal. Figure BF.54a presents the modelling results when three variants of Vs_1 are studied. All curves have the characteristic shape, while the most critical difference is revealed at $H=H_e$. Logically, the peak value of A_g attributed to H_e is directly

proportional to Ivs which is the contrast of V_s between studied materials. Thus, lower Ivs results in lower peak value of A_g, while higher Ivs yields a larger peak value of A_g. Figure BF.54b shows how the change of Vs_1 impacts the value of A_g at H_e (note: in this case Vs_0 and Fca are fixed). It can be seen, that A_g is decreasing according to power law and at Ivs≈1.15 (Vs_1≈1900 m/sec) the value of A_g is already below 1. Similar to the previous examples, at Ivs<1.15 the amplification impact of soft layer becomes less pronounced comparing to signal attenuation due to damping.

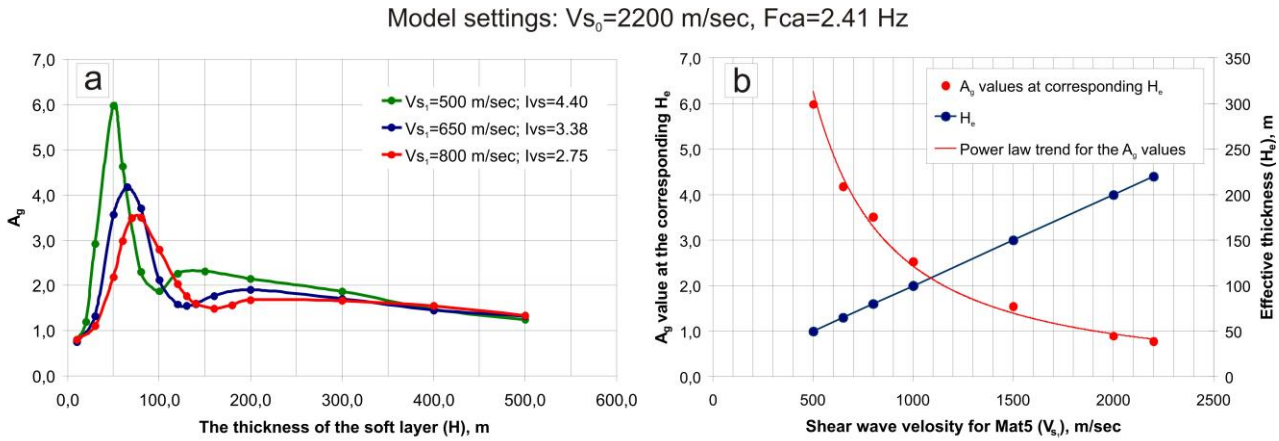

Figure BF.54: (a) Plot of A_g versus H for a changing values of Vs_1; (b) plot of H_e (blue line) and A_g values registered at H_e (red dots) versus varying values of V_{s1}.

Figure BF.55 further studies the effects of changing Ivs on the basis of tests with a fixed value of Vs_1, but with a changing Vs_0. In this case, H_e does not shift, as it is solely related to Vs_1 and H. The observed differences are only related to the modified value of A_g attributed to H_e: a higher Ivs value yields a higher value of A_g and, oppositely, a lower V_s contrast results in a smaller I_a amplification. These patterns are in agreement with the regularity shown in Figure BF.51a: the lower V_s contrast results in less intensive spectral amplification marked by a lower value of A_g. Some critical difference is observed between Figures B.54a and B.55: in the first case when Vs_0 is fixed three curves start to significantly converge after $H>3H_e$, while in the second example with fixed Vs_1 the curves are not really converging. These patterns show that distribution of A_g values is not solely related to Vs_1 and Ivs, but also dependent on the value of Vs_0.

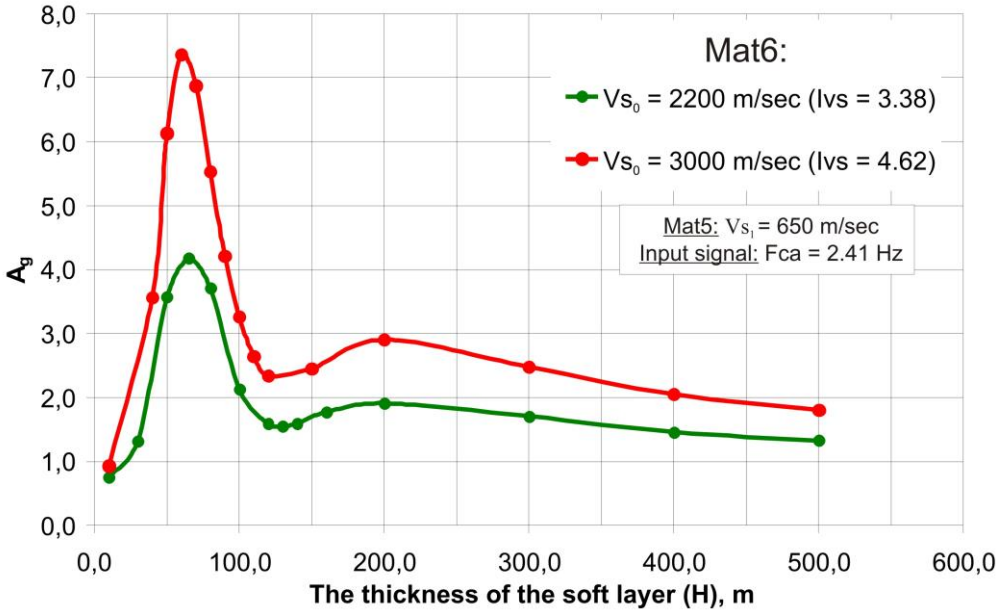

Figure BF.55: Plot of A_g versus H for models with fixed Vs_1 and varying Vs_0.

Thus, our models with simplified and regular geometry allow us to identify the amplification patterns created by the low-velocity layer lying on a harder material. The spectral studies show that this soft layer induces amplification at several frequencies: the primary amplification occurs within the range which can be reliably predicted by Vs_1 and H, while other amplified frequencies are structurally related to this primary peak. The intensity of spectral amplification is complexly determined by Ivs, Vs_0 and material damping. Generally, higher Ivs results in more pronounced spectral amplification, while material damping favours attenuation of signal.

These spectral patterns further affect the distribution of A_g values, i.e. the amplification of I_a due to pure geological effects. The peak values of A_g are always attributed to H_e which is the thickness of soft layer imposing the primary amplification at Fca. According to these rules, the spectral deamplification at $2H_e$ determines the lower value of A_g, while the secondary amplification of Fca at $3H_e$ yields the next peak amplification of I_a values. The tests show that the final distribution of A_g values is complexly determined by a set of factors which include Vs_0, Vs_1, Ivs, H, material damping and Fca. Most involved parameters can act as convenient regional predictors, as their mapping can easily be performed based on the known distribution of material properties and, in case of the Fca, on the basis of general seismological descriptors. Nevertheless, the relationships between A_g and these parameters are very complicated. This complexity does not allow us to produce simplified prediction laws which can be applied to a regional mapping of A_g. The most probable option in this case is to predict the mean values of A_g based on the mapped distribution of the selected affecting factors. The studies show that the most critical input to assess the final value of A_g is related to Ivs which is the ratio of Vs_0/Vs_1. This parameter can be conveniently mapped based on the digital geological map and applying the known distribution of V_s values. Therefore, this last parameter is in the focus of our analyses, while the links between A_g and the other impacting factors are also explored.

The simplified geometry of soft layer ensures that amplification effects are solely related to the pure geological inputs. The combined topographic-geological models are always characterized by a coupling of geological and topographic effects which cannot be directly isolated. Moreover, the geological effects in these models are more complicated, as numerous patterns of wave reflection/refraction/diffraction are created by the inclined contacts between different material types. In the next sections we review the general patterns of the geological site effects observed in our combined topographic-geological studies. The special focus of our analyses is the prediction of the regional distribution of A_g values based on the factors that were outlined as significant by the models with simplified geometry.

IV.3 Soft material: longer shaking and PGV/PGA amplification

The shear waves propagating through the material sequence easily travel from the hard material to the soft one, while in the opposite way they are subjected to reflection/refraction due to the V_s impedance contrast between the materials. Thus, the seismic energy is entrapped within the material with lower value of V_s. This process is directly related to the impacts of the geological site effects which result in longer duration of seismic shaking and amplification of peak ground motion characteristics.

Profile 3 shown in Figure BF.56 presents one of the best models to demonstrate the patterns of the geological site effects. This model includes at the syncline axis composed of Mat1 which has the lowest value of V_s within the studied material sequence (see the table of properties in Figure BF.56). Mat3 presents the next softest material which is sandwiched between Mat2 and Mat4 that are characterized by the highest V_s values. Thus, the structural position of Mat1 and Mat3 favours to entrapment of seismic energy. Figure BF.56 shows this entrapment through a set of multi-temporal x-velocity cross-sections covering 2.5 sec of modelling time. These cross-sections start at T=1.5 sec when seismic energy enters Mat3 and finish at T=4.0 sec when the main front of seismic energy is already reflected back from the model surface and is generally attenuated.

The wave entrapment within Mat3 can already be clearly seen at T=2.0 sec (see the dashed rectangles). At T=2.1 sec this entrapment results in 3-4 times higher PGV values registered at the surface of Mat3 in comparison to the top of neighbouring Mat 4 (compare the PGV values in the right part of the velocity cross-

section for T=2.1 sec). The clear patterns of wave entrapment and focusing in Mat1 can be observed starting from T=2.5 sec. The most impressive example of these patterns is presented by the last cross-section (see T=4.0 sec). At this moment the seismic energy in Mat2, Mat3 and Mat 4 is generally attenuated. Meanwhile, the seismic shaking within Mat1 is still important, as PGV values within Mat1 are 5-7 times higher than those in other materials.

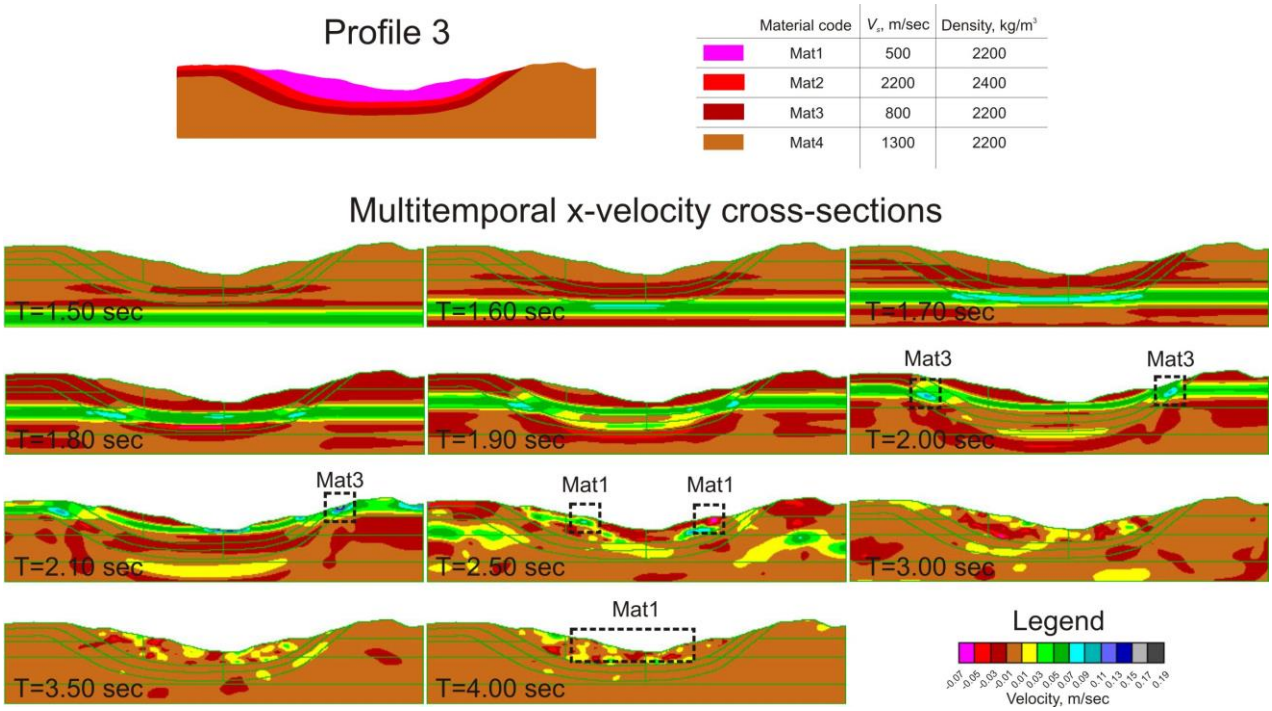

Figure BF.56: Combined topographic-geological model for Profile 3 together with multitemporal x-velocity cross-sections covering dynamic time between T=1.5 sec and T=4.0 sec (dashed rectangles denote the patterns of entrapped waves).

Figure BF.57 shows additional results for Profile 3. Here, the PGA amplification and altered duration of seismic shaking are analysed. The x-component accelerograms with associated PGA values (in terms of g) are shown for selected receivers situated withing different materials. In these analyses P3.5tg is considered as reference receiver as it is situated on a flat surface and on the hard bedrock represented by Mat2.

The comparison between acceleration recordings shows that the receivers situated on Mat1 and Mat3 (see P3.11tg, P3.17tg, P3.25tg, P3.32tg and P3.37tg) are generally characterized by a 3-5 times longer duration of seismic shaking compared to the reference P3.5tg. The receivers situated on the harder Mat2 and Mat4 (P3.35tg and P3.41tg) are characterized by a much shorter shaking which is even comparable to those registered at the local reference P3.5tg. The most expressive secondary shaking in terms of registered peak values is observed for P3.25tg. This receiver is situated above the horizontal contact between Mat1 and Mat2 and such contacts produce much intensive back-reflection of seismic energy. Oppositely, the inclined contacts at the valley rims (P3.11tg and P3.32tg) result in less expressive reflections, even though the secondary shaking is still important.

The analysis of registered PGA values shows certain regularity. Thus, the middle part of the valley composed of Mat1 (P3.17tg and P3.25tg) is characterized by PGA values that are amplified with respect to reference receiver by factors of 1.17-1.26. The PGA at P3.17tg is 10% higher than the PGA at P3.25tg: this can be explained by the coupled effects of geology and topography, as P3.17tg is situated on the hilltop and P3.25tg is situated in the topographic depression. The borders of the valley (P3.11tg and P3.32tg) are characterized by a relative PGA deamplification of about 0.71-0.85: as it will be shown in the next sections, the inclined contacts at the valley borders favour a general deamplification of seismic shaking.

The highest relative amplification of PGA marked by a factor of 1.94 is registered for Mat3 (P3.37tg). Interestingly, this material has a shorter secondary shaking compared to Mat1. Nevertheless, Mat3 imposes a much more intensive PGA amplification. These patterns can be explained through the structural settings. The layer composed of Mat3 is situated between two hard material types referred to as Mat2 and Mat4, while the thickness of Mat3 is much smaller than the one of Mat1. The lower thickness of Mat3 further results in a less prolonged secondary shaking, while more intensive PGA amplification is probably explained by wave focusing between to harder layers.

The receivers situated on the hard materials (P3.35tg and P3.41tg) are generally affected by the lateral impacts of topography. Thus, P3.35tg situated on the same Mat2 as the reference P3.5tg is marked by a relatively deamplified PGA value (factor of 0.68). This deamplification is explained through the position of P3.35tg which is situated on the inclined slope favouring to signal attenuation, while P3.5tg is located on the flat surface. A coupled effect of topography can also explain the relative PGA amplification observed at P3.41tg (factor of 1.36): this receiver is situated on the hilltop which should finally result in general signal amplification.

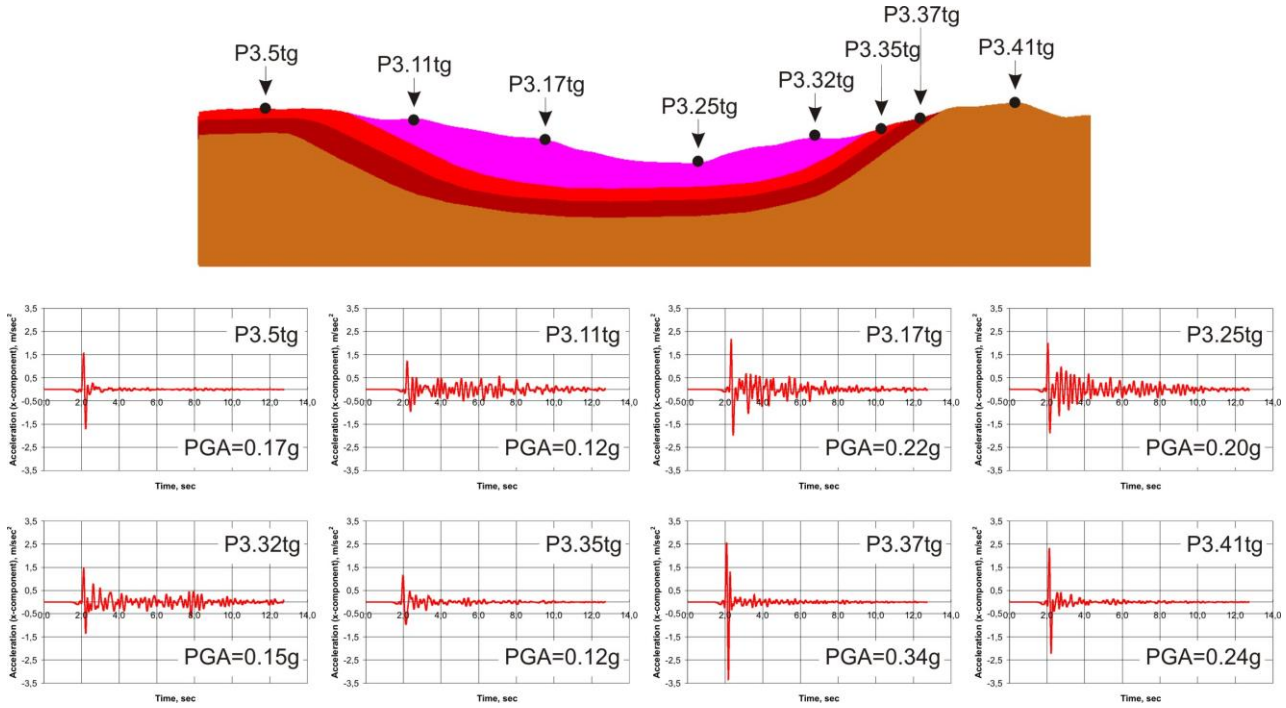

Figure BF.57: Acceleration time histories (x-component) and PGA values registered at selected surface receivers of Profile 3.

Thus, our studies show that the contrast of V_s between soft and hard materials favours entrapment of seismic energy within domains with lower V_s values. This entrapment further results in 3-5 times longer duration of seismic shaking which is impacted by structural settings, like the thickness of layer and the inclination of underground contacts. The analysis of PGA amplification reveals its complex link with the material properties, the structural position of the layers, the underground geometry and the additional topographic site effects. The last parameter is important, as certain combinations of topographic settings and the underground layer geometry can produce specific patterns when the relative PGA deamplification or amplification can reach 20-30%.

Both consequences of geological site effects, i.e. changed duration of seismic shaking and modified PGA, directly affect the value of I_a, as it is calculated based on the acceleration time history. This means that A_{tg} is also complexly depending on the combined geological, morphological and structural settings. These links are further studied by us below.

IV.4 Coupled effects of topography and geology: distribution of A_{tg}

The combinations of variable surface topography and geological settings are unlimited. The amplification effects resulting from such interactions are strongly varying. They depend on specific combinations of morphologic, geological and structural settings. Therefore, these amplification patterns can normally be determined by the site-specific studies. However, we aim at analysing general amplification principles rather than studying specific cases. The general principles can later be used to develop regional proxies allowing us to map the amplified values of I_a.

Figure BF.58 presents two snapshots from the longest Profile 1. These snapshots zoom to the valleys situated to both sides of the anticline axis. The similar structure, i.e. the valley composed of soft Mat1, is presented in Figures BF.56 and BF.57. Here we focus on the effects attributed to the valley borders. The data analysis uses the acceleration time histories and A_{tg} values recorded close to the contact between Mat1 and Mat2.

Both snapshots are characterized by a different degree of angular conformity between the model surface and the underlying contacts. The surface and the contact are conformable when they are parallel to each other and totally non-conformable when the difference between the slope angle and the inclination of the contact is equal to 90º. For instance, the surface between P1.15tg and P1.17tg is almost parallel to the contact, i.e. this part of the surface is conformable with respect to the contact. The surface between P1.40tg and P1.42tg and the underlying contact are almost non-conformable, as the difference between the slope angle and the contact inclination is larger than 50º. The other parts of model surface have an angular difference of about 5-20º that represents an intermediate level of conformity between the surface and the underground contact.

The analyses of recorded data show that receivers situated in the conformable surface are subjected to a more intensive secondary shaking (e.g., compare acceleration recordings for P1.14tg versus P1.16tg). This shaking originates from back-reflection that occurred at the underlying contact: the conformable slopes directly face these reflected waves, while the non-conformable surface seems to be located in a “seismic shadow” with respect to these reflections. This last effect, i.e. seismic shadowing, is clearly proved by the analysis of the acceleration recordings of P1.41tg versus P1.43tg. The first receiver (P1.41tg) stays in the shadow with respect to the underlying contact, as the corresponding angular non-conformity is larger than 50º. The second receiver (P1.43tg) is situated on a more conformable surface, as the respective angular difference is about 10º. This difference in surface conformity results in a significant variation of peak values: PGA at P1.41tg is almost two times smaller than at P1.43tg. In this case the modification of the secondary shaking is less obvious compared to the case of P1.14tg versus P1.16tg.

The amplification effects on a conformable surface have a direct impact on A_{tg} which is generally 25% higher than those values at less conformable surface (e.g., compare A_{tg} for P1.14tg versus P1.16tg). The strongest difference is revealed for the case when the two extreme variants are compared: A_{tg} values on highly non-conformable surfaces are up to 3.8 times smaller than those on almost conformable surfaces (e.g., compare A_{tg} for P1.41tg versus P1.43tg). The variation of A_{tg} in this last example is quite impressive and it shows the importance of related inputs.

Figure BF.58 also shows that the seismic energy is generally attenuated close to the valley borders. This attenuation can be expressed by the shorter duration of the seismic shaking (compare acceleration recordings for P1.14tg-P1.18tg with the one at P1.21tg) or by the significantly deamplified PGA (compare those values for P1.40tg-P1.43tg with the one at P1.37tg). Such attenuation patterns are related to the fact that the seismic energy more easily propagates through the horizontal contacts, while the inclined contacts at the valley borders hinder such transfer finally producing the attenuation of signal. Therefore, the receivers closest to the contact between Mat1/Mat2 (P1.21tg and P1.37tg) are marked by lower A_{tg} values compared to receivers situated farther away from this contact. These effects are less expressed in the case when contact inclination does not change: the difference of A_{tg} values is not more than 40% (compare A_{tg} for P1.21tg versus P1.17tg). A stronger difference is observed for the cases when the contact inclination becomes stepper close to surface: the difference of A_{tg} is larger than 50% and can reach the factor of 5 (compare A_{tg} for P1.37tg versus P1.41tg/P1.43tg). Nevertheless, despite this attenuation, A_{tg} at Mat1 is generally higher than A_{tg} on the neighbouring bedrock which is represented by Mat2 (e.g., compare A_{tg} for P1.35tg versus P1.37tg).

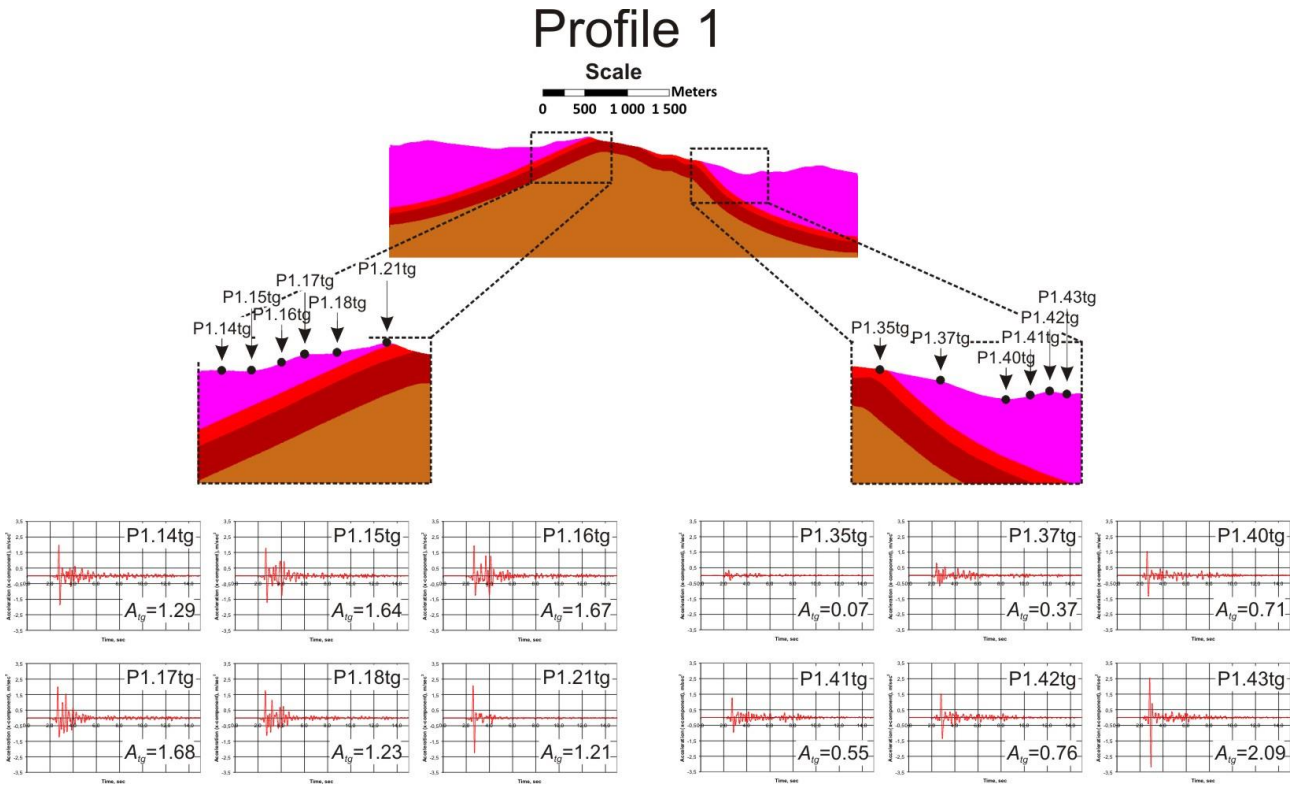

Figure BF.58: Two snapshots from the longest Profile 1 showing the acceleration time histories and A_{tg} values recorded at the rims of the valleys composed of Mat1.

The hill between P1.40tg and P1.43tg in Figure BF.58 presents an illustrative example of how topographic and geological effects can interact with each other. In the left slope the topographic amplification results in higher A_{tg} at the hilltop compared to its basis (compare A_{tg} for P1.42tg versus P1.40tg). A completely different distribution is revealed for the right slope: the hilltop is marked by a 2.7 times smaller value of A_{tg} compared to its basis (compare A_{tg} for P1.42tg versus P1.43tg). This clear difference of amplification patterns over a 300 m long hill is explained by the different degrees of conformity on both hill slopes. Thus, the left slope is marked by 50º of non-conformity with respect to the underground contact, while the right slope is almost conformable with this contact. This finally leads to the situation when along the right slope the geological site effects significantly outweigh the input of topography, as the hill basis is significantly amplified with respect to the hilltop. The left slope is much less subjected to these effects, even though some minor patterns can be revealed: the mid-slope is slightly deamplified with respect to the hill basis (compare A_{tg} for P1.41tg versus P1.40tg).

The other studied models also demonstrate how the combination of topographic and structural settings produces specific attenuation or amplification patterns. Figure BF.59 presents snapshots from Profiles 2, 4, 5 and 6 where the distribution of A_{tg} values highlights the coupled topographic and geological effects. Thus, the left snapshot of Profile 2 shows a small hill composed of Mat1 which is situated above the hard material (Mat2). This hill is generally marked by amplified A_{tg} values, while the highest value is found on the hilltop (relative crest/base amplification is at 2.5). The right snapshot of Profile 2 shows another soft material (Mat3) where the relative amplification of the convex part can reach the factor of 1.6 (compare A_{tg}=1.69 versus A_{tg}=1.06). The most illustrative example is presented by the left snapshot of Profile 4, where A_{tg} at the hilltop is almost 3.7 times larger than the one at the hill basis. Profiles 5 and 6 present some convex morphologies composed of different material types where the relative crest/basis amplification mainly ranges form 1.1 to 2.0.

The impacts of the inclined bedding can be studied on the basis of Profiles 4, 5 and 6. Thus, A_{tg} values for Mat1 in Profile 4 are generally lower than those values at other studied profiles. We relate this feature to the model geometry when the layers of Profile 4 reveal steeper inclination compared to the other models. Moreover, the axial part of the syncline with horizontal bedding of the layers is very poorly developed. All these settings of Profile 4 strongly hinder the transfer of seismic energy to Mat1. This finally yields relatively low values of A_{tg} compared to other studied models.

Profile 6 presents a good example to estimate the distance over which such inclined bedding affects the values of A_{tg}. Thus, this profile has three hills of regular and almost resembling shape. All these hills are made of unique Mat1. The pure topographic studies performed with the same model showed that these three hills are characterized by a comparable amplification of I_a values expressed via A_t (see *Chapter B.III*). The combined topographic-geological modelling shows a different distribution of I_a amplification factors, i.e. A_{tg}. Thus, the first hill which is the closest to the contact outcrop has a reversed distribution of A_{tg}: the right basis is more amplified compared to hilltop (A_{tg} = 0.62 for the hilltop and A_{tg} = 0.89 for the right base). The other hills are marked by a more characteristic distribution: the values of A_{tg} at hilltops are 2-3 times larger than those values at hill basis. Thus, we assume that the lateral impact of the inclined contact becomes insignificant near the second hill, as the topographic patterns of this hill are generally not disturbed. The horizontal distance between the contact outcrop and the second hill is 500 m, while the vertical distance between the same hill and the underground contact is around 250 m.

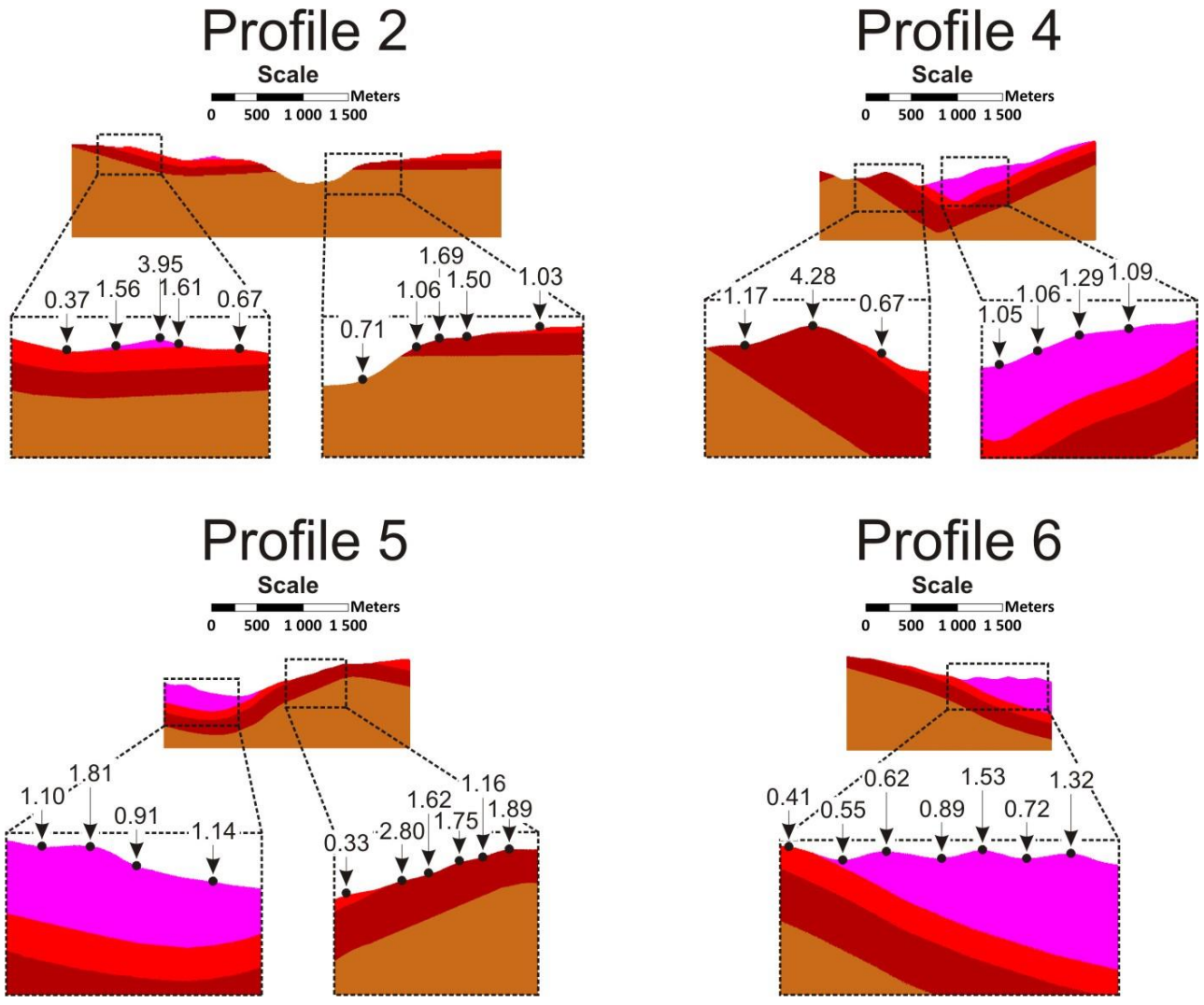

Figure BF.59: Snapshots to Profiles 2, 4, 5 and 6 presenting the patterns of coupled topographic and geological site effects via distribution of A_{tg} values.

Thus, our studies show that the final value of A_{tg} is related to the set of topographic, geological and structural settings. The V_s impedance contrast generally favours I_a amplification within soft material types, while the final value of A_{tg} can be significantly modified due to lateral impacts. For example, the inclined layer dipping generally results in signal attenuation. This attenuation further yields lower A_{tg} values, especially near the valley borders compared to the middle parts of valley. Significant impacts can originate from particular combinations of surface topography with underground layer geometry. The studies show that such specific patterns can result in 4-5 times lower/higher values of A_{tg} which can vary within a distance of 250-300 m.

The inputs of topographic site effects can generally be tracked over a distance of 500 m far from the contact outcrop or 250 m above the underground contact. Closer to contacts the pure geological effects start to considerably outweigh the topographic inputs.
The large variation of A_{tg} values is generally related to the numerous patterns of reflection/refraction/diffraction created by the inclined contacts, and by the interaction of topography and underground layer geometry. The nature of such processes is not analysed by us in more detail as it is not the primary focus of our studies. The reflected and refracted waves do not only impact the A_{tg} values, they also significantly modify the spectral properties of the seismic shaking. The variations of such spectral patterns and their links with model settings are very sensitive to site-specific conditions. The next section provides a general overview of observed spectral patterns and compares them with the results of the pure topographic studies.

IV.5 Spectral patterns: geological and topographic amplification

The spectral amplification imposed by the soft layer was first presented in *Section B.IV.2* where we tested the models with changing layer thickness and varying material properties. It was demonstrated that an idealized soft layer regularly amplifies several frequency ranges. According to Equation BE.28, the primary amplification (F_0) is quite reliably predicted through the thickness of layer (H) and the V_s of studied material. The other amplified frequencies (F_1, F_2… F_n) can be predicted on the basis of F_0, when $F_n=(2n+1)F_0$.
For our main research we use models with more complicated geometries with inclined layering and a complex interaction between surface topography and underground geology. These combinations produce the cases for which the observed spectral amplification can significantly differ from the idealized predictions. Therefore, in Figure BF.60 we apply selected receivers from Profile 3 to compare the registered spectral amplification with the one predicted according to Equation BE.28 (see F_0, F_1 and F_2 attributed to all graphs in Figure BF.60). The value of H in this case corresponds to the thickness of the soft material below any given receiver (note: this thickness is measured perpendicularly to the contact bedding). Additionally, the pure topographic spectral curves are presented for all receivers. These graphs provide an option to compare the topographic and combined topographic-geological data.
The study of presented curves suggests that both modelling cases are often characterized by the overlapping amplification patterns. For example, the P11-P32 receivers in the topographic studies are systematically amplified at low frequencies of 0.6-0.8 Hz. This range coincides with the geologically amplified peaks: i.e., for H=150-260 m and V_s=500 m/sec the predicted primary amplification is at F_0= 0.5-0.8 Hz. Due to that overlapping the topographic and geological peaks at frequencies below 1.0 Hz cannot be easily discriminated.
The higher frequency domain can also contain the overlapping amplified peaks (see, e.g., the range of 1.7 Hz at P14, 2.6 Hz at P17, 4.0 Hz at P37, etc.). Nevertheless, here the topographic and geological inputs can be discriminated at some receivers. For example, P11 is situated on the hilltop which is marked by an amplified peak at around 1.8-1.9 Hz attributed to pure topographic effects. The same peak is yielded by the topographic-geological model: we assume that this peak is related to the topographic amplification, as it lies between F_1 and F_2. The similar conclusions can be made, e.g., for P32: both studies have unique amplification at 1.9 Hz which can be attributed to the topographic amplification.
The inputs of geology and topography can be best discriminated at P21 and P25 which are situated in the topographic depression. The pure topographic studies showed a presence of small peak at 0.8-0.9 Hz, possibly related to the neighbourhood effects (see *Chapter B.III* for more details). Therefore, the peaks above 1.0 Hz observed in the combined modelling can reliably be attributed to the geological site effects. Meanwhile, only one peak can be directly explained through the predicted geological amplification (see F_2=4.1 Hz in P25). The position of the other peaks is shifted from those of F_0, F_1, F_2 and this shift can be significant. Similar peaks of unclear origin also appear for other receivers (see, e.g., 3.9 Hz in P11, 5.2 Hz in P14, 3.8 Hz in P17, etc.). Such peaks might be due to specific reflection/refraction patterns created by the curved contact between Mat1 and Mat2. These issues should further be clarified via additional tests. We do not perform these tests here, as they investigate site-specific issues which are beyond our research scope.
The spectral curve yielded for P37 by the topographic-geological model shows that the whole range after 2.5 Hz is significantly amplified. At the range of 4.0-4.5 Hz the topographic peak coincides with F_0. Another range amplified due to the topographic inputs is at 7.0-7.5 Hz. This frequency in the combined model is marked by an unusually high value of spectral ratio. This indicates that geological effects might contribute to

amplification at this frequency. It should be highlighted that the range of 7.0-7.5 Hz does not correspond to the predicted F_0 or F_1. Therefore, we assume that this amplification is due to the waves reflected or refracted from the inclined contacts between Mat3/Mat2 or Mat3/Mat4. The intensive spectral amplification registered within Mat3 results in the highest values of A_{tg} and A_g, even compared to Mat1 which is marked by a lower V_s value (see the distribution of A_g values in the next section).

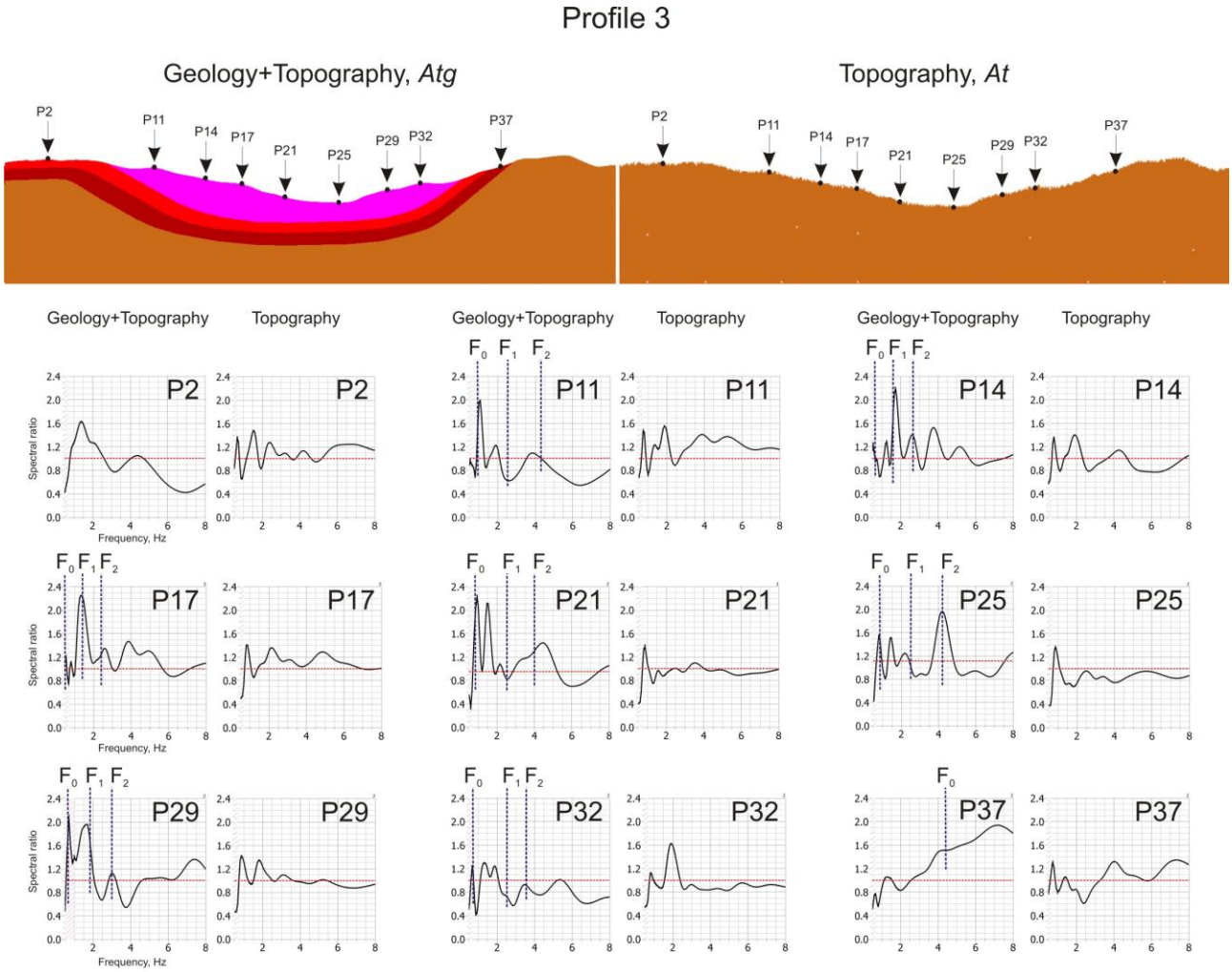

Figure BF.60: Selected surface receivers from Profile 3 together with topographic-geological and pure topographic spectral curves (F_0, F_1, F_2 are the predicted peaks produced by the underlying soft material).

Thus, we show that the combined topographic-geological spectral patterns can generally be decomposed on the basis of topographic and geological information. That discrimination is not possible when both inputs spectrally overlap, as it is observed in the case of the low frequency range in our models. Otherwise, it is proved that topographically amplified peaks can also be registered by the combined modelling. The decomposition of the topographic-geological effects yields an important conclusion regarding our way to calculate A_g: it partially proves that $A_g=A_{tg}/A_t$ is valid approach to calculate the pure geological I_a amplification factor.

In *Section B.III.8* we show a direct link between spectral amplification and final value of I_a. This link imposes that, e.g., Mat3 should have high values of A_{tg} and A_g, as this material is characterized by intensive spectral amplification. Meanwhile, we also show that observed amplification often cannot be reliably attributed to F_0-F_n, predicted according to equation BF.28. In this case, the amplified peaks are most probably related to the secondary reflections/refractions. The influence of lateral spectral effects on final value of A_g is determined by the site conditions and cannot be generalized. In the next sections we analyse the distribution of A_g over studied models and explore the ways how the mean A_g can be predicted by structural or dynamic parameters.

IV.6 Distribution of A_g and its dependence on structural settings

Figure BF.61 presents six studied models together with A_g values registered at selected receivers over different material types. The values of $A_g=A_{tg}/A_t$ express the pure geological I_a amplification factors estimated on the basis of the results of the two studies. As it can be seen, the values of A_g can significantly vary even within the same material types. Nevertheless, some regularity can be observed. Thus, the softest materials Mat1 and Mat3 are generally characterized by higher amplification factors which are explained by the higher V_s impedance contrast with respect to the underlying hard materials. The highest values of A_g are registered in Mat3. This might be explained by the structural position of Mat3: this layer is situated between two hard materials which finally results in intensive focusing of seismic energy. Two hard materials (Mat2 and Mat4) are generally marked by lower A_g values, while the lowest values are attributed to Mat2.

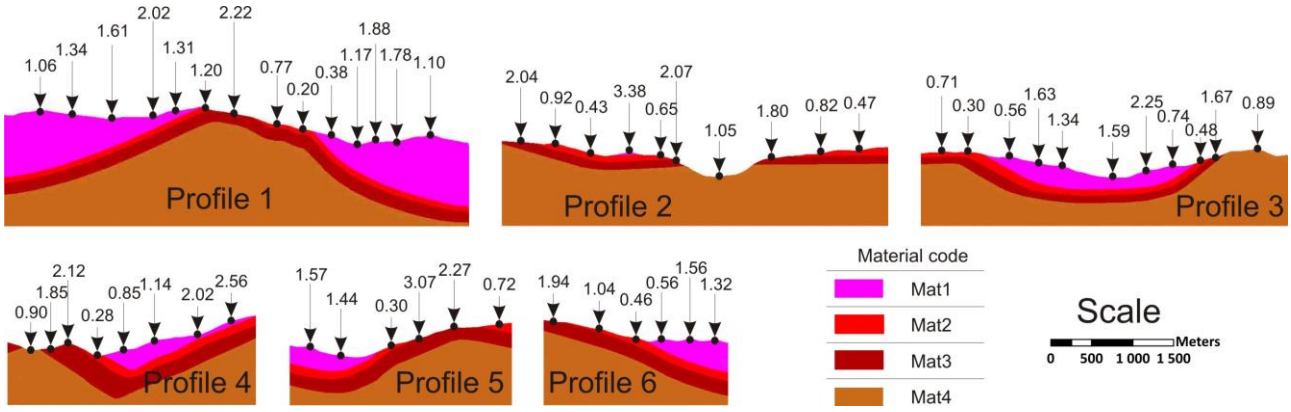

Figure BF.61: Distribution of the A_g values registered over six studied models (note: $A_g=A_{tg}/A_t$).

In the preceding sections we have demonstrated that signal amplification is strongly related to the structural settings, including the thickness of the soft material and the inclination of underground contacts. Figure BF.62a analyses how the thickness of Mat1 affects the final value of A_g (see red dots). The given distribution is further compared with A_g values yielded by tests with an idealized soft layer (see blue curve). These tests with soft layers use the same input signal as the one applied in our combined models, i.e. the Fca=4.4 Hz. This signal corresponds to the Ricker shape shear stress wave with the central frequencies of 1.4 and 3.5 Hz. Thus, Figure BF.62a shows that the tests with a soft layer produce a peak value of A_g=5.89 when its thickness is equal to H=28 m. As is explained in *Section B.IV.2*, this maximal amplification is yielded when $H=H_e=V_s/(4*Fca)$=28 m. The tests with combined models show a less regular distribution of A_g, even though some individual patterns indicate that thickness of Mat1 close to H_e can produce significant amplification (see, e.g., A_g=3.84 at H≈25 m). In general, the values of A_g for any fixed H are significantly deviating, sometimes with the factor of 2-3 between the lowest and highest values. These results imply that other factors can provide a stronger input compared with the thickness of soft sediments.

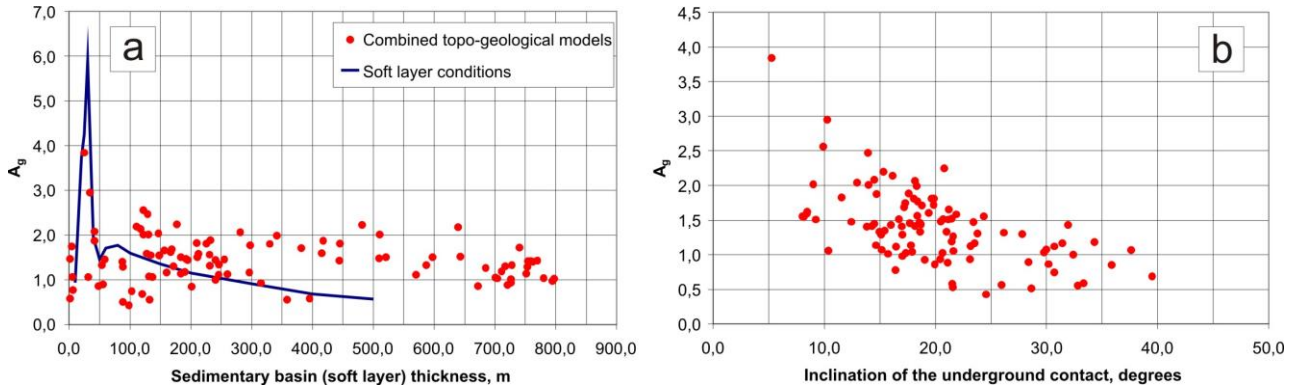

Figure BF.62: (a) Plot of A_g values versus changing thickness of Mat1 (red dots – data from combined models; blue curve – the tests with soft layer); (b) plot of A_g values versus inclination of underground contact between Mat1 and Mat 2.

Figure BF.62b plots the same A_g values versus the inclination of the underground contact between Mat1 and Mat2. The data have a negative trend which suggests that more inclined contacts produce lower values of A_g. Thus, a comparison of data indicates that the change of contact inclination from 10º up to 30º generally yields two times smaller values of A_g. This trend is logical and follows the links established in *Section B.IV.4*, where we showed that inclined contacts generally favour signal attenuation.
Meanwhile, such structural settings cannot act as convenient regional predictors, as their mapping would demand extensive data and involve laborious mapping techniques. In this case the use of the material dynamic properties (e.g., V_s) would be a better option. Their mapping may easily be performed on the basis of the digital geological maps, if the regional distribution of these parameters is known. Such relationships between A_g and dynamic properties are studied in the next section.

IV.7 Mean A_g versus dynamic properties

The distribution of A_g values within four materials is statistically analysed in Figure BF.63. The main studied parameters include the mean value of A_g (A_{gm}) and the standard deviation (D_s). During these analyses some extreme values reflecting the specific amplification patterns are filtered out. For example, the extremely high A_g = 3.38 within Mat1 of Profile 2 (see Figure BF.61) is not included into the analyses, as these specific structural settings are only met in Profile 2.
Thus, the highest A_{gm}=1.94 is attributed to Mat3 (D_s =0.24). The nature of this peak amplification within Mat3 is explained in *Section B.IV.5* where we show that its structural position between two hard materials results in significant amplification. The second highest A_{gm} =1.39 is attributed to Mat 1 (D_s=0.42). The lowest A_g values within Mat1 are normally registered near the valley borders and above the inclined contacts, while the highest A_g values are attributed to the middle parts of the valley with the horizontal bedding of underlying contacts. The statistical analysis for Mat4 returns A_{gm} =0.90 and D_s=0.14: it shows that Mat4 almost does not modify the original values of I_a. This is explained by the fact that Mat4 does not have any underlying material which could induce attenuation or amplification of I_a. Logically, the lowest value of A_{gm} =0.73 is attributed to Mat2 (D_s =0.34), as it represents the hardest material among the studied sequence. The lowest values of A_g for Mat2 are observed over Profiles 1 and 5 (see A_g = 0.2-0.3 in Figure BF.61). However, in some particular cases Mat2 can even amplify I_a (see, e.g., A_g=1.2 in Profile 1; Figure BF.61).

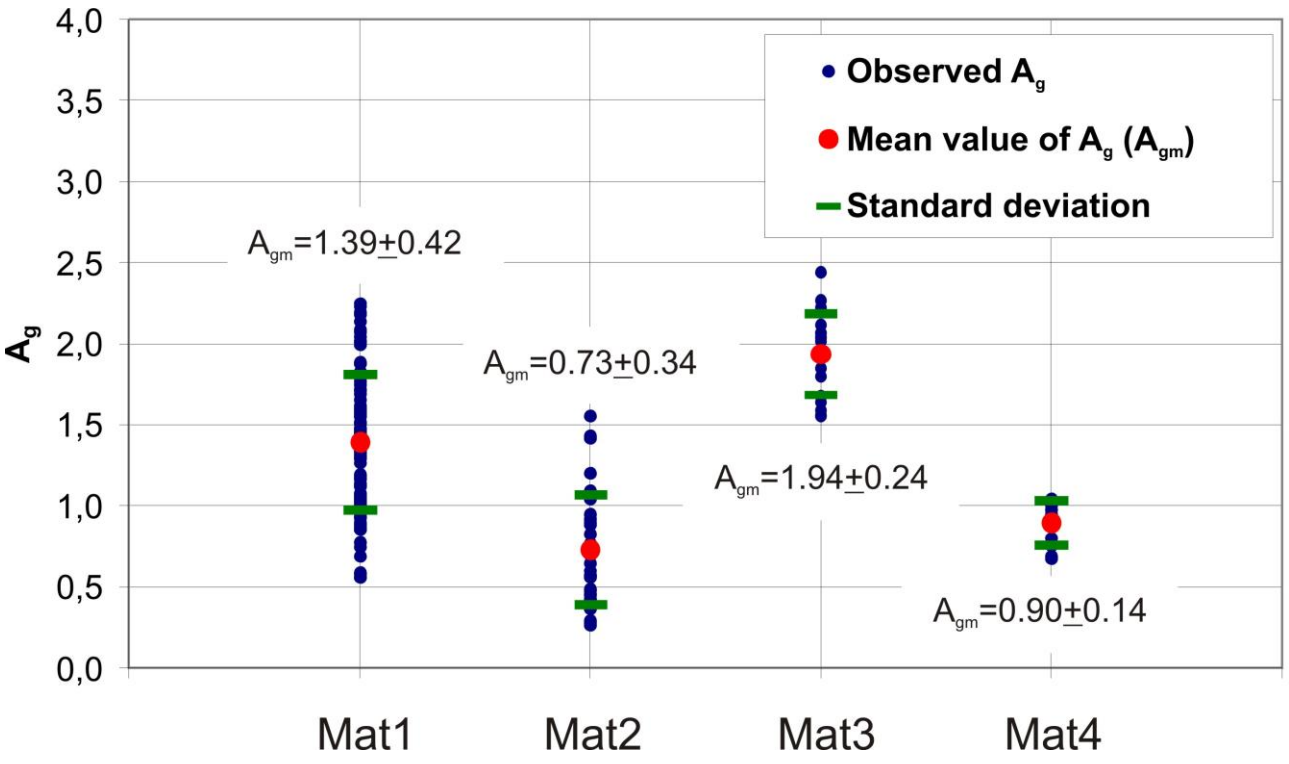

Figure BF.63: Mean values of A_g (A_{gm}) and standard deviation for four studied material types.

In the preceding sections we confirmed that amplification processes are strongly related to the contrast of V_s (I_{Vs}). Figure BF.64a plots A_{gm} values against corresponding values of I_{Vs} (note: I_{Vs} is the ratio of V_s of the underlying material to V_s of the studied material, situated above). Figures BF.64b, BF.64c and BF.64d also compare those values of A_{gm} with the contrast of the bulk modulus (I_K), the shear modulus (I_G) and the mean value between K and G (I_{KG}). According to equations BE.26a and BE.26b, K and G are complexly related to the Young's modulus (E) and the Poisson's ratio (ν) which, in turn, are determined by V_s, V_p and the material density. Similar to I_{Vs}, the values of I_K, I_G, I_{KG} represent the parametric ratios: e.g., I_K for Mat1 is equal to ratio of K of the underlying Mat2 to K for Mat1. As Mat4 does not have the underlying material, it has $I_{Vs}= I_K = I_G= I_{KG}=1$.
The review of all plots suggests that A_{gm} is generally increasing with growing parametric contrast (see the prediction laws extracted based on Mat1, Mat2 and Mat4 in Figure BF.64a-d). Nevertheless, A_{gm} for Mat3 strongly deviates from these general trends. It is explained by fact that we analysed Mat3 only in combination with the underlying Mat4, while there is also a significant parametric contrast with respect to Mat2. For instance, the I_{Vs} of Mat3 with respect to Mat4 is marked by value of 1.63, while that value of Mat3 with respect to Mat2 is even larger and equals to 2.75.
The prediction law applying I_{Vs} in Figure BF.64a suggests that A_{gm}=1.94 for Mat3 can be reached only at I_{Vs}=7.9. Such an extreme value of I_{Vs} is neither yielded by the sum, nor by the product of the specific I_{Vs}, as 1.63+2.75=4.38 and 1.63*2.75=4.47. That value of I_{Vs}=7.9 is only reached when a factor of about 2 is applied to these values. This implies that prediction laws in Figure BF.64a-d can only be applied to the cases when only one hard material is present, while the complexity related to two hard materials is not fully covered.

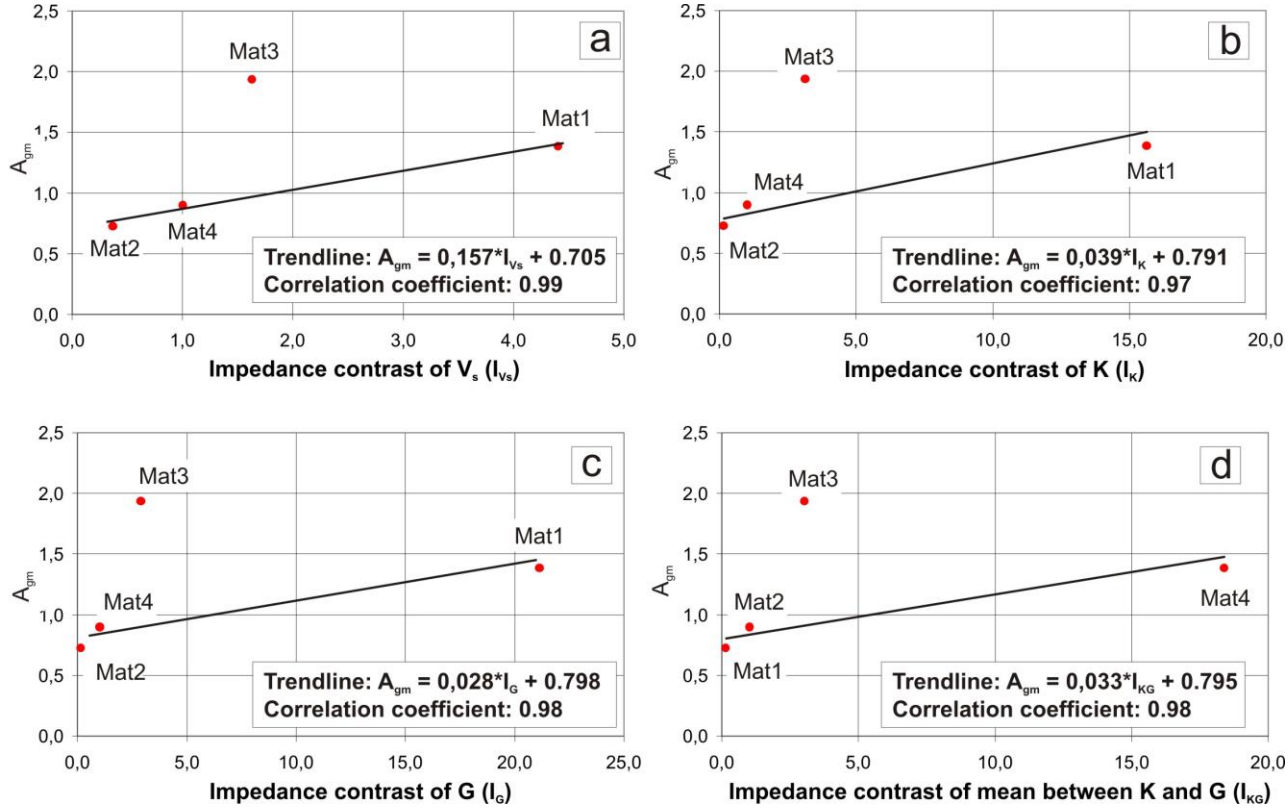

Figure BF.64: Plot of A_{gm} values versus contrast of V_s (a), bulk modulus (b), shear modulus (c), mean value between bulk and shear modulus (d) together with prediction laws extracted based on Mat1, Mat2 and Mat4 (note: Mat3 is not used to extract prediction laws, as it has extremely high A_{gm} due to its structural position between two hard materials).

We assume that in the case of no-damping and $I_{Vs}= I_K = I_G= I_{KG}=1$ the sum of slope and intercept for all prediction laws in Figures B.64a-d should be exactly equal to 1. It logically means that the absence of damping and lack of any parametric contrast with underlying material should result in no attenuation/amplification of I_a values, i.e. A_{gm}=1. As it can be seen, in our case this sum of slope and

intercept is lower than 1 and ranges between 0.83 and 0.86. This difference is explained by the Rayleigh damping of 2.0 % applied in all our tests. This suggests that the values of slope and intercept in the extracted laws are reversely related to the applied damping: higher damping results in lower values of these coefficients, while lower damping would yield higher slope and intercept.

Figure BF.64 demonstrates that in terms of final predictions of A_{gm} the laws employing K and G are not better than the one employing V_s. Actually, the application of I_{Vs} even yields a slightly better prediction compared to the laws established for I_K, I_G and I_{KG}, as it can be seen from the correlation coefficients computed the extracted prediction laws. Meanwhile, the regional mapping of I_{Vs} employs only the spatial distribution of V_s, while application of I_K, I_G and I_{KG} would additionally demand the spatial distribution of V_p and material density. It finally implies that the law employing I_{Vs} (Figure BF.64a) is the best one to predict the spatial distribution of the A_{gm} values.

V. Shear displacement versus Newmark displacement: 2D studies

V.1 Research focus and methodology

In this chapter we estimate the performance of the Newmark (1965) technique and some regional Newmark models to predict the displacements recorded in the numericalal tests. The studies are performed in the 2D domain and apply both simplified model geometry and models with real topography. The simplified geometry reproduces the rigid block sliding on an inclined plane: Newmark (1965) applies this model to develop his prediction technique. More complicated models with real topography track the triggered shear displacements in different parts of the curved slope. The modelled shear displacements are further compared with the displacements predicted by the original Newmark (1965) technique and those estimated by the regional models. The Newmark (1965) technique predicts this displacement based on the input acceleration-time history which should be integrated according to certain rules. The regional Newmark models apply a series of predictors, most commonly I_a and A_c, to estimate the triggered displacements. Thus, we evaluate the ability of both models to predict the real displacements, i.e. those which are recorded in our numericalal tests. The Newmark (1965) technique is the basis for all developments in this domain, including the regional prediction laws. Therefore, our analyses start with the model of the rigid block which is reviewed in more details below.

V.2 Rigid block: Ricker tests

Section B.I.3 presented the detailed review of the Newmark (1965) model and technique which predicts the co-seismic sliding behaviour. Figure BF.65a reproduces this model of the block sliding on a plane with an inclination of 12°. The sliding block is rigid, i.e. during dynamic modelling it does not yield the plastic deformations. All models are composed of a material with a density of 2400 kg/m^3, K=9592 MPa and G=4056 MPa. The joint tangential and normal stiffness is the same in all models (jkn=jks=10000 Pa/m). The varying model settings include the joint friction (jfric) and joint cohesion (jcoh).
According to the Newmark (1965) technique, the impacting acceleration time history (x-component) is applied to predict the co-seismic displacement of the block (Newmark Displacement or ND). The prediction is based on the double integration of the part/parts of the acceleration time history situated above the critical acceleration value (A_c, m/sec^2). This value of A_c should be calculated based on the next equation:

$$A_c = (FS - 1) * g * \sin\alpha \qquad \text{(BE.29)},$$

where FS is the Factor of Safety of the block lying on the plane, α (°) is the plane inclination (here α=12°) and g is the acceleration due to gravity (g=9.81 m/sec^2). In all our models the values of FS are automatically estimated by the UDEC code given the applied values of jfric and jcoh.
The calculations of the ND value are shown in Figures BF.65 b-d. The input signal presents the Ricker shape shear stress wave with two central frequency values (1.4 and 3.5 Hz). This signal results in a quasi-sinusoid shape of acceleration time history shown in Figure BF.65b. The studied model has jfric=15° and jcoh=0.03 MPa which result in FS=1.86 (automatically evaluated by the UDEC code). According to Equation BE.29, the calculated value of A_c corresponds to 1.79 m/sec^2 (for FS=1.86 and α=12°). This value of A_c is further applied to estimate the ND value, when the part of the acceleration-time history above the A_c=1.79 m/sec^2 is subjected to double-integration (see Figures BF.65c and d). The final result presents the curve of the cumulated co-seismic displacement shown in Figure BF.65 d. As it can be seen, the predicted Newmark displacement equals to 12.4 cm. This displacement is triggered by the part of the acceleration time history between 1.55 and 1.91 sec. The other parts of this history do not induce instability. Therefore, the predicted displacements occur only within one time interval.
Figure BF.66a further analyses how accurately this ND value predicts the modelled displacement. As it can be seen, the predicted and modelled behaviours quite reliably coincide with respect to the triggering moment (1.55 sec) and to the time when the displacement stops (1.91 sec). Some difference is observed between 1.45 sec and 1.55 sec, when the upslope-oriented acceleration (negative peak) moves the block by around 1.0 cm upslope. This pattern is not predicted by the Newmark (1965) technique which analyses only the downslope movement. Nevertheless, the difference between predicted and modelled values does not exceed 4.0%. This suggests that the ND value quite reliably predicts the modelled displacement in this case.

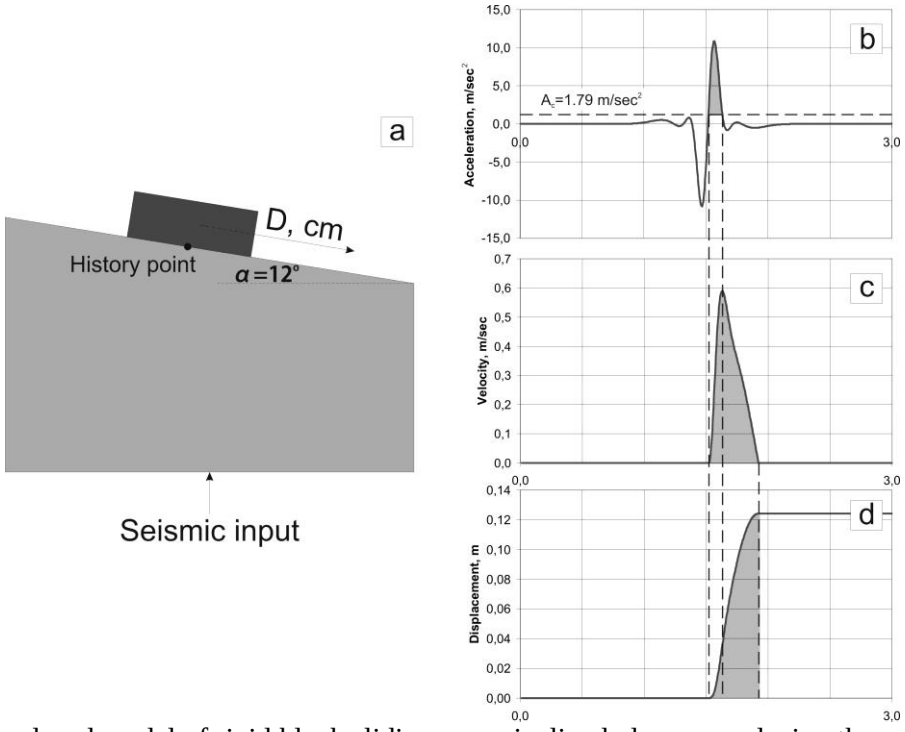

Figure BF.65: Analysed model of rigid block sliding on an inclined plane reproducing the settings employed by the Newmark (1965) technique.

Figure BF.66b analyses the results for the same model (FS=1.86, A_c=1.79 m/sec^2). In this test the input signal is inverted with respect to the one shown in Figure BF.66a (i.e., applied factor is -1). As it can be seen, the Newmark (1965) technique quite reliably predicts the modelled behaviour both in terms of triggering moment and final value of downslope displacement (relative prediction error is not more than 4.0 %). Similar to the previous case, the negative acceleration peak triggers some upslope displacement (less than 0.5 cm) which is not predicted by the Newmark (1965) technique due to its simplicity.

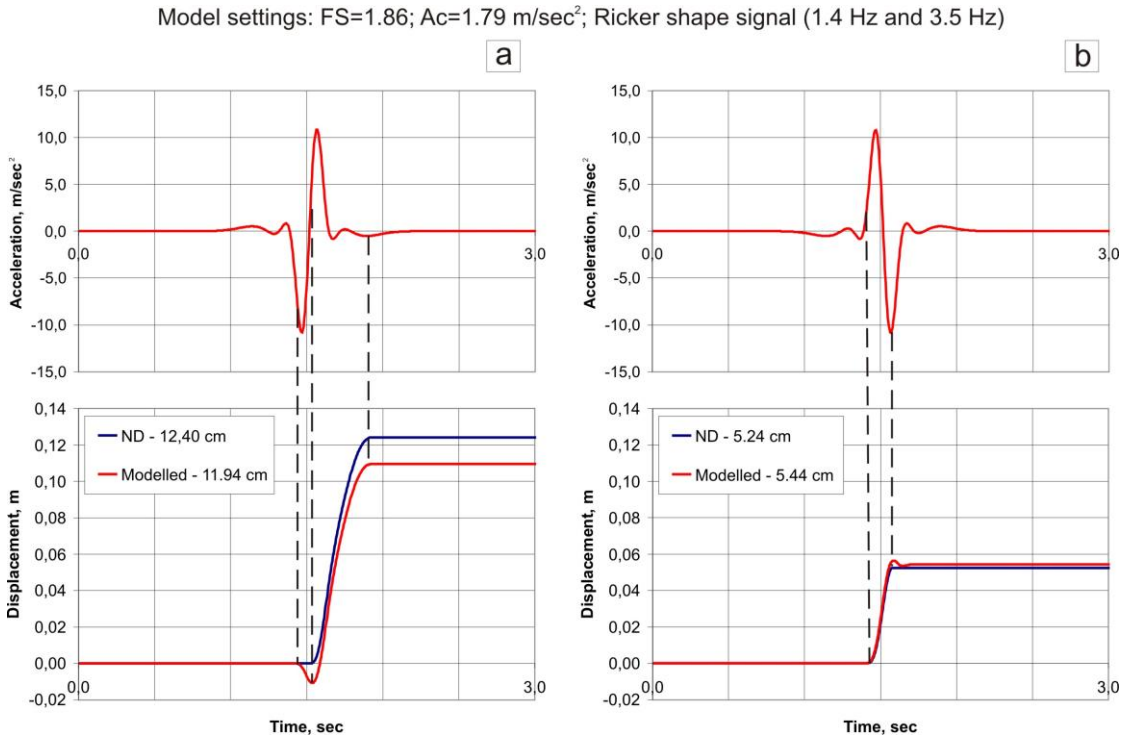

Figure BF.66: Fit between ND and modelled values of displacement and an impact of the signal shape of the final value of shear displacement.

A comparison of both cases shows that the first signal (Figure BF.66a) triggers more than two times larger displacements compared to the ones shown in Figure BF.66b (11.94 cm versus 5.44 cm). Both signals have exactly the same value of I_a=2.12 m/sec, as only a factor of -1 is applied to invert the histories. The difference is expressed via the orientation of the first acceleration pulse: in Figure BF.66a it is negative, while in Figure BF.66b it is positive. In Figure BF.66a the block starts to move after the second acceleration pulse and this displacement is not disturbed by any significant negative acceleration. In the test analysed in Figure BF.66b the sliding is triggered by the first pulse which is followed by a strong negative acceleration: this second peak clearly attenuates the downslope movements. These results show that the co-seismic sliding behaviour is directly related to the shape of impacting shaking: this sliding can be attenuated by a strong negative acceleration which can significantly affect the final value of shear displacement.
Figure BF.67 presents the results of the same model (FS=1.86 and A_c=1.79 m/sec^2) subjected to the input signals with varying PGA. Thus, the signal analysed in Figure BF.67a is marked by a 1.6 times higher PGA than the one presented in Figure BF.67b (0.88g versus 0.54g). This difference in PGA results in more than 3.5 times larger shear displacements for the first signal compared to the second one (8.34 cm versus 2.23 cm). As it can be seen, the Newmark (1965) technique quite reliably predicts the co-seismic displacement in both modelling cases, as the relative prediction error is only around 8.0-10.0 %.

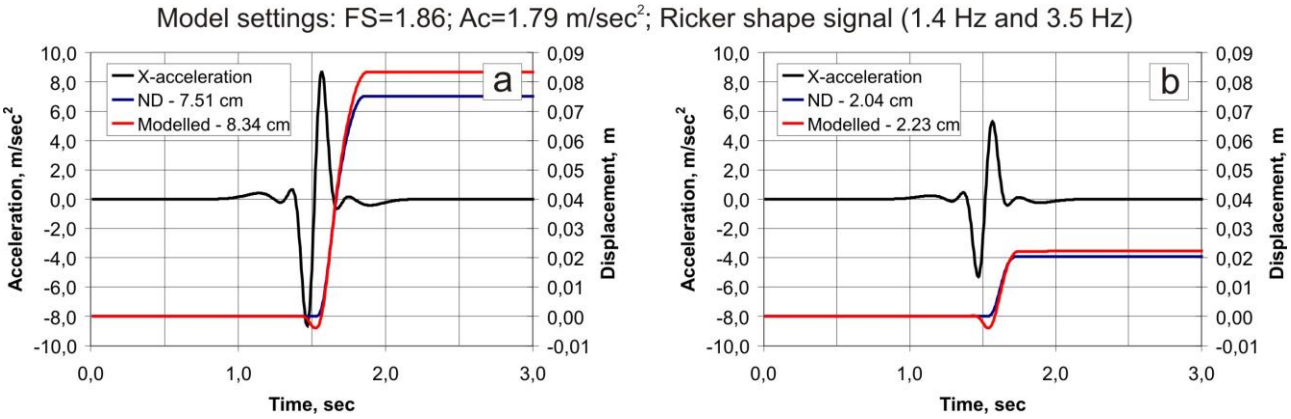

Figure BF.67: Impact of the changing input signal on final value of the shear displacement.

Figure BF.68 compares the displacement registered in two models with varying FS when A_c changes from 0.56 m/sec^2 up to 1.79 m/sec^2. Both models are subjected to the same input signal with PGA=0.80g. As it can be seen, the variation of A_c significantly affects the values of downslope displacement which change from 8.34 cm for A_c=1.79 m/sec^2 up to 20.11 cm for A_c=0.56 m/sec^2. Figure BF.68a shows that for case of A_c=1.79 m/sec^2 the difference between ND and modelled displacement is around 10.0 %. The ND value for the case of lower A_c (Figure BF.68b) significantly overestimates the modelled displacement (relative predictive error is around 40.0 %). The reason for this overestimation is analysed more in detail in the next section, where we test the signals of varying central frequencies.

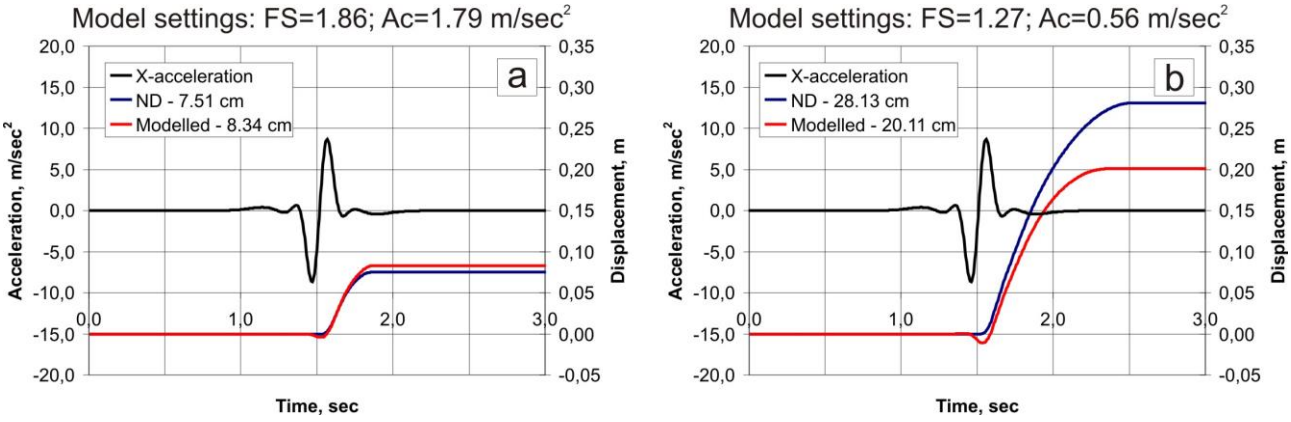

Figure BF.68: Impact of changing A_c (FS) on the final value of the shear displacement.

Thus, our tests of rigid block sliding on the inclined plane show that the Newmark (1965) technique generally provides reliable predictions of the displacements, triggered by the Ricker (1.4 and 3.5 Hz) signal. In most of the cases the predicted sliding behaviour well coincides with the modelled one, especially with respect to the triggering moment. The difference between ND and modelled displacements in most of the tests is limited to 5.0-10.0 %. This shows that in the majority of tests the Newmark (1965) technique quite reliably predicts the modelled displacement.
Nevertheless, some difference between predicted and modelled behaviour is observed. This difference is related to the simplicity of the Newmark (1965) technique which does not account for some of the problem complexities. For example, this technique cannot predict the upslope displacements which are registered in some of our tests. The Newmark (1965) technique can also yield overestimated results (up to 40 % of modelled displacement). This misfit and the displacements triggered by signals of varying central frequency are analysed in the next section.

V.3 Rigid block: the signals with varying central frequency

The model of the rigid block is subjected to sinusoid-shape signals with central frequency of stress changing from 0.25 Hz up to 2.0 Hz (Fca changes from 0.25 Hz up to 2.2 Hz). These signals are applied to the model with FS=1.86 and A_c=1.79 m/sec^2. The values of ND for all tests are calculated on the basis of the acceleration time history using the methodology shown in Figure BF.65. The results of these tests are summarized in Figure BF.69, where the ND values are plotted versus the modelled displacements. The plotted data are ordered according to increasing Fca. The last graph summarizes the results of the tests with Ricker (1.4-3.5 Hz) signal (see *Section B.V.2*).

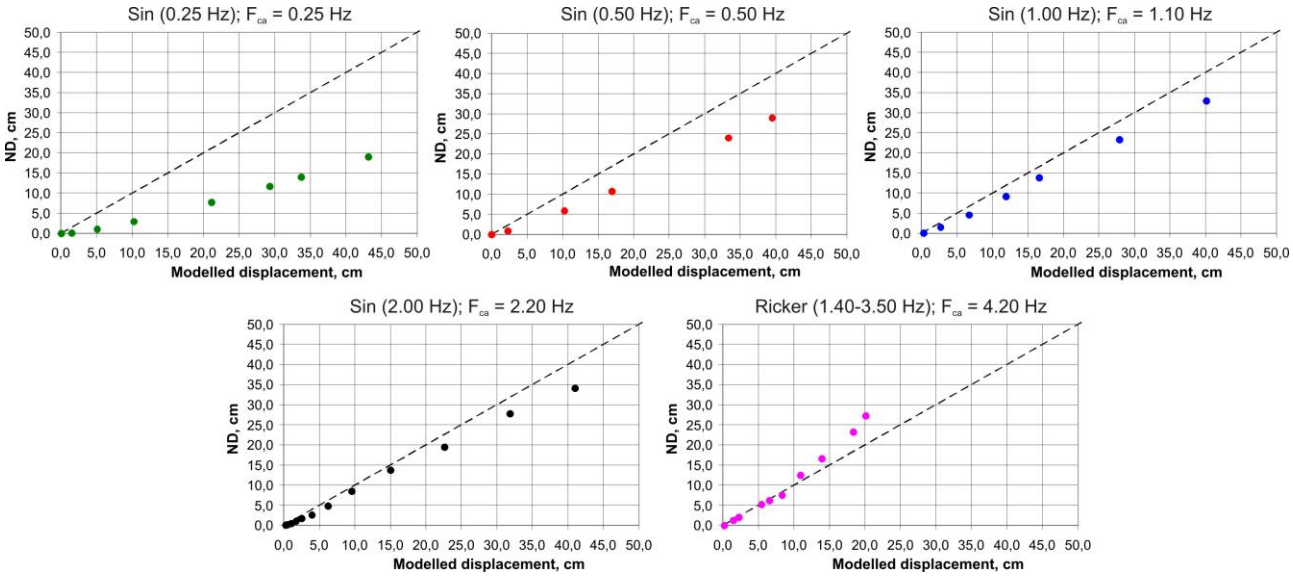

Figure BF.69: Plots of ND versus modelled displacement for signals with varying central frequency (the graphs are ordered according to increasing Fca).

Our results suggest that the worst predictions are yielded for the case of the 0.25 Hz signal, as the ND values significantly underestimate the modelled displacements (by a factor of up to 2). The rate of underestimation decreases towards the higher frequency domain, i.e., for signals with larger values of Fca. Thus, the lowest underestimation is observed for the 2.0 Hz signal for which the difference between ND and modelled displacement is limited to 15.0-20.0 %. The modelled displacements for the Ricker signal (Fca = 4.2 Hz) are even overestimated by the ND displacements, especially by those of larger than 15.0 cm (relative prediction error is up to 45.0 %). For example, Figure BF.68b shows that the ND value of 28.13 cm is predicted for the case where the Ricker signal produces only 20.11 cm of the modelled displacement.

The results of the tests with the sinusoid-shape signals are further summarized in Figure BF.70. Here, the values of modelled displacement are plotted against the I_a values calculated on the basis of acceleration recordings (x-component). The results of all tests are plotted in the form of trendlines attributed to Fca of the studied signals. As it can be seen, the value of Fca significantly impacts the relationship between I_a and modelled displacement. For example, the 0.25 Hz signal with I_a=1.5 m/sec yields 20.0 cm of modelled displacement, while the 2.20 Hz signal with exactly the same value of I_a triggers only 2.5 cm of shear displacement (i.e., the difference with factor of 8). These results have important implication in respect to the regional Newmark models. These models predict the value of ND solely based on the I_a value, while Fca is not considered as the regional predictor. Meanwhile, this parameter is included in some empirical models which predict shear displacement at the scale of a single slope (see, e.g., Saygili and Rathje, 2008; Rathje and Saygili, 2009).

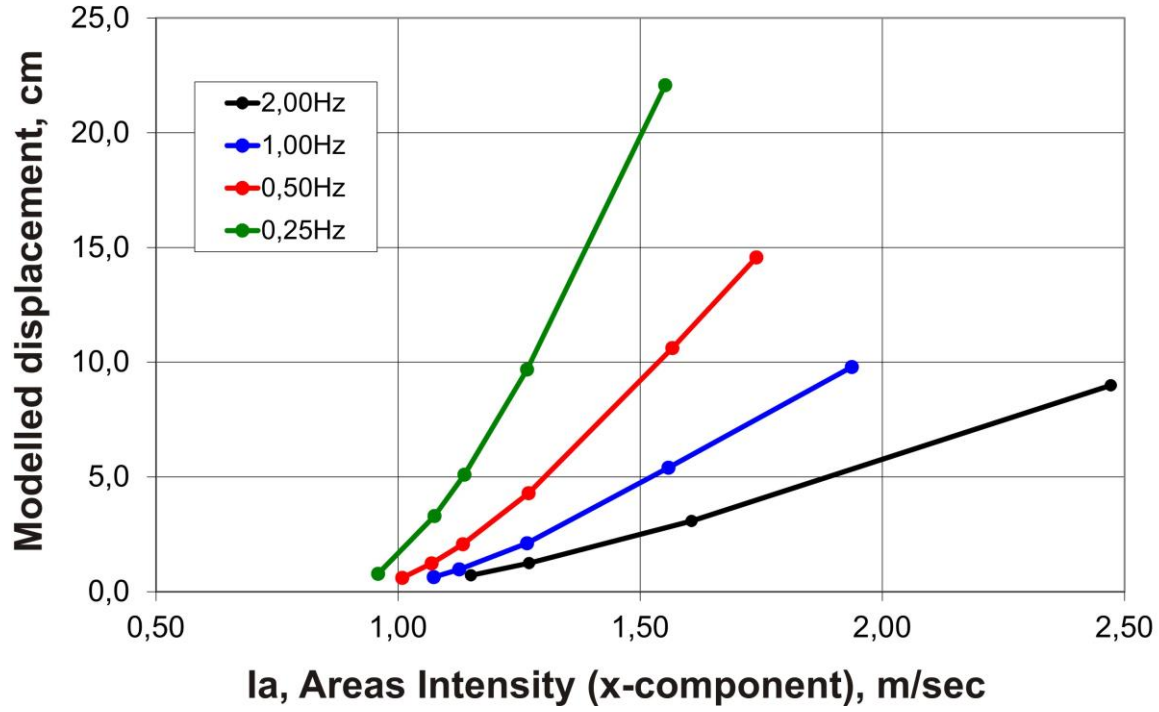

Figure BF.70: Plot of modelled displacement against I_a values for the sinusoid-shape signals of varying central frequency.

Thus, the tests with signals of varying central frequency indicate that the Newmark (1965) technique has the best performance in the range of Fca between 2.2 Hz and 4.2 Hz, when the shear displacement is below 10.0-15.0 cm. The displacement values in other ranges of Fca are less reliably predicted by the Newmark (1965) technique which can underestimate or overestimate the modelled displacements. The reason why a performance of Newmark (1965) technique is influenced by Fca is not totally clear. One possible explanation for misfit between ND and modelled displacement can be related to the inertial resistance of the moving block. For example, several studies investigated the inertial behaviour of engineering materials, soils and rocks under the dynamic conditions (see, e.g., Barbero et al., 1996; Jafari et al., 2003; Guner and Vecchio, 2012; Shui-sheng et al, 2013). These studies show that the higher rates of impulse loading or higher frequency impact provokes higher inertial resistance compared with the lower frequency shaking, which is known as the strain rate effect. Regarding our study case, the high-frequency impacts provoking higher inertial resistance may inhibit the sliding movement which finally results in smaller modelled displacements compared with the low-frequency impact. The Newmark (1965) technique may fail to reproduce such problem complexity due to the adopted simplifications. Meanwhile, such issues, including the important underestimation of modelled displacement by ND, should further be clarified by more advanced modelling analysing the change of parameters in dynamic conditions.

The tests of the rigid block sliding on the inclined plane also yield some important implications for the regional Newmark models. It is shown that the inverted orientation of the first acceleration peak for the fixed value of I_a can result in two times lower values of shear displacement. Further, Fca may play an important role: two signals with identical I_a values and varying Fca may result in significantly different values of downslope displacement. The regional Newmark models apply only I_a to characterize the impacting shaking, while the orientation of the first acceleration peak and Fca are not considered as the regional predictors. It potentially affects the reliability of the predictions yielded by the regional Newmark models. In the next section we employ our data to evaluate the performance of some existing regional models. In addition, we attempt to propose a relationship where Fca together with other conventional parameters is included as one of the predictors.

V.4 Rigid block: regional Newmark predictions

Three prediction laws were selected to estimate the performance of the regional Newmark models (Jibson, 1993 – Equation BE.30a; Jibson et al., 1998 - Equation BE.30b; Hsieh et al., 2007- Equation BE.30c):

$$\log D_n = 1.460 * \log I_a - 6.642 * A_c + 1.546 \quad \text{(BE.30a)},$$

$$\log D_n = 1.521 * \log I_a - 1.993 * \log A_c - 1.546 \quad \text{(BE.30b)},$$

$$\log D_n = 1.756 * \log I_a - 2.780 * \log A_c - 2.278 \quad \text{(BE.30c)},$$

where D_n (cm) is the co-seismic displacement value, I_a (m/sec) is the Arias Intensity and A_c is the critical acceleration (in terms of g).

Figure BF.71 plots the ND values, predicted by these regional laws, versus the modelled displacements. As it can be seen, all regional laws significantly underestimate the modelled displacement in the range of Fca below 0.5 Hz. At Fca=1.1 Hz the Jibson (1993) model starts to overestimate the modelled displacement, while two other models still underestimate the registered values of shear displacement. For the Fca=2.2 Hz signal the Jibson (1993) model significantly overestimates the modelled displacement. The models of Jibson et al. (1998) and Hsieh et al. (2007) have the best performance for Fca=2.2 Hz, even though a slight underestimation can be observed. The modelled displacement triggered by the Ricker signal (Fca=4.2 Hz) is best predicted at the range below 10.0-15.0 cm. All regional models significantly overestimate the modelled displacement of more than 20 cm triggered by the Ricker signal.

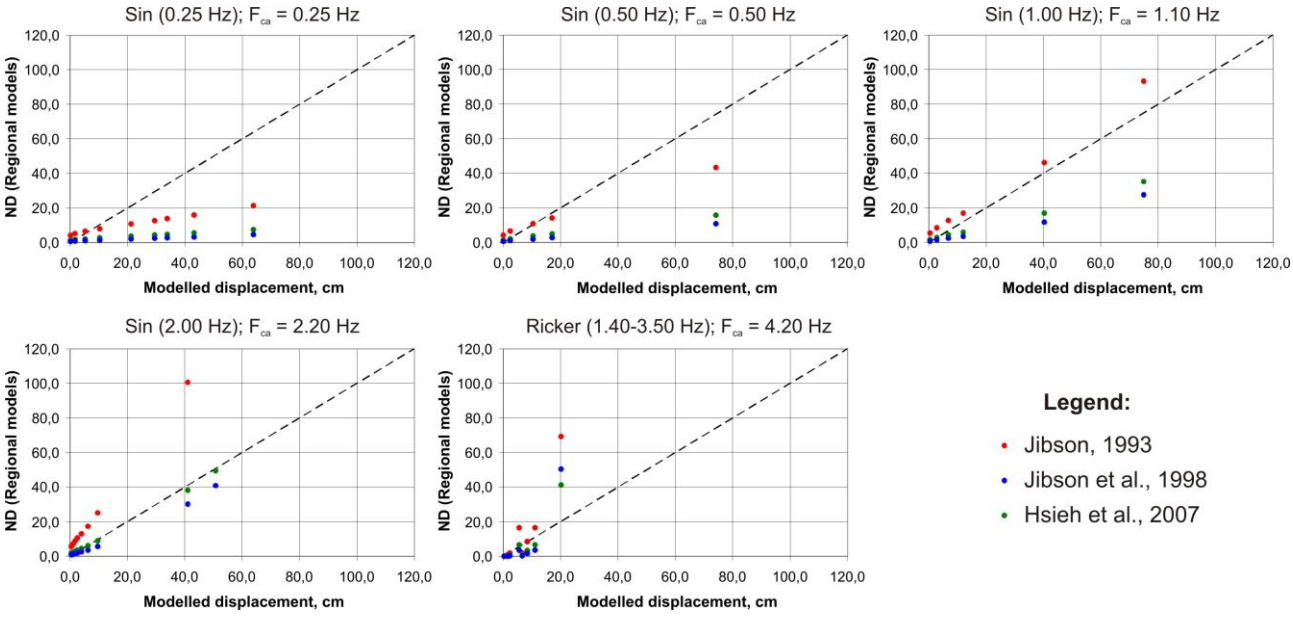

Figure BF.71: Plots of ND values predicted by three regional models versus modelled displacement for the signals of varying central frequency.

Thus, Figure BF.71 shows that the prediction performance of the analysed regional models varies depending on Fca. Figure BF.70 partially explains this misfit between predicted and modelled data: the final value of the co-seismic displacement is related to I_a, A_c and Fca, while all regional laws only use the two first predictors. Therefore, we further explore the possibility to include Fca as one of the predicting parameters.
These analyses are performed for four datasets of the modelled displacements triggered by the sinusoid signals with Fca of 0.25, 0.5, 1.1 and 2.2 Hz. Modelled displacements larger than 40 cm are filtered out from the analysed datasets, as their triggering is often related to very specific conditions. The modelled data attributed to the Ricker signal are not analysed, as only one single value of Fca=4.4 Hz was studied for that signal. The original values of the modelled displacement (via D_n), as well as its logarithm with the base of 10, often referred as common logarithm ($\log D_n$), are considered as predicted parameters. The series of tested predictors include the original values of basic parameters (I_a, Fca, A_c), their common logarithm ($\log I_a$, logFca, $\log A_c$), as well as different ratios, like $\log(I_a/Fca)$, $\log(I_a)/Fca$, $\log(A_c/Fca)$, $\log(A_c)/Fca$, etc.
The first analysis step is the cross-correlation study which outlines the parameters with the highest predictive power. Thus, it is revealed that the best fit between modelled and predicted data is obtained for the case when $\log(I_a)/Fca$ and A_c predict the values of $\log D_n$. Figure BF.72 presents those prediction laws which are attached to the plots of the predicted versus the modelled displacements. An important observation is related to the general shape of the prediction law which can be expressed as follows:

$$\log D_n = K1 * \frac{\log I_a}{Fca} - K2 * \log(A_c) + L \qquad \text{(BE.31)},$$

where K1 and K2 are the slope coefficients, and L is the intercept value.
A careful review of the prediction laws implies that values of K1, K2 and L are strongly determined by Fca. Thus, the slope coefficient K1 and K2 attributed to $\log(I_a)/Fca$ are directly proportional to Fca, while L is inversely related to Fca. The analyses of these distributions allow us to extract the linear laws which can be expressed as follows:

$$K1 = 1.7949 * Fca + 0.6899 \qquad \text{(BE.32a)},$$
$$K2 = 1.1969 * Fca + 0.0757 \qquad \text{(BE.32b)},$$
$$L = -0.2073 * Fca + 1.3790 \qquad \text{(BE.32c)},$$

Introducing these last relationships into Equation BE.31 we would get the next:

$$\log D_n = (1.7949 * Fca + 0.689) * \frac{\log I_a}{Fca} - (1.1969 * Fca + 0.0757) * \log(A_c) + (-0.2073 * Fca + 1.379) =$$
$$1.7949 * \log I_a + 0.689 * \frac{\log I_a}{Fca} - 1.1969 * Fca * \log(A_c) - 0.0757 * \log(A_c) - 0.2073 * Fca + 1.379 \qquad \text{(BE.33)}$$

Figure BF.72 suggests that this last equation quite reliably predicts the modelled displacements for all sinusoid signals. The high level of prediction performance is proven by the correlation coefficient of 0.99 for the relationship between predicted and modelled distributions. It should be noticed that Equation BE.33 may be applied only to the sinusoid signals. Nevertheless, the analysis of the Ricker data (Fca=4.2 Hz) proved the validity of the general form in Equation BE.31 for that signal. The only difference is related to K1, K2 and L which are quite far from those predicted by equations BE.32a, BE.32b and BE.32c. It suggests that the extraction of precise law for the Ricker signal would demand additional tests with varying values of Fca.
The tested numerical models have a simplified geometry of a rigid block sliding on an inclined plane. The topographic or geological amplification patterns in this case do not play a role due to the general simplicity of the model. In the next sections we analyse a model with more complicated geometry affected by pure topographic effects. These tests should assess the performance of the Newmark (1965) technique and regional prediction laws for the case when seismic energy is subjected to topographic amplification.

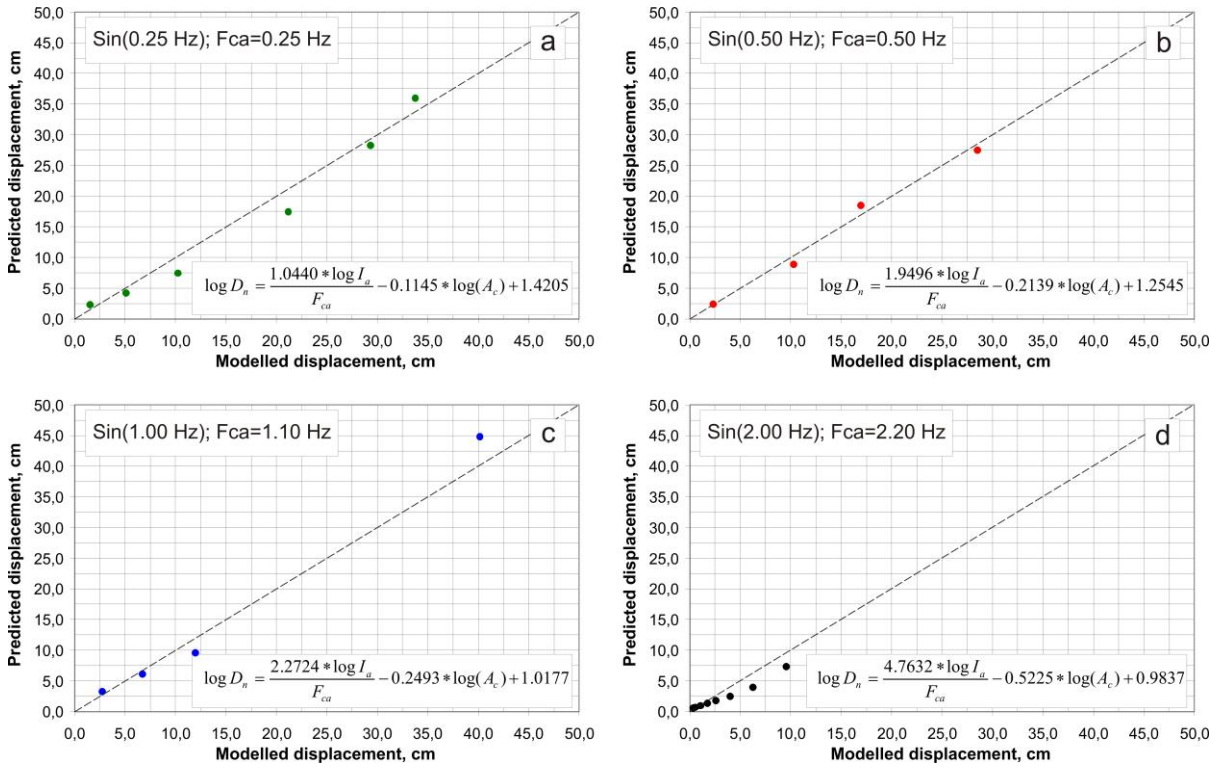

Figure BF.72: Plots of predicted displacement versus the modelled displacement for the sinusoid shape signals with Fca of 0.25, 0.5, 1.1 and 2.2 Hz (note: the prediction laws are shown in the lower right corners of graphs).

V.5 Pure topographic model: analyses settings

The studies are performed for the largest slope within Profile 4 (pure topographic settings - see Figure BF.73). The triggered displacements are tracked with eight triangle-shape elements which are distributed along the studied surface (see El1-El8 in Figure BF.73). A single material type is applied to the stable part of the model and to all sliding elements: density = 2200 kg/m^3, V_s = 1300 m/sec, K=9592 MPa, G=4056 MPa. This material type coincides to Mat4 modelled in *Chapter B.IV*.

The sliding elements are mainly situated within the convex parts of the slope. Their position favours the topographic amplification of the impacting seismic shaking. For all tests the same model geometry is used, i.e. the inclination of the contact below the sliding elements does not vary. The changing properties include contact cohesion (jcoh) and contact friction angle (jfic). The values of FS are automatically estimated through the UDEC code. As a result of varying jcoh and jfric the values of FS are ranging between 1.15 and 1.95.

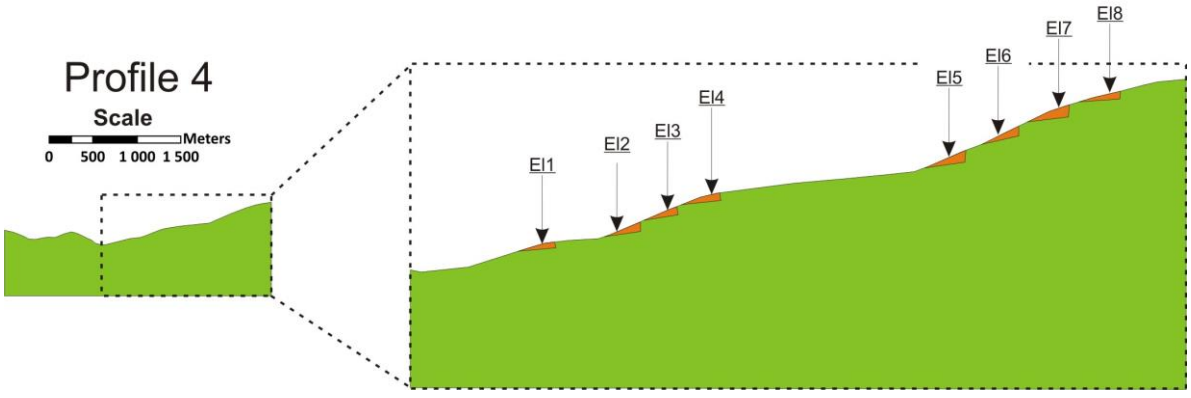

Figure BF.73: Set of the triangle-shape elements distributed along the surface of Profile 4: these elements are used to study the triggered co-seismic displacements.

Two types of Ricker shape input signals are applied in all tests (see Figure BF.74). The first signal has Fca=4.20 Hz and the second signal has Fca=1.49 Hz. The low frequency signal (Fca=1.49 Hz) is marked by almost 3 times smaller values of I_a and PGA compared to the high frequency Ricker signal (see those values in Figure BF.74). This difference is intentionally introduced, as Figure BF.70 shows that the low frequency signal normally produces larger displacements. The registered distributions of the I_a amplification values indicate that the majority of studied sites are marked by A_t values of less than 1. Only El4 under the impact of the low frequency signal has A_t=1.1 (see a position of El4 in Figure BF.73).

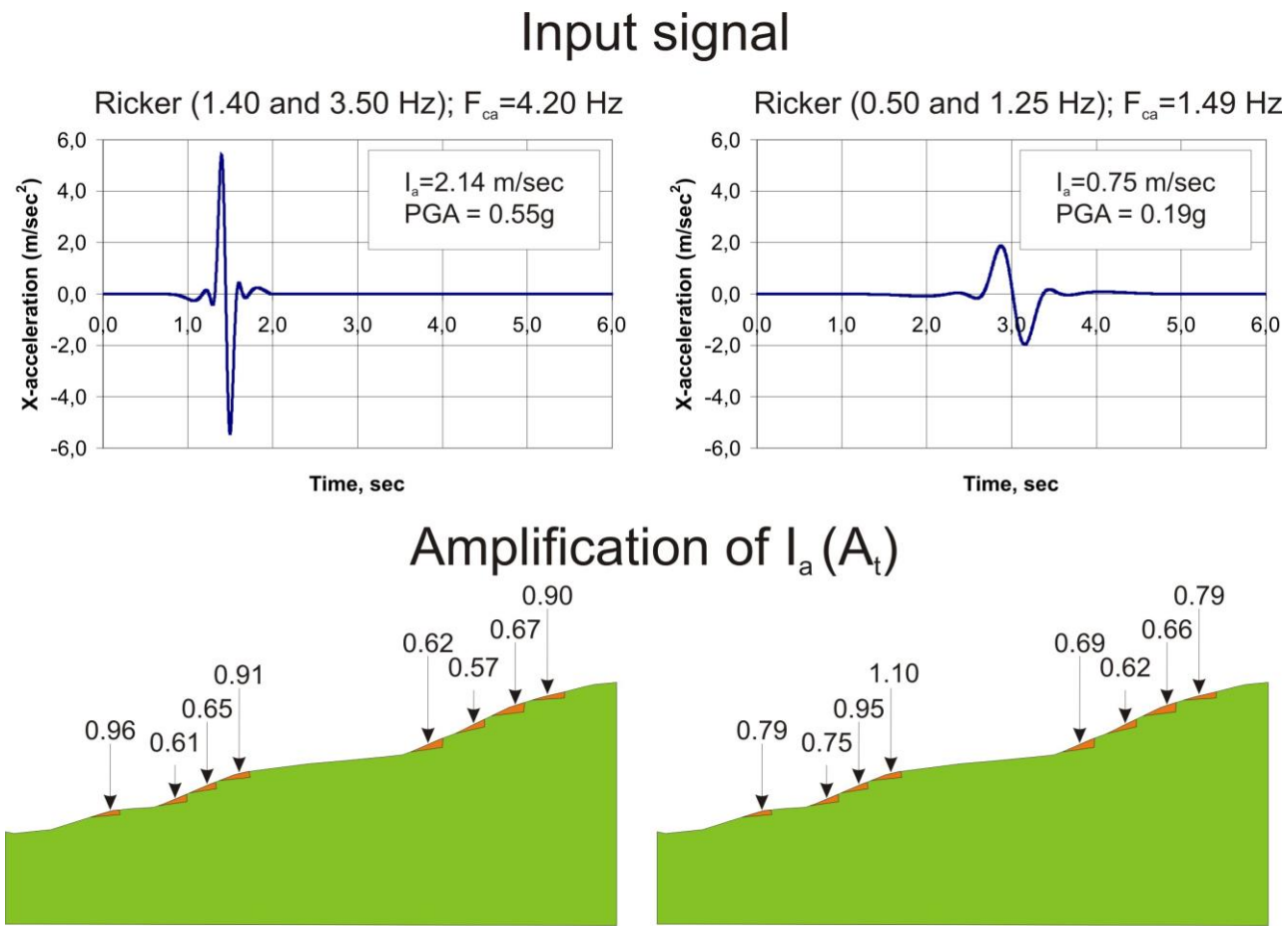

Figure BF.74: Two Ricker shape input signals presented via the acceleration-time histories (x-component) and the registered distributions of the pure topographic I_a amplification values (A_t).

V.6 Pure topographic model: Newmark (1965) technique

The acceleration time histories recorded at all studied sites are subjected to the integration according to the Newmark (1965) technique. The resulting value of ND and predicted sliding behaviour are further compared with the modelled parameters. Figure BF.75 presents the results for El6 which is situated in the upper part of the studied slope (see Figure BF.73). The applied values of jcoh and jfric yielded FS=1.26 which results in a critical acceleration of A_c=0.53 m/sec^2, considering that the plane below this sliding element has a slope of 12º. Figure BF.75 presents calculations for both input signals, i.e. for Fca=4.20 Hz and Fca=1.49 Hz.

A careful study of the results indicates that the Newmark (1965) technique accurately predicts the initial triggering moments (see the triggering at 2.07 sec for Fca=4.20 Hz and the triggering at 4.49 sec for Fca=1.49 Hz). The main phases of downslope movement are also quite reliably predicted (see, e.g., a phase between 2.72 and 2.81 sec for Fca=4.20 Hz or one at 5.87 and 6.10 sec for Fca=1.49 Hz). Nevertheless, some sliding intervals are still not predicted by the Newmark (1965) technique (see, e.g., a sliding between 2.41 and 2.72 sec for Fca=4.20 Hz). The sliding initiated at 3.63 sec for Fca=4.20 Hz and sliding initiated at

6.71 sec for Fca=1.49 Hz are somewhat unexpected, as the analysed acceleration time histories present all acceleration values below A_c (see Figure BF.75). For both tested signals the modelled displacements are underestimated by the ND values. In case of Fca=4.2 Hz this underestimation is around 20 %, while for the low frequency signal it is around 12 %.

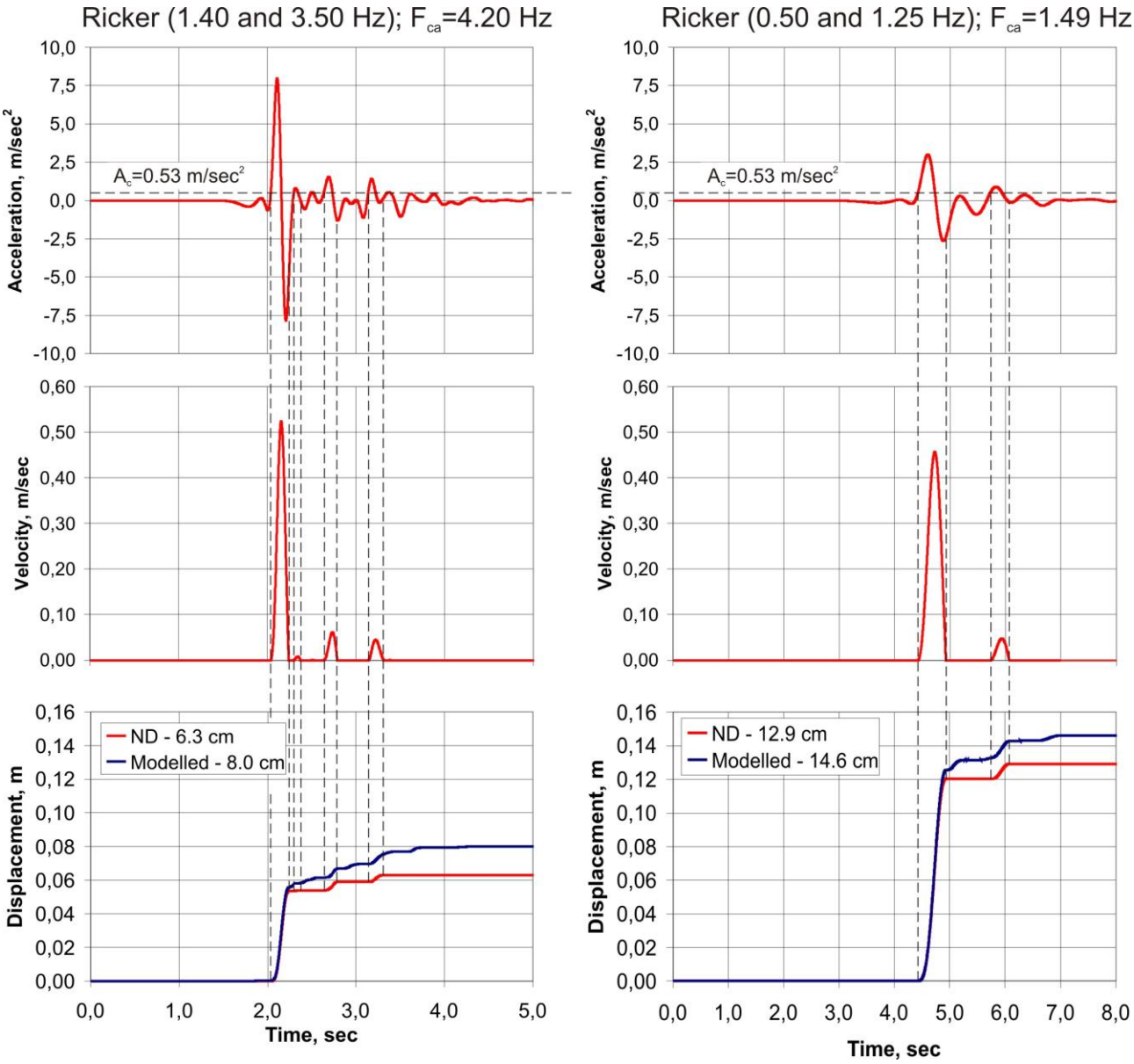

Figure BF.75: Calculation of the ND values for two Ricker shape input signals and comparison of predicted sliding behaviour versus modelled one (all data for El6 – see its position in Figure BF.73).

The result of calculations for El1 and El4 are presented in Figure BF.76. In these tests all sliding elements have FS=1.26 which corresponds to A_c=0.53 m/sec^2. The results are presented for the Fca=4.20 Hz (Figures BF.76a and BF.76b) and for the Fca=1.49 Hz (Figures B.76c and B.76d) signals. As it can be seen, the Newmark (1965) technique quite reliably predicts the triggering of the main displacement as well as the initiation of the secondary sliding (see, e.g., the sliding between 5.56 and 6.00 sec in Figure BF.76d). Nevertheless, in all tested cases the values of ND underestimate the modelled displacement. For example, Figure BF.76a shows that El1 during the second sliding interval (between 2.12 and 2.48 sec) moved around 2.0 cm further than it is predicted by the Newmark (1965) technique. The case shown in Figure BF.76b demonstrates that El4 kept sliding after 2.67 sec, while Newmark (1965) technique predicts that sliding should be stopped at this moment. This misfit between predicted and modelled behaviours results in differences between modelled displacements and ND of up to 20 %.

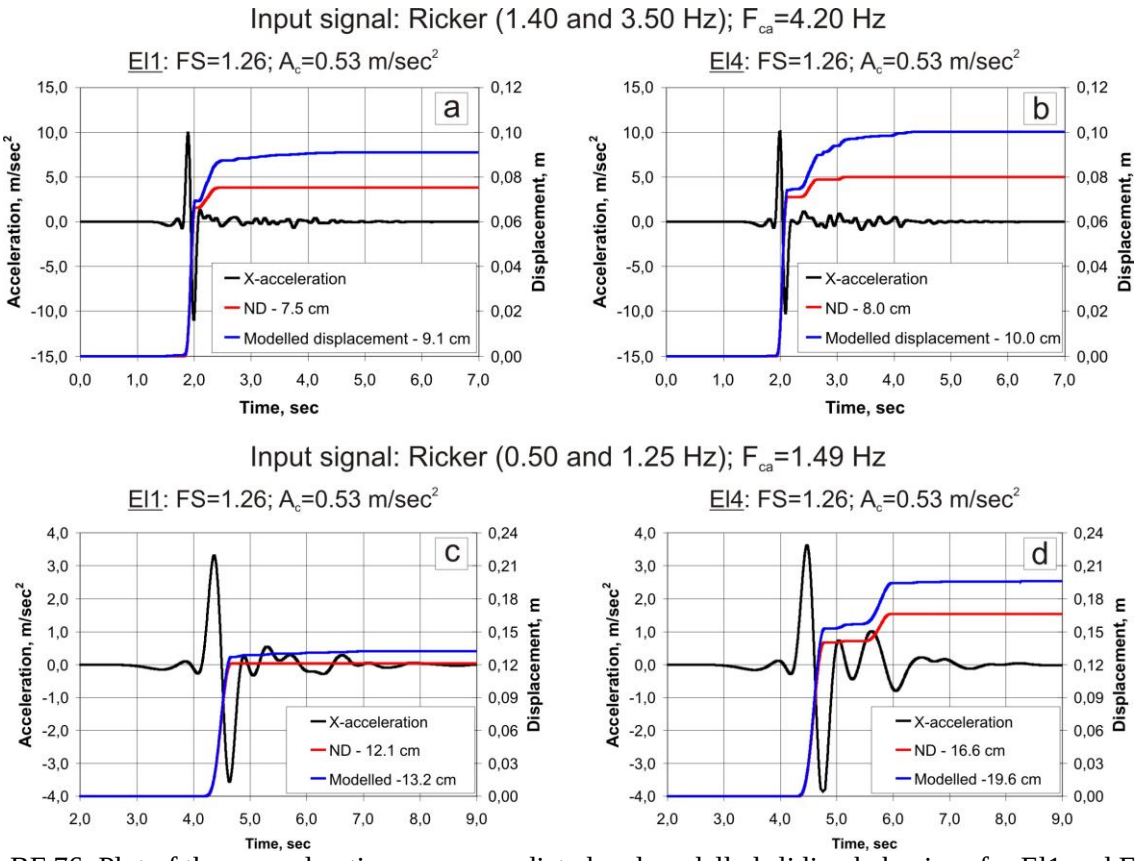

Figure BF.76: Plot of the x-acceleration versus predicted and modelled sliding behaviour for El1 and El4: the tested input signals have Fca=4.20 Hz (a, b) and Fca=1.49 Hz (c, d).

The results of all tests with both input signals are summarized in Figure BF.77, where the ND values are plotted versus the values of modelled displacement. As it can be seen, the Fca=1.49 Hz signal consistently yields higher displacements in all models, even though the I_a and PGA values are around 3 times smaller than those values for the Fca=4.20 Hz signal (see Figure BF.74). The distribution of data indicates that modelled displacement for the high frequency signal is more accurately predicted by the Newmark (1965) technique: in the majority of tests the ND values only slightly underestimate the modelled displacement, while some tests even yielded overestimation. The Fca=1.49 Hz signal is characterized by much higher underestimation of the modelled values which can reach 35-40 %. An increasing level of underestimation for the low frequency signal is in accordance with the result described in *Section B.V.3*, where it is shown that modelled displacement for the signals with lower Fca are much more underestimated than those for the higher frequency signals.

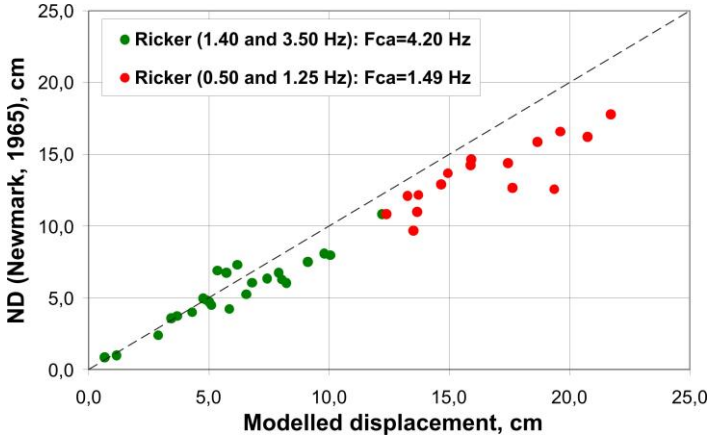

Figure BF.77: Plot of the ND values versus the modelled displacement for the cases of the Fca=4.20 Hz and Fca=1.49 Hz input signals.

V.7 Pure topographic model: regional prediction laws and updated model

The dataset of the modelled displacements are incorporated with corresponding I_a and A_c values to test the performance of selected regional models (Jibson, 1993; Jibson et al., 1998; Hsieh et al., 2007). According to Equations BE.30a-c, these regional laws predict the co-seismic displacement based on two parameters which characterize the impacting shaking (I_a) and the stability of the studied site (here, in terms of A_c).
The results of these analyses are presented in Figure BF.78, where the ND values are plotted against the modelled displacement. The model of Jibson (1993) has the worst prediction performace: the correlation coefficient for the plotted distribution is less than 0.5. The low performance of this law is mainly explained by the significant underestimation of displacements for the Fca = 1.49 Hz signal (see red dots in Figure BF.78a). Better predictions are yielded by the Jibson et al. (1998) model: the correlation coefficient is around 0.74. This law consistently underestimates the modelled displacements for both low and high frequency input signals (compare distribution for both green and red dots in Figure BF.78b). The best predictions are observed for the law of Hsieh et al. (2007): the correlation coefficient is around 0.82. This regional model presents a comparable level of performance for both input signals. Nevertheless, even this best model produces significant misfit in some cases (see, e.g., the green dot of 10.0 cm of modelled displacement versus 1.0 cm of predicted displacement in Figure BF.78c).

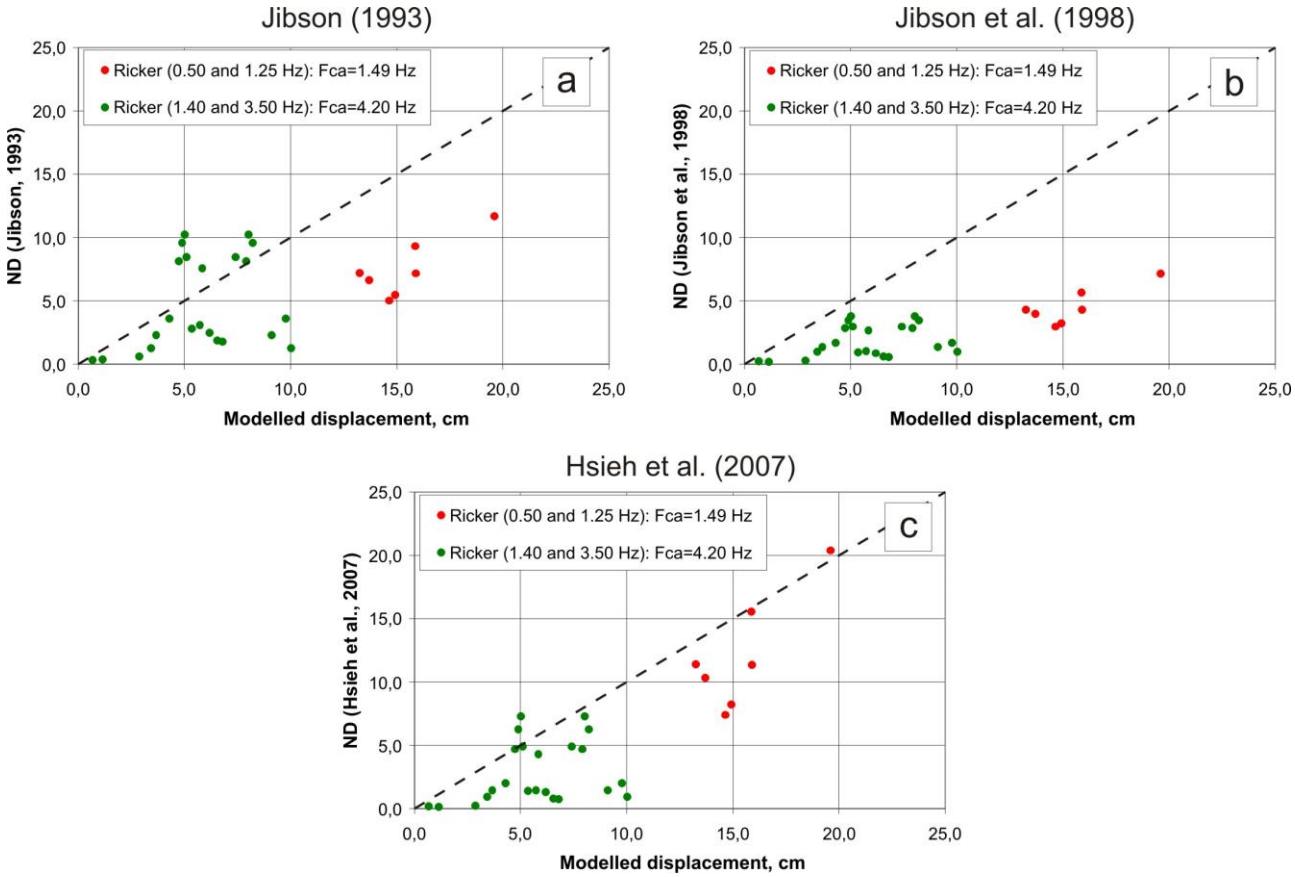

Figure BF.78: Plots of the ND values against the modelled displacements: the ND values are predicted by the Jibson, 1993 (a), Jibson et al., 1998 (b) and Hsieh et al. (2007) prediction laws.

As it is indicated in *Section B.IV.4*, the misfit between predicted and modelled values can be related to the fact that existing regional laws do not include the parameter which describes the central frequency of impacting shaking, e.g., through Fca. Meanwhile, the tests with rigid block proved an importance of Fca for the link between modelled displacement and I_a (see Figure BF.70). Therefore, we analysed the dataset attributed to the sinusoid signals and extract the prediction law where $\log D_n$ is determined by $\log(I_a)/Fca$ and $\log A_c$ (see a general shape of this law in Equation BE.31). The linear-shape laws are further used to relate the coefficient in this law with Fca. Finally, all manipulations allow us to extract the law shown in Equation BE.33.

The same statistical analysis is applied to our dataset of the modelled displacements triggered by Ricker signals with Fca of 1.49 and 4.20 Hz. The predicted parameters are the original values of the modelled displacement (D_n or in terms of its common logarithm, $\log D_n$). The series of tested predictors include the original values of basic parameters (I_a, Fca, A_c), their common logarithm ($\log I_a$, logFca, $\log A_c$), as well as different ratios, like $\log(I_a/Fca)$, $\log(I_a)/Fca$, $\log(A_c/Fca)$, $\log(A_c)/Fca$, etc.
Similar to the results obtained for the sinusoid signals, the cross-correlation reveals that $\log(I_a)/Fca$ and $\log A_c$ are the most important parameters to predict $\log D_n$. Thus, the extracted prediction laws are expressed as follows:

$$\log D_n = 0.3955 * \frac{\log I_a}{F_{ca}} - 0.7324 * \log A_c + 1.0526 \quad \text{for Fca=1.49 Hz} \qquad \text{(BE.34a)},$$

$$\log D_n = 0.4680 * \frac{\log I_a}{F_{ca}} - 0.8666 * \log A_c + 0.7293 \quad \text{for Fca=4.20 Hz} \qquad \text{(BE.34b)}.$$

Figure BF.79 plots the displacements predicted by this equation versus the modelled displacements. As it can be seen, the most reliable predictions are obtained for the low frequency signal (Fca=1.49 Hz), as the difference between predicted and modelled values is systematically smaller than 5.0 %. In general, less reliable predictions are obtained for the displacements triggered by the high frequency Ricker signal (Fca=4.20 Hz). The mean predictive error for these displacements is around 15.0 %, while extremely high errors are obtained for the displacements smaller than 2.0 cm. Meanwhile, the modelled displacements for both signals are predicted with a correlation coefficient of 0.96. This shows a very high degree of fit between the predicted and the modelled data.
The comparison between the prediction laws developed for the sinusoid- and Ricker-signals shows a certain regularity. Thus, similar to K1 in Equation BE.31, the coefficient attributed to $\log I_a/Fca$ in equations BE.34a and BE.34b has a positive trend with respect to Fca. The absolute value of the coefficient attributed to $\log A_c$ is also directly related to Fca, like it is for the sinusoid signals. Finally, the same reverse relation with respect to Fca is revealed for the intercept, which is L in Equation BE.30. Analysing those K1, K2 and L values for the Ricker type signals with respect to Fca we obtained the next linear-shape laws:

$$K1 = 0.0268 * Fca + 0.3557 \qquad \text{(BE.35a)},$$

$$K2 = 0.0495 * Fca + 0.6586 \qquad \text{(BE.35b)},$$

$$L = -0.1193 * Fca + 1.2303 \qquad \text{(BE.35c)}.$$

These last relationships are further introduced into equations BE.34a and BE.34b. Thus, the coefficient attributed to $\log I_a/Fca$ is replaced by Equation BE.35a, the coefficient of logAc is replaced by Equation BE.35b and the intercept is replaced by Equation BE.35c. Those manipulations allow us to extract the next form of prediction law:

$$\log D_n = (0.0268 * Fca + 0.3557) * \frac{\log I_a}{Fca} - (0.0495 * Fca + 0.6586) * \log(A_c) + (-0.1193 * Fca + 1.2303) = \qquad \text{(BE.36)}.$$
$$0.0268 * \log I_a + 0.3557 * \frac{\log I_a}{Fca} - 0.0495 * Fca * \log(A_c) - 0.6586 * \log(A_c) - 0.1193 * Fca + 1.2303$$

It should be noticed that this law is developed on the basis of limited data corresponding to Fca of 1.49 and 4.20 Hz. The shape of this law and especially laws predicting K1, K2 and L should further be clarified by the modelling tests using inputs with other values of Fca. Meanwhile, it is shown that the general form of the prediction law stays the same for the Ricker signals tested on a real topographic profile and the sinusoid signals tested on simplified model of sliding block. It further suggests that those additional tests with varying Fca will only update the coefficients in Equation BE.36, while the general form of the law will be preserved.

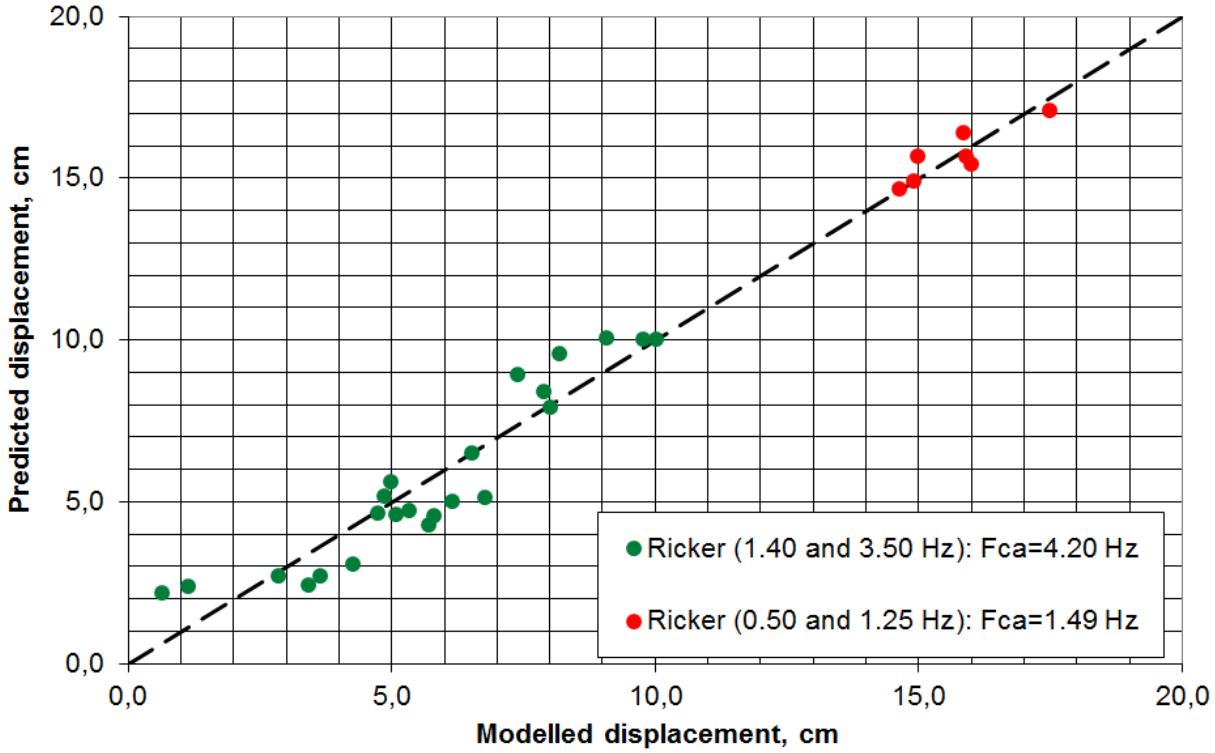

Figure BF.79: Plot of the predicted displacements versus the modelled displacements for the high- and low-frequency Ricker signals (note: the predicted displacements are those calculated according to Equation BE.34a and BE.34b).

Equation BE.36 can directly be applied to map the co-seismic displacement values acting as proxy to estimate the seismically-induced landslide susceptibility. This law includes a new parameter (Fca) which is not included in any conventional Newmark model. The regional distribution of Fca may be obtained by applying the laws of Rathje et al. (2004) which relates Fca (via mean period of seismic shaking) with the earthquakes magnitude and hypocentral distance (see equations BE.13a and BE.13b in *Section B.I.9*). The regional distributions of I_a and A_c may be obtained by applying conventional approaches. That mapping can also take into account our findings related to the pure topographic I_a amplification factors (see *Section B.IV.7*). Our next step is to explore the possibility to regionally predict the pure topographic I_a amplification factors (At). The 2D topographic modelling shows that At can be predicted based on the smoothed 2D curvature. That principle will be analysed in the next chapter through 3D dynamic modelling. These studies should establish a link between Ia amplification in the 3D domain and the 3D smoothed curvature.

VI. Proxy for mapping of the pure topographic Ia amplification factors: based on 3D studies

VI.1 Methodology

Chapter B.III presents the results of the 2D dynamic studies which analyse the pure topographic Ia amplification in terms of A_t. The studies were performed for six models made of a single material type and presenting real topographic settings. These analyses allowed us to relate the size of morphological features to spectral amplification patterns, which, in turn, determine the final value of A_t. These links finally yield the sample relationship where the value of A_t is predicted based on the smoothed curvature ($Curv_{Le}$) and the central frequency of the impacting seismic shaking (Fca). Nevertheless, this relationship cannot be directly implemented in the conventional Ia attenuation laws. The main limitation is related to the fact that 3D morphologies amplify the seismic shaking in two orthogonal directions, while the extracted law considers the amplification only along one direction.

This problem complexity is analysed in the current chapter where we study the pure topographic amplification of the Ia values in the 3D domain. The 3D dynamic studies are applied to the model with the following dimensions: 2.0 x 2.0 x 1.8 km. The model itself mainly represents the landslide-prone slope situated in the Minkush target area, Central Tien-Shan (a more detailed description of target area is presented below). The analysis considers varying Vs of the modelled material, as well as varying central frequencies of the input signals. The set of surface receivers records the acceleration time histories along two orthogonal directions. These recordings are later applied to calculate two components of the Arias Intensity (Iax and Iay) which are compared with reference values to determine the combined (in x- and y-directions) value of the Ia amplification factor (Atxy). These values of Atxy are later compared with the general curvature, the parameter which complexly accounts for the 3D shape of the real morphologies. The final goal of the studies is the development of the mapping proxy which can spatially map the distribution of the Atxy values based on the DEM of the study area and given the known values of Vs and Fca. The next section briefly reviews the target area, giving an emphasis on the environmental issues and coupled landslide risk in the surroundings of the targeted tailing site.

VI.2 The Minkush target area: mining legacy and landslide hazard

The Minkush target area is situated in the central Tien-Shan and is a former uranium mining site (see Figure BF.80). The settlement was established in 1948 in connection with the exploration activity initiated in the Kavak deposit (Nikolaev et al., 1992; Torgoev et al., 2009). The uranium mining started on 1955 and lasted until the early 70^s. The results of this activity are the numerous waste dumps and four uranium tailing sites (see Figure BF.81). During the first two years of mining (from 1955 till 1957) the processed material (*pulp*) was directly discharged into the Minkush River which led to the substantial pollution of the river network. The next five years (from 1957 till 1962) the tailing material has started to be stored in the Tuyuk-Suu tailing (see a position in Figure BF.81). From 1962 until the end of mining activity the tailing material has started to be accumulated in the Dalnee/Kak and Taldy-Bulak tailings sites situated at more than 10 km far from the Minkush village (see Figure BF.81).

The Dalnee and Kak tailings are the smallest ones: they both contain around 306,000 m^3 of tailing material. The Taldy-Bulak tailing site has approximate volume of 395,000 m^3. According to IAEA (2009) these three tailings do not pose a significant environmental threat as they are situated quite far from the settlements and the river network. The protective infrastructure of these sites is not threatened by the geohazard impacts and only minor problems due to seasonal flooding are anticipated.

The highest environmental concern is related to the biggest Tuyuk-Suu tailing which has an approximate volume of 640,000 m^3. This site is situated at a distance of less than 2.0 km far from the settlement (see Figure BF.81). The serious problems here are related to the infiltration of river water and to the gradual destruction of protective infrastructure by seasonal floods/mudflows. Due to the critical state of the Tuyuk-Suu tailing, the Minkush area is considered to be one of the most environmentally hotspot areas in the territory of Kyrgyzstan. The national responsible agencies in cooperation with international organizations try to implement a series of remediation measures on this site. The most probable action includes the relocation of the tailing materials to the Dalnee/Kak/Taldy-Bulak tailings, which are exposed to a lower level of the geoenvironmental risk.

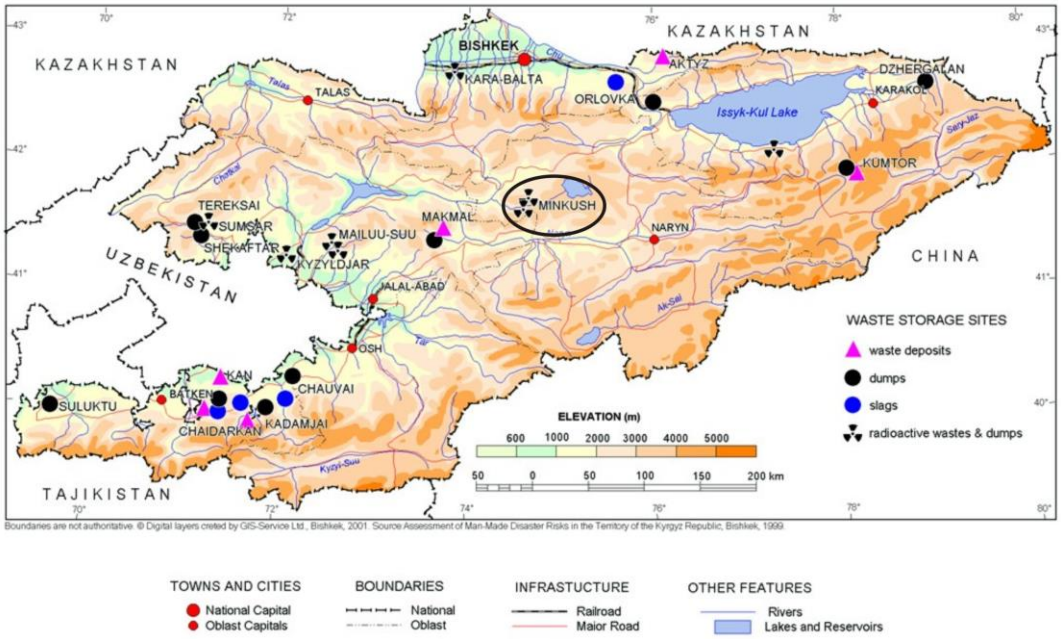

Figure BF.80: Map of Kyrgyzstan with indication of mining legacy sites (the Minkush target area is outlined by the black oval).

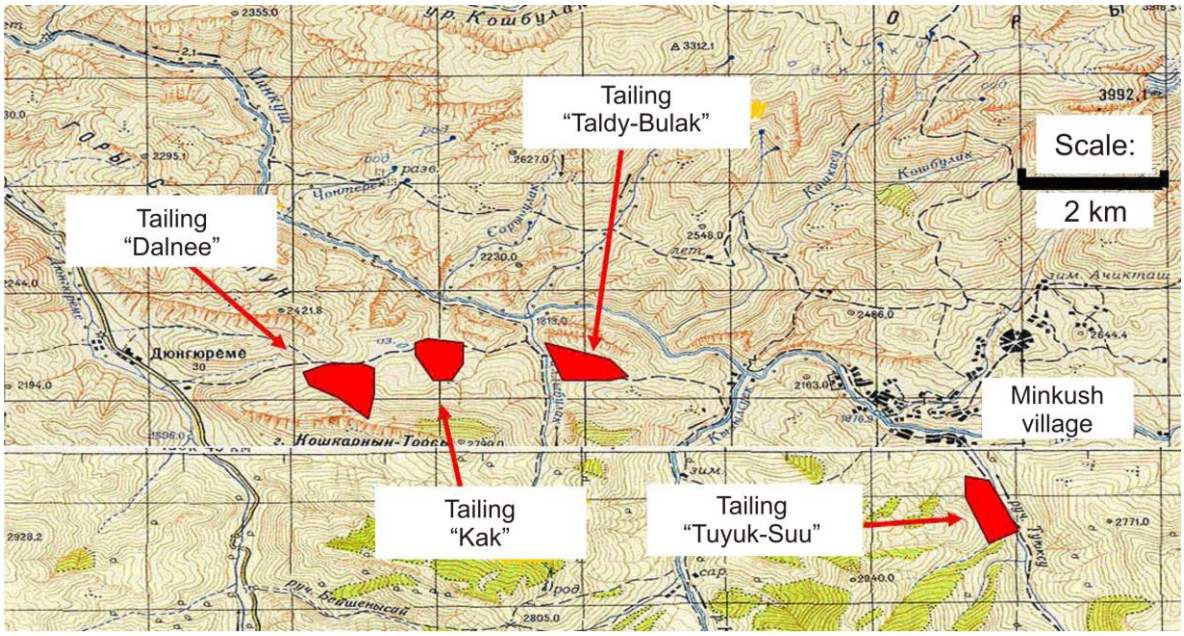

Figure BF.81: The uranium waste tailings in the surrounding of the Minkush City.

The geoenvironmental risk at the Tuyuk-Suu tailing is aggravated by the presence of an active landslide which is situated less than 200 m downstream from the lowest tailing dam (see Figures BF.82a and BF.82b). According to Torgoev et al. (2013b), this landslide has a thickness ranging between 15 and 30 m, while the volume of the sliding mass is at about 700,000 m^3. As the landslide is located downstream from the tailing, its direct impact on the tailing is unlikely (Torgoev et al., 2009). Nevertheless, the authors comment that negative impacts can originate from multiple events: landslide failure→river damming→upstream flooding→river erosion→tailing dam destruction→river pollution.

Alioshin et al. (2008) performed field studies and extensometric measurements on the Tuyuk-Suu landslide during the period between 2003 and 2010. The authors indicate that the first reactivation of this landslide occurred in the second half of 2004 (see Scarp 1 in Figure BF.83). It is supposed that this scarp appeared due to the coincidence of the high precipitation and the intense seismic activity in 2004. Additional landslide scarps are identified in 2006 and 2008 (see Scarps 2-5 in Figure BF.83). The extensometric measurements

show that the lower part of the landslide moves on average with a rate of about 4.7 cm/month, with the highest movement rates registered in spring and fall due to higher amounts of precipitation observed during these seasons. The results of extensometric measurements show that the cumulative downslope displacement at the end of the period 2004-2010 has reached the value of 4.4 m in the lower part, of 1.4 m in the middle part and of 0.4 m in the upper part of the Tuyuk-Suu landslide.

Figure BF.82: Views of the Tuyuk-Suu tailing, landslide and the Minkush village showing the high exposure of the tailing site to potential impacts of the landslide activity.

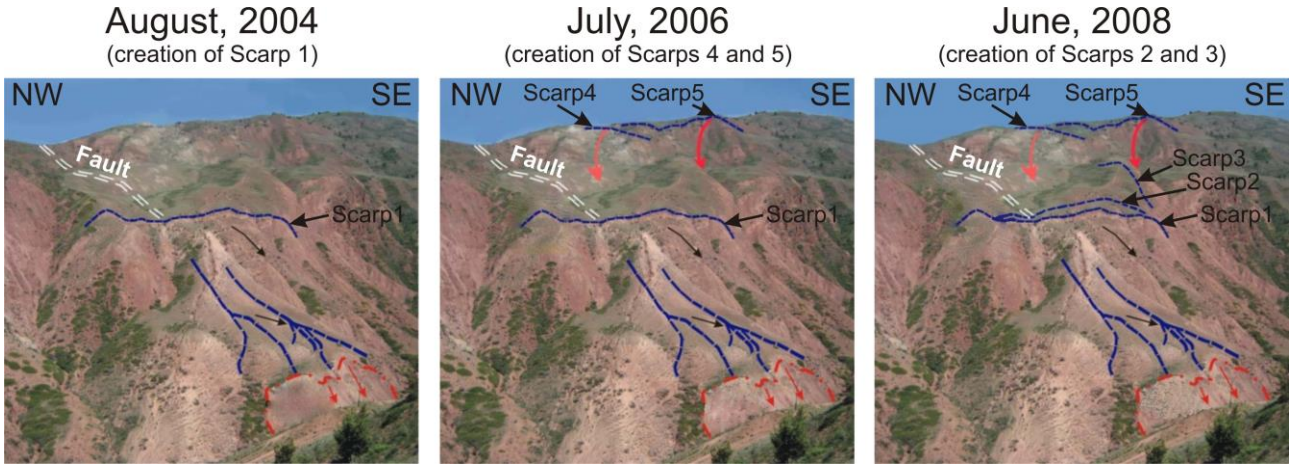

Figure BF.83: Evolution of the Tuyuk-Suu landslide from 2004 till 2008 (by Alioshin et al., 2008).

Torgoev et al. (2013b) comment that the slope movement is mainly controlled by the precipitation rate which has an influence on the underground water level in the sliding mass. However, a seismic influence on slope movements is also observed. Thus, the authors show that the seismic shaking with PGA of 0.01-0.03g (registered on rock) can trigger some downslope displacement of a few centimeters. The low level of triggering PGA may be explained by amplification effects on the landslide-prone slope. The authors assume that topographic amplification should be more pronounced compared to geological effects, as the sliding mass has relatively small thickness.

The surroundings of the Tuyuk-Suu tailing and the whole extent of the landslide-prone slope are included into the analysed 3D model composed of a single material type. Thus, only the pure topographic amplification effects can be modelled. The 3D modelling should show the range of the PGA amplification observed along the unstable slope: it should partially explain why the slope movement is triggered by the comparatively low value of PGA registered at the rock. The extraction of the 3D model, as well as critical modelling settings (studied materials, input signals, etc.) are analysed more in detail in the section below.

VI.3 3D modelling settings: model extraction, material sequence, input signals

Figure BF.84 presents a high-resolution Quickbird image of the target area with the indicated position of the Tuyuk-Suu landslide and tailing (see the red dotted outlines). The extent of the 3D model is marked by the quadratic outline with the size of 2.0x2.0 km. As it can be seen, the modelled area covers the whole extent of

the landslide-prone slope, while the tailing and landslide are situated in the middle part of it. The surface topography is shown by the perspective 3D views of the modelled area: the elevation varies from 2017 m up to 2692 m. The bottom of the model is fixed at a depth of 500 m, which means that the height of the 3D model ranges from 1517 m till 2192 m (the mean height is at around 1800 m).

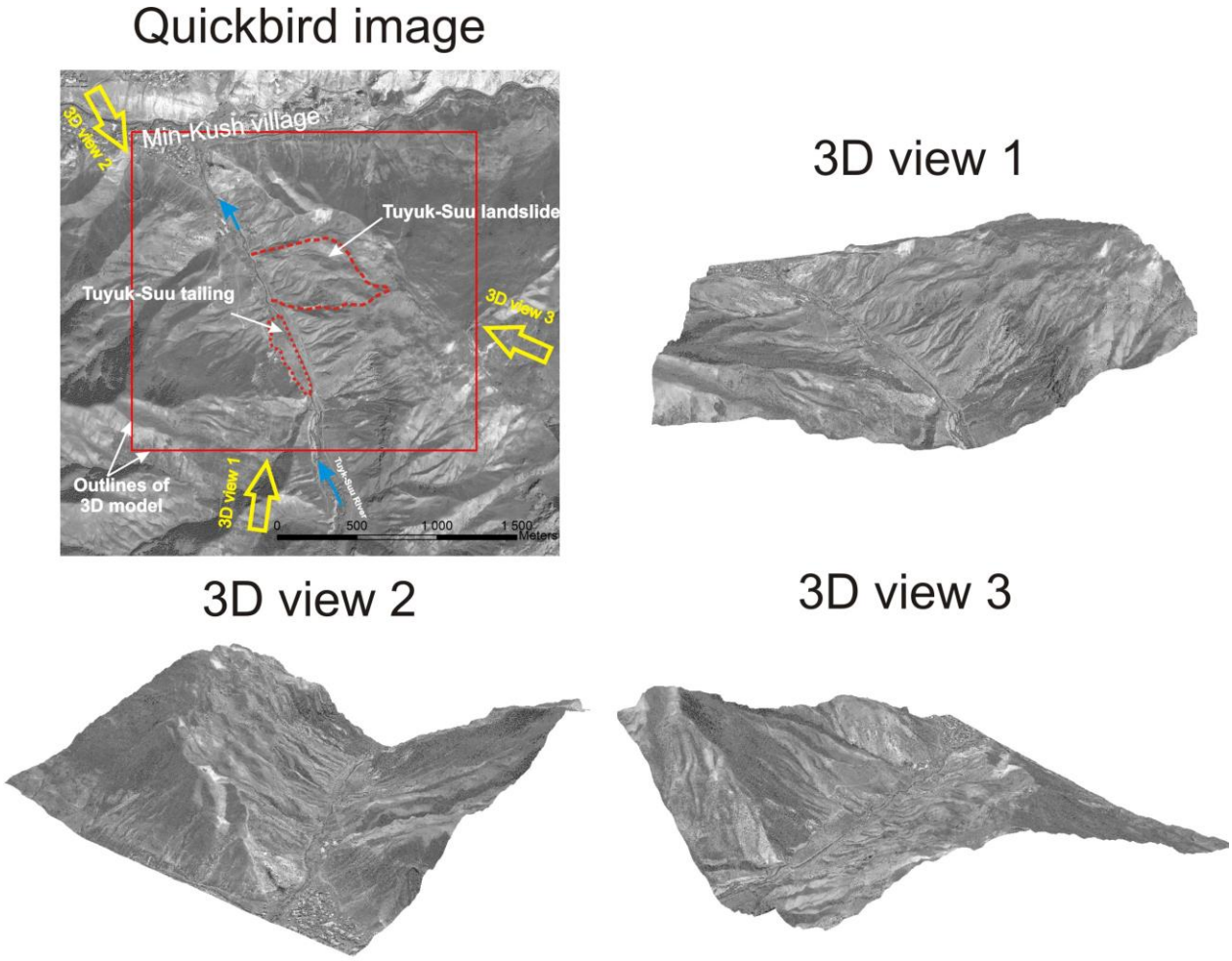

Figure BF.84: Quickbird image of the target area with indicated position of the Tuyuk-Suu tailing/landslide and extent of the 3D model (see also the direction of the three 3D views of the site shown in this figure).

The inner part of the model, from bottom up to the near-surface, is filled by cubic FD-zones with a dimension of 15.0x15.0x15.0 m (brick shape in FLAC^{3D} terminology - see Figure BF.85a). The FD-zones on the model surface have a clipped cubic shape (degraded brick mesh in FLAC^{3D} terminology - see example in Figure BF.84b). In that shape the position of the P3, P5, P6, P7 nodes (see them in Figure BF.85a) is altered according to the elevation values extracted from the SPOT DEM (note: the 20.0 m SPOT DEM is resampled at a resolution of 7.5 m to fit the 15.0 m FD-zones). The coinciding nodes of the neighbouring FD-zones exactly fit each other – that way the smoothness of the earth surface is restored (see the part of model surface in Figure BF.85b).

Figure BF.86 compares the SPOT DEM of the target area versus the surface of the 3D model represented by the degraded brick cells. As it can be seen, the original smoothness of the earth surface is well represented by the applied FD-zones. That feature is very critical regarding the modelling of seismic energy propagation. The topographic site effects mainly originate due to the wave focusing/reflection/refraction at the earth surface. Specific topographic features (such as holes, cliffs, scarps, etc.) create numerous reflection/refraction patterns which significantly differ from those created by the smoothed surface. Therefore, during the extraction of the 3D model we took care of reconstructing the original surface morphology. Figure BF.86 shows that the FD-zones with the degraded brick shape successfully accomplish this task.

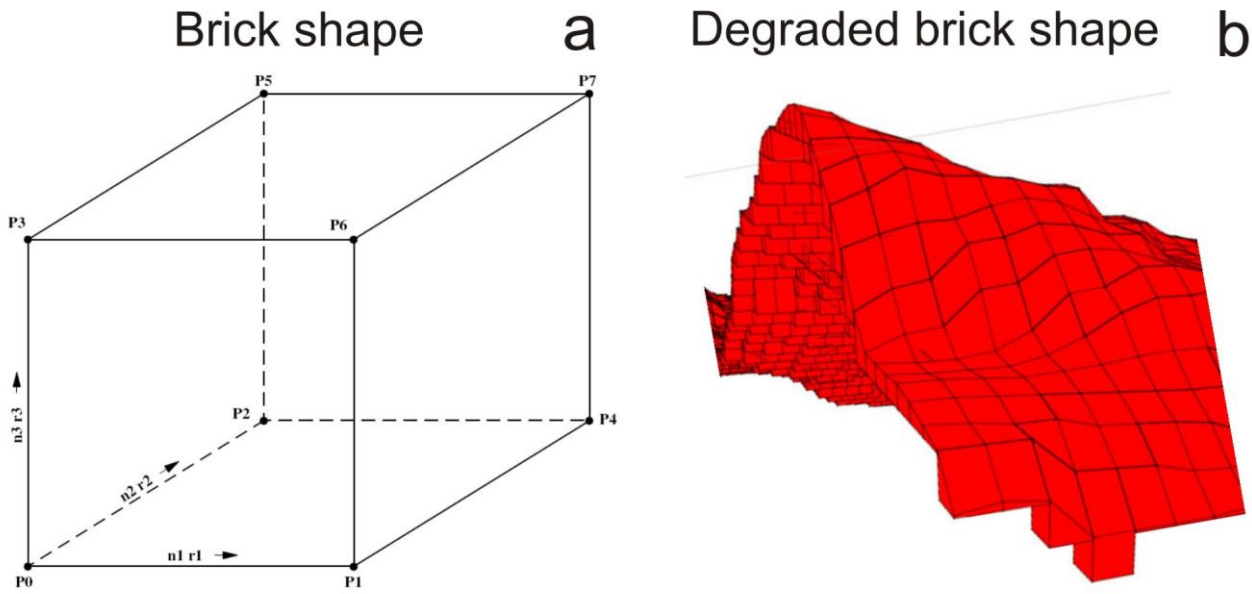

Figure BF.85: (a) Schematic representation of brick cell with the nodes forming the shape of the FD-zone (by ITASCA, 2009); (b) assemblage of the degraded brick cells which restore the smoothness of the earth surface.

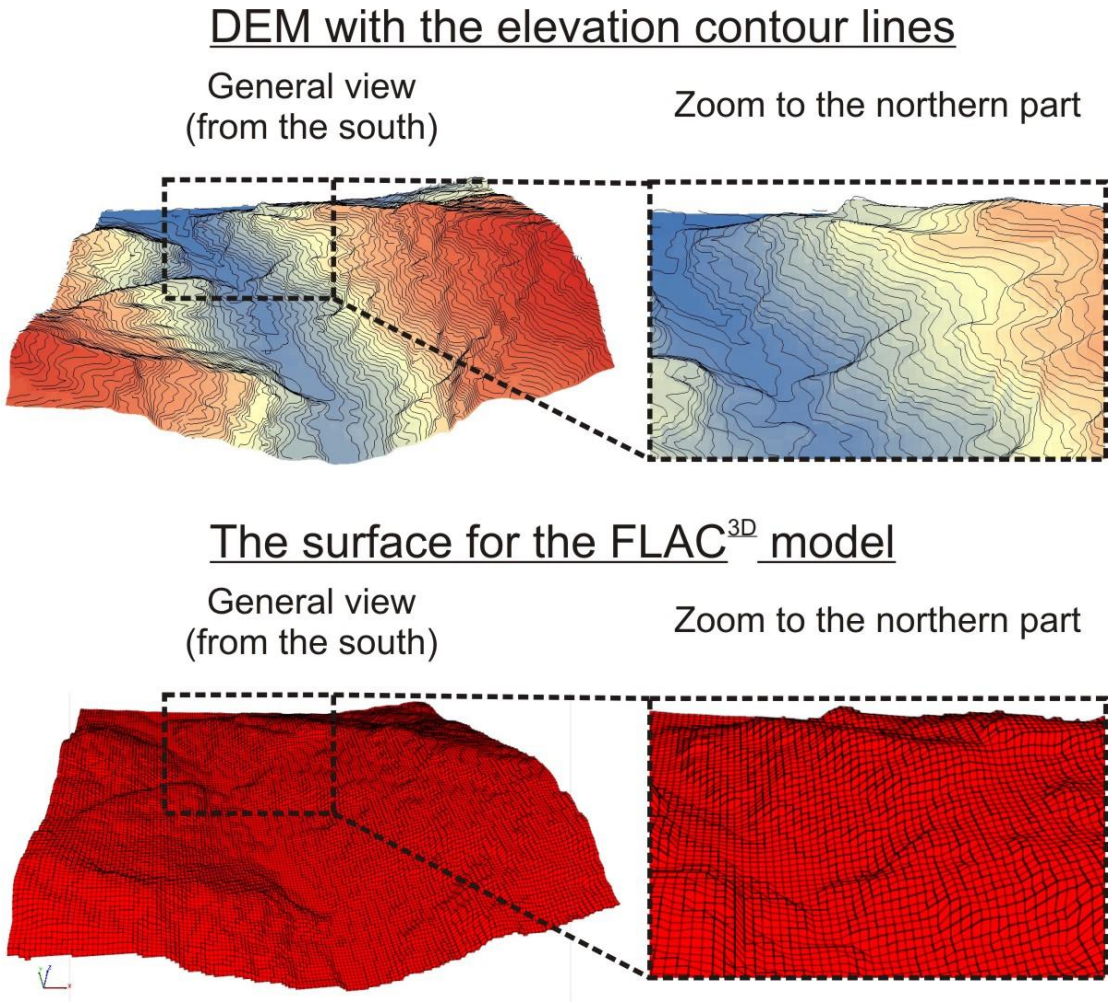

Figure BF.86: 3D views of the SPOT DEM of the target area and the extracted surface of the 3D model.

The 3D dynamic studies aimed at the modelling of the pure topographic site effects using models with uniform material types. Four main materials are studied through the sequence of the 3D dynamic tests (see Table BT.4). The most critical parameter for our studies is the shear wave velocity (V_s, m/sec). As it can be seen from Table BT.4, the analysed values of V_s range from 700 m/sec to 1400 m/sec. The applied values of V_p are equal to 1.7-1.8 of V_s, while the material density is uniform for all analysed materials and equals to 2400 kg/m^3.

Table BT.4: The material types analysed in the sequence of the 3D dynamical tests

Material	Density, kg/m^3	V_p, m/sec	V_s, m/sec	K, MPa	G, MPa
1	2400	1200	700	1888	1176
2	2400	1500	850	3088	1734
3	2400	1800	1000	4576	2400
4	2400	2600	1400	9952	4704

The model with defined geometry and assigned material properties is subjected to the same stabilization procedure which was applied for the 2D dynamic studies with the UDEC code (see *Section B.II.7*). At first, the model bottom and lateral boundaries are fixed in vertical and horizontal directions. The model with fixed boundaries is later subjected to the numerical stabilization, down to a preset minimal value of the mechanical force ratio (10^{-9}) that should be reached during iterations. After that, the free-field conditions are assigned to all lateral boundaries and the model bottom. The sequence of stabilization procedures is completed by additional iterations during which the preset minimal value of the unbalance force (10^{-9} N) is reached.
The stabilized models with assigned boundary conditions are finally subjected to the seismic loading using the Ricker shape shear stress wave as input (shear stress in both x- and y-directions). Figure BF.87a presents an input signal with a central frequency of shear stress (Fs) equal to 1.50 Hz. The resulting acceleration time histories in both x- and y-directions have quasi-sinusoid shapes (see the examples in Figure BF.87b). As it can be seen, the central frequency of the acceleration time histories (Fca=1.80 Hz) is higher than the value of Fs=1.50 Hz. The yielded PGA values for the input acceleration-time histories are not important, as the studies aim at the determination of the relative amplification of seismic shaking (in terms of Ia).

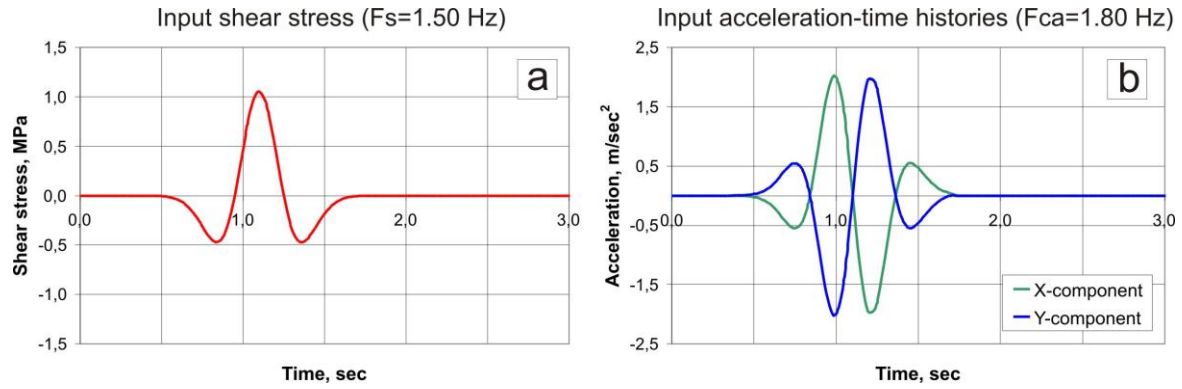

Figure BF.87: Example of the Ricker shape shear stress wave with Fs=1.50 Hz (a) which yields quasi-sinusoid acceleration time histories along both horizontal directions (b).

The studies apply varying values of Fs ranging from 0.75 to 4.0 Hz. Figure BF.88 summarizes the input acceleration time histories in terms of spectral density curves. These curves are extracted based on the x-component shaking recorded at the model bottom (reference receiver – see more details below). Figure BF.87b shows that the y-component shaking presents the inverted form of the history recorded along the x-direction, i.e. both histories correlate with each other through a factor of -1. Therefore, the spectral density curves, presented in Figure BF.88, represent the shaking along both horizontal directions. The values of Fca range between 0.98 and 4.85 Hz: these values are higher than corresponding Fs values (compare Fca and Fs in the legend of Figure BF.88). The lowest frequency signal (Fca=0.98 Hz) is characterized by the narrowest spectral width, while the signal with the highest Fca=4.85 Hz has the broadest spectral content among the applied input signals.

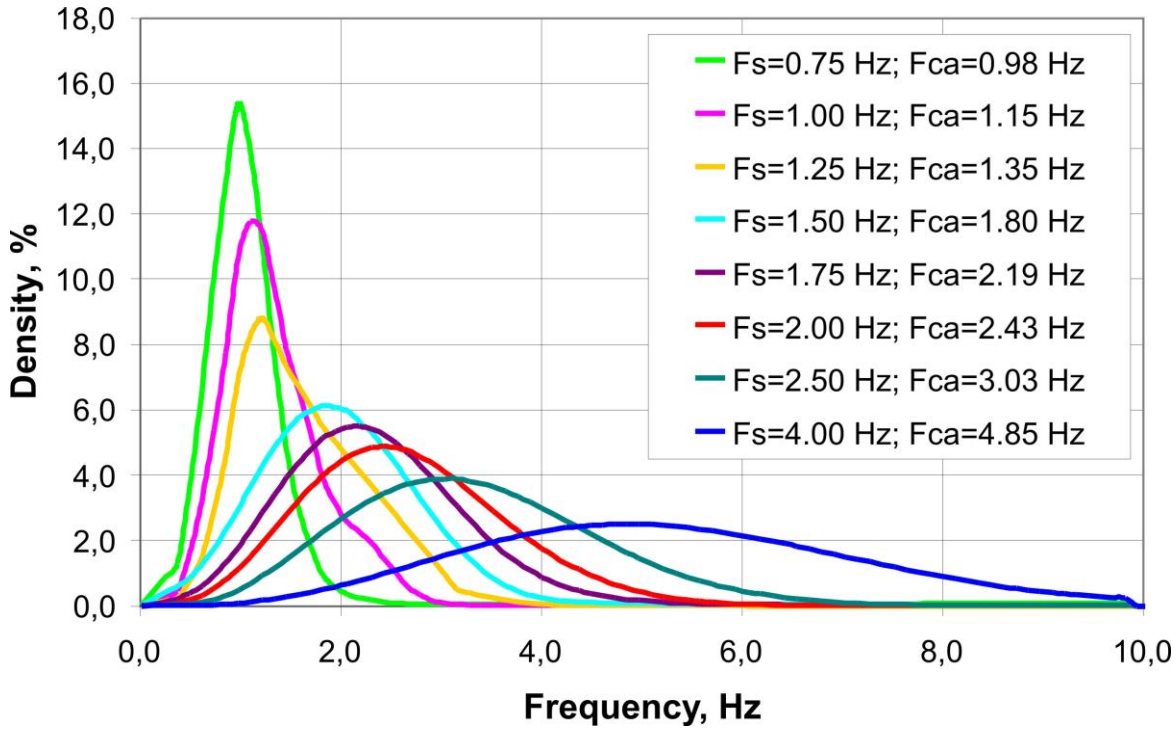

Figure BF.88: Spectral density curves for the input acceleration-time histories (note: the corresponding values of Fs and Fca are listed in the legend).

The input signal with the lowest central frequency (Fca=0.98 Hz) has the longest duration of the seismic loading which is equal to 2.5 sec. The other signals have a shorter duration of loading. For example, Figure BF.87b shows that the Fca=1.80 Hz signal develops a loading during 1.2 sec (approximately, between 0.5 and 1.7 sec). Logically, the shortest duration of the loading corresponds to the Fca=4.85 Hz signal: it is equal to not more than 0.5 sec of dynamic time.

The dynamic modelling is performed within 4.0-8.0 sec depending on the studied Vs and applied Fca value. Thus, the models with Vs=700 m/sec are cycled longer than models with higher Vs values. Similarly, the lower frequency signals have a longer duration of dynamic cycling, while the high frequency signals are modelled during shorter periods of time. The applied duration of modelling insured the full propagation of seismic energy from the model bottom up to the surface. An extended duration of cycling also allows us to record the secondary reflection/refraction patterns, created by the curved model surface.

The dynamic modelling is coupled with the parallel recording of the acceleration-time histories along both x- and y-directions. Two types of the recording network are applied: the first one is characterized by the absence of regularity in the position of the receivers (Figure BF.89a), while the history points in the second network are evenly-spaced along the central part of the model surface (Figure BF.89b). Additionally, all studied models contain one reference receiver situated 15.0 m above the model bottom (in the middle of the horizontal model plane). The reference recordings are applied to calculate the Ia, PGA as well as the spectral amplification patterns registered in different parts of the model surface.

The network of non-regularly distributed receivers contains 243 history points (see Figure BF.89a). It consists of several subsets which yield output for the specific tasks. For example, one subset of receivers tracks the amplification patterns along the whole extent of the landslide-prone slope. Another subset of receivers covers the parts of surface with varying slope angle where the earth curvature is negligible (note: both slope angle and topographic curvature correspond to the values calculated based on the 15.0 m cell size). One more subset records the shaking in flat areas (slope angle is around 0) where the topographic curvature varies.

The second network contains 414 receivers evenly-spaced over the central part of the model (see Figure BF.89b). The spacing between neighbouring receivers is equal to 60 m along the x-axis and is equal to 75 m along the y-axis. This network yields the main data applied by us to relate the Ia amplification to the

smoothed curvature. The smoothing of curvature is impacted by the model boundaries: therefore, all receivers are situated at a certain distance from them (see more details in *Section B.VI.6*).

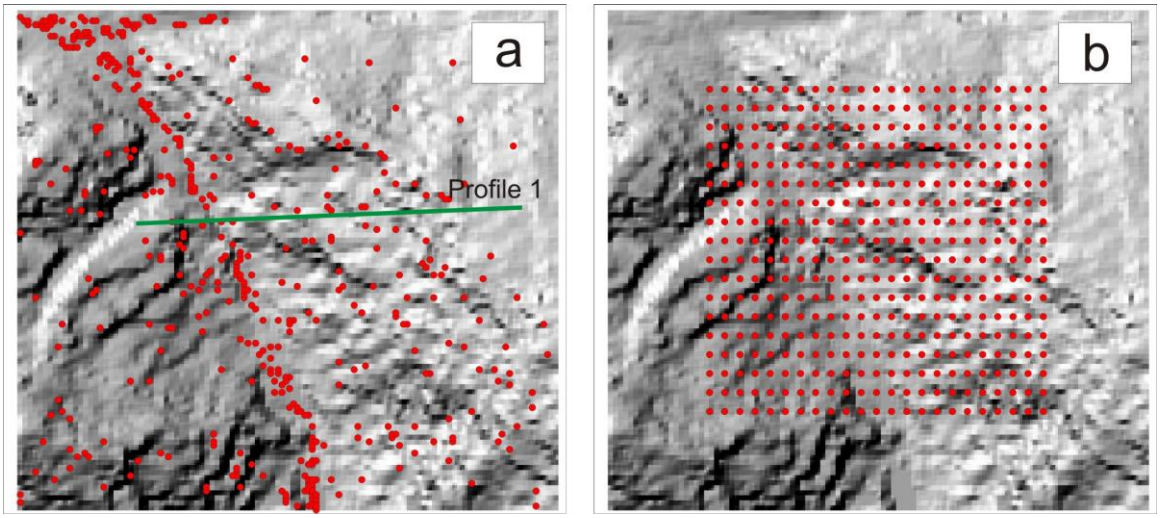

Figure BF.89: (a) The recording network with non-regularly distributed receivers (Profile 1 crosses the Tuyuk-Suu landslide); (b) the network with the receivers distributed along 60.0 x 75.0 m regular net.

The main task of our analysis is to track the total amplification of the Ia values both along both x- and y-axes. The data preparation is similar to the procedures employed for the 2D studies (see *Section B.II.8*). Thus, both orthogonal acceleration time histories are squared and integrated over the recorded time span to get the values of Iax (x-component shaking) and Iay (y-component shaking). For all surface receivers these Iax and Iay values are then summed to get the total value of Iaxy. The reference histories prior to integration are subjected to filtering and a multiplication by 2. Then, the resulting values of Iax_0 and Iay_0 are also summed to get the value of $Iaxy_0$. Finally, the value of Iaxy at all surface receivers is compared with the reference $Iaxy_0$ to get the value of the total amplification factor (Atxy):

$$Atxy = \frac{Iaxy}{Iaxy_0} = \frac{Iax + Iay}{Iax_0 + Iay_0} \qquad \text{(BE.37)},$$

where Iax and Iay (m/sec) are the x- and y-component Ia values for the given surface receiver; Iax_0 and Iay_0 (m/sec) are the x- and y-component Ia values for the reference receiver (note: Iax_0 and Iay_0 are calculated based on histories which are subjected to filtering and multiplication by 2).
The spatial distribution of Atxy is gained for the different modelling scenarios with varying values of Vs and Fca. The values of Atxy are further compared with the smoothed 3D curvature which is automatically mapped in ArcGIS by using the DEM of the modelled area. The next sections provide a detailed review of the modelling results aiming at establishing a link between Atxy and the smoothed curvature. The studies also allow us to track the amplification patterns along the landslide-prone slope.

VI.4 The Tuyuk-Suu landslide: seismic amplification patterns

According to Figure BF.84, the slope of the Tuyuk-Suu landslide has a predominant aspect of 270º, i.e. it is oriented to the west. In our 3D model the west-east direction corresponds to the x-axis. It further suggests that the shaking along the x-component is the most critical to characterize the triggering potential of the seismic loading. Therefore, the amplification patterns along this slope are solely characterized via the x-component shaking. All data are summarized over Profile 1 which crosses the landslide-prone slope along the west-east direction (see a position of profile in Figure BF.89a). The amplification patterns are outlined for the model made of Material 4 (density of 2400 kg/m^3, V_s=1400 m/sec, V_p= 2600 m/sec; see Table BT.4).

These material properties were defined on the basis of the results of the geophysical survey performed by Torgoev et al. (2013b) on this unstable slope.

Figure BF.90 summarizes the spectral amplification patterns registered in different parts of Profile 1. The presented spectral ratio curves show the surface amplification affecting the x-component shaking with respect to the reference receiver situated at the model bottom (note: the reference recording prior to analysis is subjected to filtering and multiplication by a factor of 2). The spectral ratio curves are extracted based on tests with the Fca=2.19 Hz signal. Nevertheless, as it is shown in *Section B.III.9*, the shape of the spectral ratio curve does not depend on the value of Fca, as it is solely related to the site settings (i.e., material properties, surface curvature, slope angle, etc.). Therefore, the presented curves are valid for all types of input signals.

As it can be seen, the landslide-prone slope is situated between receivers P3 and P10. The analysis of the curves suggests that this slope induces amplification at 0.80 Hz (see Peak 1 marked by the green font on all graphs). Logically, the lowest amplification at Peak 1 is revealed at the valley bottom (P3), while the crest of the slope (P10) is marked by the highest value of the spectral ratio at the range of 0.80 Hz. Peak 1 does also appear on the opposite slope (P1, P2) and on the plateau (P12): this feature is explained by the neighbourhood effect which is also confirmed by the results of the 2D studies (see *Section B.III.6*).

The crest part of the slope (receivers P9, P10, P11) is characterized by the specific shape of the spectral ratio curves, where a substantial amplification at 2.10 Hz can be identified (see Peak 2 marked by the red font). This Peak 2 is absent in the neighbouring receivers (P8, P12), which confirms that the amplification at this spectral range is induced by the part of the slope between P9 and P11.

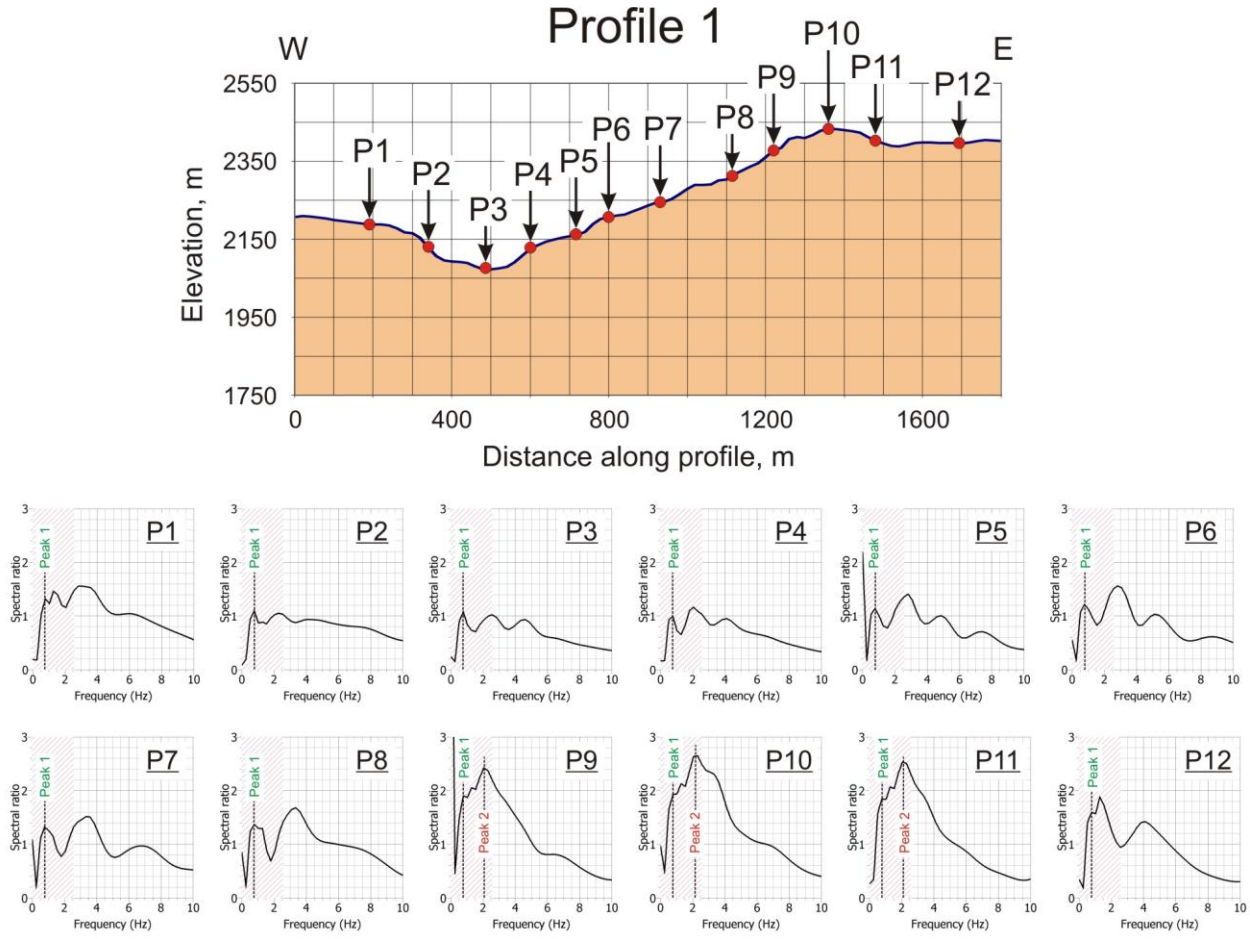

Figure BF.90: Profile 1 crossing the slope of the Tuyuk-Suu landslide and plots of the spectral ratio curves extracted at different parts of the profile (based on the x-acceleration recordings for the Fca=2.19 Hz input signal; the spectral ratio curves show amplification with respect to the bottom recording subjected to filtering and multiplication by a factor of 2).

Figure BF.91 presents the distribution of the PGA amplification factors registered for the tests with varying values of Fca. Here, the reference receiver is situated in the valley bottom and corresponds to receiver P3 in Figure BF.90. As it can be seen, the lowest crest/base PGA amplification is revealed for the Fca=4.85 Hz signal (see the value of 0.94). The highest value of the crest/base PGA amplification is registered for the Fca=2.43 Hz signal and it is equal to 1.67. The lowest frequency signal (Fca=0.98 Hz) has a moderate value of PGA amplification which is equal to 1.40. Interestingly, half of the tests show that the opposite slope (position of P1 receiver in Figure BF.90) is characterized by higher values of the PGA amplification, even though this slope has a lower height. Only the test with the Fca=3.03 Hz signal yields higher PGA amplification at the crest of the unstable slope comparing to this value on the opposite hill (1.47 versus 1.43). The test with the Fca=2.43 Hz signal yields the identical PGA amplification at both slopes (see the value of 1.67). Logically, the middle parts of the unstable slope and plateau have lower PGA amplification comparing to that value at the crest.

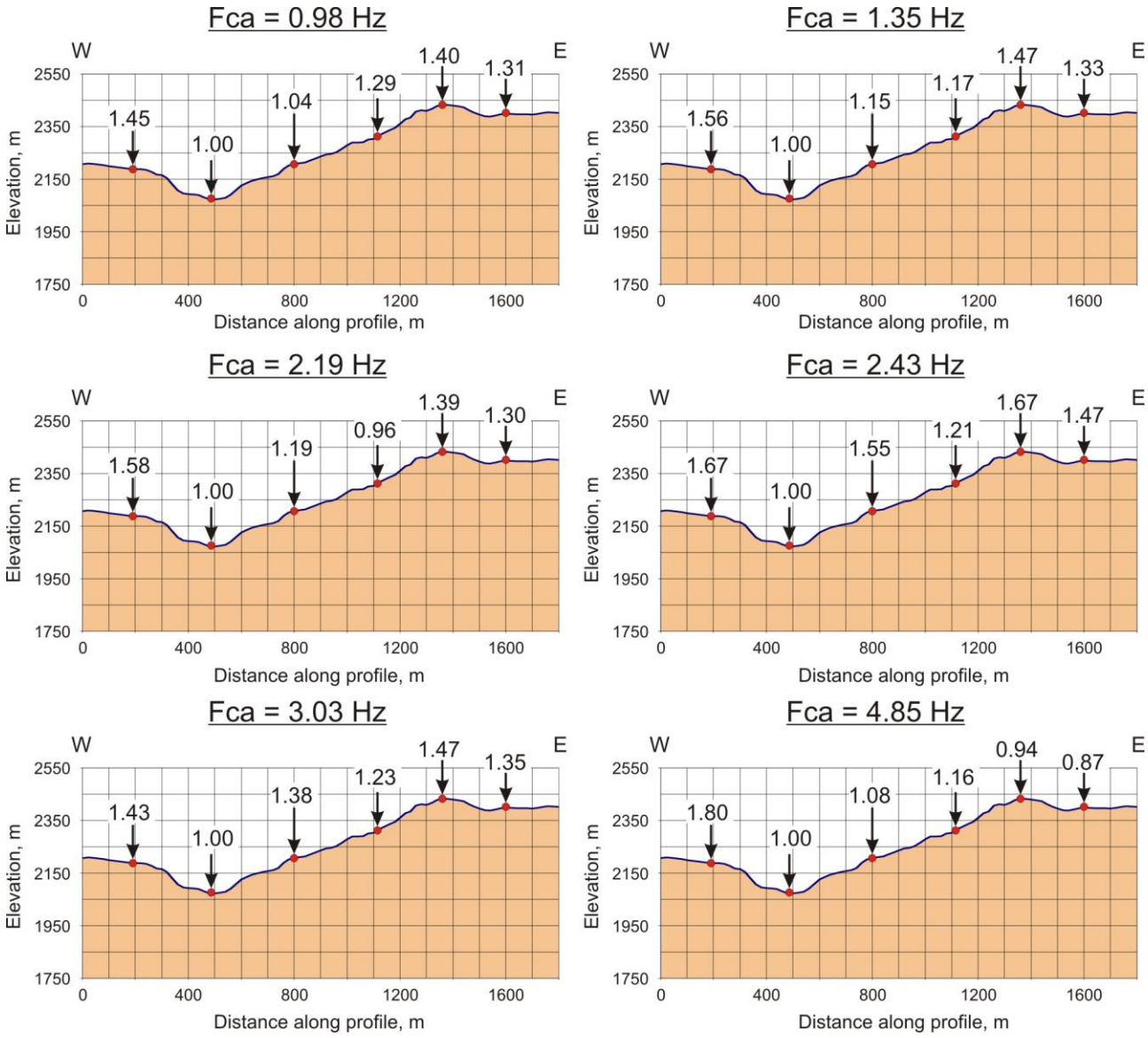

Figure BF.91: Values of PGA amplification recorded in different parts of Profile 1 applying the input signals with varying Fca (the reference receiver is situated in the valley where PGA amplification is marked by the value of 1.00).

A similar distribution of the Ia amplification factors is summarized in Figure BF.92. Here, again the reference receiver is situated in the valley bottom (see the places with Ia amplification factor equal to 1.0). Most of the tests demonstrate that the relative crest/base amplification of the Ia values is larger than 2.0. Only the high frequency signal (Fca=4.85 Hz) is characterized by a slight deamplification of the Ia value (see the value of 0.95). This feature can be explained by the spectral deamplification above 6.0 Hz which is registered in the crestal part of the studied slope (see the spectral curves for P9, P10 and P11 in Figure BF.90). According to Figure BF.88, the Fca=4.85 Hz signal has a notable portion of energy within the spectral range above 6.0 Hz: the spectral deamplification at this range results in the deamplified value of Ia.
The spectral ratio curve for the receiver P10 indicates that the crest of the unstable slope has the strongest amplification at 2.10 Hz (see Peak 2 in Figure BF.90). The Fca=2.19 Hz signal is marked by an almost coinciding central frequency: according to *Section B.III.9*, it would mean that this signal should yield the highest value of the crest/base Ia amplification factor. Nevertheless, the final value of Ia and At are also dependent on the input spectrum of the impacting shaking (see the spectral density curves in Figure BF.88). Thus, the Fca=2.43 Hz signal has a slightly broader spectral content compared to the Fca=2.19 Hz signal. This difference results in higher Ia amplification yielded by the Fca=2.43 Hz signal compared to that value obtained for the Fca=2.19 Hz signal (2.71 versus 2.29).

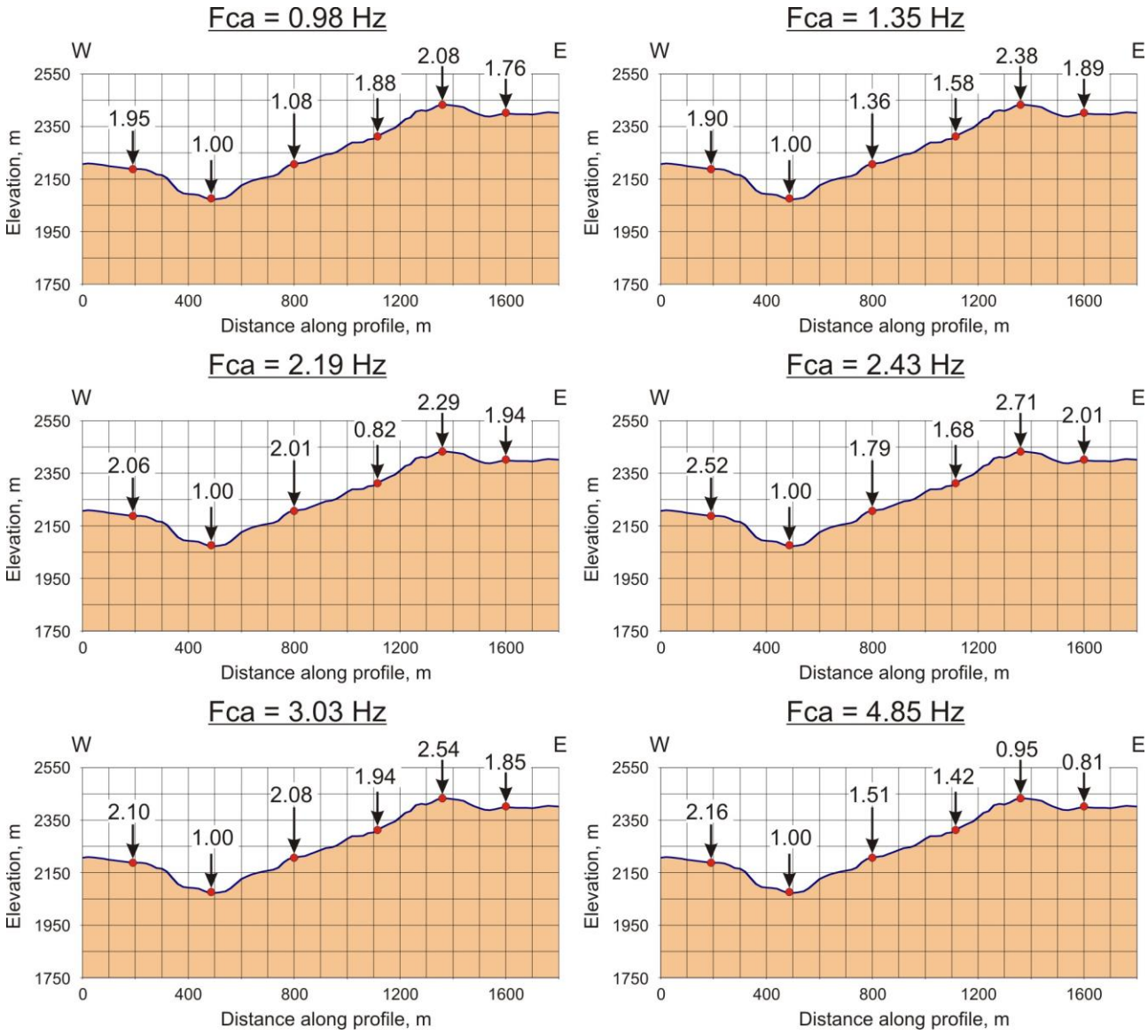

Figure BF.92: Values of the Ia amplification registered in different parts of Profile 1 applying the input signals with varying Fca (the reference receiver is situated in the valley where the Ia amplification is marked by a value of 1.00).

Alioshin et al. (2008) indicate that the Tuyuk-Suu landslide was first reactivated in 2004, partially due to a number of seismic events with magnitude (M) ranging between 3.7 and 4.5 with epicentral distances ranging between 50 and 80 km. Rathje et al. (2004) propose a law relating the central frequency of seismic shaking (Fca) to M and epicentral distance. According to this relationship, those triggering events would have been marked by 2.5<Fca<3.0 Hz. This range of Fca is very close to the one which yielded the highest PGA and Ia amplification along the studied slope. It indicates that the triggering of the Tuyuk-Suu landslide in 2004 is probably related to the topographic amplification along this slope. The results of the 3D studies further suggest that the far-distant earthquakes can also impact the stability of the Tuyuk-Suu landslide, as the Ia amplification for the low-frequency shaking exceeds the factor of 2. Small earthquakes with an epicentral distance of less than 20-30 km are anticipated to have a minor triggering potential, as the high frequency shaking is less amplified along the studied slope.
The amplification patterns along the slope of the Tuyuk-Suu landslide were analysed only for the x-components of recorded shaking. In the next sections we employ both orthogonal components of the recorded acceleration time histories to calculate the total value of Ia (Iaxy). The amplification of the Iaxy is measured via Atxy which distribution is compared with the 3D smoothed curvature. The section below presents the distribution of the Atxy values obtained for some of the performed tests. These data should provide a hint on the easiest way to predict the spatial distribution of the Iaxy amplification factors.

VI.5 General patterns of the Ia amplification in 3D domain

According to Equation BE.37, the total amplification of the Ia values in the 3D domain (studied via Atxy) is complexly related to the amplification of Ia in both orthogonal directions (expressed via Atx for Iax and Aty for Iay). The 2D dynamic studies (*Chapter B.III*) show that the single-component Ia amplification is related to the smoothed 2D curvature: the convex morphologies (hills/mountains) amplify the Ia values, while the concave features (valleys/depressions) favour deamplification. The central frequency of seismic shaking (Fca) plays an important role in these processes. The larger morphologies (curvature smoothed over larger spatial extent) have a stronger effect on the low-frequency shaking, while smaller topographic features (curvature smoothed over shorter spatial extent) influence more the high-frequency shaking.
Figure BF.93 analyses the amplification of Iax and Iay values recorded for the test with Vs=1000 m/sec and the input signal marked by Fca=2.43 Hz. Figures B.93 a and c present the oblique 3D view of the Quickbird image which is overlaid by the spatial distribution of the registered values of Atx and Aty (note: Atx=Iax/ Iax_0 and Aty=Iay/ Iay_0 – see those parameters in Equation BE.37). Additionally, the study area is crossed by two orthogonally oriented profiles (see the position of Profile 2 in Figure BF.93a and position of Profile 3 in Figure BF.93c). Profile 2 is oriented along x-axis (east-west), while Profile 3 is oriented along y-axis (north-south). The change of the topography along these profiles is presented in Figures BF.93 b and d, where the 2D distribution of Atx (Profile 2) and Aty (Profile 3) is also highlighted. This representation facilitates the data analyses, as it is focused on specific links between Atx/Aty and 2D morphology in respective directions. For example, the change of Atx can be visually compared with the concavity/convexity along the x-axis, while the same observations can be made for the distribution of Aty along the y-axis.
The 2D distribution of Atx and Aty (see Figures BF.93 b and d) confirms the systematic features revealed through the 2D dynamic studies. Thus, the concave morphologies deamplify the values of Ia (see the valleys and depressions marked by Atx and Aty values of less than 1). The hilltops and the crests of the convexities are systematically marked by the highest Ia amplification values, i.e. these sites are characterized by the maximal values of Atx and Aty. Figures BF.93 a and c indicate that the Ia deamplification can reach the factor of 0.4, while the maximal amplification is marked by the factor of 3.6 (see the distribution and legends for both Atx and Aty).
Thus, Figure BF.93 confirms that the single-component Ia amplification is directly related to the change of morphology along the corresponding direction. As it is shown in Equation BE.37, the value of Atxy depends on amplification of both Iax and Iay. It further suggests that the most expressive deamplification/amplification patterns should be revealed over the symmetric 3D morphologies, i.e. over those which are simultaneously convex or concave in both orthogonal directions. For example, the hill with symmetric shape amplifies the Ia values along both x- and y-directions, which significantly influences the final value of Atxy. The same conclusion can be made for the depression with symmetric shape, which

should deamplify the Ia values in both orthogonal directions. The assymmetric morphologies should be characterized by less expressive patterns, as basic amplification or deamplification occurs along a single direction. An elongated ridge is one example of such asymmetric feature: the site effects across the ridge should normally be much more pronounced compared to the orthogonal direction, i.e. along the ridge.

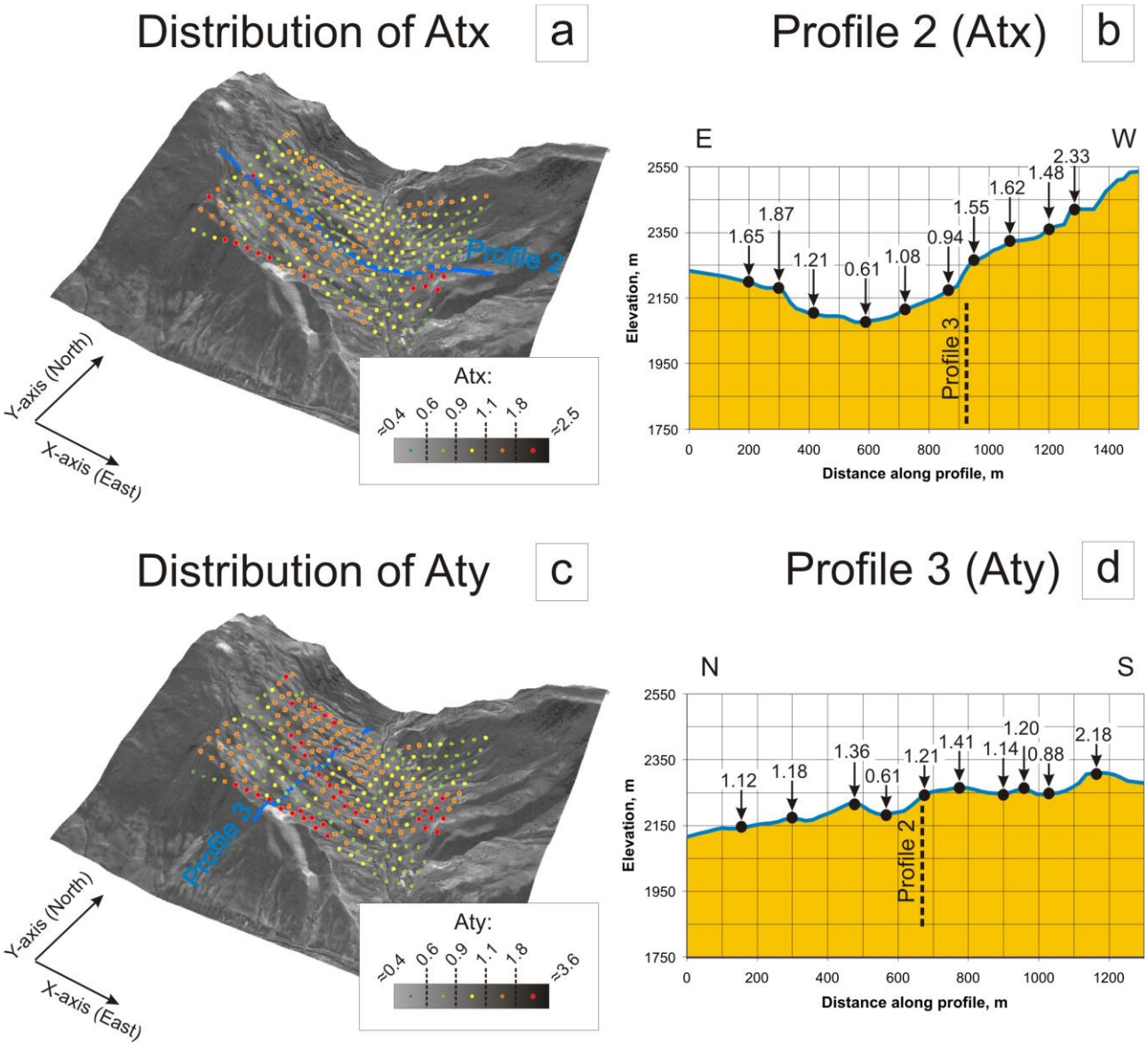

Figure BF.93: The modelling results for the tests with Vs=1000 m/sec and Fca=2.43 Hz: (a) 3D distribution of the Atx values together with the indicated position of Profile 2; (b) 2D distribution of the Atx values along Profile 2; (c) 3D distribution of the Aty values together with indicated position of Profile 3; (b) 2D distribution of the Aty values along Profile 3.

Figure BF.94 analyses the spatial distribution of Atxy for the tests with the fixed Vs=1000 m/sec, when Fca is equal to 1.15, 2.24 and 3.03 Hz. Figure BF.94a shows that for the input signal with Fca=1.15 Hz the valley is systematically characterized by Atxy<0.9. The higher frequency signals (Figures B.94 b and c) are marked by a less systematic deamplification in this part of the model, even though some basic deamplification can still be observed (in most parts of valley Atxy<1.1). This difference can be explained through the fact that the high frequency signals are more sensitive to the smaller morphologies. The general valley topography influences less the site effects over the high frequency range. Figure BF.94a indicates that the concavity of the valley starts to play a significant role if the input signal has Fca=1.15 Hz.

Figure BF.94 also shows that some of the convex morphologies induce systematic amplification, i.e. the higher values of Atxy are always observed near the crest parts of those morphologies (see the areas marked by the blue dashed outlines in Figure BF.94). According to our previous discussions, the features with systematically higher (or lower) values of Atxy should have more or less symmetric shape in both orthogonal directions. In reverse, the less symmetric features should produce less expressive amplification patterns. Such features can be found in the middle of the landslide-prone slope: they are marked by the more or less uniform values of Atxy, mainly between 1.1 and 1.8.

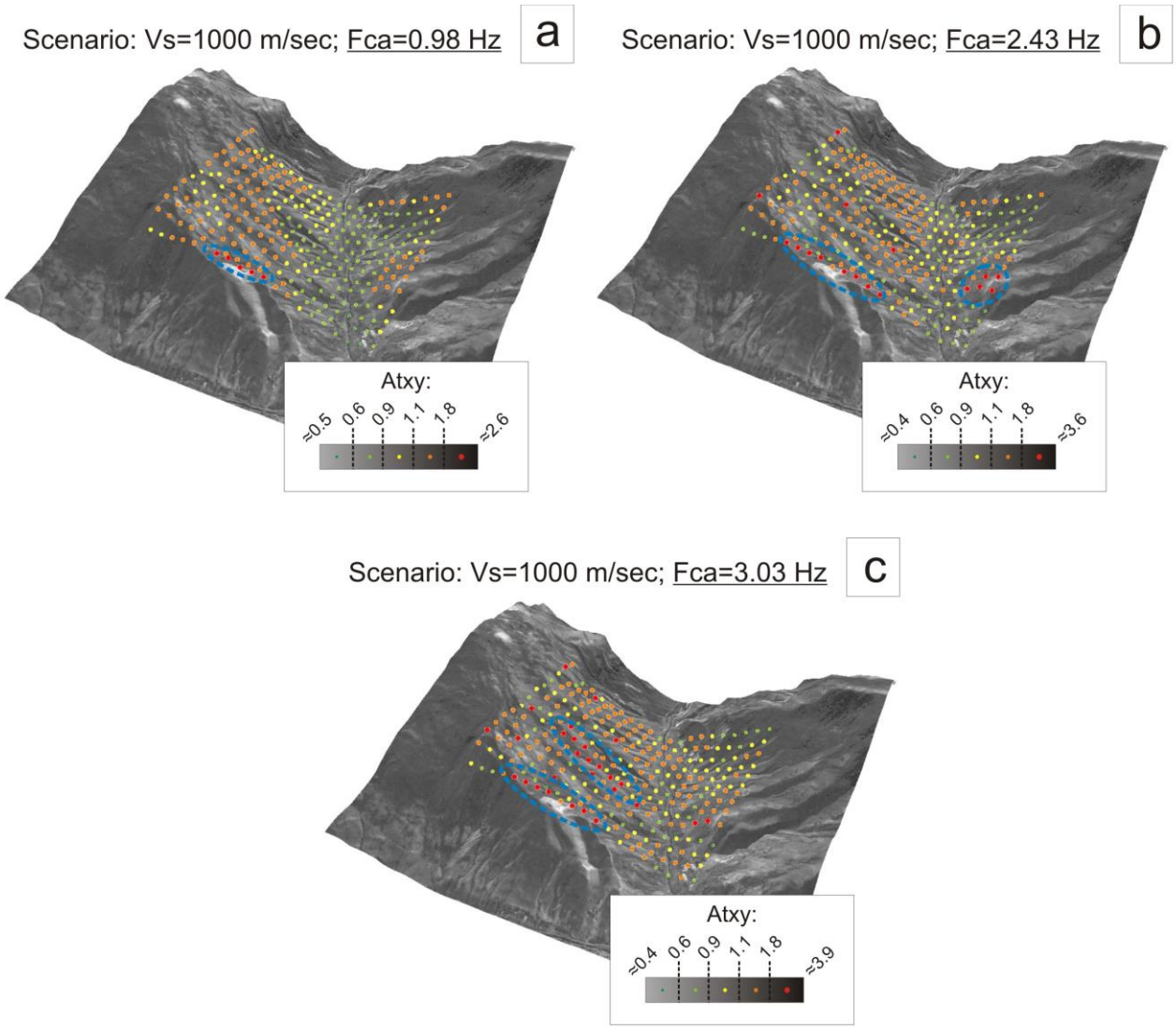

Figure BF.94: Distribution of Atxy for the tests with fixed Vs=1000 m/sec and varying Fca (blue dashed outlines mark the areas with the highest values of Atxy).

Figure BF.95 presents the distribution of Atxy for the tests with fixed Fca=1.15 Hz, but with varying Vs of the studied material (850, 1000 and 1400 m/sec). As it can be seen, in all tests the valley is characterized by the lowest values of Atxy, while the most expressive and systematic deamplification is registered for Vs=1400 m/sec (in most parts of valley Atxy<0.6). This model also has the most regular distribution of the Atxy values; here, several areas with more or less uniform ranges of Atxy can be outlined. The model with Vs=850 m/sec produces less expressive deamplification in the valley (0.6<Atxy<1.1), while it yields the highest amplification over two studied convexities (see the areas marked by the blue dashed outlines in Figure BF.95a). These convexities also amplify the Iaxy values in the models with Vs=1000 and 1400 m/sec. Nevertheless, the amplification intensity is lower for the models composed of the material with larger Vs (compare the highest Atxy values in the legends of Figures BF.95 a-c).

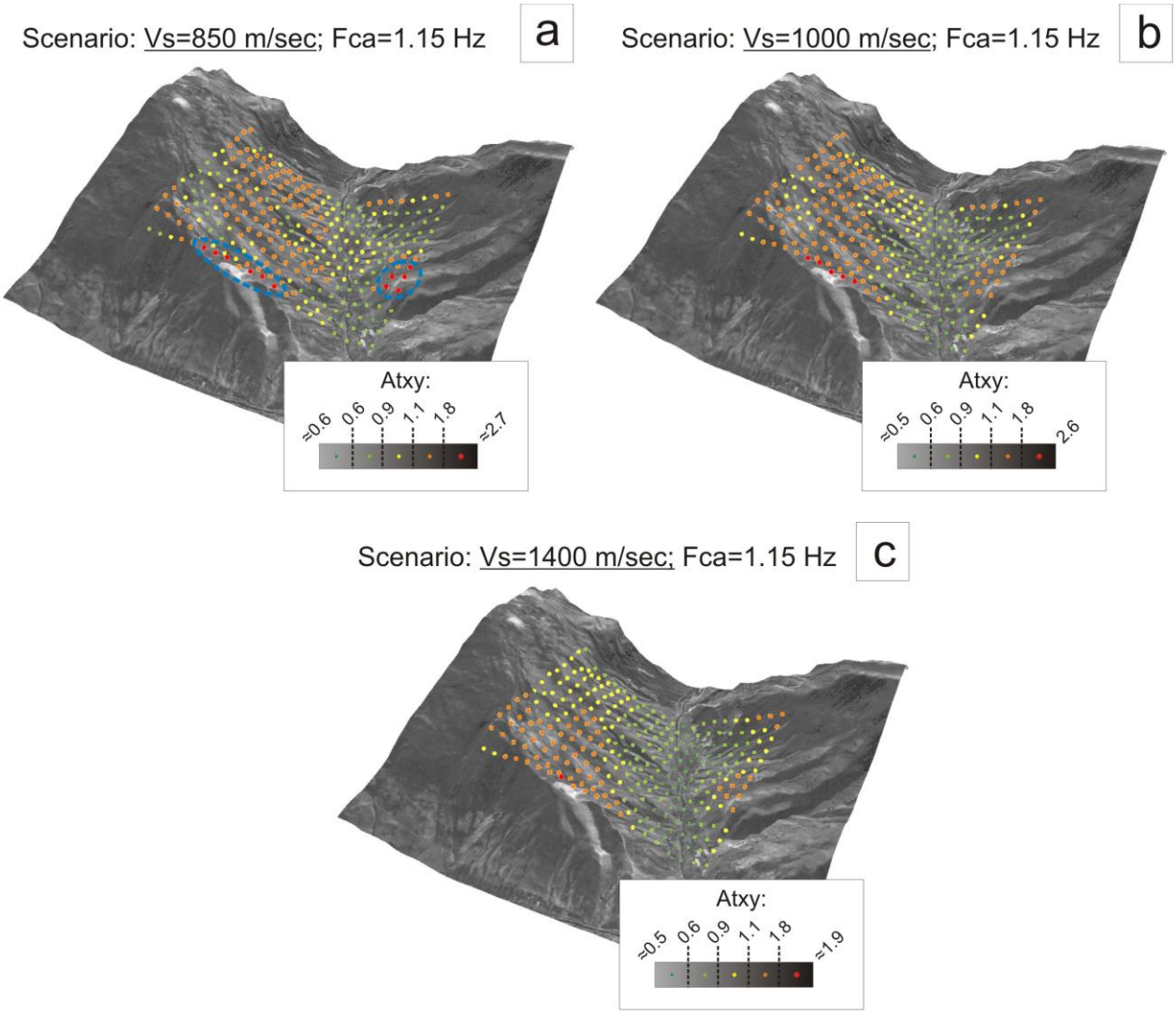

Figure BF.95: Distribution of Atxy for the tests with fixed Fca=1.15 Hz and varying Vs of the studied material (blue dashed outlines mark the convexities with the highest values of Atxy).

Thus, the qualitative analyses of the spatially distributed values of Atxy confirm the links established by the 2D studies. The convex 3D morphologies amplify the values of Iaxy, while the concave 3D features deamplify them. Logically, the symmetric morphologies produce the most expressive amplification or deamplification patterns, as the both orthogonal components of seismic shaking are impacted in the same way by the topographic site effects. The 2D dynamic studies show that the associated processes depends on two important parameters: Vs and Fca. The qualitative analyses of the 3D results reveal certain regularity regarding the impact of Fca: the low frequency shaking is impacted by the larger morphologies, while the high frequency shaking is more modified by the smaller morphologic features.
Section B.III.11 showed that the single-component Ia amplification can be predicted via the parameter called as the 2D smoothed curvature. The best predictions are yielded by the so-called effective curvature, i.e. by the curvature smoothed over the spatial extent predicted by the Geli's law. In the next sections we analyse the validity of these links in the 3D domain. The important milestone of these analyses is the way to extract the 3D smoothed curvature. Being the starting point of our analysis, this issue is reviewed in detail below.

VI.6 3D curvature: extraction and smoothing techniques

The concept of the surface curvature as the topographic index is reviewed in *Section B.III.10*. To remind, Zeverbergen and Thorne (1987) applied the polynomial function to reproduce the spatial distribution of the

elevation values extracted from the DEM of the study area. The 1st spatial derivative of that function is the slope angle and it shows the change of the elevation per unit of spatial extent. The 2nd spatial derivative of the same polynomial function shows the change of epy slope angle per unit of spatial extent and this parameter is called the surface curvature.

Figure BF.96a presents the procedure which spatially maps the 3D general curvature based on the elevation values extracted from the DEM of study area (note: for a later simplicity the term curvature reffers to the 3D general curvature). That mapping concept is adopted by the ArcGIS program which proposes convenient tools to automatically map this parameter (via Spatial Analyst/Surface/Curvature or 3D Analyst/Raster Surface/Curvature). Therefore, we applied these tools in ArcGIS to map the curvature values based on the input DEM with a resolution of 7.5 m (resampled from the 20.0 m SPOT DEM – see details in *Section B.IV.3*). Figure BF.96b presents the 7.5 m DEM of the study area and Figure BF.96c shows the raster of the automatically extracted curvature values.

Figure BF.96a demonstrates that the 3D general curvature depends on two main parameters representing the profile (D) and plan curvature (E). These components of the 3D general curvature show the change of the slope angle along both orthogonal directions. In that respect, the positive values of the 3D general curvature show that the given morphology has the predominant upward convexity, while the negative values indicate the predominant downward concavity. Perfectly flat areas should have the plan/profile/general curvature equal to 0.

It should be noted that some specific shapes can also have the 3D general curvature which is equal to zero. For example, it can be the case of an ideal saddle for which the positive plan curvature is exactly counterbalanced by the negative profile curvature (this is only true if the resolution to represent this shape is fine enough). Meanwhile, such ideal shapes are almost absent in the real conditions. Most topographic features are either convex or concave in both directions (more or less symmetric hills/depressions), or have negligible curvature in one or both directions (elongated ridge/valley or flat surface). For example, Figure BF.96b shows a part of the hillshaded DEM of the target area and Figure BF.96c presents the curvature raster extracted from this DEM in ArcGIS. As it can be seen, the highly positive curvature values mark the crest of the ridges and hills, while the highly negative curvature values are revealed at the ridge base and hill toes. The flat areas are marked by the close to zero curvature values (see the yellow areas marked by curvature between -0.1 and 0.1 in Figure BF.96c).

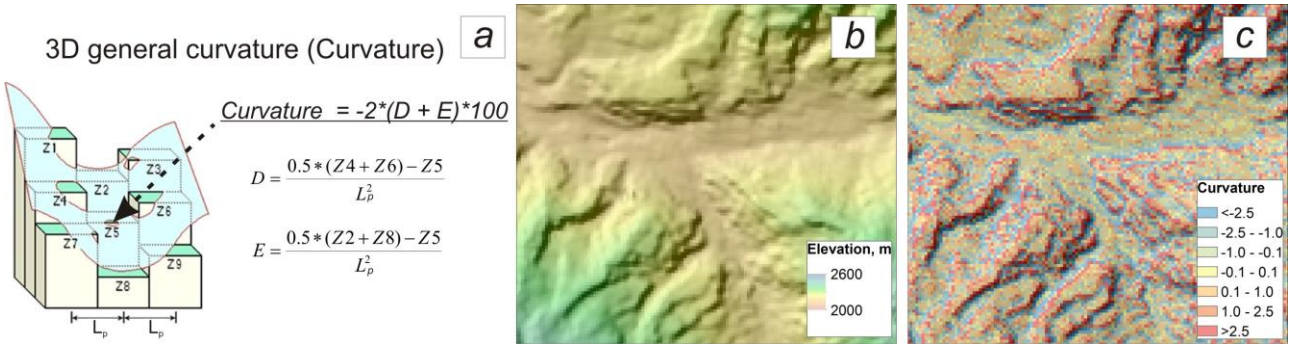

Figure BF.96: (a) Calculation of the 3D general curvature based on elevation data from DEM, where Z1, Z2…Z9 are the elevation values for the corresponding pixels (m) and Lp (m) is DEM pixel size (ESRI 2012; modified); (b) input DEM with resolution of 7.5 m; (c) automatically extracted raster of the 3D general curvature (ArcGIS tool: Spatial Analyst/Surface/Curvature; input DEM is shown in Figure BF.96b).

ArcGIS proposes the flexible and convenient solution to automatically map the values of the smoothed 3D curvature (e.g., via Spatial Analyst/Neighbourhood/Focal Statistics). That tool analyses the specific neighbourhood over each pixel and returns the predefined statistical parameter. The user can define the shape of the neighbourhood, as well as its dimensions (see the examples in Figures BF.97 a-c). The returned statistical parameters for each pixel include the mean, majority, maximum, median, minimum, minority or range over the user-defined neighbourhood.

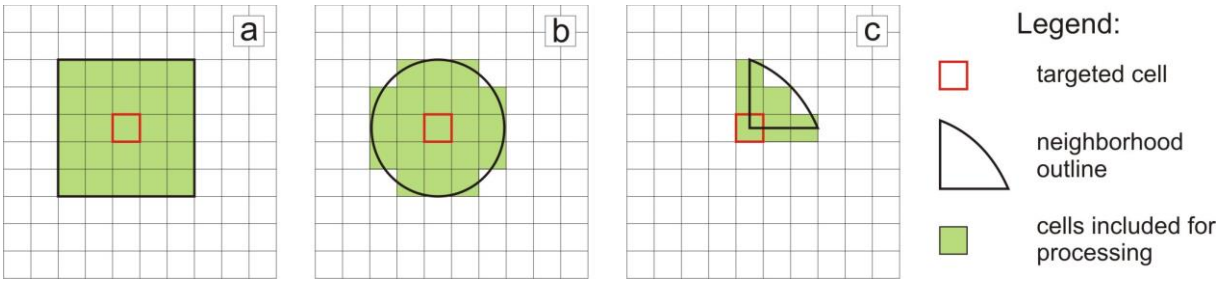

Figure BF.97: Some examples of the neighbourhood shapes available in the ArcGIS code: (a) rectangle (defined parameters: width and height in cells or m); (b) circle (defined parameter: radius in cells or m); (c) wedge (defined parameters: start and end angles in degrees, radius in cells or m).

According to *Section B.III.10*, the smoothed 2D curvature for each studied site (surface receiver) is calculated via a recurrent procedure. The first step is the collection of all curvature values located within the specified distance from the studied site. At the second step these curvature values are analysed to get the mean value which is finally referred to as the smoothed 2D curvature. In the ArcGIS terminology the smoothing of curvature means the mapping of the mean values for the input curvature raster, while the applied neighbourhood is the same as the smoothing distance in the 2D studies.

For our analyses we selected the circle to be the main shape of the processing/smoothing neighbourhood (see that shape in Figure BF.97b). The selection is based on the consideration that the amplification of the Iaxy values is mainly impacted by the average curvature along the x- and y-directions: the circle increases the weights of the curvature values along these directions compared to the curvature along other lateral directions (see the cells included for processing in Figure BF.97b). It is important to note that the size of the smoothing circle is defined via the radius (R, in terms of cells or meters). The smoothing spatial extent in the 2D studies is referred to as the curvature baseline length (L), which in the ArcGIS analyses is the double of R, i.e. L=2R.

We apply two conceptually different approaches to map the 3D smoothed curvature. The first approach is straightforward, when the input raster represents the curvature values extracted from the 7.5 m DEM (see part of that curvature raster in Figure BF.96c). This input product is further subjected to automatic smoothing applying the circle as the shape of the smoothing neighbourhood, when R ranges between 3 cells (22.5 m) and 61 cells (457.5 m). The resulting 3D smoothed curvature is referred to as $Curv3D\_1_L$, where L indicates the size of the smoothing neighbourhood or the curvature baseline length (note: L=2R). For example, $Curv3D\_1_{45}$ means that the applied smoothing radius is equal to 22.5 m (or 3 cells), which corresponds to L=2*22.5=45 m (or 6 cells).

The second mapping approach first applies the smoothing to the 7.5 m DEM (see a part of that raster in Figure BF.96b). This input DEM is subjected to the smoothing with varying values of R. Thus, each smoothing yields new smoothed DEM, such as DEM_{45} for smoothing over 45 m, DEM_{75} for smoothing over 75 m and DEM_{915} for smoothing over 915 m (note: 45, 75…915 m correspond to L=2R). All these specific raster data are further processed to map the 3D curvature values, which are defined as $Curv3D\_2_{45}$, $Curv3D\_2_{75}$… $Curv3D\_2_{915}$.

Some sample products showing the distribution of $Curv3D\_1_L$ and $Curv3D\_2_L$ are presented in Figure BF.98. As it can be seen, the presented values of R are equal to 7, 15, 29 and 55 cells, which correspond to L=105 m, 225 m, 435 m and 825 m, respectively (for a cell size of 7.5 m). The presented raster data are displayed with the varying ranges of curvature to better demonstrate the smoothing results (see the legends for all maps in Figure BF.98).

The review of the obtained ranges indicates that the increasing value of R "flattens" the study area, i.e. smoothing with larger R values returns the lower values of the 3D smoothed curvature. This link is logical, as a larger R includes a higher number of processed cells: it effectively decreases the yielded value of the mean curvature. The raster data for $Curv3D\_1_L$ are not impacted by the boundaries, as the direct smoothing of curvature values is not sensitive to the lack of data in these parts of model. The data for $Curv3D\_2_L$ contain artefacts at the rims of the study area resulted from a lack of elevation data outside of model extent. Due to these artefacts the network of the evenly-spaced surface receivers is situated at a certain distance from the model rims (see Figure BF.89). This network of receivers is used to study the links between Atxy and the 3D smoothed curvature.

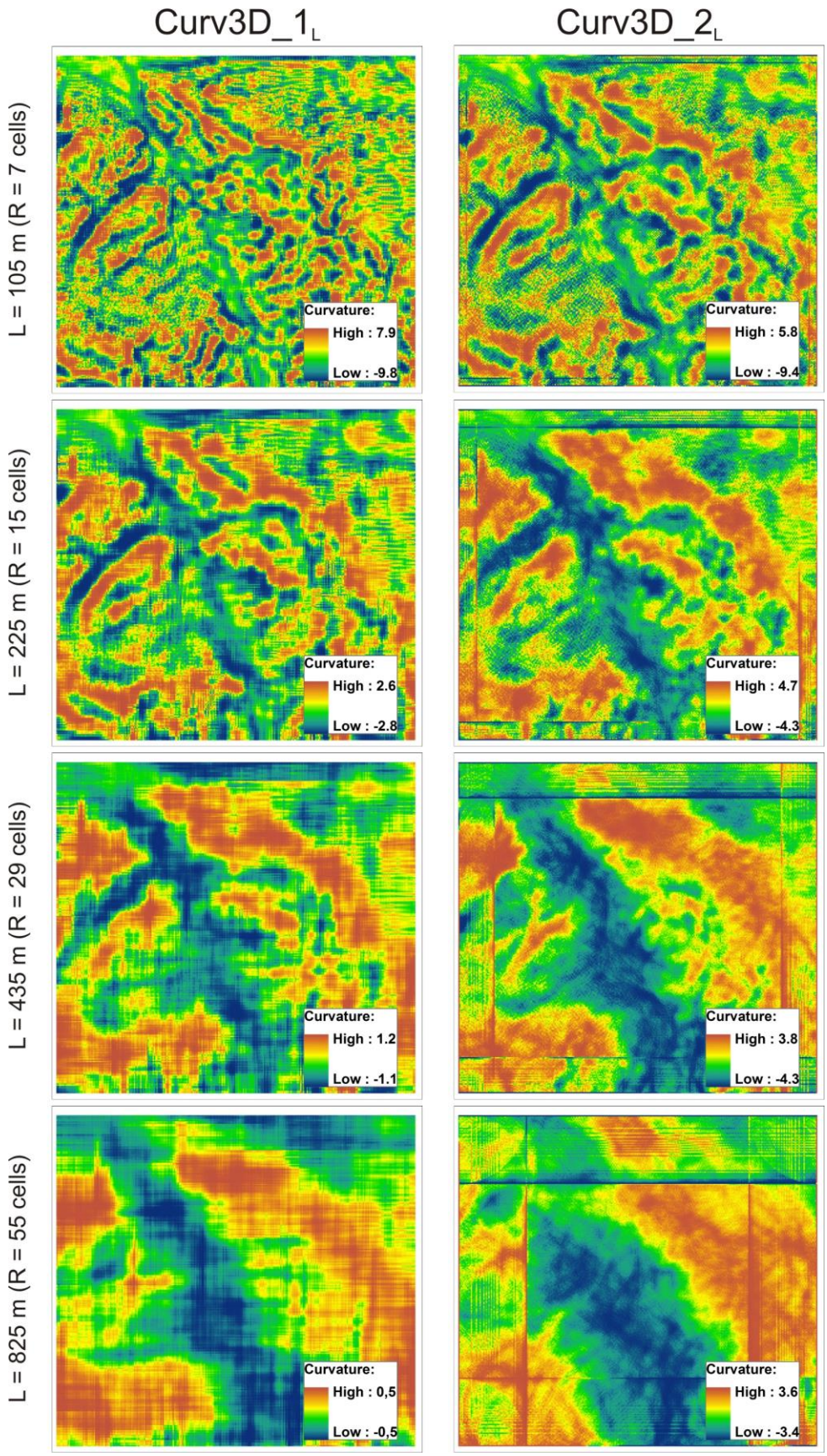

Figure BF.98: Selected examples of raster data showing the distribution of the 3D smoothed curvature (note: left column shows the results of the direct smoothing of curvature values calculated on the basis of the 7.5 m DEM; right column shows the distribution of curvature values computed on the basis of DEMs smoothed over different L; R is the smoothing radius and L is the curvature baseline length, i.e. L=2R).

Thus, the raster of the elementary curvature values and the original 7.5 m DEM are the basic products to map the Curv3D_1_L and Curv3D_2_L values, respectively. The smoothing is performed on the basis of varying L=2R which creates the dataset of the specific curvature distributions. At the next analysis step, those specific values of Curv3D_1_L and Curv3D_2_L are assigned to each receiver from the regular recording network. It finally allows us to study the links between Atxy and the 3D smoothed curvature. The next section analyses in more detail the relationships between those two parameters and proposes the way to predict the distribution of the Atxy values.

VI.7 Atxy versus 3D smoothed curvature

To further explore the link between Atxy and the 3D smoothed curvature we first analyse the modelling data for the test with Vs=1000 m/sec and a seismic input marked by Fca=1.15 Hz. Figure BF.99 presents the plots of the Atxy values versus Curv3D_1_L, where L is equal to 150, 240, 360, 450, 600, 780 and 900 m. To remind, Curv3D_1_L is the smoothing product of the elementary (original) curvature raster calculated based on the 7.5 m DEM. The graphs also contain the plot of the Atxy versus the original curvature – the linear correlation coefficient (Rcl) for a given distribution is equal to 0.22 (see the value of Rcl at each graph). As it can be seen, the highest value of Rcl = 0.76 is revealed for L=600 m, i.e. for the plot of Atxy versus Curv3D_1_{600} (see the graph marked by the dotted rectangle). Figure BF.99 also presents the distribution of Rcl versus the applied values of L. As it can be seen, the wide range of L between 360 and 890 m is characterized by correlation values of more than 0.7 (see the area filled by the green colour in the low right graph in Figure BF.99).

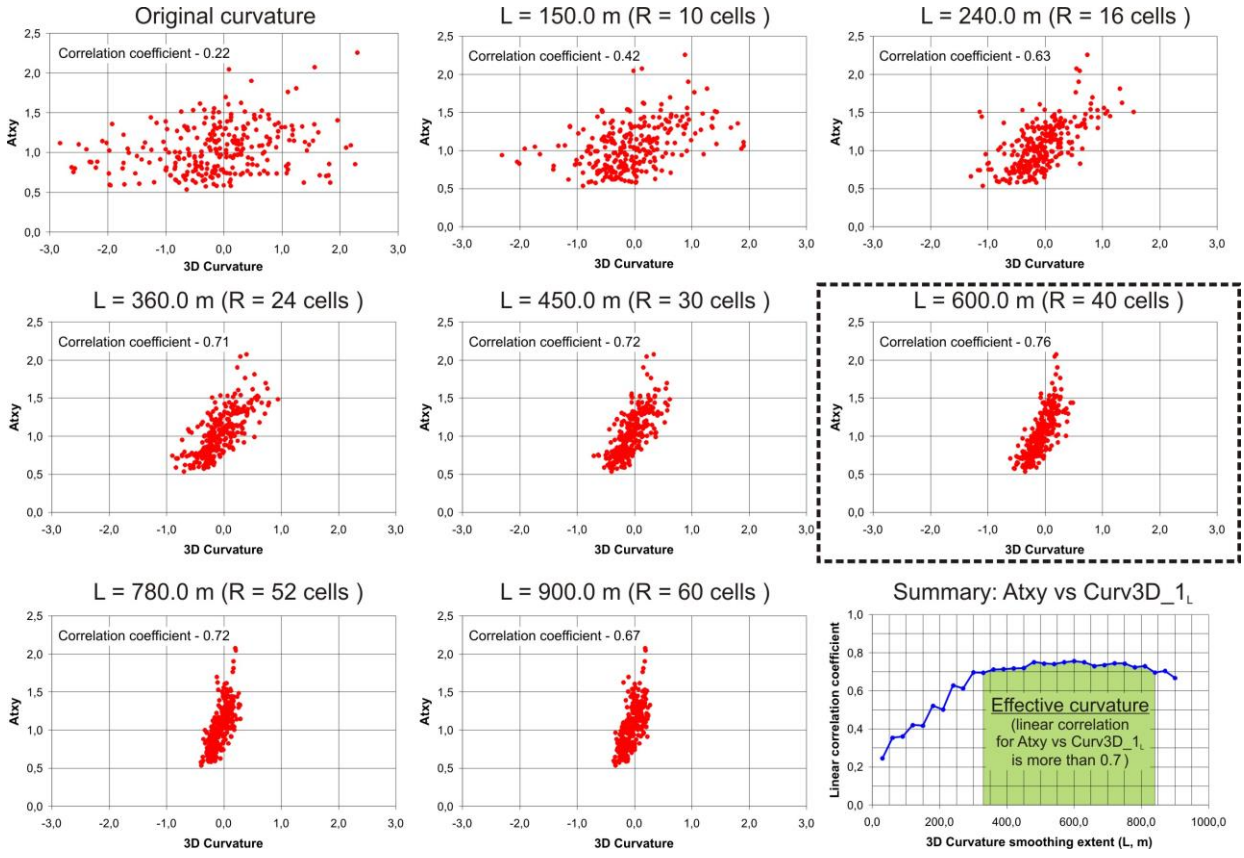

Figure BF.99: The plots of Atxy versus Curv3D_1_L for L=150, 240, 360, 450, 600, 780, 900 m together with the summary of results presented in the low right graph (note: the first graph presents the plot of Atxy versus the original curvature values; all graphs present the results for the model with Vs=1000 m/sec and Fca=1.15 Hz).

The plots of Atxy versus Curv3D_2_L are presented in Figure BF.100. The values of Curv3D_2_L are the elementary curvature values calculated based on the DEMs which are yielded by the smoothing of the 7.5 m DEM over the neighbourhood equal to L=2R (note: R is the smoothing radius). Here, the highest value of the correlation coefficient is gained for L=330.0 m (Rcl=0.79). The last summary plot reveals that the best predictions of the Atxy values are provided by the curvature smoother over L ranging between 210.0 and 450.0 m (Rcl > 0.7).

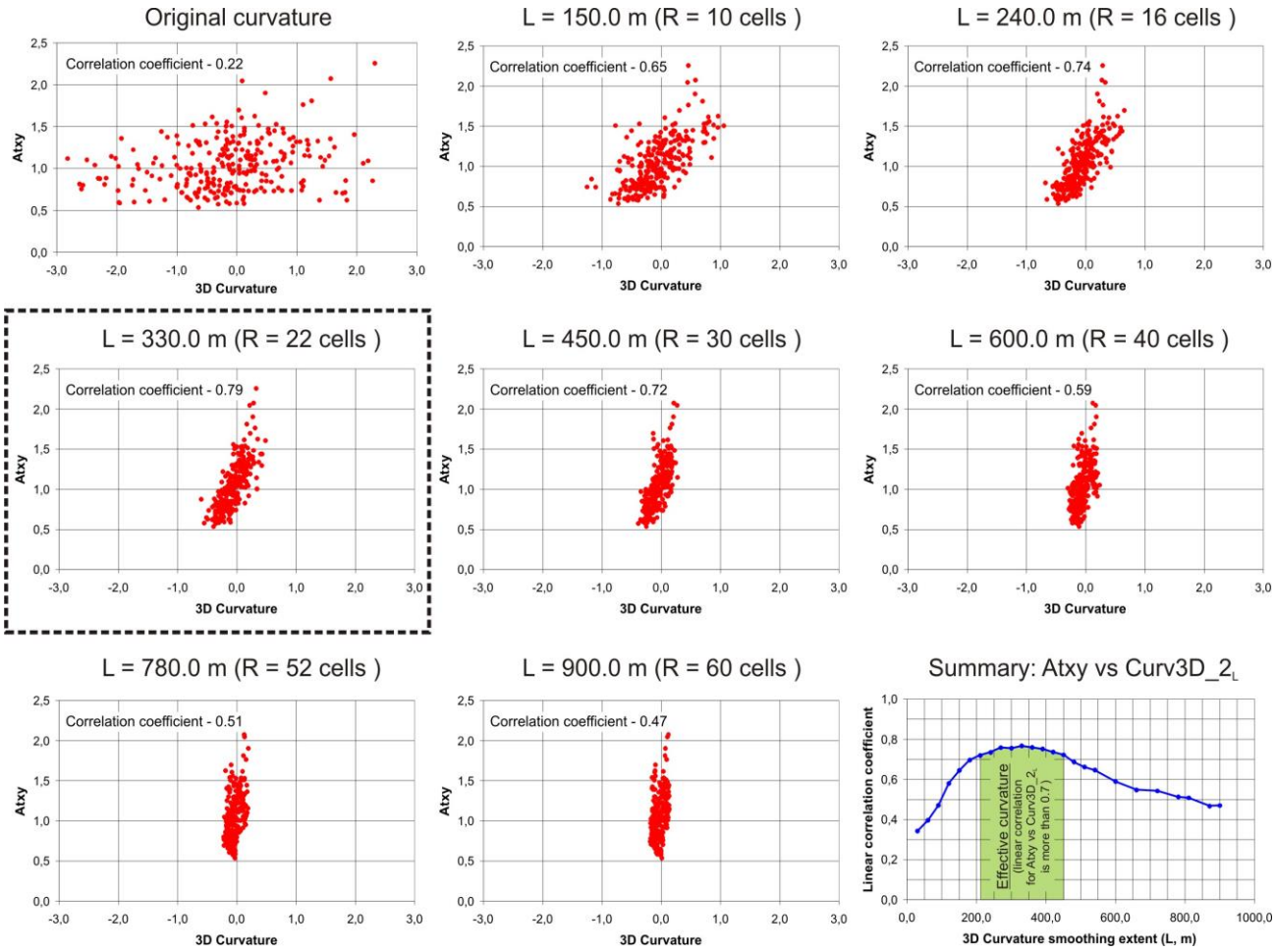

Figure BF.100: The plots of Atxy versus Curv3D_2_L for L=150, 240, 360, 450, 600, 780, 900 m together with the results summary presented in the low right graph (note: the first graph presents the plot of Atxy versus the original curvature values; all graphs present the results for the test with Vs=1000 m/sec and Fca=1.15 Hz).

Figure BF.101 analyses the distribution of the linear correlation coefficients as the function of the applied values of L. Figures BF.101 a-c present this distribution for the fixed value of Fca=1.15 Hz (Vs=850; 1000; 1400 m/sec), while Figures B.101 d-f review the data for the fixed value of Vs=1000 m/sec (Fca=2.43; 3.50; 4.85 Hz). In all graphs the data for Curv3D_1_L and Curv3D_2_L are plotted together. It facilitates the comparison of prediction performance for these two types of the 3D smoothed curvature. It also helps to define the ranges of L which yield the highest values of Rcl. According to the conventions applied in the 2D studies, the value of L with the highest correlation between Atxy and the 3D smoothed curvature is called as the effective curvature smoothing extent (Le). The curvature smoothed over Le is defined as the effective curvature (Curv3D_1_{Le} and Curv3D_2_{Le}).

A careful review of presented graphs reveals some certain regularity. Thus, the increasing Vs lead to the higher values of Le (compare those values in Figures BF.101 a-c). The link between Fca and Le is reciprocal – the higher values of Le are produced by the tests which are characterized by lower Fca (compare those values in Figures BF.101 d-f). These observation are similar to those made for the 2D studies, when the values of Le are predicted via the Geli's law (Le=Vs/Fca). Nevertheless, it can also be seen that the 3D modelling produces smaller values of Le compared to those calculated by the Geli's law. For example, the test with Vs=850 m/sec and Fca = 1.15 Hz produces a Le value of around 200 m, while Geli's law would predict a value of 740 m (850/1.15 = 740 m). The reason for such discrepancy is analysed below.

The comparison of two types of the 3D smoothed curvature shows that the curves for Curv3D_2_L are always more regular than those for Curv3D_1_L. In some cases it is hard to define the value of Le for Curv3D_1_L or the curves themselves have an irregular distribution of Rcl (see, e.g., blue curves in Figures BF.101b and BF.101c). The data for Curv3D_2_L always present more or less defined ranges of L, where the linear correlation between Atxy and Curv3D_2_L is the best. Due to these features, we select Curv3D_2_L to be the main predictor for our further analyses. Therefore, all later studies are only dealing with Curv3D_2_L, while Curv3D_1_L is no more taken into consideration.

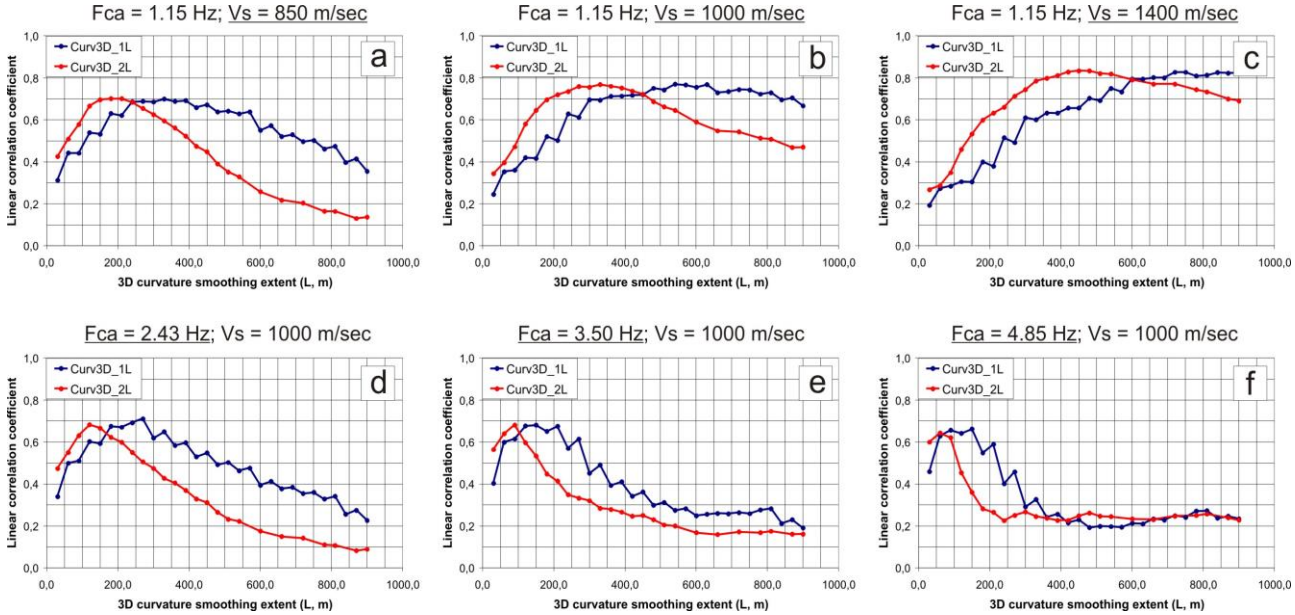

Figure BF.101: Distribution of the linear correlation values (link between Atxy and the 3D smoothed curvature) as a function of the applied values of L for the tests when: (a) Fca=1.15 Hz, Vs=850 m/sec; (b) Fca=1.15 Hz, Vs=1000 m/sec; (c) Fca=1.15 Hz, Vs=1400 m/sec; (d) Fca=2.43 Hz, Vs=1000 m/sec; (e) Fca=3.50 Hz, Vs=1000 m/sec; (f) Fca=4.85 Hz, Vs=1000 m/sec (note: blue curves mean distribution for Curv3D_1_L and red curves correspond to Curv3D_2_L).

Figures BF.102 analyses the change of Le for the link between Atxy and Curv3D_2_L. Here, the results of tests with Vs=700; 850; 1000; 1400 m/sec are summarized in four graphs. These graphs indicate the ranges of L with Rcl≥0.78 (see the black dashed lines) and the values of Le with the maximal value of Rcl (see the green dashed line). As it can be seen, in all graphs the span of L with Rcl≥0.78 often exceeds 100 m. The low values of Fca have the widest span of L which approaches the range of 300-400 m. For example, Figure BF.102a (Vs=700 m/sec) shows that Curv3D_2_{120} and Curv3D_2_{450} both predict the distribution of Atxy for Fca=0.98 Hz with Rcl=0.78, i.e. the value of Le lies somewhere between 120 m and 450 m. The higher values of Fca are marked by a narrower span of L with Rcl≥0.78: e.g., the test with Vs=700 m/sec and Fca=3.6 Hz (Figure BF.102a) shows that this span is only 60.0 m, i.e. Curv3D_2_{30} and Curv3D_2_{90} provide comparative prediction of the Atxy values.

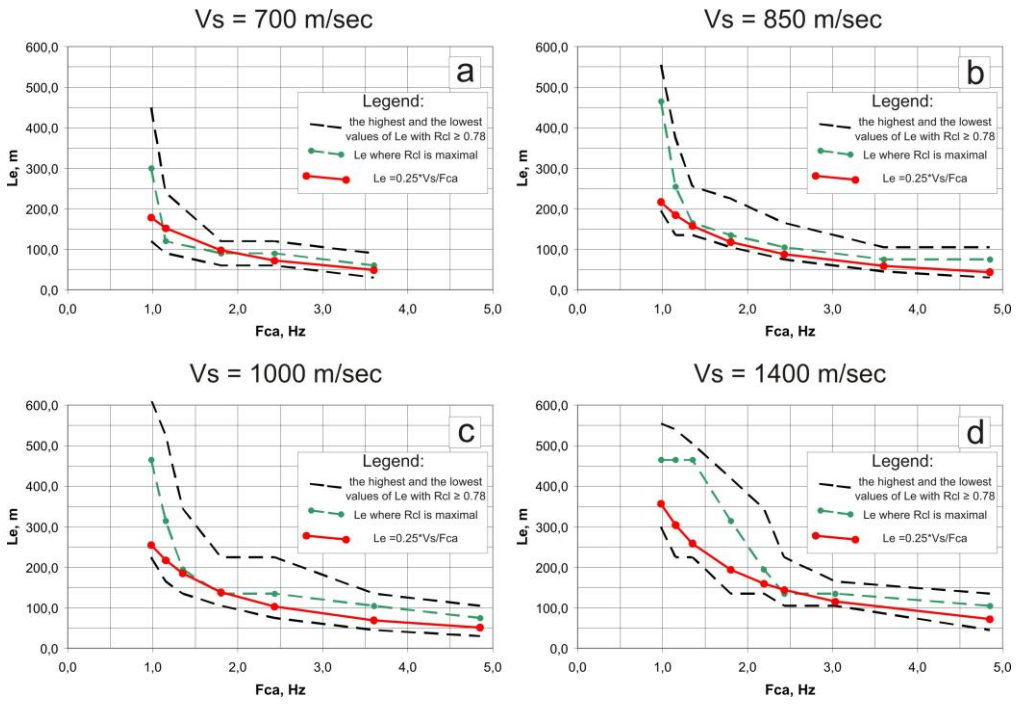

Figure BF.102: Change of Le versus Fca for the tests with Vs=700 m/sec (a), Vs=850 m/sec (b), Vs=1000 m/sec (c) and Vs=1400 m/sec (d); the ranges of L with Rcl>0.78 are outlined by the black dashed lines, Le with the maximal value of Rcl are shown by the green dashed lines and distribution of the effective smoothing length calculated as Le=0.25Vs/Le is shown by the red solid line.

The graphs in Figure BF.102 also show the values of Le calculated based on the Geli's law to which the factor of 0.25 is applied (see the red solid lines). As it can be seen, these curves always lay inside of the range of L with Rcl≥0.78, sometimes overlapping with the values of L where Rcl is maximal. It shows that the effective smoothing length (Le, m) can be reliably predicted applying the next equation:

$$Le = \frac{0.25 * Vs}{Fca} \qquad \text{(BE.38)},$$

where Vs (m/sec) is the shear wave velocity and Fca (Hz) is the central frequency of the input acceleration-time history.

To explain the difference between the Geli's law and Equation BE.38 we analyse the typical hill morphology schematically shown in Figure BF.103. Thus, the Geli's law was originally proposed to predict the spectral range amplified by a given hill/mountain. The authors showed that this amplification normally occurs at a wavelength roughly equal to a hill/mountain width (see L_H in Figure BF.103). In our studies we analyse Ia which regional distribution is predicted on the basis of the earth curvature. As it can be seen on the example of the hill in Figure BF.103, the convex morphologies are often characterized by a typical distribution of the curvature values. Thus, around a quarter of a hill width corresponding to the surroundings of the hilltop is normally marked by a positive curvature. Both slopes of the same hill are usually flat and those parts together occupy about a half of the hill surface. Finally, the lower parts of the hill are marked by a negative curvature: those parts together occupy the remaining quarter of the hill surface. It should noted, that similar distribution of curvature is normally observed for depressions: one quarter of its width (middle part) is marked by a negative curvature, both slopes with zero curvature represent half of its width and the remaining quarter (rims) is normally marked by a positive curvature. This characteristic distribution of curvature may possibly explain why Equation BE.38 introduces a factor of 0.25 in the Geli's law. Thus, the amplification of Ia is related just to the near-crest part of the whole hill, which width is roughly equal to a quarter of the whole hill width. The similar link is true for the impacts induced by concave features (depressions). The deamplification of Ia is normally related to the part of depression marked by the negative curvature: this part normally occupied aroud quarter of the whole width of given morphology.

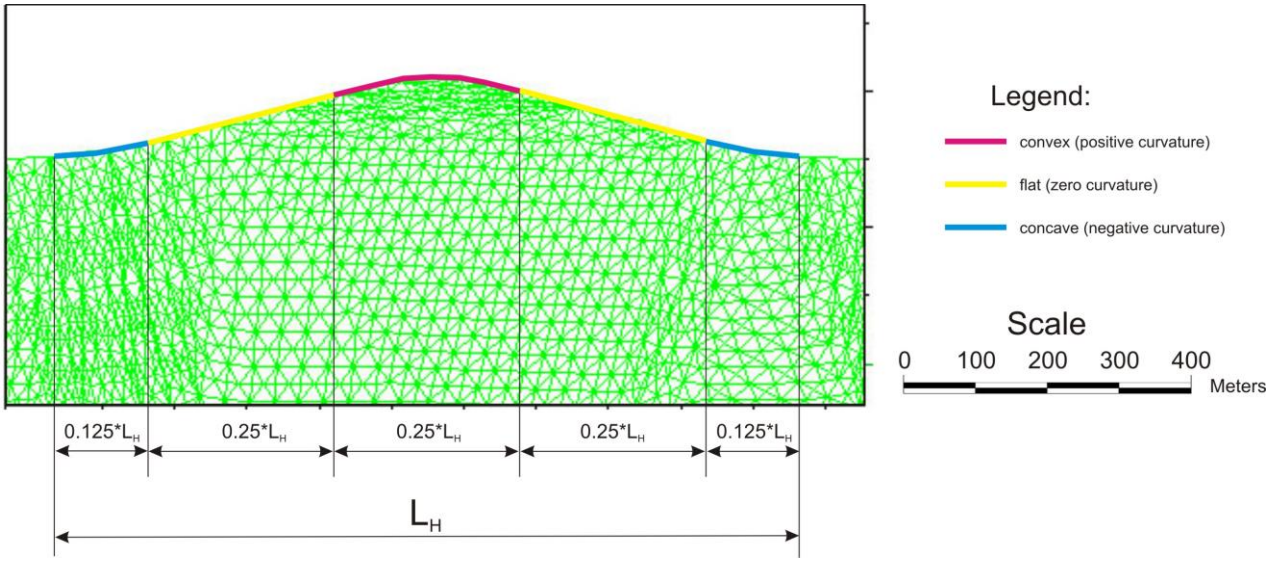

Figure BF.103: Typical hill morphology with charachteristic distribution of the curvature values.

Figure BF.104 presents a set of graphs where the values of Atxy are plotted versus Curv3D_2_{Le} (note: Le is estimated based on Equation BE.38). Nine plots demonstrate the results of tests with Vs=700; 1000; 1400 m/sec and Fca=0.75; 1.15; 2.43 Hz. As it can be seen, there is the next general form of the Atxy prediction law:

$$Atxy = K * Curv3D\_2_{Le} + 1 \qquad \text{(BE.39)},$$

where K is the slope constant and Curv3D_2_{Le} is the effective curvature.

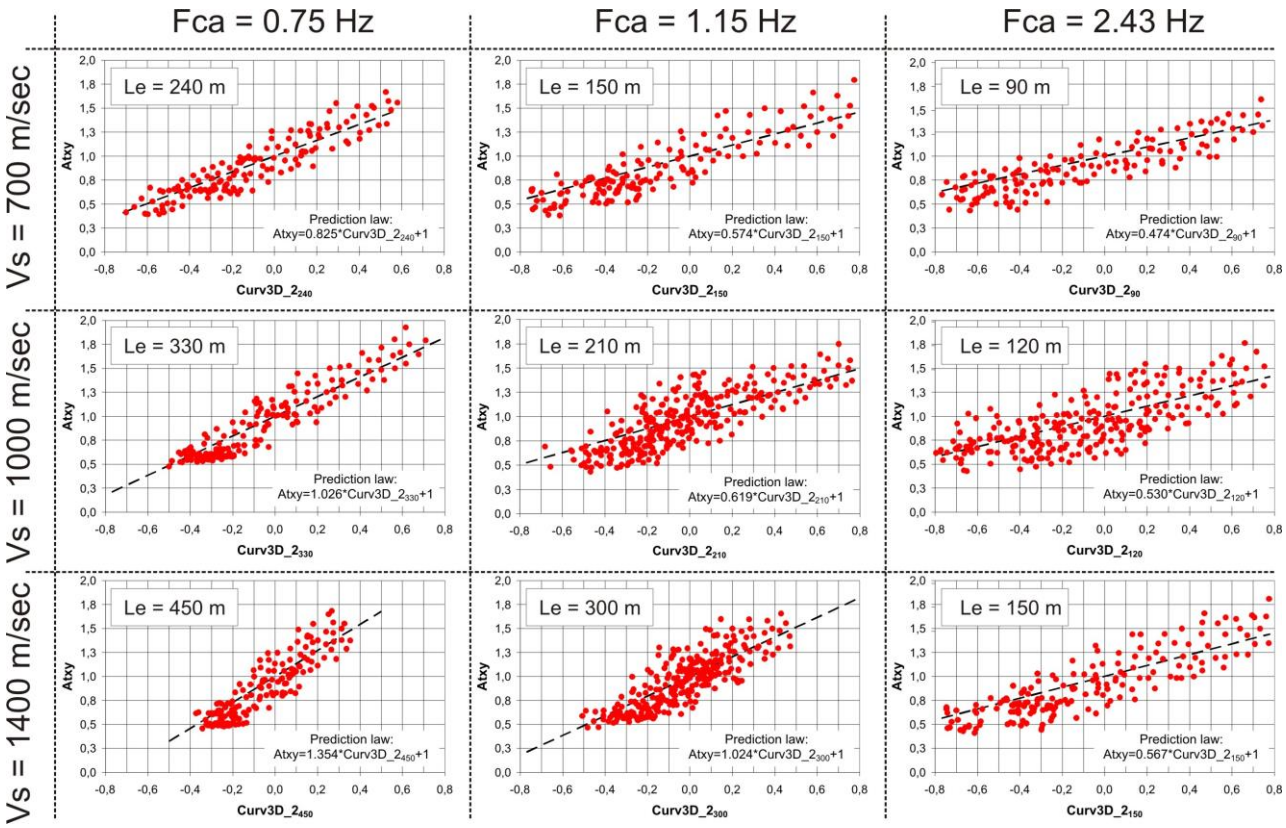

Figure BF.104: Sample plots of Atxy versus Curv3D_2_{Le} for the tests with varying Fca and Vs (note: each graph contains the linear shape prediction law; the values of Le are indicated in the upper left corner of each graph).

A detailed analysis of the graphs in Figure BF.104 indicates that the value of K in Equation BE.39 is directly proportional to Le. For example, among the nine presented graphs the highest Le value of 450 m is revealed for the test with Vs=1400 m/sec and Fca=0.75 Hz – the corresponding Atxy prediction law also has the highest K=1.354. Similarly, the lowest value of Le=90 m (Vs=700 m/sec and Fca=2.43 Hz) returns the lowest slope coefficient among all presented graphs (K=0.474).
An important conclusion originates from the comparison of the two tests which produce identical values of Le=150 m (compare the graph for Vs=700 m/sec and Fca=1.15 Hz with the graph for Vs=1400 m/sec and Fca=2.43 Hz). The Atxy prediction laws for both tests are marked by almost identical values of K (0.574 versus 0.567). It shows that the value of K in Equation BE.39 can be predicted solely on the basis of Le. Thus, Figure BF.105 plots the registered values of K versus Le for the tests with Vs=700; 850; 1000; 1400 m/sec. As it can be seen, the plotted data fit the linear shape prediction law which can be expressed by the next equation:

$$K = 0.0025 * Le + 0.2000 \quad \text{(BE.40)},$$

where K is the slope constant in Equation BE.39 and Le is the effective smoothing length.
Introducing Equation BE.40 into Equation BE.39 provides the following form of the Atxy prediction law:

$$Atxy = (0.0025 * Le + 0.2000) * Curv3D\_2_{Le} + 1 \quad \text{(BE.41)}.$$

According to Equation BE.38, the values of Le are linked to Vs and Fca. Thus, by introducing Equation BE.38 into Equation BE.41 we would get the next final shape of the Atxy prediction law:

$$Atxy = \left(0.0025 * \frac{0.25 * Vs}{Fca} + 0.2\right) * Curv3D\_2_{Le} + 1 = \left(\frac{Vs}{1600 * Fca} + 0.2\right) * Curv3D\_2_{Le} + 1 \quad \text{(BE.42)},$$

where Vs (m/sec) is the shear wave velocity, Fca (Hz) is the central frequency for the input acceleration-time history and Curv3D_2_{Le} is the effective 3D curvature.

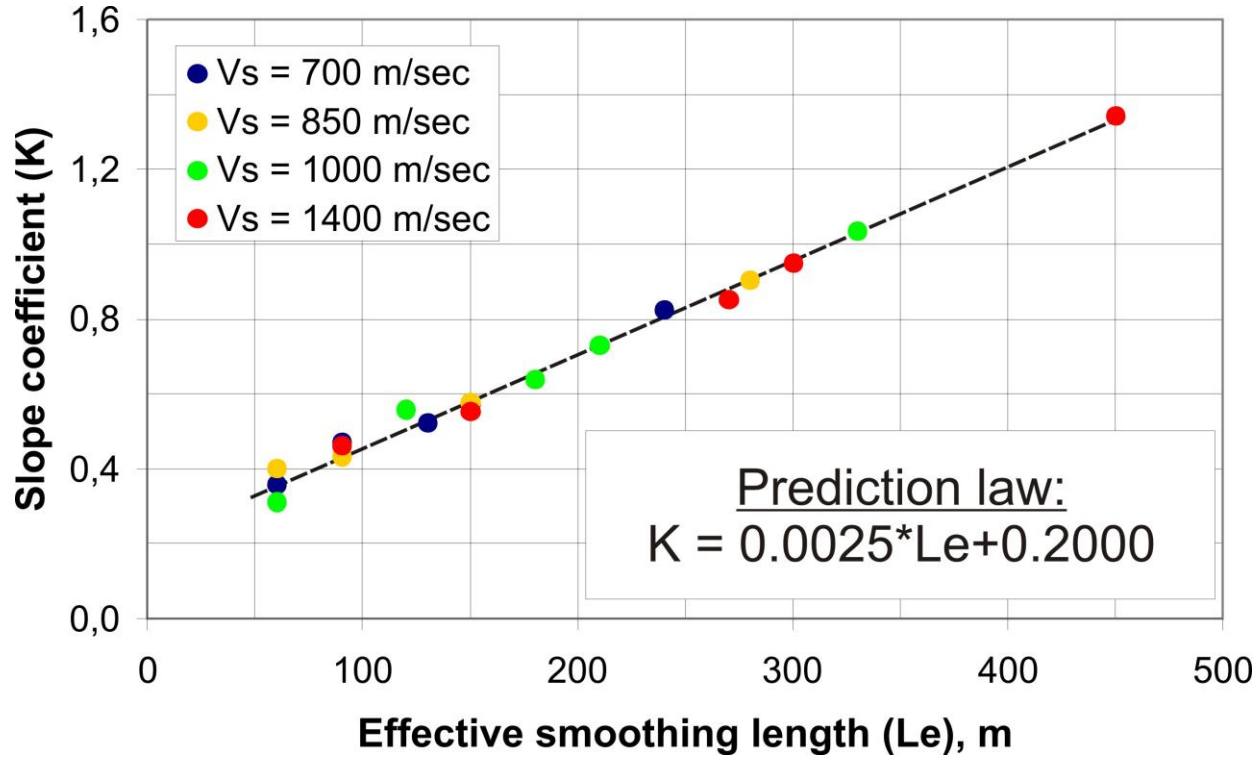

Figure BF.105: Plot of K versus Le for the set of tests with Vs=700; 850; 1000; 1400 m/sec.

The observed relationships and extracted laws allow us to define the proxy to map the values of Atxy. This mapping may be accomplished solely on the basis of the DEM of the target area. The basic input information needed for that analysis includes the Vs of the rock material and Fca of the impacting shaking. The final output that can be obtained with this proxy is the spatial distribution of the Atxy values. These values show the total amplification of Ia along both orthogonal directions, i.e. the topographic amplification of Iaxy which is the sum of Iax and Iay. The outlines of this mapping proxy as well as some test application are presented in the next section.

VI.8 Mapping proxy: outlines, application and discussion

The schematic representation of the mapping proxy is given in Figure BF.106. As it can be seen, the proxy is composed of five procedural steps. Most of these steps are automatically performed by the mapping tools embedded into the ArcGIS code. Other GIS software could certainly be applied here if they provide similar mapping tools or technical solutions.

During the first processing step (Step 1) the input DEM is resampled up/down to the pixel size of 7.5 x 7.5 m. This step is performed via ArcToolbox (Data Management/Raster/Raster Processing/Resample). The change of the DEM pixel size is compulsory, as our previous analyses are performed on the base of the 7.5 m DEM: the pixel size affects the calculation of curvature, a parameter which is further used to predict the distribution of the Atxy values.

At Step 2 the values of Vs and Fca are applied to calculate Le on the basis of Equation BE.38. This parameter is further applied at Step 3, when the input DEM is subjected to smoothing. This last procedure is performed via the focal statistics tool (Spatial Analyst/Neighbourhood/Focal Statistics) using the circle as the shape of smoothing neighbourhood and R as smoothing radius (R=Le/2). It should be noted that ArcGIS defines R either in meters or in cells: R=Le/2 corresponds to the metric measure of the smoothing radius, while in the case of cells R=Le/(2*7.5)=Le/15.

Step 4 applies the smoothed DEM to map the elementary curvature values. This mapping is automatically performed via Spatial Analyst/Surface/Curvature or 3D Analyst/Raster Surface/Curvature. The final Step 5 exploits this curvature raster to calculate the Atxy values according to Equation BE.42 (via Spatial Analyst/Raster Calculator). This raster of the spatially distributed Atxy values is the final product of the mapping proxy.

Figure BF.106: Schematic representation of the Atxy mapping proxy which consists of five procedural steps.

Figure BF.107 presents an example of mapped Atxy values for the case when Vs=1400 m/sec and Fca=1.15 Hz. Step 1 of above-listed procedure is not required, as we start with the 7.5 m input DEM (Figure BF.107a). The value of Le≈300 m is calculated according to Equation BE.38 given the known values of Vs and Fca (Step 2). The original 7.5 m DEM is further subjected to the smoothing applying R=Le/2≈150 m (the smoothed DEM is shown in Figure BF.107b; Step 3). At Step 4 the smoothed DEM is processed to get the elementary curvature raster which is shown in Figure BF.106c (note: in this example the smoothed curvature is Curv3D_2_{300}). The final raster showing the distribution of the Atxy values is presented in Figure BF.107d (Step 5). According to Equation BE.42 and given Le≈300 m the value of K is equal to 0.95, i.e. the equation used to map the Atxy values is the next:

$$Atxy = 0.95 * Curv3D\_2_{300} + 1 \quad \text{(BE.43)},$$

where Curv3D_2_{300} are the values from the raster shown in Figure BF.107c.

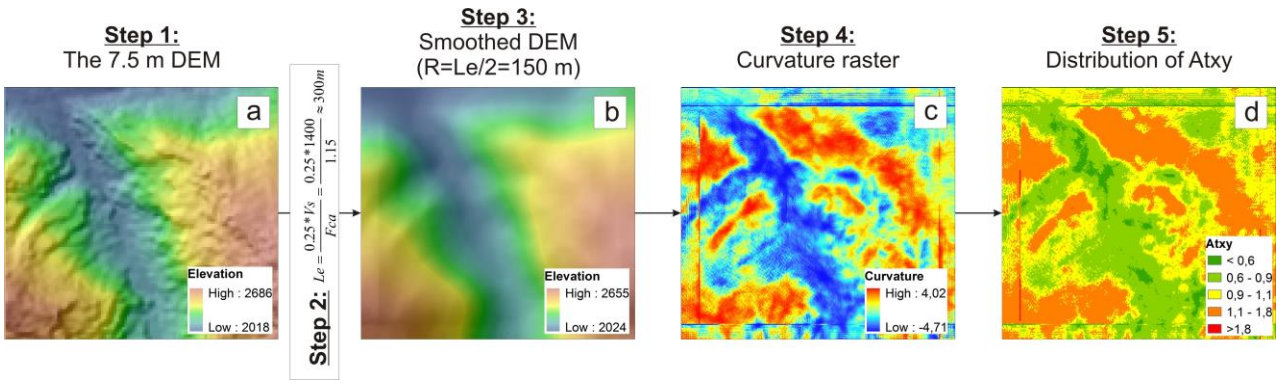

Figure BF.107: The 7.5 m DEM (a), the DEM smoothed over R=150 m (b), the elementary curvature raster (c) applied to map the spatial distribution of the Atxy values (d) for the sample case when Vs=1400 m/sec and Fca=1.15 Hz.

Figure BF.108 compares the modelled values of the Atxy versus the predicted distribution for the same test with Vs=1400 m/sec and Fca=1.15 Hz. Figure BF.108a overlays the point values of Atxy obtained through the modelling on the raster of the predicted distribution originating from Figure BF.107d (predicted values). Figure BF.108b plots the predicted Atxy values against the modelled ones (note: in the case of ideal predictions all points should lie along the blacked dashed trend line with the slope of 1). As it can be seen, the linear correlation coefficient between the predicted and modelled values of Atxy is equal to 0.8. The statistical analysis shows that the mean difference between predicted and modelled Atxy is equal to 5 %, why only several points are marked by a difference of up to 30-40 %.

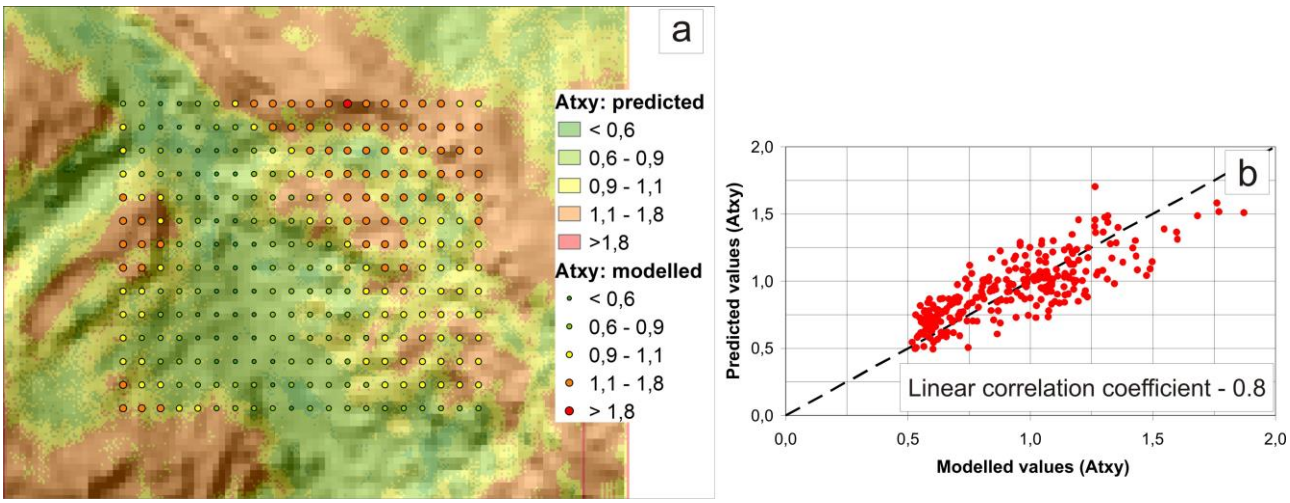

Figure BF.108: (a) Overlay of the modelled values of Atxy (regularly distributed points) over the predicted distribution (underlying raster) for the case when Vs=1400 m/sec and Fca=1.15 Hz; (b) plot of the predicted values of Atxy against the modelled ones (the black dashed line shows the trend of slope = 1; here the correlation is marked by Rcl=0.8).

An important issue is related to the case when the proposed mapping proxy should be applied to areas which are composed of different material types (varying Vs). In this case the values of Le (and R) are changing with respect to the variation of Vs. An additional complication is related to the natural variation of Fca: for instance, the near-epicentral zones of medium magnitude earthquakes (without surface rupture) are normally affected by shaking marked by higher values of Fca compared to the distant areas. In such conditions Step 3 in Figure BF.107 becomes more complicated, as R=Le/2 does not have uniform value. Two different mapping options can be applied at this step – both of them are shortly reviewed below.

The first mapping option proposes a stepwise procedure. At first, the values of Le should be mapped according to the spatially distributed values of Vs and Fca: that way the target area is partitioned into the smaller domains with uniform values of R=Le/2. At the last step, the input 7.5 m DEM is subjected to smoothing within these domains applying those specific values of R. ArcGIS does not propose any direct

solutions for such discriminate smoothing. An additional mapping option would require (regionally) variable smoothing of the input DEM to produce a set of specifically smoothed DEMs. Then, these specific DEMs should be assembled into one single product which becomes the input raster for the following calculations.
This first option looks very laborious and will possibly create numerous artefacts at the conjunction of the domains with varying R. The second mapping option proposes a much easier procedure: the mean value of R=Le/2 should be estimated based on the raster of the spatially distributed Le and, then, this mean R is applied to smooth the whole extent of the input DEM. This option has an obvious drawback as the mean radius R does not account for the specific conditions in each part of the study area. It further means that this approach would provide some averaged estimates of topographic amplification, rather than precise predictions for all specific conditions.
The proposed proxy was developed based on the DEM within which the maximal slope angle did not exceed the value of 60.0°. It suggests that this proxy may not be applied to predict the Ia amplification produced by very steep or vertical slopes, e.g. by canyon cliffs or tops of very steep ridges. The amplification principles of those steep morphologies are different from those produced by a smoother topography. An adaptation of this proxy to the case of steep topography would demand an additional study.
The mapping proxy itself may probably be improved through additional analyses. These improvements may be related to the way how the input DEM is smoothed, what type of smoothing is applied and by which law the values of Atxy are mapped. These possible studies should analyse a wide variety of input signals, as it was shown that the shape of the input signal significantly impacts the relationship between Atxy and smoothed curvature. Such specific issues are outside of our research scope.

VII. Newmark method: towards an improved mapping of landslide susceptibility

VII.1 Analysed models

In the previous sections we analyse the 2D and 3D modelling data: these studies were focused on the topographic (*Chapters B.III* and *B.VI*) and geological (*Chapter B.IV*) amplification of the Ia values, as well as on the seismically triggered downslope displacements (*Chapter B.V*). The goal of these studies is to develop mapping techniques which finally improve the conventional Newmark method adapted to map the seismically-induced landslide susceptibility in terms of Newmark displacement values (ND). Thus, the pure topographic Ia amplification factors (Atxy or simply At) are mapped based on the DEM of the study area and by applying the known distribution of Vs and Fca (see more details in *Chapter B.VI*). The pure geological Ia amplification factors (Ag) are mapped based on the known distribution of Vs using the impedance contrast values, I_{Vs} (see *Chapter B.IV*). Finally, *Chapter B.V* proposes a new law to map the values of ND based on Ac, Ia and Fca: the first two predictors are normally included in the existing Newmark displacement mapping laws, while Fca is generally not included.
In the current section we employ those developed techniques to the Mailuu-Suu target area, which has already been studied through the conventional ND mapping in *Section A.IV.2.4.* To remind, the conventional mapping applies the Ia attenuation law of Wilson and Keefer (1985), while the values of ND are mapped by using the law of Jibson (1993). Two basic earthquake scenarios are studied in *Section A.IV.2.4*: the M=6.2 earthquake in 1992 which was located at about 30 km SSE from the target area (Scenario 1) and a hypothetical M=5.5 earthquake in the Central Fault zone (Scenario 2). According to the validation studies, the model ND3 is classified as the statistically-best model for Scenario 1, while model ND7 is the best one for Scenario 2. To remind, both ND3 and ND7 represent the models of deep landslides in dry conditions.
These two models are further used as the basic products to test the advanced mapping techniques (see Table BT.5). Thus, the model ND9 applies At and Ag to map the topographically and geologically amplified values of Ia for Scenario 1: in this model the input Ia values are mapped by the law of Wilson and Keefer (1985), while the values of ND are mapped through the conventional law of Jibson (1993). The model ND10 studies the same Scenario 1 by application of all findings revealed by the modelling studies: the values of Ia are mapped with the topographic and geological amplification factors, while the values of ND are mapped via the advanced prediction law, presented in *Chapter B.V.*

Table BT.5: List of the analysed ND models in respect to the applied mapping techniques.

	Conventional Newmark mapping (Wilson and Keefer, 1985; Jibson, 1993)	Topographically amplified Ia values (based on *Chapter B.VI*)	Geologically amplified Ia values (based on *Chapter B.IV*)	Advanced ND mapping law (based on *Chapter B.V*)
ND3 (Scenario 1)	X			
ND9 (Scenario 1)	X	X	X	
ND10 (Scenario 1)		X	X	X
ND7 (Scenario 2)	X			
ND11 (Scenario 2)	X	X	X	
ND12 (Scenario 2)		X	X	X

The same mapping tests are performed for Scenario 2 (see Table BT.5). Here, model ND7 represents the results of the conventional Newmark mapping. The model ND11 applies At and Ag to the Ia values mapped by the law of Wilson and Keefer (1985), while the law of Jibson (1993) maps the values of ND. The model ND11 combines the topographically and geologically amplified values of Ia with the advanced ND mapping law.
The models extracted by the advanced mapping techniques are compared with those extracted by the conventional mapping, i.e. the models ND9 and ND10 are compared with ND3, while the models ND11 and ND12 are compared with ND7. This comparison applies the specific landslide/scarp inventories for each earthquake scenario (see more details in *Section A.IV.2.4*). The calculated values of the map-scaled density (Dm) should indicate the prediction performance of each class of the landslide susceptibility: normally, the classes of the low susceptibility should have Dm values significantly smaller than 1, while the classes of the highest susceptibility should have the largest Dm values. The distribution of the Dm values should also indicate if the advanced mapping techniques improve the prediction performance for two studied scenarios.

Table BT.5 shows that all advanced models incorporate the topographic and geological Ia amplification factors (At and Ag, correspondingly). The multiplication of At and Ag returns the values of Atg. This last parameter characterizes the combined topographic-geological amplification of the original Ia values which, in our case, are mapped by the law of Wilson and Keefer (1985). A detailed overview of the At and Ag mapping is presented in the section below, where the final distribution of the amplified Ia values is also presented.

VII.2 Distribution of Ia: introducing At and Ag

The proxy for the mapping of the pure topographic Ia amplification factors (At) is developed on the basis of the 3D modelling studies (*Chapter B.VI*). The mapping procedure applies three input rasters: the DEM of the study area, the distribution of shear wave velocity (Vs) and distribution of the central frequency values (Fca). Figure BF.109 presents these input maps needed for the mapping of the At values (note: there are two maps of Fca, as we study two earthquakes scenarios). Figure BF.109a presents the 7.5 m DEM which is resampled from the original SPOT DEM (input resolution of 20.0 m). The distribution of Vs is presented in Figure BF.108b: this raster is extracted from the digital geological map of the study area using the Vs values of the geological units introduced in *Section B.II.6*. Two maps of Fca are extracted based on the law of Rathje et al. (2004) which applies the hypocentral distance and the earthquake magnitude to calculate the mean period of the seismic shaking, Tm (note: Fca=1/Tm).

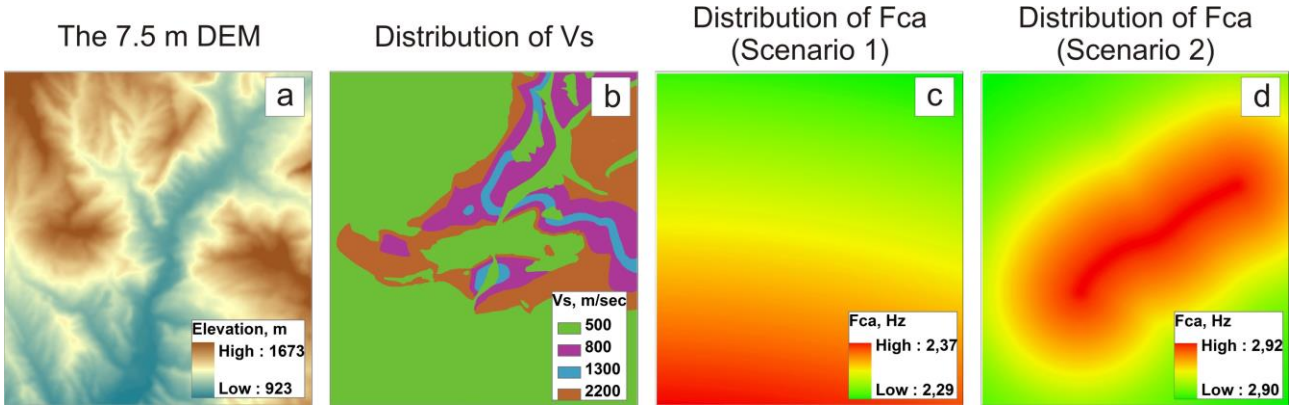

Figure BF.109: The basic raster data needed for the mapping of the At values: the 7.5 m DEM (a), spatial distribution of Vs (b) and maps of Fca for Scenario 1 (c) and Scenario 2 (d).

According to *Chapter B.VI*, the values of Le can be calculated based on the mean Vs and Fca for the target area. The statistical analysis of the Vs raster (Figure BF.109b) shows that 67% of study area are covered by the material with Vs=500 m/sec, 13% are occupied by material with Vs=800 m/sec, 3% of area correspond to Vs=1300 m/sec and remaining 17% are occupied by material with Vs=2200 m/sec. This material sequence corresponds to mean Vs ≈ 850 m/sec (0.67*500+0.13*800+0.03*1300+0.17*2200 ≈ 850 m/sec). Figures BF.109c and d indicate that the values of Fca do not vary so much: the mean Fca for Scenario 1 is 2.33 Hz and mean Fca for Scenario 2 is equal to 2.91 Hz. According to Equation BT.33, the mean Le for Scenario 1 is equal to 91.0 m, while that value for Scenario 2 is equal to 73.0 m.
The calculated values of Le are further applied for the smoothing of the input 7.5 m DEM, shown in Figure BF.109a (note: the smoothing radius is half of Le, i.e. R=Le/2). Thus, for Scenario 1 the input DEM is smoothed over R=45.5 m and for Scenario 2 the DEM is smoothed over R=36.5 m. Two smoothed DEMs are finally applied to map the values of At. According to Equation BE.42 and given the known values of Vs and Fca the next At prediction laws are applied for both scenarios:

$$At = \left(\frac{Vs}{1600 * Fca} + 0.2\right) * Curv3D\_2_{91} + 1 = \left(\frac{850}{1600 * 2.33} + 0.2\right) * Curv3D\_2_{91} + 1 \Rightarrow \text{ for Scenario 1 (BE.44a),}$$

$$\Rightarrow At = 0.4275 * Curv3D\_2_{91} + 1$$

$$At = \left(\frac{Vs}{1600 * Fca} + 0.2\right) * Curv3D\_2_{73} + 1 = \left(\frac{850}{1600 * 2.91} + 0.2\right) * Curv3D\_2_{73} + 1 \Rightarrow \text{ for Scenario 2 (BE.44b),}$$

$$\Rightarrow At = 0.3825 * Curv3D\_2_{73} + 1$$

where Curv3D_2_{91} are the smoothed curvature values extracted based on DEM_{91} and Curv3D_2_{73} are those values extracted based on DEM_{73}.
Figure BF.110 schematically represents the procedure to map the distribution of the At values for both scenarios. Figure BF.110a shows the input DEM_{91} which is applied in Scenario 1: this raster is obtained by the smoothing of the 7.5 m DEM over R=45.5 m. The smoothed DEM is further processed to extract the raster of the smoothed curvature values (Curv3D_2_{91} – see Figure BF.110b). The final raster showing the spatial distribution of the At values is presented in Figure BF.110c: here, the values of At are mapped via Equation BE.44a and using Curv3D_2_{91} as the regional predictor. During mapping of the At values around 5 % of area have unusually low (At<0.5 or even At<0) or high (At>2.5) values of At. These artefacts appear due to the fact that in *Section B.VI* the extreme values of curvature were not taken into consideration: the analysed range of the smoothed curvature lies somewhere between -1.0 and 1.0. Therefore, in the final raster all mapped values of At<0.5 get the value of At=0.5, while all values of At>2.0 are set to At=2.0: these limits correspond well to the experimental values registered in the 3D modelling studies.
The mapping products employed in Scenario 2 are presented in Figures BF.110 d-f. The smoothed DEM (DEM_{73}) is shown in Figure BF.110d: here, the 7.5 m DEM is smoothed over R=36.5 m. The raster of the smoothed curvature (Curv3D_2_{73}) is presented in Figure BF.110e. This last curvature raster is processed to extract the final distribution of the At values (see Figure BF.110f). Similar to the previous scenario, all mapped values of At<0.5 get the value of At=0.5, and all values of At>2.0 are set to At=2.0.

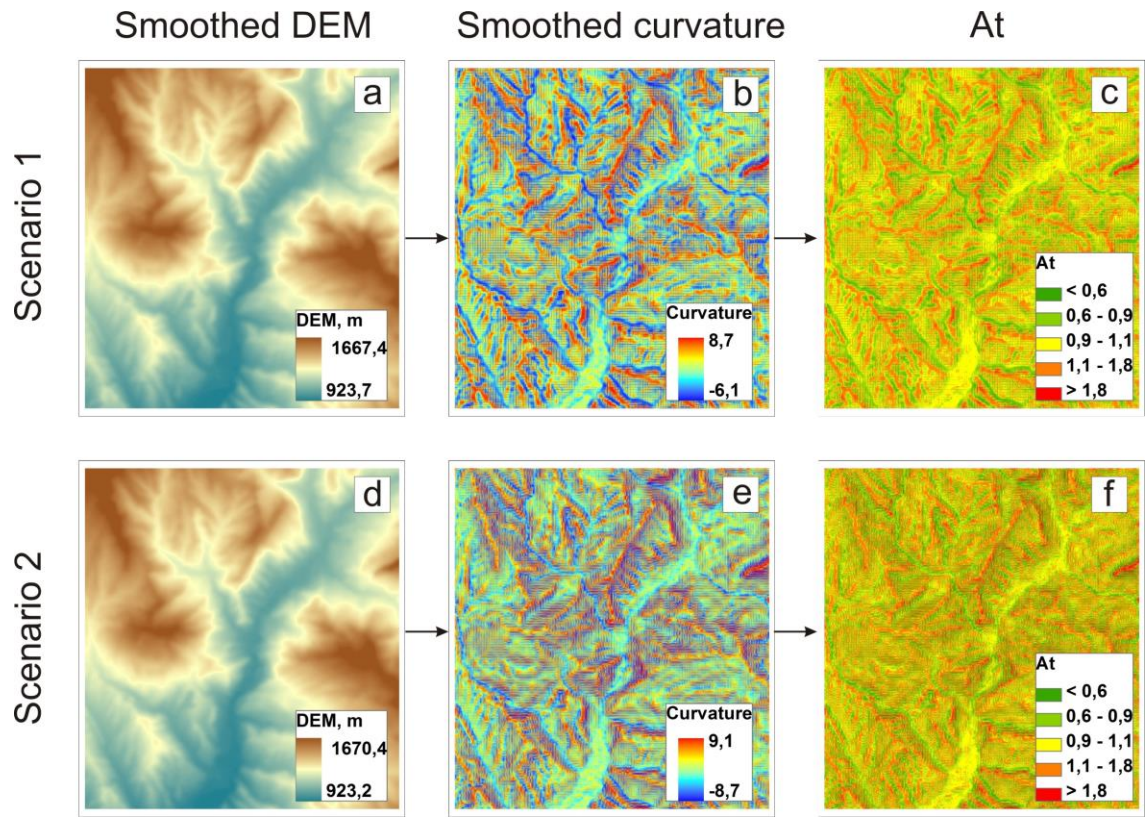

Figure BF.110: The smoothed DEM, the raster of the smoothed curvature and the final distribution of the At values gained for the both studied scenarios.

The procedure to map the pure geological Ia amplification factors (Ag) is developed based on the 2D studies described in *Chapter B.IV*. In the proposed mapping law the mean values of Ag are linked to the Vs impedance contrast of the studied layers with respect to the underlying materials (I_{Vs}). Thus, Figure BF.111a presents the distribution of the I_{Vs} values in the study area: the precise values of this parameter are estimated based on the digital geological map and partially based on the result of the 2D modelling studies, described in *Chapter B.IV*. As it can be seen, the whole area is subdivided into the domains with four different I_{Vs} values (I_{Vs}=0.36; 1.00; 1.63; 4.40).
The distribution of the I_{Vs} values is finally used to map the values of Ag (note: Ag=0.157* I_{Vs}+0.705; see Figure BF.64). The mapped distribution of Ag values is presented in Figure BF.111b: the lowest value of Ag

is equal to 0.73, while the highest one corresponds to 1.94. It should be noted that the materials with I_{Vs}=1.63 have Ag=1.94 which is higher than Ag=1.39 for the materials with I_{Vs}=4.40. This difference is explained through the fact that material with I_{Vs}=1.63 is sandwiched between two high-velocity domains which effectively increases the final value of I_{Vs} and Ag (see *Section B.IV.7* for more details).

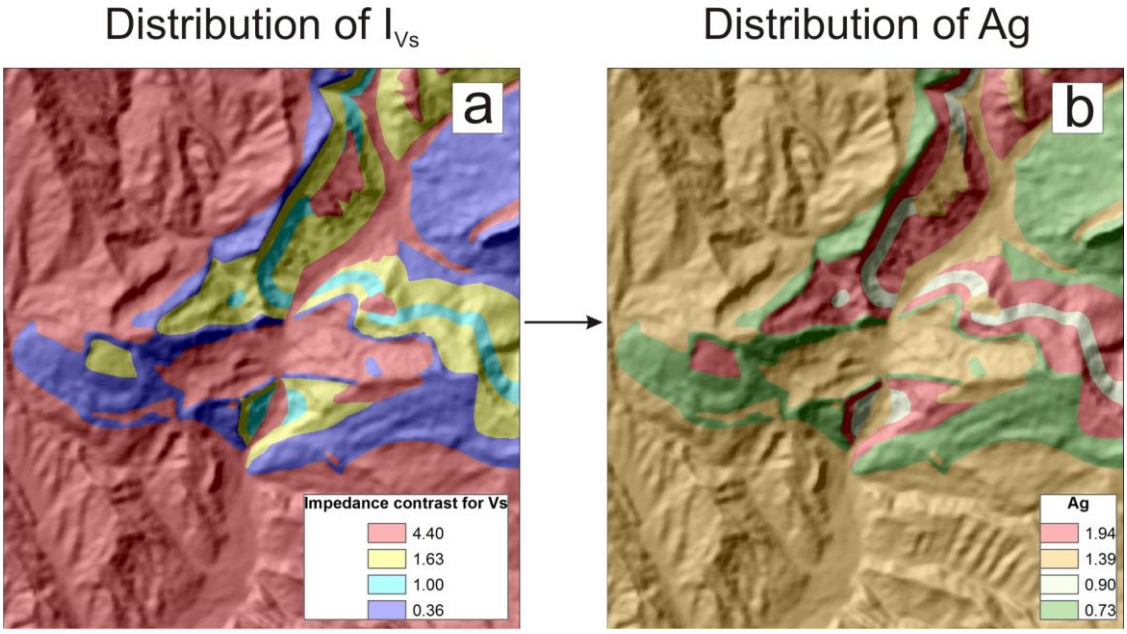

Figure BF.111: (a) The input distribution of I_{Vs} (note: this raster is extracted based on distribution of Vs shown in Figure BF.108b); (b) the mapped distribution of the Ag values.

The maps of At and Ag are further applied to get the spatial distribution of the Atg values (note: Atg=At*Ag). The values of Atg correspond to the amplification factors which show how Ia of the input shaking will be attenuated/amplified due to the combined topographic-geological site effects. Thus, Figure BF.112a shows the raster of Atg obtained for Scenario 1 and Figure BF.112b presents a similar raster for Scenario 2. It should be noted, that during mapping of Atg the identical distribution of Ag is applied for both studied scenarios (see that raster in Figure BF.111b). The values of At are taken from different maps: Scenario 1 uses the distribution shown in Figure BF.110c, while Scenario 2 applies the map presented in Figure BF.110f.

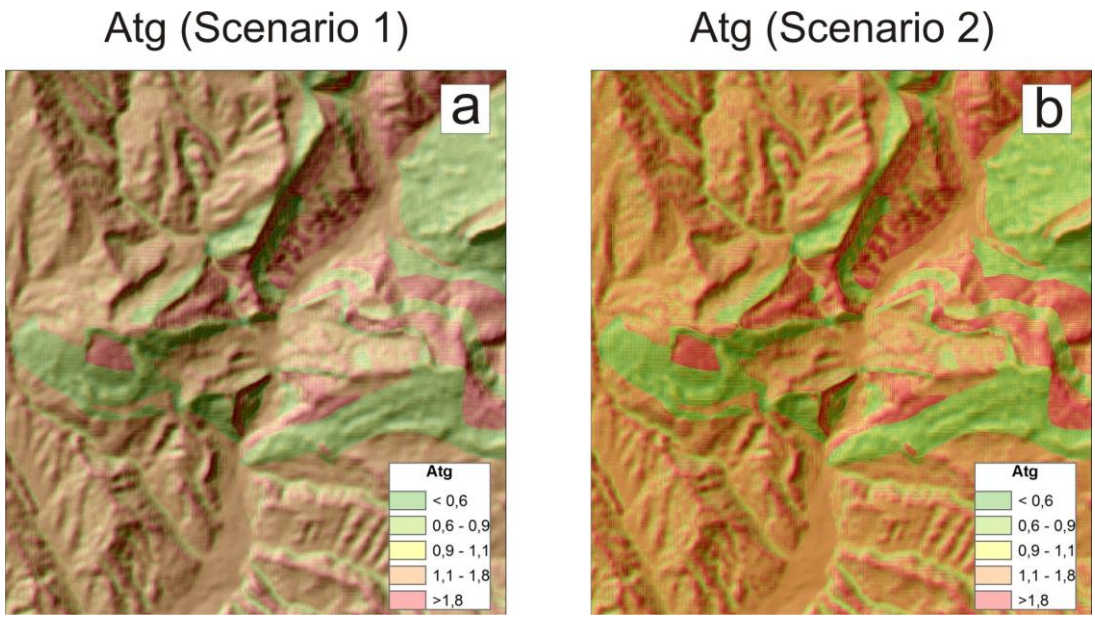

Figure BF.112: The rasters of Atg extracted for Scenario 1 (a) and Scenario 2 (b).

Finally, the original values of Ia need to be multiplied by the values of Atg representing the combined topo-geologic site effects. Figures BF.113a and BF.113c show the distribution of the original Ia values mapped by the attenuation law of Wilson and Keefer (1985) using as inputs Scenario 1 (Figure BF.113a) or Scenario 2 (Figure BF.113c). Figures BF.113b and BF.113d represent the maps of the modified Ia values, when the original Ia is multiplied by the values of Atg. As it can be seen, the amplified Ia values are quite different from those mapped by the law of Wilson and Keefer (1985). It indicates that the final values of Ia are much more sensitive to the change of Atg than to the geometric attenuation connected to the source distance.

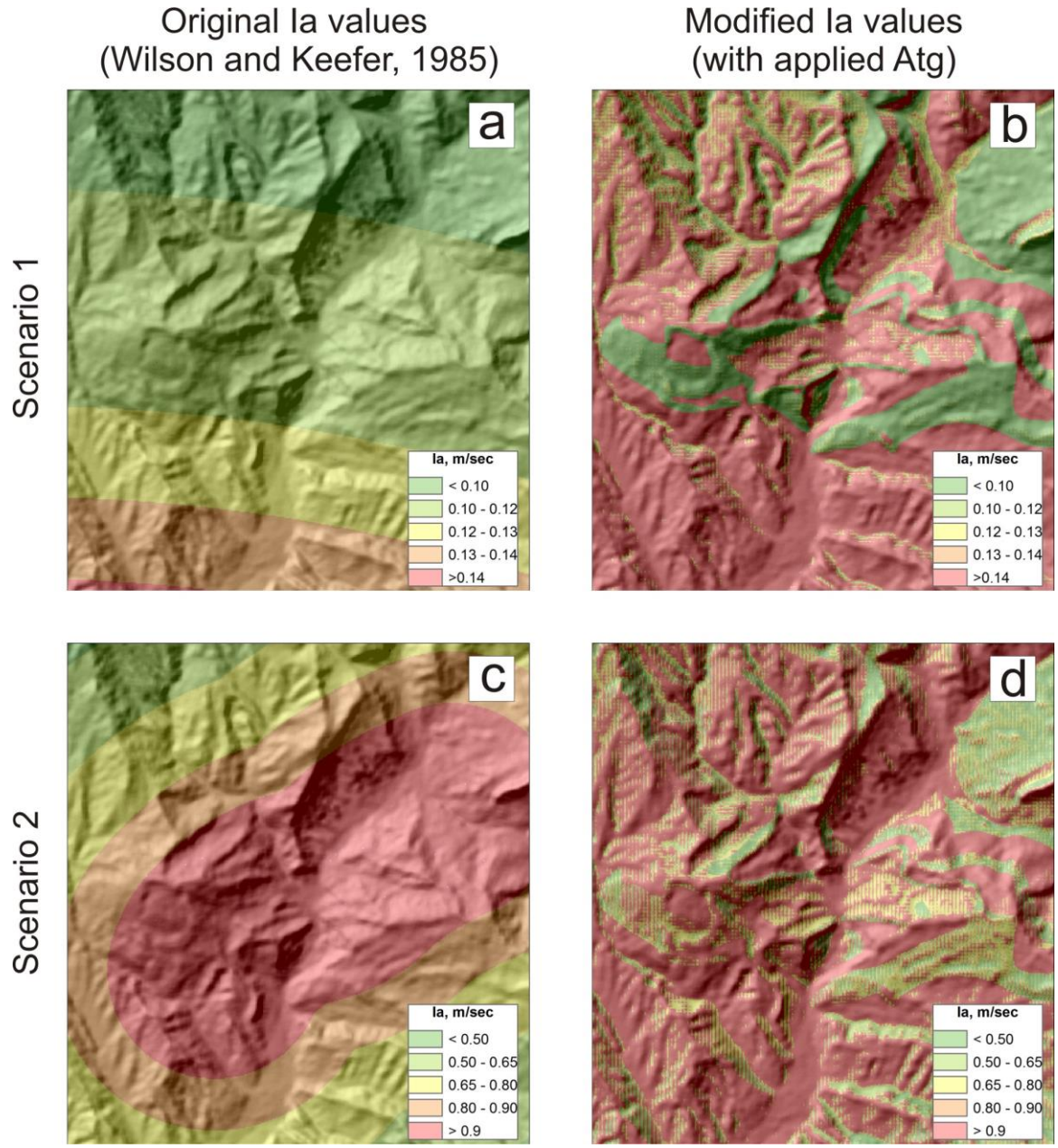

Figure BF.113: Distribution of the original Ia values mapped by the law of Wilson and Keefer (1985) for both scenarios (a and c) together with the rasters of the modified Ia accounting for the attenuation/amplification of the combined topographic-geological site effects (b and d).

According to Table BT.5, the maps of the amplified values of Ia (Figures BF.113b and BF.113d) are the input layers for the advanced Newmark mapping. The map of the critical acceleration values (Ac) represent the other input layers needed for the mapping of the ND values. This regional predictor is not modified by our advanced analyses. Therefore, these input layers correspond to those analysed in *Section A.IV.2.4*. The results of the advanced Newmark mapping applied to the two studied scenarios are presented in the following section.

VII.3 Advanced mapping and results comparison: Scenarios 1 and 2

According to Table BT.5, each earthquake scenario is studied by two types of advanced models. Thus, the first type of them combined the amplified values of Ia with the conventional ND mapping law of Jibson (1993): for Scenario 1 this model corresponds to ND9, while for Scenario 2 it is ND11. The law of Jibson (1993) maps the values of ND (D_n, cm) by using next equation:

$$\log(D_n) = 1.46 * \log(Ia) - 6.642 * Ac + 1.546 \quad \text{(BE.45)},$$

where Ia (m/sec) is the Arias Intensity (note: in the advanced models the values of Ia include the multiplication factor Atg) and Ac is the critical acceleration(in term of g).
The second types of the advanced models, i.e., ND10 for Scenario 1 and ND12 for Scenario 2 combine the amplified values of Ia with the advanced ND mapping law which is presented in *Section B.V.7* (Equation BE.36):

$$\log D_n = 0.0268 * \log I_a + 0.3557 * \frac{\log I_a}{Fca} - 0.0495 * Fca * \log(A_c) - 0.6586 * \log(A_c) - 0.1193 * Fca + 1.2303 \ ,$$

where Ia (m/sec) is the Arias Intensity (note: in the advanced models the values of Ia include the multiplication factor Atg), Fca (Hz) is the central frequency for the impacting acceleration-time history, Ac (in terms of g) is the critical acceleration value (note: corresponds to that parameter analysed in *Sub-section A.IV.2.4*).
Figure BF.114 presents the mapping results for Scenario 1. Figure BF.114a shows the model ND3 which is yielded by the conventional Newmark mapping (see more details in *Section A.IV.2.4*). It should be noted, that values of Ac for all models, including ND9 and ND10, are mapped applying the spatial distribution of the common geotechnical parameters and for the case of the deep landslides (t=20) in dry conditions (m=0). The advanced Newmark models are shown in Figures BF.113 b and c: similar to ND3 these models have five landslide susceptibility classes which are defined according to the yielded values of D_n. Thus, the class of the very low landslide susceptibility (class 1) is marked by very small displacement values between 0.0 and 0.1 cm, class 2 is marked by slightly larger ND values (0.1- 0.5 cm), class 3 – by ND values between 0.5 and 0.9 cm, class 4 - by ND values between 0.9 and 5.0 cm, while the highest susceptibility (class 5) is marked by large displacements of more than 5.0 cm.

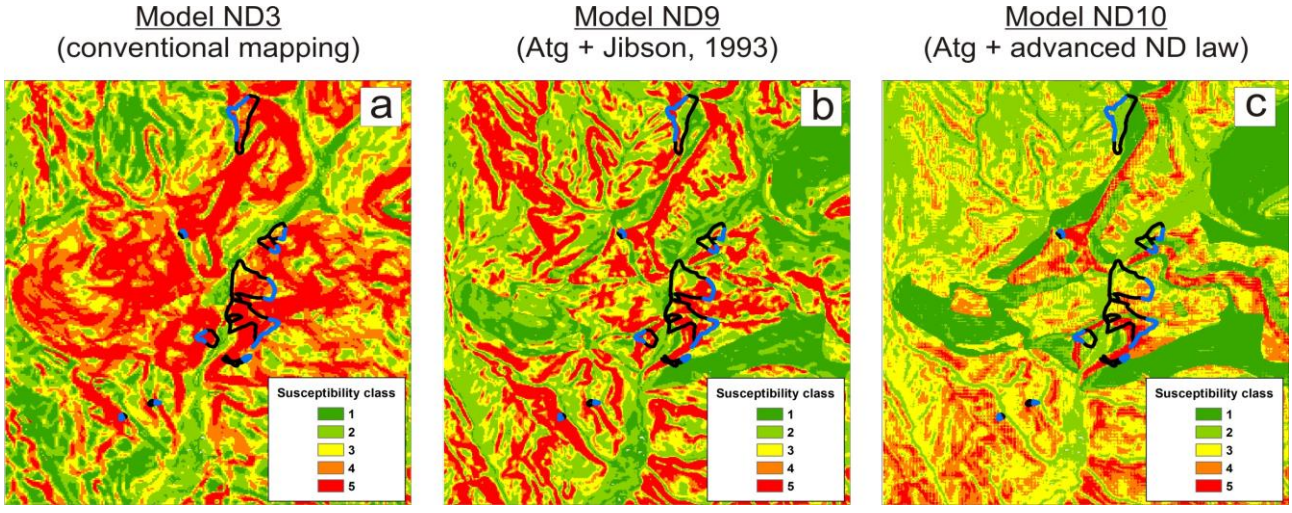

Figure BF.114: The mapping results for Scenario 1 applying the model of the deep landslide (t=20) in dry conditions (m=0): (a) model ND3 extracted by the conventional ND mapping (Wilson and Keefer, 1985; Jibson, 1993); (b) model ND9 which combines the advanced mapping of Ia (via applied Atg) with the conventional ND mapping by the law of Jibson (1993); (c) model ND10 which combines the advanced mapping of Ia (via applied Atg) with the advanced ND mapping (note: black outlines represent the landslides most likely triggered by the studied seismic event in 1992 and blue lines are the corresponding landslide scarps).

The maps shown in Figure BF.114 are overlaid by the validation set of 10 landslides which are most likely triggered by the analysed seismic event (see the black outlines). Another validation set includes the scarps of those ten landslides (see the blue lines in Figure BF.114). The landslide scarps basically represent the upper one third of each landslide outline. To better analyse a performance of the advanced mapping techniques, two additional validation sets are applied to the mapping results of Scenario 1. Those two sets include the 2007 landslides and scarps shown in Figure BF.116.
These four validation sets are further applied to calculate the values of the map-scaled density (Dm) for each susceptibility class of the extracted models. To remind, the values of Dm are the basic indicators of the model performance: the low susceptibility class (Class 1) should have the smallest Dm values, Class 3 of the landslide susceptibility should normally be marked by Dm=1, while the highest susceptibility (Class 5) should be marked by the largest value of Dm.
Figure BF.115 plots resulting distribution of the Dm values for all models of Scenario 1. As it can be seen, for three validation sets out of four, the conventional Newmark mapping (model ND3) returns better statistics comparing with the advanced mapping techniques (models ND9 and ND10). Thus, for 10 landslide outlines (Figure BF.115a) and the 2007 landslides/scarps (Figures BF.115c and BF.115d) model ND3 has the lowest Dm value in Class 1 and the highest Dm value in Class 5. Only the validation set of 10 landslide scarps (Figure BF.115b) shows an opposite distribution: models ND9 and ND10 have higher Dm values for Classes 4 and 5, while the highest Dm is revealed for model ND10. This last feature indicates that the advanced mapping techniques certainly improved the predictions in comparison with the conventional Newmark mapping.

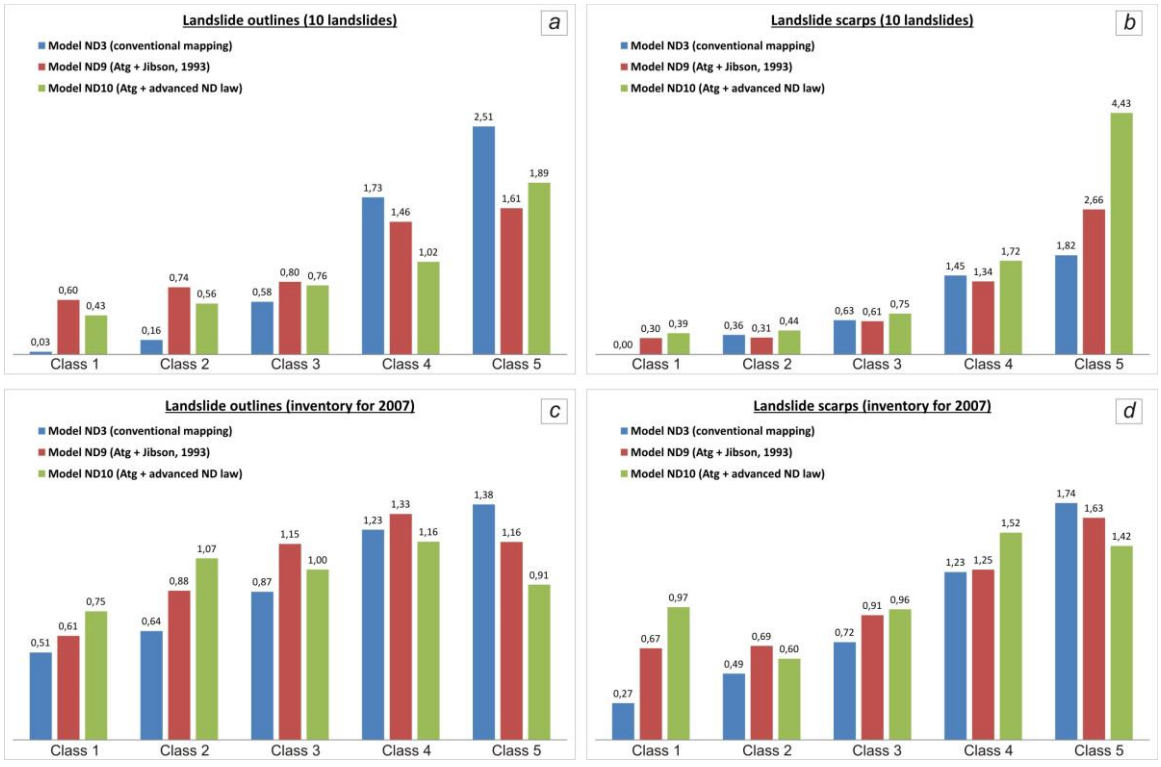

Figure BF.115: Distribution of the map-scaled density values (Dm) gained for the susceptibility classes of the models ND3, ND9 and ND10 applying the validations sets of: (a) the 10 landslide outlines most likely triggered by the studied seismic event, (b) the 10 scarps of the landslides most likely triggered by the studied seismic event, (c) the 2007 landslide outlines and (d) the 2007 landslide scarps.

Figure BF.116 shows three similar ND models for Scenario 2 analysing the M=5.5 hypothetical earthquake in the Central Fault zone. Model ND7 (see Figure BF.116a) presents the result of the conventional Newmark mapping for the case of the deep landslides (t=20 m) in dry conditions (m=0). The results of the advanced mapping are represented by the models ND11 and ND12 (see Figures BF.115b and BF.116c). Similar to Scenario 1, all models apply the same input layer of Ac which is obtained for t=20 m and m=0 given the known distribution of the conventional geotechnical parameters (see *Section A.V.5* for more details). Similar to Scenario 1, the susceptibility classes are defined according to the calculated values of D_n: the very low

landslide susceptibility (class 1) is marked by displacement values between 0.0 and 0.1 cm, class 2 is marked by slightly larger ND values (0.1- 0.5 cm), class 3 – by ND values between 0.5 and 0.9 cm, class 4 - by ND values between 0.9 and 5.0 cm, while the highest susceptibility (class 5) is marked by large displacements of more than 5.0 cm.

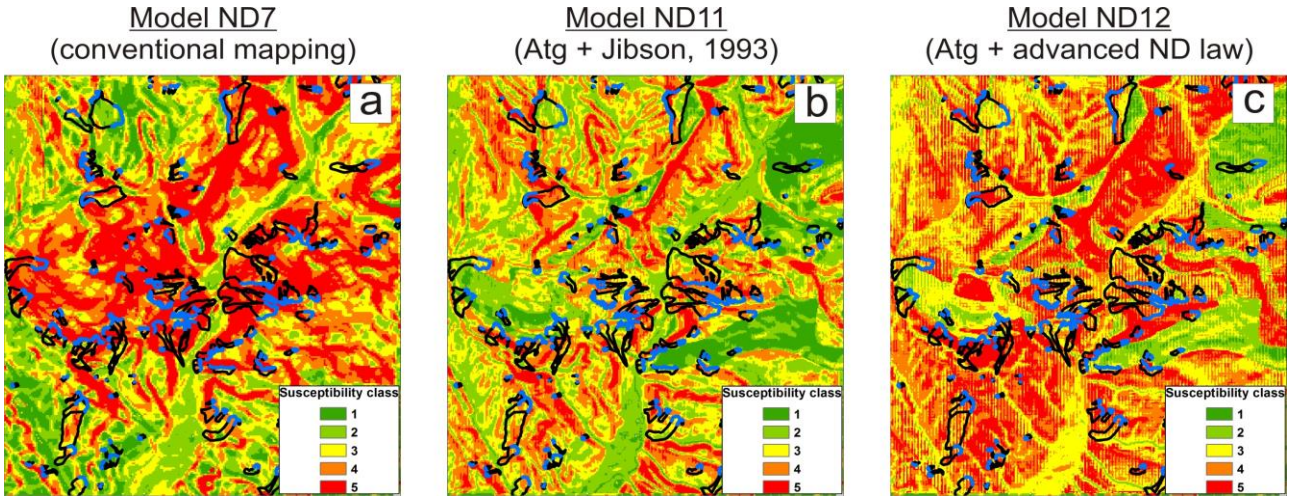

Figure BF.116: The mapping results for Scenario 2 applying the model of the deep landslide (t=20) in dry conditions (m=0): (a) model ND7 extracted by the conventional ND mapping (Wilson and Keefer, 1985; Jibson, 1993); (b) model ND11 which combines the advanced mapping of Ia (via applied Atg) with the conventional ND mapping by the law of Jibson (1993); (c) model ND12 which combines the advanced mapping of Ia (via applied Atg) with the advanced ND mapping (note: black outlines represent the landslide inventory for 2007 and blue lines are the corresponding landslide scarps).

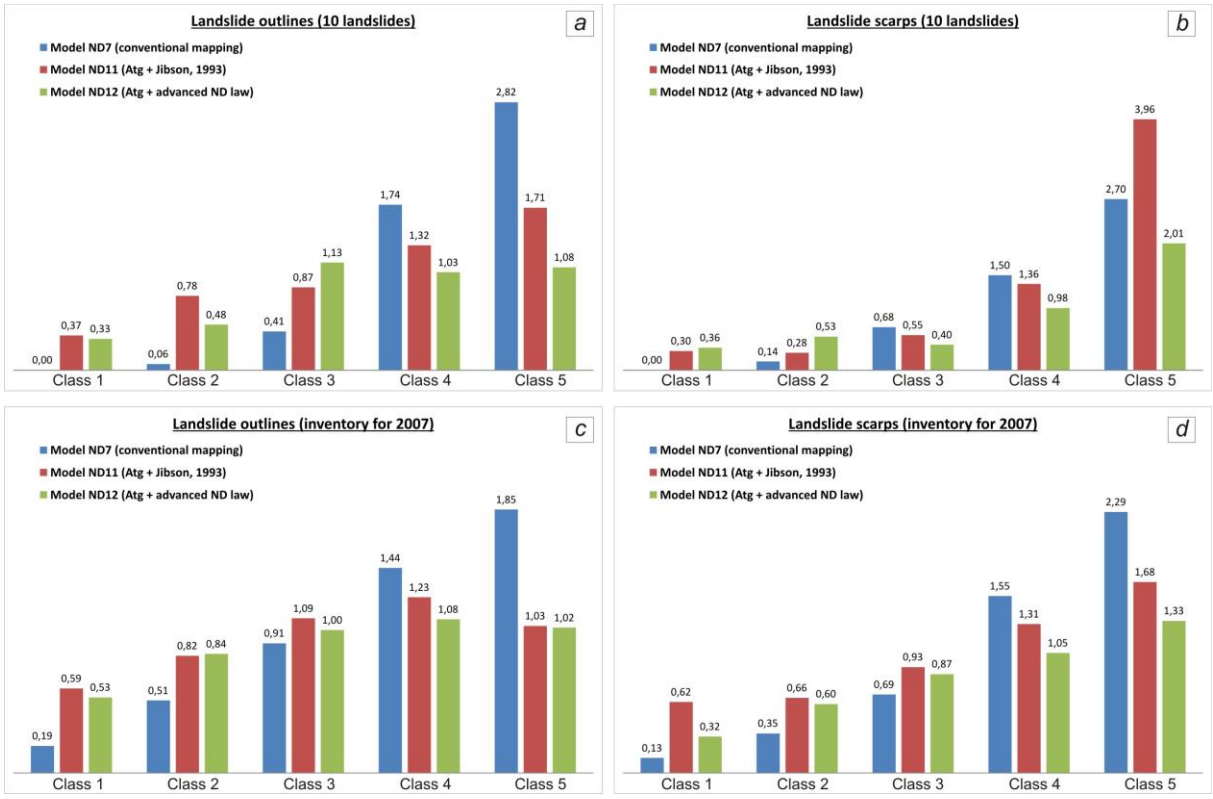

Figure BF.117: Distribution of the map-scaled density values (Dm) gained for the susceptibility classes of the models ND7, ND11 and ND12 applying the validations sets of: (a) the 10 landslide outlines most likely triggered by the studied seismic event, (b) the 10 scarps of the landslides most likely triggered by the studied seismic event, (c) the 2007 landslide outlines and (d) the 2007 landslide scarps.

The applied validation sets correspond to those used in Scenario 1: the ten landslides/scarps most likely triggered by the M=6.2 earthquake in 1992 (see Figure BF.114) and the 2007 landslide/scarps (see the black and blue outlines in Figure BF.116, correspondingly). Figure BF.117 summarizes the values of Dm calculated for all classes of extracted models. As it can be seen, the conventional Newmark mapping provides better predictions for the next validation sets: the 10 landslide outlines (Figure BF.117a) and the 2007 landslides/scarps (Figures BF.117c and BF.117d). The advanced mapping techniques provide the partially improved predictions for the case of the 10 landslide scarps (see the satistics in Figure BF.117b). This is proved by the higher value of Dm=3.96 observed for Class 5 of model ND11 in comparison with Dm=2.70 for Class 5 of model ND7 (see Figure BF.117b).

Thus, both studied scenarios yielded quite consistent results. First of all, the conventional Newmark mapping always had better performance with respect to the advanced mapping techniques for the validation sets presented by the 2007 landslides/scarps. This consistency may possibly be explained by the structure of the analysed inventories. Thus, the 2007 landslide/scarps combine different types of mass movements, including those which have a non-seismic origin. Actually, a majority of mapped landslides were either triggered by the extreme climatic conditions or their activity is complexly related to a set of different factors, including human impacts and underground water (see *Chapter A.III* for more details). These non-seismic landslides impact the final statistics, as they may fall inside the areas with the low level of the predicted landslide susceptibility.

The second consistency for both seismic scenarios is related to fact that the 10 landslide scarp indicated certain improvement provided by the advanced mapping techniques. This feature may be explained by the typical morphology of the landslide prone slopes. Thus, in such kind of slopes the landslide outline normally covers the whole extent of the sliding mass, including the central part of the landslide which is basically marked by the concave topography (note: it is true at the resolution of analysed DEM – locally the body is marked by convex shapes, but they are generally not shown at this resolution). According to the principles of the advanced mapping, the concave areas deamplify the values of Ia which return the lower D_n and the lower landslide susceptibility for such areas. This feature strongly impacts the final statistics, as some concave areas marked by low computed landslide susceptibility fall inside the landslide outlines. The landslide scarps normally have a different morphological setting: they tend to concentrate near the crest parts which are marked by the amplified values of Ia and which, in turn, increase the level of the landslide susceptibility. Therefore, the advanced mapping shows the improved statistics for the 10 landslide scarps, while for the 10 landslide outlines the results are opposite.

From the geotechnical and geomorphological points of view the landslide triggering is better characterized through the location of the landslide scarp rather than through the landslide outline. Therefore, the final performance of the advanced mapping is estimated by us through the statistics of the landslide scarps. As it is shown in Figures BF.115b and BF.117b, the application of the advanced mapping techniques really improves the statistics, as the classes of the highest landslide susceptibility are marked by the largest Dm. According to Chung and Fabbri (2003), the "powerful and effective" prediction class should have either very large (>3) or near zero (<0.2) values of Dm. Thus, class 5 of models ND10 and ND11 fall inside the indicated range: this finally indicates that the advanced mapping techniques may really improve the final predictions.

VIII. Synthesis of results

This part of thesis reviews the results of the 2D and 3D dynamic studies analysing the landslide-prone slopes in the Mailuu-Suu and the Min-Kush target areas. The numeric studies analyse the patterns of the pure topographic and topographic-geologic site effects, as well as modell the shear displacements triggered by the seismic inputs. The main focus of these analyses is put on the Arias Intensity (Ia), one of the key parameters involved in the Newmark method. This GIS-based method spatially maps the landslide susceptibility through the calculated values of the co-seismic displacement. The results of numeric studies propose the advanced mapping techniques which should improve the existing Newmark method. The elaborated mapping techniques are tested on the dataset existing for the Mailuu-Suu target area. The performance of these advanced mapping techniques is finally validated by using four different sets of landslide outlines and landslide scarps. All performed activities as well as reached milestones are summarized below.

The first type of the 2D dynamic simulations analyses the pure topographic site effects. The studied models are extracted from the geo-database of the Mailuu-Suu target area. These models are composed of unique material type, while their surfaces represented the real topographic settings restored from the DEM of the study area. All models are subjected to the dynamic loading during which the acceleration time histories are recorded over the number of surface receivers. The acceleration recordings are then used to calculate the values of Ia as well as the Ia amplification factors (At) registered in different parts of the models surface. Those registered values of At are compared with the 2D surface curvature, which represents the combined topographic index calculated on the basis of the elevation values spatially distributed over the length of the modelled profile. Through these studies we establish a link between At and the so-called 2D smoothed curvature, the parameter which represents the mean curvature over the specific neighbourhood called as the smoothing length. The statistical analysis also shows that the values of At are best predicted by the so-called 2D effective curvature, i.e. one which is smoothed over the effective smoothing length (Le). The values of Le are predicted based on the Geli's law, given the known values of the shear wave velocity (Vs) and the central frequency of the input acceleration time history (Fca). The studies finally propose the linear-shape prediction law, where At is linked to the 2D effective curvature. Meanwhile, this law cannot be directly applied in the conventional Newmark mapping, as the 3D amplification of the Ia values is marked by additional problem complexities.

This last issue is further analysed through 3D pure topographic modelling applied to the landslide-prone slope situated in the Min-Kush target area. The surface of the numerical model is restored from the 20 m SPOT DEM of the target area. The dynamic tests in the 3D domain analyse how the Ia amplification is impacted by the changing Vs of the composing material and variable Fca of the input signal. The acceleration time histories were recorded for the two orthogonal directions (x and y); this allowed us to estimate how the Ia values are amplified in the 3D domain. The resulting amplification factors (Atxy) were compared with the 3D curvature, which is automatically mapped by the ArcGIS code applying the resampled DEM of the study area. The analyses generally confirm the relationships established by the 2D studies. Nevertheless, some conceptual difference is also revealed. Thus, the 3D smoothed curvature should be mapped based on the smoothed DEM, while the 2D smoothed curvature is directly extracted based on the elementary curvature values. The second difference is related to the calculation of Le: the 2D analysis directly applies the Geli's law, while the 3D studies show that a factor of 0.25 should be used in this law to calculate the value of Le. Finally, the performed analysis allowed us to develop a mapping proxy which can be directly integrated into the conventional Newmark mapping. This proxy maps the spatial distribution of the Atxy values on the basis of elevation values included in the DEM of the study area and by applying the known values of Vs and Fca. The mapped distribution of Atxy indicates how much the original Ia values will be attenuated/amplified due to the topographic site effects.

The second type of the 2D dynamic tests analyses the topographic-geological amplification of the Ia values on the basis of the parameter Atg. The studies use the models which combine the real material sequence with the pure topographic settings. The pure geologic Ia amplification factors (Ag) are laterally assessed from the registered Atg values. The studies reveal that the geologic amplification of Ia is complexly related to a set of factors, including the underground geometry, layer inclination, distance to contact outcrop, etc. The analysis allows us to relate the mean values of Ag to the Vs impedance contrast (I_{Vs}) between the studied layer and the underlying material. Thereby, the simplified prediction law to calculate the mean Ag on the basis of I_{Vs} is elaborated. The proposed regional predictor should be mapped with the spatially distributed Vs values and applying the structural settings presented in the target area.

An additional subset of the 2D dynamic tests analyses the elasto-plastic behaviour in two types of studied models. The first type of models restored the rigid block sliding on the inclined plate, i.e. the simplified Newmark (1965) model which is the basis for all developments, including the regional Newmark mapping. The second type of model applied the real topographic profile where the elementary sliding blocks are installed in different part of the slope. The numerical tests used dynamic inputs with varying Fca to assess the triggered co-seismic displacements. The impacting seismic shaking is not subjected to any site effects in the simplified models, while in the second type of models the impacting shaking is modified due to the topographic site effects. The triggered co-seismic displacements are further compared with those values, estimated based on the Newmark (1965) model. The studies show that the Newmark (1965) model generally provides a quite reliable prediction of the co-seismic sliding behaviour. In most of the tests this technique well predicts the triggering moment, as well as the total value of the downslope displacement. However, it was also shown that the Newmark (1965) technique is performing less for the low-frequency shaking (low Fca). The modelled values of the co-seismic displacement are also compared with those predicted by some regional Newmark models. These analyses also indicate the impact of Fca on the reliability of final predictions: it is shown that these models can be applied only within specific range of Fca and for the displacement values less than 10.0-15.0 cm. The results of studies allow us to propose an advanced prediction law where ND is linked to Ia, Ac and Fca: the first two predictors are applied in the conventional Newmark mapping, while Fca is the novel parameter. The validation analysis shows that this advanced law works well for Fca>0.5 Hz and for the displacement values less than 10.0-15.0 cm.

Thus, the set of the 2D and 3D dynamic studies in elastic and elasto-plastic domains allows us to develop advanced mapping techniques which tend to improve the conventional Newmark mapping. One type of advancements account for the combined topo-geologic amplification of the Ia values conventionally mapped through the attenuation laws. This impact of the topo-geologic site effects is expressed via the values of Atg=At*Ag: the spatial distribution of At and Ag is automatically mapped applying the DEM of study area and the spatially distributed values of Vs and Fca. Another proposed advancement includes Fca as the one of the regional predictors to map the values of the Newmark displacement (ND): this law can also be conveniently applied in the conventional GIS codes, for example, in ArcGIS.

The proposed mapping proxies are finally tested over two earthquake scenarios in the Mailuu-Suu target area, which has previously been studied by the conventional Newmark model (Part A). Two types of the advanced Newmark models are extracted for each seismic scenario. The first type applies Atg to map the amplified values of Ia, while the second type combines the Atg values with the advanced ND prediction law. The mapping results are validated by applying four different validation sets of the landslide outlines and landslide scarps. These validation studies return consistent results regarding the prediction performance of the advanced mapping techniques. Thus, these techniques provide poorer predictions compared with the conventional Newmark mapping when the validation sets assemble landslides of different origin, including those triggered by the extreme climatic conditions or by the human impacts. Nevertheless, a better perfromance of the advanced techniques is proved when the validation set includes the scarps of the seismically-triggered landslides. This last feature indicates that the proposed proxies may potentially improve the existing Newmark method. Nevertherless, the final conclusion on the performance of proposed techniques should be done on the basis of a more reliable and extensive database. These studies should apply more precise input data, as well as use the validation set of the landslides/scarps which have pure seimic origin. One example of such dataset includes the thematic data collected for the numerous landslides triggered by the M=7.9 Wenchuan, China earthquake in 2008. These analyses should also outline the possible improvements of the proposed techniques: this should finally help to refine the regional Newmark methods and should make their predictions much more reliable.

Conclusions

This thesis is composed of two parts. Those two parts present different research targets and methods, but have in common the same general objective to investigate effective approaches characterising regional landslide susceptibility, hazard and, partially, also risk. These aspects are studied with the examples of two target areas situated in the Kyrgyz Tien-Shan: the Mailuu-Suu River Valley (southern Kyrgyzstan) and the Minkush area (central Kyrgyzstan). Both sites are characterised by a high level of landslide hazard. In addition, those areas represent legacy sites of former uranium mining which resulted in the storage of numerous tailings and waste rock dumps. Protective infrastructure of the tailing sites is exposed to high landslide hazards and related secondary impacts, which also elevates environmental pollution hazards. This situation urges the Kyrgyz government and international organisations to implement multiple remediation measures at the most critical sites. The selection of the remediation strategy should account for the potentially complex negative impacts of landslides on those exposed objects. Therefore, the landslide hazards in the target areas should be fully characterised regarding the possible occurrence, extent and size of the slope instabilities, also including related cascading effects.

The first part of the thesis is focused on the regional study of landslide activity in the Mailuu-Suu target area, southern Kyrgyzstan. This application-oriented part assembles several well-established approaches to map landslide susceptibility, hazard and risk in the target area. By applying spatial analysis and using high-resolution aerial/satellite imagery, we compiled a database combining the thematic information needed for further mapping activities. The first type of thematic data is represented by five multi-temporal landslide inventories which cover a period of 45 years. The time span between successive inventories is not equally distributed and ranges between 5 and 22 years. Ideally, those inventories should be equally distributed over the studied period of time. This was not possible for our analysis due to the limited availability of high-resolution imagery which was a basis for the extraction of inventories. The maps of factors influencing landslide activity are the second type of thematic data. Those factors include the geomorphological, geological and structural settings in the target area. They do, however, not cover some other important factors affecting the slope instability, such as the hydrogeological map, the areas of earth subsidence induced by former mining or the distribution of the loess cover. The extraction of those important maps was not possible due to a limited availability of input data. Thus, the inclusion of these layers could be a possible focus for further studies in the target area.

The thematic database was further used to map the landslide susceptibility applying four conceptually different approaches. Two of these methods provide qualitative results, i.e., the classification of the target area according to the expected level of landslide susceptibility expressed by a pure descriptive, non-numeric measure. Two other methods are quantitative; to each part of the target area a specific value of landslide occurrence probability was assigned. The quantitative results were than combined with the landslide inventories to map landslide hazard. That way, the landslide hazard is described both by temporal and spatial components, i.e., each part of the study area is characterised by a probability of landslide occurrence valid for a certain predictive period. Additionally, landslide hazard should also be described by other components, such as the size of triggered slope instabilities. We acknowledge that our approaches did not consider this aspect or other complexities of the target area (such as changing climatic conditions). So, the resulting landslide hazard map mainly provides answers to the two questions of ‘where’ and ‘how often’ slope failures may occur in the region of Mailuu-Suu.

Finally, by combining this map with geographic data on roads, buildings and tailings, we computed the landslide impact risk for those three groups of exposed elements. This study uses as input the vulnerability of elements with respect to landslide impacts. Due to a lack of sound data, we used some secondary features to qualitatively describe and map this component for the studied elements. The final results of these studies are represented by maps rating the clusters of objects according to the expected level of risk related to the direct impacts of the landslide failure. It is important to note that the performed studies should be considered as a very preliminary attempt to characterise landslide risk in the target area. The full analysis of risk related to the landslide impacts would demand a more advanced analysis. These possible studies should consider the ‘size’ component of landslide hazard as well as more quantitative estimates of the vulnerability of the exposed elements with respect to multiple hazard impacts - which are clearly beyond the scope of our research. Multiple types of impacts include, for example, the risk of inundation of the tailings dam due to the upstream flooding induced by the landslide damming of river. In this last case, the risk studies would also demand some engineering investigations studying the stability of the landslide dam under the pressure of the impounded water.

The thematic maps computed in Part A represent the proxy to regionally characterise the landslide activity in the Mailuu-Suu target area. Those maps provide answers to the questions of “where”, “how often” the landslides may occur and which exposed elements could be more seriously damaged. For example, such information may help improve risk prevention and mitigation activities for the exposed tailings sites. These predictions incorporated with in-situ investigations can constitute a background to select the best strategy to mitigate the risk of a given object: in the case of a tolerable level of landslide hazard some local measures can be implemented, while in the case of an intolerable hazard those tailings sites should be removed to another safer place.

One of the mapping approaches applied in Part A is the Newmark method. This method regionally predicts the seismically-induced landslide susceptibility through computed values of the co-seismic displacement. Due to the simplicity of the applied concept, this method is appealing for many researchers studying landslide hazards in seismically active regions. Nevertheless, due to the adopted simplifications, the predictions made by this method should be considered as quite uncertain or ‘vague’.

The question of how we could improve this method is the main topic of Part B of this thesis. To explore this issue we combined spatial analysis tools with outputs from 2D and 3D dynamic simulations. The studied models represent the actual topographic and geologic settings of landslide-prone slopes situated in both target areas. The modelling allowed us to track the patterns of the topographic and geologic amplification of the Arias Intensity (Ia), a factor which is also used as predictor in the empirical laws to assess Newmark Displacements at regional scale. The 2D dynamic simulations of the combined topographic-geologic models revealed that the amplification of Ia can first be predicted by the impedance contrast of the shear wave velocity (Vs). Additionally, the 2D studies of pure topographic effects showed that Ia amplification is related to the curvature smoothed over a specific neighbourhood. This concept of the pure topographic Ia amplification was further analysed through 3D studies. The results of the 3D modelling combined with classic spatial analysis allowed us to develop a simple proxy. This proxy predicts the Ia amplification in the 3D domain by means of the smoothed curvature extracted from the digital elevation model. An additional subset of 2D models analysed the shear displacements triggered by the shaking inputs. Those studies proposed a new law which allows us to regionally assess the co-seismic displacement on the basis of several predictors, including a new parameter, the one of the central frequency of the impacting shaking. This parameter has never been used before by any conventional law.

Finally, all proposed conceptual improvements were tested on the Mailuu-Suu geodatabase compiled in Part A of the thesis. The validation tests included the landslides that were the most likely triggered by seismic shaking and those that have a mixed origin. The results of the validation tests indicated that proposed techniques can really improve the predictions. This shows that the research objectives of Part B were generally achieved.

Nevertheless, we assume that the proposed techniques should be tested on a more reliable and complete database. This potential database should contain more precise input maps, as well as inventories of landslides purely triggered by the seismic shaking. For example, such kind of database could be extracted for the landslides triggered by the M=7.9 Wenchuan, China earthquake in 2008. Several authors studied the geological, geomorphological and tectonic settings of this target area, and provided precise maps of earthquake-triggered landslides. The application of the proposed techniques on such database should allow us to better assess the performance of the prediction laws and to improve related modelling and spatial analysis techniques.

References

Abbott, P. L. (2009). Mass movements. In J. L. Hahn (Ed.), Natural disasters – 7th edition. Boston, McGraw-Hill Higher Education.

Abdrakhmatov, K., Havenith, H.-B., Delvaux, D., Jongmans, D., Trefois, P. (2003). Probabilistic PGA and arias intensity maps of Kyrgyzstan (Central Asia). Journal of Seismology, 7, 203–220.

Aitmatov, I. T. and Torgoev, I. A. (2005). Geoecological processes in the mountainous areas: mathematical modeling, risk studies and geophysical survey. The report on the applied studies in the Mailuu-Suu River valley, Kyrgyzstan (in Russian).

Aki, K. and Larner, K. L. (1970). Surface motion of a layered medium having an irregular interface due to incident plane SH waves. Journal of Geophysical Research Atmospheres, 70, 933-954.

Alexander, D. E. (1989). Urban landslides. Progress in Physical Geography, 13, 157–191.

Alexander, D. E. (2002). Principles of emergency planning and management. New York: Oxford University Press.

Alioshin, U. G. and Torgoev, I. A. (2000). Radiation ecology of Mailuu-Suu. Bishkek: Ilim (in Russian).

Alioshin, U. G., Torgoev, I. A., Ashirov, G. E., Abirov, K. A., Torgoev, E. I. (2008). Evaluation of the possible outcomes of Tuyk-Suu landslide activity, Minkush City. Report on the field studies and the scientific research (in Russian).

Al-Homoud, A.S. and Al-Masri, G.A. (1999). CSEES: an expert system for analysis and design of cut slopes and embankments. Environmental Geology, 39(1), 75-89.

Al-Homoud, A.S. and Masanat, Y. (1998). A classification system for the assessment of slope stability of terrains along highway routes in Jordan. Environmental Geology, 34(1), 59-69.

Allum, J. A. E. (1975). Photogeology and Regional mapping. Pergamon Press.

Ambraseys, N. N. and Menu, J. M. (1988). Earthquake induced displacements. Earthquake Engineering and Structural Dynamics, 16(7), 985-1006.

Ambraseys, N.N. and Srbulov, M. (1995). Earthquake induced displacements of slopes. Soil Dynamics and Earthquake Engineering, 14, 59-71.

Anderson, J.G., Su, F., Zeng, Y. (2006). Characteristics of ground motion response spectra from recent large earthquakes and their comparison with IEEE standard 693. Proceedings of the 2006 SSA Meeting: 100th Anniversary Earthquake Conference, Commemorating of the 1906 San Francisco Earthquake, pp. 1–10.

Angot, A. (1909). Le treblement de terre de Provence (11 juin 1909). Annales du Berau Central Meterologique de France, 37-93.

Ardizzone, F., Cardinali, M., Carrara, A., Guzzetti, F., Reichenbach, P. (2002). Uncertainty and errors in landslide mapping and landslide hazard assessment. Natural Hazards and Earth System Sciences, 2(1), 3-14.

Arias, A. (1970). A measure of earthquake intensity. In R. J. Hansen (Ed.), Seismic design for nuclear power plants (pp. 438-483). Cambridge, Massachusetts: MIT Press.

Ashford, S. A. and Sitar, N. (1994). Seismic response of steep natural slopes. Report No. UCB/EERC 94-05, Earthquake Engineering Research Center, College of Engineering, University of California at Berkeley.

Ashford, S. A., Sitar, N., Lysmer, J., Deng, N. (1997). Topographic effects on the seismic response of steep slopes. Bulletin of the Seismological Society of America, 87(3), 701-709.

Athanasopoulos, G. A., Pelekis, P. C., Leonidou, E.A. (1999). Effects of surface topography on seismic ground response in the Egion (Greece) 15 June 1995 earthquake. Soil Dynamics and Earthquake Engineering, 18, 135-149.

Australian Geomechanics Society (2000). Landslide risk management concepts and guidelines. Australian Geomechanics, 42, 49-92.

Bard, P.-Y. (1982). Diffracted waves and displacement field over two-dimensional elevated topographies. Geophysical Journal of the Royal Astronomical Society, 71, 731-760.

Bard, P.-Y. (1995). Effects of surface geology on ground motion: recent results and remaining issues. Proc. of the 10th European Conf. on Earthquake Engineering, Vienna, pp. 305-323.

Bard, P.-Y. (2007). Ground shaking site effects: fundamentals and modeling. Lectures on site-effects, University of Granada.

Bard, P.-Y. and Bouchon, M. (1980). The seismic response of sediment-filled valleys. Part 1. The case of incident SH waves. Bulletin of the Seismological Society of America, 70, 1263-1286.

Barlow, N. (1933). Charles Darwin's Diary of the Voyage of H.M.S. Beagle. New York: Cambridge U Press.
Bebbington, M. S. and Lai, C. D. (1996). On nonhomogeneous models for volcanic eruptions. Mathematical Geology, 28, 585-600.
Berardi, R., Capozza, F., Zonetti L. (1978). Analysis of rock motion accelerograms recorded at surface and underground during the 1976 Friuli seismic period. Proceedings of the 1976 Friuli Earthquake on the antiseismic design of nuclear installation conference, Rome, Italy, October 1977.
Blaschke, T. (2010). Object based image analysis for remote sensing. ISPRS Journal of Photogrammetry and Remote Sensing, 65, 2-16.
Bogdanovich, M.M.C., Kark, J., Korolkov, B., Muchketov, D. (1914). Earthquake of the 4 January 1911 in the northern districts of the Tien Shan. Tr. Geol. Com. Ser., 89, (in Russian).
Boore, D. M. (1972). A note on the effect of simple topography on seismic SH waves, Bulletin of the Seismological Society of America, 62, 275-284.
Borcherdt, R.D. (1970). Effects of local geology on ground motion near San Francisco Bay. Bulletin of the Seismological Society of America, 60, 29-61.
Bosi, C., Dramis, F., Gentili, B. (1985). Carte geomorfologiche di dettaglio and indirizzo applicativo e carte di stabilità a base geomorfologica. Geologia Applicata ed Idrogeologia, 20(2), 53-62.
Bossu, R. and Grasso, J. (1996). Stress analysis in the intraplate area of Gazli, Uzbekistan, from different sets of earthquake focal mechanisms. Journal of Geophysical Research, 101. doi: 10.1029/96JB01182.
Bouchon, M. and Barker, J. S. (1996). Seismic Response of a hill: the example of Tarzana, California. Bulletin of the Seismological Society of America, 86, 66-72.
Bouckovalas, G. D. and Papadimitriou, A. G. (2005). Numerical evaluation of slope topography effects on seismic ground motion. Soil Dynamics and Earthquake Engineering, 25, 547–558.
Bourdeau, C. and Havenith, H.-B. (2008). Site effects modeling applied to the slope affected by the Suusamyr earthquake (Kyrgyzstan, 1992). Engineering Geology, 9, 126-145.
Bozzano, F., Lenti, L., Martino, S., Paciello, A., Scarascia Mugnozza, G. (2008). Self-excitation process due to local seismic amplification responsible for the reactivation of the Salcito landslide (Italy) on 31 October 2002. Journal of Geophysical Research, 113. doi:10.1029/2007JB005309.
Bozzano, F., Lenti, L., Martino, S., Paciello, A., Scarascia Mugnozza, G. (2011). Evidences of landslide earthquake triggering due to self-excitation process. International Journal of Earth Sciences, 100, 861-879.
Brabb, E. E. (1984). Innovative approaches to landslide hazard mapping. Proceedings 4th International Symposium on Landslides, Toronto, pp. 307-324.
Braun, A. (2010). Investigation of the landslide susceptibility in Maily-Say, Kyrgyzstan with data mining methods. Master Thesis submitted for the degree of Master of Science in "Georesources Management", RWTH Aachen, Germany, p.117.
Bray, J. D., Travasarou, T. (2007). Simplified procedure for estimating earthquake-induced deviatoric slope displacements. Journal of Geotechnical and Geoenvironmental Engineering, 133, 381-392.
Brown, C.E. (1998). Applied Multiple Statistics in Geohydrology and Related Sciences. Berlin: Springer-Verlag.
Bryant E. (2005). Land instability as a hazard. In E. Bryant (Ed.), Natural hazard – 2nd edition (pp. 249-269). Cambridge: Cambridge university press.
Bulut, F., Boynukalin, S., Tarhan, S., Ataoglu, E. (2000). Reliability of landslide isopleths maps. Bulletin of Engineering Geology and the Environment, 58(2), 95-98.
Burgmann, R., Rosen, P. A., Fielding, E. J. (2000). Synthetic aperture radar interferometry to measure Earth's surface topography and its deformation. Annual Review of Earth and Planetary Sciences, 28, 169–209.
Buslov, M. M., De Grave, J., Bataleva E. A., Batalev, V. Y. (2007). Cenozoic tectonic and geodynamic evolution of the kyrgyz Tien Shan mountains: a review of geological, thermochronological and geophysical data. Journal of Asian Earth Sciences, 29, 205-214.
Campbell, R.H. (1973). Isopleth map of landslide deposits, Point Dume Quadrangle, Los Angeles County, California; an experiment in generalizing and quantifying areal distribution of landslides. U.S. Geological Survey Miscellaneous Field Studies Map MF–535, scale 1:24,000.
Campbell, G.B. (2011). Introduction to Remote Sensing. The Guilford Press.
Cardinali, M., Reichenbach, P., Guzzetti, F., Ardizzone, F., Antonini, G., Galli, M., Cacciano, M., Castellani, M., Salvati, P. (2002). A geomorphological approach to estimate landslide hazard and risk in urban and rural areas in Umbria, central Italy. Natural Hazards and Earth System Science, 2(1), 57-72.

Carrara, A. (1978). Considerazioni sulla cartografia applicata alla stabilità dei versanti. Seminario Sottoprogetto Fenomeni Franosi, March 1978, Bari, (in Italian).
Carrara, A. (1983). A multivariate model for landslide hazard evaluation. Mathematical Geology, 15, 403-426.
Carrara, A. (1988). Drainage and divide networks derived from high–fidelity digital terrain models. In C.-J. F. Chung et al. (Eds.), Quantitative analysis of mineral and energy resources (pp. 581-597). NATO–ASI Series, Dordrecht: D. Reidel Publishing Co.
Carrara, A., Cardinali, M., Detti, R., Guzzetti, F., Pasqui, V., Reichenbach, P. (1991). GIS Techniques and statistical models in evaluating landslide hazard. Earth Surface Processes and Landform, 16(5), 427-445.
Carrara, A., Guzzetti, F. (1995). Geographical Information Systems in Assessing Natural Hazards. Dordrecht: Kluwer Academic Publisher.
Celebi, M. (1987). Topographical and geological amplifications determined from strong-motion and aftershock records of the 3 March 1985 Chile earthquake. Bulletin of the Seismological Society of America, 77 (4), 1147–1167.
Celebi, M. (1991). Topographic and geological amplification: case studies and engineering implications, Structural Safety, 10, 199-217.
Celebi, M., Prince, C., Dietel, M., Onate, M., Chavez, G. (1987). The culprit in Mexico City – amplification of motions. Earthquake Spectra, 3, 315-328.
Chaddock, R. E. (1925). Principles and Methods of Statistics. Boston Houghton Mifflin Company.
Champati ray, P. K., Dimri, S., Lakhera, R. C., Sati, S. (2007). Fuzzy-based method for landslide hazard assessment in active seismic zone of Himalaya. Landslides, 4, 101-111.
Chau, K. T., Wong, R. H. C., Liu, J., Lee, C. F. (2003). Rockfall Hazard Analysis for Hong Kong Based on Rockfall Inventory. Rock Mechanics and Rock Engineering, 36(5), 383-408.
Chung, C.-J. F. and Fabbri, A. G. (1999). Probabilistic prediction models for landslide hazard mapping. Photogrammetric Engineering & Remote Sensing, 65(12), 1389-1399.
Clough, R. W. (1960). The finite element method in plane stress analysis. In Proceedings of the 2nd Conference on Electronic Computation. American Society of Civil Engineers, Structural Division, Pittsburgh, PA, Sept. 1960.
Cluff, L. S. (1971). Peru earthquake of May 31, 1970; engineering geology observations. Bulletin of the Seismological Society of America, 61, 511-533.
Coe, J. A., Michael, J. A., Crovelli, R. A., Savage, W. Z. (2000). Preliminary map showing landslide densities, mean recurrence intervals, and exceedance probabilities as determined from historic records, Seattle, Washington. U.S. Geological Survey Open-File Report 00-303.
Comber, A. J., Fisher, P. F., Wadsworth R. A. (2005). What is land cover? Environment and Planning, 32 (2), 199-209.
Committee on the Review of the National Landslide Hazards Mitigation Strategy (2004). Partnerships for Reducing Landslide Risk. Assessment of the National Landslide Hazards Mitigation Strategy. Board on Earth Sciences and Resources, Division on Earth and Life Studies, Washington, D.C.: the National Academic Press.
Conte, E. and Dente, G. (1992). Amplification effects of wave propagation in slopes. Proceedings of the French-Italian conference on slope stability in seismic areas, May 14-15, 1992, Bordighera, Italy, pp. 181–192.
Cotecchia, V., Guerricchio, A., Melidoro, G. (1986). The geomorphogenic crisis triggered by the 1783 earthquake in Calabria (Southern Italy). Proceedings of the International Symposium on Engineering Geology Problems in Seismic Areas, Bari, Italy, vol.6, pp. 245-304
Cox, D.R. (1958). The Regression Analysis of Binary Sequences. Journal of the Royal Statistical Society. Series B (Methodological), 20, 215-242.
CRED-OFDA (2002). EM-DAT: The OFDA/CRED International Disaster Database. Centre for Research on the Epidemiology of Disasters.
Crespellani, T., Madiai, C., Maugeri, M. (1996). Analisi di stabilita di un pendio in condizioni sismiche e post-simiche. Rivista Italiana Geotech., 1, 50-61.
Crozier, M. J. and Glade, T. (2005). Landslide hazard and risk: issues, concepts and approach. In T. Glade, M. G. Anderson and M.J. Crozier (Eds.), Landslide risk assessment (pp.1-40). John Wiley.
Crovelli, R.A. (2000). Probability models for estimation of number and costs of landslides. U.S. Geological Survey Open-File Report 2000-249, 17 p.

Cruden, D. M. (2000). Some Forms of Mountain Peaks in the Canadian Rockies Controlled by their Rock Structure. Quaternary International, 68, 59-65.
Cundall, P. A. and Hart, R. D. (1985). Development of Generalized 2-D and 3-D Distinct Element Programs for Modeling Jointed Rock. Itasca Consulting Group Report to U.S. Army Engineering Waterways Experiment Station, May, 1983, published as Misc. Paper SL-85-1, U.S. Army Corps of Engineers.
Davis, L. L. and West, L. R. (1973). Observed effects of topography on ground motion. Bulletin of the Seismological Society of America, 63, 283-298.
de Marneffe C. (2010). Cartography and 3D geological modeling of the Mailuu-Suu River Valley. Master theses, University of Liege, Belgium, 126 p.
Dai, F. C., Lee, C. F., Deng, J. H., Tham, L. G. (2005). The 1786 eathquake-triggered landslide dam and subsequent dam-break flood on the Dadu River, southwest China. Geomorphology, 65, 205-221.
Danneels, G. (2004). Landslide susceptibility assessment in the Maily-Say valley (Kyrgyzstan) by means of remote sensing techniques. Master theses, University of Liege, Belgium, 111 p.
Danneels, G., Bourdeau, C., Torgoev, I., Havenith, H.-B. (2008). Geophysical investigation and dynamic modelling of unstable slopes: case-study of Kainama (Kyrgyzstan). Geophysical Journal International, 175 (1), 17-34.
DeGraff, J. V. (1985). Using isopleth maps of landslides deposits as a tool in timber sale planning. Bulletin of American Association of Engineering Geologists, 22, 445-453.
Del Gaudio, V., Pierri, P., Wasowski, J. (2003). An approach to time-probabilistic evaluation of seismically induced landslide hazard. Bulletin of the Seismological Society of America, 93, 557-569.
Del Gaudio, V., Trizzino, R., Calcagnile, G., Calvaruso, D., Pierri, P. (2000). Landsliding in seismic areas: the case of the Acquara-Vadoncello Landslide (Southern Italy). Bulletin of Engineering Geology and Environment, 59, 23-37.
Del Gaudio, V. and Wasowski, J. (2007). Directivity of slope dynamic response to seismic shaking. Geophysical Research Letters, 34(12). doi:10.1029/2007GL029842.
Delvaux, D., Abdrakhmatov, K. E., Strom, A.L. (2001). Landslides and surface breaks of the 1911 Ms 8.2 Kemin earthquake, Kyrgyzstan. Russian Geology and Geophysics, 42, 1167-1177, (in Russian).
Di Giulio, G., Cornou, C., Ohrnberger, M., Wathelet, M., Rovellii A. (2006). Deriving Wavefield Characteristics and Shear-Velocity Profiles from Two-Dimensional Small-Aperture Arrays Analysis of Ambient Vibrations in a Small-Size Alluvial Basin, Colfiorito, Italy. Bulletin of the Seismological Society of America, 96, 1915-1933.
Dietrich, E. W., Reiss, R., Hsu, M-L., Montgomery, D.R. (1995). A process–based model for colluvial soil depth and shallow landsliding using digital elevation data. Hydrological Process, 9, 383-400.
Dirik K. (2005). Advanced photogeology – lecture notes. Geological Engineering Departement, HU, 45p.
Djanuzakov, K. D., Chediya, O. K., Abdrakhmatov, K. E., Turdukulov, A. T. (1996). Seismic zonation map of Kyrgyzstan. Bishkek: Ilim, (in Russian).
Drury, S.A. (1986). Image Interpretation in Geology. Allen and Unwin, 243 p.
Dunne, T. (1991). Stochastic aspects of the relations between climate, hydrology and landform evolution. Transaction Japanese Geomorphological Union, 12, 1-24.
Elgamal, A. M., Scott, R. F., Succarieh, M. F., Yan, L. P. (1990). La Villita dam response duringfive earthquakes including permanent deformation. Journal of Geotechnical Engineering, 116, 1443-1462.
Ellis, J. (1999). NASA Satellite Systems for the Non-renewable Resource Sector. Earth Observation Magazine, 8(3), 46-48.
Ermini, L., Catani, F., Casagli, N. (2005). Artificial Neural Networks applied to landslide susceptibility assessment. Geomorphology, 66, 327-343.
ESRI (2012). ArcGIS Help Library. Retrieved from www.help.arcgis.com.
Evans, S. G. (2006). Single-event landslides resulting from massive rock slope failure: characterizing their frequency and impact on society. In S.G. Evans, G. Scarascia-Mugnozza, A.L. Strom, R.L. Hermanns (Eds.), Landslides from Massive Rock Slope Failure (pp. 53–73). NATO Science Series IV Earth and Environmental Sciences, Dordrecht: Springer.
Evans, S. G., Robertsa, N J., Ischuk, A., Delaneya, K B., Morozova, G. S., Tutubalinac, O. (2009). Landslides triggered by the 1949 Khait earthquake, Tajikistan, and associated loss of life. Engineering Geology 109 (3–4), 195-212.
Faccioli, E. (2000). The importance of earthquake site effects from an engineering point of view. In Proc. Journée d'étude de la Société Suisse du Génie Parasismique et de la dynamique des structures (SGEB) "Prévention sismique en Suisse", pp. 1-11.

Falaschi, F., Giacomelli, F., Federici, P. R., Pucinelli, A., D'Amato Avanzi, G., Pochini, A., Ribolini, A. (2009). Logistic regression versus articial neural networks: landslides susceptibility evaluation in a sample area of the Serchio River valley, Italy. Natural Hazards, 50, 551-569.

Fayyad, U., Piatetsky-Shapiro, G., Smyth, P. (1996). From Data Mining to Knowledge Discovery in Databases. AI Magazine, 17, 37-54.

Fell, R., Corominas, J., Bonnard, C., Cascini, L., Leroi, E., Savage, W. (2008). Guidelines for landslide susceptibility, hazard and risk zoning for land-use planning. Engineering Geology, 102, 99-111.

Fell, R. and Hartford, D. (1997). Landslide risk management. In D. M. Cruden and R. Fell (Eds.), Landslide risk assessment - Proceedings of the Workshop on Landslide Risk Assessment, Honolulu, Hawaii, USA, 19-21 February 1997 (pp.51-109). Rotterdam: A.A. Balkema.

Fernandez-Steeger, T. M. (2002). Erkennung von Hangrutschungssystemen mit Neuronalen Netzen als Grundlage fur Georisikoanalysen. Ph.D. Thesis, Universitat Karlsruhe.

Fernandez-Steeger, T. M., Czurda, K. (2001). Erkennung von Rutschungsgebieten mit Neuronalen Netzen, in: Zweites Forum Katastrophenvorsorge. In G. Tezla (Ed.), Extreme Naturereignisse – Folgen Vorsorge, Werkzeuge (pp.226-233), Bonn.

Fisher, R.A. (1936). The use of multiple measurements in taxonomic problems. Annales Eugenics, 7, 179-188.

Fookes, P. G. and Wilson, D. D. (1966). The geometry of discontinuities and slope failures in Siwalik Clay. Geotechnique, 16(4), 305–320.

Frankel, A. and Wennerberg, L. (1989). Rupture process of the Ms 6.6 Superstition Hills earthquake determined from strong-motion recordings, application of tomographic source inversion. Bulletin of the Seismological Society of America, 79, 515-541.

Gaziev, E. (1984). Study of the Usoy Landslide in Pamir. Proc. 4th International Symposium on Landslides, Toronto, 1, pp. 511–515

Geiger, L., Gutenberg, B. (1912). Über Erdbebenwellen. VI. Konstitution des Erdinnern, erschlossen aus der Intensität longitudinaler und transversaler Erdbebenwellen, und einige andere Beobachtungen an den Voläufern. Nachrichten von der Gesellschaft der Wissenschaften zu Göttingen, Mathematisch-Physikalische Klasse, pp. 623-675.

Geli, L., Bard, P.-Y., Jullien, B. (1988). The effect of topography on earthquake ground motion: a review and new results. Bulletin of the Seismological Society of America, 78(1), 42-62.

Gholamy, A. and Krienovich, V. (2014). Why Ricker wavelets are successful in processing seismic data: Towards a theoretical explanation. Computational Intelligence for Engineering Solutions (CIES), 2014 IEEE Symposium, September, 9-12 2014, pp. 11-16.

Ghose, S., Mellors, R. J., Korjenkov, A. M., Hamburger, M. W., Pavlis, T. L., Pavlis, G .L., Mamyrov, E., Muraliev, A.R. (1997). The Ms = 7.3 1992 Suusamyr, Kyrgyzstan, earthquake: 2. Aftershock Focal Mechanisms and Surface Deformation. Bulletin of the Seismological Society of America, 87, 23-38.

Gidrometeoizdat (1989). Applied reference book on the climate of USSR/Long-term records. Leningrad (in Russian).

Glade, T. (2003). Landslide occurrence as a response to land use change: a review of evidence from New Zealand. Catena, 51, 297-314.

Global Marketing Insights, Inc. (2005). Survey and analysis of Remote Sensing market: aerial and spaceborn. The report to National Oceanic and Atmospheric Administration, USA, 74 p.

Goodman, R.E. and Seed, H.B (1966). Earthquake-induced displacements in sand embankments. Journal of the Soil Mechanics and Foundations Division, 92, 125-146.

GO-ELS Ltd. (2008). Investigation and analysis of natural hazard impacts on linear infrastructure in Southern Kyrgyzstan: desk and field studies report. WB report № 68669.

Gorsevski, P.V., Gessler, P.E., Jankowski, P. (2003). Integrating a fuzzy k-means classification and a Bayesian approach for spatial prediction of landslide hazard. Journal of Geographical Systems, 5(3) 223-251.

Gorum, T., Fan, X., Cees, J., van Westen, C. J. (2011). Distribution pattern of earthquake-induced landslides triggered by the 12 May 2008 Wenchuan earthquake. Geomorphology, 133 (3-4), 152-167.

Graves, R.W. (1993). Modelling three-dimensional site response effects in the Marina District basin, San Francisco, California. Bulletin of the Seismological Society of America, 83, 1042-1063.

Graves, R. W., Wald, D. J. (2004). Observed and simulated ground motions in the San Bernardino basin region for the hector mine, California, earthquake. Bulletin of the Seismological Society of America, 94(1), 131–146.

Grelle, G., Revellino, P., Donnarumma, A., Guadagno, F. M. (2011). Bedding control on landslides: a methodological approach for computer-aided mapping analysis. Natural Hazards and Earth System Sciences, 11, 1395-1409.

Griffiths, D. W. and Bollinger, G. A. (1979). The effect of Appalachian Mountain topography on seismic waves. Bulletin of the Seismological Society of America, 69, 1081-1105.

Griffiths, D. V. and Prevost, J. H. (1988). Two- and three-dimensional finite element analyses of the Long Valley Dam. Technical Report NCEER-88-0015, National Center for Earthquake Engineering Research, Buffalo, NY.

Gritzner, M. L., Marcus, W. A., Aspinall, R., Custer, S. G. (2001). Assessing landslide potential using GIS, soil wetness modelling and topographic attributes, Payette River, Idaho. Geomoprhology, 37, 149-165.

Guzzetti, F., Crosta, G.B., Detti, R., Agliardi, F. (2002). STONE: a computer program for the three-dimensional simulation of rock-falls. Computers & Geosciences, 28(9), 1079-1093.

Guzzetti, F. (2006). Landslide hazard and risk assessment. PhD dissertation, University of Bonn, Germany, 389 p.

Guzzetti, F., Cardinali, M., Reichenbach, P. (1994). The AVI Project: a bibliographical and archive inventory of landslides and floods in Italy. Environmental Management, 18(4), 623-633.

Guzzetti, F., Carrara, A., Cardinali, M., Reichenbach, P. (1999). Landslide hazard evaluation: an aid to a sustainable development. Geomorphology, 31, 181-216.

Guzzetti, F., Reichenbach, P., Cardinali, M., Ardizzone, F., Galli, M. (2003). Impact of landslides in the Umbria Region, Central Italy. Natural Hazards and Earth System Sciences, 3(5), 469-486.

Guzzetti, F., Reichenbach, P., Cardinali, M., Galli, M., Ardizzone, F. (2005). Probabilistic landslide hazard assessment at the basin scale. Geomorphology, 72(1-4), 272-299.

Guzzetti, F. and Tonelli, G. (2004). SICI: an information system on historical landslides and floods in Italy. Natural Hazards and Earth System Sciences, 4(2), 213-232.

Hansen, A. (1984). Landslide hazard analysis. In D. Brunsden and D. B. Prior (Eds.), Slope instability (pp. 523-602). New York: Wiley & Sons.

Hansen, A. and Franks, C.A.M. (1991). Charachterization and mapping of earthquake triggered landslides for seismic zonation. Proceedings of the Fourth International Conference on Seismic Zonation, Stanford, California, 1, pp.149-195.

Hansen, A., Franks, C.A.M., Kirk, P.A., Brimicombe, A.J., Tung, F. (1995). Application of GIS to hazard assessment, with particular reference to landslides in Hong Kong. In A. Carrara and F. Guzzetti (Eds.), Geographical Information Systems in Assessing Natural Hazards (pp. 135-175). The Netherlands, Dordrecht: Kluwer Academic Publisher.

Hanssen, A. and Ramon F. (2001). Radar Interferometry: Data Interpretation and Error Analysis. Kluwer Academic.

Harp, E.L. and Jibson R.W. (1996a). Landslides triggered by the 1994 Northridge, California, Earthquake. Bulletin of the Seismological Society of America, 86, 319-322.

Harp, E.L. and Jibson R.W. (1996b). Anomalous concentrations of seismically triggered rock falls in Pacoima Canyon: are they caused by highly susceptible slopes or local amplification of seismic shaking? Bulletin of the Seismological Society of America, 92 (8), 3180-3189.

Harp, E. L. and Wilson, R. C. (1995). Shaking intensity thresholds for rock falls and slides: evidence from 1987 Whitter Narrows and Superstition Hills earthquake strong-motion records. Bulletin of the Seismological Society of America, 85, 1739-1757.

Harp, E.L., Wilson, R.C., Wieczorek, G.F. (1981). Landslides from the February 4, 1976 Guatemala earthquake. U.S. Geological Survey Professional Paper 1204-A. 35 p.

Harris, R., (1987). Satellite Remote Sensing: an introduction. London: Routledge and Regan Paul.

Hastie, T., Tibshirani, R., Friedman, J. (2001). The elements of statistical learning. New York: Springer.

Havenith, H.-B. (2003). Landslides triggered by earthquakes: experimental studies in the Tien Shan mountains (Central Asia) and dynamic modelling. Liège, University of Liège, PhD thesis in applied sciences, 239 p.

Havenith, H.-B., Torgoev, A., Schlögel, R., Braun, A., Torgoev, I., Ischuk, A. (2015a). Tien Shan geohazard database: landslide susceptibility analysis. Geomorphology, 249, 32-43.

Havenith, H.-B., Torgoev, I. A., Meleshko, A. V., Alioshin, Y. G., Torgoev, A. D., Daneels G. (2006). Landslides in the Mailuu-Suu valley, Kyrgyzstan: Hazards and Impacts. Landslides, 3, 137-147.

Havenith, H.-B., Torgoev, I., Torgoev, A., Strom, A., Xu, Yu., Frenandez-Steeger, T. (2015b). The Kambarata 2 blast-fill dam, Kyrgyz Republic: blast event, geophysical monitoring and dam structure modeling. Geoenvironmental Disasters, 2, 1-15.

Heenkenda, M. K., Joyce, K. E., Maier, S. W., Bartolo, R. (2014). Mangrove species identification: comparing WorldView-2 with aerial photographs. Remote Sensing, 6(7), 6064-6088.

Hollingsworth, R. and Kovacs, G.S. (1981). Soil slumps and debris flows: prediction and protection. Bulletin American Association of Engineering Geologists, 18(1), 17-28.

Hsieh, S.-Y. and Lee, C.-T. (2007). Empirical estimation of the Newmark displacement from the Arias intensity and critical acceleration. Engineering Geology, 122, 34-42.

Huang, R. and Fan, X. (2013). The landslide story. Nature Geoscience, 6, 325–326.

Humbert, M. (1977). La Cartographie ZERMOS. Modalités d'établissement des cartes des zones exposées. Publications du GFGI, 1(2), 4P.

Hungr, O. (1997). Some methods of landslide hazard intensity mapping. In D.M. Cruden and R. Fell (Eds.), Landslide risk assessment (pp. 215-226). Rotterdam: A.A. Balkema Publisher.

Hutchinson, J. N. (1988). General report: Morphological and geotechnical parameters of landslides in relation to geology and hydrology. Proceedings 5th International Symposium on Landslides, Lausanne, 1, 3-35.

Hutchinson, J. N. (1995). Keynote paper: Landslide hazard assessment. In R. Bell (Ed.), Landslides (pp. 1805-1841), Rotterdam: A.A. Balkema.

Hwang, H., Lin, C. K., Yeh, Y. T., Cheng, S. N., Chen, K. C. (2004). Attenuation relations of Arias intensity based on the Chi-Chi Taiwan earthquake data. Soil Dynamics and Earthquake Engineering, 24, 509–517.

IAEA (2009). Overview and Recommendations for Uranium Production Legacy Sites in Central Asia: An International Approach Monitoring and Regulatory Structure, Remediation, Legacy Sites Risk Assessment. Thematic report.

Iliyn, I.A. (1959). Water resources of Fergana Valley. Leningrad: Gidrometeoizdat, 248 p (in Russian).

Itasca Consulting Group, Inc. (2009). FLAC 3D — Fast Lagrangian Analysis of Continua in 3 Dimensions, Version 4.0 User's Manual. Minneapolis: Itasca.

Itasca Consulting Group, Inc. (2006). UDEC — Universal Distinct Element Code, Version 4.0 User's Manual. Minneapolis: Itasca.

Jain, P.K. (2004). Remote Sensing through satellites: a tutorial review. Microwave Journal, 47(12), 22-45.

Janbu, N. (1973). Slope stability computations–Embankment–Dam Engineering. Casagrande Volume, Wiley, New York.

Jenson, S. K. and Domingue, J. O. (1988). Extracting topographic structure from digital elevation data for geographic information system analysis. Photogrammetric Engineering and Remote Sensing, 54(11), 1593-1600.

Jibson, R. W. (1993). Predicting earthquake-induced landslide displacements using Newmark's sliding block analysis. Transportation Research Record, 1411, 9–17.

Jibson, R. W., Harp, E .L., Schulz, W., Keefer, D.K. (2006). Large rock avalanches triggered by the M-7.9 Denali Fault, Alaska, earthquake of 3 November 2002. Engineering Geology, 83, 144–160.

Jibson, R. W. (2007). Regression models for estimating coseismic landslide displacement. Engineering Geology, 91, 209-218.

Jibson, R. W. (2011). Methods for assessing the stability of slopes during earthquakes—A retrospective. Engineering Geology, 122, 43-50.

Jibson, R. W., Harp, E. L., Michael, J. A. (1998). A Method for Producing Digital Probabilistic Seismic Landslide Hazard Maps: An Example from the Los Angeles, California, Area. USGS Open-File Report 98-113.

Jibson, R.W. and Jibson, M.W. (2003). Java programs for using Newmark's method and simplified decoupled analysis to model slope performance during earthquakes. USGS Open-File Report 03-005, version 1.1.

Jongmans, D. (1989). Les phénomènes d'amplification d'ondes sismiques dus à des structures géologiques. Ann. Soc. Géol. Belg., 112, 369-379.

Jongmans, D. and Campillo, M. (1988). Répartition des dommages pendant le tremblement de terre de Liège du 8 novembre 1983: effet de source et effet de site. Colloque national du génie parasismique sur les mouvements sismiques pour l'ingénieur, St. Rémy les Chevreuses, 16 mars 1988, 23-33.

Jongmans, D. and Campillo, M. (1993). The response of the Ubaye valley (France) for incident SH and SV waves: Comparison between measurements and modeling. Bulletin of the Seismological Society of America, 83, 907-924.
Kawabata, D. and Bandibas, J. (2009). Landslide susceptibility mapping using geological data, a DEM from ASTER images and an Artificial Neural Network (ANN). Geomorphology, 113, 97–109.
Keefer, D.K. (2002). Investigating Landslides Caused by Earthquakes – A Historical Review. Surveys in Geophysics, 23(6), 473-510.
Kienholz, H. (1978). Maps of geomorphology and natural hazard of Grindelwald, Switzerland: scale 1:10.000. Arctic and Alpine Research, 10(2), 169-184.
Kramer, S.L. (1996). Geotechnical Earthquake Engineering. Prentice Hall, Upper Saddle River, NJ, 653 p.
Krestnikov, V. N. (1962). Chronology of the tectonic deformations in Pamir and Central Asia. Academy of Science of USSR (in Russian).
Köhler, A, M. Ohrnberger, F., Scherbaum, M., Wathelet, Cornou, C. (2007). Assessing the reliability of the modified three-component spatial autocorrelation technique. Geophysical Journal International, 168(2), 779-796.
Konaev, V.A. (1964). Jurassic sediments of Fergana. PhD theses, submitted for PhD in geologic-mineralogical sciences, Tashkent (in Russian).
Kuhlemeyer, R. L. and Lysmer, J. (1973). Finite Element Method Accuracy for Wave Propagation Problems. Journal of Soil Mechanics and Foundations, 99(5), 421-427.
Kunze, Ch., Schmidt, P. (2008). Internationale Erfahrungen in Sanierungsprojekten: Lermontov (Russland), Mailuu Suu (Kirgistan), Kitwe (Zambia). «Interventionen und Nachhaltigkeit im Strahlenschutz; Zusammenfassung und Bewertung der Klausurtagung der Strahlenschutzkommission», November, 13-14 2008, Berlin, Germany.
Kyrgyzgiiz (1986). The report of the engineering studies in the surroundings of Mailuu-Suu City. Frunze: Ilim, 90 p. (In Russian).
Lan, H. X., Lee, C. F., Zhou, C. H., Martin, C.D. (2005). Dynamic characteristics analysis of shallow landslides in response to rainfall event using GIS. Environmental Geology, 47, 254-267.
Le Brun, B., Hatzfeld, D., Bard, P.Y., Bouchon, M. (1999). Experimental study of the ground motion on a large scale topographic hill at Kitherion (Greece). Journal of Seismology, 3, 1-15.
Lee, C. T., Hsieh, B. S., Sung, S. H., Lin, P. S. (2012). Regional Arias Intensity Attenuation Relationship for Taiwan Considering VS30. Bulletin of the Seismological Society of America, 102(1), 129-142.
Lee, E. M., Meadowcroft, I. C., Hall, J. W., Walkden, M. (2002). Coastal landslide activity: a probabilistic simulation model. Bulletin of Engineering Geology and the Environment, 61(4), 347-355.
Lee, S., Ryu, J.-H., Lee, M.-J., Won, J.-S. (2003). Use of an articial neural network for analysis of the susceptibility to landslides at Boun, Korea. Environmental Geology, 44, 820-833.
Lin, C.-W., Shieh, C.-L., Yuan, B.-D., Shieh, Y.-C., Liu, S.-H., Lee, S.-Y. (2003). Impact of Chi-Chi earthquake on the occurrence of landslides and debris flows: example from the Chenyulan River watershed, Nantou, Taiwan. Engineering Geology, 71, 49–61.
Lin, J. S., Whitman, R. V. (1983). Earthquake induced displacements of sliding blocks. Journal of Geotechnical Engineering, 112, 44-59.
Liu, J. G., Mason, P. J., Clerici, N., Chen, S., Davis, A., Miao, F., Deng, H., Liang, L. (2004). Landslide hazard assessment in the Three Gorges area of the Yangtze river using ASTER imagery: Zigui–Badong. Geomorphology, 61(1-2), 171-187.
Liu, N., Zhang, J., Lin, W., Cheng, W., Chen, Z. (2009). Draining Tangjiashan Barrier Lake after Wenchuan Earthquake and the flood propagation after the dam break. Science in China Series E: Technological Sciences, 52(4), 801-809.
Liu, L., Zhou, J., Jiang, D., Zhuang, D., Mansaray, L. R., Zhang, B. (2013). Targeting mineral resources with Remote Sensing and field data in the Xiemisitai Area, West Junggar, Xinjiang, China. Remote Sensing 5, 3156-3171.
Lynn. H. (2010). Worldwide Overview of Large Landslides of the 20th and 21st Centuries. USGS report, retrieved 1 December 2010.
Lysmer, J. and Kuhlemeyer R. (1969). Finite Dynamic Model for Infinite Media. J. Eng. Mech., 95(4), 859-877.
Makdisi, F. I. and Seed, H. B. (1978). Simplified procedure for estimating dam and embankment earthquake-induced deformations. ASCE Journal of the Geotechnical Engineering Division, 104, 849-867.

Malamud, B. D., Turcotte, D. L., Guzzetti, F., Reichenbach, P. (2004). Landslide inventories and their statistical properties. Earth Surface Processes and Landforms, 29(6), 687-711.
Martino, S., and G. Scarascia Mugnozza (2005). The role of the seismic trigger in the Calitri landslide (Italy): historical reconstruction and dynamic analysis, Soil Dynamics Earthquake Engineering, 25.
Marble, D. F., Peuquet, D. J., Boyle, A. R., Bryant, N., Calkins, H. W., Johnson, T. (1983). Geographic information systems and remote sensing. In R.N. Colwell (Ed.), Manual of Remote Sensing (pp. 923-957). American Society of Photogrammetry, Falls Church Virginia.
Massonnet, D. and Feigl, K. L. (1998). Radar interferometry and its application to changes in the earth's surface. Rev. Geophys., 36 (4), 441–500.
Maufroy, E., Cruz-Atienza, V. M., Cotton, F., Gaffet, S. (2015). Frequency-Scaled Curvature as a proxy for topographic site-effect amplification and ground-motion variability. Bulletin of the Seismological Society of America, 105(1), 354-367.
McClelland, D. E., Foltz, R. B., Wilson, W. D., Cundy, T. W., Heinemann, R. Saurbier, J. A., Schuster, R. L. (1997). Assessment of the 1995 & 1996 floods and landslides on the Clearwater National Forest, Part I: landslide assessment. Report to the regional Forester Northern Region U.S. Forest Service.
Melchiorre, C., Matteucci, M., Azzoni, A., Zanchi, A. (2008). Articial neural networks and cluster analysis in landslide susceptibility zonation. Geomorphology, 94, 379-400.
Michie, D., Spiegelhalter, D. J., Taylor, C.C. (1994). Machine Learning, Neural and Statistical Classification. Retrieved from http://www.amsta.leeds.ac.uk/~charles/statlog/.
Miles, S. B. and Keefer, D. K. (2000). Evaluation of seismic slope-performance models using a regional case study. Environmental and Engineering Geoscience, 6, 25-39.
Minetti, L., Pelli, F., Stoutjesdijk, J. (2002). Technical review of Mailuu-Suu landslides and tailings problems and options for remediation. Technical Mission Report to the Kyrgyz Republic, February - March 9, 2002.
Ministry of Emergency Situation of Kyrgyz Republic (2013). Annual report for 2012. Retrieved from http://mes.kg/upload/kniga_2014/book_rus000.html.
Molnar, P. and Tapponnier, P. (1975). Cenozoic tectonics of Asia: effects of a continental collision. Science, 189, 419-426.
Montgomery, D. R. and Dietrich, W. E. (1994). A physically based model for the topographic control of shallow landsliding. Water Resources Research, 30(4), 1153-1171.
Montgomery, D. R., Wright, R. H., Booth, T. (1991). Debris flow hazard mitigation for colluvium–filled swales. Bulletin of Association of Engineering Geologists, 28(3), 303-323.
Moore, I. D. and Grayson, R. B. (1991). Terrain-based catchment partitioning and runoff prediction using vector elevation data. Water Resources Research, 27(6), 1171-1191.
Moore, I. D., O'Loughlin, E. M., Burch, G.J. (1988). A computer based topographic model and its hydrologic and ecological applications. Earth Surface Processes and Landforms, 13, 305-320.
Moreiras, S. M. (2004). Landslide incidence zonation in the Rio Mendoza valley, Mendoza Province, Argentina. Earth Surface Processes and Landforms, 29, 255-266.
Moreiras, S. M. (2005). Landslide susceptibility zonation in the Rio Mendoza valley, Argentina. Geomorphology, 66(1-4), 345-357.
Mouchel (2011). Landslide susceptibility mapping: literature review and findings. Technical report for the Geological Survey of Ireland, 29 p.
Munich Re (2001). Topics 2000: Natural Catastrophes — The Current Position. Special Millennium Issue, Munich, Munich Re Group.
Murillo, M. and Manuel, J. (1995). The 1985 Mexico Earthquake. Geofisica Colombiana, 3, 5-19.
Nag, P. and Kudrat, M. (1998). Digital Remote Sensing. New Delhi: Concept Publishing Company, 320 p.
Nagarajan, R., Roy, A., Vinod Kumar, R., Mukhetjess, A., Khire, M. V. (2000). Landslide hazard susceptibility mapping based on terrain and climatic factors for tropical monsoon regions. Bulletin of Engineering Geology and the Environment, 58(4), 275-287.
Nakamura, Y. (1989). A method for dynamic characteristics estimation of subsurface using microtremor on the ground surface. QR of RTRI, 30(1), 25-33.
Nathenson, M. (2001). Probabilities of volcanic eruptions and application to the recent history of Medicine Lake Volcano. In A. V. Vecchia (Ed.), U.S. Geological Survey Open-file Report 2001-324 (pp. 71-74).
Neeley, M. K. and Rice, R. M. (1990). Estimating risk of debris slides after timber harvest in northwestern California. Bulletin American Association of Engineering Geologists, 27(3), 281-289.

Nemčok, A., Pašek, J., Rybář, J. (1972). Classification of landslides and other mass movements. Rock Mechanics, 4, 71-78.
Newmark, N. (1965). Effects of earthquakes on dams and embankments. Geotechnique, 15, 139–159.
Nikitin, R. M. and Fidelli, I. A. (1974). Regional hydrological studies for the slope stability analyses on the case of Zeravshan River. Relation between surface and underground water, 2, 40-49 (in Russian).
Nikolaev, V. D. and Lykov Z. I. (1992). Report o Engineering Explorations for Designing of Technical and Economic calculations "Relocation of Tuyuk-Suu Tailings to "K" and 'Dalnee" Tailings Sites". CAF VNIPIPT (Central Asian Filial of VNIPIPT, Tashkent), 48 p (in Russian).
Nilsen, T. H. and Brabb, E. E. (1977). Slope stability studies in the San Francisco Bay region, California. Geological Society of America, Reviews in Engineering Geology, 3, 235-243.
Nogoshi, M. and Igarashi, T. (1971). On the amplitude characteristics of microtremor (Part 2). Journal of Seismological Society of Japan, 24, 26-40 (in Japanese with English abstract).
Nossin, J. J. (1989). Aerospace survey of natural hazards. ITC Journal, 3-4, 183-188.
O'Loughlin, E. M. (1986). Prediction of surface saturation zones in natural catchments by topographic analysis. Water Resources Research, 22(5), 794-804.
Önöz, B. and Bayazit, M. (2001). Effect of the occurrence process of the peaks over threshold on the flood estimates. Journal of Hydrology, 244, 86-96.
Pachauri, A. K. and Pant, M. (1992). Landslide hazard mapping based on geological attributes. Engineering Geology, 32, 81-100.
Parise, M. and Jibson, R. W. (2000). A seismic landslide susceptibility rating of geologic units based on analysis of characteristics of landslides triggered by the 17 January, 1994 Northridge, California earthquake. Engineering Geology, 58, 251-270.
Parker, H. D. (1988). The unique qualities of a geographic information system: a commentary. Photogrammetric Engineering and Remote Sensing, 55, 1589-1591.
Parseval des Chênes, M.-A. (1806). Mémoire sur les séries et sur l'intégration complète d'une équation aux différences partielles linéaire du second ordre, à coefficients constants. Mémoires présentés à l'Institut des Sciences, Lettres et Arts, par divers savans, et lus dans ses assemblées. Sciences, mathématiques et physiques. (Savans étrangers), 1, 638–648.
Pedersen, H., Le Brun, B., Hatzfeld, D., Campillo, M., Bard, P.-Y. (1994). Ground motion amplitude across ridges. Bulletin of the Seismological Society of America, 84, 1786-1800.
Peive, A. V. (1938). Tectonic scheme of the western Tien-Shan. Academy of Science of USSR, "Central Asia geology", 5 (in Russian).
Peng, W. F., Wang, C. L., Chen, S. T., Lee, S. T. (2009). A seismic landslide hazard analyses with topographic effect stidy in the 99 Peak region, Central Taiwan. Environmental Geology, 57, 537–549.
Peplies, R. W. and Keuper, H. F. (1975). Regional analysis. In R.G. Reeves, A. Anson, D. Landen (Eds.), Manual of Remote Sensing (pp.1947-1998). American Society of Photogrammetry, Falls Church Virginia.
Petley, D. N., Dunning, S. A., Rosser, N. J. (2005). The analysis of global landslide risk through the creation of a database of worldwide landslide fatalities. In O. Hungr, R. Fell, R. Couture and E. Ebergardt (Eds.), Landslide Risk Management (pp. 367–374). Amsterdam: A.T. Balkema.
Petley, D., Dunning, S., Rosser, N., Kausar, A. B. (2006). Incipient Landslides in the Jhelum Valley, Pakistan Following the 8th October 2005 Earthquake. In H. Mariu (Ed.), Disaster mitigation of debris flows, slope failures and landslides (pp. 47-56). Frontiers of Science Series 47, Tokyo: Universal Academy Press.
Pickering, K. T., Koren, T. N., Lytochkin, V. N., Silvester, D. J. (2008). Silurian-Devonian active deep-marine systems and palaeogeography, Alai Range, Southern Tien Shan, Central Asia. Journal of the Geological Society, 165, 189-210.
Pistocchi, A., Luzi, L., Napolitano, P. (2002). The use of predictive modeling techniques for optimal exploitation of spatial databases: a case study in landslide hazard mapping with expert system-like methods. Environmental Geology, 41(7), 765-775.
Pomeroy, J. S. (1978). Map showing landslides and area susceptible to sliding in Beaver County, Pennsylvania. U.S. Geological Survey Miscellaneous Field Investigation Map, MF-1160, scale 1:50,000.
Popov, V. I. (1938). Chronology of the depressions and uplifts in the western Tien-Shan. Scientific Committee of Uzbekistan, Tashken (in Russian).

Pradel, D., Smith, P. M., Stewart, J. P., Raad, G. (2005). Case history of landslide movement during the Northridge earthquake. Journal of Geotechnical and Geoenvironmental Engineering, 131, 1360-1369.
Prager, C., Zangerl, C., Nagler, T. (2009). Geological controls on slope deformations in the Koefels Rockslide area (Tyrol, Austria). Austrian Journal of Earth Sciences, 102(2), 4–19.
Preobrajensky, J. (1920). The Usoi Landslide. Geol. Comm. Papers on Applied Geol., 14 (In Russian).
Prevost, J. H. (1981). DYNAFLOW: A nonlinear transient finite element analysis program. Department of Civil Engineering, Princeton University, Princeton, NJ.
Prost, G. L. (2001). Remote sensing for geologists: a guide to image interpretation. New York: Taylor and Francis (2nd Edition), 374 p.
Qi, S., Xu, Q., Lan, H., Zhang, B., Liu, J. (2010). Spatial distribution analysis of landslides triggered by 2008.5.12 Wenchuan Earthquake, China. Engineering Geology, 116, 95-108.
Rachowiecki, R. and Beech, C. (2004). Peru. Oakland, CA: Lonely Planet, 308 p.
Raetzo, H., Lateltin, O., Bollinger, D., Tripet, J. P. (2002). Hazard assessment in Switzerland- Codes of Practice for mass movements. Bulletin of Engineering Geology and the Environment, 61(3), 263-268.
Rathje, E. M., Abrahamson, N. A., Bray, J. D. (1998). Simplified frequency content estimates of earthquake ground motions. Journal of Geotechnical Engineering, 124, 150-159.
Rathje, E. M. and Antanakos, G. (2011). A unified model for predicting earthquake-induced sliding displacements of rigid and flexible slopes. Engineering Geology, 122, 51-60.
Rathje, E. M., Faraj, F., Russell, S., Bray, J. D. (2004). Empirical relationships for frequency content parameters of earthquake ground motions. Earthquake Spectra, 20, 119-144.
Rathje, E. M. and Bray, J. D. (1999). An examination of simplified earthquake-induced displacement procedures for earth structures. Canadian Geotechnical Journal, 36, 72-87.
Rathje, E. M. and Bray, J. D. (2000). Nonlinear coupled seismic sliding analysis of earth structures. Journal of Geotechnical and Geoenvironmental Engineering, 126, 1002-1014.
Rathje, E. M. and Saygili, G. (2009). Probabilistic Assessment of Earthquake-Induced Sliding Displacements of Natural Slopes. Bulletin of the New Zealand Society of Earthquake Engineering, 42, 18-27.
Ray, R.G. (1960). Aerial Photographs in Geologic Interpretation and Mapping. U.S. Geological Survey, Professional Paper, 373 p.
Reichenbach, P., Galli, M., Cardinali, M., Guzzetti, F., Ardizzone, F. (2005). Geomorphologic mapping to assess landslide risk: concepts, methods and applications in the Umbria Region of central Italy. In T. Glade, M. G. Anderson and M. J. Crozier (Eds.), Landslide risk assessment (pp. 429-468). John Wiley.
Rial, J. A. (1996). The anomalous seismic response of the ground at the Tarzana Hill site during the Northridge 1994 southern California earthquake: a resonant, sliding block? Bulletin of the Seismological Society of America, 86, 1714-1723.
Ricker, N. (1953). The form and laws of propogation of seismic wavelets. Geophysics, 18, 10-40.
Riepl, J. (1997). Effets de site : évaluation expérimentale et modélisations multi-dimensionnelles : application au site EURO-SEISTEST (Grèce). PhD thesis, Université Joseph Fourier, Grenoble.
Risley, J. C., Walder, J. S., Denlinger, R. P. (2006). Usoi dam wave overtopping and flood routing in the Bartang and Panj rivers, Tajikistan. Natural Hazards, 38, 375–390.
Roberds, W. (2005). Estimating temporal and spatial variability and vulnerability. In O. Hungr, R. Fell, R. Couture and E. Eberhardt (Eds.), Landslide Risk Management (pp. 129-157). A.A. Balkema Publishers.
Roessner, S., Wetzel, H.-U., Kaufmann, H., Sarnagoev, A. (2002). Satellite remote sensing for regional assessment of landslide in Kyrgyzstan (Central Asia). In Forum Katastrophenvorsorge, Deutsches Komitee fur Katastrophenvorsorge e.V. (DKKV), pp. 433–441.
Rogers, A. M., Katz, L. J., Bennett, T. J. (1974). Topographical effect on ground motion for incident P waves: a model study. Bulletin of the Seismological Society of America, 64, 437-456.
Rowan, L. and Mars, J. C. (2001). Advances in lithologic mapping by using optical remote sensing measurements. Geological Society of America, 2001 annual meeting, Abstracts with Programs, 33(6).
Rygkov, O. A. (1963). Tectonics and some issues on oil content in Mezozoic-Paleosoic sediment of Uzbekistan. Academy of Science of Uzbekistan, Tashkent (in Russian).
Sabins, F. F. (1996). Remote Sensing: Principles and Interpretations. Worth Publishers Incorporated, 432 p.
Sanchez-Sesma, F. J. and Campillo, M. (1993). Topographic effects for incident P, SV and Rayleigh waves. Tectonophysics, 218, 113–125.

Sanchez-Sesma, F. J., Herrera, I., Aviles, J. (1982). A boundary method for elastic wave diffraction: application to scattering SH waves by surface irregularities. Bulletin of the Seismological Society of America, 72, 473-490.
Sarkar, S., Kanungo, D. P., Mehrotra, G. S. (1995). Landslide hazard zoning: a case study in Garhwal Himalaya, India. Mountain Research and Development, 15(4), 301-309.
Saygili, G. and Rathje, E. M. (2008). Empirical Predictive Models for Earthquake-Induced Sliding Displacements of Slopes. Journal of Geotechnical and Geoenvironmental Engineering, 134(6), 790-803.
Seed, H. B. and Martin, G. R. (1966). The seismic coefficient in earth dam design. ASCE Journal of the Soil Mechanics and Foundations Division, 92, 25-58.
Seeley, M. W. and West, D. O. (1990). Approach to geologic hazard zoning for regional planning, Inyo National Forest, California and Nevada. Bulletin of American Association of Engineering Geologists, 27(1), 23-35.
Semblat, J.-F., Duval, A.-M., Dangla, P. (2002). Seismic site effects in a deep alluvial basin: numerical analysis by the boundary element method. Computers and geotechnics, 29, 573–585.
Sepulveda, S. A., Murphy, W., Jibson, R.W., Petley D.N. (2005). Seismically induced rock slope failures resulting from topographic amplification of strong ground motions: The case of Pacoima Canyon, California. Engineering Geology, 80, 336– 348.
Seriani, G., Vuan, A., Priolo, E., Carcione, J. (2002). Development and validation of a 3D staggered Fourier pseudo-spectral method for wave modeling. In Proc. EGS XXVII General Assembly, Nice, France, EGS02-A-02795.
Schulz, S.S. (1947). Gravitational mass movements in Tien-Shan. The news of Kyrgyz Academy of Science, 8 (in Russian).
Schlögel, R. (2009). Detection of recent landslides in Maily-Say Valley, Kyrgyz Tien Shan, based on field observations and remote sensing data. PhD thesis, Université de Liège, Liège, 165 p.
Schlögel, R., Torgoev, I., De Marneffe, C., Havenith, H.B. (2011). Evidence of a changing distribution of landslides in the Kyrgyz Tien Shan, Central Asia. Earth Surface Processes and Landforms, 36(12), 1658–1669.
Schowengerdt, R. A. (2006). Models and methods for image processing. Orlando: Academic Press Inc., FL.
Schuster, R. L. and Alford, D. (2004). Usoi landslide dam and Lake Sarez, Pamir Mountains, Tajikistan. Environmental and Engineering Geosciences, 10, 151–168.
Schwardt, L. and du Preez, J. (2005). Manipulating feature space. Lecture Notes (PR414/PR813), University of Stellenbosch, South African Republic.
Seed, H. B. (1968). Landslides during earthquakes due to soil liquefaction. American Society of Civil Engineers, Journal of the Soil Mechanics and Foundation Division, 94, 1053-1122.
Seriani, G., Vuan, A., Priolo, E., Carcione, J. (2002). Development and validation of a 3D staggered Fourier pseudo-spectral method for wave modeling. In Proc. EGS XXVII General Assembly, Nice, France, EGS02-A-02795.
Sinicyn, N. M. (1948). The age of ancient erosion surfaces in the Western Tien-Shan and Alai. Soviet Geographic Community, 30(1) (in Russian).
Smith, K. (2001). Environmental hazards: Assessing risk and reducing disaster. London: Routledge.
Smith, W. D. (1975). The application of finite element analysis to elastic body wave propagation problems, Geophys. Z R. Astr. Soc., 42, 747-768.
SPSS (2004). SPSS 13.0 Command Sintax Reference. Chicago, 1994 p.
Spudich, P., Hellweg, M., Lee, W. H. K. (1996). Directional topographic site response at Tarzana observed in aftershocks of the Northridge, California, earthquake: implications for mainshock motions. Bulletin of the Seismological Society of America, 86, 193-208.
Star, J. and Estes, J. E. (1990). Geographic Information Systems: an introduction. New Jersey, Prentice Hall, Englewood Cliffs.
Steidl, J. H., Tumarin, A.G., Archuleta, R.J. (1996). What is a reference site? Bulletin of the Seismological Society of America, 86, 1733-1748.
Steiniger, S. and Hunter, A. J. S. (2013). The 2012 free and open source GIS software map – a guide to facilitate research, development and adoption. Computers, Environment and Urban Systems, 39, 136-150.
Steiniger, S. and Weibel, R (2009). GIS software – a description in 1000 words. Encyclopedia of Geography, 1-2.

Tapiador, F. J. (2009). Assessment of renewable energy potential through satellite data and numeric models. Energy and Environmental Sciences, 2, 1142-1161.

Terzhagi, K. (1950). Mechanism of landslides. In S. Paige (Ed.), Application of Geology to Engineering Practice (pp. 83-123). Geological Society of America, New York, NY.

Torgoev, A.D. (2010). GIS-based modeling of upstream flooding areas for the case of landslide damming of river. Proceedings of the Fourth Central Asia GIS Conference –GISCA'10 "Water: Life, Risk, Energy and Landuse", 27-28 May, 2010 Bishkek, Kyrgyzstan, pp. 60-65.

Torgoev, I .A. and Alioshin, Y. G. (2009). Geoecology and impact, created by the mining activity in Kyrgyzstan. Bishkek: Ilim, 239 p., in Russian.

Torgoev, I. A., Aleshin, Y. G., Daneels, G., Torgoev, A., Ashirov, G. (2005). The risk assessment and monitoring of landslides in the Tien-Shan Mountains of Kyrgyzstan. Proceedings of International Symposium on "Landslide Hazards in Orogenic Zone from the Himalaya to Island Arcs in Asia", September, 2005, Nepal, Katmandu.

Torgoev, I. A., Alioshin, Y. G., Havenith, H.-B. (2002). Impact of uranium mining and processing on the environment of mountainous areas of Kyrgyzstan. In P.-F. Merkel and Wolkersdorfer (Eds.), Uranium in the aquatic environment (pp. 93-98). Berlin Heidelberg: Springer.

Torgoev, I. A., Havenith, H.-B., Strom, A. (2013a). Impact of 3000-t blast on unstable slopes near the Kambarata-2 HPP site, Kyrgyzstan. Landslide Science and Practice, Section "Risk Assessment, Management and Mitigation", 6, 37-42.

Torgoev, A. D., Lamair, L., Torgoev, I. A., Havenith, H.-B. (2013b). A review of recent case studies of landslides investigated in the Tien-Shan using microseismic and other geophysical methods. Proceedings of the International Symposium on Earthquake-Induced Landslides, Kiryu, Japan, 2012.

Torgoev, I. A., Niyazov, R., Havenith, H.-B. (2013c). Tien-Shan landslides, triggered by earthqukes in Pamir-Hindukush zone. Proceedings of the Second World Landslide Forum – 3-7 October 2011, Rome, Italy.

Travasarou, T., Bray, J. D., Abrahamson, N. A. (2003). Empirical attenuation relationship for Arias intensity. Earthquake Engineering & Structural Dynamics, 32, 1133–1155.

United Nations Development Program (2013). Human development report 2013: The rise of the South (human progress in the diverse world).

Uromeihy, A. and Mahdavifar, M. R. (2000). Landslide hazard zonation of the Khorshrostam area, Iran. Bulletin of Engineering Geology and the Environment, 58(3), 207-213.

U.S. Dept. of the Interior (1970). The Peru Earthquake: a Special Study. Bulletin of the Atomic Scientists, 26(8), 17–19.

Vandenhove, H., Quarch, H., Clerc, J., Lejeune, J., Sweeck, L., Sillen, X., Mallants, D., Zeevaert, T. (2003). Remediation of uranium mining and milling tailing in Mailuu-Suu district of Kyrgyzstan. Report on Tacis Project N◦ SCRE1/N◦38.

Vandine, D. F., Moore, G., Wise, M., Vanbuskirk, C., Gerath, R. (2004). Chapter 3 - Technical Terms and Methods. In Wise et al. (Eds.), Landslide Risk Case Studies in Forest Development Planning and Operations (pp. 13-26). Ministry of Forests, Forest Science Program, Abstract of Land Management Handbook 56.

van Asch, Th. W. J., Buma, J., van Beek, L.P.H. (1999). A view on some hydrological triggering systems in landslides. Geomorphology, 30(1-2), 25-32.

van Dijke, J. J. and van Westen, C. J. (1990). Rockfall hazard: a geomorphologic application of neighborhood analysis with ILWIS. ITC Journal, 1, 40-44.

van Westen, , C. J., van Duren, I., Kruse, H. M. G., Terlien, M.T.J. (1993). GISSIZ: training package for geographic information systems in slope instability zonation. ITC Publication number 15(2).

Varnes, D. J. (1978). Slope movements: types and processes. In R. L. Schuster and R.J. Krizek (Eds.), Landslide analysis and control (pp. 11-33). Washington, National Academy of Sciences, Transportation Research Board Special Report 176.

Varnes, D. J. and IAEG Commission on Landslides and other Mass-Movements (1984). Landslide hazard zonation: a review of principles and practice. The UNESCO Press, Paris, 63 p.

Verstappen, H. T. (1983). Applied geomorphology: Geomorphological survey for environmental development. Amsterdam: Elsevier Scientific Publishing Co.

Wald, D. J., Helmberger, D. V., Hartzell, S. H. (1990). Rupture process of the 1987 Superstition Hills earthquake from the inversion of strong–motion data. Bulletin of the Seismological Society of America, 80, 1079-1098.

Wang, D., Pu, R., Gong, P., Yang, R. (1995). Predicting forest yield with an artificial neural network and multiple regression. Hong Kong, Chinese University of Hong Kong.
Ward, T. J., Li, R. M., Simons, D. B. (1981). Use of a mathematical model for estimating potential landslide sites in steep forested drainage basins. IAHS Publication, 132, 21-41.
Wartman, J., Bray, J. D., Seed, R. B. (2003). Inclined plane studies of the Newmark sliding block procedure. Journal of Geotechnical and Geoenvironmental Engineering, 129, 673-684.
Wathelet, M., Jongmans, D., Ohrnberger, M., Bonnefoy-Claudet, S. (2008). Array performances for ambient vibrations on a shallow structure and consequences over Vs inversion. Journal of Seismology, 12, 1-19.
WebFinance Inc. (2015). BussinessDictionary. Retrieved from www.businessdictionary.com.
Wieczorek, G. F., Wilson, R. C., Harp, E. L. (1985). Map showing slope stability during earthquakes in San Mateo County California. USGS Miscellaneous Investigations Map I-1257-E, scale 1:62,500.
Williams, J. (2001). GIS Processing of Geocoded Satellite Data. UK, Chichester: Springer-Praxis Publishing, 368 p.
Wilson, R. C. and Keefer, D.K. (1983). Dynamic analysis of a slope failure from the 6 August 1979 Coyote Lake, California, earthquake. Bulletin of the Seismological Society of America, 73, 863–877.
Wilson, R. C. and Keefer, D. K. (1985). Predicting areal limits of earthquake-induced landsliding. In J.I. Ziony (Ed.), Evaluating Earthquake Hazards in the Los Ángeles Region: An Earth-Science Perspective (pp. 317-345). U.S. Geological Survey Professional Paper 1360.
WP/WLI - International Geotechnical societies' UNESCO Working Party on World Landslide Inventory (2001). A suggested method for reporting landslide remedial measures. Bulletin Engineering Geology and the Environment, 60, 69-74.
Wright, R. H. and Nilsen, T. H. (1974). Isopleth map of landslide deposits, southern San Francisco Bay Region, California. U.S. Geological Survey Miscellaneous Field Studies Map MF-550, scale 1:250,000.
Xu, Ch., Xu, X., Dai, F. (2014). Three (nearly) complete inventories of landslides triggered by the May 12, 2008 Wenchuan Mw 7.9 earthquake of China and their spatial distribution statistical analysis. Landslides, 11(3), 441-461.
Yesilnacar, E. and Topal, T. (2005). Landslide susceptibility mapping: A comparison of logistic regression and neural networks methods in a medium scale study, Hendek region (Turkey). Engineering Geology, 79, 251-266.
Yin, Y., Wang, F., Sun, P. (2009). Landslide hazards triggered by the 2008 Wenchuan earthquake, Sichuan, China. Landslides, 6(2), 139-152.
Zadeh, L. A. (1975). The concept of a linguistic varabile and its application to approximate reasoning. Information Science, 8, 199-249.
Zeverbergen, L. W. and Thorne, C. R. (1987). Quantitative analysis of land surface topography. Earth Surface Processes and Landforms, 12, 47-56.
Zhang, D. and Wang, G. (2007). Study of the 1920 Haiyuan earhquake-induced landslides in loess (China). Engineering Geology, 94, 76-88.
Zimmerman, M., Bichsel, M., Kienholz, H. (1986). Mountain hazards mapping in the Khumbu Himal, epal, with prototype map, scale 1:50,000.